INFORMATION TO USERS

This manuscript has been reproduced from the microfilm master. UMI films the text directly from the original or copy submitted. Thus, some thesis and dissertation copies are in typewriter face, while others may be from any type of computer printer.

The quality of this reproduction is dependent upon the quality of the copy submitted. Broken or indistinct print, colored or poor quality illustrations and photographs, print bleedthrough, substandard margins, and improper alignment can adversely affect reproduction.

In the unlikely event that the author did not send UMI a complete manuscript and there are missing pages, these will be noted. Also, if unauthorized copyright material had to be removed, a note will indicate the deletion.

Oversize materials (e.g., maps, drawings, charts) are reproduced by sectioning the original, beginning at the upper left-hand corner and continuing from left to right in equal sections with small overlaps. Each original is also photographed in one exposure and is included in reduced form at the back of the book.

Photographs included in the original manuscript have been reproduced xerographically in this copy. Higher quality 6" x 9" black and white photographic prints are available for any photographs or illustrations appearing in this copy for an additional charge. Contact UMI directly to order.

UMI

A Bell & Howell Information Company
300 North Zeeb Road, Ann Arbor, MI 48106-1346 USA
313/761-4700 800/521-0600

Computer Simulations Studies:

I-Dynamics of Brittle Crack Propagation.

II-Brittle To Ductile Transition Temperature.

Volume I

by

Behzad Massoumzadeh

A dissertation submitted to the Graduate Faculty in Physics in partial fulfillment of the requirements for the degree of Doctor of Philosophy, The City University of New York.

1995

UMI Number: 9530902

Copyright 1995 by
Massoumzadeh, Behzad
All rights reserved.

UMI Microform 9530902
Copyright 1995, by UMI Company. All rights reserved.

This microform edition is protected against unauthorized
copying under Title 17, United States Code.

UMI

300 North Zeeb Road
Ann Arbor, MI 48103

©1995

Behzad Massoumzadeh

All Rights Reserved

This manuscript has been read and accepted for the Graduate Faculty in Physics in satisfaction of the dissertation requirement for the degree of Doctor of Philosophy.

3/31/95
Date

C. R. Fischer
Chair of Examining Committee

3/31/95
Date

Joseph B. Krieger
Executive Officer

Karl Strauch

Kay Tergaonkar

L. A. Lanari

B. Tondiglia VIC2

Supervisory Committee

The City University of New York

ABSTRACT

Computer Simulations Studies:

I-Dynamics of Brittle Crack Propagation.

II-Brittle To Ductile Transition Temperature.

by

Behzad Massoumzadeh

Advisor: Professor Rutherford Fischer.

Molecular Dynamics Simulations Technique is used to investigate the effect of geometry of the crack-tip on the local stress distribution, the influence of the interatomic potential law on the crack-tip velocity of the brittlely propagating cleavage cracks, dynamics and energetics of brittle fracture, and brittle-to-ductile transition temperature on a variety of two-dimensional (triangular) crystals. The main goal of these investigations is to model the general fracture phenomena, rather than to make predictions for a particular crystal. The simulations results indicate that the discreteness of the lattice limits the degree of the geometric blunting. The interatomic potential is found to be the most important factor in determining the upper limit for the magnitude of the terminal crack-tip velocity. The transition from the brittle behavior to ductile failure, as the temperature of the system is increased, is recognized by the observation of the first thermally activated spontaneous emission of blunting dislocation from the crack-tip prior to any breakage of the crack-tip interatomic bond. The simulations results indicate that BDT in investigated solids are gradual.

To My Wife Nafisseh Berendji

and

My Sons Armin and Ramtin.

Preface

Molecular Dynamics Simulations Technique is used to investigate the effect of geometry of the crack-tip on the local stress distribution, the influence of the interatomic potential law on the crack-tip velocity of the brittlely propagating cleavage cracks, the dynamics and energetics of brittle fracture, and the brittle-to-ductile transition temperature on a variety of two-dimensional (triangular) crystals.

Since, at present there is no sophisticated detailed interatomic potential to simulate the detailed thermo-mechanical properties of a given solid, and due to economic restrictions which have forced us to perform the simulations on two dimensional solids, the main goal of these investigations is set to model the general fracture phenomena, rather than to make predictions for a particular crystal. In this regard the details of the interatomic potentials used in these simulations is not significant. The first part of the simulation is performed at absolute zero temperature.

In a series of simulations, sensitivity of crack-tip stress distributions to the variations on the crack-length, and the crack-tip geometry, on the atomic scale, was investigated. The two-dimensional triangular Johnson or Lennard-Jones solids subjected to a remotely applied tensile constant load or constant displacement were used in these studies. Surprisingly, no significant difference in the local stress distributions was observed between very sharp (narrow) and

blunt (wide) cracks. However, wide cracks with irregularly shaped crack-tips (termed "the wide-jagged crack") displayed appreciably lower local stresses at the vicinity of the crack-tip. At the crack-tip (CT), magnitude of the maximum stress concentration was about a factor of ten lower than that predicted by the classical elasto-static continuum treatments of elliptically shaped cracks. However, at a distance r from the crack-tip of a crack of half-crack length c, in the $0.1 < r/c < 1.5$ range, the simulations results are in close agreement with the stress distributions predicted by the elasto-static continuum theories for the elliptic cracks. The lack of any variations in going from the "narrow" to the "wide" cracks suggests that there is an effective radius of the crack-tip which controls the magnitude of the crack-tip stresses. The simulations results indicate that the discreteness of the lattice limits the degree of the geometric blunting, at least within the size scale readily accessible with the present simulations. The conventional continuum analysis is found to account for the functional dependence of the local stresses on the crack-length, but not for the magnitude of the local stresses. On the other hand, the nonlocal theory of Eringen is found to account for the order of magnitude of the local stresses but not its functional dependence.

Dynamic properties of brittlely propagating cleavage cracks are investigated in another series of molecular dynamic simulations. The interatomic potential is found to be the most important factor in determining the upper limit for the magnitude of the terminal crack-tip velocity, as well as the degree of brittleness, plastic deformations at the vicinity of the propagating

crack-tips, and in leading to the spontaneous emission of dislocations from the atomically sharp crack-tips. Under carefully controlled conditions, Johnson empirical potential results in a considerably more brittle behaviour than the 6-12 Lennard-Jones potential, and results in a higher limiting crack-tip velocity. In addition to Johnson and Lennard-Jones potentials, in order to investigate the effect of interatomic potentials on the degrees of brittleness of fast-running crack-tips, and on the normalised terminal crack-tip velocity, a 3-body covalent potential was constructed, and used in a series of simulations. These covalent potentials are constructed by including an angular resistance term to the Lennard-Jones or Johnson potentials. The lattice rigidity is varied over a very wide range by changing the amplitude of the angular resistance, a^*. The normalised terminal crack-tip velocity, V_T/ C_1, is increased, by a factor of two to four with increasing a^*, saturating at about $V_T/ C_1=0.42$.

Simulations results for the energetics of Johnson solid for the quasi-static extension of internal cracks are in very good agreement with the continuum predictions. During the quasi-static crack-extension under a remotely applied constant tensile load, the ratio of the work done by the external load to the increase in the stored elastic strain energy of the system is about 1.94 which is in reasonably good agreement with the elasto-static continuum value of 2.00 for a linear elastic solid.

Energetics of brittlely propagating cleavage cracks are presented in detail for various sample sizes, loading conditions, and crack-lengths.

These results are compared to each other, to those obtained from the quasi-static simulations, and to the continuum predictions. These comparisons clarified some previously misinterpreted computer simulations results [1,2].

Fairly good agreement is obtained between the simulations results for the critical applied fracture stress, σ_c, needed to initiate the brittle propagation of cleavage crack for varieties of the internal cracks, sample-sizes, loading scheme, and the predictions of the Griffith criterion, σ_G.

For the pre-cleaved and critically loaded 2D-Johnson solid, the normalised crack-tip velocity versus normalised crack-length curves are presented for a variety of sample size and loading conditions. The measured terminal velocity is about 0.25 of the longitudinal sound velocity in the medium, independent of the sample-size and loading conditions. The rapid acceleration of the brittlely propagating crack to the terminal velocity as well as the magnitude of the terminal crack-tip velocity, V_T, is in accord with the laboratory observations, but deviates significantly from the predictions of the continuum based theories. Mott [3] and Freund [4-6] formulations are, therefore, reviewed in sufficient detail. The "crack-tip configurational" model is developed which shows some promise for overcoming the objections to the previous theoretical formulations. Inertial effects are likely more important than either Eshelby [7] or Freund [4-6] conclude.

At high constant applied load, and hence, high deformations, in the 2D-

Johnson solid, by the time the crack-length is tripled, the rapidly moving crack-tip emits a pair of blunting dislocations which results in the immediate blunting of the crack-tip. The crack-tip stress concentration factor is reduced considerably immediately after the emission of the blunting dislocations which shield the crack-tip from the influence of the remotely applied stresses. The crack-tip is arrested for a significant amount of time up to a point where these emitted dislocations is moved sufficiently far away from the crack-tip, and the crack-tip stress is raised back to its maximum value of the cohesive stress of the solid. The emission of the blunting dislocations from the tip of the fast-running crack tip is, probably, thermally activated due to the local adiabatic heating of the immediate vicinity of the rapidly moving crack-tip.

The nature of stress distributions at the immediate vicinity of the brittlely propagating crack-tip is at variance with the linear elastic continuum predictions. Dynamic local crack-tip stress distribution is very similar to the static stress distribution, and is independent of the crack-length, sample-size, loading scheme, and the magnitude of the crack-tip velocity.

The final set of the molecular dynamic simulations is designed to explore the brittle-to-ductile transition temperature of a pre-cracked critically loaded two-dimensional (triangular) covalent Lennard-Jones solid with the angular resistance amplitude of $a^*=0.2$, (LJCOVa.2). The fundamental question to be answered is to find which factors influence, and determine the form and magnitude of the brittle-to-ductile transition (BDT) temperature, T_C. Constant

enthalpy ensemble is used in these studies. The transition from the brittle behavior to ductile failure, as the temperature of the system is increased, is recognised by the observation of the first thermally activated spontaneous emission of blunting dislocation from the crack-tip prior to any breakage of the crack-tip interatomic bond. While truly brittle cleavage fracture, as well as truly ductile fracture is observed in going from very low temperatures to a relatively high temperature, the transition from the brittle to ductile fracture seems to cover a relatively long range. Pin-pointing a temperature as the brittle-to-ductile transition temperature seems highly dependent on the adopted definition of the brittle-to-ductile transition temperature. The simulations results are presented in detail, and analysed in terms of the available theories. It is concluded that the brittle-to-ductile transition temperature in the pre-cleaved critically loaded 2D-LJCOVa.2 is gradual, and the experimentally observed sharp BDT in Si is not due to the emission of the thermally activated dislocations from the crack-tip, but rather, probably, as predicted by Hirsch et al. [8-11] is due to the activations of the preexisting dislocations or dislocation sources in the pre-cleaved solid.

I am grateful for the cooperation and support of many professors, scientists, colleagues and research facilities during the preparation of this manuscript. Special mention is due to Professor Arthur Paskin, who provided the original motivation for the venture, maintained close interest throughout the research, gave much useful advice, and supported me financially through his grants. Unfortunately, towards the final stages of the completion of the work Professor A. Paskin passed away suddenly. I was fortunate that Professor

Rutherford Fischer of Queens College volunteered his services and accepted to be my mentor. I gratefully acknowledge the invaluable efforts of Professor Fischer's in the final editing of this manuscript and helping me to complete my graduate studies at CUNY. Among others who have left their imprint on the following pages through their valuable advise, constructive criticism and unconditional support, are Professor G. J. Dienes, and Dr. Karl Sieradzki. I am thankful to Dr. K. Shukla who cooperated with me in preparation of a major part of this manuscript. I am grateful to Professor Tom Kiewicz of Brooklyn College, Professor Lawrence Ferrari and Professor Alexander Lisyansky of Queens College who accepted to be members of my supervisory committee. I am also grateful to the faculty at the Physics Department of Queens College who maintained a close interest in the present research and provided valuable support and advise. Among them special mention is due to Professor Rafanelli, Professor Narciso Garcia, Professor J. Neuberger, and Professor I. Lazar. Acknowledgement is made of Brookhaven National Laboratory who enabled me to work at its facilities. I am also grateful to my parents for their constant support and understanding throughout my education. Finally, I express my deepest appreciation to my wife Nafisseh Berendji for her commendable patience and unconditional love and support.

This research was performed under the auspices of the U.S. Department of Energy, Division of Material Science, Office of Basic Energy Sciences under Contract No. DE-AC02-76CH00016 and at Queens College by N.S.F under Grant No. DMR/8301775.

Table of Contents

Volume I

Title page.	i
Approval page.	iii
Abstract.	iv
Preface and Acknowledgements.	vi
Table of Contents.	xiii
List of Symbols.	xvii
List of Tables.	xix
List of Illustrations.	xxix
Introduction.	1
II. Atomistic Approaches to the Crack Problem.	65
II.1A. Molecular Dynamics: Outline of the Techniques at 0 Kelvin.	70
II.1B. The Interatomic Potentials.	71
II.1C. Simplifications.	74
II.1D. Verlet Method for Solving Newton's Equation of Motion.	75
II.1E. Constant Externally Applied Tensile Load Simulations; Outline of the method.	81
II.1F. Fixed External Displacement (Fixed-Grips) Simulations; Outline of the Method	88
II.1G. Elasto-Static Considerations: Outline of the Method.	90
II.1H. Limitations, Advantages, and the Credibility of the Present Molecular Dynamic Simulations	92

II.2. Elasto-Static Molecular Dynamic Simulations. 95

II.2A. Outline of the Method. 96

II.2B. Major Computer Simulations Results 96

i. Mechanical Properties of the Two-Dimensional Triangular Johnson, and Lennard-Jones Crack-Free Solids. 96

ii. Mechanical Properties of the 2D- Triangular Lennard-Jones Covalent Solid at Absolute Zero Temperature. 101

II.2C. Sample-Size Effect: Constant Applied Tensile Displacement. 102

II.2D. The Two-Dimensional Solid Containing an Internal Crack. Elasto-Static Considerations and Griffith's Energy-Balance Theory. 104

II.2E. Major Computer Simulations Results. 109

II.2F. Stress Distribution Around an Internal Elliptical Crack in a Plate Under Constant Applied Tension. 113

II.2G. Inglis-Griffith's Elliptical Crack in a Plate Under Simple Tension. 117

II.2H. Eringen's Nonlocal Theory. 125

II.2I. Molecular Dynamic Simulations of the Effect of the Atomic Crack-Tip Geometry on Local Stress: Outline of the Method. 130

II.2J. The Effect of Atomic Crack-Tip Geometry on the Local Stress Distributions: The Simulations Results. 133

II.2K. The Effect of Atomic Crack-tip Geometry on the Local Stress Distribution, and on the Dynamic Behavior of Critically Loaded Cracks: Discussion of the Simulations Results. 142

II.2L. The Credibility of the Simulations Results. 151

II.2M. The Effect of Atomic Crack-Tip Geometry on Local Stress Distributions: Conclusions. 154

II.2N. Local Stress Distributions in the Vicinity of Internal Cracks in the 2D-Lennard-Jones Solids Subjected to Elevated Remotely Applied Constant Tensile Stresses or Strains. 157

II.3. Dynamic Crack Propagations. 161

II.3A. The Theoretical Quasi-Static Analysis of the Velocity of the Brittlely Propagating Crack-Tip 166

II.3B. Crack-Tip Velocity; Major Simulations Results 195

II.3C. The Crack-Tip Configurational Model 210

II.3D. Crack-Tip Velocities of Brittlely Propagating Cleavage Cracks; Conclusions 216

II.3E. Remotely Applied Constant Critical Tensile Stress (or Strain) Necessary for the Initiation of Brittle Propagation of an Internal Cleavage Crack; Major Simulations Results 224

II.3F. Remotely Applied Constant Tensile Critical Stress (or Strain) Necessary for the Initiation of Brittle Propagation of an Internal Cleavage Crack; Conclusions 230

II.3G. Energetics of Brittlely Propagating Cleavage Cracks; Major Simulation Results 232

II.3H. Energetics of Brittlely Propagating Cleavage Cracks; Conclusions 242

II.3I. Computer Simulations of Dynamic Cracks; Summary 245

Volume II

III. Brittle-to-Ductile Transition Temperature. 249

III.1. Finite Temperature Molecular Dynamic Technique 249

III.2. Interatomic Potentials 257

III.3. Thermo-Mechanical Properties of the Two-Dimensional Triangular Covalently Bonded Lennard-Jones Solid, LJCOVa.2; Major Simulations Results 260

III.4. Brittle-to-Ductile Transition Temperature; Major Simulations Results 263

III.4A Series; Major Simulations Results 263

III.4B Series; Major Simulations Results 274

III.5. Brittle-to-Ductile Transition Temperature; Conclusions 284

III.6. Simulations Results for the "Corrected" Two-Dimensional Triangular Covalent Lennard-Jones Solid with a*=0.2 294

III.7. Simulations Results of the Investigation of the BDT Temperature of the Pre-Cleaved Two-Dimensional Triangular Johnson Solid 312

III.8. Brittle-to-Ductile Transition Temperature; Summary 319

Tables 328

Illustrations 413

Appendix A 532

Bibliography 535

LIST OF SYMBOLS

c	half-crack length,
V_C	crack-tip velocity,
V_T	crack-tip terminal velocity,
C_0	longitudinal sound velocity,
C_1	dilational wave velocity,
d	interatomic spacing,
ε_o	unit of energies,
M	Young's modulus,
M^*	effective Young's modulus,
μ	shear modulus,
e	conventional (or engineering) strain,
ε	natural (or true) strain,
s	conventional (or engineering) stress,
σ	natural (or true) stress,
$2w$	width of the sample,
H	the height of the sample,
W	work done by the external load on the system.,
E_{el}	elastic strain energy of the system,
E_{ke}	kinetic energy of the system,
E_{me}	mechanical energy of the system,

Δ	change (in energies),
K_B	Boltzmann's constant,
NBB	number of broken bonds,
NNBB	number of new broken bonds,
ρ	radius of curvature; density,
r	radial distance,
T	temperature,
T_m	melting temperature,
T_C	critical temperature (BDT temperature),
BDT	brittle-to-ductile transition,
BDTT	brittle-to-ductile transition temperature,
DBT	ductile-to-brittle transition,
K	Kosterlitz-Thouless parameter,
t	time,
δ	basic time interval,
ν	Poisson's ratio,
a*	coefficient of covalent resistance,
LJ	Lennard-Jones potential,
J	Johnson potential,
LJCOVa.2	modified LJ potential with a*=0.2,
COR.LJCOVa.2	"corrected" LJCOVa.2.

List of Tables

[Table. II.1.1.] Conversion factors and units for the two-dimensional triangular Lennard-Jones solid.

[Table. II.1.2.] The Johnson Potential.

[Table. II.1.3.] Conversion factors and units for the two-dimensional triangular Johnson solid.

[Table. II.1.4.] Energetics of the quasi-static crack extension in a 2D-triangular array of 10704 atoms interacting via the Johnson potential and arranged in 79 rows (79X135) subjected to the remotely applied constant tensile load of 1.50. All energies are given for the half-sample.

[Table. II.1.5.] The comparison of the critical engineering stress, S , true stress, σ, engineering strain, e , and true strain, ε, values from the simulations and the corresponding Griffith (fracture) stress, σ_G, and e_G .

[Table. II.2.1.] Mechanical properties of the two-dimensional triangular (modified) Johnson solid with the angular resistance, a*. Sample size: 18x19, defect-free sample under the constant applied load, S, and absolute zero temperature. The simulation results.

[Table II.2.1B] Analytical calculation of Young's Modulus, M, Shear Modulus, μ,

and Poison's ratio, ν, for nominal applied strain, e. Johnson Potential ($a^*=0$).

[Table II.2.2.] Mechanical properties of the two-dimensional "modified" Lennard-Jones, LJCOVa.2, solid with the angular resistance of $a^*=0.2$ as a function of temperature.

[Table II.2.2A] Simulations results for LJCOVa $a^*=0.2$, sample: 32x19, temperature $K_BT=0$ ε_0.

[Table II.2.2B] Simulations results, for LJCOVa $a^*=0.2$, sample:18X19, applied load, σ =0.25.

[Table II.2.2C] Simulations results, for LJCOVa $a^*=0.2$, sample:18X19.

[Table. II.3.1.] Experimentally observed limiting crack-tip velocities.

[Table. II.3.2.] Simulations results for the crack-tip velocity as a function of a^*.

[Table. II.3.3.] Approximate values of the elastic wave velocities for common engineering materials.

[Table. II.3.4.] The theoretical values of the limiting terminal velocity of brittlely propagating cleavage crack. Eshelby and Mott's theoretical predictions for the crack-tip velocity for $c_0=3.75$. Eshelby's velocity is normalised to the Shear velocity, $C_2=0.612\ C_1$, and Mott's velocity is normalised to $V_C = .25C_1$ and

V_C=.44C_1.

[Table. II.3.5.] Forces acting on atoms near the crack-tip for 2D-triangular Lennard-Jones solid of 10704 atoms arranged in 79 rows. The initial number of broken bonds in the half-sample was 19. At the start of the run the first broken bond is at the atomic position #59.

[Table. II.3.6.] The dynamic simulations results of the brittlely propagating internal cracks in a two-dimensional triangular Lennard-Jones solid under constant critical applied strain.

[Table. II.3.7A] Comparison of the simulations results regarding the change in the mechanical energy of varieties of systems during the brittle propagation of the internal cracks. The slopes are calculated graphically from Fig. II.3.24, 26 & 31. Constant Applied Load.

[Table. II.3.7B] Comparison of the simulations results regarding the change in the mechanical energy of varieties of systems during the brittle propagation of the internal cracks. The slopes are calculated graphically from Fig. II.3.24, 26&31. Constant Applied Strain

[Table II.3.8A1.] Run: JN7LD, Type of loading: "fast", sample size: 79x135, c_o=3.75, critical load, σ_C= 3.37. Changes in the energies of the system are given with respect to the energies of the pre-cracked critically loaded sample.

[Table II.3.8A2.] Run: JN7LD, Type of loading: "fast", sample size: 79x135, c_o=3.75, critical load σ_C= 3.37. Changes in the energies of the system are given with respect to the energies of the "perfect" critically loaded sample.

[Table II.3.8B1.] Run: JN13LD, Type of loading: "fast", sample size: 79x135, c_o=6.75, critical load, σ_C= 2.45. Changes in the energies of the system are given with respect to the energies of the pre-cracked critically loaded sample.

[Table II.3.8B2.] Run: JN13LD, Type of loading: "fast", sample size: 79x135, c_o=6.75, critical load, σ_C= 2.45. Changes in the energies of the system are given with respect to the energies of the "perfect" critically loaded sample

[Table II.3.8C1.] Run: JN19LD, Type of loading: "fast", sample size: 79x135, c_o=9.75, critical load, σ_C= 1.90. Changes in the energies of the system are given with respect to the energies of the pre-cracked critically loaded sample.

[Table II.3.8C2.] Run: JN19LD, Type of loading: "fast", sample size: 79x135, c_o=9.75, critical load, σ_C= 1.90. Changes in the energies of the system are given with respect to the energies of the "perfect" critically loaded sample.

[Table II.3.8D.] Run: JN19LD, Type of loading: gradual, sample size:79x135, c_o=9.75, critical load, σ_C= 1.90.

[Table II.3.8E] Run: JN7SRN, Type of loading: gradual, sample size: 79x135, c_o=3.75, critical strain, ε_C=0.0615. Changes in the energies of the system are

given with respect to the energies of the "perfect" critically loaded sample.

[Table II.3.8F] Run: JN13SRN, Type of loading: gradual, sample size:79x135, c_o=6.75, critical strain, ε_C= 0.0470. Changes in the energies of the system are

given with respect to the energies of the "perfect" critically loaded sample.

[Table II.3.8G] Run: JN19SRN, Type of loading: "fast", sample size:79x135, c_o=9.75, critical strain, ε_C= 0.0410. Changes in the energies of the system are given with respect to the energies of the "perfect" critically loaded sample.

[Table II.3.8H] Run: JN19SRN, Type of loading: gradual, sample size:79x135, c_o=9.75, critical strain, ε_C= 0.0410. Changes in the energies of the system are given with respect to the energies of the "perfect" critically loaded sample.

[Table II.3.8.1] Summary: Normalised Crack velocity V_T/C_1, sample size: 79x135, c_o=9.75, JN19SRN: critical strain, ε_c= 0.0410, and JN19LD: critical load, σ_c= 1.90. Crack-tip velocities, V_C, are calculated graphically from the graph of c(t) vs t. Note that the normalised crack-tip terminal velocity lies in the range of 0.249-0.273. Only, the acceleration period is effected by the loading scheme. It is slower for the gradual type of loading.

[Table II.3.8.2] Summary: Change in the "normalised" mechanical energy of the system as a function of crack length. Sample size: 79x135, c_o=9.75, JN19SRN: critical strain, ε_c= 0.0410, and JN19LD: critical load, σ_c= 1.90.

[Table II.3.9] Summary. Comparison of the major simulations results concerning the magnitude of the terminal crack-tip velocity, change in the mechanical energy of the system, and theoretical predictions.

[Table II.3.10A] The simulation results for the 2D-triangular modified Lennard-Jones, LJCOVa, solid with the angular resistance, a*=1.0, and a*=3.0. Crack half-length, c_o=3.75, and the applied load, S_a=3.00. Sample size is 39X65. Time interval=0.01.

[Table II.3.10B] The simulation results for the 2D-triangular modified Johnson, JOHNCOVa, solid with the angular resistance, a*=0.30, a*=0.75, a*=1.0, and a*=3.0. Crack half-length, c_o=3.75, and the applied load, S_a=4.00. Sample size is 39X65.

[Table II.3.10C] Simulation results for the 2D-triangular modified Johnson, JOHNCOVa, solid with the angular resistance, a*=0.30, a*=0.75, a*=1.0, and a*=3.0, and the 2D-triangular Lennard-Jones, LJCOVa, with a*=0.5 and a*=3.0. The change in mechanical energy, $-\Delta E_{me}=\Delta(E_{el}-W)$, is given with respect to c=4.25. Crack half-length, c_o=3.75, and the applied load, (S_a=3.00 for LJCOVa, and S_a=4.00 for JOHNCOVa). Sample size is 39X65.

[Table II.3.10D] Simulation results for the 2D-triangular modified Lennard-Jones, LJCOVa, solid with the angular resistance, a* ={2.0, 4.0, 6.0, 8.0, 10.0}. Crack half-length, c_o=3.75, and the applied load, S_a=3.00. Sample size is 39X65. Time interval is 0.01.

[Table III.4A1] Temperature $K_BT= 0\ \varepsilon_o$, LJCOVa.2 a*=.2, sample size: 32x19, c_o=3.75d, time interval is 0.01, critical load, σ_c =2.10.

[Table III.4A2] Temperature $K_BT= 0.02\ \varepsilon_o$, LJCOVa.2 a*=.2, sample size: 32x19, c_o= 3.75d, time interval is 0.01, critical load, σ_c = 1.90.

[Table III.4A3] Temperature $K_BT= 0.02\ \varepsilon_o$, LJCOVa.2 a*=.2, sample size:32x19, c_o= 3.75d, time interval is 0.01. Applied load σ_a=2.0. *OVERLOADED*.

[Table III.4A4] Temperature $K_BT=0.046\varepsilon_o$, LJCOVa.2 a*=.2, sample size: 32x19, c_o= 3.75d, time interval is 0.01, critical load, σ_c = 1.90.

[Table III.4A5] Temperature $K_BT=0.056\varepsilon_o$, LJCOVa.2 a*=.2, sample size: 32x19, c_o= 3.75d, time interval is 0.01, critical load, σ_c= 1.80.

[Table III.4A5*] Temperature $K_BT=.056\varepsilon_o$, LJCOVa.2 a*=.2, sample size: 32x19, c_o= 3.75d, time interval is .01, applied load σ_a=1.90. *OVERLOADED*.

[Table III.4A6] Temperature $K_BT=0.060\varepsilon_o$, LJCOVa.2 a*=.2, sample size: 32x19, c_o= 3.75d, time interval is 0.01, critical load, σ_c= 1.80.

[Table III.4A7] Temperature $K_BT=0.060\varepsilon_o$, LJCOVa.2 a*=.2, sample size: 32x19, c_o= 3.75d, time interval is 0.01, critical load, σ_c = 1.80. The history of the run is different from that of III.4A6.

[Table III.4A8] Temperature $K_BT=.0628\varepsilon_o$, LJCOVa.2 a*=.2, sample size: 32x19, c_o= 3.75d, time interval is 0.01, critical load, σ_c = 1.80.

[Table III.4A9] Temperature $K_BT=.0625\varepsilon_o$, LJCOVa.2 a*=.2, sample size: 32x19, c_o= 3.75d, time interval is 0.01, critical load, σ_c = 1.80. The history of the run is different from that of the III.4A8 run.

[Table III.4A10] Temperature $K_BT=0.075\ \varepsilon_o$, LJCOVa.2 a*=.2, sample size: 32x19, c_o= 3.75d, time interval = 0.01, critical load, σ_c = 1.80.

[Table III.4A] **SUMMARY**: III.4A SERIES; Brittle-to-Ductile Transition Temperature in the covalently modified Lennard-Jones solid, LJCOVa.2 a*=.2, c_o=3.75d, sample size: 32x19, time interval = 0.01.

[Table III.4B1] Temperature $K_BT=0.0193\ \varepsilon_o$, LJCOVa.2 a*=.2, sample size: 64x39, c_o= 3.75d, time interval = 0.01, critical load, σ_c = 2.40.

[Table III.4B2] Temperature $K_BT=0.0680\ \varepsilon_o$, LJCOVa.2 a*=.2, sample size: 64x39, c_o= 3.75d, time interval = 0.01, critical load, σ_c = 2.20.

[Table III.4B3] Temperature $K_BT = 0.0904\ \varepsilon_o$, LJCOVa.2 a*=.2, sample size: 64x39, c_o= 3.75d, time interval = 0.01, critical load, σ_c = 2.00.

[Table III.4B3*] Temperature $K_BT = 0.0892\ \varepsilon_o$, LJCOVa.2 a*=.2, sample size: 64x39, c_o= 3.75d, time interval = 0.01, applied load σ_a = 2.10 > critical load.

[Table III.4B4] Temperature K_BT=0.105 ε_o, LJCOVa.2 a*=.2, sample size: 64x39, c_o= 3.75d, time interval is 0.01, critical load, σ_c = 1.80.

[Table III.4B] SUMMARY, LJCOVa.2 a*=.2, c_o=3.75d, sample size: 64x39, time interval = 0.01.

[Table III.5] Summary. The simulations results of III.4A and III.4B series are summarised and compared to each other.

[Table III.6A1] Temperature K_BT=0.0193 ε_o, COR.LJCOVa.2, sample size: 64x39, c_o= 3.75d, time interval = 0.01, critical load, σ_c = 2.30.

[Table III.6A2] Temperature K_BT=.0634 ε_o, COR.LJCOVa.2, sample size: 64x39 c_o= 3.75d, time interval = 0.01, critical load, σ_c = 2.10.

[Table III.6A2*] Temperature K_BT= 0.062 ε_o, COR.LJCOVa.2, sample size: 64x39, c_o= 3.75d, time interval = 0.01, critical load, σ_c = 2.20.

[Table III.6A3] Temperature K_BT= 0.0675 ε_o, COR.LJCOVa.2, sample size: 64x39, c_o= 3.75d, time interval = 0.01, critical load, σ_c = 2.20.

[Table III.6A4] Temperature K_BT= 0.0790 ε_o, COR.LJCOVa.2, sample size: 64x39, c_o= 3.75d, time interval = 0.01, critical load, σ_c = 2.00.

[Table III.6A5] Temperature K_BT = 0.0857 ε_o, COR.LJCOVa.2, sample size:

64x39, c_o= 3.75d, time interval = 0.01, critical load, σ_c = 2.00.

[Table III.6A6] Temperature K_BT= 0.104 ε_o, COR.LJCOVa.2, sample size: 64x39, c_o= 3.75d, time interval = 0.01, critical load, σ_c = 1.95.

[Table III.6A6*] Temperature K_BT= 0.104 ε_o, COR.LJCOVa.2, sample size: 64x39, c_o= 3.75d, time interval = 0.01, σ_a =2.0 > σ_c =1.95: "OVERLOADED".

[Table III.6A8] Temperature K_BT= 0.136 ε_o, COR.LJCOVa.2, sample size: 64x39, c_o = 3.75d, time interval = 0.01, critical load, σ_c = 1.80.

[Table III.6] **Summary:** BDT in the 2D-triangular COR.LJCOVa.2 solid, a*=.2, sample size: 64x39, c_o=3.75d, time interval = 0.01.

[Table III.7] **Summary** of the search for the brittle-to-ductile transition temperature in the 2D-triangular Johnson solids, c_o=3.75d, time interval = 0.01.

[Table III.8] **Overall summary** of the search for the BDT in the 2D-LJCOVa.2 and 2D-COR.LJCOVa.2 solids.

[Table III.9] **Conclusion**: Brittle-to-Ductile Transition Temperature in the 2D-LJCOVa.2 and 2D-COR.LJCOVa.2 solids.

LIST OF ILLUSTRATIONS

[Fig. II.1.1.] The two-dimensional triangular lattice of 79 rows and 135 columns in odd rows with the centrally located internal crack of 38 broken bonds correspondent to the initial half-crack length c_o=9.75d between the 39th and 40th rows. Mirror symmetry about the central vertical axis is used. The half-sample mode I opening is illustrated.

[Fig. II.1.2.] Pair-wise 6-12 Lennard-Jones interatomic potential and the corresponding interatomic force against the interatomic spacing.

[Fig. II.1.3a.] Pair-wise Johnson empirical interatomic potential versus the interatomic spacing. The potential has an inflection point at r/d=1.17189 (maximum in the force) and goes to zero at r/d=1.3147.

[Fig. II.1.3b.] The interatomic force versus the interatomic distance for the Lennard-Jones and Johnson potentials. The arrow indicates the maximum force the bond may sustain at the r values indicated. Note that the shapes of the forces are quite different. The Johnson interatomic force falls off much more rapidly past the maximum than is the case with the Lennard-Jones interatomic force.

[Fig. II.1.4.] Half-sample with two extra columns of atoms. Column n+1 and n+2 are mirror images of columns n-1 and n-2 about the central axis n.

[Fig. II.1.5.] The crack shapes investigated (only a portion of the half-sample shown): (a) A narrow crack of 38 broken bonds c_o=9.75d; (b) The wide crack. In this configuration the narrow crack was widened by removing four rows of atoms; (c) The "wide-jagged crack" created by removing 8 rows of atoms. The crack-tip atom is atom no. 58 on the 39th row. The crack-length is the same for all of these cracks.

[Fig. II.1.6.] In the case of the constant external displacement simulations, the calculated forces (stresses) on the individual atoms in the uppermost and lowermost rows are not constant.

[Fig. II.2.1.] The deformed elementary triangular cell under a uniform tensile strain, ε.

[Fig. II.2.2.] The tensile force, F, versus the applied strain for the two dimensional triangular Johnson solid.

[Fig. II.2.3.] Young's Modulus, M, versus the applied strain for the two-dimensional triangular covalently modified Johnson and Lennard-Jones solids.

[Fig. II.2.4.] Poisson's ratio, ν, versus the applied strain for the two-dimensional triangular Johnson solid.

[Fig. II.2.5.] Young's Modulus, M, versus the applied strain. The crosses (full circles) represent the simulations results of a defect-free 2D-triangular Johnson

solid under a given constant applied strain (or stress). The line is the theoretical behavior of the modulus of elasticity of the system against strain.

[Fig. II.2.6a.] The tensile stress versus the applied strain for the 2D-triangular LJCOVa.2 solid with $a^*=0.2$.

[Fig. II.2.6b.] The force versus strain curves for the Johnson and Lennard-Jones 2D-triangular solid. The arrows indicate the points of instability.

[Fig. II.2.7a.] Young's modulus, $\langle M \rangle_t$, versus the externally applied load for LJCOVa.2 solid as a function of temperature.

[Fig. II.2.7b.] Modulus of elasticity, M, versus strain curves for Johnson and Lennard-Jones solids. The arrows indicate the points of instability of the solids.

[Fig. II.2.8.] μ /M ratio versus a^* for the covalently modified Lennard-Jones and Johnson solids.

[Fig. II.2.9a.] Young's modulus, M, versus the applied strain. The full circle represents three sample-sizes spanning a factor of 4 in the plate-area. The moduli are identical within 0.1% independent of the sample-size. The straight line is the theoretical behavior of the modulus against strain for a perfect sample.

[Fig. II.2.9b.] Young's modulus, M, and the shear moduli versus the increase in

the amplitude of the angular resistance, a*, for a 2D-triangular "covalent" solid held together by the modified Lennard-Jones and Johnson potential.

[Fig. II.2.9c.] The functional dependence of the modulus of elasticity, M*, on the sample-size. The simulation data is plotted as 1/M* against c^2. The straight line is the empirical fit to the simulations results. All samples have the identical sample size of 79x135 under the critical constant external strain, and containing varieties of centrally located internal cracks of initial half-crack length c_o={3.75, 6.75, and 9.75}.

[Fig. II.2.10.] Energetics of the Griffith crack in uniform tension. Data for glass from Griffith's paper: γ_s=1.75Jm^{-2}, E=6.2X10^{10}Nm^{-2}, σ=2.63X10^{6}Nm^{-2} selected to give equilibrium at c=10 mm.

[Fig. II.2.11.] The pre-cleaved two-dimensional triangular Lennard-Jones solid under the externally applied critical tensile load. Due to the mirror symmetry used in these simulations only half-sample is demonstrated in this figure. The whole sample may be obtained by the reflection about the right-hand side vertical column of this figure. External constant tensile forces (loads, σ_a) are applied to the individual atoms of the uppermost and lowermost horizontal boundaries, i.e., 1st and 39th rows. Lines are drawn between the interacting atoms, i.e., between those atoms which are less than 1.6d apart. (a) Brittle propagation of the cleavage crack of initial half crack-length, c_o=19.75d, under the applied constant tensile load of σ_a=0.50. (b) The incipient dislocation nucleation at the crack-tip of initial half crack-length, c_o=9.75d, under the

applied tensile load of σ_a=1.30. The extra lines designate the atoms which have moved into the interaction range of their second neighbors. (c) Dislocation formed at the lower end of the crack tip at σ_a=1.30 and c_o=19.75d. The generated dislocation is, eventually, moved away from the crack-tip towards the loaded horizontal surfaces of the specimen. Note that the system is heavily overloaded.

[Fig. II.2.12.] The arrest and blunting of an internal crack in a two-dimensional triangular Lennard-Jones crystal, subjected to the remotely applied constant tensile critical load at the horizontal boundaries of the specimen, due to the emission of blunting dislocations at the crack-tip. The emitted dislocations, eventually, moved to the loaded horizontal surfaces of the sample and produced a jug there. Only a portion of the specimen is illustrated.

[Fig. II.2.13.] The arrest and blunting of brittlely propagating cleavage crack of initial half crack-length, c_o=3.75d, in a two-dimensional triangular Johnson crystal subjected to the critical applied constant tensile load of 3.37 at the horizontal surfaces of the specimen. Immediately after the emission of blunting dislocations at the crack-tip the brittlely propagating internal crack got blunted. As illustrated in Fig. II.3.14 the blunting dislocations were generated at step 460, the crack was then arrested for about 200 time steps, and the brittle propagation of the blunted crack-tip renewed at time step 645 as the emitted dislocations moved away from the crack-tip zone and their shielding effect was, therefore, removed. A new set of dislocations were emitted at step 801, and the above process was repeated again. The emitted dislocations, finally,

propagated to the loaded horizontal boundaries of the specimen. In the 2D-triangular Johnson solid the dislocation shows up as missing bonds as atoms move out of the short range of the interatomic potential (r>1.3147d).

[Fig. II.2.14.] The local stress distributions due to (a) circular hole and (b) elliptical hole in an infinite plate subjected to the remotely applied constant tensile loads at the horizontal boundaries of the specimen.

[Fig. II.2.15.] Griffith's model for a crack system: a pre-cleaved plate subjected to the remotely applied loads at the boundaries. The important elements of the system are illustrated as: an elastic body, E, containing an internal crack, S, of length, 2c, subjected to the externally applied loads, L, at the boundaries.

[Fig. II.2.16.] The local stress concentration factor, σ_y/σ_a, of an internal elliptical hole of c=3b. Note that the major perturbations to the applied stress field occur only within the characteristic length of c from the physical boundaries of the hole, with the greatest stress gradients confined to the highly localised region within the distance of the order of the radius of curvature of the hole, ρ, surrounding the position of the maximum concentration.

[Fig. II.2.17.] Uniform loading configurations for plane cracks with straight fronts. This model is used for the derivations of the local stresses in the vicinity of the internal cracks. The thickness of the plate is conveniently taken to be unity in the two-dimensional problem, and infinity in the 3D problems.

[Fig. II.2.18.] Hoops stress distribution along the crack-line, $p(x)= \sigma_y(x,0)/\sigma_a$, for the variety of the crack-lengths from Eringen's non-local treatment of the crack problem.

[Fig. II.2.19.] Eringen's Material Function, $C(\nu)$, depends on the Poisson's ratio only, and it falls into the region $0.845 \geq C(\nu) \geq 0.676$ for $\nu=0$ to 0.5. For $\nu=0.25$, $C(\nu)=0.713$.

[Fig. II.2.20.] The stress concentration (distribution) factor, F-1, along the column of the crack-tip atom, i.e., at r=0, atom no. 58 of Fig. II.1.5, at the central crack row (row 39 of Fig. II.1.5) and at several surrounding rows. F-1 is the contribution from the crack itself, and the remotely applied nominal tensile stress is about E/10000 in magnitude. E is Young's modulus of the solid.

[Fig. II.2.21.] Brittle propagation of the "wide" crack of Fig. II.1.5b at a constant critical applied strain of 0.0305.

[Fig. II.2.22.] Dislocation generation at the sharp corner of the wide jagged crack of Fig II.1.5c at the critical externally applied strain of 0.0350. The emitted dislocation, characterised by the cross hatching has left a ledge at the crack-tip by gliding away from the crack-tip toward the loaded horizontal surface of the specimen.

[Fig. II.2.23.] Local stress concentration factor, F-1, at the crack-tip, i.e., at r=0 as a function of half-crack length for four narrow cracks. Simulations results are

illustrated as open circles. The solid line passing through these points demonstrate a linear dependency of stress concentration factor, F-1, on the crack length. The broken line represents the theoretical calculation of Inglis-Griffith-Goodier (IGG) for an elliptical hole of b=0.5d (equations II.2.51-52). Eringen's non-local prediction for the stress concentration factor (eq. II.2.58) is also shown for the purpose of comparisons.

[Fig. II.2.24.] Log-Log plot of the stress distribution factor, F-1, as a function of r/c. The simulations results for the narrow and wide cracks of c_o=9.75d are indistinguishable and, therefore, illustrated with a single symbol (open circles). The wide-jagged crack simulations results are shown as solid triangle. The solid lines are IGG's theoretical predictions for an elliptic hole of c/b=20 or 50, and for a circle (c/b=1) calculated by means of equations II.2.51-53.

[Fig. II.2.25.] The simulations data of Fig. II.1.5 plotted as F-1 versus $(c/2r)^{1/2}$. The theoretical prediction of IGG is given as broken line (slope=1). Note that the solid line fit to the data has neither the correct slope nor does it pass through the origin.

[Fig. II.2.26.] The simulations data for four narrow cracks of different lengths plotted as F-1 versus $(c/2r)^{1/2}$. The number adjacent to the symbols are the half crack lengths, c. The broken line illustrates the correct theoretical slope of one. Note that the solid line fit to the data has neither the correct slope nor does it pass through the origin. Most of the simulation data fall between the thin elliptical (c/b=20), and infinitely thin crack ($F-1=(c/2r)^{1/2}$) lines. No systematic

$r^{-1/2}$ dependence is observed.

[Fig. II.2.27.] Labelling of the interatomic bonds and mass points (atoms) at the immediate vicinity of the crack-tip.

[Fig. II.2.28.] Displacements of a few atoms on the two central rows in the vicinity of the crack-tip are plotted against the atomic positions for a 2D-triangular Lennard-Jones solid (79X135) subjected to varieties of remotely applied constant displacements, containing an internal crack of c_o=9.75d.

[Fig. II.2.29.] The local forces acting on the individual atoms on the two central rows in the vicinity of a narrow crack, c, in a 2D-triangular Lennard-Jones solid subjected to four very different applied constant strain, i.e., ε= 0.01, 0.02, 0.028, 0.029. Note that the critical strain for the initiation of fracture for this crack of c_o=9.75 in the same sample size, i.e., 79 rows by 135 columns was 0.0293.

[Fig. II.3.1.] Dynamic plane-crack system. V_c is the crack-tip velocity. R denotes the domain which receives the stress-wave "message" from the crack-tip.

[Fig. II.3.2.] The calculations of Robert and Wells that provided their limiting crack-tip velocity of $0.38C_1$.

[Fig. II.3.3.] Dynamic stress distribution in the 2D-triangular Johnson solid. Curve (a) is the static stress distribution for the centrally located internal crack of the initial half-crack length c_o=3.75 corresponding to 7 broken bonds in the

half-sample. Curve (b) is 331 steps later where there are 11 broken bonds in the half sample, and the crack-tip is accelerating. Curve (c) represents the system 93 steps later, where there are 15 broken bonds in the half-sample and the crack-tip velocity is saturated to its constant terminal value. The static and dynamic local stress distributions are very similar and is obviously crack-tip velocity independent. The critical (fracture) stress is 3.37.

[Fig. II.3.4.] Dynamic stress distribution in the 2D-triangular Lennard-Jones solid of 10704 atoms arranged in 79 rows (79X135). Curve #1 is the static stress distribution for an initial crack of 19 broken bonds in the half-sample. Curves 2-7 are those of the propagating cleavage crack. The relative strain, e/e_G is 1.036 at time step 3600 (stable crack). The relative strain is 1.054 for all other curves (see Table II.3.5). The static and dynamic stress concentration and distributions are very similar.

[Fig. II.3.5.] Normalised crack-tip velocity versus the normalised crack-length, c/c_o, where c_o is the initial half-crack length. C_1 is the velocity of the waves of dilation in the 2D-Johnson solid = $[E/\rho(1-\nu^2)]^{1/2}$ = $(9E/8\rho)^{1/2}$ for ν =1/3. The sample size is 79X135.

[Fig. II.3.6.] Normalised crack-tip velocity versus the normalised crack-length, c/c_o, where c_o is the initial half-crack length. C_1 is the velocity of the waves of dilation in the 2D-Johnson solid = $[E/\rho(1-\nu^2)]^{1/2}$ = $(9E/8\rho)^{1/2}$ =7.65 for ν =1/3. Sample size: (•) 159X135, σ_c=2.15; (X) 79X135, σ_c=1.90.

[Fig. II.3.7.] Normalised crack-tip velocity versus the normalised crack-length, $c-c_o$, where c_o is the initial half-crack length. C_1 is the velocity of the waves of dilation in the 2D-triangular covalently modified Johnson solid which is $(9E/8\rho)^{1/2}$ for $\nu = 1/3$. The shape of this curve is representative of the development of the crack-tip velocity in the varieties of the covalently bonded 2D solid (Table II.3.2).

[Fig. II.3.8.] The variation of the normalised terminal crack-tip velocity with the amplitude of the angular resistance, a^*.

[Fig. II.3.9.] Plots of the crack-tip velocity against crack-half length in the 2D-triangular Lennard Jones and Johnson solid for varieties of sample sizes.

[Fig. II.3.10.] Experimental results for the crack-tip velocity in sapphire tested in the moistened nitrogen gas (relative humidities indicated).

[Fig. II.3.11.] Comparison of the observed crack propagation results with predictions of a propagating strip yield zone model for steel foil sheet in tension.

[Fig. II.3.12.] A typical dynamic brittle propagation. Number of new sequential breaking of the interatomic bonds between rows 39 and 40, NNBB, is plotted against the time step. Initial number of broken bonds in half-sample was 19, corresponding to c_o=9.75d. The sample is under remotely applied constant critical strain of 0.041.

[Fig. II.3.13.] Computer simulations results of the brittle propagation of the centrally located internal narrow crack of initial half-crack length c_o=9.75d, corresponding to 19 initial broken bonds in half-sample in a 2D Johnson's solid of 21544 atoms arranged in 159 rows, subjected to a remotely applied constant critical load of 2.15. Number of new broken bonds, NNBB, is plotted against the time step. The slope of this curve at a given time step is the instantaneous crack-tip velocity at that point.

[Fig. II.3.14.] The crack arrest caused by dislocation generation at the crack-tip of a running crack of the initial half-crack length of c_o=3.75d, in a 2D-triangular Johnson solid of 10704 atoms arranged in 79 rows under the remotely applied constant critical tensile load of 3.37. A pair of dislocations were emitted, symmetrically, from the crack-tip (Fig. II.2.13) 460 time steps after the removal of the critical damping. Immediately after dislocations nucleation, the crack-tip got blunted, the principal stresses at the crack-tip was reduced for a considerable length of time. By the time step 645, where the brittle propagation of the crack-tip was renewed along its initial path, the emitted dislocations had moved away from the crack-tip toward the loaded horizontal surfaces of the specimen, and the normal stresses at the crack-tip had risen back to the theoretical cohesive (fracture) strength of the material. After 801 time steps following the removal of the critical damping, a second pair of blunting dislocations were emitted from the fast-running crack-tip, and the crack was arrested again for a significant amount of time.

[Fig. II.3.15] The simulations results illustrated in this figure for the two-

dimensional triangular covalent Lennard-Jones solid of $a^*=1.0$ is typical of these series. The internal crack of $c_o=3.75$ has propagated brittlely to a crack of instantaneous half crack-length c=16.25, i.e., $c/c_o=4.33$ by the end of this run as demonstrated in the last image in this figure. Note that the crack surface is very clean, and no evidence of any plastic deformation is present.

[Fig. II.3.16.] The simulations results of the brittlely propagating internal crack of initial half crack-length $c_o=3.75$ in a two-dimensional triangular Johnson solid of sample size 79x135, and subjected to the critical external load of 3.37. The system is damped, i.e., the kinetic energy of the sample is reduced at every step by a given amount. Note that there is no observable plastic deformation in the vicinity of the running crack-tip. Comparison of these results with those of JN7LD run reveals the fact that indeed the observed generation of a pair of dislocations at the tip of the running crack-tip in JN7LD run is due to the generated adiabatic heating in the vicinity of the running crack-tip. Note also the very smooth surface of the propagated crack.

[Fig. II.3.17] The schematic representation of the distance parameters at the crack-tip.

[Fig. II.3.18] Interatomic bond lengths against the time step during the steady propagation for the several interatomic bonds in the vicinity of the crack-front

[Fig. II.3.19] Typical raw data of the Number of New Broken Bonds, NNBB, vs the time step for a very brittle solid (Johnson solid with $a^*=3.0$).

[Fig. II.3.20] The change in the energies of the critically loaded, σ_c=2.15, pre-cleaved, c_o=9.75, sample of 159x135, as a function of the number of new broken bonds, NNBB, during the brittle propagation of internal crack. As demonstrated clearly in this figure, the work done by the externally applied load on the sample during the brittle propagation of the crack, ΔW, is essentially zero, and practically, all of the driving (fracture) energy is provided by the strain potential energy of the specimen. The behavior of the system strongly resembles that of fixed-grips loading conditions. The reason for this particular behavior is none other than the fact that the externally applied load at the horizontal boundaries of the specimen, due to the relatively large height of the sample, H, does not detect the initiation of the brittle propagation of the cleavage internal crack until almost the end of the run. This is due to the fact that, the information about the initiation of the fracture travels with the longitudinal sound velocity in the strained medium. Therefore, naturally, due to the relatively large height of the specimen, it takes relatively longer time for this information to reach the outer horizontal boundaries of the specimen, and hence, being detected by the externally applied loads there. So, obviously, the applied loads would not respond to the undetected events, and all of the fracture energy has to be provided by the stored strain potential energy in the body. Hence, the system behaves as if it was loaded under a fixed constant displacement at its boundary, or as if the specimen was infinitely large. In this regard, it is therefore, not unreasonable to assume that practically, the largest simulated sample of 159X135 resembles an infinite sample loaded to the critical load at infinity, i.e., Griffith's theoretical sample.

Due to economic restrictions, the simulations was terminated after the fast-running crack-tip was arrested. Of course, if the simulations were not discontinued, the externally applied load would have detected the events taking place at the crack tip and would have responded to it by working on the specimen. The system then would have behaved in a manner similar to the behavior of our middle-size sample of 79X135.

[Fig. II.3.21] The change in the energies of the critically loaded σ_c=1.90 pre-cleaved c_o=9.75 sample of 79x135, as a function of the number of new broken bonds, NNBB, during the brittle propagation of internal crack.

[Fig. II.3.22] The change in the energies of the critically loaded σ_c=1.45 pre-cleaved c_o=9.75 sample of 39x135, as a function of the number of new broken bonds, NNBB, during the brittle propagation of internal crack.

The fracture energy is provided almost entirely by the work done by the externally applied constant load at the horizontal boundaries of the specimen, ΔW. The elastic strain energy of the system is practically constant during the brittle propagation of the internal cleavage crack, and therefore, its change is zero. The fracture energies resemble more of a double cantilever mode than those of mode I tensile fracture. $\Delta E_{el} \approx 0.0$ indicates that the solid behaved like two rigid bodies above and below the crack-line, during the crack growth. Due to the relatively short height of the sample, the information about the initiation of the fracture reaches the applied load only after 4 new crack-tip interatomic bonds are broken, and the externally applied constant load

responds to this event by working on the sample. During the sequential breaking of the first four crack-tip interatomic bonds, the fracture energy is essentially provided by the released strain potential energy in the specimen. Immediately after the detection of the onset of the fracture by the applied load at the horizontal boundaries of the specimen, the applied load takes over the role of the sole provider of the fracture energy, by increasing the work done on the sample proportional to c. However, the rate of change of the mechanical energy of the system, i.e., the driving force is identical for all sample sizes, implying that the terminal crack-tip velocities must be identical and therefore sample-size independent.

[Fig. II.3.23] The change in the mechanical energy of the pre-cleaved critically loaded 2D-triangular Johnson solid as a function of the number of new broken bonds, NNBB, during the brittle propagation of the internal crack of c_o=9.75d. Sample size (•) 159x135, σ_c=2.15; (x) 39x135, σ_c=1.45; (□)79x135, σ_c=1.90.

[Fig. II.3.24] The decrease in the elastic strain energy, ΔE_{el} of the pre-cleaved c_o=9.75 critically loaded σ_c=2.15 2D-triangular Johnson solid of sample size 159x135, vs c^2 during the brittle propagation of the internal crack.

Just past the initial stage of the brittle propagation of the cleavage crack, the functional dependence of the decrease in the elastic strain potential energy, $-\Delta E_{el}$, of the system on the instantaneous half crack-length, c, is the one predicted by the elasto-static continuum theory, i.e., $-\Delta E_{el}$ is a linear increasing function of c^2. However, the slope of the linear regression line is

.206, about 30% lower than the elasto-static predicted value of $\pi\sigma^2/M^*$=0258. Notice that this relationship is valid throughout the history of the growth of the running crack, even during the acceleration stage of the moving crack-tip where the velocity is much smaller than the terminal velocity and it is changing very rapidly. It is worth noting that the simulations results for the quasi-static crack extension are in good agreement with the predictions of the elasto-static continuum theories, being within 5% of them as demonstrated in Fig. II.3.25 and Table II.1.4.

[Fig. II.3.25] Energetics of the quasi-static crack extension as a function of c. The predictions of the quasi-static continuum theories are illustrated as $\pi c^2\sigma^2 / 2M^*$, for the comparison purposes.

[Fig. II.3.26] The change in the mechanical energy of the critically loaded pre-cleaved c_o=9.75 2D-triangular Johnson solid vs c^2 during the brittle propagation of the internal crack. Sample size: (•) 159x135, σ_c =2.15; (x) 79x135, σ_c =1.90; (o) 39x135, σ_c=1.45.

[Fig. II.3.27] The change in the energies of the critically loaded (under constant critical strain of ε_c= 0.061) pre-cleaved c_o=3.75 sample of 79x135, as a function of the number of new broken bonds, NNBB, during the brittle propagation of internal crack.

[Fig. II.3.28] The change in the energies of the critically loaded (under constant critical strain of ε_c= 0.047) pre-cleaved c_o=6.75 sample of 79x135, as a

function of the number of new broken bonds, NNBB, during the brittle propagation of internal crack.

[Fig. II.3.29] The change in the energies of the critically loaded (under constant critical strain of ε_c=0.041) pre-cleaved c_o=9.75 sample of 79x135, as a function of the number of new broken bonds, NNBB, during the brittle propagation of internal crack.

[Fig. II.3.30] The change in the "normalised mechanical energy" of the critically loaded pre-cleaved 2D-triangular Johnson solid, $-\Delta E_{me}/(\pi c^2 e^2 M^*)$ for constant external strain, and $-\Delta E_{me} M^*/(\pi c^2 s^2)$ for constant external stress, versus "normalised square of crack length", $(c/c_o)^2$ during the brittle propagation of the internal crack for varieties of sample sizes, loading conditions, and initial crack lengths.

[Fig. II.3.31] The change in the mechanical energy of the critically loaded pre-cleaved 2D-triangular Johnson solid, $-\Delta E_{me}$ vs c^2/M^* during the brittle propagation of the internal crack.

(Δ) 159x135, σ_c =2.15, c_o=9.75; (□) 39x135, σ_c=1.45, c_o=9.75;

(●) 79x135, σ_c =1.90, c_o=9.75; (X) 79x135, σ_c=3.37, c_o=3.75;

(o) 79x135, σ_c =2.45, c_o=6.75.

[Fig. II.3.32] The change in the mechanical energy of the critically loaded pre-cleaved 2D-triangular Johnson solid, $-\Delta e_{me}$, versus c^2M^* during the brittle propagation of the internal crack. Sample size: (⅄) 79x135, ε_c=0.061, c_o=3.75;

(+) 79x135, ε_c=0.047, c_o=6.75; (●) 79x135, c_o=9.75, ε_c=0.041 (O fast).

As demonstrated clearly, independent from the sample-size, i.e., H and c/W, initial half crack-length, c_o, or the loading scheme, the decrease in the mechanical (fracture) energy of the system is linear in c^2, in accord with the predictions of the elasto-static continuum theories of Griffith-Mott. Comparisons of Fig. II.3.30-32 indicate that M* corrections, i.e., the replacement of E by the effective instantaneous Young's modulus of the critically loaded specimen, M*, do not significantly influence the functional dependency of ΔE_{el}. However, it affects the slope of these linear functions. Therefore, the effect of M* corrections may be observed in the quantitative differences between those of the simulations results and the theoretical predictions as demonstrated in Table II.3.6.

[Fig. II.3.33] The change in the kinetic energy of the critically loaded pre-cleaved 2D-triangular Johnson solid, ΔE_{ke}, vs the Number of New broken bonds, during the brittle propagation of the internal crack.
(∇) 159x135, σ_c=2.15, c_o=9.75; (■) 79x135, σ_c =1.90, c_o=9.75; (x) 39x135, σ_c=1.45, c_o=9.75; (+) 79x135, σ_c=3.37, c_o=3.75; (⊕) 79x135, ε_c=.061, c_o=3.75; (•) 79x135, σ_c=2.45, c_o=6.75; (o) 79x135, ε_c=0.047, c_o=6.75.

[Fig. II.3.34] The change in the kinetic energy of the critically loaded pre-cleaved 2D-triangular Johnson solid, ΔE_{ke}, vs c^2 during the brittle propagation of the internal crack.

[Fig. II.3.35] The change in the kinetic energy of the critically loaded pre cleaved 2D-triangular Johnson solid, ΔE_{ke}, versus $c^2V_c^2$ during the brittle propagation of the internal crack.

[Fig. II.3.36] The change in the kinetic energy of the critically loaded pre-cleaved 2D-triangular modified Lennard-Jones solid with $a^*=1.0$, ΔE_{ke}, vs $(V_c c/C_1 M^*)^2$ during the brittle propagation of the internal crack.

[Fig. III.1A] Schematic diagram showing the relationship between allowable stress level and flow size. Solid line represents material fracture toughness K_C; dashed lines show the effect of plasticity.

[Fig. III.1B] Failure stress against temperature for intrinsic silicon; ○, brittle cleavage; ●, ductile failure.

[Fig. III.2] Orientation between the crack and the dislocation glide planes in 3D Si.

[Fig. III.3] Load-deflection curves for three temperatures bracketing a brittle-to-ductile transition.

[Fig. III.4] Critical stress intensity factors at fracture or flow versus temperature for five cross-head speeds showing the respective brittle-to-ductile transition.

[Fig. III.3.1] The (time averaged) linear coefficient of expansion of the LJCOVa.2 solid as a function of the temperature.

[Fig. III.3.2] The (time averaged) modulus of elasticity, $\langle M \rangle_t$, versus the equilibrium temperature of the 2D LJCOVa.2 solid, K_BT.

[Fig. III.3.3] Young's modulus, M, versus the externally applied load for the 2D-triangular LJCOVa.2 solid with $a^*=0.2$ at zero Kelvin.

[Fig. III.3.4] The (time averaged) density of the LJCOVa.2 solid, $\langle \rho \rangle_t$, as a function of the equilibrium temperature of the system, K_BT.

[Fig. III.3.5] Kosterlitz-Thouless parameter

$$K = [33d/28][M/K_BT] \geq 16\pi \qquad \text{for Solid} \qquad \text{III.3.4}$$

is plotted against the K_BT. The extrapolation of K to 16π discloses $K_BT_M \approx .34\varepsilon_o$ for the melting temperature of LJCOVa.2 solid which is in a surprisingly good agreement with the simulations results.

[Fig. III.4A1] The critically loaded $\sigma_c=2.1$ pre-cleaved $c_o=3.75d$ LJCOVa.2 solid is at $K_BT=0$. The simulations results are tabulated in Table III.4A1.

[Fig. III.4A2] The critically loaded $\sigma_c=1.9$ pre-cleaved $c_o=3.75d$ LJCOVa.2 solid is at $K_BT=0.02\ \varepsilon_o$. The simulations results are tabulated in Table III.4A2.

[Fig. III.4A3] The overloaded σ=2.0 pre-cleaved c_o=3.75d LJCOVa.2 solid is at K_BT=0.02 ε_o. The simulations results are tabulated in Table III.4A3.

[Fig. III.4A4] The critically loaded σ_c=1.90 pre-cleaved c_o=3.75d LJCOVa.2 solid is at K_BT=0.046 ε_o. The simulations results are tabulated in Table III.4A4.

[Fig. III.4A5] The critically loaded σ_c=1.80 pre-cleaved c_o=3.75d LJCOVa.2 solid is at K_BT=0.056 ε_o.

[Fig. III.4A5*] The overloaded σ=1.90 pre-cleaved c_o=3.75d LJCOVa.2 solid is at K_BT=0.056 ε_o. The simulations results are tabulated in Table III.4A5*.

[Fig. III.4A6] The critically loaded σ_c=1.80 pre-cleaved c_o=3.75d LJCOVa.2 solid is at K_BT=0.060 ε_o. The simulations results are tabulated in Table III.4A6.

[Fig. III.4A7] The critically loaded σ_c=1.80 pre-cleaved c_o=3.75d LJCOVa.2 solid is at K_BT=0.060 ε_o. The simulations results are tabulated in Table III.4A7. The history of the run is different from that of III.4A6.

[Fig. III.4A8] The critically loaded σ_c=1.80 pre-cleaved c_o=3.75d LJCOVa.2 solid is at K_BT=.0628 ε_o. The simulations results are tabulated in Table III.4A8.

[Fig. III.4A9] The critically loaded σ_c=1.80 pre-cleaved c_o=3.75d LJCOVa.2 solid is at K_BT=0.0625 ε_o. Simulations results are tabulated in Table III.4A9. The history of the run is different from that of III.4A8.

[Fig. III.4A10] The critically loaded σ_c=1.80 pre-cleaved c_o=3.75d LJCOVa.2 solid is at K_BT=0.075ε_o. The simulations results are tabulated in Table III.4A10.

[Fig. III.4B1] The critically loaded σ_c=2.40 pre-cleaved c_o=3.75d LJCOVa.2 solid is at K_BT=0.0193ε_o. The simulations results are tabulated in Table III.4B1.

[Fig. III.4B2] The critically loaded σ_c=2.20 pre-cleaved c_o=3.75d LJCOVa.2 solid is at K_BT=0.068 ε_o. The simulations results are tabulated in Table III.4B2.

[Fig. III.4B3] The critically loaded σ_c=2.00 pre-cleaved c_o=3.75d LJCOVa.2 solid is at K_BT=0.0904ε_o. The simulations results are tabulated in Table III.4B3.

[Fig. III.4B3*] The overloaded σ_a=2.10 pre-cleaved c_o=3.75d LJCOVa.2 solid is at K_BT=0.0892ε_o. Simulations results are tabulated in Table III.4B3*.

[Fig. III.4B4] The critically loaded σ_c=1.80 pre-cleaved c_o=3.75d LJCOVa.2 solid is at K_BT=0.105 ε_o. The simulations results are tabulated in Table III.4B4.

[Fig. III.6A1] The critically loaded σ_c=2.30 pre-cleaved c_o=3.75d COR.LJCOVa.2 solid is at K_BT=0.0193 ε_o. The simulations results are tabulated in Table III.6A1.

[Fig. III.6A2] The critically loaded σ_c=2.10 pre-cleaved c_o=3.75d COR.LJCOVa.2 solid is at K_BT=0.0634 ε_o. The simulations results are tabulated in Table III.6A2.

[Fig. III.6A2*] The overloaded σ_a=2.20 pre-cleaved c_o=3.75d COR.LJCOVa.2 solid is at K_BT=0.062 ε_o. The simulations results are tabulated in Table III.6A2*.

[Fig. III.6A3] The critically loaded σ_c=2.20 pre-cleaved c_o=3.75d COR.LJCOVa.2 solid is at K_BT=0.0675 ε_o. The simulations results are tabulated in Table III.6A3.

[Fig. III.6A4] The critically loaded σ_c = 2.00 pre-cleaved c_o = 3.75d COR.LJCOVa.2 solid is at K_BT = 0.0790 ε_o. The simulations results are tabulated in Table III.6A4.

[Fig. III.6A5] The critically loaded σ_c=2.00 pre-cleaved c_o=3.75d COR.LJCOVa.2 solid is at K_BT=0.0857 ε_o. The simulations results are tabulated in Table III.6A5.

[Fig. III.6A6] The critically loaded σ_c=1.95 pre-cleaved c_o=3.75d COR.LJCOVa.2 solid is at K_BT=0.104 ε_o. The simulations results are tabulated in Table III.6A6.

[Fig. III.6A7] The "critically" loaded σ=1.90 pre-cleaved c_o=3.75d COR.LJCOVa.2 solid is at K_BT=0.120 ε_o.

[Fig. III.6A8] The "critically" loaded σ_c=1.80 pre-cleaved c_o=3.75d COR.LJCOVa.2 solid is at K_BT=0.136 ε_o. The simulations results are tabulated in Table III.6A8.

[Fig. III.6A9] The "critically" loaded σ=1.60 pre-cleaved c_o=3.75d COR.LJCOVa.2 solid is at $K_B T$=0.170 ε_o.

[Fig. III.7A1] The critically loaded σ_c=2.40 pre-cleaved c_o=3.75d 2D-triangular Johnson solid is at zero Kelvin.

[Fig. III.7B1] The critically loaded σ_c=2.50 pre-cleaved c_o=3.75d 2D-triangular Johnson solid is at 295 Kelvin. Sample size is 39x64.

[Fig. III.7C1] The critically loaded σ_c=3.37 pre-cleaved c_o=3.75d 2D-triangular Johnson solid is at absolute zero temperature. Sample size is 79x68.

[Fig. III.7C2] The critically loaded σ_c=2.80 pre-cleaved c_o=3.75d 2D-triangular Johnson solid is at 110 Kelvin. Sample size is 79x68.

[Fig. III.7C3] The critically loaded σ_c=2.60 pre-cleaved c_o=3.75d 2D-triangular Johnson solid is at 296 Kelvin. Sample size is 79x68.

[Fig. III.7C4] The critically loaded σ_c=2.30 pre-cleaved c_o=3.75d 2D-triangular Johnson solid is at 404 Kelvin. Sample size is 79x68.

[Fig. III.7C4*] The overloaded σ_a=2.40 pre-cleaved c_o=3.75d 2D-triangular Johnson solid is at 404 Kelvin. Sample size is 79x68. The critical load is 2.30.

I. ***INTRODUCTION***

The mechanical failure of materials through fracture is a subject of obvious economic importance and is of considerable interest to materials engineers and solid state physicists.

Through the ages, the applications of materials in engineering design have posed difficult problems. Shaping and production of materials was once the main problem. With the improved skill of metal working, applications of metals in structures increased, progressively. Then, it was experienced that, structures built of these materials did not always behave satisfactorily, and unexpected failures often did occur.

The rapidly increasing use of metals in the nineteenth century caused the number of accidents to reach very high levels. The number of people killed in railroad accidents in Great Britain was about two hundred per year during 1860-1870. Most of the accidents were the result of derailing caused by fracture of wheels, axles or rails. Anderson [12] has made an interesting compilation of accident reports from the last two hundred years. Some of these accidents were certainly due to a poor design, but it was gradually discovered that material deficiencies in the form of preexisting flaws could initiate cracks and fractures. The failures often occurred under conditions of low stresses (several ships failed suddenly in the harbor) which made them seemingly inexplicable. The fractures were truly brittle: they were accompanied by no, or very little plastic deformation. It turned out that the brittle fracture of steel was promoted by low

temperatures, and by conditions of triaxial stress such as those existing at the tip of sharp notch, crack, or a flow. Under these circumstances, structural steel can fracture by cleavage without any noticeable plastic deformations. Above a certain temperature, called the "brittle-to-ductile transition (BDT)" temperature, the steel behaves in a ductile manner. The basic mechanisms of BDT is governed at the crack tip by atomic processes [13].

The fracture of solids may be considered as the formation of new surfaces in the medium, in a thermodynamically irreversible manner. The essential feature of the phenomenon is the rupture of cohesive bonds in the material. The fracture of solids may be classified into two broad categories: brittle, and ductile fractures. Ductile fracture is usually associated with large deformations, high rates of energy dissipations, and slow fracture velocities. The surface of the fracture is rough in the ductile mode of failure. Brittle fracture, on the other hand, is a low energy failure, which takes place in a catastrophic manner. The surface of the cleavage crack is smooth, and very shiny.

As quoted in the prologue to a paper by Tipper [14], Mott stated in 1949 that: "quite apart from its practical importance, fracture is the most interesting property of solids to theoreticians because it is the least understood property, no progress having been made beyond the 1924 Griffith's crack theory. It is not known how cracks exist, nor what cause them. Experimental work has made clear what happens during fracture, but not how it occurs." The situation is not very different at the present time. The theoretical study of fracture process

requires the simultaneous consideration of macroscopic effects, the nature of the material, and the microscopic phenomena. At microscopic level, one is interested in the events taking place in the material within distances of the order of 10A°. The approach should use quantum theory. At the other extreme, where one is interested in the phenomena taking place in the material at a distance of 0.01 cm and up, the material may be considered as a homogeneous continuum, and tools of thermodynamics and continuum mechanics may be used to study the phenomena.

The description of a crack in a solid with an applied external tensile load or strain is rather simple to envision. One has a semi-infinite periodic three-dimensional array of atoms interacting with one another via an interatomic potential. A crack is inserted in the solid and load is applied externally to appropriate surfaces. If the load is sufficiently large, the crack grows and the solid ultimately fractures. Why is the phenomenon so much more difficult to treat than other problems encountered in the solid state physics? In the most fundamental phenomena in solids, the periodicity of the solid is used to reduce the problem to an examination of a simple representative cell or region. Hence, the infinite number of atoms is not a serious problem. In the case of a crack, with its finite extension and the resulting long-range strain field, such reductions are prohibited [15]. Hence, due to the highly complex nature of the problem, lack of full physical understanding, and insufficient mathematical tools, at the present time, there is no consistent single theory dealing with all the relevant aspects of fracture, and the fracture theories tend to treat the phenomenon from only one of the three points of view, namely: statistical mechanics, continuum

mechanics, and micro structural approaches. In every case, one has to resort to simplified models to try and gain insight into the role of cracks in brittle fracture. In every approach, some trade off has been made between giving up some aspect of the phenomenon in nature for some simplifications that enables one to carry out a quantitative study [15].

In 1776 Coulomb [16] expressed the view that fracture of a solid would occur, if the maximum shear strain at some point in the material, surpassed a critical value characterizing the mechanical strength of the material. Although the suggestion is of no more than a historic interest, it may be noted as the oldest of a number of "empirical" critical stress, or critical strain relations [17].

From the beginning of this century, much attention has been paid to the problem of the sudden breaking of components. In 1920, Griffith [18] proposed an explanation of fracture strength of glass, based on the idea that glass contains crack-like flaws. Griffith reasoned that the largest crack-like flaw would become self-propagating when the rate of the release of the stored strain energy in the solid becomes greater than the rate of spending energy by the extending crack. Taking account of this energy approach, but without going into detail about the fracture process at the crack tip, Griffith established a fracture criterion [18,19], which forms the basis of modern day fracture theories.

During 1938, a statistical concept of mechanical strength was introduced. A widely known exposition of this viewpoint, sometimes referred to as a "worst flaw" theory is due to Weibull [20], who showed that fracture

strength might be expected to depend upon the extent of the region of the greatest stress, as well as the magnitude of the stress. The fracture mechanics, based on the statistical mechanics approach, simplify and idealize the material with respect to the kinetics of its atomic structure, and on the other hand, ignore its local geometry and mechanism with respect to micro structures and stress state. Hence, these theories provide some phenomenological insight, but not a satisfactory quantitative theory. At this level, the approach is quite general, and is applicable to all solids.

The macroscopic theories of fracture assumes the existence of cracks, voids, or other imperfections, which may readily act as fracture nuclei. The size of these imperfections is assumed to be sufficiently large compared to the characteristic dimensions of the micro structure to justify the use of the tools of continuum mechanics. Theses theories consider the material to be a homogeneous continuum with certain, usually, idealized properties. They approach the problem from an entirely field point of view, using the tools of the continuum mechanics, and classical thermodynamics.

In the macroscopic approach to the fracture problem, it becomes necessary to devise a model for the actual phenomenon, and postulate a "criterion" for fracture. Among such criteria, one may mention the "maximum strain criterion" proposed by McClinton [21], Krafft and Irwin [22]; the "critical stress intensity factor" criterion of Barenblatt [23], which may be considered as a maximum stress, or an energy criterion, depending on the interpretation of the stress intensity factor [24]; and the "energy-balance" criterion [3-6,18-19]. In

general, all energy-balance criteria are based on a simple classical thermodynamics notion that the fracture will continue to propagate, if for a unit increase in fracture surface, the increase of externally added, or internally released energy is greater than the amount of stored and dissipated energies. Fracture is a kinetic phenomenon, hence, there should be a balance between the rates of input, stored, dissipated, and kinetic energies. Partly due to the generality and physical soundness of the underlying principle, and partly due to its flexibilities, energy-balance criteria form the basis of, by far, the most used and accepted fracture theories. As mentioned above, the first energy-balance theory was formulated by Griffith [18,19] for the fracture of ideally brittle materials in which surface energy is the only source of energy dissipation. The subsequent theories have dealt mainly with the modifications, and generalizations of Griffith's work. Among the notable generalizations of the Griffith's energy-balance concept, one may note the work done by Rivlin and Thomas [25], who studied the tearing of a rubber vulcanite, and introduced the concept of "characteristic tear energy" to replace the "surface free energy" term in the Griffith's theory. This theory has been very useful in the investigation of high energy type fracture, and has been successfully applied to the fracture of polymers [26-29]. The modifications to the Griffith's theory offered by Orowan [30], and Irwin [31] deal with the introduction of the plastic work as an additional source for "energy-dissipation", extending the application of the theory to the fracture of metallic materials. Probably, the most significant extension of Griffith's theory was made by Mott [3] who included the kinetic energy term in the energy-balance equation, in the investigation of the dynamics of fracture. Roberts and Wells [32], recognizing the finite sample effect, modified Mott's

theory, and derived an expression for the velocity of propagation of a cleavage crack. A different approach was taken by Eshelby [7] who used the continuum mechanics wave equation for the displacements resulting from the stresses to obtain an expression for the stress intensity factor, and for the crack tip velocity. Freund [4-6] investigated the "dynamic crack propagation" analytically, and compared his results to the experimental results available at the time. Freund's approach is seemingly different from that of Mott's, but his approach is also based on the concept of the conservation of energy, using the "dynamic" stress intensity factor based on continuum mechanics. In these theories, the rate of the change of the dissipative energy with respect to the fracture area, called the "surface free energy", "tear energy", "fracture energy", or "fracture toughness", plays an important role. It is considered to be an intrinsic property of the material, and is dependent on the environmental conditions, temperature, strain rate, type of loading, and the nature of the material.

For those who concern themselves primarily with the question of when fracture occurs, as engineers do, the methodology of fracture mechanics appear to be totally adequate as a predictive tool. However, if one starts to ask why fracture occurs, things start to go wrong. For, the critical process of crack propagation occurs in the immediate vicinity of the crack-tip, where the linear elastic continuum solutions show singularity. Thus, in inquiring how stresses remotely applied at the outer boundaries of a specimen transmit to the crack-tip, there is a limit as to how far we may go with the conventional fracture mechanics. The way engineers circumvent this difficulty is to write down an empirical "criterion" for the possible extension of the preexisting crack, in terms

of various parameters which characterize the intensity of the locally concentrated stress field; the distribution of stresses within the field being taken to be invariant. A similar disregard for geometrical details is adopted in the description of flaws simply as "micro cracks", a scaled down version of the well-defined cracks whose characteristic dimensions may be determined by the empirical testing procedures. In short, engineering fracture analysts concern themselves with the mechanics, as distinct from the mechanisms of the crack growth. Therefore, if we wish to understand fracture process at a fundamental level, our attention must turn to the latter aspect. In fracture, as in any thermodynamics process, the final answers must be sought at the atomic or molecular level. For, it is the nature of the cohesive bonding between the constituent atoms in the solid which ultimately determines the resistance to the propagation of the crack. A quantitative understanding and description of micro structures including regions in the vicinity of the defect on an atomic level could lead to very powerful insights, predictive and, therefore, possible preventive capabilities in material science and engineering. It is very difficult to study real materials, in atomic level, experimentally at the present time. Hence, one must resort to simplified models to try to gain insight into the role of preexisting cracks in the brittle fracture process. Therefore, various discrete or lattice models have been proposed. If we are to predict the behavior of materials at a macroscopic level, we have to begin with some structural models of solid with a great number of atoms. Modeling involves two basic steps:

i. The construction of a model incorporating the key physical features of the system.

ii. Calculations, analytically by computer simulations of the physical characteristics of interest.

The limitations of the results are, then, those of the model itself. Modeling may lead to very significant insights. But, it is essential to determine which parts of the results are (or may be) artifacts of the model, and which parts are general and relevant to the real physical system being modeled [15]. Because of the complications of the problem under investigation, there are various approaches. In each case, some tradeoffs have been made between giving up some aspects of the phenomena in nature for some constraints and simplifications in the model, which enable one to carry out a quantitative study. Each model has emphasized a different aspect of the real phenomena. Tradeoffs vary between the sample size, the interatomic potentials, dimensions, and boundary conditions. If the semi-infinite periodic nature of the system is of major concern, then one is led to the "lattice statistics" methods [15] the key feature of which is the treatment of an infinite number of atoms via some oversimplified unrealistic interatomic potentials in one or two dimensional discrete lattices. The method varies, somewhat, with the particular problem under investigation [33-35]. In the "hybrid lattice statics model" a very small crystalline region near the crack tip, where both the atomic structure and interatomic interactions are treated explicitly, is embedded in an outer "infinite" medium where the interatomic force law and also the atomic structure are simplified [15, 36-38]. The boundary matching between the inner and outer regions, the appropriateness of the embedded medium, and the simplifications of the outer region are the major approximations in this method [15]. For long-

range potentials the serious tasks to overcome are those of the lattice mismatch, force mismatch, and the image forces at the boundary. The image forces at the boundary may impede the possible movements of defects.

If the nature of the interatomic interactions and of the atomic motions are the major concern, one is led to the molecular dynamic techniques, which may be used on an unconstrained ensemble of a "large" number of atoms interacting via realistic interatomic forces. Here, of course, the question is how "large" is large enough to represent and simulate the behavior of the corresponding macroscopic systems. Finite memory of computers, the dynamic nature of the method, and therefore the computation time, the available time in the main-frame super-computers for a given investigator, and specially choosing a realistic interatomic potentials are major limitations of this techniques.

Aside from fatigue, perhaps the most serious concern of material engineers, when it comes to practical fracture control, is the worry that a material may undergo an unexpected transition from its "normal" strength to a much lower and dangerous value, because of some unforeseen change of conditions, either of the material, or in the way it is used. In general, parameters which control the strength of the material, once it is fabricated, are temperature, strain rate, and the external chemical environment. The transition in fracture from an energy absorbing ductile mode to a brittle cleavage mode is an important limitation of crystalline solids in their use in structures [39]. Many materials are inherently brittle at very low temperatures in the sense that cleavage cracks can propagate without absorbing any plastic work. However,

with increasing temperature these inherently brittle solids generally pass through a transition in which plastic processes at the tip of a propagating crack become increasingly significant, and energy absorption, correspondingly, increases [40]. The stress concentration that arise at the tip of a crack may induce the plastic deformation in their neighboring material, and this plastically strained region is known to modify the conditions for the propagation of the crack. Despite the importance of the crack tip relaxation by dislocations in the fracture problem, only very few observations have been done under well defined loading conditions [41].

Fundamental understanding of the factors controlling the brittle, or the ductile behavior, and the brittle to ductile transition are of particular interest for the solid state community, material science, as well as, engineering and design societies. It is essential, however, to recognize the limitations in the application of the transition temperature philosophy to the component design. The defined transition temperature will depend not only on the measurement criteria, but also on the thickness of the specimen [42], and the initial crack length. As demonstrated in Fig. III.1A, a notched bar with crack length, $2c_1$, would be brittle at room temperature, but the same material with a crack length, $2c_3$, would exhibit tough behavior. Since the brittle region of this curve is truncated by the onset of the plastic deformation when the applied stress reaches the material yield strength, the brittle domain may be expanded simply by lowering the test temperature. For this reason, a wide range of the "transition temperatures" may be obtained simply by changing the specimen thickness of the sample and/or initial crack. Therefore, transition temperature values

obtained in the laboratory bear little relation to the performance of the full scale components thereby necessitating a range of correction factors [42].

A necessary condition for fully brittle cleavage is that no generation or motion of dislocation in the vicinity of the crack tip may occur during the propagation of the crack. There can be energy absorption and even crack blunting due to the motion of preexisting dislocations, the extent of which will depend on the dislocation density. However, if dislocation nucleation can occur at the crack tip, this will result in the crack blunting and energy absorption, even if the density of preexisting dislocations is very low.

Pre-cleaved single crystals of materials such as silicon exhibit a very sharp transition from brittle to ductile behavior with increasing temperature, and it seems likely in cases such as this, that the BDT is due to the onset of dislocation nucleation [40].

A crack cannot run rapidly through a solid unless the rate of the release of the strain energy with the growth of the crack is at least equal to the work done in producing new areas of the crack surface. The work done by the applied stress per unit area of fracture, γ_p, is a property of the material which depends upon the state of stress and upon the temperature. A truly brittle substance is one in which $\gamma_p=2\gamma_s$, where γ_s is the specific surface free energy of the solid at the temperature in question. A ductile crystal fails by plastic shear, through the motion of dislocations, and the measured values of γ_p then rise to as much as $10^5\,\gamma_s$.

The boundary between ductility and brittleness is not a sharp one. Any crystal which can be cleaved must be inherently capable of propagating brittle cracks, at least at low temperatures. It becomes ductile under certain conditions, where these cracks are prevented from forming or from propagating [43]. The atomic displacements near the crack tip are, in the limit of long initial cracks and small applied stresses, a property of the solid. For, they depend on the interatomic forces, on the modes of failure, i.e., cleavage or slip, and on the failure stresses of these modes [43].

The stress field near the crack tip in a linearly elastic solid is of the form

$$\sigma_{ij} = K (2\pi r)^{-1/2} b_{ij} (\theta) \qquad \text{III.1}$$

where K is the stress intensity factor, and (r,θ) are polar coordinates with its origin at the crack tip [33]. At the crack tip where $r \rightarrow 0$ as the interatomic cohesive bonds are stretched beyond the region of harmonic behavior, nonlinear treatment of the problem is required. As the stress intensity at the crack tip increases, lattice failure will eventually occur at the tip in the nonlinear region. The failure can occur by bond rupture in either tension or shear, which will determine whether the behavior is inherently brittle or ductile [40].

Davidenkov and Wittman [44] in 1937 proposed the so called "classical" theory of the brittle-to-ductile transition temperature. They suggested that the existence of a transition temperature in the solid is due to the difference in the way the resistance to shear and cleavage changes with the temperature. The

relative value of these two intrinsic properties of the material determines whether the fracture will be ductile or brittle. Above the transition temperature, the flow stress is reached before the fracture stress, while below the critical transition temperature the fracture stress is reached first. Decreasing the temperature, and increasing the strain rate, both, have this effect. Even though this picture of the brittle-to-ductile transition temperature does not provide the structural details embodied in the dislocation theory of the BDT, it does give an easy to grasp working model.

Kelly, Tyson, and Cottrell (KTC) in their historic 1974 paper [43] pointed out that at the tip of a sharp crack, when the K level is high enough to generate cleavage, it is also in the range to initiate spontaneous shear breakdown. They investigated whether a crack can propagate in a fully brittle manner in a particular material by calculating the mode of failure at absolute zero temperature at the tip of a crack in a crystal that contains no preexisting dislocations. They proposed that "if the ratio of the largest tensile stress to the largest shear stress close to the tip of an equilibrium crack in the crystal is grater than the ratio of the ideal cleavage stress to the ideal shear stress, then a fully brittle fracture is possible" [43]. In the converse case they assumed that some dislocations must be generated in the process of cracking, and that the work of fracture will necessarily be larger than the surface energy. Therefore, inherently brittle failure would be observed if

$$(\sigma/\tau)_{id} < (\sigma/\tau)_{max} \qquad \text{III.2}$$

Here the subscripts "id" and "max" refer to the ideal properties of a perfect lattice and to the maximum values attained at a crack tip, respectively. This model correctly predicts the ductility of the fcc metals, and the brittle nature of diamond, but is not sufficiently detailed to make predictions for the wide range of intermediate materials [45].

Rice and Thomson in their classic 1974 paper [46] extended KTC approach, and analyzed the problem in terms of dislocation emission from the crack tip. They reasoned that if the shear breakdown occurs at the crack tip, the result is dislocation emission, suggesting that ductile behavior will occur when a crack tip spontaneously emits dislocations before fracture. The emitted dislocations would reduce the stress intensity at the crack tip by blunting and shielding the crack tip by effectively exerting a back-stress on the crack [46]. They proposed that after the emitted dislocation expands under the external stress field as concentrated by the presence of the crack; an atomically sharp crack would have been blunted by one atomic plane. This blunted crack will then be trapped at the original lattice position until the externally applied stress is increased substantially (when, probably further blunting dislocations may be possible). Crystals for which dislocation emission is spontaneous may be expected to be good candidates for essentially plastic opening of the crack. On the other hand, crystals for which there exists a large energy barrier for the dislocation emission, may be expected to be good candidates for brittle cleavage. In order for a dislocation to blunt a crack, it is necessary for the Burgers vector to have a component normal to the crack plane and to intersect the crack line along its whole length. They calculated the stability of a sharp

crack against the emission of a blunting dislocation for varieties of crystals in two dimensions, and the energy to form a stable loop of dislocation from the crack tip in three dimensions. Rice and Thomson then calculated forces acting on a dislocation which had been emitted from the crack tip of an atomically sharp crack tip. They found a critical distance from the crack tip, ξ_c, beyond which the generated dislocation would be repelled from the crack, and could therefore be considered to be emitted. Their criterion for ductility is that the critical distance, ξ_c, should be less than the dislocation radius, ξ_d. Qualitatively, Rice and Thomson found that crystals whose dislocations have wide cores and small values of the parameters $\mu b/\gamma$, i.e., $\mu b/\gamma \leq 7.5$ to 10, were ductile, while crystals with narrow cores and large values of $\mu b/\gamma$ were brittle. They treated the problem within the approximation of the linear elasticity and Peierls model of dislocation .

However, both RT and KTC treatments required approximations in their quantitative development. The stress analysis of the linear elasticity was used to evaluate $(\sigma/\tau)_{max}$ and forces on dislocations in the immediate vicinity of the crack tip. On the other hand, plausible models of the nonlinear and atomistic behavior of materials are required to evaluate $(\sigma/\tau)_{id}$ and the dislocation structure. Since it is essential to have a clear description of crack tip processes and energetics in order to understand the effect of temperature, it is important therefore, to evaluate predictions of these treatments in order to gauge the validity of approximations used.

Tyson [40] in analyzing and comparison of KTC and RC models concluded that in the presence of thermal vibrations, the crack motion may be understood on the basis of Rice and Thomson's theory [46] for the dislocation nucleation at the crack tip. However, Rice and Thomson [46] predicted a very large energy barrier to dislocation emission from the crack tip for the crystals they investigated. Such materials, therefore, must remain brittle even close to their melting temperature. This is contrary to the experimental observations. Silicon, for example, undergoes a very sharp brittle to ductile transition at about $(2/3)T_m$, where T_m is the melting temperature of Si [45]. However, the prohibitively high activation energy of 111 ev calculated initially by Rice and Thomson [46] for the nucleation of small dislocation loops from the crack tip for Si has been questioned, and more recent estimates and different saddle-point configurations suggested much smaller values [47-50]. All of these theoretical estimates are subject to large uncertainties in the calculations [8]. Tyson [40] also concluded that KTC criterion is both necessary and sufficient for the brittle-to-ductile transition, although the sufficiency was not proven. Both RC and KTC models deal with essentially atomic properties of the crack tip by quasi-elastic means [51], and they are physically equivalent as pointed out by Lin [52]. The difficulties associated with accurately estimating forces on dislocations in highly nonlinear region at the crack tip must be realized. The critical distance, ξ_c, at which a straight dislocation is in unstable equilibrium, is only of the order of the Burgers vector, b, and the application of the linear continuum elasticity in this region is clearly an oversimplification [40]. More exacting attempts have addressed the problem via computer simulations with two dimensional atomic models. However, since only inadequate interatomic force laws exist for atoms

in the vicinity of such a severe distortion as a critically loaded crack, these calculations also have major limitations and the predicted results are, at the best, a qualitative and general descriptions of the phenomena, and therefore inapplicable to any real material. Thus, the current theoretical situation is not satisfying from a quantitative point of view [51], though considerable qualitative insight is available. Experimentally it has been established that at least under certain conditions dislocation emission and cleavage can coexist in the same material. It does not seem to be possible to present an electronic theory of dislocation cores and crack tips in bcc transition metals which are in the center of the fracture problem [47]. Instead, the electronic aspect has become more transparent in semiconductors with diamond structure, which undergo a macroscopic brittle to ductile transition at about sixty percent of their absolute melting temperature [53]. Haasen [47] pointed out that the brittle-to-ductile transition is determined by the dislocation mobility and not by the nucleation process.

St. John [54] was the first to study the brittle-to-ductile transition temperature, experimentally, in mode I on pre-cleaved "dislocation-free" silicon single crystal between -196°C and 1000°C at various strain rates. Monocrystalline silicon was chosen for several reasons, in spite of the fact that this material possesses only partial covalent bonding [54]. Dislocation glide in Si is strongly rate-dependent, appreciable movement occurs only above 600°C. The glide systems are easily analyzed because of their similarity to the fcc glide systems. Furthermore, Si is particularly amenable to large scale analysis of dislocation arrangement by X-ray topography. Silicon can easily be obtained in

the form of large, essentially dislocation-free, single crystals, which aids considerably the interpretation of X-ray topographs [54]. Finally, there are extensive data available on dislocations and their velocities under various conditions of stress, temperature, and doping in Si [48, 55-56] which makes it an ideal material to use in the brittle-to-ductile transition, BDT, investigations [45]. St. John [54] found that the transition from pure cleavage to the general yielding at the crack tip occurred over several degree Centigrade, and that the BDT temperature was rate dependent with an activation energy of 1.9 ev. This value is reasonably close to 1.8 ev found by Kannan [57] for the glide of screw and 60° dislocations in silicon at similar temperatures. St. John's direct observations by Lang X-ray topography showed that the number of emitted dislocations from a static crack tip increases rapidly in the transition region. The resolved dislocations in the X-ray topographs were all in the screw or 60° orientation [54]. The trapezoid shape of the thin Si plate provides on the crack-line loading in mode I, a high K at a relatively low nominal stress, and also only a weak dependence of K on the initial crack length. Fig. III.2 shows the crystallography with respect to the crack. Fig. III.3 shows St. John's load-deflection curves at three temperature bracketing a brittle to ductile transition. At the lower temperatures, the specimen fractures at an average critical stress-intensity factor $K_C=9.37\times10^7$ dynes/cm$^{3/2}$ where

$$K_C = [2E\,\gamma_i / (1-\nu^2)]^{1/2} \qquad \text{Plane Strain} \qquad \text{III.3}$$

and γ_i is the fracture surface-energy for the fracture initiation which is determined to be 2700 ergs/cm^2 at the room-temperature. E is Young's modulus

being 1.55×10^{12} dynes/cm² and ν=0.215 is Poisson's ratio. An average fracture surface-energy, γ_a, of 2300 ergs/cm² is obtained from the crack-arrest data which results in

$$\gamma_a / \gamma_i = 0.85. \qquad \text{III.4}$$

It can be seen in Fig. III.3 that the load at fracture increases rapidly from values typical of low-temperature fracture [54], while, X-ray topography shows the formation of a limited plastic zone before the specimen fractures. The curve for the highest temperature in the series exhibits general yielding as the applied load-deflection goes through a maximum value with increasing T. Fig. III.4 shows, in the stress-intensity form, the temperature dependence of maximum loads attained in the load-deflection curves for 29 specimens tested at five different cross-head speeds. The abruptness of the BDT is evident. The rapid increase in fracture load is a manifestation of the rate dependence of a crack-tip blunting mechanism. The X-ray topographs by St. John [54] and more recently by George et al. [48, 55] give the shape of the plastic zone in the region of the original crack tip. No dislocations were ever observed at the static crack tips in the low temperature plateaus of K_C, nor in connection with moving crack tips. In the plastic zone George et al. [48, 55] counted 10^6 dislocations per cm² within a radius of 100 μm, and 10^4 /cm² somewhat beyond, altogether about several hundred dislocations. St. John [54] concluded that, at low temperatures, a greater strain-energy release-rate was required to initiate than to maintain propagation, and that the excess strain-energy release at the onset of propagation will be transformed into the kinetic energy of the crack.

The rapid increase of the fracture load within the transition temperature range for any particular deflection rate, according to St. John [54] is due to the rate-sensitive production and/or glide of dislocations from the crack-tip into previously "dislocation free" solid. The mechanical stability of the initially atomically-sharp crack is strongly influenced by the resultant crack-tip blunting. The singular aspect of these fracture experiments is the complete dependence of crack-tip blunting on the nucleation and glide of dislocations from the crack tip, since the initial dislocation density is zero. The crack-tip radius is, therefore, the sum of the elastic component, ρ_e, and a plastic component, ρ_p

$$\rho = \rho_e + K^2 / 2E\sigma_y \qquad \text{III.5}$$

where σ_y is the yield-stress.

Empirically, the dislocation velocity, V, may be described as a function of the applied force per unit length, F, acting on the dislocation [58]

$$V=DF^n \exp(-U/K_BT) \qquad \text{III.6}$$

where D and n are material constants, U is the activation energy of the dislocation and K_B is Boltzmann's constant. The force, F, acting on any particular glide system (glide plane, n_i, and Burgers vector, b_j) in the case of an isolated dislocation in the crack-tip region is given by

$$F=n_i . \sigma_{ij} . b_j \qquad ; i, j = 1,2,3$$

$$\sigma_{ij}=[K/(2\pi r)^{1/2}] \sigma_{ij}(\theta /2) \qquad \text{III.7}$$

where σ_{ij} is the crack-tip stress tensor. The polar coordinates (r, θ) are centered on the crack tip (Fig. III.2) and K is the stress-intensity factor. For each of the twelve glide systems the force per unit dislocation length is

$$F_i = [a_o K/2(3\pi r)^{1/2}]\, F_i(\theta/2) \qquad ; i=1,2...12 \qquad \text{III.8}$$

where a_o is the lattice parameter. The radial velocity with which a particular force level, F_i, moves away from the static crack-tip during loading is

$$r^\circ = [a_o^2 F_i^2(\theta/2)/6\pi\,][KK^\circ / F_i^2) \qquad \text{III.9}$$

where K° is the applied stress-intensity rate which may be assumed constant for a given applied displacement rate, δ°. Therefore, the dislocation velocity is an increasing function of the applied stress while the radial velocity of the force-field increases with decreasing force. This implies that a dislocation moving away from the crack tip will be accelerated or decelerated according to whether the instantaneous velocity is less or greater than that of the surrounding stress field. Hence, the effective yield stress is

$$F_{iy} = \{L\,\delta^\circ\, K \exp(U/K_B T)\}^{1/(n+2)} \qquad \text{III.10}$$

where,

$$L = [Ha_o^2 F_i^2(\theta/2)] \;/\; [6\pi\, D\, C\, f_i(\theta/2)] \qquad \text{III.11}$$

where C is the elastic compliance of the system and H is the constant of proportionality between the load and the stress-intensity factor. For an ideally

plastic material n approaches infinity. Silicon represents the opposite extreme, since the parameter n approaches the Newtonian limit of one [59].

The effect that the parameter n has on the abruptness of the BDT may be appreciated by realizing that

$$d/dT\ [\ \Delta K/K_O\ ] \approx [U/(n+2)]\ [\ \Delta K/K_O\ ]/K_B T^2 \qquad \text{III.12}$$

where $\Delta K = K_C - K_O$. The term $U/(n+2)$ is therefore an important material parameter in determining whether a solid will have an abrupt BDT.

In St. John's view [54] blunting of the crack tip was regarded to be responsible for the BDT. The transition temperature is then determined by the nucleation and glide of dislocations which blunt the crack tip. The BDT was identified as an event determined only by the thermally activated migration of dislocations [54]. The plastic zones which developed at high temperatures were investigated by reflection X-ray topography. However, dislocations close to the crack tip could not be resolved by this technique. The beginning of plasticity, therefore, could not be studied in detail [54].

Haasen [47] reanalyzed St. John's measurements in 1983, and modified his theoretical treatment. In order to develop a consistent theoretical description of the dynamics of formation of the plastic zone and to come to a quantitative comparison, he avoided some conceptual difficulties and complications (like the "yield stress" of a dislocation-free material). The maximum crack tip stress

acting perpendicular to the fracture plane depends on the crack tip radius ρ as

$$\sigma_{max} = 2K / (\pi\rho)^{1/2} \qquad \text{III.13}$$

He argued that, if σ_{max} reaches the cleavage stress E/10, then fracture occurs. As in St. John's treatment, ρ is the sum of an elastic and a plastic component, the latter produced by the crack surface ledges of n dislocation loops emitted from the tip. The former, i.e., ρ_e, must be several Burgers vector large $\tilde{n}_o$ b

$$\rho = b[\tilde{n}_o+n(t)] \qquad \text{III.14}$$

The production rate of new dislocation is assumed to be governed by the rate at which they move away from the tip

$$n^\circ = V (\tau^*) / \Delta \qquad \text{III.15}$$

where Δ is the spacing in the dislocation train and, τ * is the stress that determines their velocity V. We may calculate τ^* from

$$V (\tau^*) = r^\circ (\tau^*) \qquad \text{III.16}$$

where τ^* is the component of the stress tensor σ_{ij} in the slip system

$$\sigma_{ij} = [K/2\pi r] \Psi(\theta) = \tau^* / \mu \qquad \text{III.17}$$

Haasen estimated τ^* to be larger than 10 MPa, and $\Delta \approx Gb/\tau^* \approx 1\mu m$. Haasen [47] estimated the BDT temperature, T_c, where cleavage still occurs in the presence of blunting from

$$\delta^{\circ} K_c / c \exp(-U/K_B T c) = [(E/20)(\pi b/2\Delta)^{1/2}]^{m+2} [\mu\Psi / \pi^{1/2}]^m . B_o \qquad \text{III.18}$$

He concluded that the BDT occurs if the dislocation velocity becomes larger than the rate of spreading of the stress contour. Brede and Haasen [60] in 1988 in an attempt to investigate the importance of the dislocation velocity for the BDT temperature, performed several fracture experiments on the pre-cleaved dislocation-free silicon single crystals at elevated temperatures. They used the well known doping dependence of the dislocation velocity in Si to obtain the detailed information about the conditions in the plastic zone. They observed that [60] at high temperatures dislocations are generated at an applied stress intensity lower than the critical stress intensity for inducing cleavage in the dislocation-free silicon single crystal samples at room-temperature. As a consequence of this, the plastic zone which develops around the crack tip is saturated before the tensile stress at the crack tip reaches the cohesive stress. Because of the saturation of the plastic zone, they concluded that the BDT temperature is determined by the velocity at which dislocations move outward from the crack tip at low shear stress existing in the vicinity of the shielded crack [60]. They pointed out that the dislocation generation at the crack tip is only a necessary condition for the brittle to ductile transition, the sufficient condition being that dislocations must be able to move away sufficiently quickly from the crack tip, to relax the local stresses at the crack tip before the

cleavage occurs. As expected, the n-type doping lowered the BDT temperatures and the activation energy calculated from the Arrhenius plot of the loading rate vs. the transition temperatures compared to St. John [54] and Michot's [61], because of the dislocation-velocity enhancing Patel-effect. Using the dislocation behavior at low shear stresses, where in addition to the "non-local" electronic Patel-effect "local" elastic interactions between dislocations and impurities lower the dislocation velocity and yield a minimum shear stress necessary to move dislocations, Brede and Haasen [60] quantitatively explained their BDT results at lower loading rates and temperatures. They concluded that a saturated plastic zone develops around the crack tip before the cohesive stress is reached. They reasoned that this is due to the fact that the applied stress intensity to generate dislocation is distinctly smaller than the critical applied stress intensity to induce cleavage at room temperature. The velocity with which dislocations move outward from the crack tip is then the velocity at the low shear stress existing in the saturated plastic zone. Hence, the dislocation nucleation rate is determined by the dislocation velocity at low shear stress, because dislocations just generated exert a back stress on the crack tip. Brede and Haasen [60] concluded that the BDT occurs when the nucleation rate at the critical situation is just high enough to compensate the increasing applied stress intensity by shielding and blunting due to a sufficiently high dislocation nucleation rate. They also found that the applied loading rate at the BDT temperature was proportional to the dislocation velocity. Furthermore, it turned out that because of the change of the dislocation distribution in the plastic zone with the applied stress intensity, the critical situation exists only at a certain applied stress intensity. This leads to extremely sharp transitions

which were found in the experiments. Therefore, besides the activation energy of the dislocation movement, the "starting stress" plays an important role in the BDT. Behrensmeier, Brede and Haasen [62] calculated the "starting stress", τ_c, in 1987 by measuring the average spacing, Δ, between two dislocations. They used

$$\tau_c = \pi\mu\, b / (4\,\Delta) \qquad \text{III.19}$$

where μ is the shear modulus and b is the Burgers vector for the dislocation arrangement ahead of a loaded mode-I crack according to the Bilby-Cottrel-Swinden fracture model. The results indicated that a higher starting stress which drives dislocations faster, results in a lower BDT temperature. Note that Brede and Haasen [60], and Michot [63] had followed the pioneering studies of St. John [54] in using the pre-cracked double cantilever type specimens of "dislocation-free" silicon single crystals for which the applied stress intensity factor K is approximately independent of the initial crack length.

In a series of investigations Hirsch, Roberts and Samuels [8-11, 45] used four point bend type specimen containing small surface cracks (mostly 13 μm radius, parallel to (111) cleavage plane), introduced by indentation [11] and studied the fundamental processes involved in the BDT in Si. They also found that a sharp transition, characterized by a rapid increase in the fracture stress with temperature, occurs at a temperature, T_c, that depends on the strain rate and doping of the material used [45]. They found that the activation energies were equal to those for dislocation glide. At temperatures above the sharp

transition region, their specimen deformed by macroscopic plastic yielding. Etch pitting experiments showed that below T_c no significant dislocation activities occurred, and the sharp BDT was associated with a *sudden* growth of well defined dislocation arrays from *certain* points on the precursor flow *before* the fracture occurred. Samuels and Roberts [45] argued that Haasen's 1983 model [47] did not take into account the interactions between the dislocations emitted from the crack tip and that these interactions are, indeed, important in determining dislocations behavior. In Haasen's model [47] it was assumed that the dislocation nucleation occurred relatively easily at the crack tip, and that the rate of blunting was controlled by the rate at which dislocations could move away from the crack tip, i.e., by the dislocation velocity, and the BDT occurred when the crack tip blunting was so fast that the critical intensity factor for the fracture at the crack tip, K_C, was not reached even though the applied K rose above it. Samuels and Roberts [45] tested St. John's [54] conclusions that the loading rate dependence of T_c is controlled by dislocation velocity. They used etch pitting method to make the direct observation of the dislocation arrangements near T_c in the n, p and intrinsic Si crystals to clarify the controlling mechanisms of the BDT. They concluded that [45]:

I. Dislocation glide controls the BDT in Si.

II. For the identical strain rates, n type doping lowers the BDT temperature relative to the intrinsic Si.

III. The BDT in Si is controlled by the dislocation velocity in the material.

IV. There is a genuine effect of the initial crack size on T_c. Specimens containing larger cracks are brittle at higher temperatures.

V. The transition is marked by a substantial increase in stress to fracture, whereas the etching experiments have revealed that the transition is also characterized by the *emission* of a large number of dislocations. No dislocation is seen at temperatures just below T_c. The sharpness of the transition suggests that some sort of dislocations come from the four points on the crack front where the tangent to the crack front lies in a slip plane. However, owing to the inherently poor resolution of the etching technique, one *cannot* distinguish between dislocation emissions from the crack tip or near tip sources.

VI. Some dislocations have been emitted during loading at T_c, as they cannot be associated with the propagating crack.

VII. Dislocations generated in the immediate vicinity of the crack at or above T_c shield and/or blunt the crack, reducing the stress intensity at the tip.

VIII. At the transition temperature, specimens still fracture in an apparently brittle manner but at a fracture stress typically about 80 percent greater than the "base level". This increase in the stress to fracture was found to be associated with the generation of a large number of dislocations, mostly from four favorable sites around the crack front where the tangent to the crack front lies in a slip plane. However, as mentioned above, it is not clear from

these experiments whether these dislocations are nucleated at the crack tip or generated by pre-existing near-tip sources. It has been shown that most of these dislocations were indeed generated during loading and not as the crack propagated.

IX. More detailed experiments indicate that during a test at T_c some sort of nucleation event occurs and dislocations start to be generated as K reaches K_C. It should be noted, however, that this is not the same as the minimum K required for dislocation nucleation under the static loading conditions, ca. $0.3K_C$. For the fracture stress at the transition to be higher than the room temperature value, dislocations must reduce the stress intensity at the crack tip, either by blunting , or by shielding the crack.

Hirsch et al. [8] analyzed the experimental data of Samuels and Roberts [45] and developed a dynamic crack tip shielding model to describe the BDT of pre-cracked crystals in constant strain rate experiments. They concluded that:

i. Existing dislocations in the crystal moving to the crack tip control the sharp BDT observed in bulk Si, where they generate new sources that cause rapid shielding of the crack, no matter how low the pre-existing dislocation density in the solid may be. Once the crack tip sources are formed, it is possible to promote the nucleation by Rice-Thomson mechanism at the crack tip [64]. Even if it was so, T_c is still primarily controlled by the time it takes for an existing dislocation to reach the crack tip and to form the sources.

ii. If no stable source is present within the appropriate radius r_o, the BDT is controlled by other processes, for example by the Rice-Thomson's [46] nucleation mechanism. This may be the situation in experiments on pre-cracked thin foils of Si by Chiao and Clark [65], who have reported the emission of dislocations from cracks in the absence of any pre-existing dislocation in the crystal. The experiments of Ohr [50] on thin foil specimens also show that nucleation of dislocations at crack tips in bcc metals can occur without the need for pre-existing dislocation in the material. The operation of the Rice-Thomson mechanism should result in a soft (gradual) transition.

iii. If the energy barrier for the nucleation of dislocations at the crack tip becomes zero for a value of K less than ca. $0.9K_{Ic}$, then the transition should be soft (gradual) and dislocations should be generated, which is not observed in the experiments of Samuels et al. [45]. However, if the nucleation of dislocations by the Rice-Thomson mechanism becomes spontaneous at $K \approx K_{Ic}$ its effect are unlikely to be observable in the present experiments [45] because dislocation generation by the crack tip sources would be much faster as they operate at $K_n << K_{Ic}$.

iv. The main parameter controlling the BDT is the dislocation velocity. Any mechanism that reduces the average dislocation velocity is likely to increase T_c. Such mechanisms of course also increases the yield stress. It is difficult to predict the effect of work hardening: an increase in dislocation density may reduce T_c, but an internal stress opposing dislocation motion may have

the opposite effect. An obstacle to the dislocation motion may stop the dislocation emission at the crack tip source and may cause cleavage.

Silicon presents an extreme example of the effect of pre-existing dislocations on the BDT because the crack is so sharp and the density of existing dislocations so low that dislocations have to be nucleated at or close to the crack tip before screening takes place by the emission of dislocation avalanches. When dislocations already exist at or near the crack tip, or are formed at small values of stress intensity, and the loops generated by different sources by the crack-tip stress overlap, screening is not dependent on the nucleation of dislocations, but depends only on the rate at which dislocations move away from the crack tip.

Hirsch and Roberts [11] proposed a second possible nucleation mechanism in 1991 appropriate to long straight cracks that would result in sharp transition, which assumes the existence of other dislocations in the crystal. The theory involves the distance between existing sources along the crack front as a structure sensitive parameter, and the experiments of Brede and Haasen [60], of Michot [63], and of Michot and George [66] were interpreted in the light of this treatment. Hirsch et al. [11] concluded that:

i. The sharp BDT occurs because of the need to nucleate a high density of crack tip sources which emit dislocations which rapidly shield the crack. Sources are nucleated:

a. By existing dislocations distant from the crack tip moving to the crack tip. T_c is controlled by the time taken for the external dislocations to reach the crack before $K \approx K_{IC}$. T_c depends on the existing dislocation arrangements. The sharpness of the BDT is controlled by the distance between the crack tip sources at the end of nucleation phase.

b. By dislocations emitted from a few preferential sites (spacing $2d_{l,crit}$) along the crack tip, moving along the tip, and creating new sources spaced at $2d_{f,crit} << 2d_{l,crit}$. T_c is controlled by the time available to the initial loops to move $d_{l,crit}$ before K reaches K_{IC}. T_c is structure sensitive. The sharpness of the BDT is controlled by $d_{f,crit}$.

ii. When crack-tip sources are already present, and any nucleation is negligible, the transition is soft.

iii. The strain-rate dependence of T_c is controlled by the activation energy controlling dislocation velocity, not by the activation energy for the loop nucleation.

Hirsch et al. suggested that: "even for dislocation-free Si there appear to be some sites where the slip can start at $K < K_{IC}$. So far, there is no evidence for a thermally activated homogeneous nucleation mechanism for dislocation loops. Even the direct observations of Si [65] are compatible with their nucleation of special sites".

M. Khantha, D. P. Pope, and V. Vitek [67-69] studied the brittle-to-ductile transition, BDT, and developed a new model (KPV) that describes the dual nature of the BDT, i. e., the massive generation of dislocations at the transition temperature T_C and the strain-rate dependence of this behavior. They started by criticizing the existing models that in these models the BDT was considered to be either controlled by the generation of a single dislocation [46,70-71] or by the mobility of a group of dislocations [8, 60, 72]. They further argued that in both these approaches, it was essential to throw in supplementary conditions in order to recognize the transition temperature. In the nucleation-based models, a certain rate of dislocation nucleation at the BDT is considered [73], and in the mobility-based models [8] it is assumed that an avalanche of dislocations is emitted at T_C. Khantha et al. [68] concluded that "the issue that needed to be resolved is not whether dislocation nucleation or dislocation mobility is the rate-controlling factor [73] but how the two effects can be treated simultaneously without ad hoc assumptions in order to obtain a complete description of the phenomenon".

Khantha et al. [67-69] used the fact that macroscopically two distinct features are affiliated with the BDT [54, 74-75]. (i) An abrupt massive generation of dislocations which gives rise to a sharp BDT above a characteristic temperature T_C, and in the transition zone, the fracture toughness, K, increases expeditiously with temperature. (ii) In most materials, T_C is a function of the applied rate of stress intensity, $\dot{K}$.

Khantha et al. [68] argued that "a sudden well defined transition in a narrow temperature range cannot occur if the underlying process is thermally activated as is assumed in the existing models. This is because the characteristic feature of a thermally-activated phenomenon is that it occurs in a continuous manner over wide range of temperature". In the KPV model [67-68], the BDT is *not* a thermally induced phenomenon in the common sense, but rather a *thermally activated instability* that gives rise to a sudden massive dislocation generation. M. Khantha, D. P. Pope, and V. Vitek [67-68] presented a statistical mechanics two-dimensional model (KPV) based on the Kosterlitz-Thouless [72] concept of dislocation screening and spontaneous dislocation generation leading to the BDT. An analytical expression for the transition temperature was derived [67-68]. In KPV model the abrupt onset of ductile behavior corresponds to a cooperative instability of many small dislocation dipoles induced chiefly by thermal fluctuations and advanced by the applied stress, resulting in a vast increase in the free dislocation concentration. The instability occurs well below the melting temperature. This instability corresponds to the spontaneous dissociation of dislocation dipoles in 2D and unstable expansion of small dislocation loops in three dimensions. The principal feature of KPV model [67-68] is a cumulative temperature-and-stress dependent dislocation effect caused by the interaction between *many dislocation dipole nuclei* that co-exist at any finite temperature. In KPV model the screening gets stronger with increasing temperature and ultimately gives rise to a collective dislocation instability above a certain temperature. This phenomenon is physically distinct from the conventional dislocation shielding of the crack-tip stress field [51], and does not exist if thermal fluctuations are not

considered explicitly. The criterion for the spontaneous massive dislocation generation derived from this approach contains identical physical parameters to the pioneering model of Rice-Thomson [46] describing the instability of a single dislocation loop. KPV model [67-69] tries to explain how above a critical temperature for a given stress level in a solid a massive dislocation generation abruptly becomes possible .

In the limit of zero stress, KPV model reduces to the Kosterlitz-Thouless theory of the melting transition [76-77], and in the opposite limit of zero temperature Rice-Thomson result [46] for the brittle-to-ductile transition is obtained. The effect of dislocation mobility on the strain-rate dependence of T_C is investigated in [69].

A particular correlation between the strain-rate dependence of T_C and the temperature dependence of the dislocation velocity, V, has been observed in silicon [11, 54] and is suggested in intermetallic solids [75]. The BDT temperature is found to depend on the loading rate according to an Arrhhenius-type kinetic equation [78]. The appropriate association is found by comparing plots of $\ln(K')$ versus $1/T_C$ and $\ln(V)$ versus $1/T_C$. It is often discovered that the behavior is almost identical in both and the graphs have nearly equal slopes. This indicates that the strain-rate dependence of T_C is related to the dislocation mobility [11, 78-79].

A comprehensive representation of the BDT, however, requires a good understanding of both dislocation generation and mobility effects. M. Khantha

[69] explains how effects related to dislocation dynamics can be incorporated to the instability criterion [68] and analyzes the strain-rate dependence of T_C.

KPV model [67-68] considers the *massive generation of dislocations* at T_c as a *necessary* condition for the BDT. As long as there is no crack tip interatomic bond broken, and the failure is purely due to the generation of the blunting dislocations at the crack tip, the fracture is ductile by definition. The massive dislocation generation at T_C may be assumed necessary only in the macroscopic level. Because, in the macroscopic level the emission of the first blunting dislocation may not be detected. Besides, if the behavior is ductile, the system must fail by the continuous process of the dislocation generation at the crack tip. Ultimately, we may expect to observe a massive number of emitted dislocations from the crack tip. M. Khantha et al. [67-69] start from the fact that in the existing models, the BDT is viewed either as a competition between crack propagation and thermally induced nucleation of a single dislocation at the crack tip [46, 71, 73] or as a thermally activated generation of a single dislocation mobility-controlled dynamic process [8]. Then they [67-69] argue that "the physical understanding of the phenomenon remains incomplete because a thermally activated mechanism of dislocation generation or mobility does not lead to a sudden well-defined transition at a characteristic temperature with a dramatic increase in the fracture toughness without imposing ad hoc conditions [8, 73]". But the existing description of the abrupt or sharp transition is based on the macroscopic definition of the BDT temperature. In these models the solid is heavily overloaded when the transition takes place. The applied load (or applied stress intensity) is gradually increased after the emission of the

first blunting dislocation until the complete failure of the solid. Because as stated clearly by A. S. Argon [49] the emitted dislocations at the crack tip produce shielding at the crack tip that reduces both the crack tip tensile stresses and the shear stresses on the inclined planes. They also blunt the crack. The brittle propagation of the crack may continue under adequately increased stress intensity conditions to keep the crack tip tensile stress constant [49]. At a certain configuration a small increase in temperature or a decrease in the crack velocity permits the generation of a new set of dislocations that leads to additional shielding and blunting which tip the balance against the crack-tip tensile stresses [49]. This results in the BDT. Obviously, the increase in the applied load may cancel out the shielding effect of the emitted dislocations and as a result a massive dislocation generation is occurred. Argon's analysis [49] shows that traditional activation analyses that do not consider the discrete atomic nature of the crack tip material and its nonlinear reaction overestimate the energetics of the phenomenon by an order of magnitude or more.

Unlike the conventional models which describe the stress-induced instability of a single dislocation at the crack tip, Khantha et al. [67-68] assumed a thermally activated instability of *many small loops* in the presence of an applied stress. The creation of many atomic-size loops by thermal activation induces a temperature-dependent *cooperative screening* effect that enhances the ensuing advancement of the loops. However, it is not clear on what bases they have assumed the existence of *many small loops*. On the other hand, our MD simulations indicate that the emission of a single blunting dislocation from

the crack-tip immediately reduces the crack tip stress intensity and blunts and arrests the (moving) crack tip for a significant amount of time. Our observations suggests that unless the emitted dislocation moves far enough away from the crack (or is absorbed back to it), the tip remains inactive, i.e., neither any crack-tip interatomic bond breaks nor any new dislocation is generated at the tip. Hence, the concept of the "cooperative screening" is somewhat ambiguous. Of course, at $T \geq T_C$ no crack-tip interatomic bond may break and the pre-cracked critically loaded solid may fracture purely by the continuous emission of dislocations from the crack tip. Hence, a massive number of dislocations must be generated *during* the fracture at $T \geq T_C$. Therefore, the "cooperative screening" could be considered as the effective shielding or screening of the crack tip due to the emitted dislocations *during* the fracture and not at the *onset* of the ductile behavior.

The concept of dislocation screening was originally introduced by Kosterlitz and Thouless (K-T) [76] in a totally diverse circumstance of 2D phase transition. They showed that [76] the mutual interactions between numerous dislocation dipole nuclei leads to a *dislocation screening phenomenon* which permits a cooperative dissociation of the dislocation dipoles to occur above a certain temperature. In the K-T theory [76], the unstable dissociation of dislocation dipoles is driven only by the thermal fluctuations, without the assistance of any external stress. It evolves close to the melting temperature and leads to a dislocation-mediated melting transition [77, 80]. Similar to our MD simulations, in the KPV model [67-69] both of the thermal fluctuations and applied stress assist the dislocation generation. This produces a K-T type

instability at the Griffith stress at a certain temperature well below the melting temperature which corresponds to the BDT [67-68].

The concept of screening is closely related to the fact that in two dimensions, dislocation dipoles with separation slightly larger than the dislocation core radius, r_0, have energies of the order of 1-2 ev and may be induced by thermal activation at finite temperatures [76]. The presence of a given thermal fluctuation that induces a dislocation dipole of size r, suggests that dipoles of size smaller than r exist with higher probability [68]. Therefore, a loaded solid contains a limited density of tightly bound dislocation dipoles of various sizes at a certain finite temperature. The loops grow on average with increasing temperature and/or stress until an unstable configuration is achieved beyond which they may expand freely and lead to ductile behavior [68]. The dissociation of dipoles at the instability produces a significant concentration of "free" dislocations in the material [67].

Besides the elastic strain due to the externally applied loads, the creation of the dislocation dipoles by thermal activation generates some plastic strain in the solid. The total energy of the system is a sum of the elastic energy of the solid in the absence of dislocations U^0, the elastic energy of the dipoles U^d, the work done in forming the dipoles U^w, and the interaction energy between the dislocations belonging to different dipoles U^{int} [67-68, 81]. The analysis of this complex system becomes tractable if the reaction of the system to the externally applied load is considered in terms of the total strain via the concept of an "effective shear modulus" or an "effective susceptibility" [67-68].

The effective susceptibility diverges when the dislocation dipoles dissociate and plastic flow begins. Instead of explicitly assuming the existence of plentiful dislocation dipoles, Khantha et al. [67-68] considered the presence of just one test dipole in an elastic medium characterized by the effective properties due to the existence of all other dipoles. Then they wrote [67-68] the total energy of the system as a sum of the reduced elastic energy of the solid expressed in terms of the effective moduli and the energy of the test dipole.

In KPV model [67-68] a larger dislocation dipole is screened by the existing smaller dipoles in the solid and its energy is lowered. The apparent change in the local properties helps more dipoles to be nucleated by the thermal activation resulting in a cumulative effect. Thus the production of abundant atomic-size dislocation dipoles induces a temperature-dependent *cooperative screening effect* that assists the subsequent increase of the dipoles with rise in temperature and/or stress. When the entropy is sufficiently ample to overcome the mutual interaction between the dislocations at a certain temperature and stress level, the susceptibility diverges due to the cooperative spontaneous dissociation of the dipoles and gives rise to the onset of the ductile behavior [67-68].

Khantha et al. [67-68] considered a dislocation-free pre-cracked elastic solid which was loaded in mode I. They assumed the shear stress σ to act on a slip plane that was coincident with the crack plane. They hypothesized that at a finite temperature, there was a small density of bound dislocation dipoles nucleated by thermal activation near the crack tip. Khantha et al. [67-68]

identified the BDT as caused by the *unstable spontaneous dissociation of dipoles* that led to a rapid increase in the density of free dislocations.

Khantha et al. [67] introduced a scale-dependent polarizability, $\varepsilon(r)$, which took into account the screening due to all dipoles of separation smaller than r. $\varepsilon(r)$ is related to the susceptibility $\chi(r)$ by $\varepsilon(r) = 1 + 4\pi\chi(r)$. For a constant stress, there is a critical temperature T_c corresponding to the radius r_c beyond which $\varepsilon(r)$ increases rapidly. This temperature can be defined by the implicit equation

$$T_c = [1/2K_B] \{q^2 / \varepsilon(r_c) - (\sigma b r_c) / 2\}, \qquad \text{III.20}$$

where $q^2 = [\mu_0 B_0 / (\mu_0 + B_0)] b^2 / 2\pi = [\mu_0 / (1-\nu)] b^2 / 4\pi$, μ_0 and B_0 are two-dimensional shear and bulk moduli in the absence of dislocations, ν represents Poisson's ratio, b, r_0, and E_0 are the Burgers vector, core radius, and core energy of dislocation, respectively. At $T \geq T_C$ the average-size thermally activated dipoles become unstable and dissociate spontaneously, and therefore the density of free dislocations increases very rapidly.

Khantha et al. [67] eliminated r_c and expressed T_C as the solution of a nonlinear equation

$$(\beta_c)^{-1} = \mu_0 b^3 [1 - 2\pi \exp(-\beta_c E_C b + \sigma b^2 \beta_c r_0/2)] / [8\pi(1-\nu)(1 + \sigma b^2 \beta_c r_0/4)], \qquad \text{III.21}$$

where $\beta=1/ K_B T$. Note that T_C is expressed in terms of the parameters that occur in the physical Hamiltonian. Equation III.21 evaluates a temperature above which a sudden massive dislocations generation occurs in an initially dislocation-free solid containing a sharp crack subjected to an applied stress, σ. The spontaneous nucleation of dislocations occurs at the crack tip due to the stress concentration, and blunts the crack-tip [46]. The stress σ in equations III.20-21 is therefore the local stress near the crack tip when the Griffith-like criterion for brittle crack propagation is satisfied [67-68]. Above T_C extensive generation of dislocation suddenly becomes possible at this stress level and the solid fails in ductile manner.

The phenomenological description of a cooperative instability in KPV model tries to explain the abrupt rapid rise in the dislocation concentration observed above a critical temperature. KPV model also tries to show why brittle fracture occurs below T_C even when the material contains a high density of pre-existing dislocations. The reason lies in the fact that the blunting and arrest of a crack demands a *continuous unceasing* emission of dislocations at the crack-tip giving rise to a diverging intensity of "free" dislocations. Khantha et al. [67-68] analysis shows that a sudden massive dislocations generation above a critical temperature induces the BDT. The statistical mechanics based model [67-68] tries to explain how an extensive and cooperative dislocation generation instability occurs due to a thermally induced dislocation screening effect. The spontaneous generation of dislocations become energetically favorable above a certain critical temperature when the screening leads to scale-invariant dislocation interactions.

The KPV approach tries to give an alternative view for investigation of the BDT not only in terms of crack tip activity but also by merely exploring the temperature dependence of the plastic flow in crystals not containing cracks. When the solid is not pre-cracked, most materials display brittle behavior at low temperatures and become ductile above a characteristic temperature. The continuous generation of dislocations is a pre-requisite for the onset of ductile behavior and it is hard to think that the manner of dislocation nucleation could deviate considerably depending on whether a pre-existing crack is present or absent in a solid. According to Khantha et al. [68] an impressive confirmation of the applicability of the KPV model to the extensive description of tensile ductility may be established in the investigation of yield and flow behavior as a function of temperature in whiskers. In the case of Si whiskers [82], it was discovered that the onset of plastic flow appeared abruptly above a certain temperature, entirely analogous to the BDT observed in bulk single crystals with a crack.

In the third paper M. Khantha [69] investigated the dynamics of a bunch of dislocations in the vicinity of a crack subjected to Mode III loading. He considered [69] an empirical velocity-stress power-law for the thermally induced dislocation motion. The correlation between the temperature dependence of the dislocation mobility and the strain-rate dependence of T_C was then derived by incorporating the analytical dynamical solutions in the static criterion [67-68] for the cooperative instability. M. Khantha [69] concluded that "the strain-rate dependence of T_C is due to a combination of the scale-invariant thermal dislocation screening which causes the BDT and the self-similar stress-induced dynamics of dislocations (or loops) in the vicinity of the crack tip".

The new model [67-69] not only tries to explain the qualitative nature of the phenomenon but also considers in conjunction the influence of strain-rate effect in the onset of the BDT. M. Khantha et al. [67-69] tried to establish that both dislocation generation and dislocation dynamics play eminent roles in the BDT but in separate aspects of the problem. In M. Khantha's model [69], the two separate effects are treated in a unified manner. The KPV model offers an alternative mechanism for dislocation generation at finite temperatures in addition to stress-driven Frank-Read sources. The results [67-69] reveal the significance of thermally-induced cooperative effects in the context of the BDT which may also be of relevance to the general problem of dislocation generation and of plastic flow in solids.

In his latest investigation of the BDT in silicon M. Brede [83] carried out computer simulations of the crack-tip shielding dynamics using the general formalism of R. Thomson et al. [51, 64]. M. Brede [83] concluded that

1. A gradual transition from cleavage to semi-brittle fracture with a relatively small homogeneous plastic zone precedes a sharp transition to general ductility. The local shear stresses in the plastic zone are determined by the shielding provided by the sum of all dislocations.

2. The fracture toughness between both transitions is independent of temperature, yielding a plateau region. The plateau region is a direct result of the shielding dynamics at increasing temperatures, and the sharp transition to ideal ductility may be attained only if additional shielding is

supplied. In the computer simulations this supplementary shielding was accomplished by considering a certain emission configuration for dislocations in opposite glide directions. The assumed configuration corresponds to the emission of a single dislocation loop on a glide plane which intersects the crack tip at a single point. The loop encloses the crack tip. The transition occurs at the temperature, where the maximum of the local stress intensity factor K_I remains just below the Griffith-value.

K. J. Hsia, and A. S. Argon [13] experimentally investigated the micro mechanisms of the BDT of cleavage fracture in silicon single crystals. They used a modified novel experimental technique developed by Brede et al [84] to study the crack arrest by propagating a cleavage crack against a temperature gradient. One may use this technique to measure the BDT temperature of a running cleavage crack without explicitly differentiating the controlling crack tip mechanism. They used a laser imaging technique to measure the crack-tip velocity. The crack arrest temperature which fundamentally corresponds to the BDT temperature was measured as a function of the crack-tip velocity. Hsia et al. [13] used an etch-pitting technique to inspect the dislocation configuration at or near the crack arrest front. Their experimental results on silicon single crystals indicates that even if dislocations are generated at the crack tip, they do not generally provide sufficient blunting or shielding to lead to the BDT. Hsia et al. [13] concluded that the rate-limiting mechanism for the BDT in silicon single crystals was dislocation mobility rather than dislocation generation. Similar behavior has been reported by Dewald et al. [85] in GaAs and MgO. They noticed that even though dislocations could be nucleated at or

around a cleavage crack tip, this did not prevent the crack-tip from brittlely propagation [85]. Burns and Webb [86] have reported similar observations of brittlely propagating cracks carrying with them growing plumes of dislocations in LiF.

Hsia et al. [13] based on their preliminary experimental results concluded that high dislocation velocity and a massive dislocation density were needed to arrest a brittlely propagating cleavage crack. They observed that for a running cleavage crack in silicon single crystals, dislocations could be continuously emitted from the crack tip at a temperature slightly lower than the crack-tip arrest temperature. These nucleated dislocations could not move far enough away from the crack-tip to result in effective shielding because of low mobility [13].

Hsia et al. [13] reported that in silicon single crystals, attaining the crack arrest temperature did not often bring about general yielding of the solid. If the loading is continued, a reversal of fracture mode from crack blunting to reinitiation of cleavage may take place. This is consistent with the mobility limiting mechanism of the BDT. After the arrest of the crack-tip, if the loading is continued the fracture mode is determined virtually by the competition between the applied loading rate and the growth rate of the crack tip plastic zone. This is very similar to those experienced in the static experiments [45, 54, 60, 63]. When dislocations are sluggish, the growth rate of the plastic zone may not be able to compete with the applied loading rate, and hence the brittle propagation of the cleavage crack may be re-initiated. On the other hand, for

materials in which dislocation velocity is large, such as in some b.c.c. transition metals and possibly some intermetallic compounds, once dislocations are emitted they move away from the crack with a very high velocity. The dislocation nucleation near the crack tip could continue non-stop to produce more blunting and ductile tearing. In these solids, a ductile to brittle transition could take place only under elevated strain rates by nucleating a microcrack in the vicinity of the blunted crack tip [87].

K. Maeda, H. Nishioka, N. Narita and S. Fujita [88] studied the BDT by the novel method of indentation fracture experiments performed at a constant loading rate (CRIC method). The indentation fracture, IF, test is based on the fact that a microcrack created in the vicinity of an indent gets arrested when the stress intensity factor affiliated with the crack drops beneath the fracture toughness of the solid [89]. The CRIC method [78] have demonstrated promising potentials for its use in the investigation of the BDT in small crystals. Employment of CRIC method to GaAs indicated [78] that the apparent fracture toughness K_{IC}, experimentally reflected in the length of indentation-induced cracks, displayed a sudden rise above a critical temperature T_C. It was found that [78] the BDT temperature was an Arrhenius-type function of the loading-rate. The activation energy was found to be very close to that of dislocation motion in GaAs [78]. In the pioneering CRIC method [78], however, the existence of an "incipient crack" had to be assumed. The "incipient crack" was a hypothetical crack that functioned as a pre-crack. In the modified two-step CRIC method this ambiguity was removed by creating a well-defined pre-crack in the first indentation for the ensuing CRIC experiment. Employment of this

technique to an n-GaAs single crystal revealed [88] that the growth of the crack was suppressed when the applied loading rate was less than a given value. Maeda et al. [88] assumed an Arrhenius-type kinetics and estimated the activation energy to be 1.8 ± 0.5 ev, which was fairly close to the glide activation energy of ß dislocations in n-GaAs. In the experiments of Maeda et al. [88] the BDT occurred when the plastic zone, represented by dislocations distribution, grew adequately to enclose the whole crack. They assumed that the growth rate of the plastic zone in the indentation of the Ga face was controlled by the mobility of β dislocations. K. Maeda et al. [88] concluded that the apparent activation energy controlling the BDT was close to the glide activation energy of β dislocations.

V. R. Nitzsche and K. J. Hsia [79] developed a model to investigate the dislocation mobility controlled BDT. They assumed the model material to experience elastic rate-dependent plastic deformation, with plastic strain rate calibrated with dislocation mobility. They adopted a simple isotropic rate-dependent plasticity theory to take care of the effects of dislocation motion. They assumed the plastic strain to obey an Arrhenius-type law with a power law dependence on stresses. Except for a coefficient, the dependence of strain rate on temperature and stress can be uniquely found from the experimental data of dislocation velocity in specific materials. They considered the BDT to take place when enclosing plastic zone shielded the crack such that the tip never achieved the critical stress intensity for cleavage. They used the finite element method to determine the crack tip shielding due to plastic deformation.

V. R. Nitzsche et al. [79] used the finite element software ABAQUS [90] to compute the response of the pre-cracked sample subjected to various temperatures and loading conditions. Since plastic deformation evolves continuously as the applied load is increased gradually, the characteristic of the problem is effectively the transient response of the crack tip fields. Most atomistic models using dislocation theories [8, 49, 83] take into account the crack tip and dislocations interactions, but are unequipped to consider the continually evolving stress fields in the vicinity of the crack tip during the transient period. V. R. Nitzsche et al. [79] , however, take into account the constantly changing stress distribution and redistribution during loading. Their results display that at the BDT temperature, the stress distributions for various applied loading rates in the plastic zone are nearly equal at a crack tip stress intensity level close to K_{IC}. Their computational results also demonstrate that the stress singularity is significantly reduced due to the plastic deformation. These results are consistent with atomistic simulations of M. Brede [83] and Hirsch et al. [11], and with experimental results of G. Michot et al. [91].

V. R. Nitzsche et al. [79] adopted the elastic zone concept of Z. Suo, C. F. Shih and A. G. Varias [92] to develop their current model. In the elastic zone concept of Z. Suo et al. [92] no plastic deformation takes place within the elastic zone very near the crack tip, and it is indicated that dislocation activities in the immediate vicinity of the crack tip do not have a significant impact on the crack tip stress fields. Furthermore, the presence of an elastic zone essentially erects a barrier to the onset of plastic deformation. This is analogous to a barrier to dislocation generation.

V. R. Nitzsche et al. [79] identified the dimensionless group that influenced the DBT, and investigated the impacts of different dimensionless parameters on the BDT. Their computer simulations results indicate that as the stress exponent n increases, the BDT gets sharper. They concluded that a BDT controlled by the generation of dislocations would be much sharper than a dislocation mobility controlled BDT, because the nucleation barrier virtually functions as an on/off device. Before the barrier is overcome, the fracture toughness is identical to the intrinsic cleavage toughness with no crack tip shielding. Once the nucleation barrier is defeated the behavior should be purely ductile. The computer simulations results of V. R. Nitzsche et al. [79] imply that crystals with a higher stress exponent n are more likely to obey dislocation nucleation controlled BDT, whereas those with a lesser n tend to have a dislocation mobility controlled BDT. Si, Ge, and GaAs have relatively small stress exponents n (about 1.4 to 3.0), whereas materials like Fe-3%Si, LiF and W have much higher stress exponents (about 20 to 40) for dislocation mobility. Experimentally [13, 85] it has been shown that in Si, GaAs and MgO dislocation generation is easier than dislocation mobility. On the other hand, D. Hull, P. Beardmore and A. P. Valintine [93] in the experimental investigation of the crack propagation in single crystals of tungsten have observed that the BDT was rather gradual. Note that W has high value of stress exponents n.

The simulations results of V. R. Nitzsche et al. [79] also indicate that the sharpness of the BDT is a function of the applied loading rate. The BDT is very sharp at lower loading rates, as the loading rate increases the BDT gets more gradual. Therefore, their simulations results imply that at lower loading

rates the BDT is dislocation nucleation controlled , and at high loading rates dislocation mobility controls the transition. V. R. Nitzsche et al. [79] predicted that under quasi-static loading generated dislocations had sufficient amount of time to glide away from the crack tip, and thus to lead to the dislocation nucleation controlled BDT.

Amand George and Gérard Michot [94] experimentally studied the generation of dislocation loops at crack tip and the development of the plastic zone in precracked silicon single crystals. The silicon samples were precracked at room temperatures and loaded at $T \geq 900$ K under constant mode I strain rate. They paid special attention to the early stages of plastic zone formation. In situ observation by synchrotron X-ray topography were supplemented by chemical etching after fracture. According to their observations dislocation emission seems to be very heterogeneous along the crack front. They emphasized that depending on the experimental conditions, loop nucleation may be an important parameter of the BDT. They demonstrated that real plastic zones were much more complicated than the simple dislocation arrays used in the reported computations [8, 45, 47, 60-62], with 3D arrangements and activation of unexpected slip systems.

Contemporary studies [41, 45, 54, 60, 95-98] have established the fact that silicon is a perfect crystal for the investigation of the foremost fundamental processes involved in the BDT. Most of the experimental studies on silicon single crystals indicate that the BDT in this solid is accompanied by the dislocation emission from sources at, or nearby crack tip [41, 45, 60]. Models

based on these observations have been developed for the BDT [8, 10-11, 83]. On the other hand, several teams have been performing experiments on the BDT in other single crystals among them are FeSi [99], Mo [100], sapphire [101], Ge [102], MgO [103], NiAl [104], and TiAl [96]. The experimental results indicate that the BDT in these solids displays a very complicated behavior, and it is associated with the dislocation nucleation at the crack tip and the dislocation mobility [96, 99-104]. Experimental observations indicate that materials that initially have high concentration of dislocations before testing (Mo [100], MgO [103], Ge [102], TiAl [96]) display a gradual BDT, where the fracture stress increases steadily with rising temperature. On the other hand crystals which are essentially dislocation free (Si [41, 45, 54, 97-98], Al_2O_3 [95]) experimentally exhibit a sharp BDT, with an abrupt increase in the stress to fracture over a narrow temperature range. Of these materials hydrogen-embrittled Fe-Si [99], MgO [103], and TiAl [96] display stable crack growth, SCG, by microcleavage processes enhanced by dislocations prior to the ultimate fast fracture.

Experimental investigations indicate that the activation energy for the BDT is identical to that for dislocation glide in Si [95-98], Ge [102] and sapphire [101]. Both experimental results and models indicate that BDT is controlled by the dislocation shielding of the crack tip in these materials. S. G. Roberts, A. S. Booth and P. B. Hirsch [96] reviewed these models. Using the fact that modifications of the dislocation sources in tests samples may be employed to improve the DBT temperature and the "shape" of the BDT [98], Roberts et al. [96] concluded that realistic setting of dislocation sources in the BDT models

was crucial in attaining the proper simulations of experiments [11, 83]. They pointed out [96] that a simple model based on a single developing array of dislocations could account for most characteristics of the BDT [8, 11]. They also introduced their recent results on TiAl, and presented their novel model of stable crack growth, SCG. Roberts et al. [96] reported that γ-TiAl displayed a BDT that obeyed an Arrhenius law with an activation energy of 1.34 ev.

Experimental results imply that SCG is exclusive to crystals with a high concentration of grown-in mobile dislocations and perhaps to solids with a high stress exponent n for the dislocation motion. Experimentally SCG has not been encountered in Si [41, 45, 54, 60, 97-98], and Ge [102] which are virtually dislocation free, and have relatively small stress exponents (about 1.4 to 3.0). SCG has the following characteristics [96].

(1)The growth of the crack is by "unzipping" sideways of a tiny forward step.

(2)Dislocation progress is virtually associated with every forward step.

(3)The intersections of dislocation arrays with the facade of the crack do not go far beyond the crack tip at any stage.

Roberts et al. [96] concluded that a constructive model therefore should feature a local dislocation processes to raise the effective crack tip stress intensity K_e to above K_{Ic}, possibly at steps in the crack front. Note that the effective crack tip stress intensity K_e is the local stress intensity as modified by

the shielding effects of the dislocations. The crack must be stable after each forward step as long as $K_e<K_{Ic}$. The stable crack growth, SCG, by microcleavage processes enhanced by dislocations may have the following features [96].

(1) Dislocation half-loops on a plane that locally intersects the crack front are emitted by a source at or nearby the crack tip. These loops quickly expand along the crack front.

(2) The dislocation loops stretch round to the "underside" of the crack at a step in the crack front. Portions of the loops that extend beyond the crack step are antishielding to the crack, and therefore they amplify the local stress intensity.

(3) The stress intensity at the step surpasses K_{Ic} when adequate amount of dislocations loop round the step. Then the step grows quickly until it intersects the slip plane again, and K_e drops below K_{Ic} once more [95]. Subsequently every antishielding dislocations "below" the crack plane will be attracted back to the crack tip and will be absorbed.

This procedure is repeated at every crack step and the crack advances by small-scale micro-cleavage [96]. This process leads to the creation of dislocation bands left behind the crack front. Each band is affiliated with an "unzipping" crack step. Ensuing a crack jump, when the local effective crack tip stress intensity at the crack tip K_e eventually surpasses K_{Ic} the fast fracture

will occur. Due to the shielding dislocations, the applied stress intensity K at fast fracture is higher than K_{Ic} [96].

S. G. Roberts, M. Ellis and P. B. Hirsch [95] used models based on the simulations of dislocation dynamics in the vicinity of crack tips to analyze and estimate the experimental results of the BDT in Si, Ge, Al_2O_3 and Mo. The simulations results rely on the position, type and nucleation parameters of the dislocation source(s). Selection of source features proper to the material and experimental settings yields the superb fit to experimental results [95-96]. They concluded that the BDT in precracked silicon and sapphire could be explained by a two-stage dynamic model based on the dislocation movement to the immediate vicinity of the crack tip [95]. In Si and Ge, where the stress-temperature-velocity relations are available, the BDT temperatures are predicted accurately. The shape of the BDT may be predicted by the computer simulations of the dynamic progress of dislocation arrays near the crack-tip if the pre-existing dislocation arrangements in the crystal are given. S. G. Roberts et al. [95] performed experiments to verify these predictions. In sapphire, where these data are not accessible, the dislocation velocities may be estimated using the model. They measured dislocation velocities in sapphire experimentally and found reasonably good agreement with the predicted values. They also studied the BDT in semibrittle materials (b.c.c. metals and oxides), where the BDT may be controlled by the pre-existing dislocations via the slow, stable crack propagation. In Mo the stable crack growth is limited and the estimated fracture stress-temperature curve by their model is fairly accurate.

F. C. Serbena and S. G. Roberts [102] experimentally investigated the BDT in precracked germanium single crystals. They pointed out that any heat treatment to reduce the residual stress of indentations in Ge would produce dislocations in the vicinity of the crack tip. The presence of dislocations at or very near the crack tip at $T<<T_C$ leads to the creation of many crack tip dislocation sources. In Ge the plastic zone consists of a high dislocation concentration generated by numerous closely spaced sources around the crack. This gives rise to a gradual BDT in Ge where the fracture stress increases steadily with temperature. The BDT temperature in Ge is an Arrhenius-type function of the applied loading rate indicating that the BDT is controlled by dislocation mobility [102].

Serbena and Roberts [102] assumed that the crack tip sources were already formed in the vicinity of the crack tip, consistent with the etching experiments which exhibited dislocation activity nearby the crack below T_C. Serbena and Roberts [102] performed computer simulations of the shielding effect of an evolving crack tip dislocation array using the modified version of a model developed earlier [8, 10-11, 95]. The model used by Serbena and Roberts [102] simplifies the real crack tip/dislocation geometry, and assumes the movement of straight and parallel edge dislocations on inclined slip planes which are coincident with the crack front [8,10-11, 95, 102]. In these computer simulations they used the equations of R. Thomson [51] to evaluate the stresses on each dislocation, and the dislocation shielding of the crack. Each dislocation is then moved according to its calculated velocity, v, using the data of Patal and Chaudhari [105],

$$v = A\,(\tau / \tau_o)^n \quad \exp(-U/ K_B T), \qquad \text{III.22}$$

where τ, T, n, and U are the stress, temperature, the stress exponent factor, and the activation energy, respectively. For germanium n is 1.3, U is 1.56 ev and the constant A is equal to 1.05 $X10^{-5}$ m/s with τ_o equal to 1 Pa. The time interval for each cycle of the computer simulations is chosen so that dislocations move no more than 1/3 of the distance to their nearest neighbors. In every cycle, each dislocation is advanced according to its calculated velocity, and the crack tip stress intensity is evaluated from the new dislocation position. The applied stress intensity is increased according to the experimentally measured values of the applied stress intensity rate, $\dot{K}$. The sources may emit dislocations in each cycle. The distance of the sources from the crack tip was selected such that the first dislocation would be emitted at a stress intensity equal to that observed experimentally, i.e., $K_N=0.2K_{IC}$. A new dislocation will be nucleated as soon as the stress on the dislocation at the source is sufficient to move it away from the crack tip. The nucleated dislocations must travel a given critical distance, d_{crit}, in order to shield the most vulnerable section of the crack tip. The model assumes that fracture will occur when the local effective shielded crack tip stress intensity K_e reaches K_{IC} (taken to be 0.6 MPa.$m^{1/2}$ [106-107]). K_N and d_{crit} control the estimated value of T_c, the predicted shape of the BDT, and the length of the dislocation array at fracture. The model fits the experimental results best for low values of d_{crit} (0.1-0.5 μm). This corresponds to the experimental observations that dislocations reach the crack during the early states of the tests and immediately begin to multiply along the crack front to form many crack tip sources.

The object of the present molecular dynamic simulations is to clarify the role of dislocations nucleation at the crack tip and their mobility on the BDT temperature and its sharpness in a dislocation-free pre-cracked 2D triangular Lennard-Jones covalent solid. There is no dislocation source in the solid. Therefore, the BDT is purely due to the nucleation and emission of dislocations from the crack tip, if any. According to Hirsch et al. [8]: "the operation of the Rice-Thomson mechanism should result in a soft transition". Although there are still questions on the mechanism of the transition, there is a general agreement in the literature that:

I. BDT in Si is very sharp.

II. T_c is controlled by the activation energy for dislocation velocity in the solid.

Although Hirsch's model [11] describes the relevant experiments in a consistent manner it remains speculative, since at the present time no evidence on $d_{l,crit}$ is available. This fact is recognized correctly by Hirsch et al. [11]. On the other hand, Brede-Zhang-Haasen's (BZH) model for the sharp BDT in Si does not involve a nucleation stage. Hirsch et al. [11] has shown that the quasi-static treatment used by BZH is internally inconsistent. Therefore, since experimentally it is impossible to create and verify a source/dislocation-free specimen at the present time, it remains for the computer simulations to investigate the BDT and its characteristics in a pre-cracked covalently bonded hard solid. However, since only inadequate force laws exist for atoms in the immediate vicinity of the severe distortions at the crack tip, and due to the

economic restrictions imposed by the use of computers (for example the use of 2D solid instead of a 3D material, and therefore the use of triangular lattice instead of the diamond structure), these calculations also have major limitations, and the results are inapplicable to any solid, directly.

It is well known that, when the sharp crack is mechanically stable in the solid, there will always be a saddle-point configuration of a dislocation loop of finite size through which, in principle, the loaded crack can emit a dislocation by the thermal fluctuations of the constituent atoms at the crack tip [51]. Realizing that no adequate interatomic potential laws yet exist for real materials, the present molecular simulations will be carried out on two dimensional triangular lattice points interacting via the Lennard-Jones covalent potential. The mechanical properties of this potential is described in sufficient detail in the later sections. The aim is to model the general fracture phenomena at high finite temperatures rather than to make any particular predictions for any particular material.

Due to the atomistic nature of the Rice-Thomson [46] criteria, i.e., the emission of dislocation from the atomically sharp crack tip before the cleavage-brittle propagation of the crack takes place, we adopt this criterion for the recognition of the brittle to ductile transition. This choice will also assist us in the evaluation of Hirsch et al. model which suggests that the sharp transition observed experimentally in Si is due to the presence of the pre-existing dislocations or dislocation-sources in the crystal, and that the Rice-Thomson mechanisms of the emission of dislocation from the crack tip would result in a

gradual BDT.

The objective of the present research is to determine the susceptibility to cleavage of selected systems, to correlate this property with the ideal cohesive and shear strengths of the crystal, and to investigate the brittle to ductile transition temperature and its characteristics in a covalent 2D triangular solid. The molecular dynamic simulation technique is used in these studies. The role of the crack-tip geometry and crack-length on the near-tip stress distributions, and the atomistic aspects of dynamic cleavage crack propagations at zero Kelvin temperature are studied in the first part of the dissertation. In the second part, the BDT of a covalent 2D triangular solid is studied using the MD computer simulations techniques. The simulations results are of fundamental interest.

The program has been carried out mainly in three stages:

I. The "static" simulations with the emphasis on the local stresses in the vicinity of the crack-tip and energetics of the system.

II. The "dynamic" simulations with the emphasis on the velocity of the brittle cleavage crack propagations, local stress distributions in the vicinity of the moving crack-tip, and energetics of the system. These series of investigations are performed at absolute zero temperature.

The mechanical properties of the selected systems, sample-size effects,

and the role of interatomic potentials on the said properties are studied in detail.

III. The brittle to ductile transition temperature and its characteristics are investigated in a 2D triangular covalent solid. The mechanical properties of the selected systems at finite temperature are also studied.

The plan of the present work is as follows: Chapter II contains the main body of the absolute zero temperature molecular dynamic simulations. In this section some relevant theories is reviewed in detail. The atomistic approaches to the fracture problems are reviewed in section II.1. The simulations results will be compared to, and interpreted in terms of these theories in the later chapters. MD simulations techniques used in the investigations, its simplifications, advantages, tradeoffs, limitations, and the interatomic potentials employed in the simulations are presented in section II.1. The section II.2 contains the mechanical properties of Johnson, Lennard-Jones, and "covalent" three-body potentials. Major simulations results of the "static" simulations exploring the effect of atomic crack-tip geometries on the local stresses are described, discussed, and compared to the continuum mechanics predictions, as well as, non-local theory of Eringen in this section. Theoretical developments concerning the sample size effect is discussed in II.2C. Griffith energy-balance theory is analyzed in section II.2D. The major computer results of the "static" simulations are cited and discussed in II.2E. The local stress distribution around an internal elliptic crack in a plate under simple tension is discussed in II.2F. Eringen's non-local theory is discussed in II.2H. The molecular dynamic

simulations of the effect of atomic crack-tip geometry on the local stresses is explained in section II.2I. The simulations results concerning this matter is cited in section II.2J. These results are discussed in the following section II.2K. The credibility of the computer simulations results is investigated in section II.2L. Section II.2M contains conclusions. Dynamic crack propagations is analyzed in the section II.3. This section begins by a short introduction, followed by the theoretical quasi-static analysis of the velocity of a cleavage propagating crack. Major simulations results of the crack-tip velocity is discussed in section II.3.B. The following section contains the conclusions. The crack-tip configurational model is developed in the section II.3.C. The energetics of the dynamic simulations is analyzed in the following section.

In section III.1 the molecular dynamic simulations at finite temperature is discussed. The interatomic potentials used in these simulations are discussed in section III.2. The mechanical properties of the two dimensional triangular Lennard-Jones-covalent (LJCOVa.2) solid at finite non-zero temperatures is studied in the following section, III.3. The simulation results of the search for the brittle-to-ductile transition temperature of the pre-cleaved LJCOVa.2 solids of various sample size is discussed in III.4. The simulation results are analyzed and compared to the available experimental and to the theoretical predictions in section III.5. The simulations results of the investigation of the brittle-to-ductile transition temperature of the pre-cleaved "corrected" Lennard-Jones-covalent (COR.LJCOVa.2) solids is cited and analyzed in section III.6. A brief report regarding the investigation of the behavior of the 2D-Johnson solid at finite non-zero temperatures is given in the section III.7. Finally, the simulations results of

the search for the brittle-to-ductile transition temperature is summarized in the section III.8.

The following sections contain Tables, illustrations, Bibliography, and Appendix.

II. *Atomistic Approaches to the Crack Problem.*

For a mathematical field quantity to represent a physical field, certain conditions must be satisfied. Basic to these conditions are the length and time requirements which arise from the discrete inner structure of bodies and the inner transmission time signals. All materials are made up of some sub-bodies which are attracted to each other by interatomic forces. We can associate an inter characteristic length, λ, with a given body [108]. In fracture, as in any thermodynamic processes, the final answers must be sought at the atomic or molecular level. For, it is the nature of the cohesive bonding between the constituent atoms in solids which ultimately determines the resistance to the propagation of a crack. This is particularly so in the case of perfectly brittle solids, where the critical rupture process is confined to an atomic-scale size about the crack-tip [33]. The inner characteristic length, λ, therefore, may be taken to be the atomic distance. In addition, with these sub-bodies there is associated a time scale, τ, (or frequency, ω) which may be the minimum transmission time of a signal (or an associated frequency) from one sub-body to the next. In fracture case, this may be taken to be an atomic or molecular relaxation time (or a related frequency). Associated with the external stimuli and geometrical and surface discontinuities is an external characteristic length, c, and time, τ_o, (or frequency, ω_o). The domain of applicability of a continuum theory depends on the ratios

$$[\lambda/c\,,\ \tau/\tau_o \ (\text{or}\ \ \omega/\omega_o)] \qquad \text{II.1.1}$$

All classical field theories intrinsically assume that $\lambda/c<<1$, and generally $\tau/\tau_o<<1$. Clearly, we cannot expect a reasonable treatment of the physical phenomena when these conditions are violated. In fact, this turns out to be the case for many important classes of physical problems among which we may cite: fracture of solids, state of stress at a crack-tip or dislocation core, micro-crack growth, fatigue, etc. [108]. However, practitioners often too busy with the difficulties of problems at hand, have forgotten or disregarded the underlying assumptions of the classical field theories that make these theories inapplicable to their problems. When such efforts did not bear fruit (as it is natural that they should not) then a "patch work" was made to mend some part of the field equation with arbitrary parameters and functions so that the result can be brought within the vicinity of experiments for that particular problem. Fracture of solid is one of these situations, where these approaches, having some convincing power, proliferated in the literature [108]. The critical process of crack propagation must occur at the very crack-tip, and here the linear-elastic continuum solutions show singularity. Thus, in inquiring how stresses remotely applied at the outer boundaries of a specimen transmit to the crack tip, there is a limit as to how far we may go with the conventional fracture mechanics. Therefore, if we wish to understand the "mechanisms" of fracture processes at a fundamental level, we must either develop theories that can reach the atomic and molecular regions [108] or expand the existing atomic theories.

Real materials are complicated in their inner structures. Imperfections, impurities, dislocations, holes, micro-cracks are widespread. Binding forces are almost certainly long ranged and involve multi-body effects [109]. These facts

when combined with the colossal number of differential equations, especially when quantum effects are taken into account, make it impossible to employ any atomic theory for real materials at this point.

On the other hand, while an atomic approach provides physical insight into the problem, it inevitably involves greater complications in analysis. Besides, since it is very difficult to study real materials at the atomic scale experimentally, the use of computer simulations to study model materials have been of growing importance [110] . Indeed, it is only with the advent of modern computers that dynamic investigations of the fracture problem at the atomic level have become possible [1-2, 110-118]. While computer simulations are not the ultimate desired microscopically controlled experiments, they may serve as a preliminary step in the atomistic level investigations of events occurring at the crack tip.

Modeling may lead to very significant physical insights, but it is essential to determine artifacts of the model and distinguish them from the general and relevant physical results [15]. Classically, the picture that one conjures up is an assembly of point masses, representing atoms held in some equilibrium configuration by means of non-linear cohesive bonds. The internal energy of the system, then, comprises of potential and kinetic components. The potential energy determines the intrinsic strength of the solid, while the kinetic energy determines the thermal properties [33]. Modeling involves two basic steps:

i. The construction of a model incorporating the key physical features of the system.

ii. The calculation of the physical characteristics of interest.

Then, the limitations of the results are those of the model itself [15].

In principle, the construction of a realistic model is perfectly straight forward: Construct a representative lattice for the given structure, then introduce a crack, followed by the allowance of the system to relax to its equilibrium configuration in accordance with some refined interatomic potential function. Why is this phenomenon so much more difficult than the other problems encountered often in solid state physics? In the most fundamental phenomena in solids, the periodicity of the solid is used to reduce the problem to an examination of a simple representative cell or regions. Hence, the infinite number of atoms is not a major problem. In the case of the crack, with its finite extension and resulting long-range strain fields, such reductions are not permitted. Besides, the fundamental descriptions of the interatomic interactions in the solid are not available at present. The ensuing equilibrium differential equations become intractable. The finite memory of even present day super-computers, and despite their high speeds, the limited time available to a given investigator due to economic restrictions still impose sever limitations on the size of the crystal model that may be handled. One is faced with the choice of either restricting consideration to relatively small crystallite containing at most a few thousand atoms, or devising some unrealistic hybrid atomistic-continuum model. In the hybrid lattice statics model a very small crystalline region, where the calculations are done with relatively realistic interatomic force laws, is embedded in an infinite elastic continuum. The size of the area of the crystal modeled to the atomic detail in this model is restricted to the order of several

hundred to several thousand atoms by computational costs. Often, this is too small for the atomic level effect to be considered negligible at the boundaries, and one of the major problems in the applications of this technique is the determination of the boundary conditions to be applied to the crystalline region [119]. At the other end of the scale, molecular dynamic simulations may be used on an unconstrained system of a relatively large number of atoms interacting via a reasonably realistic interatomic potential. Here, of course, the question is how large is large enough to simulate the behavior of the corresponding real macroscopic system [15].

II.1A. *Molecular Dynamics: Outline of the Techniques at 0 Kelvin.*

The computer simulations of the atomic motion in solids by the molecular dynamics (MD) technique has been treated extensively in the literature [114-115, 120]. Basically, Newton's differential equations of motion are solved simultaneously by a numerical method for a relatively large number of interacting atomic mass points, representing the constituent interacting atoms of the solid. The interatomic interactions are, in general complicated non-linear long-ranged force laws for real materials. In brief, the molecular dynamic simulations [121-124] are carried out on a two-dimensional triangular lattice illustrated in Fig II.1.1. The largest sample, in the present simulations, consisted of 21544 atoms arranged in 159 rows. Mirror symmetry about the central vertical axis was used to reduce the computational time, and therefore its cost. The full sample contained a centrally located internal crack and was subjected to the mode I opening configurations either under an externally applied constant load, i.e., Dead-Weight, or a constant applied external strain or displacements, i.e., Fixed-Grips. The initial central internal crack was introduced to the solid by cutting a given number of interatomic bonds by prohibiting the interatomic interactions between the given atoms at the center of the solid. For example, the interatomic bonds between a given number of atoms, depending on the length of the initial central crack, were cut between the specified atoms on rows 39 and 40 for 79x135 sample size, as illustrated in Fig. II.1.1. No atom was removed physically from the system, unless otherwise specifically mentioned.

II.1B. *The Interatomic Potentials*

As pointed out in the previous section, an interatomic potential has to be assumed in order to perform the molecular dynamic simulations. Some of the dynamic properties of the running crack, such as the terminal velocity, sample size effect, strain rate effect, as well as the degree of the brittleness of the sample depends very much on the nature of these interatomic potentials. Other properties such as the local stress distribution, and the acceleration processes of the running cleavage crack appears to be primarily influenced by the discrete atomic nature of the crystalline solid. In any case, it is clearly important to define and discuss the interatomic potentials employed in the MD simulations, and the resultant mechanical properties of the crystal. It is also important to recognize that, since no interatomic potential suitable to simulate a real solid especially in the highly sensitive region of the immediate vicinity of critically loaded crack is available at the present, the simulation results at best represent the general properties of a propagating crack. The lack of existence of a reasonable potential to represent a real solid is the major limitation of the MD techniques.

Four types of interatomic potentials were employed in the present MD simulations:

i. **The Lennard-Jones (LJ) 6-12 potential** characteristic of the interatomic interactions in the rare gas crystals (Fig II.1.2) was used in the form

$$\Phi_{ij}(r_{ij}) = [(d/r_{ij})^{12} - 2(d/r_{ij})^{6}]\,\varepsilon_o - \Phi(1.6d) \qquad \text{II.1.2}$$

with all energies measured in units of ε_o, and distances r_{ij} in units of d, the equilibrium spacing. Because of the economic considerations, the LJ potential was truncated at r=1.6d, well beyond the interatomic distance of 1.11d where the interatomic force is maximum and slightly less than the second-neighbor distance, $\sqrt{3}$d, i.e., after the introduction of the internal crack [1-2, 15, 121] forces were calculated between all atoms within 1.6d. Conversion factors and units for 2D triangular LJ solid is given in Table II.1.1.

ii. **Johnson's [125] empirical potential.** This potential was originally developed to simulate α-iron. It is used in the form

$$\Phi_n(r_{ij}) = -A_n (r_{ij} - B_n)^3 + C_n (r_{ij}) - D_n \qquad \text{II.1.3}$$

where, $\{A_n, B_n, C_n, D_n ; n=1,2,3\}$ are constants giving a continuous composite potential over three ranges of r_{ij}. These constants and ranges of this polynomial potential are given in Table II.1.2. Conversion factors and units for the 2D-triangular Johnson solid are tabulated in Table II.1.3. The Johnson potential is illustrated in Fig II.1.3. As indicated in this figure, the Johnson potential has an inflection point at r/d = 1.17189. Consequently, the interatomic force is maximum at this point. A major difference with the Lennard-Jones potential is the fact that Johnson potential goes smoothly to zero at r/d=1.31470. Another major difference between these two pair-wise

interatomic potential is that the Johnson interatomic force, as demonstrated in Fig. II.1.3b, falls off much more rapidly past the maximum than is the case with the Lennard-Jones interatomic force. The mechanical properties of the two-dimensional Johnson solid is studied in the section II.2B.

iii. ***Three-body covalent potentials.*** The 2D triangular Lennard-Jones (or Johnson) solids are in the vicinity of ductile-brittle behavior. Most of the continuum based formulations are developed for perfectly brittle cleavage crack, with no plastic deformations associated with the running crack. Therefore, in order to study the influence of the relative brittleness of the fracture on the dynamic properties of the running crack, by realizing that many brittle materials exhibit directional bonding between their constituent atoms, a covalent potential was developed by modifying the pair-wise Lennard-Jones (or Johnson) potentials, by adding an angular resistance to them. It is worthy to note that the construction of these three-body interatomic potentials were extremely important for the investigation of the brittle to ductile transition temperature. For, as indicated above, the 2D Lennard-Jones (or Johnson) solids were in the vicinity of the ductile-brittle behavior, and any small variation in the boundary conditions, crack shapes, strain rate and loading conditions may drive the behavior either way [15] even at absolute zero temperature.

The rigidity and therefore the degrees of brittleness of these solids may be varied to investigate the influence of the degree of brittleness or rigidity of the solid on the various static or dynamic properties of the fracture. These

covalent potentials are given by

$$(1/2)\,\Sigma'_{ij}\,\Phi(r_{ij}) + (1/6)\,\Sigma'_{ijk}\,[\Phi_{ijk}+\Phi_{jki}+\Phi_{kij}] \qquad \text{II.1.4}$$

where,

$$\Phi_{ijk} = \Phi(r_{ij})\Phi(r_{ik})\,[2a^{*}\,(\mathrm{Cos}\theta_{ijk} - \mathrm{Cos}\theta_{o})\,] \qquad \text{II.1.5}$$

where a^* is the amplitude of the angular resistance, θ_{ijk} is the angle between r_{ij} and r_{ik}, and θ_o is the original angle between r_{ij} and r_{ik} in the perfect defect-free unstrained specimen. The lattice rigidity was varied over a wide range by varying a^*. Mechanical properties of these solids are studied in section II.2B.

II.1C. *Simplifications.*

Due to economic restrictions, the computer simulations could proceed only if some simplifying assumptions were made. The most important trade-off was made on the dimensionality of the system. The limitation of the computer memory, and the high cost of calculations imposed sever limitations on the size of the crystal model which could be handled. This limitation forced us to give up on the third dimension, and simulate a two-dimensional triangular lattice. Due to the similar restrictions, the LJ potential had to be truncated at a distance slightly less than the initial second-neighbor distance. Two-dimensional triangular lattice is the simplest system supporting shear stability in the near neighbor approximation. The two-dimensional square lattice would posses a

minimal shear stability only when second-neighbor interactions are included [112]. The triangular lattice is isotropic, and therefore, the comparison of its properties with those of the isotropic continuum is possible. The two-dimensional triangular lattice has the same strain energy as a two-dimensional continuum when the first-neighbor Hookian interaction is considered. Preliminary studies [1-2] have established the credibility of the molecular dynamic simulations of the 2D triangular LJ solid [15]. The sample size limitations, the proximity of the boundaries to the crack-tip, and the nature of boundaries may produce some serious artifact. The credibility of the computer simulations results, therefore, has to be discussed in order to determine which part of the results are (or may be) the artifact of the model and which parts are general and relevant to the real physical system being modelled [15]. Finite, and very limited three dimensional model would not necessarily produce more realistic results [113]. The size restriction is not due to any limitation of the molecular dynamic techniques, but merely due to the restrictions imposed on by the use of computers to implement the technique.

II.1D. *Verlet Method for Solving Newton's Equation of Motion.*

The calculations were performed using the Verlet method [126] for solving Newton's differential equations of motion for every point mass in the system, simultaneously. Basically, Newton's differential equations were solved numerically [127] by approximating them as difference equations

$$r_i(t+\delta) = -r_i(t-\delta) + 2r_i(t) + [F_i/m]\delta^2 \qquad \text{II.1.6}$$

where $\mathbf{r}_i(t)$ is the position of the ith atom at time t, m is its mass, and $\mathbf{F}_i$ is the net force on it calculated from the interatomic potential, $\Phi(r_{ij})$ as

$$\mathbf{F}_i = -\Sigma'_{ij} \nabla\Phi(r_{ij}) + \mathbf{F}_{i,ext} \qquad \text{II.1.7}$$

where $\mathbf{F}_{i,ext}$ is the external force on the ith atom, if any.

The choice of the approximation schemes for solving Newton's differential equation of motion is as much a matter of economics determined by the accounting practices of the research establishment as by the mathematical merits. Present calculations have achieved an accuracy in the energy of one part in a million by using a short time step, δ=0.08 $d\sqrt{(m/\varepsilon_o)}$ for the static calculations, δ=0.02 $d\sqrt{(m/\varepsilon_o)}$ for dynamic calculations at zero Kelvin temperature, and δ=0.01 $d\sqrt{(m/\varepsilon_o)}$ for all finite temperature simulations. Further reduction in the time step, δ, did not make the calculations more accurate over reasonable time steps. The basic limitation of the MD technique is this time duration, δ, which should be chosen in such a way that neither disturbs the basic physical principles (like that of the conservation of energy), nor to prolong, unnecessarily, the calculations. It is worthy to note that due to the small duration in time 10^{-10} sec., which can be handled by MD techniques, only those physical phenomenon with the characteristic times of this order may be handled by this method [108]. As we were charged by the BNL computer facilities for the product of memory and time used, the Verlet central difference method is as cost effective as other more elaborate techniques which require the use of a larger amount of computer memory [127]. The main difference

between the Verlet method and Nordsiek-Gear method is in the number of previous positions or equivalently the number of higher order time derivatives used to predict the present position of an atom. More computer memory may be used to obtain a higher precision per time step in the Nordsiek-Gear method. This may be exchanged by a longer time interval for a comparable accuracy in the Verlet method. Som [115] found that in the CDC7600 computer at BNL using the Nordsiek-Gear method of order seven with comparable accuracy to the central difference method and a given time duration, δ, time intervals of four to six times as long may be used for the same precision, and a cost reduction of about a factor of two resulted for a medium size sample simulations. However, the long memory requirement in the Nordsiek-Gear method made the required time to collect a comparable accurate result so long that Som abandoned this method. In transferring to the Cray 2 computer facilities, assuming a similar accounting procedure, no attempt was made to alter the code regarding the Verlet method.

At absolute zero Kelvin temperature, equilibrium was achieved by inserting the critical damping parameter, β, into the equation of motion. The difference equation II.1.6 was therefore replaced by

$$\mathbf{r}_i(t+\delta) = \mathbf{r}_i(t) + \beta[\mathbf{r}_i(t) - \mathbf{r}_i(t-\delta)] + [\mathbf{F}_i/m]\delta^2 \qquad \text{II.1.8}$$

The critical damping removes a portion of the kinetic energy of every mass point in the system at each time step. This artificial decrease of the kinetic energy of the system speeds up the equilibration process, and therefore,

reduces the economic costs of these simulations. The smaller the value of β, the more energy is extracted from the system. But, since this reduction in the kinetic energy of the system is directly related to the velocity of every given atom in the solid, too large or too small value of β prolongs the equilibration time. There is only a narrow domain of β which causes a sharp reduction in the equilibration time. Obviously, if we are interested in the quantitative properties of the propagating crack or of a dynamic configuration, or if the study is performed at a finite non-zero temperature, damping should be removed. Because otherwise, unaccounted amount of energy is extracted from the system, and therefore as a result the system is no longer an adiabatic one; the temperature of the solid is reduced artificially, and the crack-tip velocity is too small. Hence, all of the dynamic and finite non-zero temperature simulations were performed using β=1 which corresponds to the adiabatic configuration.

The potential, kinetic, and total energies, modulus of elasticity of the system, atomic positions, velocities, forces, and the total number of interatomic bonds were monitored throughout. The atomic positions and velocities were stored at a given time step, in order to continue the run, or to plot the positions of mass points and unbroken interatomic bonds, in order to make the dynamic *behavior* of the fracture visual.

The forces were calculated between the mass points, i.e., atoms which were initially nearest neighbors. After the introduction of the crack, forces were calculated between all atoms within the range R. The value of R was set to 1.6d for LJ potential, and 1.3147d for the Johnson potential. A table of interacting

atoms, where neighbors of every atom are identified was constructed. This table was updated periodically, or immediately after any serious disturbances in the solid (like that of any atom moving out of the range of its assigned neighbors, i.e., when a bond at the crack-tip broke). This type of updating is necessary in the investigation of the dynamic properties of the fracture, where there are considerable deformations in the vicinity of the running crack and local atoms in this region keep moving in and out of the interaction range of each other.

Mirror symmetry about the central axis, n, required a special treatment of the atoms of the two immediate right columns of it. Fig. II.1.4 shows these two mirrored columns of n+1 and n+2 produced respectively by the reflection of the n-1 and n-2 columns of the left hand side part of the solid about the central vertical axis n. Hence, one half of the sample plus two columns of atoms mirrored into the neglected half of the solid was only used in the simulations. Therefore, for example, our largest sample of 159 rows with 135 atoms in the odd rows and 136 atoms in the even rows were simulated by using a sample of 159 rows with only 70 atoms in each row. The last two columns passing through 69th and 70th atoms of the odd rows are the mirror images of the 67th and 66th atoms of the odd rows about the central (mirror) axis passing through 68th atoms of the odd rows. The horizontal positions of the central axis are fixed to their initial perfect lattice values.

The mirror symmetry facility could not be used for the finite non-zero temperature computer simulations. Because otherwise, part of the system, i.e.,

atoms of the central axis would be partially frozen, and therefore would be kept artificially in a temperature much lower (about half) than the rest of the solid. Non-zero finite temperature MD simulation technique is discussed in section III.1 in detail.

The zero K simulations were performed both at constant externally applied tensile load (dead-weight) and constant external tensile strain (fixed-grips). The finite non-zero temperature simulations were done only at constant externally applied tensile load.

II.1E. Constant Externally Applied Tensile Load (Dead-Weight) Simulations; Outline of the Method

In the case of the constant applied tensile stress simulations, the external tensile force was applied to the individual atoms of the uppermost and lowermost rows. All external boundaries were free to move. The atomic positions of the constituent atoms of the solid, regardless of the presence of the internal crack, under a small constant external tensile load are almost identical to those of the perfect sample. The crack-tip region, depending on the interatomic potential, external load, and crack length may be excluded from the above statement. Therefore, for the purpose of a considerable saving on the computation time, the vertical positions of individual atoms in the sample were scaled to a value of strain corresponding to the applied external tensile load. The sample, then, takes relatively very short time to reach its equilibrium configuration [15]. The detailed knowledge of the modulus of elasticity and the stress-strain relation of the perfect sample is a necessity for this purpose. The mechanical properties of the 2D triangular LJ, Johnson, and covalent solids, therefore, had to be studied in detail prior to the investigation of the fracture problem in these solids. Since the crack-tip region is considerably deformed due to the high stress concentrations in the vicinity of the crack-tip when the remotely applied tensile stress is large, the vertical positions of individual atoms were scaled from those of the perfect sample under infinitesimally lower applied tensile stress. The sample, then, was allowed to relax to its proper new equilibrium state, with the aid of the critical damping. The critical damping, along with the vertical scaling procedure, may not be employed when the

applied tensile load is about the critical Griffith stress. This is because of the extreme sensitivity of the critically loaded crack-tip to any motion or displacement of the atoms in its immediate neighborhood. Any externally induced disturbance in the immediate vicinity of the critically loaded crack-tip may artificially aid or delay the propagation of the crack. These simulations represent, virtually, the quasi-static loading schemes, and are identified as the "gradual" simulations in the present studies. To investigate the loading rate affect, a few simulations were performed using a different procedure. In these studies, the "perfect" sample was brought to a reasonable equilibrium by scaling and damping under the critical load identical to the corresponding "gradual" simulations. The crack was then introduced to the solid, and the critical damping of the system was continued for a few hundred time steps in order to minimize the shock wave introduced to the system during the introduction of the crack into the solid. Damping was then removed and the crack was allowed to propagate [122].

To explore the sample-size effect a set of samples with various initial crack-length were simulated. Different sample sizes of 39x135, 79x135, and 159x135 were simulated to investigate the effect of the height of the sample on the various dynamic properties of running crack. These set of simulations were also essential to clear out some previously misinterpreted simulation results in the literature [1,2].

Because of the spatial configuration of the crack, it was found that we may estimate the half-crack length, c, from the total number of broken bonds in

the sample, NBB_{tot}, by

$$c = [NBB_{tot} + 1]/4. \qquad \text{II.1.9}$$

The total number of mass points in the full sample may be calculated using

$$[NAOR][NR+1]/2+[NAOR+1][NR-1]/2 \qquad \text{II.1.10}$$

where,

NAOR = The number of atoms in the odd row of the full sample.

NR = Number of rows of the sample.

For example, the total number of atoms in the largest sample of 159x135 is

$$(135)(159+1)/2 +(136)(159-1)/2 =21544 \text{ atoms}$$

The total number of atoms in the 79x135 sample was 10704, and in the 39x135 sample was 5184.

To study the energetics of the running crack under the critical externally applied stress, σ_c, the energetics of the "perfect" sample subjected to the identical critical load and at perfect equilibrium were needed as the reference point. Hence, after the determination of the critical external load, σ_c, necessary to initiate the brittle propagation of the crack, the perfect sample was "scaled" from a previous run to the σ_c, and brought to its equilibrium state by critically damping the system. This procedure was repeated for every individual run,

where we were interested in the energetics of the system.

All interatomic potentials used in these simulations were non-linear, except a short run where the Hookian potential was used to investigate the possibility of supersonic crack-tip velocities reported in the literature. The deviation from the continuum linear elastic theory may be ascribed primarily to the nonlinear behavior of these solids. When the externally applied tensile load (or strain) is large, or when a crack is introduced into the solid, the modulus of elasticity of the sample is reduced. The self-consistency requires that this be taken into the account along with the sample size effect. Hence, the effective modulus of elasticity, M*, correction represents a self-consistent approach for the evaluation of the finite sample size effect, and is analogous to the laboratory experimental compliance measurement.

Since all external boundaries of the sample are free to deform, the horizontal distance between the interatomic atoms are contracted because of the function of Poisson's ratio. Therefore, the constant external tensile forces on the individual atoms of the uppermost and lowermost rows, rather than stresses which would involve some arbitrary length, are given. The externally applied stress may be defined as the applied tensile force per unit length

$$\sigma = F / r_2 \qquad \text{II.1.11}$$

As illustrated in Fig. II.2.1 with $r_{o1}=r_{o2}\equiv d\equiv 1$, the relevant equations are

$$r_2 = r_{o2} - \nu\varepsilon \equiv 1 - \nu\varepsilon \qquad \text{II.1.12}$$

and,

$$\varepsilon = 2\Delta / \sqrt{3} \qquad \text{II.1.13}$$

where ν is Poisson's ratio, ε is the strain, and Δ is the tensile elongation of the height, i.e., $h_O=\sqrt{3}/2$ of the elementary triangular cell.

The comparison of the local stress distribution around the static and running cracks is an important issue in the evaluation of the dynamic crack propagation theories. Some of the earlier MD simulations of running cracks [15, 114, 128-129] indicated disagreement between the local stress distribution in the vicinity of the crack-tip at the atomic level and those derived from the conventional linear elastic continuum concepts. For example, the critical load for dislocation generation at the crack-tip was not significantly reduced by the widening the crack produced by the ledge left behind by the dislocation [114, 128]. The singularity at the crack-tip by the continuum theories is, naturally, never observed in the atomistic simulations of the fracture. In a discrete lattice the crack tip stress is bound, i.e., there is no singularity. The maximum value which it may achieve occurs at the initiation, and/or during the brittle propagation of the cleavage crack. The maximum value of stress corresponds to the cohesive strength of the material. These observations were made at very high stress levels on a non-linear elastic material (2D-triangular LJ solid). For a quantitative comparison with continuum theory it was clearly necessary to carry out simulations for the stress concentration factor on a variety of cracks, and crack geometries at very small applied loads where the stress-strain

behavior is for all practical purposes, linear.

The effect of geometrical blunting was investigated by simulating the response of the cracks of Fig II.1.5 to a remotely applied nominal tensile load. These cracks are very similar to the ones observed in the earlier dynamic simulations [15, 123]. The influence of crack length on the local crack tip stress was also studied but only on narrow cracks (constant b) of various lengths [Fig. II.1.5a]. The medium sample of 10704 atoms arranged in 79 rows is used in these set of simulations.

The narrow crack was formed by cutting the interatomic bonds [2, 111-112] between a given number of atoms in the 39th and 40th rows, i.e., those atoms were prevented from interacting with each other [Fig. II.1.5a]. This corresponds to the insertion of a very thin knife to create the crack, and keeping the knife there to prevent the undesired healing of the crack. This form of cracks were our "normal" mode I internal cracks used as the initial cracks in all of the simulations, unless otherwise mentioned.

The wide crack [Fig. II.1.5b] was formed by removing four rows of given atoms. The crack tip is located on the 58th atom of the 39th row. The effective "half-crack length", c, is 9.75d.

The "wide-jagged" crack was created by removing eight rows of atoms and by cutting some additional bonds as illustrated in the Fig. II.1.5c. The effective half-crack length, c, is 9.75d.

The detailed study of the effect of the atomic crack-tip geometry on the local stresses was done on the 2D-triangular Lennard-Jones solid. To investigate the effect of the interatomic potential on the local stresses, a few simulations were also performed on the 2D-triangular Johnson solid.

II.1F. *Fixed External Displacement (Fixed-Grips) Simulations; Outline of the Method*

In this case a given constant strain was applied by specifying and maintaining the vertical displacements of the individual atoms in the uppermost and lowermost rows of the specimen, with all other atomic motions free to adjust. To cut down the equilibration time, and therefore the cost of the computation, vertical positions of individual atoms in the sample were scaled to their appropriate values according to the applied strain. Equilibrium at absolute zero temperature was attained by the insertion of the critical damping parameter, β, into the equation of motion.

All other procedures/calculations of the fixed external displacement and constant applied tensile load simulations were done in the similar manner. In the case of the fixed-grips simulations, the calculated forces (stresses) on the individual atoms in the uppermost and lowermost rows of the sample were not constant. The force on the individual atoms along the horizontal boundaries directly above and below the crack line was lower than the force on the other individual atoms along the same rows but toward the vertical boundary of the sample [Fig. II.1.6]. The system is partially unloaded because of the reduction in the magnitude of the strain (potential) energy of the solid due to the introduction of the crack into the sample. This makes the appropriate stress to use in the definition of the stress concentration factor unclear, and introduces some uncertainty into it. In the case of the constant load simulations the forces on the individual atoms in the lowermost and uppermost rows are constant by

definition. The results of the constant externally applied tensile load simulations are, therefore, the only quantitative data which could be compared to the theoretical predictions [121].

II.1G. *Elasto-Static Considerations*: *Outline of the Technique*

To evaluate the elasto-static continuum predictions a set of MD simulations were carried out in a 2D-triangular array of 10704 atoms interacting via Johnson potential and arranged in 79 rows under the constant externally applied tensile load of 1.50 ε_o/d. Varieties of crack lengths were used in these simulations. The constant applied load of 1.50 is less than the critical load of 1.90 necessary for the initiation of the brittle propagation of the longest crack of half-length c_o=9.75d [Table II.1.4-5] studied in these simulations. An initially defect-free sample was brought to its equilibrium by the critical damping of its kinetic energy. The question of equilibrium is of great importance in these studies, and was judged to have been achieved when small and equal fluctuations of alternating sign of the order 10^{-6} ε_o were observed in the energies of the solid. The kinetic energy of the sample, with or without crack, at equilibrium is expected to be zero. This is equivalent to achieving absolute zero temperature. The change in the potential energy of the system, ΔE_{pe}, and the work done by the external load on the solid, ΔW, were calculated with respect to the corresponding values of the loaded defect-free sample. Each broken bond corresponds to a single unit of the potential energy, ε_o. Therefore, the free surface energy, γ_S, is equal to ε_o. The surface energy of the cleavage crack of half-length c is therefore

$$E_S = 4c\gamma_S \equiv 4c\varepsilon_o \qquad \text{II.1.14}$$

The change in the strain potential energy, ΔE_{el}, stored in the elastic medium is

therefore given by

$$\Delta E_{el} = \Delta E_{pe} - NBB \qquad \text{II.1.15}$$

The number of broken bonds in the solid at a given time, NBB, and potential energy of the solid, E_{pe}, are monitored throughout the run. The results of the simulations are presented in Table II.1.4.

II.1H. *Limitations, Advantages, and the Credibility of the Present Molecular Dynamic Simulations*

The principal limitation of the MD simulation is the small duration in time of the events $\tau \approx 10^{-10}$ sec., which may be handled by this technique. Let τ_o be the associated characteristic time with the external stimuli and the geometrical and surface discontinuities (cracks). Only if $\tau/\tau_o \approx 1$, the individual fields of sub bodies are important and the collaborative action of sub bodies (atoms) are influenced by their individual responses substantially [108]. Therefore, only those phenomenon in which the characteristic times are of this order ($\tau_o \approx 10^{-10}$ sec.) may be investigated by this technique.

Despite the speed and memory capacities of present day super-computers (like Cray2 which is used in a major part of the present work), the economic factor still imposes a sever limitation on the size of the crystal model that may be handled [33]. Therefore, only a limited number of atoms could be involved in the simulation. Even though this is not due to any limitation of the technique, in practice it is an intrinsic and integrated part of it, because, we need computers to employ the MD technique. This serious limitation is the principal limitation of the present work, which forced us in compromising on the third dimension and limit the investigation to a 2D solid. The use of a more realistic multi body long-range interatomic potential was also prohibited because of these economic restrictions. Due to the similar intolerance, we were limited to the investigation of very few varieties of crack-lengths and loading conditions. Sometimes, we had to submit overnight jobs because of their

relative cheapness. On the other hand, a job which would not take more than few minutes of the computer time, were delayed by the computer facilities for several hours due to the use of the computer by the other investigators. Computer simulations, in this regard, are very time-consuming, specially when a dynamic situation is involved, where in order to submit a new job at a given load or at higher step the results of a job at lower load or lower time step is required.

The time step, δ, in the equation of motion II.1.8 had to be chosen very carefully. For, a larger time step would probably result in the violation of some basic physical principles (like that of the conservation of energy), and in dynamic simulations may result in the complete destruction of the sample. On the other hand, very small time step would prolong the computation, unnecessarily. Similar care must be taken in choosing the critical damping parameter, β, as discussed early.

Periodic boundary conditions can not be used in the simulations of the crack problem due to the undesired crack-tip interaction with each other. Only mirror symmetry about the central axis could be employed in the zero temperature simulations which saved about fifty percent in the computation cost. In the finite non-zero temperature simulations mirror symmetry could not be employed and the "mirror" had to be removed.

On the other hand, the MD technique is a powerful method. A realistic semi-empirical interatomic potential can be used. The model system can be

completely unconstrained, except for the correct boundary conditions. With the appropriate attention to the required accuracy [127] in the simulation, the results are exact within the framework of the model. Thus, there is no question that the molecular dynamic calculations do not yield interesting "accurate" data, but always the problem to be resolved is how much of the results arise from the simplifications in the interatomic potential as well as the geometry [15].

The major argument favoring the credibility of the molecular dynamic simulations is the fact that the energetics of the 2D-triangular LJ solid [1] or Johnson solid [122] are in close agreement with predictions of continuum mechanics. The fact that the crack-tip velocities rapidly attain a constant terminal value which is less than the sound velocity in the solid is in accord with the experimental observations [1, 15, 122-124] and is another argument for the credibility of the molecular dynamic simulations technique.

Most of the limitations stated earlier are imposed on us by the economic restrictions by the use of computers to implement the technique. By the advent of super-computers, this limitation could be negligible in the near future. For, the use of 21544 atoms in the MD simulations was unthinkable even few years ago [111-113].

II.2. *Elasto-Static Molecular Dynamic Simulations*

II.2A. *Outline of the Method*

In all elasto-static MD simulations, the system was brought to equilibrium under a constant externally applied tensile load, σ_a , (or a fixed external strain, ε_a) smaller than the critical external load, σ_c, (or critical external strain, ε_c) before the insertion of the internal crack into the system. Equilibrium at absolute zero Kelvin was attained by scaling of the sample and the insertion of the critical damping factor into the equation of motion as described in detail in the section II.1C. Then, an internal centrally located crack of a given length was created in the solid by cutting a specific number of interatomic bonds across the central rows of the solid (Fig. II.1.5a). The removal of a few atoms were needed only if we were interested in the creating of a specific crack geometry.

II.2B. *Major Computer Simulations Results*

i. *Mechanical Properties of the Two-Dimensional Triangular Johnson, and Lennard-Jones Crack-Free Solids*

The elastic properties, at infinitesimal applied strain, ε_o, (or stress, σ_o) of a 2D-triangular solid held together by a central force are well known [130]. This solid is isotropic. It has been realized that the application of the predictions of the three dimensional elasticity theory to a two-dimensional solid leads to

certain inconsistencies [112, 130]. Detailed analysis leads to the conclusion that for a 2D system, the elasticity results of 3D plane-stress may be used, and Lam's parameters, λ and μ, [131] are equal for this isotropic solid. The modulus of elasticity at infinitesimal applied strain, M_o, and Poisson's ratio, ν, are given by

$$M_o = 4\,\mu(\lambda + \mu)/(\lambda+2\mu) = (8/3)\mu \qquad \text{II.2.1}$$

and,

$$\nu = \lambda/(\lambda+2\mu) = 1/3 \qquad \text{II.2.2}$$

For any nonlinear elastic solid, such as Johnson (or Lennard-Jones) solid, as the strain (or stress) is increased, Poisson's ratio, Young's modulus of elasticity, and the shear modulus become functions of the strain (or stress). Young's modulus and Poisson's ratio may be calculated theoretically for a homogeneous deformed elementary triangle, or measured directly by the MD simulation on the solid for a given external applied strain (or stress). For a uniform applied strain, Young's modulus and Poisson's ratio may be calculated from the balance of forces from the deformed elementary triangular cell [15, 123] as illustrated in Fig. II.2.1 with $r_{01} = r_{02} \equiv d \equiv 1$, the relevant equations are

$$\varepsilon = 2\,\Delta / \sqrt{3} \qquad \text{II.2.3}$$

$$r_1^{\,2} = (3/4)[1+\varepsilon]^2 + (1/2)^2\,[1-\nu\varepsilon]^2 \qquad \text{II.2.4}$$

and,

$$r_2 = 1-\nu\varepsilon \qquad \text{II.2.5}$$

where Δ is the tensile elongation of the height, i.e., $h_o=\sqrt{3}/2$ of the elementary triangular cell. The corresponding tensile force, F, may be calculated from the interatomic central potential $\Phi(r)$ as

$$F = 2\,(\sqrt{3}/2)\,(1+\varepsilon)\,(1/r_1)(d/dr_1)\Phi\,(r_1) \qquad \text{II.2.6}$$

Poisson's ratio, ν, is determined by minimizing of the potential energy of the system with respect to ν, i.e., by imposing the equilibrium condition

$$d\Phi/d\nu = 0 \qquad \text{II.2.7}$$

Using the appropriate interatomic potential, $\Phi(r)$, the equation II.2.7 yields

$$2[d\,\Phi\,(r_1)/dr_1\,][dr_1/d\nu\,]+[d\,\Phi\,(r_2)/dr_2\,][dr_2/d\nu\,]=0; \qquad \text{II.2.8}$$

$dr_1/d\nu$, and $dr_2/d\nu$ may be calculated from equations II.2.4-5 producing

$$dr_2/d\nu = -\varepsilon \qquad \text{II.2.9}$$

and

$$dr_1/d\nu = -(1/4)(1-\nu\varepsilon)\,\varepsilon/r_1 \qquad \text{II.2.10}$$

Young's modulus of elasticity $M(\varepsilon, \nu)$ is given by

$$M(\varepsilon, \nu) = \sigma/\varepsilon = F/(\varepsilon r_2) = F/\varepsilon\,(1-\nu\varepsilon). \qquad \text{II.2.11}$$

Note that Young's modulus, M, is defined as the stress over the strain and not as the differential of stress w.r.t. the strain.

For the Johnson's potential

$$\Phi_n(r_{ij}) = -A_n(r_{ij} - B_n)^3 + C_n(r_{ij}) - D_n$$

where $\{A_n, B_n, C_n, D_n ; n=1,2,3\}$ are constants giving a continuous composite potential over three ranges of r_{ij} [Table II.1.2-3]

$$d\Phi/dr = -3A_n(r_{ij} - B_n)^2 + C_n \qquad \text{at} \quad r=r_{ij} \qquad \text{II.2.12}$$

Therefore, for a given value of the tensile strain, ε, the following equations may be solved interactively with an error in the sixth figure

$$-[(1-\nu\varepsilon)\varepsilon/2r_1][-3A_n(r_1-B_n)^2+C_n]-\varepsilon[-3A_n(r_2-B_n)^2+C_n]=0$$

$$r_1^2 = (3/4)[1+\varepsilon]^2 + (1/2)^2[1-\nu\varepsilon]^2 \qquad \text{II.2.4}$$

and,

$$r_2 = 1-\nu\varepsilon \qquad \text{II.2.5}$$

The results of these calculations are illustrated in Fig. II.2.2-9 as the force, F, Young's modulus, M, and Poisson's ratio, ν, vs. the applied strain, ε. The maximum force of 9.088 ε_o/d occurs at the applied strain of ε=0.2605 [Fig. II.2.2]. The corresponding Young's modulus is M=36 ε_o/d^2 as demonstrated in

Fig. II.2.5. Beyond this point the system is metastable. Note that the data given in these figures are passed this point.

A series of molecular dynamic simulations were carried out over a range of constant applied stress, strain and sample sizes. The results of these computer simulations are shown in the Fig. II.2.5&9 together with the theoretical Young's modulus, M, (solid line) calculated by the above equations in the region of interest. The excellent agreement of the theory and the computer simulation is reassuring. In the region of interest the strain dependency of the modulus of elasticity may be given by

$$M = M_o - \alpha\varepsilon \qquad \text{II.2.13}$$

where $M_o=60.13\ \varepsilon_o/d^2$ and $\alpha=46.104$, as illustrated in Fig. II.2.5.

For the two-dimensional triangular Lennard-Jones solid, for a given value of the applied tensile strain, ε, the theoretical values of Young's modulus and Poisson's ratio are calculated through the interactive solution of the following set of equations, with an error in the sixth figure [15]

$$r_1^{\,2} = (3/4)[1+\varepsilon]^2 + (1/2)^2\,[1-\nu\varepsilon]^2 \qquad \text{II.2.4}$$

$$r_2 = 1-\nu\varepsilon \qquad \text{II.2.5}$$

$$\varepsilon(1-\nu\varepsilon)[r_1^{-14}-r_1^{-8}]+2[r_2^{-13}-r_2^{-7}]=0. \qquad \text{II.2.14}$$

R_1 and r_2 are shown in Fig. II.2.1. The results of these calculations are shown in Fig. II.2.6-9 as the tensile stress, σ, Young's modulus, M, and Poisson's ratio, ν, against the applied strain, ε. As illustrated in the figure II.2.6, the maximum stress of 4.8902 ε_o/d^2 occurs at the applied strain of 0.15. The corresponding Young's modulus, and Poisson's ratio are 32.6013 ε_o/d^2 and 0.094971, respectively, at this point [Fig. II.2.7b]. Beyond this point the system is metastable. The data presented in Fig. II.2.6-7 are given past this point. The computer simulations results [115] are in excellent agreement with the predictions of the theory. In the region of interest, the functional dependency of Young's modulus on the applied strain, ε, is given by [15]

$$M = M_o - \alpha\varepsilon \qquad \text{II.2.13}$$

with M_o = 83.14 ε_o/d^2 and α = 414 ε_o/d^2 as illustrated in Fig. II.2.7.

However, in the presence of a crack and during the "brittle" propagation of the crack, the system may be deformed in a highly inhomogeneous manner in the vicinity of the critically loaded crack-tip, and there may exist regions which are deformed way past the stability point, but are stabilized by the surrounding atomic matrix.

In order to demonstrate the very different response upon the compression of the solid with a rapidly varying repulsive potential, the calculations was carried out for the 2D-triangular Lennard-Jones solid under compressive forces. The results are illustrated in Fig. II.2.6-7.

ii. *Mechanical Properties of the 2D-Triangular Lennard-Jones-Covalent Solid at Absolute Zero Temperature*

Analytical calculations are no longer simple for the "covalent" solid where besides the radial deformation of the interatomic bonds the angular deformations also have to be taken into the account. Consequently, the mechanical properties of this solid is determined only by the computer simulations in these studies. The modulus of elasticity decreases by the increase in the applied strain. Young's modulus, M, as well as the shear moduli, μ, increases with the increase in the amplitude of the angular resistance, i.e., the degree of the rigidity of the solid, a*. However, as illustrated in Fig. II.2.8-9 the functional dependency of the shear moduli of the system on a* is considerably larger than that of the Young's moduli, i.e., μ/M also increases with the increase in a*. Therefore, the rigidity of the solid increases considerably by increasing a*.

II.2C. *Sample-Size Effect; Constant Applied Tensile Displacement.*

When a crack is introduced to a finite sample subjected to an external constant tensile displacement (fixed-grips), the modulus of elasticity of the system will be reduced as its consequence. The reduction in Young's modulus is due to the reduction in the strain energy of the finite sample because of the creation of free internal surfaces when the crack is introduced to the system. In the elasto-static approximation, the strain-energy in the test piece in the crack-free solid subjected to the externally applied tensile strain, ε, is given by

$$E_{el} = A\varepsilon^2 M/2 \qquad \text{II.2.15}$$

where A is the area of the plate. The strain energy of the sample after the introduction of the crack may be written as

$$E'_{el} = A\varepsilon^2 M^*/2 \qquad \text{II.2.16}$$

The reduction in the stored energy of the system subjected to the applied strain, ε, because of the introduction of the crack may be written as

$$\Delta E_{el} = A\varepsilon^2 [M^*-M]/2 \qquad \text{II.2.17}$$

where M^* is the effective Young modulus of the cracked sample under the external applied tensile strain, ε. To evaluate M^*, a theoretical estimate of ΔE_{el} is needed. As the exact form of the strain energy of a nonlinear system

subjected to large strains at the presence of small cracks are not known, it is assumed that it is of the conventional form with the linear modulus replaced by the effective nonlinear modulus, M*. Therefore, we may write

$$\Delta E_{el} = -\pi\sigma^2 c^2 / M^* = -\pi\varepsilon^2 c^2 M^* \qquad \text{II.2.18}$$

where σ is the externally applied stress. Hence

$$-\pi\varepsilon^2 c^2 M^* = A\varepsilon^2 [M^*-M]/2 \qquad \text{II.2.19}$$

Solving this equation for the effective modulus implies that

$$M^* = M/[1+2\pi c^2 /A]. \qquad \text{II.2.20}$$

This is similar to the form obtained by Berry [132] with the linear modulus replaced by the nonlinear modulus, M, at the applied constant tensile strain. A series of computer simulations using a 2D triangular Johnson solid, as illustrated in Fig. II.2.9c, shows that the above approximation is, indeed, a very reasonable one to calculate the effective modulus of the system. The question of the use of the "effective" modulus of elasticity in the case of "static" MD simulations of 2D-triangular Johnson solid will be investigated in section II.2E.

II.2D. *The Two-Dimensional Solid Containing an Internal Crack. The Elasto-static Considerations and Griffith's Energy-Balance Theory*

The first explanation of the discrepancy between the observed and "theoretical" fracture strength of solids was offered by Griffith [18]. Griffith reasoned that the largest crack-like flaw produces a stress concentration of sufficient magnitude so that the theoretical cohesive strength is reduced at the crack-tip subjected to a nominal externally applied tensile stress which is well below the theoretical value. The catastrophic propagation of the crack occurs when the rate of release of the mechanical energy of the system becomes greater than the rate of increase of the surface energy of the extending crack. According to the linear elasticity theory, for any solid subjected to a constant applied tensile stress during the formation of the crack

$$\Delta W_L = 2 \Delta E_{el} \qquad \text{II.2.21}$$

where ΔW_L is the work done by the remotely applied tensile load normal to the plane (line) of the crack, and ΔE_{el} represents the change in the internal strain-energy of the system due to an incremental growth of the crack. The mechanical-energy of the system is defined as

$$E_{me} = - W_L + E_{el}. \qquad \text{II.2.22}$$

For an internal elliptical crack of the half-length, c, the local stress and strain fields are calculated by Inglis [133]. Integrating the strain-energy density

computed from the solution of Inglis over dimensions large compared to the crack length, the internal strain potential energy of the sample during the formation of the crack in 2D (i.e. plane-stress condition in 3D) is given by

$$\Delta E_{el} = -\pi\sigma_a^2 c^2 / E \qquad \text{II.2.23}$$

where E is Young's modulus of the solid. The surface-energy, E_S, due to the formation of the crack in the solid is

$$\Delta E_S = 4c\gamma_s \qquad \text{II.2.24}$$

where γ_s is the free-surface energy of the brittle material. The change in the total energy, ΔE_{tot}, of the system resulting from the creation of the crack is

$$\Delta E_{tot} = \Delta [- W_L + E_{el}] + \Delta E_S \qquad \text{II.2.25}$$

The first (composite) term favors the extension of the crack, while the second term opposes it. According to the thermodynamical approach of Griffith, the internal crack subjected to the tensile applied load of, σ_a, will start propagation if any incremental increase in the crack length produces no change in the total energy of the system. i.e.,

$$d/dc [\Delta E_{tot}] = 0 \qquad \text{II.2.26}$$

$$d/dc [4c\gamma_S - \pi\sigma_a^2 c^2 / E] = 0 \qquad \text{II.2.27}$$

This requirement for unstable equilibrium [see Fig. II.2.10] produces a critical applied tensile stress, σ_G, required to initiate the propagation of the crack of half-length, c_o, in a brittle solid in the plane-stress (2D) condition

$$\sigma_G = [2E\gamma_s / \pi c_o]^{1/2} \qquad \text{II.2.28}$$

This can be accomplished most conveniently by Buckner's [134] procedure. Buckner recognized the fact that the change in the internal strain energy of the sample subjected to a remotely applied tensile load normal to the crack line, σ_a, due to the introduction of a finite crack of half-length, c, was equal to one-half of the work done by stress (of equal magnitude but opposite in sign to the applied stress) acting on the crack-face. If the center of the crack is taken as the origin of the coordinate system, the crack face displacement is given by Westergaard's [135] solution for the plane stress Griffith problem

$$\vartheta(x) = (2\sigma_a / E) \; [c^2 - x^2]^{1/2} \qquad \text{II.2.29}$$

Consequently, for the internal crack, work is done at four separate surface segments of the crack. Therefore, the net change in the mechanical energy of the system, due to the introduction of the crack is

$$\Delta E_{me} = -4 \int (1/2) \sigma_a \vartheta(x) dx$$

or,

$$\Delta E_{me} = -\pi \sigma_a^2 c^2 / E \qquad \text{II.2.30}$$

Applying Griffith's energy-balance concept implies that

$$\sigma_G = [2E\gamma_S / \pi c_o]^{1/2}.$$

The implication is that, for a given internal crack of half-length, c_o, there is a critical value of the applied stress, σ_a, above which the total energy of the sample is lowered by the catastrophic propagation of the crack, below which the total energy is decreased by rehealing of faces of the crack. Griffith's energy-balance concept is strictly a (static) thermodynamic balance of energy changes with crack length, ignoring the kinetic energy of the system and any change in its entropy, and furthermore postulating that the release of the mechanical energy of the system is absorbed entirely by the creation of the free crack surfaces. Hence, it is assumed that the separation of the crack surfaces is totally elastic in the presence of no irreversible plastic deformation in the vicinity of the crack-tip. Griffith's initial experiments were made on a glass sample, but there are indications [136] that his results were influenced by the stress-corrosion due to water vapor and that, in the absence of this agent his value for the strain-energy release rate would have been significantly larger than $2\gamma_s$. Better evidence for the Griffith's criteria is found in the cleavage of mineral materials. It is claimed that thin mica sheets can be cleaved in a thermodynamically reversible manner in vacuum, i.e., if the remotely applied tensile load is reduced the crack faces will be rehealed. It is interesting to note that the word "cleave" itself has both meaning of "split" (as cleofan akin to the German word klieben: to slice), and to "adhere, cling or binding together" (as cleofian, clifian, to adhere, akin to German Kleben) [137]. The term "true

cleavage" is usually reserved for this type of reversible processes [136].

In the earlier MD simulations of the 2D-triangular Lennard-Jones solid it was claimed that [1] nonlinearity and finite sample size effect may be taken into account by replacing the modulus of elasticity E, in the above equations, by M*, the effective Young's modulus of the solid subjected to a constant externally applied tensile stress (or strain) and containing an internal crack of half-length, c. M* is calculated throughout the simulations as the average stress over average strain on the solid, i.e., M* is determined from the slope of the secant to the stress-strain of the sample at a prescribed value of stress (or strain).

II.2E. *Major Computer Simulations Results*

In order to determine how closely the behavior of the internal crack in the two-dimensional Johnson solid followed the predictions of the continuum based elasto-static theories, a series of computer simulations were performed on a pre-cracked loaded 2D-triangular Johnson solid. Detailed studies were performed on a solid consisted of 10704 atoms arranged in 79 rows. Mirror symmetry about the central vertical axis was used in order to reduce the computation time. The solid was brought to equilibrium under a constant applied load of 1.50 ε_o/d before the insertion of the internal crack into the sample. The internal crack of various lengths (Table II.1.4) was created by cutting the specific number of interatomic bonds across the central rows of the sample (Fig. II.1.5a). The externally applied constant tensile load was less than the critical tensile load required to initiate the propagation of the longest internal crack of half-length, c_o=9.75d. The computer simulations results for this series of the investigation are tabulated in the Table II.1.4. The reference point for the energies are those of the crack-free solid under the identical externally applied tensile load of 1.50 ε_o/d at perfect equilibrium. Each broken bond corresponds to a single unit of potential energy, ε_o. Hence, the free surface energy per unit length, γ_s, is taken to be 1 ε_o.

The change in the strain potential energy of the sample, ΔE_{el}, results from the formation of the free surfaces of the crack in the sample. It is therefore calculated as

$$\Delta E_{el} = \Delta E_{pe} - NBB_{tot} \qquad \text{II.2.31}$$

where NBB_{tot}, the total number of broken interatomic bonds, correspondent to the free surfaces of the created internal crack. Along with the simulations results the continuum predictions are listed as $\pi\sigma_a^2c^2/M^*$, $\pi s_a^2c^2/M^*$, $\pi\varepsilon_a^2c^2M^*$, $\pi\varepsilon_a^2c^2M$, $\pi\varepsilon_a^2c^2M_o$, $\pi e_a^2c^2M^*$, and $\pi e_a^2 c^2 M$ in Table II.1.4.

True strain or natural strain, ε, is defined by Ludwik [138] as

$$\varepsilon = \int_{L_o}^{L} dc/c = \ln[L/L_o] \qquad \text{II.2.32}$$

True strain is related to the conventional (engineering) strain $e = \Delta L/L_o$ through

$$\varepsilon = \ln[L/L_o] = \ln[e+1] \qquad \text{II.2.33}$$

On the other hand, true stress is the instantaneous load divided by the cross-sectional area (width in 2D) of the sample over which it acts. For an elementary triangle (Fig. II.2.1) under the external tensile load F

$$\text{True stress} = \sigma = F/r_2 \qquad \text{II.2.34}$$

and

$$\text{Engineering stress} = s = F/r_{20}. \qquad \text{II.2.35}$$

It is very unfortunate that in the analysis of computer simulation results [15, 114, 121-122] the engineering stress, s, was confused with the true stress. For dead-weight (constant applied tensile load) simulations, this confusion has led to some unrealistic assumptions and conclusions [122]. The comparison of $\pi\sigma_a^2c^2/M^*$, $\pi s_a^2c^2/M^*$, $\pi\varepsilon_a^2c^2M^*$, $\pi\varepsilon_a^2c^2M$, $\pi\varepsilon_a^2c^2M_o$, $\pi e_a^2c^2M^*$, and $\pi e_a^2c^2M$ listed in Table II.1.4, with the simulations results, i.e., $-\Delta E_{me}$ tabulated in the same table for various crack-lengths, clearly indicates that the $\pi\varepsilon_a^2c^2M_o$ values are closest to the simulations results (except for c_o=9.75d case which $\pi\varepsilon_a^2c^2M$ is the closest). Therefore, based on these observations, we may conclude that in the analysis of the simulations results:

i. The true strain, ε, rather than the engineering strain, e, should be used.

ii. The use of engineering stress, s, should be definitely avoided, and instead the true stress, σ, must be used in the calculations and analysis.

iii. There is no need to replace E, the modulus of elasticity of the perfect solid subjected to an infinitesimal applied tensile stress, with any kind of "effective" Young's modulus M*. We may replace E with the modulus of elasticity of the crack-free sample under the given working applied tensile stress for the longer crack cases.

For the varietues of the initial crack-lengths investigated in these simulations, the change in the strain potential energy, ΔE_{el}, of the sample, and the change in the work done by the externally applied tensile load on the

system, ΔW_L, during the formation of the internal crack in the pre-loaded sample are both systematically slightly larger than the predicted values of the continuum elasto-static theories. However, the change in the mechanical energy, ΔE_{me}, of the system is surprisingly identical to the theoretical predicted values, within the accuracy of the calculations. Independent from the crack-length and "effective" Young's modulus, the ratio $\Delta W_L/\Delta E_{el}$ is 1.94 in all cases, deviating only three percent from the continuum predictions of 2.00.

The mentioned minor deviations from the predictions of the linear elasto-static continuum values may be imputed to the nonlinear-elastic behavior of Johnson's solid. We may conclude that the elasto-static molecular dynamic simulations of the two-dimensional Johnson's solid is in reasonably good agreement with the predictions of the linear elasto-static continuum theories. This is indeed reassuring.

II.2F. *Stress Distribution Around an Internal Elliptical Crack in a Plate Under Externally Applied Constant Tension*

The next logical step in characterizing the response of the solid to a remotely applied constant tensile load or displacement is to investigate the local stress and strain distributions in the vicinity of the internal crack, and then develop a quantitative criterion regarding a critical condition by which the internal crack would propagate. As demonstrated in the previous sections, the overall mechanical properties of the solid are well described by simple extension of the linear elasto-static theories, namely, if necessary, by replacing the linear modulus by the nonlinear modulus of elasticity arising from the highly nonlinear stress-strain curves characterizing the solid held together by a nonlinear interatomic force. It is therefore necessary to discuss next the local stresses in the vicinity of the crack-tip region to complete the comparisons of the theoretical predictions and computer simulations results.

The fracture of a solid, in general, develops from minute origins which are embedded in a larger field of inelastic or plastic strain. Knowledge of the complex patterns of distortion which characterize such early stages of fracture is for the most part qualitative [139]. For a microscopic crack, the emission of dislocations may produce considerable blunting at the crack-tip. This phenomena is, also, observed in some computer simulations [15, 114] of a running crack which emits dislocations under an externally applied tension, at a point of its development (Fig. II.2.11-13). In the most extreme cases, the geometry of the crack-tip resembles a rectangle (Fig. II.2.12). The condition of

fracturing which closely resembles these types of internal cracks is conceptually possible in any solid material. Pertinent change in the crack geometry in a crystalline solid, generally is produced because of the nucleation and emission of blunting dislocations at or near the crack-tip which eventually move away from the crack tip. If these nucleated dislocations are unable to move away from the vicinity of the crack-tip, they will be attracted back to the blunted crack-tip and will be absorbed by the crack, and as a result the crack-tip will be re-sharpened. Rice and Thomson [46] have shown that in some materials sharp cracks are not stable against the nucleation of dislocations and the crack widens or gets blunted by an amount described by the component of the Burger's vector perpendicular to the line defining the position of the crack-tip. The conventional treatment of the phenomena has been largely based on the continuum approaches. According to the continuum based theories, the blunting process affects the local stresses in the vicinity of the crack-tip in two ways:

i. ***The Physical blunting.*** The nucleated dislocations shield the crack-tip from the remotely applied tensile load in such a way as to reduce the crack-tip stress intensity factor by an amount proportional to $1/\sqrt{r}$; where r is the distance between the crack-tip and the emitted dislocation. Only after the emission of an avalanche of dislocations, or after trapping of a large number of emitted dislocations at a distance relatively close to the crack-tip, the physical blunting is significant. The emitted dislocations from the atomically sharp running crack, generally, move away from the crack-tip, and therefore, only temporarily may reduce the stress concentration at the crack-tip.

ii. ***The geometric blunting.*** The emitted dislocations from the crack-tip widens it by the ledge left behind. Weertman [140] and Friedel [141] predicted that the stress intensity factor for a crack of radius of curvature, ρ, scales as $\sqrt{(d/\rho)}$. Here, ρ is larger than the atomic dimensions, but is small compared to the crack-length. The form of this relation is consistent with the Inglis's expression [133] for stresses at the tip of a narrow elliptical crack. The geometric blunting effect should, therefore, be significant for initially sharp cracks.

The earlier molecular dynamic simulations results [15, 114, 128] were not in agreement with the predictions of the continuum based theories. For example, the critical load (i.e. fracture stress), and stress intensity factor, F, for the emission of dislocations from the crack-tip, was not significantly reduced by widening of the crack produced by the ledge left behind by the emitted dislocations [16]. These observations were made at very high stress levels on a nonlinear (Lennard-Jones) elastic solid.

For a quantitative comparison with the predictions of the continuum based theories, it was therefore necessary to carry out a series of MD simulations on a variety of cracks under the remotely applied nominal tensile loads where the stress-strain behavior is, for all practical purposes, linear.

The conventional treatment of the problem is at the macroscopic level, and is based on the continuum approach of Inglis [133] on the stress concentration of blunted elliptic cracks; Sneddon [142] on stresses and strains in the vicinity

of "penny-shaped" cracks in an infinite solid; Williams [143] and Irwin [144] on infinitely sharp cracks. The following section provides some theoretical insight into the approach of Inglis. Then Eringen's application of the non-local continuum theory to an internal crack, and his prediction of the stress distribution along the crack line will be reviewed in some detail.

The results of the present computer simulations, then, will be presented, analyzed, and finally compared to the continuum based predictions.

II.2G. *Inglis-Griffith's Elliptical Internal Crack in a Plate Under Simple Tension*

The stress concentration factor, F, is defined as the ratio of the local stress, σ_y, to the nominal applied tensile stress, σ_a. For a small elliptic hole of semi-major axis, c, and semi-minor axis, b, oriented with its major axis (along X) normal to a uniform nominal applied tensile stress, σ_a, (parallel to Y) in an infinite plate (Fig. II.2.14) the maximum stress at the ends of the major axis of the hole (X = ±c) is found to be

$$\sigma_y (\pm c , 0) = \sigma_a (1 + 2c/b) \qquad \text{II.2.36}$$

or, if the radius of curvature of the tip is ρ, then

$$\rho = b^2 / c \qquad \text{II.2.37}$$

and,

$$\sigma_y (\pm c , 0) = \sigma_a [1 + 2 (c/ \rho)^{1/2}] \qquad \text{II.2.38}$$

Inglis [133] has shown that II.2.38 may be used, with a negligible error, even for cracks that are of elliptical geometry only near the crack-tip. Note that, even though equations II.2.36-37 give identical results for the ellipse, they lead to entirely different crack-length dependencies for the stress concentration. F-1, the contribution arising from the surface discontinuity to the stress concentration factor at the crack-tip, is proportional to the crack length, 2c, if the crack-length is varied but the crack-width, 2b, is kept constant. On the other

hand, if the crack-length, 2c, is varied while the radius of curvature at the crack-tip, ρ, is kept constant, F-1 is proportional to $\sqrt{c}$. For a very narrow slit as $b/c \rightarrow 0$, the stress concentration factor goes to infinity.

Following Inglis [133] for identical configurations, but for a uniform biaxial applied tensile stress, σ_a, on an infinite plate (Fig. II.2.15) for the local stress σ_y (X, Y) along the major axis of the crack (y=0), but normal to its plane, Griffith developed the following equation

$$\sigma_y (X,0)/ \sigma_a = \sinh(2\alpha)[\cosh(2\alpha)+ \cosh(2\alpha_o)-2]/[\cosh(2\alpha)-1]^2 \qquad \text{II.2.39}$$

The elliptical coordinates (α,β) are related to the Cartesian coordinates (X,Y) as

$$X + iY = c \cosh(\alpha + i\beta) \qquad \text{II.2.40}$$

where α_o defines the elliptical crack under consideration. In terms of r, the radial distance from the crack-tip to the field point, along the major axis of the crack (Y=0) equation II.2.39 may be expressed as

$$\sigma_y (r,0)/ \sigma_a = \left\{(1+ r/c)/ \{(1+r/c)^2-[1-(b/c)^2] \}^{1/2} \right\} x \left\{1+ (b/c)^2 /\{(1+r/c)^2-[1-(b/c)^2]\}\right\}. \qquad \text{II.2.41}$$

Here r is actually identical to X, the horizontal distance of the field point from the crack-tip. The relative values of r/c and b/c compared to 1, defines the region of interest, and eventually determines the behavior of the crack-tip. The

particular case of c=3b is illustrated in Fig. II.2.16. As clearly demonstrated in this figure, σ_y drops from its peak at the crack-tip and approaches to the value of the applied stress, σ_a, asymptotically at large values of X. The major disturbance to the applied stress field, therefore, occurs within a distance of the order of c from the boundary of the crack, with the greatest stress gradients confined to the highly localized region of the order of, ρ, surrounding the position of the maximum concentration at the crack-tip. The half-crack length, c, is therefore considered as the characteristic length of the system [33]. Within a distance r of the order of the characteristic length from the crack-tip, if the bluntness contribution b/c is included, the leading term of the equation II.2.41, along the major axis of the elliptic hole, may be written (for r/c<<1) as

$$\sigma_y(r,0)/\sigma_a \approx \left\{1/\ [(2r/c) + (b/c)^2\ ]^{1/2}\right\} x \left\{1+ (b/c)^2/[2(r/c)+(b/c)^2\ ]\right\} \qquad \text{II.2.42}$$

It is evident from the Fig. II.2.25 that the effect of the contribution of bluntness factor, b/c, is noticeable even when it is of the order of 1/10 to 1/20. The $1/[2(r/c)]^{1/2}$ dependency of the stress concentration often quoted for the extremely narrow slits where b/c vanishes, is no longer valid for an internal crack of finite length and thickness. Thus, for microscopic cracks where the minimum value of the thickness of the crack, b, could not be less than the interatomic spacing, d, the simple $1/[2(r/c)]^{1/2}$ dependency should not be expected in the immediate vicinity of the crack-tip, where r/c and b/c may be collateral values. For the field points far away from the crack-tip, i.e., r/c>1 eq. II.2.41 along the major axis of the elliptic hole may be approximated with

$$\sigma_y(r,0)/\sigma_a \approx 1 + (b/c)^2/(1+r/c)^2. \qquad \text{II.2.43}$$

Therefore, σ_y/σ_a asymptotically varies as $(r/c)^{-2}$ and finally approaches unity at a distance far away from the crack-tip, i.e., at r>>1. This result is independent of b/c and therefore should be valid for a variety of crack-tip geometries, including both blunted and sharp cracks. Notice that, if σ_y/σ_a does not have $[2(r/c)]^{-1/2}$ dependency in the immediate vicinity of the crack, the conventional use of stress-intensity factor is, then, questionable.

The stress intensity factor **K** (for Kies, one of Irwin's collaborators) is a convenient way of describing the stress distribution around a flaw, provided that the following near crack-tip approximations for the stress distribution (Fig. II.2.17) are valid

$$\sigma_x = [K/(2\pi r)^{1/2}]\, f_-(\theta) \qquad \text{II.2.44}$$

$$\sigma_y = [K/(2\pi r)^{1/2}]\, f_+(\theta)$$

and,

$$\tau_{xy} = [K/(2\pi r)^{1/2}] \sin(\theta/2) \cos(\theta/2) \cos(3\theta/2)$$

where $f_{\pm}(\theta)$ are the following geometrical factors

$$f_{\pm}(\theta) = \cos(\theta/2)\,[1 \pm \sin(\theta/2) \cos(3\theta/2)]. \qquad \text{II.2.45}$$

Values of **K** for many crack-tip configurations, and varieties of loading conditions may be calculated with the aid of elasticity theory. An excellent compendium of **K** factors is given by Paris and Sih [145-147]. For a sharp elastic crack in an infinitely wide plate, **K** is defined as

$$\mathbf{K} = \sigma_a (\pi c)^{1/2} \qquad \text{II.2.46}$$

For a plate of width, W, loaded in tension with a centrally located crack of half-crack-length c, the stress intensity factor, **K**, may be written as

$$\mathbf{K} = \sigma_a (\pi c)^{1/2} \{ (W/\pi c) \tan(\pi c/W) \}^{1/2} \qquad \text{II.2.47}$$

If two flaws of different geometries have the same value of **K**, then the stress fields around each of the flaws are identical.

In examining computer simulations results in the vicinity of the crack-tip, the validity of the stress intensity factor and its usefulness in this region will be investigated. The dependency of fracture (critical) stress on the bluntness of the crack-tip may be evaluated by using the more general expression for the formation energy of the crack which includes its shape dependency explicitly. Following Griffith [18], the fracture (critical) stress for the onset of the fracture may be expressed as

$$\sigma_c = \sigma_G [1+(b/c)^2]^{1/2} \qquad \text{II.2.48}$$

where σ_G is the Griffith's critical stress (eq. II.2.28) for an extremely narrow slit (when b/c vanishes). The critical stress for a circular hole (b=c) is therefore $\sqrt{2}$ times that of a narrow slit. On the other hand, the stress concentration factor at the crack tip, F_o, is very sensitive for the ratio b/c as

$$F_o = [1+2c/b] \qquad \text{II.2.49}$$

While it is three for a circular hole (c=b), F_o is extremely large for very narrow cracks, i.e., $F_o \rightarrow \infty$ as $b \rightarrow 0$. Nevertheless, the trend is verifiable in the computer simulations and is investigated in the following section.

Inglis-Griffith's results are very convenient for examining asymptotic behavior of the stress concentration factor, and crack-tip geometry dependence of the fracture (critical) stress. However, since they are given for biaxial loading configuration, for the purpose of the quantitative comparisons with the present simulations results for the local stresses, σ_y, along the major axis of varieties of crack-tip geometries with the continuum elasto-static predictions for elliptic cracks, Goodier's [148] formulations are used. For the local stress along the major axis of the ellipse

$$\sigma_y(r,0)/\sigma_a=1 + [(1+m)/(\beta^2-m)] + \{(1-m^2)/[2(\beta^2-m)^2]\} \times \{1+\beta^2+2\beta^2[(1-\beta^2)/(\beta^2-m)]\} \qquad \text{II.2.50}$$

where

$$b/c = (1-m)/(1+m) \qquad \text{II.2.51}$$

and,

$$\beta=(1+m)[(1+r/c)/2] + (1/2)\ [(1+m)^2\ (1+r/c)^2\ -4m]^{1/2} \qquad \text{II.2.52}$$

For extremely narrow slit $m\rightarrow 1$ and for a circular hole m=0. In the m=1 limit, in the immediate vicinity of the crack-tip ($r/c << 1$)

$$\sigma_y/\sigma_a = 1 + 2/(\beta^2-1) \approx\ 1 + 1/(2r/c)^{1/2} \qquad \text{II.2.53}$$

while far away from the crack-tip, i.e., $r/c>>1$ along the crack line (Y=0)

$$\sigma_y(r,0)/\sigma_a \approx 1 + 1/[2(r/c)^2] \qquad \text{II.2.54}$$

These results are similar to the biaxial results of Inglis (eqs. II.2.42-43) except that near the crack-tip, the biaxial results (eq. II.2.42) have no contributions from the applied load, i.e.,

$$\sigma_y/\sigma_a \approx 1/\ (2r/c)^{1/2} \qquad \text{II.2.55}$$

This also shows up in the stress concentration factor. The uniaxial results of Goodier [104] (eqs. II.2.50-52) when combined with equation II.2.36 for circular hole (c =b or m=0) yields $F_o=3$, while the biaxial result of II.2.42 yields $F_o=2$ for the circular hole. It may be noted that the $1/\sqrt{r}$ dependency of $\sigma_y(r,0)/\sigma_a$ is valid only for the very limited region of

$$b/c << r/c << 1 \qquad \text{II.2.56}$$

Further, for a finite b (as opposed to the unrealistic approximation of infinitely sharp slits) the strict $1/\sqrt{r}$ dependency, indeed, should not be observed. From the above equations for the near-crack-tip approximation, i.e., $r/c<<1$, it is F-1 and not F which varies as $1/\sqrt{r}$. Besides, even then, b/c, the crack-tip bluntness factor, would have a significant contribution to σ_y/σ_a. In the computer simulations the near crack-tip region of $r/c \approx 0.1$ to 1 is observable comprehensively. But for very small cavities in the $r/c<<1$ region, only the very crack-tip point, i.e., r=0 is describable. While conceptually for long cracks the $r/c<<1$ region is observable, there are certain difficulties arising from the sample-size limitations. Therefore, there are sample size effects for very long cracks, which are difficult to compensate for, quantitatively. Hence, in the present simulations only the crack-tip and intermediate distances from the tip are available for any meaningful quantitative comparisons with the predictions of continuum based theories.

II.2H. *Eringen's Non-local Theory*

In a series of papers Eringen et al. [108, 149] applied the non-local continuum theory to the problem of a line crack. They started by criticizing the Griffith's criterion that:

i. The surface energy, γ_s, is that of a fluid. For solids there may be other energies arising from surface stresses.

ii. The ellipse shrinking to a crack may not be uniform, i.e., other shapes may give different limits.

iii. Worst of all, the crack-tip stress is infinite in Griffith's formulations no matter how small the applied tensile load may be.

Eringen et al. [108, 149] argued that many advances prior to 1977 in fracture mechanics were all influenced by Griffith's criterion for the fracture of materials, and that there was no rational theory which predicted the observed finite stress at the tip of a sharp crack. They accused the work of Barenblatt [23], Dugdale [150], and others [108] being "semi-rational and to some extent, patched-up theories", which had eliminated some of the objections to the Griffith's criterion, but nevertheless "replacing old objections by new ones". They concluded that "of course, arguments may also be advanced by insisting that there is no such thing as a sharp crack. The crack-tip always has a small radius of curvature even if we produce a crack by removing one line of atoms.

Therefore, the singularity is superficial and is the result of the mathematical idealizations. While this is true, we have no way of measuring the curvature at the crack-tip for these limiting situations (experimentally). For example, by the removal of one layer of atoms to form a crack do we get positive or negative curvature? What is its magnitude? Since the stress at the crack-tip is highly sensitive to the curvature, according to Inglis' solution of elliptic hole problem in the absence of definitive answers to these questions, no specific progress is possible" [108].

Remarkably, the application of the non-local theory to a line crack by these workers [108, 149] not only predicted finite stress everywhere, but also allowed them to unify the fracture criteria in a physically sound basis, attributing the fracture process to bond failure. They also arrived at Griffith's criterion for brittle fracture with the extra benefit that Griffith's surface energy, γ_s, is now fully determined. Furthermore, they were able to calculate the atomic cohesive stress which was in agreement with those known from the atomic theory of lattices and experiments. Because of the importance of Eringen's work in removing the stress singularity at the crack-tip and their development of stress concentration, here a brief account of their results will be presented.

The global balance laws of non-local continuum mechanics are identical to those of classical continuum mechanics. In the classic field theories, a strong assumption is made, namely that the balance law is considered valid for every part of the body, however small it may be. This is called localization. In the non-local theory this assumption is abandoned. Thus, the non-local theory contains

certain residuals which must be integrated to zero. These residuals are the effects of all other points of the body on the point of interest. The recognition and determination of these residuals is an integral part of the theory.

With this account, leaving out many of the interesting details in the non-local theory, we state here the solution of the crack problem, in which the crack surface is free of traction and a remotely applied uniform uniaxial tension, σ_a, at $Y=\infty$ stretches the plate as illustrated in Fig. II.2.17, from Eringen's 1977 classic work [108].

The Hoop stress distribution, F(x), along the crack line is demonstrated in Fig. II.2.18. The local stress, $\sigma_y(x,0)$, has a finite maximum at the crack tip and thereafter reduces smoothly to the classical elasticity solution. The stress concentration factor, F_{oE}, (the subscript E stands for Eringen) is given by

$$F_{o\,E} = \sigma_y(0,0)/\sigma_a = C(\nu)\,[2c/d]^{1/2}. \qquad \text{II.2.57}$$

Eringen's material function $C(\nu)$ is shown in Fig. II.2.19. It is a function of Poisson's ratio ν only, and it falls into the region $0.676 \leq C(\nu) \leq 0.845$ for $\nu=0.0$ to 0.5. For Poisson's ratio of 0.2, Eringen's material constant $C(\nu)$ is 0.713. We may observe that:

i. The Hoop stress (and for that matter all stress components) is finite everywhere, as long as the atomic distance $d \neq 0$. In the continuum limit of the

"vanishing interatomic spacing", i.e., as $d \rightarrow 0$, the classical square-root singularity appears.

ii. Eringen's finite stress concentration factor F_{oE} has the $\sqrt{c}$ dependency on the crack-length similar to the eq. II.2.38 rather than the c dependency of the eq. II.2.36 for an elliptic crack of semi-major axis c.

iii. By equating the maximum stress to the failure stress, Eringen [108, 149] established a failure criterion that "when $(\sigma_y)_{max} = f_{max}$ = cohesive stress, fracture will occur". This most natural criterion is not only physical in nature because of attributing the fracture to the failure of interatomic bonds (in a complete consistency with the natural process of the fracture in our MD simulations), but it also agrees with the engineering failure criterion commonly used in structural mechanics. Incorporating this argument with the equation II.2.57 it follows that

$$\sigma_{yy}(0,0) = f_{max} = \text{cohesive stress} = \sigma_c C(\nu) \quad [2c/d]^{1/2} \qquad \text{II.2.58}$$

Therefore,

$$\sigma_c^E = [\, f_{max} / C(\nu)] \quad (d/2c)^{1/2} \qquad \text{II.2.59}$$

Comparing this equation to the Griffith's critical stress

$$\sigma_G = [2E\gamma_S / \pi c\,]^{1/2}, \qquad \text{II.2.28}$$

we note that these equations are identical. Therefore, Eringen's critical stress σ_c^E is equivalent to Griffith's stress σ_G for the initiation of the brittle propagation of a crack of half-length c in a solid, but with the external benefit that

$$C_G \equiv [\, d/2C^2\,(\nu)\,]\, f^2_{max} = \sigma_c^{\,2}\, c \qquad \text{II.2.60}$$

is now fully determined. No poorly known constant such as surface energy, γ_s, appears in the above formula. Notice that C_G is material dependent and is a material property. This seemingly very simple and obvious result has been under extensive experimental investigations. The stress intensity factor (sometimes called engineering fracture toughness) $\mathbf{K}_I$ in this formulation takes much simple and more definitive value

$$\mathbf{K}_I = \sigma_a\,(\pi c)^{1/2} = (\pi C_G)^{1/2} \qquad \text{II.2.61}$$

iv. While the accuracy of experimentally measured values of surface-energy, γ_s, are often questioned, if we equate σ_c given by II.2.59 to the Griffith's expression II.2.28 we obtain

$$\gamma_s = (\pi d/4E)\ [f_{max}/C(\nu)]^2. \qquad \text{II.2.62}$$

II.2l. *The Molecular Dynamic Simulations of the Effect of the Atomic Crack-Tip Geometry on Local Stress; Outline of the Method*

The molecular dynamic technique is described in the section II.1 in detail. Here, only the specifics directly related to the investigation of the effect of the geometry of the crack-tip on the local stresses is described.

The detailed MD simulation was performed on the two-dimensional triangular Lennard-Jones solid of 10704 atoms arranged in 79 rows as illustrated in Fig. II.1.5. Johnson's two-dimensional triangular solid was used only in a few simulations, for comparison purposes. Identical results were obtained. The solid under investigation was either loaded at its horizontal surfaces to a nominal externally applied tensile constant load (dead-weight), or to a constant external tensile displacement (fixed-grips).

The effect of the geometrical crack-tip blunting is investigated by simulating varieties of crack-shapes and sizes. These studies were performed by varying the width of the crack, 2b, and/or by changing the shape of the crack-tip at a fixed half-crack length of c_o=9.75d. The crack geometries investigated are shown in Fig. II.1.5.

In order to compare the simulations results to the available theories described in the previous sections, the stress concentrations at the crack-tip as well as the local stress distributions were obtained for varieties of crack-lengths of the sharpest crack (Fig.II.1.5a). The width of the sharpest crack used in

these studies is the minimum possible width of any crack in this solid, i.e., it is the width of the interatomic distance between two consequent rows of this two-dimensional triangular solid 2b = ($\sqrt{3}$ /2)d. Note that these are the narrowest possible cracks in the atomic level in this solid. As discussed earlier in detail, these narrow slits are produced by cutting the interatomic bonds between a given number of atoms in the 39th and 40th rows. The wide central cracks demonstrated in Fig II.1.5b, are created by removing four given rows of atoms at the center of the solid. Fig. II.1.5c illustrates the "wide-jagged" central crack which is formed by removing eight given rows of atoms at the center of the sample, in addition to cutting a few interatomic bonds at the boundaries of the crack-tip in order to obtain the desired crack-tip geometry. These crack-tip configurations are very similar to those observed (Fig. II.2.12) in some dynamic simulations of running cracks [15, 114] as mentioned in the previous sections. The simulations results for both types of loading scheme used in these investigations are similar. But, in the case of fixed-grips type of loading of the sample, the calculated forces (stresses) on the particular atoms in the uppermost and lowermost rows of the sample are not constant. The tensile force on an individual atom on the horizontal boundaries of the solid directly above and below the crack is lower than the tensile force on the atoms toward the vertical boundaries of the sample under constant externally applied tensile displacement. This is due to the fact that the insertion of the crack into the stretched sample under a constant applied displacement reduces the stored strain potential energy of the sample. This reduction in the stored strain energy of the solid is not uniform, and naturally, mostly concentrated in the vicinity of the inserted crack. The processes of this particular type of unloading is very

simple to visualize: during the equilibration process after the introduction of the crack to the sample, the atoms directly above and below the physical crack get closer to each other in the vertical dimension because of widening of the crack itself. The decrease in the interatomic distances of these atoms results in the reduction in the potential energy and the interatomic forces between these atoms on the neighboring rows directly along the column of the crack. The distribution of stresses on the horizontal surface of the sample under a fixed applied tensile displacement at the horizontal boundaries and at the presence of a central internal crack is illustrated in Fig. II.1.6. The non-constancy of these tensile forces makes the appropriate stress used in the definition of the stress concentration factor, F, unclear and introduces some unaccountable uncertainties in its determination. However, since by definition, the stresses on individual atoms on the uppermost and lowermost rows of the sample is constant in the case of the constant applied tensile load simulations, the stress concentration and local stress distributions are definitive in these simulations, and therefore, the simulations results for these simulations are the only quantitative results presented here. The results of the constant displacement simulations are very similar to those of the constant applied stress simulations. The very small differences may be attributed to the sample-size effect and the uncertainty in the calculations of F described above.

II.2J. *The Effect of Atomic Crack-Tip Geometry on the Local Stress Distributions: The Simulations Results*

The main purpose of the present investigation is to study the dependency of the local stress distribution on the crack-tip geometry. The crack-tip geometries investigated are illustrated in Fig. II.1.5, and referred to as the narrow (Fig. II.1.5a), wide (Fig. II.1.5b), and wide-jagged (Fig. II.1.5c) cracks. Detailed simulations are performed on the internal cracks of half-length c_o=9.75d, a length which corresponds to 38 broken bonds between specific atoms of the 39th, and 40th rows in the very center of the rectangular two-dimensional triangular array of 10704 atoms arranged in 79 rows as illustrated in (Fig. II.1.5). Approximating these cracks of half-length c_o=9.75d with their equivalent elliptic holes, the narrow crack corresponds to an ellipse of c/b≈22.5, the wide crack may be approximated with an "ellipse" of c/b≈4.5, and the wide-jagged crack may be approximated with an elliptic hole of c/b≈2.5. A nominal constant tensile stress of 10^{-4}E was applied externally to the individual atoms of the uppermost and lowermost horizontal surfaces of the sample. The local stresses at every atom of the loaded sample in its equilibrium state at zero Kelvin temperature may be determined accurately. The effect of the crack-tip geometry on the stress distribution is investigated by plotting F-1 along the column of the crack-tip atom (at r=0) against row number in Fig. II.2.20. F-1 is solely the contribution of the crack itself to the stress concentration factor F.

In analysis of Fig. II.2.20 one may observe that the stress concentration factor, F, in accordance with the experimental observation, has a maximum at

the crack tip with the characteristic sharp fall off for narrow (sharp) crack (hollow circles in the figure). But surprisingly, the stress concentration factor, F, for the wide-crack (solid circles) is almost identical to that of the narrow cracks. We may therefore conclude that the crack-tip atom is identical in both configurations, and that the wide crack should behave similarly to the narrow crack under identical loading conditions. To check the validity of this conclusion at high externally applied stresses, both systems were gradually loaded to their correspondent externally applied critical constant tensile strain where the brittle propagation of the cracks were initiated. The wide crack, indeed, behaved surprisingly similar to the narrow crack. The critical applied tensile strain of 0.0305 was needed to initiate the brittle propagation of the wide crack, a value slightly higher than 0.0295 the critical applied strain needed for the initiation of the brittle propagation of the narrow crack. Note that everything, except the width of the crack and the geometry of their tips, are identical for both of these cracks. As it is illustrated in Fig. II.2.21, the removal of four rows of atoms had no significant effect on the dynamic properties of the narrow crack. Indeed, a brittlely propagating narrow crack is initiated at the tip of the wide crack and therefore, both cracks propagate brittlely by the sequential breaking of identical interatomic bonds between the specific atoms of the 39th and 40th rows.

On the other hand, as demonstrated in Fig. II.2.20, the stress concentration factor in the vicinity of the wide-jagged crack is totally different from those of the narrow and wide cracks. The stress concentration factor, F, is depressed along the center (row 39) of the wide-jagged crack by almost a factor of three, but rises at the sharp corners of this crack (along the 35th, and

43rd rows). Therefore, a totally different dynamic behavior from those of the narrow and wide cracks is expected for the wide-jagged crack. To investigate the validity of this conclusions, the externally applied constant strain was gradually increased to its critical value where the propagation of the wide-jagged crack was initiated. Indeed, dynamically, the wide-jagged crack behaved in a completely different manner than those of the narrow and wide cracks. The wide-jagged crack did not show any activities till the externally applied tensile strain reached its critical value of 0.0350, where as demonstrated in Fig. II.2.22, a dislocation was emitted from the upper sharp corner (tip) of the crack upward. Note that the fixed-grips type of loading induces brittleness by suppressing the conditions for the nucleation and emission of dislocations at the crack-tip [1, 15]. Thus, the wide-jagged crack acts as a blunted crack, like those observed dynamically [15] and illustrated in Fig. II.2.12. Note also that the critical constant strain for the nucleation of the dislocation at the upper lips of the wide-jagged crack is about 20% higher than the critical cleavage tensile strain required for the initiation of the brittle propagation of the narrow and wide cracks.

The stress distribution in the immediate vicinity of the crack-tip is essential for the determination of the behavior of the crack at fracture. In order to render the accessible immediate vicinity of the crack-tip for the detailed study of the stress profiles to $r/c \approx 0.01$, longer narrow cracks were needed to be simulated. Since the smallest increment of r is the interatomic spacing, d, in order to study the region $r/c \approx 0.01$, the half-crack length c must be a large multiple of d. The longest crack that could be studied without having any

serious size-effect was a narrow crack of c_o=35.75d correspondent to 142 broken bonds in the full sample. This required a sample of 20816 atoms arranged in 79 rows as opposed to 10704 atoms used for the rest of the present simulations.

To investigate the functional dependency of the stress concentration factor, F, on the crack-length, 2c, four narrow (sharp) cracks of half-crack lengths c_o=3.75d, 9.75d, 19.75d, and 35.75d correspondent to 7,19,39, and 71 initially broken interatomic bonds at the very center of the half-sample were also simulated. The stress concentration factor at the crack-tip of these narrow cracks, under remotely applied nominal constant tensile uniaxial stress of about 10^{-4}E in magnitude were obtained at the equilibrium state of these loaded pre-cracked samples. The simulation results are compared to their corresponding theoretical values. The sample-size effect has been found to be negligible at the crack-tip. Therefore such a comparison is logically possible and conclusive. The simulations results of the four narrow cracks are plotted in Fig. II.2.23 as F-1 versus c. Along with these simulations results (open circles) the theoretical predictions of Eringen (eq. II.2.57) and Goodier (eqs. II.2.50-52 for b=0.5d) are also plotted for visual comparison purposes. As demonstrated in Fig. II.2.23, F-1 is a linear function of the crack-length , c, for the simulations results of the four narrow cracks investigated; a behavior similar to the theoretical predictions of Goodier, but with different slope. Inglis-Griffith-Goodier's (IGG) theoretical predictions for the concentration factor for an elliptic crack is linear in c with the slope of 2/b. But, clearly, for a reasonable value of b=0.5d for the width of the narrowest crack possible in the simulated solid, IGG theory overestimates the

stress intensity factor. Eringen's theory, on the other hand, predicts square root dependency on the crack length, i.e., $F_E \propto \sqrt{c}$. While, this predicted functional dependency contradicts the observed dependency of the stress concentration factor on the crack-length, the simulations results are closer in magnitude to the predicted values of Eringen in the range accessible for the present computer simulations. This closeness in magnitude is possibly fortuitous, because, at higher values of c, if the linear dependency of the stress concentration factor is still valid, the deviation between the Eringen's F-1 and those of the simulations results is an increasing function of the crack-length. It remains for future studies to investigate this point. Note that the F-1 value for the smallest crack is slightly higher than the value given by the slope of the linear line, and those of the largest crack is slightly lower. This may indicate a different functional dependency of the stress concentration factor on the crack-length. However, at the present, with the available data, and the accessibility limitations of the simulation on the crack length, it is impossible to answer these questions.

The stress concentration factor, F, along the major axis of an elliptic hole, as seen in the earlier section, conventionally (eqs. II.2.50-54) is given in terms of r, the radial (horizontal) distance from the tip of the crack. To explore the crack-tip geometry dependency, and functional dependency of the stress concentration factor on r along the crack-line (Y=0), the simulations results for the varieties of the crack investigated are plotted in Fig. II.2.24 as Log-Log plot of F-1 versus r/c, and in Fig. II.2.25-26 as F-1 against $(c/2r)^{1/2}$. Along with the simulations results, the theoretical continuum predictions for the stress concentration factor is plotted by means of equations II.2.50-51 for narrow

cracks c/b=20 and c/b=50 (they are essentially the same in the range accessible for the present computer simulations), and for a circle c/b=1, over the range of $0.01 \leq r/c \leq 10$. Also shown are the asymptotic dependence of F-1 far away from the crack tip, namely $(1/2)(c/r)^2$, and at the small distances from the tip, i.e., $(c/2r)^{1/2}$. The simulations results for the narrow and wide cracks are practically indistinguishable, hence, one set of points (open circle) is assigned for them in the Fig. II.2.24. While the crack tip (r=0) values, as already discussed, differ drastically from the values predicted by the continuum theories for the equivalent elliptical holes, the F-1 values in the $0.1 \leq r/c \leq 1.50$ range are in surprisingly excellent agreement with the IGG calculations for an elliptical hole of c/b=20 (or 50). As noted earlier, widening the crack by removing four rows of atoms has no significant influence on the stress concentration factor.

Although the crack-tip (r=0) value of the stress concentration factor is significantly different from the predicted values of IGG continuum theories, the computer simulations results in the range of $0.1 \leq r/c \leq 1.50$, are essentially identical to the theoretical calculations of IGG for a circular hole, c/b=1. The wide-jagged crack (Fig. II.1.5c), therefore, resembles a highly blunted crack in this range, and its dynamic behavior at high applied loads may be understood on this basis.

The functional dependency of F-1 on r/c, as illustrated in Fig. II.2.24, over the range accessible for the computer simulations where the simulations results may be compared to the theoretical predictions at relatively very small or

very large r/c is not very simple, certainly nothing like the $1/\sqrt{r}$ dependency predicted by the IGG theory.

Continuum theory predicts $1/\sqrt{r}$ dependency for the stress concentration factor, F, in the vicinity of extremely narrow cracks (eq. II.2.53). Stress distribution data are therefore conventionally plotted against $1/\sqrt{r}$. To explore the functional dependency of the stress concentration factor, the simulations results are plotted as F-1 against $(c/2r)^{1/2}$ in Fig. II.2.25. The stress distributions along the crack line for the narrow and wide cracks are essentially identical, and show an approximate $1/\sqrt{r}$ dependency over a considerable range in r. However, the line through the data points does not go through the origin, nor does it have the "right" slope. As already illustrated in Fig. II.2.24, the simulations results for narrow and wide cracks are closer to the theoretical values for an elliptic hole of c /b=20 (or 50). Part of the theoretical curve for the stress concentration factor in Fig. II.2.25-26 may be approximated by the $1/\sqrt{r}$ dependency, but the slope is correct only over a very limited range. Besides the line through the data points does not go through the origin. As a consequence of the last item, i.e., the presence of an additional constant, the Log-Log plot of Fig. II.2.24 shows nothing like the $1/\sqrt{r}$ dependency over the same range of r.

On the other hand, the wide-jagged crack shows the $1/\sqrt{r}$ dependency for the stress concentration factor only over the very limited region of $0.3 \leq r/c \leq 1.0$. The slope of the linear line through the simulations data, over this range, is the correct value of one. This line, too, does not pass through the origin, and intercepts the Y-axis at -0.68. Due to the presence of this constant, similar to

the case of the narrow and wide cracks, the Log-Log plot of Fig. II.2.24 does not show any $1/\sqrt{r}$ dependency over this range. Note that for the wide-jagged crack, unlike the narrow and wide cracks, we do not observe any $1/\sqrt{r}$ dependency in the immediate vicinity of the crack tip, i.e., for $r/c < 0.3$.

Fig. II.2.26 demonstrates a similar plot of the stress concentration factor, F-1, versus $(c/2r)^{1/2}$ for four narrow cracks of different lengths investigated in the present simulations. Most of the data points fall between the theoretical predicted values of IGG for a thin elliptical crack of c/b=20 (or 50), and for an infinitely thin slit. The simulations data for the longest crack of c_o=35.75d, however, fall outside of this range in the vicinity of the crack tip. The crack-tip (r=0) behavior is excluded from this plot. Although it is possible to find a reasonable regression line with a high correlation coefficient for each set of data points in the Fig. II.2.26, but neither one of these lines pass through the origin, and none of them has the theoretical slope of one. Therefore, it may be concluded that no systematic $1/\sqrt{r}$ dependency exists for these simulations data points, and the simulations resylts are not describable by any universal function of r/c. As demonstrated in Fig. II.2.23, the linear dependency of F-1 on c is valid only at the crack-tip for the narrow cracks.

Note that there is some uncertainty about the exact location of the crack-tip, i.e., r=0. This uncertainty would certainly make the investigation of the immediate vicinity of the "crack-tip" somewhat ambiguous. The mentioned uncertainty is a natural consequence of the discreteness of the crystal. Forces may be calculated *only* on the mass points representing the atoms. These

atomic positions may not necessarily coincide exactly with the natural "crack-tip" at any given time. Furthermore, the "crack-tip" is shared between two rows of atoms, and an unbroken interatomic bond connects these two atoms a distance d apart. Hence, the exact location of the crack-tip is ambiguous to a certain degree which leads to an uncertainty in locating the origin of the coordinate system (r=0), and therefore an ambiguity in the analysis of the points in the immediate vicinity of the physical crack-tip. Therefore, due to the mentioned difficulties, and because of the particular shape of the narrow crack used in these simulations, a particular definition, namely

$$c = (NBB_{tot}+1)/4 \qquad \text{II.2.63}$$

was adopted for the calculation of the half-crack length, c. However small, this definition of c introduces some uncertainty to the present calculations.

II.2K. *The Effect of the Atomic Crack-Tip Geometries on the Local Stress Distribution, and on the Dynamic Behavior of Critically Loaded Cracks; Discussion of the Simulations Results*

The central aim of the present computer simulations is to investigate the crack-tip geometry dependence of the local stress distributions and the dynamic behavior of varieties of critically loaded cracks. The consequences of the emission of blunting dislocations from the crack tip are also studied in these simulations.

Continuum based theories totally ignores the discrete nature of lattice points in the crystals, and their idealizations and simplifications lead to the non-physical stress singularity at the crack-tip of an infinitely thin slit, no matter how small the remotely applied tensile constant load may be. Obviously, there is no such a thing as infinitely thin slit of b=0, or infinite stress at any point of any crystal in nature. Eringen's application of the non-local theory to the crack problem, however, removes the stress singularity of the classic continuum theory, and establishes a failure criterion by attributing the fracture phenomena to the failure of the interatomic bonds and, hence, to the cohesive stress. In order to establish the effect of the discrete nature of the lattice points in the crystalline solid on the local stress distributions in the vicinity of varieties of internal cracks, the results of the present simulations are compared to the predictions of the classical continuum theory of Inglis-Griffith-Goodier (IGG) [133, 18, 148] as well as those of Eringen's [108, 149] non-local theory.

The narrow and wide cracks of the same crack-length (Fig. II.1.5a,b) have essentially identical stress distributions everywhere in the solid (Fig. II.2.20, II.2.24-25) under duplicate conditions. Therefore we may conclude that, provided the effective crack-length and the crack-tip geometry are not altered in the atomic level, simple removal of several numbers of atomic layers around the horizontal boundaries of the crack would have no significant effect on the local stress distribution of the crack and on the dynamic behavior of the crack. The narrow crack (Fig. II.1.5a) is equivalent to an elliptic hole of c/b=22.5. On the other hand, the wide crack (Fig. II.1.5b) corresponds to an ellipse of c/b=4.5. The classical continuum theory of IGG predicts totally different stress distributions for these two types of elliptic holes, namely, according to the equation II.2.36, the stress concentration factor F_o-1 at the tip (r=0) of the narrow and wide cracks are 45 and 9, respectively. The simulations results for these two cracks, as illustrated in Fig. II.2.20, are not only identical, but much lower than those predicted by the classical continuum theory, being 3.3 at the "crack-tip". Eringen's non-local theory, however, predicts an identical value of 3.19 for the stress concentration factor which is surprisingly very close to the simulations results for the narrow and wide cracks of c_o=9.75d. To investigate the validity of the Eringen's stress concentration factor further, a set of narrow cracks of various crack-lengths, i.e., c_o=3.75d, 9.75d, 19.75d, and 35.75d under a remotely applied nominal constant tensile load were simulated. The stress concentration factor, F_o-1, for this set of narrow cracks are plotted against half-crack length, c, in Fig. II.2.23. The stress concentration factor demonstrates a linear dependency on c, as predicted by the classical continuum theory (eq. II.2.36), but with the slope which is an order of magnitude smaller than the one

assumed by the continuum theory. However, Eringen's stress concentration factor at the crack-tip (eq. II.2.57) is a parabolic function of half-crack-length c. Therefore, the reasonable agreement of Eringen's value for the crack of half crack-length c_o=9.75d must be mostly fortuitous.

Eringen's main contribution to the physics of fracture was his recognition of the fact that the local stress at a point in a crystalline solid is not only a function of the strain at that point, but it also must depend on the strains at the other points in the neighboring region. Taking Eringen's non-local view into account, the identical results of the wide and narrow cracks for the stress concentration factor at the crack tip, and its much lower than the classical continuum value, must no longer be of any surprise. Most of the reduction in the stress concentration is apparently due to the non-local effects in the immediate vicinity of the crack-tip which smear out the local stress over a region of the order of the interatomic distances. The non-local effects, therefore, not only remove the classical continuum's crack-tip singularity, but it also reduces the maximum stresses at the crack tip (or anywhere in the solid) to a value smaller than the cohesive strength of the interatomic bonds. Naturally, the interatomic bonds will break when the local stress at any point of the crystal reaches its maximum value of the cohesive strength of the solid.

The identical value of the stress concentration factor for the wide c/b=4.5 and narrow c/b=22.5 cracks suggests that, it is in fact the effective radius of the crack and not the ratio of c/b which influences the stress concentration factor F. By examining the local bond configuration in the immediate vicinity of the crack-

tip of both wide and narrow cracks (Fig. II.1.5a,b), one may conclude that they are very similar to each other at the atomic level. Further, the stress distribution along the column of the crack atom (Fig. II.2.20) and along the crack-line (Fig. II.2.24-25) for the narrow and wide cracks are practically indistinguishable, which confirms the resemblance in the "shape" of the crack-tip configuration in the narrow and "wide" cracks. Thus, to the degree that the crack-length and the interatomic bonds at the crack-tip determine the stress distribution in the vicinity of the crack-tip, the narrow and wide cracks with their similar crack-tip bonding configurations should, in fact, behave similarly.

The lack of any variation in F upon widening the crack implies that the wide crack should behave similarly to the narrow cracks under the identical conditions. To assure the brittle behavior of the crack in this solid (i.e., the 2D-triangular Lennard-Jones solid) at remotely applied critical loads, the computer simulations had to be performed in the fixed-grips mode. Earlier computer simulations [128] have concluded that fixed-grips type of loading in a finite-size sample reduces the tendency of the dislocation nucleation at the crack tip, and therefore it enhances brittleness. The conventional continuum theory predicts that the critical stress should be larger for blunter or wider cracks. Neglecting the changes in the Young's modulus, the critical strain should therefore increase in going from the narrow crack of $2b=\sqrt{3}/2$ d to the wide crack of $2b=5\sqrt{3}/2$ d. Using the equation II.2.48 for the crack of half-length $c_o=9.75d$ we obtain

$$\sigma_c\,[\textit{wide crack}] = 1.0234\sigma_c\,(\textit{narrow crack}] \qquad \text{II.2.64}$$

Using e_c=0.0295 for the narrow crack implies e_c=0.0302 for the wide crack, if the identical modulus of elasticity is assumed. Surprisingly, the critical strain for the initiation of the brittle propagation of the wide crack was e_c=0.0305, only one percent higher than the theoretical IGG value. The trend is therefore as expected.

Because of the nonlinear behavior of the modulus of elasticity and the increasing departure from the linear elasto-static (nominal strain) theory, the stress concentration factor for externally applied large constant loads (or displacements) are not the same as the values derived from the remotely applied nominal stresses used to obtain the local stress distributions as discussed earlier. At the remotely applied stresses (or strains) just below the critical stress, for the narrow and wide cracks the F_o-1 values are 1.64 and 1.70, respectively. The comparable values for very small applied stresses are 3.3 and 3.2. Note that, for the Lennard-Jones two-dimensional triangular solid, the "crack-tip" is no longer the physical boundary of the crack and solid, but rather, by definition it is the atomic position which experiences the largest force. As the crack develops, the "crack-tip" moves few atomic positions in front of the physical crack tip. The previous investigations of the local stress profiles around the "crack tip" of a static and a running crack [1, 115] showed that while at the low external strains, the maximum stress is on the atom located at the lower corner of the physical corner of the physical crack, r^L_c, i.e., the 58th atom on the 39th row, just before the initiation of the brittle propagation of the crack the maximum force is on r^U_{c-2}, i.e., on the 57th atom on the 40th row. Labeling of bonds and atoms in the vicinity of the crack tip is illustrated in Fig. II.2.27.

The stress profile of running cracks will be investigated in the following sections; however, it is clear that the critical stress variations with the crack length cannot be deduced from the low stress linear behavior of Fig. II.2.23.

The simulations results for a variety of narrow cracks are plotted in Fig. II.2.26 as the stress concentration factor, F-1, against $(c/2r)^{1/2}$. The continuum theory of IGG predicts a slope of unity for an infinitely sharp slit as illustrated by the upper straight line which passes through the origin. The lower curve in this figure is the expected stress concentration factor for an elliptical crack of c/b=20 (or 50). The line passing through the data points does not pass through the origin. The simulations results for the two relatively long cracks lie mostly between the two theoretical curves. The simulations data in the intermediate vicinity of the crack, i.e., $0.1 \leq r/c \leq 1.5$ lie closer to the IGG calculations for an elliptic hole of c/b=20 (and 50). In the immediate vicinity of the crack-tip, i.e., r/c<0.1, the simulations results for the longest crack of c_o=35.75d with c/b=86.59, lie above the theoretical calculations for infinitely sharp slit. It is difficult to understand why the longest crack has stresses near the crack tip (but not at the tip) which are higher than those predicted by the continuum theory for an infinitely sharp crack. Further, the stress dependence on $1/\sqrt{r}$ is not the same as the theoretical prediction for a finite elliptic hole, because the theory predicts a slope of unity for the stress concentration factor.

The stress concentration factor at the "crack-tip" (r=0) was plotted against c for four narrow cracks in Fig. II.2.23. The simulations results show a reasonable linear dependency between F_o-1 and half-crack length, c. Indeed,

conventional continuum theory for the elliptical cracks predicts a linear dependence albeit with a slope about an order of magnitude larger than the one observed in the simulations. While some of this discrepancy may be accounted for by the uncertainty in the location of the crack-tip for the shorter cracks, it becomes less important for the larger cracks, and obviously can not explain a systematic order of magnitude reduction in the concentration factor.

The wide-jagged crack has a very different bond configuration in the center of the vertical boundaries of the crack. It has also a larger effective radius than the narrow and wide cracks. Indeed, if it is the effective radius or the degree of the bluntness of the crack tip which is the determining factor in influencing the stress concentration, we should expect a lower stress concentration factor for the "wide-jagged" crack. The local stress distribution in the immediate vicinity of the crack might also be expected to resemble those of blunted or very much widened cracks. Actually this is exactly the case, as it is evident from Fig. II.2.24 the stress distribution for the wide-jagged crack is in excellent agreement with the predicted values of continuum theory (eqs. II.2.50-52) for a circular crack, c/b=1.

A remotely applied critical strain of 0.0350 was needed to generate a dislocation at the upper lips of the crack. Up to this strain the crack did not show any significant activity. The nucleated dislocation, as demonstrated in Fig. II.2.22, gradually moved away from the upper corner of the crack toward the upper loaded horizontal surface of the sample. Thus, in agreement with the predictions of Fig. II.2.24 at remotely applied nominal stress, the wide jagged

crack, indeed resembles a highly blunted crack (Fig. II.2.22) with the dislocation generation at the crack tip occurring at the increased value of the applied strain. For a circular crack, the continuum theory predicts (eq. II.2.48) a critical strain of $\sqrt{2}$ of the critical strain for the narrow crack. Using 0.0295 for the critical strain of the narrow crack, we obtain 0.0417 for the critical strain needed to initiate the brittle propagation of the wide-jagged crack. However, a dislocation was emitted at the applied strain of 0.035, before any crack-tip interatomic bond broke. Therefore, not only the trend is in accord with the theory, but indeed if the system is to behave in a ductile manner, the dislocation nucleation at the crack-tip must take place before the maximum stress at the crack tip reach the cohesive strength of the material. The predicted value of 0.0417 is the value of the applied strain where the stress concentration has reached its maximum value at the crack-tip and the interatomic bond at the crack tip is about to break.

Simulations of the two-dimensional triangular Johnson's solid at remotely applied nominal stresses, for the cracks of Fig. II.1.5, produced identical results to those of the Lennard-Jones solid discussed in detail. For all practical purposes, the stress-strain relationship is linear for both potentials as illustrated in figures II.2.2, and 2.6. Thus, the identical response of the varieties of cracks in both solids to the nominal applied stress should not be of any surprise.

Therefore, the discreteness of the lattice rather than the details of the interatomic potential is the determining factor in controlling the stress

concentration in the immediate vicinity of the internal cracks and the degree of the geometric blunting of the crack-tip in crystalline solids.

II.2L. *The Credibility of the Simulations Results*

The major argument favoring the credibility of the present molecular dynamic simulation is the surprisingly close agreement of the computer simulations results for the stress concentration factor, F-1, of the narrow and wide cracks (Fig. II.1.5a,b) with the Inglis-Griffith-Goodier's continuum based theoretical calculations for an elliptical hole of c/b = 20 (or 50) within the $0.1 \leq r/c \leq 1.50$ range, as illustrated in Fig. II.2.24. Note that the "crack-tip" is taken as the origin of the coordinate system. An equally important fact supporting the credibility of these simulations is the identical results of the two-dimensional triangular Johnson and Lennard-Jones solids subjected to the remotely applied nominal stresses (or strains) for the cracks of figure II.1.5 under identical conditions. Both solids show a linear stress-strain relation, for all practical purposes at nominal stresses. These agreements are reassuring both for those using continuum mechanics and for those using molecular dynamics simulations.

Surprisingly close agreement of the critical (fracture) strain for the initiation of the brittle propagation of the wide crack, e_c=0.0305, with the corresponding value predicted by the continuum theory e_G=0.0302 is also encouraging.

The emission of a dislocation from the tip of the wide jagged crack at the elevated remotely applied constant strain of e_c=0.0350 is quite credible for several reasons. First of all, as it is evident from the Fig. II.2.24, the local

stress distributions in the range accessible for the present simulations for the wide-jagged crack subjected to a remotely applied constant tensile stress is in excellent agreement with those of IGG calculations for a circular crack. Second, the wide-jagged crack closely resembles the configuration observed for a running crack which is blunted and arrested as a result of the emission of a dislocation from its tip (Fig. II.2.12). The wide-jagged crack has a larger effective crack-tip radius than the narrow or wide crack. It has also a particular bond configuration at the center of the vertical boundaries of the crack. It is therefore to be expected that the local stress concentration factor for this crack would be lower (Fig. II.2.20), and would resemble those of a blunted crack. Further, from the "static" molecular dynamic simulations at both fixed-grips and dead-weight types of loading, it is apparent that the two dimensional Lennard-Jones solid must be just in the vicinity of the ductile-brittle behavior. Small variations in the boundary conditions, geometry of the crack, loading conditions, and sample size may drive the behavior of the fracture in this solid either way [15]. Finally the Rice-Thomson [46] model for the nucleation of a dislocation at the tip of a crack, stresses the importance of the immediate vicinity of the crack tip in determining the behavior of the fracture of the solid. As the near crack tip region is well described in the molecular dynamic simulations [15], the generation and emission of dislocations from the crack-tip is observable and realistic in this technique, and the quantitative results are reasonably accurate.

The resemblance of the dynamic behavior of the wide crack under the remotely applied tensile critical displacement, to those of the brittlely propagating narrow cracks are quite interesting and educational. This particular

act proves that the local stress distribution in the immediate vicinity of the loaded crack at nominal stress (or strain) may be used quite successfully to predict the behavior of the fracture at elevated applied stresses (or strains). This property of the crystalline solids may be incorporated to the non-destructive engineering testing for practical purposes.

II.2M. *The Effect of Atomic Crack-Tip Geometry on the Local Stress Distributions: Conclusions*

We close this section by concluding that:

1. There is no such a thing in nature as an infinitely sharp or thin crack. The real crack always has a finite (however small) radius of the crack-tip curvature and a finite thickness. Even if we produce a crack in a crystalline solid by preventing (by any means possible) the interatomic interactions of a given number of atoms on the two adjacent planes (i.e., somehow, we produce the thinnest crack possible in the solid, as we have done in the present simulations for the "narrow cracks"), the width of the produced crack can not be less than the distance between the two adjacent planes of the solid. The stress singularity at the crack-tip predicted by the conventional continuum theory for an infinitely thin (sharp) crack is therefore an artifact of the mathematical idealization and an oversimplification of the problem.

2. The stress concentration factor at the tip of the (narrow and wide) crack in a crystalline solid subjected to a remotely applied tensile stress (or strain) is finite and a factor of order lower than the predicted value of the classical continuum mechanics for an equivalent elliptical hole in a continuous medium subjected to the identical boundary conditions. Non-local effects in the immediate vicinity of the crack-tip smear out the local stresses over a region of the order of interatomic spacing of the crystalline solid. This results

in the considerable reduction in the stress concentration factor in the vicinity of the tip.

3. The maximum value of the local stresses on any atom in the solid (and hence at the crack-tip), σ_y, is the cohesive stress of the solid. When the "crack-tip" atom achieves the maximum fracture (cohesive) stress of the solid, the interatomic bond at the crack-tip will fail and the crack will propagate brittlely.

4. It is the "effective" radius of the crack-tip and not the relative width of the crack, c/b, which affects the local stress concentration. The bonding configurations, in the atomic level, in the immediate vicinity of the crack-tip, and the crack length determine the local stress concentration factor. Larger effective crack-tip radius, and smaller crack-length would produce smaller crack-tip stress concentration factor.

5. The simulations results, as illustrated in Fig. II.2.23 in the range accessible for the present simulations, shows a linear dependency of the stress concentration factor at the crack tip to the half-crack length, c. The empirical relationship may be written as

$$F_o - 1 = 0.339\, c \qquad \text{II.2.65}$$

6. The discreteness of the lattice in the crystalline solids rather than the interatomic potentials (at least for the pair-wise potentials investigated here) is the determining factor in controlling the local stress concentration factor and in deciding the degree of geometrical bluntness of the crack.

7. The fracture behavior at the elevated remotely applied stress may be determined by the investigation of the stress profile in the vicinity of the crack-tip loaded to a remotely applied nominal stresses. This fact may be incorporated to the non-destructive engineering testing for practical purposes.

8. The F-1 values, in the $0.1 \leq r/c \leq 1.5$ range, are in surprisingly excellent agreement with the theoretical continuum based predictions of Inglis-Griffith-Goodier (IGG) for an elliptical hole of c/b=20 (or 50) for the wide and narrow cracks, and for the circular hole of c/b=1 for the wide-jagged cracks.

9. Continuum theory predicts that the critical stress should be larger for the blunter or wider cracks. The trend is as expected.

10. The (fracture) stress for the emission of dislocation from the crack-tip must be less than the required critical applied stress for the initiation of the brittle fracture. The trend is as expected for the emission of dislocation from the crack-tip of the wide jagged crack which takes place at the remotely applied constant tensile stress of 0.0350, a value about 16% smaller than the predicted critical (fracture) stress of 0.0417 for the initiation of the brittle propagation of an equivalent elliptical whole.

The simulations results are quite credible and of significant academic and practical importance.

II.2N. *Local Stress Distributions in the Vicinity of internal Cracks in the Two-Dimensional Triangular Lennard-Jones Solids Subjected to Elevated (lower than the critical) Remotely Applied Constant Tensile Stresses or Strains*

The local stress concentration factor for an internal crack in a two-dimensional triangular Lennard-Jones solid subjected to a remotely applied elevated (lower than the critical) tensile loads (or displacements) are investigated. The simulations results deviate from those of the identical cracks subjected to remotely applied constant nominal tensile loads (or displacements) discussed in detail in the previous sections. This is due to the non-linearity of the modulus of elasticity of the solid and the increasing departure of it from the linear elasto-static nominal strain theory at elevated applied tensile strains.

The interatomic bonds, and the atomic positions in the immediate vicinity of the crack tip are labeled in Fig. II.2.27, where "c" refers to the critical interatomic bond, i.e., d_c is the length of the interatomic bond to be broken next, and r^U_c is the atomic position of the critical atom on the upper surface of the crack.

The atomic displacements of few atoms on the two central rows of the sample in the vicinity of the crack-tip are plotted against the atomic positions for the pre-cracked Lennard-Jones solid containing an internal "narrow" crack of c_o=9.75d under varieties of remotely applied constant tensile displacement in Fig. II.2.28. The simulations data for the highest remotely applied strain of

0.0290 represent the atomic displacements in the vicinity of the crack-tip just before the initiation of the brittle propagation of the crack at the critical applied constant tensile strain of 0.0295.

The local stress distribution corresponding to the atomic displacements of the Fig. II.2.28 are illustrated in Fig. II.2.29. Note that the position of the maximum stress (force) which defines the location of the "crack-tip" moves forward as the remotely applied tensile displacement is increased for this solid. This phenomena is the direct consequence of the particular shape of the Lennard-Jones interatomic potential (and force) as illustrated in figures II.1.3b, and II.2.6b. The Johnson interatomic force falls off very rapidly past its maximum. The crack-tip atom, i.e., the position of the maximum stress is practically identical to the physical boundary of the solid and the internal crack in the Johnson solid, i.e., it is always the atomic position at the tip of the physical crack. On the other hand, the Lennard-Jones interatomic force falls off relatively smoothly after it reaches to its maximum as the interatomic distances increase. Because of this inherent difference from the Johnson interatomic force law, the crack-tip moves about two atomic positions forward in the critically loaded Lennard-Jones solid. Notice that because of the specific geometry of the narrow internal cracks, the crack-tip alternates between the two central rows as the crack propagates brittlely by breaking the interatomic crack tip bonds consecutively. For example as illustrated in Fig. II.2.29, at the elevated applied constant strain of 0.0290 just below the critical (fracture) strain, the maximum force is at r^{U}_{c-2}, i.e., two atomic positions ahead of the geometric crack tip. The two interatomic bonds at the geometric crack-tip is

stretched beyond the stability point of the interatomic bond (Fig. II.2.6b), but are not broken immediately due to the fact that they are physically trapped in the complex force field of the surrounding region. This is exactly what the non-local theory tries to explain. The actual value of the maximum force observed in the simulations for the 2D-triangular Lennard-Jones solid was 4.6, a value very close to the theoretical maximum stress of 4.85 sustainable in the crack-free solid (Fig. II.2.6b).

For the remotely applied constant tensile strain of 0.0290, the corresponding average applied stress at the horizontal boundaries of the sample is calculated to be 1.90 which gives the stress concentration factor of F_o-1=1.42 at the "crack-tip", $r^U_{c\text{-}2}$. Note that the stress concentration factor at the physical crack-tip, r^U_c, of the identical crack of c_o=9.75d subjected to the remotely applied constant nominal stress of 10^{-4}E was F_o-1=3.3.

However, as mentioned above, the crack tip atom for the 2D-triangular Johnson solid subjected to an externally applied constant tensile stress (or strain) remains the same as the physical crack tip, r^U_c, for the entire range of the applied tensile stress (or strain) smaller than the critical (fracture) applied constant stress (or strain). Yet, similar to the behavior of the Lennard-Jones solid, while the maximum stress concentration factor F_o-1 is 3.3 at the remotely applied nominal stress of 10^{-4}E, it is 1.60 at the elevated applied stresses just below the critical stress required for the initiation of the brittle propagation of the crack in the 2D-triangular Johnson solid.

Therefore, the stress concentration factor may not be extrapolated from the low-stress linear elasto-static values, for the highly non-linear solid subjected to a remotely applied elevated constant tensile loads or displacements.

II.3. Dynamic Crack Propagation.

This far only the static systems have been considered. It is well known that if a net force acts on any volume-element within a pre-cracked solid, that element will be accelerated and will thereby acquire some kinetic energy. This system is then a *dynamic* one, and inertia forces must be included in the equations of motion of the body. The word "dynamic" has been used to imply the crack propagation processes accompanied by rapidly occurring changes in the crack-structure geometry, and where those changes are not necessarily well described by a sequence of static equilibrium states and hence the inclusion of inertial forces are necessary.

A phenomenological classification of the problem in the dynamic fracture mechanics might include five specific focal points: The initiation of the rapid propagation of the crack, ensuing of the crack path, the speed of the propagation of the crack, crack branching, and the arrest of the crack. In practice, two kinds of dynamic fracture mechanics problem have received most attention [151]. They are:

1. Bodies with the stationary cracks which are subjected to very rapidly varying applied loads.

2. Bodies under fixed or slowly varying applied loads, which contain rapidly propagating cracks.

By far most attention and efforts have been focused on the second category. Accordingly, the second classification will be considered in the present investigation.

When the externally applied load on a pre-cracked solid reaches its critical value, the system acquires a kinetic energy by the virtue of the inertia of the material surrounding the rapidly separating walls. A running crack is typified by a rapid acceleration toward a "terminal velocity" [33] governed by the lowest speed of the propagation of elastic waves in the solid. In most (but not all) test pieces, the propagating crack divides the material into two or more fragments. Note that while the demarcation between the "rapid" and "slow" crack propagation is difficult to fix in a formal way, the distinction is usually not difficult in practice.

At present, like all other branches of fracture mechanics, the bulk of applications in dynamic fracture mechanics assumes linear elastic conditions. The development of this aspect of dynamic fracture mechanics is fairly complete [151]. Current research efforts are focused on incorporating the elasto-plastic and other forms of *nonlinear* material behavior into the dynamic treatment of the phenomena.

A thorough coverage of the areas related to the dynamic fracture mechanics may be found in the fourth chapter of Kanninen and Popelar's excellent book of "Advanced Fracture Mechanics" [151]. The authors have done a great deal of work in this subject, and 138 references are listed at the end of

the section. The classical books of Broek [152] and of Lawn and Wilshaw [33] have also addressed dynamic processes in the fracture, but they are largely limited to the quasi-static concepts. Several comprehensive review articles are contained in Liebowitz's Fracture Treatise [153]; of these articles, Erdogan's [154] is particularly noteworthy. In addition, there have been a number of papers reviewing the specific aspects of dynamic fracture. The most notable of these are the articles of Achenbach [155], Freund [156], Rose [157], Francois [158], Kanninen [159], Kamath [160], Nilsson [161], and Dienes and Paskin [15]. Further, three volumes of conference proceedings entirely devoted to the dynamic fracture mechanics are also worth noting [162-164]. Lawn and Wilshaw [33] have also included two chapters (6&7) in their book investigating the micro structural and atomistic aspects of the crack propagation which is of vital interest to the present studies.

While a great deal of attention has been successfully directed towards understanding of the critical stresses required to initiate fracture in a solid, the mechanism of the crack propagation processes itself is not well understood [165]. The models on which calculations for the dynamic cracks have been based vary considerably in their approaches. Mott's [3] approach was very similar to the thermodynamical approach of Griffith [18], except that he included the neglected kinetic energy term in his detailed energy balance modification of Griffith's formulation of the problem. Mott's calculations predicted a limiting velocity for the brittlely propagating cleavage crack-tip in terms of an undetermined constant. Roberts and Wells [32] modified Mott's formulation of the problem and concluded that the limiting crack-tip velocity in brittle materials

must be $0.38C_0$, where C_0 is the longitudinal sound velocity in the material. Freund [4-6] approached the problem from a seemingly different angle. His formulation of the brittlely propagating crack is based on the continuum mechanics and the stress intensity approach. In this formulation for the mode I loading configuration, the terminal velocity of the brittlely propagating cleavage crack is C_R, where, $C_R=0.58C_0$ is the Rayleigh velocity of the solid. However, the crack-length dependency of Freund's formulation [165] to the first degree approximation is identical to that obtained by Mott. On the other hand, Eshelby [7] approached the problem from a totally different point of view. He used a continuum mechanics wave equation for the displacements resulting from the stresses in pre-cracked critically loaded brittle solid. In this equation the velocity of sound has its usual role. Eshelby finally obtained a relationship for the stress intensity factor and the crack-tip velocity. The limiting crack-tip velocity in this formulations for the Mode III deformation is the shear wave velocity in the material, C_S. The crack-length dependency of the crack-tip velocity in this calculation is similar to that of Mott.

Because of the relative importance of Mott [3] and Freund's [4-6] formulations to the present investigations, they will be reviewed in some detail in the following section in order to examine the underlying assumptions in this analysis, and to see if the computer simulations could be used to differentiate between them. The simulations results will be compared to the predictions of these continuum based theories. As both formulations yield an identical crack-length dependency, it is left for the examination of the underlying assumptions that one may determine the validity and applicability of either formulation. The

purpose of the present analysis is to highlight the component parts in these formulations rather than to critique the mathematical bases of the calculations.

II.3A. *The Theoretical Quasi-Static Analysis of the Velocity of the Brittlely Propagating Crack-Tips*

Historically, the first quantitative theoretical prediction of the speed of a rapidly propagating cleavage crack was given by Mott [3] in an extension of the Griffith's approach. Mott considered an infinitely large brittle body subjected to a remotely applied constant tensile stress, σ_a, containing an internal propagating through crack of instantaneous half-length c(t). Mott's main contribution was his recognition of the fact that for a dynamic situation the kinetic energy term must be included in the energy balance. The kinetic energy is produced due to the motion of the constituent atoms as a direct consequence of the separation of the surfaces of the crack and its propagation. The idea is perfectly straight forward: one simply includes the kinetic energy of the system in the calculation of the total energy of the solid, and then seeks the unstable thermodynamic equilibrium configuration of it. In his analytical attempt to estimate the effect of the kinetic energy in determining the unstable configuration of the system, Mott made the following assumptions [3]:

1. The local stress and strain fields about the running crack are identical to those of the elasto-static crack of the identical crack-length, and under the same boundary conditions.

2. The crack speed is small in comparison to the shear-wave velocity in the material.

3. The fracture (free) surface energy, γ_s, is not crack-tip velocity dependent, and remains constant throughout the fracture.

Thus, if u and v are the components of the displacement of a given point in the continuum, c(t) is the instantaneous half-crack length, and dc/dt is small compared to the shear-wave velocity in the material, the components of the velocity of an element at (X,Y) in the plate may be written as

$$u^{\bullet} = V_c \left(\partial u/\partial c \right)_t$$

$$v^{\bullet} = V_c \left(\partial v/\partial c \right)_t \qquad \text{II.3.1}$$

where $V_c = dc/dt$ is the instantaneous crack tip velocity. Noting that $(\partial u/\partial t)_C = 0$ under the conditions of constant applied loading of the sample, the kinetic energy of such a disturbed point in the plate may be written as

$$(1/2)\rho V_C^{\,2} \left[(\partial u/\partial c)^2 + (\partial v/\partial c)^2 \right] dx\, dy \qquad \text{II.3.2}$$

where ρ is the mass per unit area, i.e., mass-density of the plate. We may now integrate this kinetic energy density over all such disturbed elements in the medium within the domain R which has received the information about the propagation of the crack (Fig. II.3.1). R is limited by the distance that elastic waves carry the information from the crack-tip region during the brittle propagation of the crack. Therefore, the kinetic energy of the system may be calculated from

$$E_{ke}=(1/2)\rho\,(V_c)^2 \iint_R [\,(\partial u/\partial c)^2+(\partial v/\partial c)^2]dxdy \qquad \text{II.3.3}$$

Mott argued that since u and v are proportional to $c\sigma_a/E$, $\partial u/\partial c$ and $\partial v/\partial c$ would be proportional to σ_a/E. Here E is the modulus of elasticity of the solid. He also argued that since c is the only characteristic dimension in the material, using the second presumption to assume that the domain R embraces the entire plate, the area integral in the equation II.3.3 would be proportional to c^2. Hence, the expression for the kinetic energy of the system may be written as

$$E_{ke} = (1/2)k\,\rho\,V_c^{\,2}\,(c\sigma_a/E)^2 \qquad \text{II.3.4}$$

where k is a numerical constant to be determined. The total energy of the system due to the presence of the crack was, then, obtained by adding the kinetic energy to the diminution of the mechanical energy and the surface energy increase due to the presence of the crack in an infinitely large (continuum) plate subjected to a tensile applied stress, σ_a, at infinity. The total energy of the system, E_{tot}, therefore may be expressed as

$$E_{tot}=(1/2)k\rho V_c^{\,2}(c\sigma_a/E)^2-\pi(c\sigma_a)^2/E+4\gamma_s c \qquad \text{II.3.5}$$

Mott reasoned that since the total energy of the system must be constant due to an incremental increase in the crack length, its derivative with respect to the crack length must be zero. Making the questionable assumption that $dV_c/dc=0$, i.e., the acceleration of the crack is zero and it has picked up a constant (terminal) velocity V_c instantly at the moment it began to

propagate, and using the following Griffith's relationship for the surface energy of the system

$$\gamma_s = \pi c_o \sigma_a^2 / 2E \qquad \text{II.3.6}$$

where c_o is the initial half-crack length, Mott calculated the velocity of the crack-tip to be of the following form

$$V_c = (2\pi/k)^{1/2} \, (E/\rho)^{1/2} \, (1 - c_o / c)^{1/2} \qquad \text{II.3.7}$$

which predicts a limiting terminal crack-tip velocity

$$V_T = (2\pi/k)^{1/2} \, (E/\rho)^{1/2} \qquad \text{II.3.8}$$

From this expression Mott concluded that: "the velocity of propagation, under uniform stress, of a crack in a material that is not ductile, will tend toward a value of the order of the velocity of sound in the material, and which is independent of the stress applied or of the atomic cohesive forces across the cleavage plane".

As pointed out by Berry [132] and Dulaney & Brace [166], the equation II.3.7 is in error because of the conceptually erroneous assumption $dV_C/dc=0$. While their approaches were entirely different, however, they reached essentially the same result. The more straight forward approach of Dulaney and Brace [166] takes the equation II.3.5 of Mott as its starting point, and like Mott

introduces the definition of the initial half-crack length c_o from Griffith's calculations to eliminate the (free) surface energy, γ_s. They assumed the logical initial condition that the crack-tip starts the propagation from rest, i.e., $V_c=0$ at $c(t)=c_o$. Then, replacing γ_s in the equation II.3.5 by its Griffith value from equation II.3.6, and requiring the conservation of total energy of the system at any given instant, they concluded that

$$(1/2)k\rho V_c^2(c\sigma_a/E)^2-\pi(c\sigma_a)^2/E+2\pi cc_o\sigma_a^2/E= \pi c_o^2\sigma_a^2/E \qquad \text{II.3.9}$$

The instantaneous crack tip velocity may be obtained by solving this equation for V_c

$$V_c = (2\pi/k)^{1/2}\ (E/\rho)^{1/2}\ (\ 1 - c_o\ /c\ ) \qquad \text{II.3.10}$$

which produces the identical terminal crack-tip velocity, V_T, as the value predicted by Mott, namely

$$V_T = (2\pi/k)^{1/2}\ C_0 \qquad \text{II.3.11}$$

where $C_0 = (E/\rho)^{1/2}$ is the longitudinal wave velocity in the material.

Thus the problem is reduced to the evaluation of the unknown constant of Mott's expression for the kinetic energy of the system, k, and going back and investigating the validity of the key assumptions on which this solution is based.

To evaluate k, Robert and Wells numerically solved [32] the integral given in the equation II.3.3, and then plotted the quantity $(2\pi/k)^{1/2}$ against r/c (Fig. II.3.2), where r is the radius of the domain R as illustrated in Fig. II.3.1. This was done partly because of the fact that outside the circle $r=C_1t$ the material is practically undisturbed and the kinetic energy density is therefore zero in this region. Here $C_1=[E/\rho(1-\nu^2)]^{1/2}$ is the velocity of the waves of dilatation, and ν is Poisson's ratio. In order to find the proper value of k, it was further assumed that:

1. The velocity of waves of dilatation is identical to the longitudinal wave velocity in the material.

2. The initial half-crack length, c_o, is very small compare to the instantaneous half-crack length c(t).

The farthest wave front travels a distance equal to r, the radius of the domain R, during the dynamic propagation of the crack-tip, t, which may be estimated to be

$$r = C_0t = c_o(k/2\pi)^{1/2}. \qquad \text{II.3.12}$$

Thus for $\nu=0.25$, it is found that

$$r/c_o = (k/2\pi)^{1/2} = 2.62 \qquad \text{II.3.13}$$

which gives a lower limit of

$$(2\pi/k)^{1/2} = 0.38. \qquad \text{II.3.14}$$

Therefore, Mott-Berry-Dulaney expression for the crack-tip velocity of a propagating cleavage crack in a perfectly brittle material may be written as

$$V_c = 0.38C_0 \left(1 - c_o/c \right) \qquad \text{II.3.15}$$

which estimates the terminal crack-tip velocity to be

$$V_T \approx 0.38\ C_0$$

Note that the typical longitudinal wave velocity, C_0, is about 5000 km/s.

Note that since in the numerical evaluation of the velocity of the waves of dilatation the Poisson's ratio of 0.25 was used, the effect of the first assumption on the final results is therefore insignificant. But strictly speaking, the second assumption is valid only for $t \rightarrow \infty$, or $c \rightarrow \infty$. However, for a reasonably large values of t (or c), and considering all other approximations involved, its effect may also be neglected. Besides, at least qualitatively, the results are consistent with the experimental observations that the terminal velocities, in fact, do exist for the propagating cracks. It seems that these experimentally observed crack-tip terminal velocities do not depend upon the manner of producing the crack nor upon the magnitude of the applied load, provided that it is sufficient to

initiate the propagation of the crack. Indeed, experimentally measured values for the terminal velocities of brittlely propagating cracks (in glass or in metals), as well as the results of the present computer simulations as illustrated in Table II.3.1-2, typically lie in the range of about $0.20C_0$ to $0.40C_0$. Of course, the simple-minded calculations given above should be regarded as no more than a rough guide to the magnitude of the terminal crack-tip velocity. Different treatments tend to produce different values for the terminal crack-tip velocities as demonstrated in Table II.3.4. In fact, it is not even certain which form of the elastic wave velocities actually controls the terminal velocity of the brittlely propagating cracks. There are many who argue, for instance, that the maximum velocity attained by any moving surface discontinuity should be identified with the velocity of Rayleigh surface waves $C_R=0.58C_0$ (for $\nu=0.25$). However, the crack propagation relations obtained are very definitive in their predictions that the crack-tip velocity cannot exceed a theoretical upper limit that is governed by an applied elastic wave speed. Winkler et al. [167] suggested that under the normal kinds of loading conditions, the upper limit for the crack-tip speed must arise from the restriction on the flow of energy onto the crack-tip. That is, since the crack-tip propagation at speeds less than the Rayleigh velocity C_R is an energy-absorbing process, the rate at which it may proceed depends upon the rate at which sufficient energy can be supplied to the vicinity of the running crack-tip. In general, the external load is applied at the outer boundaries of the specimen at a finite distance from the crack-tip. Therefore, the energy is transmitted through the material at a rate which is restricted by the lowest velocity of the elastic waves in the medium. Winkler et al. [167] demonstrated that when the external load is applied directly to the crack-tip by a laser

impulse, the resulting crack-tip speeds may greatly exceed those normally observed. Moreover, they succeeded in producing crack-tip velocities from one to two orders of magnitude above C_R using this technique.

An objection to the theory as outlined above may be raised on the ground that, in computing the available elastic energy from the static solution, it is essentially assumed that the stress wave velocities are infinite. On the other hand in the evaluation of the kinetic energy, the finitude of the propagation velocity of the elastic disturbances is observed.

In the actual problem of a large pre-cracked plate subjected to a remotely applied constant tensile load at its outer boundaries, the applied load is increased gradually up to its critical value necessary to initiate the propagation of the crack. The available energy to overcome the dissipation and the increase in the kinetic energy of the system only comes from the released potential energy within a circular region of radius C_1t, where C_1 is the velocity of the waves of dilatation in the plate. Outside this region the system is undisturbed and the state of the local stresses are those of the static uniform tension and hence the atomic velocities are zero. In the large-scale specimen during the crack propagation the atomic disturbance may not extend to the outer boundaries of the solid, and therefore the applied load at the boundary would not detect the events taking place at the crack tip. Hence, the work done by the remotely applied load on very large sample, ΔW, is zero, and all of the energy necessary for the creation of new surfaces and increase in the kinetic energy must come from the released strain energy, ΔE_{el}, from the circular

region of the radius $r=C_1t$ about the crack-tip. This is an important factor in the development of the crack-tip velocity, and the error introduced through replacing this energy by its static equivalent given by

$$\Delta(W - E_{el}) = - \pi\sigma^2c^2/E \qquad \text{II.3.16}$$

is difficult to estimate analytically, but is unlikely to be negligible. This point will be investigated extensively in the following section based on the data collected in the present simulations and the published computer simulations results [15].

On the other hand, in a small-scale specimen (taking c as the characteristic dimension), the emitted stress waves not only may extend to the boundaries (thereby offering a convenient means for the "acoustic detection" of the propagating cracks), but also may suffer reflection at the outer boundaries and hence interact with the advancing crack-tip, and therefore possibly affect its path and behavior. In addition, if the external load is applied relatively fast, it may function like an effective wave generator. If the interaction between the reflected stress waves from the boundary surfaces of the specimen and the propagating crack-tip slightly disturbs the motion of the crack-tip, a rather complex pattern of surface undulations may result. This is the well known "Wallner line" pattern [168], the naturally occurring analogue (and the historical precursor) of the ultrasonic modulation technique [33]. Like the ultrasonically induced surfaces, the Wallner lines may be interpreted as a visual record of the instantaneous crack-tip positions. On the other hand, if the interaction is strong, the resulting crack deflection may be abrupt, and in the crystalline solids the

crack-tip may deviate from its natural path entirely onto an adjacent cleavage plane [33].

The further objection which is often raised to Mott's theory lies primarily in its quasi-elastic assumptions for the local distribution of stress and displacement fields [151, 154]. Since the energy exchange takes place in the immediate vicinity of the crack-tip, any misrepresentation of the local stress and strain fields in this region may alter the results even though if the gross fields far away from the crack-tips would resemble those of the static values. A comparison of the local stress distributions around stationary crack, and those of fast running crack-tip is therefore essential in the evaluations of the dynamic crack propagation theories. In this regard, it should be recalled that, as demonstrated in the section II.2, the stress distribution around a crack-tip in a discrete lattice differs from the linear elastic continuum descriptions. In a discrete lattice, the maximum value that the local stress may attain occurs at fracture, and this value is bounded by the cohesive stress of the interatomic bonds. The molecular simulations results analyzed in detail in the section II.2 exhibit a $1/\sqrt{r}$ dependency for the stress concentration factor for the narrow and wide cracks (Fig. II.1.5a,b) over a considerable range of $0.1 \leq r/c \leq 1.5$ in agreement with the continuum predictions. However, in these computer simulations we have found no evidence of noticeable crack-tip velocity dependency of the stress intensity factor over the range accessible to the simulations. It is evident from Fig. II.3.3&4 and Table II.3.5 that the static local stress distribution for narrow cracks is indeed very similar to the dynamic stress distributions, independent from the magnitude of the crack-tip velocity and the

loading scheme. Therefore, our simulations results supports Mott's very controversial presumptions that "the stress and displacement fields for the dynamic problem are the same as those for the elasto-static problem with the same length". This point will be investigated extensively in the following sections.

A great many works have been concentrated on the evaluations of the "dynamic" stress intensity factor. We refer those who are interested in this aspect of the development of the dynamic fracture mechanics to the excellent book of Kanninen and Popelar's "Advanced Fracture Mechanics" [151], which has covered it extensively. Among these "dynamic approaches" the work of Freund [4-6] which appeared in 1972 is noticeable. By using a slight numerical approximations his results may be applied to Mott's problem, i.e., an internal propagating crack in an infinite medium subjected to a remotely applied load to obtain

$$V_c = C_R \left(1 - c_o / c \right) \qquad \text{II.3.17}$$

where C_R is the Rayleigh velocity. The ratio C_R/C_0 varies from 0.54 to 0.62, depending upon Poisson's ratio. For ν=0.25 Rayleigh velocity is C_R=0.58C_0. The crack-length dependency of Freund's crack-tip velocity, in the first degree approximation, has the same form as the corrected form of Mott's quasi-static crack growth, yet, it is about 50% higher at every stage of the growth of the crack up to and including the terminal velocity. While the observed crack-tip velocities in the present simulations as well as the real-life experiments tend to

agree somewhat better with the terminal velocity predicted by the corrected form of Mott $V_T=0.38C_0$ than Freund's prediction, i.e., $V_T=C_R=0.58C_0$, it is left for the examination of the underlying assumptions that one may determine the validity and applicability of either formulation. The purpose of the present analysis is to highlight the component parts in these formulations rather than to critique the mathematical bases of the calculations. An attempt will be made to distinguish between the basic definitions of the physical quantities used and their mathematical equivalents. For example, in the energy balance equations the released energies must be equal to the consumed energies. Carelessness in defining these quantities may cause confusion in distinguishing between the measured quantities and their mathematical equivalents.

In the current terminology, the elastic strain or mechanical energy release rate or alternatively, the crack driving force is given the symbol G in the honor of Griffith, and is defined as

$$G = (dW/dA) - (dE_{el}/dA) \qquad \text{II.3.18}$$

where W and E_{el} are the external work done on the body and the strain potential energy of the system, respectively, and A=4Bc is the surface area of the internal crack in the sample of thickness B.

Therefore, in our two-dimensional system, G may be defined as

$$G = (1/4)\, d(W-E_{el})/dc. \qquad \text{II.3.19}$$

Energy balance statement of the critical condition for the extension of the crack is then given by

$$G = G_C \qquad \text{II.3.20}$$

where G_C represents the resistance of the solid to the extension of the crack. While the quantity G_C was originally called the fracture toughness, despite the fact that they are not numerically equal it is now the quantity K_c which is generally so called. This is a consequence of the predominance of K-based expressions for the propagation of the crack in engineering fracture mechanics [151]. We will, properly, name G_C the energy consumption rate.

The energy consumption rate G_C in general consists of the free surface energy of the material γ_s, the plastic energy per unit length extension of the crack γ_p, the rate of the kinetic energy increase due to the crack growth, the adiabatic heating in the vicinity of the fast running crack-tip, the change in the kinetic energy of the sample because of the possible shock generated in the pre-cracked body during the loading of the sample, plus all other possible energy dissipation-consumption mechanisms in the solid during the crack growth.

The two-dimensional triangular Johnson solid is brittle at absolute zero temperature, and there is little or no evidence of observable significant plastic deformation present in the vicinity of the running crack-tip during the brittle propagation of the cleavage crack. We may therefore assume that the energy

consumed during the brittle propagation of the cleavage crack in the Johnson solid is simply that arising from the increase in the kinetic energy of the system E_{ke} and the free surface energy E_s. The surface energy, E_s, may be given as

$$E_s = 4\gamma_s c \qquad \text{II.3.21}$$

where γ_s is simply the depth of the (Johnson) potential ε_o, i.e., the net gain of $1\varepsilon_o$ by the total potential per broken interatomic bond. Therefore by definition, the surface energy E_s is not a function of the crack-tip velocity or any other "dynamic" properties, and trough ε_o it is material dependent, and for a given solid it is a linear function of the half-crack length c.

In the analysis of the results of the present simulations, care will be taken to distinguish between the measured value of G and its mathematical equivalent.

It was shown earlier that, Mott [3] simply set the crack driving force equal to the energy consumption rate. For our system we may write it as

$$G = (1/4)\, d(W-E_{el})/dc = \gamma_s + (1/4)\, dE_{ke}/dc \qquad \text{II.3.22}$$

The computer simulations data are the instantaneous values of the kinetic energy E_{ke}, potential energy of the system E_{pe}, total number of broken bonds NBB_{tot}, and the work done by the externally applied tensile load at the horizontal boundaries of the sample W. The instantaneous half-crack length is

calculated directly from NBB_{tot} through $c=(NBB_{tot}+1)/4$. The instantaneous crack tip velocity may be calculated from the slope of the graph of the instantaneous crack length c(t) versus time t.

Our simulations results will be compared to the predictions of the continuum based theories. It is therefore worthwhile to note that in the equation II.3.9:

i. The kinetic energy of the system E_{ke} is proportional to $c^2V_c^2$.

ii. The elastic potential of the sample E_{el} is proportional to c^2.

iii. The surface energy E_S is proportional to c.

Hence, according to equation II.3.9 the terminal crack-tip velocity can be approached but only for very long instantaneous crack-lengths $c(t) >> c_o$, where E_{ke} is much larger than E_S. Thus, according to equations II.3.22 and II.3.9, if the kinetic energy of the system is not large compared to the surface energy term, the constancy of the crack-tip velocity cannot be explained successfully by Mott's formulation.

Freund's [4-6] approach is also based on the conservation of energy principle. He, too, uses the tools of continuum mechanics in his formulation of the problem. But he evaluates E_{el}, W, and E_{ke} in an entirely different manner, and with seemingly very different assumptions. Yet, Freund's predicted history

of the development of the crack-tip velocity (eq. II.3.17) is qualitatively similar to that of corrected Mott's formulation (eq. II.3.10), but only about 50% greater at every stage of the crack growth up to and including the terminal state.

Freund introduced an energy flux term, F, defined as

$$F \equiv d[W-(E_{el}+E_{ke})]/dt \qquad \text{II.3.23}$$

It is very unfortunate that this formulation has blended the energy release rate $d(W-E_{el})/dt$, with an energy consumption term dE_{ke}/dt. It is therefore impossible to compare directly and in detail, the energy flux F of Freund, with either Mott's formulation or with the results of the computer simulations, where the energy release and the energy consumption terms are explicit and readily available directly for the quantitative analysis. Furthermore, for systems in which the remaining energy term is only the energy consumed in the creation of the new crack surfaces, conservation of energy yields a very simple form for the right hand side of equation II.3.23, which gives little physical insight into the detailed mechanism of the crack propagation. This is even more evident when the quantitative forms for F and dE_s/dt are introduced via Freund's formulation. The detailed and direct comparisons of Freund's results and the computer simulations results are further complicated by the confusing terminology used by Freund. He sets the energy flow rate equal to $V_c G_F$ (where F subscript is added here to distinguish Freund's G and G defined by equation II.3.19). G_F is defined as a "dynamic energy release rate"

$$G_F = d[W-(E_{el}+E_{ke})]/dA = d(W-E_{el})/dA - dE_{ke}/dA$$
$$= G - dE_{ke}/dA \qquad \text{II.3.24}$$

where A=4Bc is the crack surface area for an internal crack of half-length c in a body of thickness B.

In our two-dimensional solid, Freund's "dynamic energy release rate" G_F may be written down as

$$G_F = G - (1/4)dE_{ke}/dc \qquad \text{II.3.25}$$

Unfortunately, Freund's "dynamic energy release rate" G_F is a blend of the conventional energy release rate G, and the rate of the increase in the kinetic energy generated during the crack growth which is a form of the energy consumption rate. It should be noted that, even though initially the kinetic energy (consumption) rate is small, this term would become significant and comparable to the (conventional) energy release rate G as the crack is propagated to a size large compared to its initial length. Therefore, Freund's "dynamic energy release rate" is far from being an energy release rate. Rather, it is essentially the difference between the two comparable energy terms of energy release and energy consumption rates, and therefore, it must be quite small and insignificant in its magnitude.

Freund derived an explicit relationship for F. For mode I deformation, F may be written as

$$F = 2V_cG_F = 2V_c\,[A(V_c)\,\mathbf{K}^2(V_c,c)]/E \qquad \text{II.3.26}$$

where $A(V_c)$ is an analytical relation which is an explicit function of V_c. $\mathbf{K}(V_c,c)$ is a dynamic stress intensity factor which is an explicit function of the instantaneous crack length and crack-tip velocity in the immediate vicinity of the running crack-tip. We may write it as

$$\mathbf{K}(V_c,c) = \mathbf{K}(V_c)\,\mathbf{K}(0,c) \qquad \text{II.3.27}$$

where $\mathbf{K}(0,c)$ is the static stress intensity factor. Freund evaluated $A(V_c)\mathbf{K}^2(V_c)$ and obtained an approximated form of it in terms of the crack-tip velocity V_c and Rayleigh velocity C_R in the following form

$$A(V_c)\mathbf{K}^2(V_c) \approx (1 - V_c/C_R) \qquad \text{II.3.28}$$

For a system in which the only energy consumption term is the surface energy term, the conservation of energy (for the left hand side of equation II.3.26) yields

$$F = 2V_CG_F = 2V_Cd[(W-E_{el})-E_{ke}]/dA = 2V_CdE_S/dA$$
$$= 2V_C\gamma_s \qquad \text{II.3.29}$$

On the other hand, for the right hand side of the equation II.3.26 we may write

$$F = 2V_c[A(V_c)\,\mathbf{K}^2(V_c,c)]/E$$

Or,

$$F/2V_c \approx (1-V_c/C_R)\, K^2(0,c)\, /E$$

$$= (1-V_c/C_R)\pi\sigma^2 c/E \qquad \text{II.3.30}$$

Using Griffith's critical load, i.e.,

$$\sigma_G = (2E\gamma_s/\pi c_o)^{1/2}$$

we may write equation II.3.30 as

$$(1-V_c/C_R)(2E\gamma_s/\pi c_o)(\pi c/E) = \gamma_s \qquad \text{II.3.31}$$

which implies

$$V_c = C_R\,(1-c_o/c). \qquad \text{II.3.17}$$

Although the basic assumptions of Mott [3] and Freund [4-6] are at complete variance, the crack-tip speed history predicted by this equation is that arising from the corrected form of Mott's theory, namely

$$V_c = 0.38C_0(1-c_o/c) \qquad \text{II.3.15}$$

except that Freund's crack-tip velocity is about 50% higher at every stage of its development up to and including the terminal state. Mott [3] used the quasi-static equilibrium value of the crack driving force by assuming the similarity of

the local stress and strain fields of the running and stationary cracks. On the other hand, Freund explicitly evaluated the dynamic contribution to the crack driving force through the calculation of the velocity dependence of the "dynamic intensity factor" $\mathbf{K}(V_c,c)$ in the immediate vicinity of a running crack.

In analysis of Freund's formulation, we may note that the right hand side of equation II.3.31, i.e., γ_s, is a property of the material and it is constant. By definition, γ_s is independent of the crack-length and crack-tip velocity. Therefore, according to the equation II.3.31, the product of $A(V_c)\mathbf{K}^2(V_c)$, which is explicitly only a function of the crack tip velocity, and $\mathbf{K}^2(0,c)/E$, which is just an explicit function of the crack-length, is a constant, γ_s. This is in absolute violation of the basic definition of the stress intensity factor $\mathbf{K}(0,c)$, which is defined as

$$\mathbf{K}(0,c) \equiv \sigma_a \ (\pi c)^{1/2} \qquad \text{II.3.32}$$

Thus, the evaluation of the "dynamic" stress intensity factor

$$A(V_c)\ \mathbf{K}^2(V_c) \approx (1-V_c/C_R) \qquad \text{II.3.28}$$

must be incorrect, and therefore, the constancy of the terminal crack-tip velocity may not be explained on the basis of Freund's formulation.

It is important to note that in Mott's formulation [3] the terminal crack-tip velocity is possible only after the running crack-tip propagates to a length

substantially larger than its initial length and the kinetic energy of the system is much larger than the increase in the surface energy of the sample. Therefore, if the terminal crack-tip velocity is achieved much earlier at a relatively shorter crack-length $c/c_o \approx 2$, and the increase in the kinetic energy of the system is of the order of the change in the surface energy of the sample, Mott's formulation is unable to explain the constancy of the terminal crack-tip velocity.

Therefore, in Freund's formulation, as well as in Mott's analysis of the brittlely propagating cleavage crack, the constancy of the terminal crack-tip velocity, practically, is not permitted. Yet, indeed, the constant terminal crack-tip velocity is directly observed in the present and previous computer simulations [1, 15] as well as in the laboratory experiments [151, 169-170]. In the reported experiments of Kobayashi et al. [170] the crack-tip velocity is essentially constant over a range in the stress intensity factor of about two. Furthermore, experimentally observed crack-tip acceleration period as well as those of the computer simulations does not agree with either Mott or Freund's continuum based theories. In particular, as it is clearly illustrated in Figure II.3.5-12, the crack-tip velocity reaches its terminal constant value much sooner than predicted by these theories at a much smaller relative value of c/c_o. By the time the crack-length is doubled, i.e., $c/c_o \approx 2$, the crack-tip velocity has attained its maximum terminal constant value and saturated. We will return to this point in the discussion of the simulations results and in the course of the development of the "crack-tip configuration" model in the following sections.

A somewhat hypothetical but a complete mathematical equivalent of Mott's formulation is that of a plate at the presence of a centrally located brittlely propagating cleavage crack under the influence of the pressure P, acting on the crack surfaces. Here, the work done by the pressure P on the body, W, is the product of the pressure P and the total volume of the gap formed by the fracture surfaces, E_{el} is the elastic potential energy stored in the circular region $r=C_1t$ about the brittlely propagating crack-tip, E_{ke} is the kinetic energy of this region, and E_s is the change in the surface energy of the body which is assumed to be $4\gamma_s c$. Note that the initial values of all of these quantities are zero, and hence the total energy of the system is zero, $E_{tot}=0$. At a later time, t, conservation of energy requires that

$$W = E_{el}+E_{ke}+E_s \qquad \text{II.3.33}$$

Since the quantities W, E_{ke}, and E_{el} are proportional to c^2, but E_s is proportional to c, for the relatively large values of the instantaneous half-crack length c(t), the dissipation term may be ignored. Thus, the propagation of the crack becomes the motion of a surface disturbance in a non-dissipative medium. Such a motion is known to have the velocity of Rayleigh surface waves [171] which is the velocity of edge dislocations in the body [172].

However, it should be pointed out that the conclusion that $V_T=C_R$ is based on the following assumptions:

i. The crack is constrained to run along a straight path.

ii. The fracture surface energy γ_s is independent of the crack-tip velocity.

iii. The sample is infinitely large.

iv. The loading conditions at infinity during the crack growth remain unchanged.

In a real situation, none of these presumptions seems to be true. The fracture surface energy in general is not constant, and for high crack velocities, for real materials, it seems to be an increasing function of the crack-tip velocity [154]. Also, as pointed out earlier, for the plate of finite size, the reflected waves from the outer boundaries of the sample complicates the analytical picture. However, it is not difficult to show qualitatively that in the case of fixed-grips type of loading, the reflected waves have the effect of the superimposed compression and hence, tend to reduce the crack-tip velocity [1].

It must be emphasized that, while the stresses about the stationary cracks are such that the extension of the crack in general occurs in the line of the crack, there might be a tendency for the crack to curve or branch out at the elevated crack-tip velocities [173]. Yoffe [173] calculated the stress state ahead of a rapidly propagating crack, $\sigma_{\theta\theta}(r,\theta)$, using a Fourier expansion method which was rather lengthy. He plotted $\sigma_{\theta\theta}(r,\theta)$ versus θ, and finally from this plot concluded that there was a critical velocity of about $0.6C_2$ for the crack-tip, above which the angle for which the maximum value of $\sigma_{\theta\theta}(r,\theta)$ occurs, changes

from $\theta=0$ to some non zero finite value, and the crack path is therefore changed. Here C_2 denotes the shear wave speed in the medium and is given by

$$C_2 = (\mu/\rho)^{1/2} \qquad \text{II.3.34}$$

where μ is the shear modulus of the specimen, and ρ is the density of the medium.

Similarly, Cotterel [174] reasoned that while the crack extension normally proceeds along a local symmetry line where the principal stress normal to the line is a maximum, but at high crack-tip velocities two such lines are developed which causes the branching of the propagating crack. Clark and Irwin [175] suggested that the successful crack branching implies that a limiting crack-tip velocity has been nearly achieved. They used the fact that the observed limiting crack speeds were roughly half of the Rayleigh velocity, and wrote that "damping processes rather than inertia of the material dominate in setting the value of V_T. Thus, we regard the running crack as subsonic, over-damped, low inertia disturbance moved ahead by a driving force G. Until the value of G begins to overdrive the crack toward crack division, the crack speed increases and decreases in phase with the force" [175]. In agreement with the observations reported by Schardin [176], Clark and Irwin [175] found that the crack speed just before the branching was nearly the same as that of the most advanced crack in a multiple crack pattern. Hence, in contrast to Yoffe's argument [173], the crack does not branch solely because it has reached some critical velocity, but as Clark and Irwin [175] suggested "It seems best therefore

to regard attainment of a critical K (or G), rather than a crack-speed-induced modification of the stress pattern, as the primary factor controlling crack division". On the other hand, Congleton and Petch [177] found that the crack branching may occur at speeds well below the limiting speed. Even though we did not observed any crack branching phenomena in the present computer simulations, it was observed by Gohar [114] and Paskin et al. [2] at very low crack-tip velocities of $V_T \approx 0.1C_0$ in their computer simulations of a two-dimensional Lennard-Jones solid. At present, no universal crack branching criterion exists [168].

As mentioned earlier, Winkler, Shockey, and Curran [167] argued that, under the normal loading conditions, the upper limit for the crack-tip velocity must arise from the restriction on the flow of energy (driving force) to the crack tip. To prove their view, Winkler et al. [167] applied the external load directly to the crack tip by a laser impulse. The resulting crack-tip velocities greatly exceeded those normally observed. Furthermore, they succeeded in producing the crack-tip velocities from one to two orders of magnitude above the Rayleigh velocity C_R by this method. However, while the results of Winkler et al. [167] are important for the establishment of a theoretical framework for the prediction of the upper limit for the crack-tip velocities, of more practical significance is the role of the plastic deformations in the immediate vicinity of the crack tip in governing the crack-tip velocity. Stroh [178] developed a simple crack growth model in which the fracture energy was associated with the crack-tip plasticity, and hence, dependent upon the temperature and strain rate. Therefore the transition from brittle to ductile behavior with increasing temperature may be

explained qualitatively on this basis. The operation of any plasticity and branching processes contribute to the fracture resistance, and might therefore be expected to prevent the crack-tip velocities from reaching their theoretical limits [33]. Furthermore, the plasticity processes, which operate in the immediate vicinity of the crack tip in all but most brittle solids, generally become less evident as the crack accelerates. However, adiabatic heating at the tip of a fast-running crack may actually enhance plasticity in certain materials.

As is evident from Table II.3.2 and Fig. II.3.7-8, the normalized terminal crack-tip velocity for the most brittle solid simulated in the present studies ($a^* \geq 3$) seems to saturate at about $0.4C_0$. There is no observable plasticity associated with the running (or static) cracks in the simulated covalent solids. However, the two-dimensional Lennard-Jones, and Johnson solids are in the vicinity of brittle-ductile behavior. Specially in the Lennard-Jones solid, smallest variation in the boundary conditions and/or crack shapes may drive the behavior either way [15, 114]. Rice-Thomson's model [46] for the nucleation and emission of blunting dislocations at the crack-tip, stresses the importance of the events taking place in the immediate vicinity of the crack-tip in determining the brittle-ductile behavior of the fracture. Rice and Thomson [46] showed that there is a narrow range for which the activation energy for the dislocation nucleation is low enough that the thermal energy may blunt the crack by the process of dislocation emission from the crack tip. Indeed this may explain not only the observed relatively low terminal crack-tip velocities of the two-dimensional Lennard-Jones and Johnson solids in these simulations, but also the mechanism of the process of observed dislocation

nucleation at the tip of running crack-tip (Fig. II.2.12-13). As illustrated in Fig. II.2.13, the fast-running crack in the 2D-Johnson solid got arrested for quite a long time immediately after the emission of a blunting dislocation from its tip. The local stresses at the crack tip was decreased as a result of the generation of these blunting dislocations which shielded the crack tip from the influence of the remotely applied load. The local crack-tip stresses gradually increased to its pre-arrest critical value only after the emitted dislocations moved sufficiently away from the crack-tip toward the outer boundaries of the solid. The arrested crack-tip resumed its brittle propagation only after the local crack-tip stress attained back its maximum value. This process will be discussed in sufficient detail in the following sections. However, it is important to note at this point that the two-dimensional triangular Lennard-Jones and Johnson solids are not ideal brittle solids (as is evident from the emission of dislocations from the crack-tip of running cracks in these solids), and an undetermined energy dissipation takes place at the crack-tip zone in these solids. This would naturally prevent the crack-tip velocities from attaining their upper limiting theoretical values predicted for the perfectly brittle solids through equations II.3.5&9.

A different approach was taken by Eshelby [7] who used a theorem of Bateman [179] to find the elastic field near the tip of an anti-plane crack which starts moving in an arbitrary manner. He considered a case where the crack-tip starts from rest and moves arbitrarily, the crack being initially of finite length. His analysis is, however, limited to the initial motion in the following sense. In a region close enough to the tip of a static crack, the elastic field, which is independent of the crack-length and the details of the loading, is completely

characterized by a single parameter, the stress intensity factor. Realizing that for the initial dynamic motion of a crack-tip the nature of loading mechanism is irrelevant until the disturbance produced by the motion of the crack-tip has reached the surface-boundaries of the sample, Eshelby [7] used the continuum mechanics wave equation for the displacements, w, resulting from the stresses, in the anti-plane strain state

$$\nabla^2 w - (1/C_2)^2 \partial^2 w/\partial t^2 = 0 \qquad \text{II.3.35}$$

where

$$C_2 = (\mu/\rho)^{1/2} \equiv V_S \qquad \text{II.3.34}$$

is the shear wave velocity, μ is the shear modulus of the specimen, and ρ is the density of the medium. Solving this equation yields

$$\sigma_{zy} = (2\pi)^{-1/2} K_{III} X^{-1/2} \quad ; \; X>0 \qquad \text{II.3.36}$$

for the stress ahead of the crack in its plane. Then he set the crack-tip in motion by using Bateman's theorem [179] and developed a relationship for the crack-tip velocity. The limiting velocity in this formulation for the Mode III deformation is the shear velocity C_2 in the medium. The crack-length dependence of the crack-tip velocity is given by

$$V_c = V_S [\, 1 - (c_o/c)^2 \,] / [\, 1 + (c_o/c)^2 \,]. \qquad \text{II.3.37}$$

II.3B. *Crack-Tip Velocity*; *Major Simulations Results*

Major results of the present investigations concerning the crack-tip velocity at absolute zero Kelvin temperature, on a variety of two-dimensional triangular solids containing various initial internal narrow cracks of different half-crack length c, and either subjected to the remotely applied constant tensile loads σ_a at the horizontal surface-boundaries of the specimen, i.e., dead-weight, or under the remotely applied constant tensile displacements, i.e., fixed-grips are illustrated in Fig. II.3.5-9. The raw simulations data for the calculation of the instantaneous crack-tip velocities are the instantaneous values of the number of new broken bonds NNBB at a given time step. The computer simulations results of the two typical brittlely propagating cleavage crack are demonstrated in Fig. II.3.12-13 as the plot of the number of new broken bonds NNBB versus the time steps t. The instantaneous crack-tip velocity is graphically determined as the instantaneous slope of such a plot at a given time step t. An interatomic bond is considered to be broken when the interatomic distance between the two initially-immediate neighbors exceeds 1.31470d for Johnson solid and 1.60d for Lennard-Jones solid at which the interatomic potential and force is set to zero.

The detailed simulations for the pair-wise Johnson's potential were performed on a two-dimensional triangular array of 10704 atoms arranged in 79 rows, i.e., 79 x 135, at absolute zero Kelvin temperature. To study the crack-length dependency and therefore indirectly the sample-size dependency of the crack-tip velocity a variety of the centrally located internal narrow cracks of half crack-length c_o=3.75d, 6.75d, and 9.75d were investigated. The internal cracks

were introduced between the given atoms of the two adjacent rows of 39 and 40 at the very center of the specimen by preventing these atoms from interacting with each other. As discussed earlier, this corresponds to the insertion of infinitely thin knife into the sample and keeping it there to avoid any possible re-healing of the initial crack. The pre-cracked specimen was then loaded at its outer horizontal boundaries to either an applied constant tensile load or an applied tensile displacement. The mirror symmetry about the central column of the specimen was used in order to reduce the computation time and therefore its cost.

Previous computer simulations [1-2, 15, 114-115] have established the fact that the two-dimensional Lennard-Jones solid is in the vicinity of brittle-ductile behavior at absolute zero temperature. Our preliminary investigations showed that even though the 2D-triangular Johnson solid is more brittle than the Lennard-Jones solid but it is also in the vicinity of brittle-ductile behavior. The detailed studies of Gohar [114] and Som [115] indicated that for any border-line solid, slightest change in the boundary conditions, loading scheme, and crack configurations may drive the fracture behavior either way. It has been demonstrated that the dead-weight type of loading, elevated applied loads, small initial crack-length, and relatively small size sample favor the ductile behavior [2, 15, 114]. On the other hand, the fixed-grips type of loading, long initial crack-length, and very fast increase in the applied load, i.e., high strain-rate induce brittleness [1-2, 15, 115, 123]. The shorter initial crack length favors dislocation nucleation at the crack-tip probably because of the high applied critical load needed to initiate the fracture, and hence large deformations of the

specimen particularly at the very sensitive zone of the immediate vicinity of the crack-tip. Small-size sample also favors dislocations emission from the crack-tip under the constant applied load conditions, probably due to the high deformations of the specimen during the dynamic development of the crack. On the other hand, the fixed-grips type of loading induces brittleness, apparently due to the fact that in this loading scheme the vertical atomic displacements are limited, and therefore the deformations at the crack-tip zone is very restricted.

As illustrated in Table II.3.8A1-II.3.8H, all of the brittlely propagating cleavage cracks in the Johnson's solid ended up being arrested due to the emission of the blunting dislocation from the fast-running crack-tip. The local crack-tip stress dropped significantly immediately after the nucleation of the blunting dislocation at the crack-tip. The crack-tip stress gradually increased only after the emitted dislocation left the crack-tip zone and as it moved toward the surface-boundary of the specimen. As illustrated in figure II.2.13 and II.3.14, the arrested crack-tip was stationary for a considerable amount of time, and only after the crack-tip stress rose to its pre-arrest maximum value, the crack resumed its brittle propagation. The processes of the initiation of the brittle propagation of the cleavage crack, the emission of a pair of blunting dislocations from the fast-running crack-tip, the arrest of the crack, the considerable reduction in the local stress concentration factor due to the shielding effect of the emitted dislocations, the gradual and smooth increase of the local normal stress at the crack-tip to the cohesive strength of the material after the emitted dislocation moved away from the crack-tip zone, the resumption of the brittle propagation of the crack, and the repetition of the

whole process happened for all of the simulated internal cracks in the two-dimensional triangular Johnson solid.

The detailed study of this event was performed on the crack of initial half crack-length c_o=3.75d which corresponds to seven initial broken bonds in the half-sample (Fig. II.2.13). The critical applied tensile load of 3.37 was needed to initiate the brittle propagation of this crack. Simulations results for this run is plotted in figure II.3.14 as the number of new broken bonds NNBB against the time step t. As illustrated in this figure, 460 time steps after the removal of the critical damping and after 11 new crack-tip interatomic bonds were sequentially broken along the original crack line, i.e., when c(t=460)=9.25d, or c/c_o=2.5 a pair of dislocations were emitted symmetrically from the fast-running crack tip at 60 degrees to the axis of the original crack-line toward the horizontal surface boundaries of the specimen as illustrated in figure II.2.13. The fast-running crack-tip stopped and got blunted, immediately after the symmetric generation of the blunting dislocations. The crack-tip was arrested for about two hundred time steps during which the emitted dislocations moved away from the now stationary-blunted crack-tip, symmetrically along 60 degrees to the original axis of the crack-line toward the loaded horizontal boundaries of the specimen. Immediately after the generation of the blunting dislocations at the crack-tip, the stress concentration factor at the crack-tip is reduced by a factor of four due to the shielding effect of the emitted dislocations. The normal stress at the crack tip, as the emitted dislocations left the crack-tip zone and as they were moving away from the crack-tip, gradually increased to its maximum value of the cohesive strength of the material at the time step 645 where the arrested-

stationary crack-tip resumed its brittle propagation along its original path (Fig. II.2.13) and proceeded with near constant terminal crack-tip velocity (Fig. II.3.14). It is interesting to note that the geometry of the blunted crack-tip just before the resumption of the brittle propagation of the crack (Fig. II.2.13), resembles the "wide crack" (Fig. II.1.5b) studied in section II.2. As illustrated in figure II.2.13, the second pair of blunting dislocations were generated at the crack-tip at time step 801. At this point the total number of 21 new interatomic bonds were broken along the original path of the crack. The fast running crack-tip stopped immediately after the nucleation of the new pair of dislocations. Note that by this time, the stress waves generated at the onset of the brittle propagation of the initial crack is reflected back from the surface boundaries of the specimen and is superimposed on the local stresses due to the emitted dislocations and the surface discontinuities forming a very complex pattern in the vicinity of the crack-tip. Eventually a complex pattern of dislocation nucleation coupled with propagation of the crack and changes in the propagation path took place, and the simulations were terminated.

The instantaneous normalized crack-tip velocities V_T/C_1 for a variety of initial crack-lengths c_o=3.75d, 6.75d, and 9.75d are plotted against the "normalized" crack-length c/c_o in Figure II.3.5. The crack-tip velocities are normalized by the velocity of waves of dilatation C_1 in the medium subjected to the given applied critical tensile stress or strain

$$C_1 = (9M/8\rho)^{1/2} \qquad \text{II.3.38}$$

where M is the modulus of elasticity of defect-free specimen subjected to the appropriate remotely applied constant critical tensile load or displacement. Note that M is less than its elastic equivalent $M_0 \equiv E$ for non-linear potentials like Johnson or Lennard-Jones interatomic potentials which deviate from the elastic behavior at elevated stresses as illustrated in Fig II.2.3&5.

The runs indicated as the "gradual" in Figure II.3.5 represent simulations results obtained for virtually quasi-static loading conditions. In the "gradual" runs, the critical load was approached very slowly by increasing the applied load in less than one percent increments until the load is sufficient to initiate the brittle propagation of the crack. In these runs the system is in reasonably good equilibrium before each increase of the applied load.

In the "fast" loading procedure the defect-free solid was brought to equilibrium by scaling and critical damping at remotely applied constant critical load. The internal crack of given initial crack-length was then introduced to the loaded solid and the critical damping was continued for a few hundred time steps in order to minimize the shock-wave produced by the creation of the internal cut in the sample. Damping was then removed and the internal crack was allowed to propagate.

All of the simulations data in figure II.3.5 correspond to the sequential breaking of the crack-tip interatomic bonds between atoms of the 39th and 40th rows which is the original crack line (plane in 3D), and therefore represent the brittle propagation of the cleavage crack under Mode I loading conditions.

There is no significant difference in the curves of figure II.3.5, and the terminal crack-tip velocities seem to be virtually independent of either initial crack-length or loading scheme. The loading rate, however, seems to influence the early stage of the acceleration of the running crack. The slope of the curves representing the so called "fast" runs in figure II.3.5 is higher than all others. The "fast" type of loading seems to accelerate the crack-tip to its constant terminal velocity much faster than other type of loadings. In any case, by the time the crack has grown by fifty percent (hundred percent for the "gradual" runs) the crack-tip velocity is saturated to a constant terminal value which is independent of the initial crack-length, method of loading and the magnitude of the remotely applied constant tensile stress or strain. This acceleration period of the propagating crack is extremely fast, in accord with the experimental observations as illustrated in Fig. II.3.10-11, but contrary to the predictions of the existing theories. The magnitude of the normalized terminal crack-tip velocity $V_T/C_1 \approx 0.24$ is much smaller than the theoretical predictions of Mott, $V_T/C_0 \approx 0.38$, and Freund, $V_T/C_0 \approx 0.58$. Note that for Poisson's ratio of $\nu=1/3$, velocity of waves of dilatation $C_1=\{E/[\rho(1-\nu^2)]\}^{1/2}$ may be approximated by the longitudinal sound velocity $C_0=\{E/\rho\}^{1/2}$ in the medium. It should be noted also that E is replaced by M, the modulus of elasticity of the defect-free specimen under the applied critical tensile load σ_c, in the calculations of these velocities. This replacement is a self-consistent approach for the representation of the finite size sample and the non-linear behavior of the interatomic potential, and is analogous to the laboratory compliance measurement. The slightly higher terminal velocity of the "gradual" run of the crack of initial half crack-length $c_o=9.75$ subjected to the remotely applied constant critical load of $\sigma_c=1.90$ does

not represent a statistically significant deviation from the average terminal velocities achieved by other simulated cracks under various loading conditions in the Johnson's solid.

To study the sample size effect, specially that of the height of the sample, on the acceleration stage and the terminal velocity of the crack-tip in the two-dimensional Johnson solid, a larger sample of 21544 atoms arranged in 159 rows, 159X135, and a smaller sample of 5184 atoms arranged in 39 rows, 39X135, both containing an internal narrow crack of initial half crack-length c_o=9.75 under the remotely applied constant tensile load of 2.15 and 1.45, respectively, were simulated. The simulations results of the tallest sample were extremely instrumental in the clarification of the sample size effects regarding the energetics of the dynamic crack. The simulations results for the tallest sample are plotted in Fig. II.3.13 as the number of new broken bonds NNBB against the time step. Instantaneous crack-tip velocity is calculated from the slope of this curve at the given time step. The graphically obtained crack-tip velocities are plotted in Fig. II.3.6 as the normalized crack-tip velocity V_C/C_1 versus the normalized crack length c/c_o. To investigate the effect of the height of the sample on the crack-tip velocities, the simulations results of the medium size specimen 79x135 are plotted along with the simulations data of the tallest sample in this figure. Note that the critical applied tensile load necessary for the initiation of the brittle propagation of the cleavage crack in both of these samples were approached very carefully and extremely slowly. Once the size-effect on the modulus of elasticity M, and through that on the velocity of waves of dilatation C_1 is taken care of, as clearly demonstrated in figure II.3.6, the

simulations results are very similar, and there is no evidence of the sample-size effect on the crack-tip velocities. Thus, we may conclude confidently that the crack-tip terminal velocity in the two-dimensional triangular Johnson solid is $0.24C_1$ and it is achieved relatively quickly by the time the instantaneous crack length is doubled, i.e., $c/c_0 \approx 1.50$ to 2.0.

Previous computer simulations of Paskin et al. [1] which was performed on a two-dimensional triangular Lennard-Jones solid for a variety of sample sizes and initial crack-lengths (Fig. II.3.9) concluded that "Because of size effects, manifested primarily as a geometrical constraint, the terminal velocity attained in the present simulations is less than the one predicted by Mott. The size dependence of the terminal velocity indicates that considerably larger sample would have to be used for a proper comparison of the magnitude of the terminal velocities with the theoretical predictions". The largest terminal crack-tip velocity obtained by Paskin et al. [1] for the 2D Lennard-Jones solid was $V_T=0.113C_0=0.127C_1$ [see Table II.3.6] about fifty percent of the terminal crack-tip velocity observed in the present computer simulations of the two-dimensional Johnson solid $V_T=0.24C_1$. Yet, comparing the history of development of the crack-tip velocities in both system (Fig. II.3.6&9) indicates that indeed they are very similar, i.e., in both solids the crack-tip is accelerated to its constant terminal velocity by the time the instantaneous crack-length is doubled, i.e., $c/c_0 \approx 1.50$ to 2.0.

As mentioned earlier, the 2D-triangular Lennard-Jones solid is in the immediate vicinity of ductile-brittle behavior. The two-dimensional triangular

Johnson solid is more brittle, but all of the propagating cleavage cracks in this solid were eventually arrested for relatively long time due to the emission of a pair of blunting dislocations from the fast-running crack-tip, by the time the instantaneous crack-length was quadrupled, i.e., $c/c_o \approx 3$ to 4 (Fig. II.2.13 and Table II.3.8A1-8H). The generation of dislocations at the crack-tip is probably thermally activated due to the local adiabatic heating in the immediate vicinity of the running crack-tip (compare Fig. II.2.13 and II.3.16). Considering the fact that the total kinetic energy of the system was about $E_{ke} \approx 14$ to 30 ε_o for an ensemble of 10704 atoms at the moment of the crack-tip arrest, we may conclude that the 2D triangular Johnson solid is also in the vicinity of ductile-brittle behavior and it is only relatively brittle compared to 2D Lennard-Jones solid. Therefore, it is logical to assume that the relatively larger magnitude of the terminal crack-tip velocity of Johnson solid in comparison to that of Lennard-Jones solid, is possibly due to the relative brittleness of the former solid. Therefore, we may conclude that the terminal crack-tip velocity is potential and hence material dependent, and the more brittle the material is the larger the terminal crack-tip velocity in the solid is.

To evaluate this conclusion, a two-dimensional triangular solid with controllable degrees of brittleness was needed. So, it was created through the construction of a "covalent" interatomic potential by adding an angular resistance to the Lennard-Jones and the Johnson pair-wise interatomic potentials, i.e., equations II.1.4-5 as discussed earlier. The lattice rigidity is varied over a wide range by varying a*, the amplitude of the angular resistance.

The cost of the computer simulations of the "covalent" solids is overwhelming. It is at least quadrupled. But fortunately "covalent" solids are very rigid and practically no plastic deformations under ordinary loading conditions is expected, which would constitute itself on the considerable reduction in the sample-size dependency of the crack-tip velocities.

It is evident from Fig. II.3.5-6&9 that the acceleration of the crack-tip toward the constant terminal crack-tip velocity is very fast and the terminal crack-tip is usually reached by the time the instantaneous crack-length is doubled. It is independent of the sample size, initial crack-length, the loading scheme, or the material. It is only a weak function of the strain-rate. This fact is supported by the experimental observations (Fig. II.3.10-11). The overloading effect on the terminal crack-tip velocity is also minimal, and it affects only the early stage of the development of the velocity of the running crack-tip.

Hence, we compromised on the sample size, and decided to perform the simulations on a two-dimensional triangular array of 2476 atoms arranged in 39 rows, 39X63. These specimen contained a centrally located internal crack of half crack-length c_0=3.75d between the 19th and 20th rows, and they were slightly overloaded. This reduced the computational cost considerably, because the search for the critical applied load is usually very time consuming and very costly. The mirror symmetry was also used for the purpose of the reduction in the computation time and cost. The shorter time increment of 0.01 was used because otherwise the desired accuracy of one part in one million in the total energy of the system could not be achieved.

The pre-cracked sample was promptly loaded, properly scaled in the vertical directions, and critically damped for a few hundred time steps. The covalently modified Lennard-Jones solid LJCOVa was loaded to σ_a=3, and the covalently modified Johnson solid JNCOVa was loaded to σ_a=4. Note that the system is somewhat overloaded. The brittle propagation of the cleavage crack was initiated only few time steps after the removal of the critical damping. The fracture was perfectly brittle and very fast, and ran through the specimen dividing the sample to two equal parts. No plastic deformation of any kind was observed throughout the simulations.

The simulations results illustrated in Fig. II.3.15 for the two-dimensional triangular covalent Lennard-Jones solid of a^* = 1.0 is a typical run of these series. The internal crack of c_0=3.75 has propagated brittlely to a crack of instantaneous half crack-length c=16.25, i.e., c/c_0=4.33 by the end of this run as demonstrated in the last image in this figure. Note that the crack surface is very clean, and no evidence of any plastic deformation is present. Local normal stress distribution along the crack line of the fast-running crack-tips of Fig. II.3.15 was very similar to those of the quasi-static crack extension. The resemblance of the local stress distribution of the static and dynamic cracks are striking, in accord with our simulations results for the pair-wise potentials, but in contradiction with the theoretical predictions of Freund and other "dynamic" fracture theories.

The simulations results for the instantaneous "normalized" crack-tip velocities V_C/C_1 are plotted against the "normalized" instantaneous crack-

lengths c/c_o, for the "covalently modified" Johnson solid of various a* in figure II.3.7. The simulations results for the terminal constant crack-tip velocities of the covalently modified Lennard-Jones solid, LJCOVa, as well as those of the covalently modified Johnson solid, JNCOVa, are tabulated in Table II.3.2 as a function of the angular resistance amplitude, a*. These data are plotted in Fig. II.3.8 as the normalized terminal crack-tip velocity, V_T/C_1, against the amplitude of the angular resistance, a*.

Note that "pure" 2D-triangular Lennard-Jones solid, i.e., a*=0, is basically ductile, favoring dislocation generation at the crack-tip over the initiation of brittle propagation of the cleavage crack at absolute zero temperature [1, 114]. The initiation of the brittle propagation of cleavage crack in this solid was only possible under the fixed-grips type of loading [1], and the corresponding data in this solid is therefore taken under constant tensile displacement. Due to the significant influence of the sample-size on the terminal crack-tip velocities [1, 114], the data obtained for the larger sample of 79X135 where the sample-size effect seems to be minimal [1] are used here.

Except for the case mentioned above, i.e., LJ a*=0 care was taken to create exact identical initial and boundary conditions for all other investigated solids. Sample size 39X63, initial half crack-length c_o=3.75d, applied constant tensile load at the horizontal boundaries of the solid σ_a=3 >σ_c for LJCOVa and σ_a=4>σ_c for JNCOVa, basic time step δ=0.01, and free boundaries were identical for all of the investigated cases. Only the intensity of the angular resistance a* was varied for these solids. Increasing a*, increases the rigidity of

the solid. Hence, the degree of brittleness of the solid, the magnitude of the modulus of elasticity M, and the velocity of the waves of dilatation C_1 increases as a^* is increased.

Investigation of the simulations results summarized in Table II.3.2 and illustrated in Fig. II.3.8, indicates that the normalized terminal crack-tip velocity V_T/C_1 increased by a factor of 2 to 4 with increasing a^*, but saturated at $V_T/C_1 \approx 0.42$ at $a^*=3.0$. Note that while the velocity of waves of dilatation in the specimen C_1 is increased only by a factor of 1.50, crack-tip terminal velocities have been multiplied by a factor of six with the increase in a^* up to $a^* = 3.0$. Any further increase in a^* resulted in no significant change in the normalized crack-tip velocity, i.e., C_1 and V_T increase proportionally for $a^*>3.0$. Therefore, we may conclude that the maximum attainable terminal crack-tip velocity in a two-dimensional solid is

$$V_T \approx 0.42C_1 \qquad \text{II.3.39}$$

Our simulations results are certainly in accord with the experimental observations as illustrated in Table II.3.1. Note that Roberts and Well's prediction of the limiting terminal velocity of $V_T \approx 0.38C_0 \approx 0.41C_1$ for a brittlely propagating cleavage crack in a perfectly brittle specimen is identical with our computer simulations observations. Considering all of the assumptions and approximations which they made in reaching this conclusion, makes this identity questionable. Particularly, it is worth recalling that the early acceleration period of the development of the brittlely propagating cleavage crack predicted by

Roberts and Wells, i.e., corrected Mott's theory, differ substantially from those of our computer simulations results as well as laboratory observations.

The simulations results regarding the crack-tip velocities do not agree with any of the continuum based formulations. The crack-tip velocity reaches its terminal value much faster than the predicted process of Mott or Eshelby formulations. Further and perhaps more importantly the terminal crack-tip velocities as summarized in Table II.3.2 strongly depend on the interatomic potential holding the solid together, and span all the way from $0.1C_1$ to $0.42C_1$, and are not simply related to any of the elastic wave velocities in the medium. Therefore, there is a need for another theory which would take all of the above facts into account. We have developed such a theory in section II.3C which is even though very simple, but yet, is capable of overcoming some of the stated objections to the existing theories.

II.3C. *The Crack-Tip Configurational Model*

The detailed analysis of the computer simulations results indicates that the continuum based theories are inadequate in the explanations of the extremely rapid acceleration of the brittlely propagating cleavage crack to a constant terminal velocity. These theories are developed for perfectly brittle propagation of cleavage cracks and naturally the dependence of the terminal velocity on the degree of brittleness or the interatomic potentials is not explicitly present in the analysis of these theories, and therefore cannot be explained by these theories. A simple atomistic model, therefore, is developed which shows some promise for overcoming some of the objections to the continuum based formulations.

Our computer simulations observations have established that the normalized terminal crack-tip velocity is a very sensitive function of the degree of brittleness or rigidity of the specimen. On the other hand, it is clearly evident pictorially (Fig. II.3.15) from the simulations results that the more brittle (rigid) solid supports sharper brittle propagation of cleavage cracks with relatively no plastic deformations in the vicinity of the fast-running cleavage cracks. The activation energy for the dislocation nucleation at the crack tip increases as the solid becomes more rigid. Depending on the degree of the rigidity of the crystal, the thermal energy or the adiabatic heating in the immediate vicinity of the running crack-tip may not provide sufficient energy for the emission of the blunting dislocation at the crack-tip.

As it is discussed in a sufficient detail in the preceding sections, the

"pure" two-dimensional Lennard-Jones and Johnson solids are borderline materials. Even though under carefully controlled conditions, the two-dimensional triangular Johnson solid $a^* = 0$ demonstrates considerably more brittle behavior than the LJ solid does, yet, there is evidence of high plastic deformations in the immediate vicinity of the running crack in this solid, which eventually give rise to the generation of a pair of dislocations at the running crack-tip (Fig. II.2.13 & 3.14) which results in the immediate arrest of the crack. Therefore, it may be concluded that the crack-tip velocity is related to the "crack-tip configuration" effects. The lesser plastic deformation in the vicinity of the running crack is, the higher the terminal crack-tip velocity would be. The limiting terminal crack-tip velocity is associated with no deformation of any kind at the atomically sharp running crack-tip. This also explains why the normalized terminal velocity did not respond to any further increase of the rigidity of the "covalent" solid for $a^*>3.0$. Although other approaches may suggest limiting terminal crack-tip velocity to be one of the stress wave velocities, but the configurational effects on the atoms in the vicinity of the running crack-tip might prevent the crack tip atom from attaining the expected velocity during the time available to it in moving one lattice distance d. Let τ be the available time to the maximum local crack-tip stress to move forward by one lattice spacing, d, in the direction of the brittle propagation of the cleavage crack as illustrated in Fig. II.3.17. During this time, τ, the crack-tip atom itself moves physically a distance δ transverse to the crack-line. The terminal crack-tip velocity then may be written as

$$V_T = d/\tau = (d/\delta)\, \underline{V}_y \qquad \text{II.3.40}$$

where $\underline{V}_y$ is the average velocity of the crack-tip atom in the direction transverse to the crack-tip line, i.e., along the Y-axis. If the initial transverse velocity of the crack-tip atom is small compared to the instantaneous transverse velocity of this atom V_{fy} at T, then

$$\underline{V}_y \approx V_{fy}/2. \qquad \text{II.3.41}$$

The bond stretching process at the crack-tip region of a typical run is investigated and the results are plotted as the interatomic bond length against time steps during the steadfast brittle propagation of the cleavage crack for several interatomic bonds in the immediate vicinity of the fast-running crack-tip in Fig. II.3.18. As the first bond breaks, the second bond directly in front of it in the direction of the propagating crack grows smoothly, while the third bond in the same direction oscillates with a rather small amplitude as the maximum force switches from one atom to another one on the alternating adjacent row of the crack line, i.e., for example from the crack-tip atom on the 39th row to the new crack-tip atom on the 40th row and vice versa, and the crack tip geometry alternates as illustrated in Figure II.3.17. The process is continued smoothly. The crack tip velocity, V_c may be related to the "bond velocities", i.e., the slope of the curves in Fig. II.3.18. We may therefore conclude from Fig. II.3.18 that the assumption of the initial transversal crack-tip velocity being small compared to its instantaneous value V_{fy} at T is reasonable. V_{fy} may be calculated from the vertical component of the net force on the crack-tip atom Fy

$$V_{fy}^2 = 0+2(F_y/m) \qquad \text{II.3.42}$$

where F_y/m is the average "constant" acceleration of the crack tip atom transverse to the crack-line, i.e., in Y direction. For an interatomic force which drops off very rapidly beyond its maximum as in the case of the Johnson's interatomic potential, F_y may be approximated by the vertical component of the maximum force F_{my}. For a triangular lattice (Fig. II.2.1), F_{my} is related to the maximum interatomic force, i.e., the cohesive strength of the bond directed along the bond, F_m, through

$$F_{my} = (\sqrt{3}/2)\, F_m \qquad \text{II.3.43}$$

Therefore, the limiting terminal crack-tip velocity V_T for an interatomic force law which drops very fast beyond its maximum point like Johnson's potential in a two-dimensional triangular crystal may be calculated from

$$V_T = (d/2)\, \{[\sqrt{3}\, F_m\,]/[\delta\, m]\}^{1/2} \qquad \text{II.3.44}$$

All of quantities in this equation are explicitly measurable in the computer simulations.

Since the approximations made in the course of development of the equation II.3.44 are reasonably valid for the two-dimensional triangular Johnson crystal, the limiting terminal velocity of the fast-running cleavage crack in this solid may be evaluated through this equation. The simulations result for δ using the largest sample, i.e., 159X135, c_o=9.75d, and σ_c=2.15 ε_o/d^2 during the steadfast brittle propagation of the cleavage crack in Johnson solid is

$$\delta=0.4d \qquad \text{II.3.45}$$

Using $F_m=4.85\ \varepsilon_o/d$ for the maximum interatomic Johnson force, the equation II.3.44 yields

$$V_T=2.29\ (\varepsilon_o/m)^{1/2} \qquad \text{II.3.46}$$

Normalization with respect to the velocity of the waves of dilatation, $C_1=7.57\ (\varepsilon_o/m)^{1/2}$, yields

$$V_T=0.30C_1 \qquad \text{II.3.47}$$

The simulations results for the terminal crack-tip velocity in 2D-triangular Johnson potential is

$$V_T=0.24C_1 \qquad \text{II.3.48}$$

Considering the approximations made in the process of the development of equation II.3.44, the agreement between the simulations results and the predicted values of the "crack-tip configurational" model is very good.

On the other hand, for a potential that falls off relatively slowly beyond its maximum point (as the Lennard-Jones interatomic force law does) the net force on the physical "crack-tip" atom is nominal, and the equation II.3.44 is no longer valid. In such a case, to evaluate the net transverse force F_y on the physical

"crack-tip" atom (not where the maximum local normal stress is concentrated) the Taylor expansion about $r_m+\epsilon$ is made. Here r_m is the interatomic distance where the interatomic force is maximum, and ϵ is small compared to r_m. The normal force F_y on the physical "crack-tip atom", therefore, may be written down as

$$F_y \approx [\delta/2]\, F_y'(r_m+\epsilon) \qquad \text{II.3.49}$$

The factor 1/2 appears because the interatomic force varies in this region, and therefore, an average is calculated for F_y'. Considering that

$$F_y'(r_m+\epsilon) = [\sqrt{3}/2]\, F'(r_m+\epsilon) \qquad \text{II.3.50}$$

the equation II.3.42 may be written as

$$V_{fy}^2 = 0+2\delta(\delta/2)(\sqrt{3}/2)|F'(r_m+\epsilon)|/m \qquad \text{II.3.51}$$

Combining it with equation II.3.40-41 yields

$$V_T=d\{[\sqrt{3}\,|F'(r_m+\epsilon)|]/8m\}^{1/2} \qquad \text{II.3.52}$$

Since $r>r_m$, F' is negative and therefore the absolute magnitude of it has to be used in the above equation. For the two-dimensional triangular Lennard-Jones solid, $\epsilon\approx 0.1d$ leads to reasonable agreement with the terminal constant crack-tip velocity of the earlier simulations [1, 15] (see Table II.3.2).

II.3D. *Crack-Tip Velocities of Brittlely Propagating Cleavage Cracks; Conclusions*

In the light of the simulations results presented and discussed in the preceding section we may conclude that:

i. The terminal crack-tip velocity is a very sensitive function of the degree of brittleness or rigidity of the solid. In accord with the experimental observations tabulated in Table II.3.1, the computer simulations results indicate that the limiting terminal crack-tip velocity in the most brittle (rigid) two-dimensional triangular solid is

$$V_T \approx 0.42 C_1 \qquad \text{II.3.39}$$

where $C_1=(9M/8\rho)^{1/2}$ is the velocity of the waves of dilatation in the medium for the Poisson's ratio of 1/3. This velocity is often approximated with the longitudinal velocity of sound, $C_0=(M/\rho)^{1/2}$, in the solid.

The simulations results are summarized in Table II.3.2, where the crack-tip velocities V_T normalized with respect to the velocity of waves of dilatation in the solid C_1 are tabulated against the intensity of the rigidity of the specimen a^* (Fig. II.3.8). Increasing a^*, increases the rigidity and the degree of brittleness of the solid. Normalized crack-tip terminal velocities increase markedly by increasing a^*, but saturate at V_T/C_1 of about 0.42 at $a^*=3.0$. Normalized crack-

tip velocities V_T/C_1 are insensitive for any further increase in the degree of brittleness or rigidity of the solid, a*.

It is interesting to note that, while the magnitude of the velocity of waves of dilatation C_1 is increased by a factor of 1.5, the crack-tip terminal velocities is multiplied by a factor of six as a* is increased. The degree of dependency of V_T and C_1 to a* is the same afterward for any a*>3.0.

We may therefore conclude that the limiting terminal crack-tip velocity for any (two-dimensional triangular) solid is a sensitive function of the degree of brittleness of the solid as illustrated in Fig. II.3.8, and for perfectly brittle solid it is about $0.42C_1$. The terminal crack-tip velocity is independent of the initial crack-length, sample-size, and the magnitude of the remotely applied tensile load. This limiting terminal crack-tip velocity is in accord with the experimental observations (Table II.3.1), and the theoretical considerations that crack speed cannot exceed a theoretical upper limit which is connected to an elastic wave speed. As suggested by Winkler, Shockey and Curran [167], under the normal kinds of loading conditions, the upper limit for the crack-tip velocity probably is due to the limitations on the flow of driving energy to the crack-tip. That is, as Kanninen [151] pointed out "since crack propagation at speeds less than C_R must be an energy absorbing process, the rate at which it can proceed depends upon the rate at which sufficient energy can be supplied to the crack-tip process region. Usually, the load is applied at a distance from the crack-tip whereupon the energy must be transmitted through the material at a rate that is restricted by the elastic wave speeds". This analysis indicate that a running

crack-tip in a tensile brittle solid is limited by the speed at which sonic waves can travel within the elastic medium, but does not provide us with a quantitative value for this upper limitations. There exists a limit to the size of the domain R, beyond which the rigid solid is undisturbed by the fast moving crack. By taking the boundary R to be a circle of radius r centered on the crack tip, Robert and Wells estimated the cut off as the distance $r=C_0t$ traveled by the elastic waves in the time t taken for the crack to extend through $c\approx V_T t$ at terminal velocity. As mentioned earlier, they obtained the upper limit for the crack-tip velocity in a very brittle tensile specimen to be

$$V_T \approx 0.38C_0 \approx 0.4C_1$$

an astonishingly good agreement with the experimental observations (Table II.3.1) and with the simulations results for very brittle materials.

ii. The early acceleration stage of the development of the crack-tip velocity is very fast. By the time the crack-length is doubled, i.e., $c/c_o \approx 1.5$ to 2, the crack-tip has reached to its maximum constant terminal velocity. The acceleration period is only dependent on the rate of applying the externally applied tensile load. But, regardless of any initial or boundary conditions, sample size, initial crack-length, or even the degree of brittleness or rigidity of the solid, as long as the brittle propagation of the cleavage crack is possible, the crack-tip reaches its terminal constant velocity very fast.

The implications of these observations, regarding a crack-tip equation of motion, is that the inertial effects are likely more important than the analytical predictions of either Mott [3], Eshelby [7], or Freund [4-6]. The very rapid acceleration of the internal cracks from rest to the terminal velocity, V_T, is not consistent with the functional form of $V_c=V_T(1-c_o/c)$, regardless of the magnitude of the terminal crack-tip velocity, V_T. The magnitude of V_T is set by the crack-tip configuration effect which was discussed in detail in the preceding section.

iii. The dynamic stress distribution along the "cleavage plane" (crack-line) of the fast-running crack is independent of the crack-tip velocity, and is very similar to the static stress distribution along the crack axis. The simulations results in this regard is in accord with Mott's very controversial presumption, but inconsistent with the "dynamic fracture theories" including Freund's predictions [4-6]. Freund's analysis [4-6] predicts a decreasing stress intensity distribution with increasing velocity. The simulations results do not show any measurable effect of the crack-tip velocity on the stress distributions along the crack line (Fig. II.3.3-4). It should be noted that, Freund's formulations do not predict any significant effect of the crack-tip velocity on the stress intensity distribution until the crack-tip velocity is about $0.5C_R$. Terminal crack-tip velocities in the Johnson and Lennard-Jones solids are less than this value, and therefore, it may be argued that Freund's analysis is inapplicable for these solids. Yet, the observed terminal velocities for more rigid solids of the covalently bonded crystals are higher enough to evaluate Freund's predictions for the velocity dependency of the crack-tip stress intensity. We did not observe any velocity

dependence of the crack-tip stress distribution even for these extremely brittle solids.

iv. If there is any type of plastic deformation present during the crack growth, part of energy is dissipated. Therefore, only a portion of the fracture energy is available for breaking the interatomic bonds at the crack-tip, and hence, the crack-tip is unable to attain its theoretical limit, where no energy dissipation is assumed.

v. Continuum based theories have failed in the prediction of the terminal crack-tip velocities for the relatively brittle solids. The terminal crack-tip velocities in these solids are less than the upper theoretical limits which are derived for the very brittle materials. The operation of any plasticity and branching processes contributes to the fracture resistance, and prevents crack velocities from reaching the upper limit reached by the sharp cracks in very rigid specimen.

In the "crack-tip configuration" model, the crack-tip terminal velocity is not explicit function of any elastic wave velocities in the medium. Rather, according to this model it is the explicit form of the interatomic potential and its derivative at distances appreciably larger than the equilibrium lattice spacing that determines the magnitude of the crack-tip terminal velocities. Therefore, continuum theories which are based on the elastic behavior of the material at near equilibrium interatomic distances are not appropriate. Further, because of the explicit dependency of the inertial equations on δ, as soon as the vertical

displacement of the crack tip atom from its original position reaches a value of the order of δ, the crack-tip terminal velocity is approached. Therefore, according to the "crack-tip configuration" model, the acceleration stage of the crack-tip is expected to be short, and the crack-tip maximum velocity should be reached relatively fast, in complete agreement with the experimental observations as well as the simulations results.

It should be noted that in the "crack-tip configurational" model, a change of the medium would produce almost an immediate change in the crack-tip velocity. If the medium is such that the local forces are less than F_m (for the new medium) the crack instantly will be arrested. Understanding the underlying mechanism of the crack-tip arrest phenomena is of the great practical as well as academic interest, and may be considered as a future project.

vi. Owing to the nonlinear elastic behavior of the interatomic potentials used in these simulations, there is a considerable ambiguity regarding the values of the elastic wave velocities to be used in assessing the crack-tip terminal velocity. Elastic wave velocities in the highly strained and plastically deformed region around the running crack will certainly be lower than the elastic wave velocity in the defect-free nominally strained specimen. Elastic wave velocities are also a decreasing function of temperature. Increasing temperature in the immediate vicinity of the fast-running crack-tips due to the local adiabatic heating will therefore reduce the elastic wave velocities in the crack-tip zone. Therefore, the rate of transmitting energy and information through the material at the region surrounding the crack-tip is lower than its

corresponding rate for the rest of the material. However, the appropriate manner of quantitative evaluation of the elastic wave velocities in the immediate vicinity of the fast-running crack is not known.

We may also argue, accordingly, that since the crack-tip zone of a fast-running cleavage crack in a perfectly brittle medium (like the 3-body covalent solid used in these simulations) is not (highly) deformed or strained, the elastic wave velocities in this region would be very close to those of the rest of the specimen. Therefore, if the limiting terminal crack-tip velocity is

$$V_T \approx 0.42 C_1, \qquad \text{II.3.39}$$

the simulations results for very brittle solids would be very close to this limiting elastic wave velocity. Here $C_1=(9M/8\rho)^{1/2}$ is the velocity of waves of dilatation in the loaded solid, where M is the modulus of elasticity of the defect-free specimen under the identical applied tensile load of $\sigma_a \geq \sigma_c$.

On the other hand, for a solid which is relatively brittle, like the two-dimensional triangular (pair-wise) Lennard-Jones or Johnson solid, the crack-tip zone is highly deformed and therefore the magnitude of elastic wave velocities in the immediate vicinity of the running crack-tip is reduced. Hence, if we assume C'_1 to be the velocity of the waves of dilatation in the highly deformed crack-tip zone, C'_1 is only a fraction of C_1, i.e.,

$$C'_1 = nC_1 \qquad ; 0 < n \leq 1 \qquad \text{II.3.53}$$

Therefore, if we assume $V_T \approx 0.42C'_1$ for these solids, this would yield

$$V_T = 0.42nC_1 \quad ; 0 < n \leq 1 \qquad \text{II.3.54}$$

which may be of the order of the measured crack tip terminal velocities in these computer simulations.

Therefore, if it was possible to measure the magnitude of the *local velocity* of waves of dilatation in the highly strained, deformed and heated vicinity of the fast-running crack in the relatively-brittle specimen, the problem would be resolved satisfactorily.

II.3E. *Remotely Applied Constant Critical Tensile Stress or Strain Necessary for the Initiation of Brittle Propagation of an Internal Cleavage Crack; Major Simulations Results*

Griffith's criterion for the initiation of the brittle propagation of an internal cleavage crack in a tensile plate subjected to a remotely applied constant tensile load or displacement is evaluated through the investigation of the critical tensile constant applied loads or strains necessary for the onset of the varieties of brittlely propagating cleavage cracks in the two-dimensional triangular crystalline solids of various sizes subjected to a variety of loading schemes and different boundary conditions.

For the detailed studies a two-dimensional triangular Johnson solid of 10704 atoms arranged in 79 rows, 79X135, was chosen. Three different centrally located internal cracks of initial half crack-lengths c_o=3.75d, 6.75d, and 9.75d corresponding respectively to 7, 13, and 19 initial broken bonds in the half-sample were simulated under either remotely applied constant tensile load, i.e., dead-weight or applied constant tensile displacement, i.e., fixed-grips. As described in detail earlier, in a typical search for the critical load necessary for the initiation of the brittle propagation of the initial crack, the pre-cracked specimen is loaded at its horizontal boundaries to a load slightly smaller than Griffith's stress for the given initial crack-length. The initial narrow internal crack of the desired crack-length, $2c_o$, was created at the center of the defect-free medium size specimen, 79X135, between the 39th and 40th rows of it by the procedure described earlier. Equilibrium was then obtained by the

combined effort of scaling of the pre-cracked-loaded specimen in the vertical direction according to the corresponding Young's modulus, and the insertion of the critical damping factor into the equation of motion. After a reasonable equilibrium was attained, the critical damping was removed and the externally applied constant load was increased in about one percent increments until the onset of the brittle propagation of the initial crack. After each incremental increase in the applied load a sufficient time was given to the applied information to reach the crack-tip. Meanwhile the system would reach its new equilibrium configuration. Therefore, the loading scheme was quasi-static. Note that all external boundaries of the specimen are free to move, and the pre-cracked pre-loaded specimen is at absolute zero temperature just before the onset of the fracture, i.e., zero Kelvin MD simulations. Any further rise in the temperature would be either due to the adiabatic heating in the vicinity of the fast-running crack-tip, or some possible plastic deformations in the specimen and most probably in the vicinity of the crack-tip. Even though the process of the introduction of the internal crack to the specimen, as well as the abrupt increase in the applied load would introduce a shock-wave to the system which would in turn increase the temperature of the specimen, the critical damping of the system and proper scaling of the atomic positions mostly reduce and possibly eliminates the rise in the temperature induced by the shock-waves. Therefore, at the onset of the brittle propagation of the internal crack, the temperature of the specimen must be zero Kelvin which corresponds to the zero kinetic energy of the sample. Later, as the crack-tip propagates, due to the adiabatic heating in the vicinity of the running crack-tip, the temperature, and therefore the kinetic energy of the specimen increases accordingly.

In the case of the constant applied displacement or fixed-grips studies, as described earlier in detail, the constant external strain of $\varepsilon<\varepsilon_G$ was applied by specifying and maintaining the vertical displacement of the individual atoms on the uppermost and lowermost rows, i.e., the horizontal boundaries of the specimen. The process of the introduction of the centrally located internal cracks of given initial crack-length and the critical damping of the system for the purpose of the reduction of the introduced shock-waves to the system and the substantial saving in the computation time in attaining the static equilibrium were identical to the case of the dead-weight studies discussed above. After the removal of the critical damping, the externally applied constant strain was increased in the increments of about one percent until the brittle propagation of the initial internal crack was initiated. A sufficient time was given for the system to reach its new static equilibrium state and for the information about the applied strain to reach the crack-tip before the external applied strain was increased. Therefore, the loading scheme was quasi-static.

A larger sample of 159X135 and an smaller one of 39X135 both containing an initial centrally located internal narrow crack of half crack-length c_o= 9.75d under an applied constant tensile load were also simulated in order to investigate the effect of the height of the sample on the critical loads.

Griffith's criterion for the initiation of the brittle propagation of an internal cleavage crack, as described earlier in detail, predicts that for an internal crack of the initial half crack-length c_o in an *infinite perfectly brittle* plate subjected to a remotely applied constant load, the brittle propagation of the cleavage crack

will be initiated at

$$\sigma_G = (2E\gamma / \pi c_o)^{1/2} \qquad \text{II.2.28}$$

where E is Young's modulus of the specimen under a *nominal* tensile load. For a constant level of the applied tensile strain at the boundaries Griffith's relation may be represented as

$$\varepsilon_G = \sigma_G / E = (2\gamma / \pi E c_o)^{1/2}. \qquad \text{II.3.55}$$

Simulations results for the critical fracture stress or strain for the initiation of the brittle propagation of a variety of narrow internal cracks in remotely loaded two-dimensional triangular Johnson solids of various sizes are summarized in Table II.1.5a&b. The simulations results tabulated in Table II.1.5b demonstrates the effect of the height of the specimen on the critical load. Note that the identical sample of 79X135 was used for the simulations data listed in Table II.1.5a, and the width of the sample (135 column) and the initial half crack-length (9.75d) were identical for the simulations results reported in Table II.1.5b.

The effect of the width of the sample on the critical fracture stress may be studied by the comparison of the simulations results and the theoretical prediction [145, 33] of

$$\sigma_C = m(c/W)\,\sigma_G \qquad \text{II.3.56}$$

where

$$m(c/W) = \{(2W/\pi c)\tan(\pi c/2W)\}^{1/2}$$

Note that at the limiting case of c<<W, i.e., an internal crack of half crack length c in an infinite plate, $m(c/W) \rightarrow 1$. The simulations results along with the predictions of equations II.2.28 & II.3.55-56 are summarized in Table II.1.5a. The true stress σ and the true strain ε are also listed along with their engineering equivalents S and e in this table.

The overall agreement between the simulations results and Griffith's critical stress or strain was surprisingly good, being within seven percent of each other.

It is interesting to note that we have generally found good agreement with the predictions of the elasto-static continuum theories regarding energetics and critical fracture stress or strain [1, 114] despite the sharp disagreement we have reported regarding the details of the local stress distributions in the vicinity of the crack-tip.

Surprisingly, the height of the sample, H, has quite a significant effect on the magnitude of the critical fracture stress. The critical fracture stress is smaller for the shorter sample, and larger for the taller one, however, it is within eight percent of Griffith's stress. This is probably due to the fact that in the shorter sample, as we will study in detail in the following section, the fracture energy is provided mostly by the work done on the specimen by the externally

applied loads at the horizontal surface boundaries of the sample. This may, in fact, be the analogue of a double cantilever mode rather than Mode I fracture in a tensile solid.

It is evident from Fig. II.3.22 that the change in the elastic strain energy of the system during the brittle propagation of the cleavage crack, in the shorter sample of 39X135, is negligible compared to the work done by the external load on the system, ΔW. However, the rate of change of the mechanical energy of the system, i.e., the driving force, is identical for all sample sizes, implying that the terminal crack-tip velocities must be identical and therefore sample-size independent.

II.3F. *Remotely Applied Constant Critical Tensile Stress or Strain Necessary for the Initiation of the Brittle Propagation of an Internal Cleavage Crack; Conclusions*

In the light of the simulations results presented above, we may conclude that:

i. The simulations results for the critical applied constant tensile load to initiate the brittle propagation of cleavage crack in a two-dimensional triangular Johnson solid at absolute zero Kelvin are within seven percent of Griffith's fracture stress.

ii. The height of the sample has a significant effect on the critical fracture stress. The shorter sample requires smaller critical applied stress to initiate the fracture. The shortest sample 39x135 resembles the fracture at the tearing mode. Almost all of the fracture energy is provided by the work done on the specimen by the applied load at the horizontal boundaries of the shortest sample, and there is no significant changes in the strain energy of the solid during the brittle growth of the crack (Fig. II.3.22).

iii. The value of the true critical fracture strain ε_C is much closer to Griffith's value (eq. II.3.55) than the engineering critical strain e_C.

It is worthwhile to note that, the critical fracture stress for the initiation of the brittle propagation of a variety of internal cleavage cracks in a 3D Johnson solid α-iron were within ten percent of Griffith's value in the simulations results

reported by deCelis, Argon and Yip [180], in close agreement with our 2D results. deCelis et al. [180] also simulated 3D copper held together by the Morse interatomic pair-wise potential, and found it ductile in the sense that dislocations were emitted from the crack-tip before any crack-tip bond broke. The dislocation nucleation at the crack-tip occurred at about $0.8\sigma_G$, twenty percent below Griffith's fracture stress. These results are similar to the simulations results for the 2D triangular Lennard-Jones solid under constant applied tensile load [114].

II.3G. *Energetics of Brittlely Propagating Cleavage Cracks; Major Simulations Results*

The energetics of a variety of narrow internal cracks of initial half crack-length c_o=3.75d, 6.75d and 9.75d in the two-dimensional triangular Johnson solid of various sample-size of 39X135, 79X135, and 159X135 subjected to the remotely applied constant critical tensile load or displacement at the horizontal boundaries of the specimen are studied in detail during the brittle propagation of the internal cleavage crack. The simulations results will be compared to the reported computer simulations results of the quasi-static crack-extension and to the predictions of existing continuum based elasto-static theories discussed earlier.

The simulations results indicate that the size of the height of the sample, H, is the critical parameter in the partition of the mechanical energy release during the brittle propagation of the cleavage crack, between the work done by the externally applied tensile load at the outer horizontal surfaces of the sample on the specimen, ΔW, and the change in the elastic strain potential energy of the system, ΔE_{el}.

Note that all energies, i.e., ΔW, ΔE_{el}, ΔE_{me}, and ΔE_{ke} are reported with respect to those of the defect-free specimen subjected to the identical applied load or displacement and boundary conditions, unless otherwise mentioned.

The detailed investigations are performed on the medium size 79X135

specimen. By varying the initial half crack-length c_o, but keeping the width of the sample 2W constant, we make it possible to study the sample-size effect on the energetics of the system.

The effect of the finite height sample size on the energetics of the system during the brittle propagation of the internal cleavage crack was investigated by studying energetics of three specimen of the identical width, 2W=135 columns, but very different height, H=39, 79 and 159 rows. These samples contained identical centrally located internal narrow crack of initial half crack-length c_o=9.75d corresponding to 19 broken bonds in the half-sample, and were subjected to the externally applied constant tensile critical load at the horizontal boundaries. These three simulations are of the "gradual" type, i.e., the pre-cracked specimen is first loaded to a load just below the critical load and is brought to a reasonable equilibrium by the combined effort of scaling and critical damping. After the removal of the critical damping, the applied load was increased gradually in the small increments of less than one percent until the critical load to initiate the brittle propagation of the initial internal crack is reached.

The simulations results are plotted as the change in the energetics of the sample during the brittle propagation of the crack, i.e., ΔW, ΔE_{el}, and ΔE_{ke}, versus the number of new broken bonds NNBB in Fig. II.3.20-22.

The critical applied fracture load of 2.15 is required to initiate the brittle propagation of the internal crack of initial half crack-length c_o=9.75d in the

largest simulated sample of 159X135. After 13 new crack-tip interatomic bonds broke sequentially, by the time $c/c_o \approx 1.7$, the crack-tip velocity saturated to the constant terminal velocity of $V_T=0.24C_1$. The fast-running crack-tip was arrested because of the emission of a pair of blunting dislocations at the crack-tip and the run was terminated by us due to the economic restrictions.

The simulations results are plotted in Fig. II.3.20. As demonstrated clearly in this figure, the work done by the externally applied load on the sample during the brittle propagation of the crack, ΔW, is essentially zero, and all of the driving fracture energy is provided practically by the strain potential energy of the specimen. The behavior of the system strongly resembles that of fixed-grips loading conditions. The reason for this particular behavior is no other than the fact that the externally applied load at the horizontal boundaries of the specimen, due to the relatively large height of the sample H does not detect the initiation of the brittle propagation of the cleavage internal crack until almost the end of the run. This is due to the fact that the information about the initiation of the fracture travels with the longitudinal sound velocity in the strained medium. Therefore, due to the relatively large height of the specimen, it takes relatively longer time for this information to reach the outer horizontal boundaries of the specimen and hence being detected by the externally applied load there. Obviously, the applied load could not respond to the undetected events, and all of the fracture energy has to be provided by the stored strain potential energy in the body. Hence, the system behaves as if it was loaded under a fixed constant displacement at its horizontal boundaries, or as if the specimen was infinitely large. In this regard, it is therefore not unreasonable to assume that practically,

the largest simulated sample of 159X135 resembles an infinite sample loaded to the critical load at infinity, i.e., Griffith's theoretical sample. Of course, if the simulations were not discontinued, the externally applied load at the horizontal boundaries of the sample would detect the events taking place at the crack tip, and would respond to it by working on the specimen. The system then would behave in a manner similar to the behavior of our middle-size sample, 79X135. The emission of a pair of blunting dislocations from the tip of the fast-running crack in 2D Johnson solid is independent of the sample size, the initial crack-length, or loading scheme. It is probably due to the adiabatic heating in the immediate vicinity of the fast-running crack-tip, and is the clear indication of the fact that the two-dimensional triangular Johnson solid is in the vicinity of ductile-brittle behavior. The activation energy for the dislocation nucleation in this solid is small enough to be provided by the nominal increase in the local crack-tip temperature.

Thus, as is well put by Erdogan [154] "in the actual problem of a large plate subjected to loads at infinity, which are increased slowly up to values sufficient to initiate fracture and then held constant, the available energy to overcome the dissipation and increase in the kinetic energy comes from the released elastic potential within a circular region of radius C_1t, where C_1 is the dilational wave velocity in the plane stress ... The error introduced through replacing this energy by its static equivalent given by

$$\Delta(W - E_{el}) = \pi\sigma_a^2 c^2 / E \qquad \text{II.3.57}$$

may be difficult to estimate, but is unlikely to be negligible... It is obvious that outside this circle, the stress state is that of uniform tension and velocities are zero". This point is investigated by plotting the decrease in the elastic stored energy of the system, $-\Delta E_{el}$, versus c^2 in Fig. 3.24. Just past the initial stage of the brittle propagation of the cleavage crack, the functional dependence of the decrease in the elastic strain potential energy of the system, $-\Delta E_{el}$, on the instantaneous half crack-length c is the one predicted by the elasto-static continuum theory, i.e., $-\Delta E_{el}$ is a linear increasing function of c^2. However, the slope of the linear regression line in Fig. II.3.24 is 0.206, about thirty percent lower than the elasto-static predicted value of $\pi\sigma^2/M^*=0.258$. Notice that this relationship is valid throughout the history of the growth of the running crack, even during the acceleration stage of the moving crack-tip where the velocity is much smaller than the terminal velocity and it is changing very rapidly. It is worthy to note that the simulations results for the quasi-static crack extension are in good agreement with the predictions of the elasto-static continuum theories, being within five percent of them as demonstrated in Fig. II.3.25 and Table II.1.4.

The externally applied constant tensile critical load of $\sigma_c=1.45$ is required to initiate the brittle propagation of the internal crack of initial half crack-length $c_o=9.75d$, in the short sample of 39X135. The brittlely propagating crack-tip accelerated to the terminal constant velocity of $V_T\approx 0.25C_1$ by the time the crack length was doubled. The simulations results are plotted in Fig. II.3.22 as the change in the energies of the specimen during the brittle propagation of the internal cleavage crack, versus the number of new broken bonds, NNBB. The

fracture energy is provided almost entirely by the work done by the externally applied constant load at the horizontal boundaries of the specimen, ΔW. As demonstrated in Fig. II.3.22, the elastic strain energy of the system is practically constant during the brittle propagation of the internal cleavage crack, and therefore, its change is zero. The fracture energies resemble more of a double cantilever mode than those of mode I tensile fracture. $\Delta E_{el} \approx 0.0$ during the crack growth, indicates that the solid behaved like two rigid bodies above and below the crack-line. Due to the relatively short height of the sample, as illustrated in Fig. II.3.22, the information about the initiation of the fracture reaches the applied load only after four new crack-tip interatomic bonds are broken. The externally applied constant load at the horizontal boundaries of the specimen responded to this event by working on the sample. During the sequential breaking of the first four crack-tip interatomic bonds, the fracture energy is essentially provided by the released strain potential energy in the specimen. Immediately after the detection of the onset of the fracture by the applied load at the horizontal boundaries of the specimen, the applied load takes over the role of the sole provider of the fracture energy, by increasing the work done on the sample proportional to c^2.

The intermediate sample of 79X135 showed a mixed behavior. Neither ΔW, nor ΔE_{el} changes as a function of c^2. The simulations results for the typical "gradual" case of the initial crack of $c_o=9.75d$ which required the applied critical tensile constant load of $\sigma_c=1.90$ to begin its brittle propagation, is illustrated in Fig. II.3.21 as the change in the energies of the system against the number of new broken bonds, NNBB. As demonstrated, ΔW increases quite

rapidly in the initial stage of the propagation of the cleavage crack, i.e., up to the point where $c/c_0 \approx 1.4$ during which the strain energy of the system also increases, but the kinetic energy is relatively small and almost constant. During this period the work done on the sample not only provides the necessary energy for the continuation of the fracture, but it also provides some additional energy which is stored in the potential energy of the body. At this point ΔE_{el} has its maximum, while ΔW shows an inflection. Afterward, ΔE_{el} decreases smoothly, while ΔW continues its increase but with the relatively lower slopes, indicating that the fracture energy is shared between the work done on the sample by the externally applied load and the release in the stored strain energy of the specimen. After this point the kinetic energy of the system first very slowly and then smoothly increases, and toward the end of the run it is comparable to the other forms of energies of the specimen. Simulations data for the middle size sample 79x135 containing a variety of centrally located initial cracks under remotely applied constant critical load and/or displacement are tabulated in Table II.3.8A1-II.3.8H. Figure II.3.21 is a representative of the mixed behavior of the energetics of the middle size sample 79X135 during the brittle propagation of the variety of the internal cracks studied.

The strong dependency of the partition of energies on the height of the sample during the brittle propagation of the internal crack was totally misunderstood in the previous simulations, where it was misinterpreted as the "failure of Griffith's energy criterion" [2], or as the strain rate effect [15].

However, surprisingly the sample size, i.e., height dependency has completely disappeared in the functional dependency of the change in the mechanical energy of the system, ΔE_{me}, on the instantaneous half crack-length, c, during the brittle propagation of the internal cleavage crack. This particular behavior is demonstrated in Fig. II.2.23 by plotting the change in the mechanical energy of the system, ΔE_{me}, against NNBB for the three samples of the identical width, i.e., 135 columns and initial crack-length c_o=9.75d but very different heights, i.e., 39, 79, and 159 rows subjected to quasi-static or "gradual" critical applied tensile load at their horizontal surface boundaries. As illustrated in this figure, ΔE_{me} are almost identical for these specimen even though their heights differ by a factor of two to four. The change in the mechanical energy of the system during the brittle propagation of the internal crack, $-\Delta E_{me}$, for these three samples are plotted against c^2 in Fig. II.2.26. As demonstrated clearly in this figure, $-\Delta E_{me}$, is a linear function of c^2 as predicted by the elasto-static continuum theory of Griffith-Mott, however, with a different slope, indicating the quantitative difference between the predictions of the elasto-static continuum theories and the computer simulations results for the dynamic cracks. Note that as demonstrated in Fig. II.3.25 and Table II.1.4, the simulations results for the quasi-static extension of the internal cracks are almost identical to the predictions of the elasto-static continuum theories. This may indicate that the quantitative difference discussed above as well as the sample-size, i.e., height dependency of ΔW and ΔE_{el} are in fact the *dynamic effect,* which elasto-static based theories are incapable of handling.

The energetics of constant displacement simulations are presented in

Fig. II.3.27-29 as the change in the various energies of the system during the brittle extension of the cleavage crack, against NNBB.

The change in the mechanical energy of the two-dimensional triangular Johnson solid of various sample sizes containing a variety of narrow internal cracks is plotted versus c^2 in Fig. II.3.30, against c^2/M^* for constant applied stress simulations in Fig. II.3.31, and against c^2M^* for constant applied strain simulations in Fig. II.3.32. As demonstrated clearly in Fig. II.3.30, independent from the sample-size, i.e., H and c/W, initial half crack-length c_o, or the loading scheme, the decrease in the fracture mechanical energy of the system is linear in c^2 in accord with the predictions of the elasto-static continuum theories of Griffith-Mott. Comparisons of Fig. II.3.30-32 indicate that M* corrections, i.e., the replacement of E by the effective instantaneous Young's modulus of the critically loaded specimen M*, do not significantly influence the functional dependency of ΔE_{me}. However, it affects the slope of these linear functions. Therefore, the effect of M* corrections may be observed in the quantitative differences between those of the simulations results and the theoretical predictions as demonstrated in Table II.3.7.

The increase in the kinetic energy of the specimen during the brittle growth of the cleavage crack of various initial half crack-length, sample size, and loading conditions are plotted against NNBB, c^2, and $c^2V_c^2$ in Fig. II.3.33-35. The simulations results do not reveal any particular functional dependency of the kinetic energy on c^2 and/or $c^2V_c^2$ as predicted by Mott's theory. Our observations indicate that:

i. The boundary conditions influences the build up of the kinetic energy. Overall, the kinetic energy of the system at a given instantaneous crack-length and crack-tip velocity is lower for the fixed-grips than for the dead-weight loading conditions. This is probably due to the restrictions put on the vertical displacements of the constituent atoms in the constant displacement loading scheme.

ii. Comparisons of the simulations results for the three different sample sizes reveals the fact that the height of the sample influences the build up of the kinetic energy of the system during the brittle propagation of the crack. For a given instantaneous crack-length and crack-tip velocity, the kinetic energy of the tallest simulated sample 159X135 is the lowest, while those of the shortest simulated specimen 39X135 is the highest. Because of this sample-size dependency, only the kinetic energy of the tallest sample, where the expected sample-size dependency is minimum, may be analyzed and compared to the theoretical predictions. Note that the applied critical load for the initiation of the fracture is lowest for the shortest sample, i.e., σ_c=1.45, and highest for the tallest one, i.e., σ_c=2.15.

iii. There is an influence of the strain rate on the development of the kinetic energy of the system. For the given instantaneous crack-length, crack-tip velocity, and boundary conditions, the kinetic energy of the system is higher for the "fast" type of loading.

II.3H. *Energetics of Brittlely Propagating Cleavage Cracks; Conclusions*

In the light of the simulations results presented in the preceding section for the brittlely propagating cleavage crack in the two-dimensional triangular Johnson solid, and those of the quasi-static extension of the internal cracks presented in section II.2, and comparisons of these simulations results to those of the quasi-static continuum theories of Griffith-Mott we may conclude that:

i. There is a strong influence of the height of the sample on the partition of the change in the fracture mechanical energy of the system during the brittle propagation of the internal cleavage crack, ΔE_{me}, between the work done on the specimen by the externally applied load at the outer horizontal boundaries of the sample, ΔW, and the change in the stored strain potential energy of the body, ΔE_{el}.

The change in the fracture mechanical energy of the system, ΔE_{me}, is essentially independent of the sample-size, initial crack-length, boundary conditions, the magnitude of the applied load, and the loading scheme. As illustrated clearly in the figure II.3.26, just past the very initial acceleration stage of the brittlely propagating cleavage crack, the change in the fracture mechanical energy of the system is linear in c^2 as predicted by the elasto-static continuum theories of Griffith-Mott, except for the fact that as demonstrated in Table II.3.7 the slope of the linear regression line between the simulations data differs from the theoretically expected values. Therefore, even though the functional dependency of the change in the fracture

mechanical energy of the system is exactly what is expected by the theory, there is a quantitative difference between the simulations results and the expectations of Griffith-Mott's theories.

ii. Energetically, as demonstrated clearly in Fig. II.3.20&24, there is a strong resemblance between the tallest simulated sample of 159X135 under the remotely applied constant tensile critical load at the horizontal boundaries of the sample, and the simulations results for the fixed-grips method of loading of the specimen during the brittle propagation of the internal cleavage crack (Fig. II.3.27-29). The fracture energy in this particular system is provided almost entirely by the stored strain potential energy released during the fracture up to the arrest of the crack, ΔE_{el}. The work done on the system by the external critical constant load, ΔW, is essentially zero during this period. In the deeper investigation of the simulations results we recognize that due to the relatively large size of the height of the specimen, the information about the onset of the fracture has not reached to the horizontal boundaries of the sample. Therefore, the initiation of the fracture is not detected by the externally applied load at these outer boundaries until a much later time where the fast-running crack-tip is already arrested due to the emission of a pair of blunting dislocations from the crack-tip. The slight increase in the magnitude of ΔW toward the end of the run is observable in Fig. II.3.20. The simulations was discontinued by us few steps after the arrest of the crack due to the economic restrictions and the fact that the behavior of the system was clearly predictable. The occurrence of the situation is widely recognized in the literature [151, 154], but there is a great confusion in some others [2,

15, 114]. Note that we may calculate the average longitudinal wave velocity in the strained sample from the information provided by the Fig. II.3.20.

iii. The simulations results for the increase in the kinetic energy of the system are not in accord with the predictions of the linear elasto-static continuum theory of Mott. The kinetic energy of the system is a very complicated function of the sample size, i.e., height, instantaneous crack-length, crack-tip velocity, boundary conditions, and the loading scheme. This is probably due to the fact that the two-dimensional triangular Johnson solid is in the vicinity of the brittle-ductile behavior. In this solid, there are sufficient plastic deformations in the vicinity of the critically loaded crack-tip, and the fast running crack-tip is eventually arrested due to the emission of a pair of blunting dislocations from the crack-tip. The more brittle system of the covalently modified Lennard-Jones solid (Fig. II.3.36) shows a reasonable linear relationship between the increase in the kinetic energy of the system and $(cV_c/C_1M^*)^2$. Therefore, probably because of the energy dissipations due to the plastic deformations in the crack-tip zone, the functional dependency of the kinetic energy of the Johnson solid does not follow the predicted form of the linear elasto-static theory of Mott. Mott's theory was developed for the cleavage fracture in the perfectly brittle plate.

It is worth noting that the simulations results for the energetics of quasi-static crack extension, as illustrated in Table II.1.4, and Fig. II.3.25 are in reasonable agreement with the predictions of the linear elasto-static continuum theories.

II.3l. *Computer Simulations of Dynamic Cracks: Summary*

Because of the rather long and bulky volume of the present investigations discussed above, it is beneficial to summarize the simulations results:

i. The acceleration of the brittlely propagating crack tip to the constant terminal crack-tip velocity is in accord with the laboratory observations and much faster than the predicted period of the elasto-static continuum based theories. By the time the crack length is doubled, the instantaneous crack-tip velocity is saturated to its terminal constant value. The quick rise of the crack velocity is independent of the sample-size, initial crack length, loading scheme, and most importantly the interatomic potential law. It seems that the faster the applied load is, i.e., the higher the strain rate is, the quicker the rise in the velocity of the crack would be.

ii. The terminal velocity of the brittlely propagating cleavage crack is strongly dependent on the interatomic potential law holding the crystalline solid together. The more brittle or rigid the material is, the higher the terminal constant velocity of the crack-tip velocity would be. The limiting terminal velocity is $V_T=0.42C_1$, where C_1 is the velocity of the waves of dilatation in the material. It seems that no particular elastic wave velocity in the solid directly governs the terminal velocity of the brittlely propagating cleavage cracks. The "crack-tip configurational" model reasonably explains the phenomena and overcome the objections to the elasto-static continuum theories.

iii. The local stress distributions for the fast-running crack-tip is crack-tip velocity independent and resembles the quasi-static stress distributions as presumed by Mott, but in sharp disagreement with the predictions of the dynamic fracture theories. The maximum local normal stress is limited by the cohesive stress of the interatomic bonds in the solid, and therefore is a material property and independent of the crack-length, crack-tip velocity, loading scheme, boundary conditions, and the sample size. The discreteness of the crystalline solid at the atomistic level is responsible for this phenomena.

iv. The magnitude of the externally applied critical constant tensile load or displacement required for the initiation of the brittle cleavage crack in a tensile plate is in very close agreement with the predictions of the elasto-static continuum theories. It is sample size dependent, being small for shorter sample and large for the taller specimen, within five percent of Griffith's fracture stress.

v. The fracture mechanical energy of the system during the brittle propagation of the internal crack, ΔE_{me}, is proportional to c^2 in the qualitative agreement with the predictions of the continuum theories, but quantitatively there is a difference of about thirty percent between these two values. Note that this is only a dynamic phenomena, because the quasi-static simulations results discussed in the preceding sections are in reasonable agreement with the theoretical expectations, being within five percent of them. The functional

dependency of the ΔE_{me} is independent of the sample size, crack-tip velocity, loading scheme, interatomic potential and boundary conditions.

vi. The work done on the sample by the externally applied tensile constant critical load at the horizontal boundaries of the specimen, ΔW, and the change in the stored elastic potential energy of the specimen, ΔE_{el}, during the brittle propagation of the cleavage crack, are strongly sample-height dependent. The tallest sample simulated behaves like the infinite plate of Griffith which is loaded at infinity, or those of the specimen under fixed displacement, i.e., the fracture energy is entirely provided by the stored elastic energy of the solid, and $\Delta W \approx 0.0$. The shortest sample in the height resembles a mode III fracture, where the change in the strain energy of the solid during the fracture is almost zero, and the fracture energy is provided almost entirely by the work done on the sample by the externally applied load. The applied load at the outer boundaries of the specimen in the tallest sample does not detect the onset of the fracture at the crack-tip until a much later time, due to the fact the information about the initiation of the brittle propagation of the cleavage crack travels with the longitudinal velocity in the strained specimen.

vii. The kinetic energy of the sample is a very complicated function of the sample-height, loading-scheme, boundary conditions, interatomic potential, crack-length, and the crack-tip velocity. Even in the tallest Johnson solid it does not follow the predictions of the elasto-static theories. Probably, the energy dissipations due to the plastic deformations in the crack-tip zone are

responsible for this phenomenon. The increase in the kinetic energy of the covalently bonded modified Lennard-Jones solid of $a^* = 1.0$ is in close agreement with the expectations of the continuum based theories.

viii. The fast-running crack-tip in the two-dimensional Johnson solid is arrested by the time the crack-length is quadrupled, by the symmetric emission of a pair of blunting dislocations from the moving crack-tip. The dislocation nucleation at the crack-tip is probably thermally activated due to the adiabatic heat generated in the immediate vicinity of the fast-running crack because of the fast displacements of atoms in this region. This phenomenon also indicates that the two-dimensional Johnson solid is in the vicinity of brittle-ductile behavior.

Computer Simulations Studies:

I-Dynamics of Brittle Crack Propagation.

II-Brittle To Ductile Transition Temperature.

Volume II

by

Behzad Massoumzadeh

A dissertation submitted to the Graduate Faculty in Physics in partial fulfillment of the requirements for the degree of Doctor of Philosophy, The City University of New York.

1995

III. *Brittle-to-Ductile Transition Temperature*

III.1. Finite Temperature Molecular Dynamics Technique

The MD technique at absolute zero Kelvin temperature is described in the earlier sections in detail. Here, we will emphasize on the parts related to the introduction of the thermal energy to the specimen.

Similar to the zero Kelvin temperature simulations, due to the economic restrictions imposed on us by the use of computer facilities, we had to compromise on the third dimension, and a two-dimensional triangular array of atoms interacting via a given interatomic potential is used in these simulations.

The finite non-zero temperature was introduced to the system via the controlled random displacements of the atoms from their static frozen equilibrium positions, and then allowing the system to relax. The time-average temperature, strain, Young's modulus, potential energy, total energy, center of mass velocity, and mean square value of thermal fluctuations MSTFL of the system was monitored throughout the run. When the fluctuations in the temperature MSTFL was "sufficiently" small, it was assumed that these values were representing the equilibrium values of the physical entity of interest. What is meant by "sufficiently" small as well as other parts relating to the establishment of equilibrium are discussed in Appendix A. For the dynamic properties, the time step in the calculations δ=0.01 gave one part in 10^6 accuracy in the total energy of the system.

Due to the extreme sensitive nature of the immediate vicinity of the crack-tip especially when the pre-cracked sample is loaded and at high temperatures, we were forced to elect the constant enthalpy adiabatic ensemble procedure. This procedure introduces some problems, the principle one being the reduction in the temperature of the system as the applied load is increased. The isothermal molecular dynamics technique is well known. The temperature of the system is monitored throughout, and in every given time step by randomly increasing or reducing the atomic velocities by an appropriate amplitude, the average constant temperature is achieved and maintained. But because of the extremely sensitive nature of the loaded crack-tip region, any arbitrary change in the position and/or velocity of any atom in the immediate vicinity of the crack-tip might result in an unpredictable unnatural behavior of the crack-tip.

The average temperature of the specimen was calculated from the total kinetic energy of the system

$$T = [1/2NK_B]\sum_i m_i v_i^2 \qquad ; i=1,2,3...N \qquad \text{III.1.1}$$

where K_B is Boltzmann's Constant, N is the total number of atoms in the specimen, m_i is the mass of the ith atom which is taken to be unity in our system of units, and v_i is the velocity of the ith atom. This is due to the fact that at high-temperature limit, in the quasi-harmonic approximations, each mode has a kinetic energy of $K_BT/2$.

After the system was judged to have reached equilibrium, the temperature, potential energy, total energy, strain, Young's modulus, MSTFL, velocity of the center of mass, and angular momentum of the system about its center of mass were averaged over the last several hundred time steps of the simulations. The values reported are these time averaged thermal equilibrium values, unless specifically mentioned.

The sample size problem is reduced and eliminated in some theoretical MD calculations dealing with various thermodynamical properties of the solid [127] by assuming a periodic boundary condition. Unfortunately here we not only are prevented from using these well known facilities because of the complications associated with the interacting periodic crack-tips, but in addition, we are not even allowed to use the "mirror symmetry" used in the absolute zero temperature fracture simulations of the previous sections. For, otherwise, we would produce a non-physical temperature gradient at the mirror.

To reduce the shock wave introduced to the system during the introduction of the crack to the specimen, or when the externally applied constant tensile load was increased, in the zero-temperature MD simulations the kinetic energy of the system was critically damped and finally reduced to zero. Here, because the kinetic energy of the system is directly connected to the temperature of the system through equation III.1.1, we are prevented from using this facility either, otherwise, the temperature of the system would be consistently and undesirably reduced. To circumvent this problem, the thermal energy is introduced to the pre-cracked loaded sample which is in its zero-

temperature equilibrium state. Because, then we are able to use the critical damping facilities during the introduction of the crack to the specimen as well as during its loading at its boundary at absolute zero temperature. The MD simulations is therefore similar to those of the zero temperature runs, described in detail in the previous sections, up to the point where the desired temperature is introduced to the system by displacing the atoms randomly from their zero-temperature equilibrium positions.

Prior to the MD simulations of the fracture problem at finite temperature, the mechanical properties of the system as a function of the temperature was investigated in a sufficient detail. Besides the obvious academic interest in the thermo-mechanical properties of the solid, the detailed quantitative knowledge of the mechanical properties of the solid as a function of temperature would assist us in achieving the desired thermo-mechanical equilibrium much faster. A full sample of 18X19 is used in these studies, the details of which may be found in the following sections.

For the purpose of a significant amount of saving in the equilibration time and therefore computation cost, at the moment of the introduction of the temperature to the system the specimen was scaled in both dimensions according to the proper linear coefficient of expansion α obtained earlier. The vertical position of every atom in the system was also scaled according to the proper Young's modulus at the given temperature and applied tensile load.

It is customary to give the brittle-to-ductile temperature BDT of the solid

in the units of the melting temperature of the material, T_M. Therefore, the melting temperature of the material was investigated. A full sample of 18X19 was used in these studies. The detail of the search for the melting point temperature of the covalently modified two-dimensional triangular Lennard-Jones solid with $a^* = 0.2$, LJCOVa.2, is given in the following sections. T_M, calculated from the Kosterlitz-Thouless parameter **K** is in close agreement with the simulations results.

As mentioned earlier in the introduction, here we have adopted the Rice-Thomson's [46] criterion for the brittle-to-ductile transition, i.e., the emission of the first blunting dislocation from the crack-tip prior to the breakage of any crack-tip bond.

For the low temperature runs, first the system was loaded to an applied external load below the critical (Griffith) stress at absolute zero temperature. The specimen was scaled uniformly in the Y-direction according to the proper value of the Young's modulus. The critical damping factor was introduced to the Newton's equation of motion in order to reduce the shock wave produced during the loading procedure, and therefore to save on the equilibration time. The centrally located internal narrow crack of initial half-length of c_o=3.75d, corresponding to 14 broken bonds in the full sample, was then introduced to the loaded specimen by artificially preventing a number of given atoms in the center of the sample from interacting, i.e., by setting the interatomic force between the specified atoms in the center of the specimen to zero and maintaining this throughout the simulations in order to prevent any possible undesired re-

healing of the initial crack. The critical damping was continued for a few hundred steps till a reasonable static mechanical equilibrium at absolute zero temperature was attained. Then, the critical damping parameter was removed, and the loaded pre-cracked specimen was heated up to the desired temperature by randomly displacing every atom in the sample according to the proper amplitude which was found earlier in the investigations of the thermo-mechanical properties of the solid. The sample was scaled in both dimensions according to the corresponding value of the coefficient of expansion. The system was then allowed to relax, and the thermo-mechanical equilibrium was considered to be attained when the fluctuations in the temperature, MSTFL, were sufficiently small (Appendix A). After the thermal equilibrium was achieved, the externally applied constant tensile load at the horizontal boundaries of the specimen was increased in increments of less than five percent, until either the brittle propagation of the cleavage crack was initiated at the crack tip by breaking the interatomic bond there, or until the stationary crack-tip got blunted and a blunting dislocation was nucleated at the crack-tip.

The emitted dislocation from the crack-tip usually blunts the crack-tip and shields it from the influence of the externally applied load and therefore initiate the ductile fracture of the specimen. Sometimes the applied load is not sufficient to give the nucleated dislocations the necessary kinetic energy in order to separate themselves from the crack-tip and move away from the crack. These generated but unstable dislocations, eventually, are attracted back to the crack-tip, and finally are absorbed by the crack. If such an event takes place, the blunted crack-tip gets back its original sharp and atomically narrow

configuration. In these situations we have to proceed with increasing the applied load with about one to two percent until a dynamic effect takes place at the crack-tip. The vertical positions of the constituent atoms were uniformly scaled according to the corresponding Young's modulus at the moment of each increase in the applied load. Before any increase in the magnitude of the externally applied tensile load, a reasonable time was given to the system in order to reach to its new equilibrium state.

Unfortunately, due to the fact that the simulations are performed in the constant enthalpy ensemble, increasing the magnitude of the externally applied tensile load results in the reduction in the equilibrium temperature of the system. The reason for this phenomenon lies in the fact that the interatomic potentials used in these simulations are highly nonlinear. The increase in the external load is associated with the expansion of the solid, increase in the volume of the specimen, and stretching of the interatomic bonds especially at the highly sensitive, possibly deformed and strained crack-tip zone. Since the system is adiabatic and therefore no heat exchange may take place with the universe, the increase in the volume would result in the reduction of the temperature of the system. This is not a major problem at the low temperature simulations, but it becomes a problem later when we try to pinpoint the BDT temperature. As mentioned earlier, the critical load is a function of the temperature. On the other hand, any change in the applied load immediately affects the temperature of the system. Therefore, since due to the high cost of these runs we are economically constrained to simulate very limited number of temperatures, it becomes practically impossible to pinpoint the desired

temperature. Possibly for the future studies of the phenomena, it is advisable to rather choose the isothermal ensemble instead, with a restrictions that the atomic velocities of every atom in the ensemble but those of the crack-tip zone may be varied on a regular basis to keep the kinetic energy and therefore the equilibrium temperature of the system constant. This would resolve the mentioned problem, and simultaneously would not artificially induce any change in the behavior of the system.

For the high temperature studies, the procedure was slightly different. A loaded pre-cracked sample at a lower temperature, in a reasonable equilibrium, was reheated by randomly displacing every atom in the sample from their present finite temperature atomic positions according to a given amplitude. Then the system was allowed to relax to its new equilibrium state. Note that the lower temperature sample should not be under applied load of higher than eighty percent of the zero temperature critical fracture stress. Reheating procedure has the following advantages over the direct heating of the sample from the absolute zero temperature

1. It reduces the computation time significantly.

2. Preliminary investigations showed that the direct random displacement of atoms from their absolute zero temperature equilibrium positions of the pre-cracked loaded sample requires a rather large amplitude which would sometimes create some unpredictable and undesired behavior of the free surface interatomic bonds, especially those of the horizontal

surfaces of the sample where the external tensile load is directly applied. This is due to the fact that the surface and corner atoms have fewer interacting neighbors than those of the internal atoms. Therefore, amplitude of the oscillations of these atoms in general are larger than those of the internal atoms. Now particularly if these large amplitude oscillating boundary atoms are subjected to a relatively high externally applied tensile stress before a reasonable thermal equilibrium is attained, there is always a chance of losing these directly loaded boundary atoms, which in turn may completely alter the behavior of the crack. Because, by losing these atoms we actually lose the contribution of the externally applied force locally at the column of that atom, i.e., the system is in fact locally unloaded. This is equivalent to the surface peal off and sublimation in the laboratory. Gradual heating of the sample by multiple random re-displacements of the atomic positions prevents the initial high amplitude vibrations of the boundary atoms and therefore reduces considerably the chance of undesired local unloading of the system at high-temperature and large applied-loads.

III.2. ***Interatomic Potentials***

To study the BDT temperature, we naturally needed a material that is inherently brittle at very low temperature. The previous studies have shown that the two-dimensional triangular Lennard-Jones and Morse solids are in the vicinity of brittle-ductile behavior at absolute zero temperature. But two-dimensional triangular Johnson solid, as was shown in the previous sections, is relatively

brittle at zero Kelvin. Because of the importance of iron in practice, and since Johnson solid is often used to simulate the properties of α-iron, therefore, it was natural for us to choose the two-dimensional triangular Johnson solid as the subject of our studies. But unfortunately the behavior of the high temperature fracture in the 2D Johnson solid was very complex and difficult to interpret. The simulations were therefore terminated. Major simulations results will be reported briefly in section III.7.

The particular behavior of the two-dimensional triangular Johnson solid at the high temperatures, and since this solid is only relatively brittle at absolute zero temperature, led us to the believe that in order to be able to investigate the brittle to ductile transition temperature, we may need a crystalline solid which is very brittle at absolute zero temperature. Such a solid was in fact developed in the course of the investigation of the terminal velocity of brittlely propagating cleavage crack, as reported in the previous sections. As discussed earlier, the 3-body covalent potential was constructed by modifying the pair-wise potential, $\Phi(r_{ij})$, by adding an angular resistance to it

$$U= (1/2) \sum'_{ij} \Phi(r_{ij}) + (1/6) \sum'_{ijk} [\Phi_{ijk}+\Phi_{jki}+\Phi_{kij}] \qquad \text{II.1.4}$$

Where

$$\Phi_{ijk} = \Phi(r_{ij})\Phi(r_{ik}) [2a^* (Cos\theta_{ijk} - Cos\theta_o)] \qquad \text{II.1.5}$$

and θ_{ijk} is the angle between r_{ij} and r_{ik}, and a^* is the amplitude of the angular resistance.

The radial pair-wise potential $\Phi(r_{ij})$ was chosen to be the Lennard-Jones potential truncated at r=1.60d, and a*=0.2. The activation energy for the dislocation nucleation for the higher a*s are extremely large, and therefore, can not be provided by the thermal energy.

The 2D-triangular covalently modified Lennard-Jones solid with a*=0.2, LJCOVa.2, is very brittle at zero temperature, and fortunately unlike the 2D-triangular Johnson and Lennard-Jones solids, its brittleness is independent of the sample-size. On the other hand, being able to create the absolutely dislocation-free, defect-free specimen, unlike the real world, is trivial in the computer simulations. So, we may investigate the possibility of the thermally activated dislocation emission from the crack-tip directly, and therefore, evaluate the possible effects of the preexisting dislocations on the reported sharpness of BDT in covalently bonded materials like silicon. Hirsch model [8] for the BDT in Si predicts that the sharp BDT is due to the preexisting dislocations or its sources in the original specimen, and that if the BDT was solely due to the Rice-Thomson's [46] mechanism, i.e., due to the dislocation emission from the crack-tip, the BDT would be soft. Computer simulations are the only reliable tool that would be able to answer with high precision the questions raised.

III.3. *Thermo-Mechanical Properties of The Two-Dimensional Triangular Covalently Bonded Lennard-Jones Solid, LJCOVa.2. Major Simulations Results*

Thermo-mechanical properties of the LJCOVa.2 solid were investigated as a function of temperature. A small sample of 18X19 was chosen in these simulations.

i. The time averaged linear coefficient of expansion of the solid as a function of the temperature was studied by the gradual heating of the specimen up to the melting point, i.e., multiple random re-displacements of the atomic positions with a rather small amplitude. The simulations results are tabulated in Table II.2.2B, and plotted in Fig. III.3.1 as the linear coefficient of expansion against temperature.

ii. The time averaged modulus of elasticity, strain, Kosterlitz-Thouless parameter, and average density were studied as a function of temperature and external load. The simulations results are tabulated in Table II.2.2B&C and plotted against temperature in Fig. III.3.2-5.

iii. Conventionally, the BDT temperature is expressed in terms of the melting point temperature T_M of the solid. Therefore, a series of high temperature simulations was performed to pinpoint the melting point of the LJCOVa.2 crystalline solid. At the melting point, there is a large increase in the atomic diffusion and atoms occasionally jump into the new positions more distant

than their initial second neighbor [127]. Because of the atomic book-keeping scheme used in the simulations, the contribution of these atoms to the total potential energy of the system and to the total number of interacting neighbors are lost. This results in a systematic drift of the total energy and the total number of interacting neighbors. In addition, if the specimen has a free surface as our sample does, because the sublimation temperature is lower than the melting point, the surface boundary atoms are sublimated before the melting point is reached. Therefore, in the studies like ours where the investigation of the melting point temperature is not the main concern we may estimate the melting temperature from the high temperature behavior of the system. The temperature of $K_BT_M=0.33\ \varepsilon_o$ is therefore estimated for the melting point temperature of the 2D-LJCOVa.2 solid. Kosterlitz-Thouless parameter for solid state is defined as

$$K =[4d^2/K_BT]\{[\mu(\mu+\lambda)]/[2\mu+\lambda]\}\geq 16\pi \qquad \text{III.3.2}$$

Considering the 2D Lennard-Jones solid we may justify

$$\mu \approx (3/8)\lambda \equiv (3/8)M \qquad \text{III.3.3}$$

which results in

$$K =[33d^2/28][M/K_BT] \geq 16\pi \qquad \text{III.3.4}$$

K calculated from III.3.4 is plotted against K_BT in Fig. III.3.5. Extrapolation of

K to 16π discloses the theoretical melting point temperature K_BT_M of about 0.34 ε_o, which is in surprisingly good agreement with the simulations results for the melting point temperature of the LJCOVa.2, i.e., K_BT_M=0.33 ε_o.

III.4. *Brittle-to-Ductile Transition Temperature; Major Simulations Results*

Simulations results are summarized in Table III.4A, III.4B, and III.6A. The details of these simulations are described below.

III.4A Series. *Major Simulations Results*

The molecular dynamic simulations were performed on a sample of two-dimensional array of 598 atoms interacting via LJCOVa.2 potential and arranged in 19 rows. The full sample is illustrated in Fig. III.4A1.A.

III.4A1. This run was performed at absolute zero temperature. The purpose was to make sure that the 2D-LJCOVa.2 solid is perfectly brittle with no ductile tendencies at zero Kelvin, and to evaluate the critical fracture stress. The critical applied constant tensile stress of σ_c=2.1 was needed to initiate the brittle propagation of the cleavage crack in the 2D-LJCOVa.2 solid at absolute zero temperature. The simulations results are tabulated in Table III.4A1. The brittle propagation of the cleavage crack was very clean and symmetric, and the specimen was cleaved brittlely with no observable plastic deformations, as illustrated in Fig. III.4A1.

III.4A2. The temperature K_BT was 0.02 ε_o. The brittle propagation of the cleavage crack was initiated at the critical fracture stress of 1.90 at about ten percent below the zero temperature fracture stress. The simulations results are tabulated in Table III.4A2 and illustrated in Fig. III.4A2. The propagation of the

internal crack was brittle, but the symmetry observed in the zero-temperature simulations between the left hand side crack tip (LHSCT) and the right hand side crack tip (RHSCT) is broken due to the thermal fluctuations of the crack-tip atoms.

III.4A3. The temperature of the specimen for this run was also $K_BT=0.02\ \varepsilon_o$, but the system was slightly overloaded. The simulations results are tabulated in Table III.4A3, and demonstrated in Fig. III.4A3. Even though both III.4A2 and III.4A3 runs shared the identical temperature of $K_BT=0.02\ \varepsilon_o$ and history, the behavior of the crack in III.4A3 was quite different from that of III.4A2. While both crack-tips propagated brittlely in III.4A2 run, the RHSCT of III.4A3 immediately got blunted and a dislocation was emitted downwards which eventually moved to the lower horizontal surface of the specimen forming a step there. Meanwhile, the LHSCT of III.4A3 run propagated brittlely by breaking the crack-tip bonds sequentially. The variations in the behavior of III.4A2 and III.4A3 runs may be interpreted as the strain rate or overloading effect. The strain-rate effect will be investigated further and discussed in the following sections. It is interesting to note that the LHSCT in III.4A3 propagated twice faster than that of III.4A2 crack-tips. It is not very clear, at this point, that the increase in the LHSCT velocity in III.4A3 is due to the extra energy available to the crack-tip because of the overloading of the sample, or due to the change in the spatial configuration of the crack because of blunting of the RHSCT, or due to the fact that the fracture energy is shared by the two brittlely propagating crack-tips in III.4A2, while in the III.4A3 run since the LHSCT is arrested, the total fracture energy is available to the brittle propagation of the RHSCT.

However, the zero-temperature simulations reported in section II.3 showed no significant effect of the overloading and strain-rate on the magnitude of the terminal velocity of the brittlely propagating crack-tips. There is no reason to assume that the finite temperature behavior of the crack is different from those of the zero-temperature behavior in this aspect. Therefore, the first mechanism may be comfortably overruled. Furthermore, although the change in the physical configuration of the crack itself and the resulting sharper RHSCT may have some effect on the terminal velocity of the propagating crack-tip, however, this effect based on our observation in the process of the investigations of the crack-tip geometry reported in section II.2 is insignificant as long as the crack-tip is atomically sharp. Therefore, it seems that the latter mechanism may have the dominant effect. Because, the energy needed to move the emitted dislocation is much smaller than the energy needed to break an interatomic bond during the brittle propagation of the cleavage crack.

III.4A4. The temperature of the specimen was $K_BT=0.0462\ \varepsilon_o$ at the critical fracture stress of 1.90. The first LHSCT bond broke 338 steps after the applied load was increased to 1.90 from its previous value of 1.80. The simulations results are tabulated in Table III.4A4 and illustrated in Fig. III.4A4. The RHSCT did not show any activity (Fig. III.4A4A) till five LHSCT interatomic bonds cleaved and, eventually, was arrested and blunted (Fig. III.4A4B) due to the emission of a blunting dislocation upwards which finally moved to the upper horizontal surface of the sample forming a step there. Meanwhile, at step 13621, i.e., 621 steps after the applied load was increased to its critical value of 1.90, and 283 steps after the first LHSCT cleaved, the first RHSCT broke

brittlely. The consecutive breaking of the RHSCT continued afterward (Fig. III.4A4C). It is interesting to note that the LHSCT was arrested and inactive immediately after the emission of the blunting dislocation upward, till this dislocation moved to the upper surface of the specimen. Only after the specimen was slipped the LHSCT resumed its brittle propagation. But after three new LHSCT bonds were broken brittlely a new blunting dislocation was emitted upward and the LHSCT got arrested again. The run was terminated at this point. No dislocation activity was observed at the RHSCT-zone throughout the run. The behavior of the crack may still be interpreted as brittle. But, clearly, the thermal fluctuations of the crack-tip atoms have affected the behavior of the solid. Not only does the observed zero temperature symmetrical behavior of the LHSCT and RHSCT no longer exist in the higher finite temperature, but the thermally activated dislocation generation has also become a possibility at finite temperature. As illustrated in Fig. III.4A1, the zero-temperature 2D-LJCOVa.2 solid is perfectly brittle with no possibility of dislocation emission throughout the brittle propagation of the crack. The arrest of the LHSCT due to the emission of the thermally activated blunting dislocation, and the resumption of its brittle propagation after the emitted dislocation moved away from the crack-tip (to the surface of the solid) is very similar to the behavior of the zero-temperature 2D-Johnson solid. We may interpret the dislocation nucleation at the LHSCT after five CT bonds are broken as a sign that the activation energy of the dislocation generation is slightly higher than the value the initial temperature of the specimen could provide. Therefore, the adiabatic local crack-tip heating of the sample due to the dynamic propagation of the LHSCT is needed to provide it. It is also becoming clear that the very rigid and brittle zero-temperature 2D-

LJCOVa.2 is getting softer and relatively ductile as a direct result of raising the temperature of the system, a phenomenon regularly observed in nature.

III.4A5. The K_BT was 0.056 ε_o at the critical fracture stress of 1.80. The applied tensile load was increased from 1.70 to the fracture stress of 1.80 at step 12500. The simulations results are tabulated in Table III.4A5 and illustrated in Fig. III.4A5. The RHSCT almost immediately got blunted (Fig. III.4A5A), but no dislocation was generated at the crack-tip. Instead a micro-hole was nucleated at the lower row of the RHSCT between 8th and 9th rows (Fig. III.4A5B), which after five sequential breaking of the interatomic bonds between 8th and 9th rows emitted a blunting dislocation downward. The propagated micro-crack then got blunted, and immediately arrested afterward (Fig. III.4A5C). The emitted dislocation moved downward to the lower surface of the sample. Meanwhile, first LHSCT bond broke at step 12669; 169 steps after the applied load was increased to 1.80. The second LHSCT bond followed it by breaking at step 12703, but was rehealed later at step 12753. This bond broke again at step 12830. Then the LHSCT got blunted, and eventually emitted a dislocation downwards which moved to the lower surface of the sample. The blunted-arrested LHSCT was inactive after the dislocation nucleation. Even though the "plane" of the original crack-line was changed for the propagated RHSCT, we may interpret the behavior of the crack as brittle. Note that, clearly, the behavior of the fracture is gradually changing from the *perfectly brittle* to a *relatively brittle* fracture with the strong plastic deformations and tendencies for dislocation generation at the crack-tip. It is impossible to detect experimentally the change of the plane of the crack by one atomic space as well as detecting

breaking of only two crack-tip bonds before the dislocation nucleation at the crack-tip.

III.4A5*. An overloaded run with the applied tensile load of σ_a=1.90 > σ_c=1.80 and exact identical history of the III.4A5 run is available for this analysis. The initial behavior of the crack was identical to that of the III.4A5 run. But, the behavior of the fracture was different and more complicated as it developed. The simulations results are tabulated in Table III.4A5* and illustrated in Fig. III.4A5*. The RHSCT kept changing the plane (line) of its propagation. In 600 steps the crack-tip propagation plane was changed three times. The LHSCT got blunted and emitted a dislocation downwards after two CT bonds broke consecutively. The emitted dislocation eventually propagated to the lower boundary surface of the specimen, and produced a step there (Fig. III.4A5*C).

III.4A6. The temperature of the sample under the critical stress of 1.80 was K_BT=0.0600 ε_o. The applied load was increased from 1.70 to 1.80 at step 13500. The simulations results are tabulated in Table III.4A6 and illustrated in Fig. III.4A6. Both LHSCT and RHSCT bonds broke simultaneously (Fig. III.4A6A) at step 13548, probably due to the slight shock introduced to the system at the moment of increasing the applied load. However, the LHSCT interatomic bond was rehealed at step 13659, while the second RHSCT bond broke at this moment. Later, at step 13671, the new broken RHSCT bond rehealed, whereas, the first LHSCT bond broke again. At step 13751, 251 steps after the critical fracture stress of 1.80 was applied to the system, there were two LHSCT and two RHSCT broken bonds, and both crack-tips were struggling

to nucleate a dislocation. At step 13808, finally, the RHSCT succeeded in the emission of a blunting dislocation upward which eventually propagated to the upper horizontal boundary of the sample and produced a step there at step 13997. LHSCT also got blunted and nucleated a dislocation at its lower corner. This dislocation was unsuccessful in its attempts to break away from the LHSCT. It stuck around and eventually resulted in the nucleation of a micro-hole (Fig. III.4A6C) which propagated between the 7th and 8th rows and finally joined the blunted LHSCT (Fig. III.4A6D). The system seems to behave in a mixed brittle/ductile mode. Depending on the adopted definition of the ductility versus brittleness of the solid, the interpretation of the behavior of the solid may go either way. While macroscopically, the behavior of the fracture may be interpreted as ductile, here, since we have adopted the Rice-Thomson [46] mechanism, i.e., the emission of blunting dislocations from the crack-tip before breaking of the crack-tip bond, we may think of it as "semi-brittle". It is very clear that we are in the brittle-to-ductile transition temperature zone.

III.4A7. The specimen under the critical load of 1.80 is at the equilibrium temperature of $K_BT=0.0600\ \varepsilon_o$, like III.4A6 run. But the history of this particular run is at variance with that of III.4A6 run. The externally applied tensile load was increased from 1.70 to its critical value of 1.80 at step 11500. The simulations results are tabulated in Table III.4A7 and illustrated in Fig. III.4A7. At step 11878, both crack-tip bonds broke (Fig. III.4A7a). At step 12049, both crack tips were relatively sharp, and four LHSCT and two RHSCT bonds were already broken consecutively during the last 549 steps (Fig. III.4A7b). Starting at this time step both crack-tips struggled to generate a dislocation. They finally

succeeded in the emission of blunting dislocations downwards (Fig. III.4A7c) which eventually moved down to the lower surface of the specimen (Fig. III.4A7d). The behavior of the crack is therefore mixed, and may be interpreted to be in the brittle-to-ductile transition range.

Since the only difference between the III.4A6, and III.4A7 runs were their history of evolution we may therefore conclude that the loading history of the specimen has a definite effect on the behavior of the fracture, at least, in the sensitive zone of the brittle-to-ductile transition.

III.4A8. The sample under the critical tensile load of σ_c=1.80 was at K_BT=0.0628 ε_o. The externally applied load was increased from 1.70 to the critical value of 1.80 at time step 12000. The simulations results are tabulated in Table III.4A8 and illustrated in Fig. III.4A8. The LHSCT almost immediately showed a strong tendency to get blunted (Fig. III.4A8a). Before the LHSCT succeeded in the dislocation nucleation and got completely blunted, the first RHSCT bond broke at step 12158 (Fig. III.4A8b). Eventually, the LHSCT emitted a blunting dislocation downwards and got blunted (Fig. III.4A8c). The RHSCT, on the other hand, was sharp throughout and was propagating brittlely with no observable significant sign of plasticity in its vicinity. The emitted dislocation from the LHSCT was gliding downward during this time, and finally, ended up in moving to the lower horizontal surface of the specimen and causing a slip of one Burger's vector in the sample (Fig. III.4A8d). There were six RHSCT broken bonds at this point.

The LHSCT is perfectly ductile, while the RHSCT is clearly brittle. The brittleness of the RHSCT may be induced by the change in the spatial configuration of the crack. This behavior is similar to that of the overloaded sample at $K_BT=0.02\ \varepsilon_o$ observed earlier (Fig. III.4A3c).

III.4A9. The specimen under the critical load of $\sigma_c=1.80$ was at $K_BT=0.0625\ \varepsilon_o$, almost identical to those of III.4A8 runs. Yet, the loading history of these two runs were totally different.

The externally applied load was increased from 1.70 to 1.80 at the time step 14000. Both crack-tips were inactive for 650 steps. The simulations results are tabulated in Table III.4A9 and illustrated in Fig. III.4A9. Both crack-tip bonds broke at time step 14651 (Fig. III.4A9a). Then both crack-tips struggled to emit a blunting dislocation (Fig. III.4A9b). At step 14693, the second LHSCT bond broke. At step 14754, finally, the LHSCT succeeded in emitting a blunting dislocation downward, and the RHSCT got sharper as a result (Fig. III.4A9c). The emitted dislocation from the LHSCT glided to the lower horizontal boundary of the sample, resulting in the slip of the solid by one Burgers vector. While LHSCT was inactive during this period, the RHSCT, on the other hand, was propagating brittlely (Fig. III.4A9d).

III.4A10. The sample under the critical load of 1.8 was at the thermal equilibrium of $K_BT=0.075\ \varepsilon_o$. The applied load was increased from 1.70 to 1.80 at the time step 22000. The simulations results are tabulated in Table III.4A10 and illustrated in Fig. III.4A10. Both crack-tips, as illustrated in Fig. III.4A10a,

showed strong tendencies to emit a blunting dislocation downward and get blunted. The LHSCT first succeeded in the emission of a blunting dislocation downward (Fig. III.4A10b). The RHSCT lost its interest in the dislocation nucleation (probably as a result of the dislocation generation in the LHSCT and therefore the resultant change of the spatial configuration), resharpened but remained inactive (Fig. III.4A10b) for another 450 time steps. About 100 steps after the emitted dislocation from the LHSCT reached the lower surface and produced a step there, the brittle propagation of the RHSCT was initiated. After four RHSCT broke consecutively between the time step 22639 and 22803, the RHSCT struggled to emit a blunting dislocation downward which finally succeeded in doing so at step 22938. This dislocation moved to the lower surface. The RHSCT is blunted at this point, but a bond at the LHSCT between 8th and 9th rows broke and few more LHSCT interatomic bonds followed it between 8th and 9th rows (Fig. III.4A10d). By the time step 23500, the RHSCT has emitted four blunting dislocations, which three of them have already moved to the lower horizontal surface of the sample.

The fracture has definitely shown the atomistic characteristics of ductile behavior (Fig. III.4A10d). Therefore, the fracture is perfectly ductile at the equilibrium temperature of $K_BT_C=0.075\ \varepsilon_o$. Hence, if we assume the melting point temperature is sample-size independent and $K_BT_M\approx0.33\ \varepsilon_o$, then we may conclude that the system is ductile at $T_C\approx0.25T_M$.

Note that the critical applied fracture load was constant between $K_BT=.056\ \varepsilon_o$ and $K_BT_C=.075\ \varepsilon_o$, and we did not observe any sharp increase in

the fracture stress reported in the literature (St. John [54], Haasen et. al. [39, 60, 62], Hirsch et. al. [8-11], Michot et. al. [66, 181-183]). Note also that practically all of the experiments reported are those of the specimen under variable applied load, and none of these reported experimental observations have reported a tensile dead weight (constant stress) mode of loading. The brittle-to-ductile transition in this simulation is apparently gradual (soft) as opposed to all experimentally reported investigations of the BDT temperature in Si which have been all very sharp.

The adopted definition for the BDT temperature by experimentalists is that the fracture stress rises at the transition temperature from that of the cleavage stress to the yield stress. All of the reported experiments insist on the sharpness of the transition point. Therefore, even if the "transition" was sharp in terms of its macroscopic definitions there is always a chance that we would miss this "very narrow zone" in the temperature, because as stated earlier, the finite temperature runs are extremely expensive and the search for the BDT temperature had to be discrete and limited. We did not see any significant increase in the fracture stress, and unless that we missed this sharp (step-function type) increase in the applied load, we may conclude that the BDT is soft in terms of the macroscopic definition of the brittle-to-ductile transition.

III.4B Series. ***Major Simulations Results***

Sample size effect was studied by increasing the sample size by factor of four. The III.4B series of BDT studies were performed on a two-dimensional triangular array of 2296 atoms arranged in 39 rows (Fig. III.4B1). Simulations results are summarized in Table III.4B.

III.4B1. The loading history of this run is summarized in the Table III.4B1. The equilibrium temperature of the specimen under the critical load of σ_a=2.40 was K_BT=0.0193 ε_o with MSTFL=1.87X10^{-4}.

The temperature was introduced to the defect-free perfect sample by randomly displacing atoms from their absolute zero temperature equilibrium positions. The specimen was scaled in both dimensions according to the proper linear coefficient of expansion. The system was then allowed to relax for 5000 time steps. Then the crack was introduced to the heated system and another 1500 steps were given to it to reach to a reasonable thermal equilibrium. The system was at the equilibrium temperature of K_BT=0.0219 ε_o, with MSTFL=2.22X10^{-4}, at time step 6000. At step 6500, the externally applied load of σ_a=0.25 was applied to the atoms of the uppermost and lowermost rows of the sample. The system was scaled uniformly in the vertical direction according to the corresponding Young's modulus. Another 500 steps was given to the pre-cracked loaded system to relax. Then, the externally applied load was increased in increments of 0.25 every 201 steps up to σ_a=1.50. From this point on up to σ_a=1.80, the applied tensile load was increased by 0.10 every 201

steps. Note that at the moment of every increase in the applied load, for the purpose of the considerable saving in the computation time, the vertical scaling of the atomic positions also took place. At the time step 8000, the external load was σ_a=1.80, the temperature of the system was K_BT=0.0201 ε_o, with MSTFL of 2.13X10^{-4}. This increase in the applied load was followed by another series of the incremental increase of 0.10 every 300 steps. At the time step 10600, the applied load had reached to its critical value of σ_c=2.40, where, the equilibrium temperature was K_BT=0.0193 ε_o with MSTFL=1.87X10^{-4}.

The first RHSCT broke at 10816. This was followed by non-symmetric sequential breakage of the left and right hand side crack-tip interatomic bonds. At step 11087, there were four LHSCT and seven RHSCT brittlely broken interatomic bonds. Both crack-tips were sharp throughout (Fig. III.4B1b). At time step 11100 both crack-tips were struggling to nucleate dislocations. The LHSCT gave up this struggle and the 5th LHSCT bond broke at this point, but the RHSCT was already arrested and its struggle to emit a dislocation seemed succeeding. At time step 11263 the RHSCT, finally, succeeded in the emission of a blunting dislocation downwards (Fig. III.4B1c), which was eventually propagated down to the lower horizontal surface of the sample, causing the specimen to slip by one Burger's vector (Fig. III.4B1e). At this point, there were nine broken LHSCT interatomic bonds, and the LHSCT was sharp (Fig. III.4B1c). A second dislocation was emitted at time step 11400 from the already blunted RHSCT, but this time upward. There were 13 broken LHSCT interatomic bonds at this time step. Fig. III.4B1d, clearly, demonstrates the effect of the emission of blunting dislocations from the crack-tip. The RHSCT

was arrested and blunted for about 500 time steps while the LHSCT was completely sharp throughout and there were 18 broken LHSCT interatomic bonds at this point. Both emitted dislocations moved to the horizontal boundaries of the specimen and produced the configuration demonstrated in Fig. III.4B1e. There are 23 cleaved LHSCT interatomic bonds at this point.

Therefore, we may conclude that the fracture is relatively brittle at $K_BT=0.0193\ \varepsilon_o$. Heating up the sample brakes the observed absolute zero temperature symmetry in the behavior of the left and right hand crack-tips, and softens the solid. A considerable plastic deformation is induced, and multiple thermally activated dislocation are nucleated at the RHSCT.

The effect of the emission of blunting dislocation on the arrest of the brittlely propagating RHSCT is very similar to the arrest of propagating cleavage cracks in the two-dimensional Johnson solid at zero-temperature. The detailed studies, reported in the earlier sections, showed that the emitted dislocation actually reduces the crack-tip stress intensity level by a large factor by shielding the crack-tip from the influence of the remotely applied load. We also demonstrated that the arrested crack remains inactive up to the point where the emitted dislocation is far enough from the crack-tip or moved to the surface of the sample in order for the crack-tip stress intensity to increase to the cohesive strength of the interatomic bonds for the breakage of any bond in the solid.

Note also that the crack-tip velocity unlike the absolute zero temperature

simulations is very irregular from the very beginning of the initiation of the brittlely propagating cleavage crack, jumping up and down and never saturating to a constant terminal value. This is partially due to the thermal fluctuations of the crack-tip atoms, and partially due to the interactions between the emitted dislocations and the crack-tips. Note that the emitted dislocations are in motion, and their distance from the crack-tip, and therefore the interacting force with the crack-tips are continuously changing.

III.4B2. The pre-cracked sample under the critical fracture stress of σ_c=2.20 was at the equilibrium temperature of K_BT=.068 ε_o with RHSCT = $0.9X10^{-4}$.

The defect-free perfect sample of III.4B1 run at K_BT=0.0219 ε_o was reheated at time step 5000 by randomly displacing its constituent atoms from their new equilibrium position with a given amplitude. Then the specimen was allowed to relax for 2000 time steps. At time step 7000 the temperature of the system was K_BT=0.0760 ε_o with MSTFL of $2.43X10^{-4}$. At this point the centrally located internal crack of fourteen initial broken bonds was introduced to the solid, and the specimen was given sufficient time to reach to its new equilibrium state. Afterward, the externally applied load was increased gradually: first at the increments of 0.25 up to σ_a =1.50, followed by the incremental increase of 0.1 every few hundred steps. At step 9400, the critical fracture stress was 2.20. The equilibrium temperature of the specimen was K_BT=0.068 ε_o at this point.

The simulations results are tabulated in Table III.4B2 and illustrated in Fig. III.4B2. The first RHSCT interatomic bond broke at time step 9456, just 56

steps after the critical load was attained. At time step 9481, the first LHSCT bond broke, and the LHSCT showed a strong tendency to emit a dislocation upward. Note that due to the geometry of the crack-tip, and the slip system of the two-dimensional triangular solid, if a dislocation is to be emitted upward, the first crack-tip interatomic bond must necessarily be broken. There were two broken RHSCT interatomic bonds at this step (Fig. III.4B2a). The LHSCT finally succeeded in the emission of a blunting dislocation upward. The LHSCT got blunted as a result (Fig. III.4B2b), and remained arrested afterward throughout the simulations. On the other hand, the RHSCT propagated brittlely. After four consecutive breaking of the crack-tip interatomic bonds, the RHSCT got blunted and nucleated a blunting dislocation at its lower corner (Fig. III.4B2c). But the emitted dislocation on its way down nucleated a micro-hole which was unable to propagate brittlely and it too got blunted and emitted a dislocation downwards (Fig. III.4B2d). From this point on, both crack-tips and the nucleated-blunted micro-hole were inactive. The emitted dislocations were gradually moving towards the horizontal loaded surfaces of the specimen, where, the simulations was terminated at time step 10000.

The LHSCT is perfectly ductile. The only broken LHSCT interatomic bond was necessary for the emission of a dislocation upward. This is dictated by the spatial crack-tip configuration and the slip system in this two-dimensional solid. Even though the RHSCT also finally got blunted and the fracture is certainly due to the dislocation emission, the four broken RHSCT interatomic bonds prior to the dislocation emission and crack-tip blunting makes it difficult to interpret the behavior of the fracture. These broken bonds could be a direct

result of the broken-symmetry and the configuration change in the crack-tip geometry due to blunting-effect of the LHSCT. We may therefore interpret the fracture behavior being in the brittle-to-ductile transition zone.

III.4B3. The simulations results are tabulated in Table III.4B3 and illustrated in Fig. III.4B3. The defect-free perfect sample at $K_BT=0.0219\ \varepsilon_o$ was heated up by randomly displacing its new equilibrium atomic positions by a given amplitude. The specimen was expanded on both dimensions according to the coefficient of expansion. The system was allowed to relax for 2000 time steps. At the time step 7000 the average equilibrium temperature of the system was $K_BT=0.103\ \varepsilon_o$ with MSTFL=$3.62X10^{-4}$. At time step 7000 the centrally located internal crack of half-crack length $c_o=3.75d$ was introduced to the system. Starting at time step 7100, the applied load was increased by 0.25 every 151 time steps up to $\sigma_a=1.50$, where the increments of the increase in the external load changed to 0.1. At time step 8305 the applied load was increased to the critical fracture tensile load of $\sigma_c=2.00$. The equilibrium average temperature of the specimen was $K_BT=0.0904\ \varepsilon_o$ with MSTFL=$7.3X10^{-4}$ at time step 8400. Both crack-tips showed strong tendencies to generate dislocations. The LHSCT succeeded first by emitting a blunting dislocation upwards and naturally breaking one bond at its crack tip due to the configurational necessity at time step 8621 (Fig. III.4B3a). At this point the first RHSCT bond also broke. At time step 8649 the second RHSCT bond broke. At time step 8674 the LHSCT is completely blunted, and the emitted dislocation is gradually gliding away from the CT toward the upper loaded horizontal boundary of the specimen. The RHSCT, on the other hand, stopped and started a relatively long struggle to nucleate a

dislocation. This struggle finally resulted in blunting the RHSCT and the generated dislocation, up to the end of the run, was unable to move away from the crack-tip and was stuck to the upper corner of the RHSCT (Fig. III.4B3b).

The LHSCT is perfectly ductile at $K_BT=.09\ \varepsilon_o$ and $\sigma_c=2.00$. The RHSCT is definitely more ductile than III.4B2 run. There were only two broken RHSCT bonds prior to the dislocation nucleation at the crack-tip here, while there were four broken RHSCT bonds in III.4B2. But unlike III.4B2 run, the generated dislocation at the RHSCT in III.4B3 stuck to the crack-tip and was unable to separate itself from the tip for about 350 steps. Note that the critical fracture stress here is about ten percent lower than that of III.4B2 run.

The fracture behavior is clearly not brittle, but we may not be able to characterize it as perfectly ductile because of the particular behavior of the RHSCT. Therefore, we may interpret the fracture to be in the brittle-to-ductile transition zone.

III.4B3*. The history of the evolution of this run was identical to that of III.4B3 runs, except that, prior to initiation of any observable activities at the crack-tips, the applied load was increased from 2.00 to $\sigma_a=2.10$ at time step 8456. Therefore the system is *overloaded* by five percent. The temperature of the system was $K_BT=0.0892\ \varepsilon_o$ with $MSTFL=2.23X10^{-4}$ at time step 8500. The simulations results are tabulated in Table III.4B3* and illustrated in Fig. III.4B3*. Surprisingly, even though the specimen was overloaded by five percent no significant activity was observed till time step 8618 where the first RHSCT

interatomic bond broke (Fig. III.4B3*a). Few steps later at time step 8631 the first LHSCT interatomic bond broke and the CT immediately showed a very strong tendency to nucleate a dislocation. At time step 8646 the second RHSCT bond broke. At time step 8677 the generated dislocation at the LHSCT finally was able to separate itself from the crack-tip and glide upward. During this period the RHSCT had already started a struggle to emit a dislocation upward. The third RHSCT bond broke at time step 8689, but the generated dislocation at the upper corner of the RHSCT had stuck to it up to time step 8850 where the third broken RHSCT bond was rehealed (Fig. III.4B3*c). At time step 8863 the RHSCT initiated a new struggle to emit a dislocation downwards. The RHSCT formed a peculiar shape at 8901 (Fig. III.4B3*d). While the nucleated dislocation at the upper corner of the RHSCT was still stuck to it, the generated dislocation at the lower corner of the RHSCT separated itself from the crack-tip at step 8962 and gradually moved downwards. At the final step of 9000 both crack-tips were blunted and the emitted dislocation from the LHSCT continued its voyage toward the upper horizontal loaded surface of the specimen. During this time the generated dislocation at the lower corner of the RHSCT was gliding downwards toward the lower horizontal surface of the sample (Fig. III.4B3*e).

Probably the most interesting aspect of this overloaded sample is the generation of the blunting dislocation at the lower corner of RHSCT. This is most likely due to the extra energy available to the system because of overloading. It is not clear however, why with the extra energy available to the system because of overloading of the sample, the nucleated dislocation at the

upper corner of the RHSCT was still unable to break away from the attractive force of the crack-tip.

Similar to III.4B3 run we may conclude that the fracture is in the brittle-to-ductile transition zone.

III.4B4. The pre-cracked loaded sample of III.4B2 at $K_BT=0.075\ \varepsilon_o$ and subjected to the applied constant tensile load of $\sigma_a=1.50$, was heated up by randomly displacing the equilibrium atomic positions of its constituent atoms by a small given amplitude. The system was then allowed to relax to the temperature of $K_BT=0.110\ \varepsilon_o$ with MSTFL of $2.06X10^{-4}$ up to time step 9000. At time step 9038, the applied load was increased to 1.70. This was followed by another increase in the applied load at time step 9323, where it was increased to the critical fracture stress of 1.80. Note that every increase in the applied load was accompanied by the vertical scaling of the atomic positions. The equilibrium temperature of the sample, subjected to the critical fracture of 1.80, was $K_BT=0.105\ \varepsilon_o$ with $MSTFL=1.22X10^{-4}$. The simulations results are tabulated in Table III.4B4 and illustrated in Fig. III.4B4. Both crack-tips showed very strong tendencies to nucleate dislocations (Fig. III.4B4a). While a blunting dislocation was generated at the lower corner of the already blunted LHSCT at step 9618, the RHSCT gave up its struggle to nucleate a dislocation, and was resharpened again (Fig. III.4B4b). At time step 9851 the generated dislocation at the lower corner of the LHSCT finally separated itself from the attractive influence of the crack-tip and started gliding downwards towards the lower horizontal loaded surface of the specimen. Fig. III.4B4c demonstrates the

system at time step 10000 where the LHSCT is completely blunted and the generated dislocation continues its glide towards the lower horizontal loaded surface of the specimen. On the other hand the RHSCT did not show any significant activity during this period for about 700 time steps (Fig. III.4B4b-d).

Since the LHSCT got blunted and emitted a blunting dislocation which was able to move away from the attractive influence of the crack-tip and, on the other hand since the RHSCT was almost inactive throughout the run, we may therefore conclude that the fracture is perfectly ductile according to the atomistic definition of ductility [46].

III.5. *Brittle-to-Ductile Transition Temperature; Conclusions*

Based on the simulations results reported in the preceding section, and considering the reported experimental observations and the theoretical understandings of the brittle-to-ductile transition temperature reviewed earlier in the introduction, we may conclude that

i. If it is assumed that the melting point temperature T_M is not sample-size dependent, we may conclude that BDT is gradual and sample-size dependent in the covalently modified two-dimensional triangular Lennard-Jones solid with a*=0.2, LJCOVa.2. For the larger sample of 64x39 BDTT is $T_C \approx 0.35T_M$ and for the smaller sample size of 32x19 it is $T_C \approx 0.25T_M$. The magnitude of the BDT temperature is in accord with the experimental observations. But practically all of the experimental observations on the pre-cracked dislocation-free Si have agreed on the sharpness of the brittle-to-ductile transition temperature. The differences between the simulations results and the laboratory observations will be investigated further, below.

ii. The externally applied critical fracture stress decreases by increasing the equilibrium temperature of the system, and finally saturates to $\sigma_c=1.80$ well below the critical stress to initiate the brittle propagation of the cleavage crack at absolute zero temperature, i.e., $\sigma_c=2.40$ for the large sample-size of 64x39 and $\sigma_c=2.20$ for the small-size sample of 32x19.

iii. At the applied critical fracture stress of $\sigma_c=1.80$ and $T_C \approx 0.35T_M$ for the large

sample and $T_C \approx 0.25T_M$ for the small sample, the first blunting dislocation is emitted from the crack-tip before any crack-tip bond is broken. Note that while the BDT temperature is apparently sample size-dependent, the critical applied stress for the emission of the blunting dislocation, i.e., initiation of the ductile fracture is identical for both of the investigated samples and therefore is not sample size dependent.

iv. Ductility of the fracture at the atomistic level is recognized by the emission of the first blunting dislocation from the crack-tip prior to the breakage of any crack-tip bond.

v. There was a significantly large range of temperature (about $0.10T_M$) where it was difficult to interpret the behavior of the fracture to be either brittle or ductile. Therefore, we may conclude that the brittle-to-ductile transition in the pre-cracked dislocation-free 2D-LJCOVa.2 is very soft and gradual.

vi. Contrary to the experimentally observed sharp brittle-to-ductile transition in the pre-cleaved dislocation-free single-crystal Si [9, 11, 45, 54, 60, 181], the simulations results indicate that the BDT in the two-dimensional triangular covalently bonded Lennard-Jones solid with $a^*=0.2$, LJCOVa.2, is very gradual (soft). The interpretation of the simulations results, and the direct comparisons of them with those of the laboratory observations are complicated due to the following facts:

- Experimentally with the available technology it is impossible to create a completely dislocation-free dislocation-source-free legitimate laboratory-size specimen. Therefore, the experimentally observed dislocations are indistinguishable between the ones emitted from the crack-tip, the preexisting dislocations which are attracted to the crack-tip, and dislocations which are emitted by various dislocation sources in the specimen [8-11, 60]. Any claim that the observed dislocations in the fracture experiments are definitely those emitted from the crack-tip due to the thermal fluctuations of the atoms in the immediate vicinity of the crack-tip is baseless.

- The brittle-to-ductile transition is, unfortunately, very much dependent on the adopted definition of the BDT. St. John [54], Michot et. al. [61, 66, 94, 181-183], Haasen et. al. [39, 47, 60, 62], and Hirsch et. al. [8-11, 95-96, 101] have adopted the definition which is expressed clearly by Hirsch and Roberts [11] as "Fig. III.1B shows the variation of failure stress with temperature for a typical strain in the Oxford experiments. Below T_C the fracture is entirely brittle and fracture stress is independent of temperature; it is controlled through the Griffith criterion by the low temperature critical stress intensity factor for brittle fracture, K_{IC}. Above T_C the whole specimen deforms plastically and behaves in a ductile manner, at a stress determined by the upper yield stress. At T_C there is a jump in the stress intensity factor at failure K_{IF} from K_{IC}, the low-temperature critical stress intensity factor, to a higher value the maximum of which is limited by the upper yield stress. The jump takes

place in a temperature range of a few degrees, and in this transition region the fracture is essentially brittle, but occurs at values of $K_{IF}>>K_{IC}$. Similar behavior is observed in the experiments of Michot [63, 66] and of Brede and Haasen [60]" [11]. This is just a macroscopic definition and ignores completely the question of the dislocation nucleation at the crack-tip prior to breakage of the crack-tip interatomic bonds.

Two theories have been formulated to interpret the brittle-to-ductile transition. Hirsch et. al. [8] predicts that dislocations observed in the etch pits studies are emitted from the discrete sources along the crack front which in turn shield the crack. They ignore the blunting of the crack, and their criterion for the brittle-to-ductile transition is that the local shielded stress intensity factor, K_{IE}, must be less than the critical stress intensity factor for the brittle fracture, K_{IC}, everywhere along the crack front for all values of the applied stress intensity factor, K_I, up to the value at which macroscopic yield takes place. Hirsch et. al. [8, 11] then developed a dynamic crack-tip shielding model which predicts that the sharp transitions are obtained *only* if the crack-tip dislocation sources are nucleated at values of K_{IO} *just below* K_{IC}. These sources sending out avalanches of dislocations which shield the whole crack-tip very quickly, reduce the local shielded stress intensity factor, and therefore produce an extremely sharp transition in Si. Hirsch et. al. [8, 11] identified the movement of existing dislocations in the crystal to the crack-tip where they transform into dislocation sources as the mechanism of the nucleation of these sources at K_{IO}. This mechanism is obviously inapplicable to the present computer simulations where

the initial sample is totally dislocation-free and source-free. Hirsch et. al. [8] predicted that "the operation of the Rice-Thomson mechanism should result in a soft transition" [8], and that "if the nucleation of dislocations by Rice-Thomson mechanism becomes spontaneous at K_I - K_{IC}, its effects are unlikely to be observable in the present experiments..." [8]. Samuels and Roberts [45] have recognized that "owing to the inherently poor resolution of the etching technique one cannot distinguish between dislocation emission from the crack-tip or near-tip sources" [45]. Therefore, if Hirsch et. al. [8] are correct in their prediction that "the nature of the brittle-ductile transition in Si is sharp because no significant generation takes place at the crack-tip until crack-tip sources are generated at K_{IO} just below K_{IC} ..." [8], then our simulations results in the 2D-LJCOVa.2 pre-cracked dislocation-free dislocation-source-free solid is in complete agreement with the predictions of Hirsch et. al. [8, 11].

The second theory in an attempt to explain the brittle-to-ductile transition temperature in the pre-cleaved Si was developed by Haasen and his coworkers [39, 60]. Haasen's criterion for the BDT is that at T_C as the applied stress is increased, the maximum tensile stress at the crack-tip σ_y passes through a maximum value which is just less than E/10, where E is modulus of elasticity of the solid. E/10 is the predicted approximate value of the cohesive strength of the solid. Brede and Haasen in their 1988 paper [60] suggested that "at high temperatures, dislocations are generated at an applied stress intensity lower than the critical stress intensity for inducing cleavage in the dislocation-free samples at room temperature. As a consequence of this, the plastic zone which develops around the crack-tip is saturated before the tensile stress at the

crack-tip reaches the cohesive stress. Because of saturation of the plastic zone, the brittle-to-ductile transition temperature is determined by the velocity at which dislocations move outward from the crack-tip at low shear stress existing in the vicinity of the shielded crack" [60]. They further argued that "because of the change of the dislocation distribution in the plastic zone with the applied stress intensity, the critical situation exists only at a certain applied stress intensity. This leads to the extremely sharp transitions which were found in the experiments" [60].

In their experiments Brede and Haasen increased the applied stress at a given rate (Hirsch et. al. [8] also did so) till the specimen fractured completely. On the other hand, in the present simulations, the externally applied critical (fracture) stress σ_c is the *minimum* applied constant load necessary for either the initiation of the brittle propagation of the cleavage crack, or to cause the emission of the first blunting dislocation from the crack-tip prior to breakage of any crack-tip interatomic bond. Therefore, the critical fracture stress σ_c in the present simulations is not equivalent to the "fracture stress" of Haasen's experiments [39, 60] or experiments of Hirsch et. al. [8-11] which was the applied stress necessary for the fracture of the specimen. Our MD simulations is in complete agreement with Brede and Haasen's [60] predictions that at high temperatures, dislocations are generated at the applied stress intensity which must be lower than the critical stress intensity for inducing cleavage in the dislocation-free samples at low temperatures.

On the other hand, neither the etch pitting experiments of the Oxford group, nor the Sirt-etched SEM micrography technique of the Gotlinge group, nor the Transmission Electron Microscopy (TEM) technique used by Ohr [184] in situ observations of the plastic deformations occurring at the crack-tips under stress, nor the High Voltage Electron Microscopy (HVEM; E>1Mev), nor the X-ray Topography (XRT) [185-186] used by Michot and George [181] are capable of detecting the *first* blunting dislocation emitted from the crack-tip. Therefore, all of experimental criterion for the recognition of BDT have been other than Rice-Thomson criterion of the emission of the first blunting dislocation from the crack-tip prior to the breakage of any crack-tip interatomic bonds.

We have shown that the thermally activated dislocation emission from the crack-tip in the 2D-LJCOVa.2 solid under the externally applied load is possible (Fig. III.4A & III.4B series). Once emitted, these dislocations move rapidly away from the crack-tip region towards the loaded boundary surfaces of the specimen, creating a dislocation-free zone (DFZ). The emission of the thermally activated dislocations from the crack-tip occurs at an applied stress (load) which is lower than the critical applied (Griffith) stress necessary for the initiation of the brittle propagation of the cleavage crack at low temperatures. Once a dislocation is emitted from the crack-tip, the crack-tip gets blunted (Fig. III.4A5-10, III.4B2-4) and the stress intensity factor at the crack-tip is lowered to a value well below the cohesive force of the crystal. Therefore the crack-tip is shielded from the influence of the remotely applied stress by the emitted dislocations. The blunted-arrested crack-tip remains inactive for a considerable length of time until the generated dislocation moves away from the crack-tip

zone or is absorbed back to the tip. Earlier we showed that at absolute zero temperature the crack-tip stress intensity is lowered immediately after the emission of the blunting dislocation from the crack-tip. It gradually increases as the emitted dislocation glides away from the crack-tip zone toward the loaded surfaces of the specimen, up to its maximum value (corresponding to the cohesive stress of the crystal) where a new crack-tip bond breaks. The generation of the blunting dislocations at the crack-tip is only a necessary condition for the brittle-to-ductile transition. The sufficient condition, as pointed out by Brede and Haasen [60], is that these nucleated dislocations must glide away sufficiently quickly from the crack-tip zone to relax the local crack-tip stress before any cleavage occurs (compare Fig. III.4B3b and III.4B3*b-e). The simulations results indicate that if these nucleated dislocations do not attain sufficient velocity to break away, they are often absorbed back to the arrested-blunted crack-tip. If such an event takes place, the crack-tip gets sharper, resumes its activity and may propagate brittlely.

Simulations results clearly demonstrate that any dislocation nucleation at the crack tip results in the immediate arrest of the crack. The crack-tip remains arrested and inactive up to the point which the emitted dislocation glides sufficiently far away from the crack-tip, or is absorbed back to the tip. This argument holds for both static and dynamic crack-tips, and it is independent of temperature, sample-size, or loading scheme (Fig. III.4B1, III.4B2, III.4A7b-c, III.4A9b-d, III.4A10).

Robb Thomson in his 1986 review of Physics of Fracture [51] argued that "The crucial question of whether a material will be capable of sustaining a brittle crack stably in a cleavage mode, without blunting the tip and arresting the bond-braking process, will be determined by the emission of dislocations at the tip rather than by absorption of externally generated dislocations. The reason is that the externally generated dislocations must collide with the tip in order to blunt it, which is an unlikely event, whereas dislocations emitted from the crack blunt the tip by definition". On the other hand, Hirsch et. al. [9] suggested that "silicon presents an extreme example of the effect of existing dislocations on the BDT, where the crack is sharp and the density of existing dislocations is so low that new sources have to be nucleated at or close to the crack-tip, before screening takes place by the emission of avalanches of dislocations" [9]. Hirsch and Roberts [11] furthermore argued that "the sharp transition arises from the need to nucleate a high density of the crack-tip sources which emit dislocations which rapidly shield the crack-tip. Sources are thought to be nucleated either by existing dislocations distant from the crack-tip moving to the crack-tip, or by dislocations emitted from a few preferential sites along the crack-tip moving along the crack-tip. The nucleation stage controls T_C, which is structure sensitive,..." [11].

However, while the present computer simulations results are in accord with the necessary and sufficient conditions for the brittle-to-ductile transition suggested by Thomson et. al. [46, 51, 64, 187] and Haasen [39, 60] in a dislocation-free specimen, it is impossible for us at this stage to evaluate the importance of the external sources suggested by Hirsch, which may halt a

cleavage crack, because we simply do not have such sources in our defect-free specimen. Therefore, even though the argument of Robb Thomson [51] seems logical, since his suggested mechanism as well as Haasen's [39, 60] model for the brittle-to-ductile transition does not count for the shape of the BDT, and since the observed brittle-to-ductile transition is gradual (soft) in the present simulations in agreement with the predictions of Hirsch [8], while all of experimentally reported BDT were extremely sharp, we could not reject Hirsch's model [8, 11]. It remains for the further computer simulations, either to simulate a 3D Si using an appropriate interatomic potential law which is fitted to all of thermo-mechanical properties of Si in a defect-free pre-cleaved Si specimen, or to introduce preexisting dislocations or dislocation sources in the present 2D-LJCOVa.2 solid for example by the "warm pre-stressing" effect, to evaluate the importance of the existing dislocations or its sources in the shape of the brittle-to-ductile transition in silicon.

III.6. *Simulations Results for the "Corrected" Covalently Modified Two-Dimensional Triangular Lennard-Jones Solid with a*=0.2, COR.LJCOVa.2*

The goal of the present simulations is to model the general fracture phenomena rather than to make predictions for the behavior of a particular crystal. In this regard, the details of the interatomic potential law is not significant. Towards the end of the investigations it was discovered that in the construction of the covalent potential (eq. II.1.4-5) used in the calculations of the computer simulations of III.4A and III.4B series θ_o was replaced with 60 degrees, i.e., the original angle between r_{ij} and r_{ik} in the perfect defect-free unstrained specimen at absolute zero temperature. There is no question that this choice is true for the near neighbors, but when the system is plastically distorted, particularly when a dislocation is nucleated and the second neighbors come into the interaction range of few atoms, θ_o is no longer 60 degrees. Therefore Φ_{ijk} and hence the interatomic potential U for these new interacting atoms in the following equations must be treated in a different manner from those of the first neighbors.

$$U= (1/2) \sum'_{ij} \Phi(r_{ij}) + (1/6) \sum'_{ijk} [\Phi_{ijk}+\Phi_{jki}+\Phi_{kij}] \qquad \text{II.1.4}$$

where,

$$\Phi_{ijk} = \Phi(r_{ij})\Phi(r_{ik}) [2a^* (Cos\theta_{ijk} - Cos\theta_o)] \qquad \text{II.1.5}$$

where θ_{ijk} is the angle between r_{ij} and r_{ik} and a^* is the amplitude of the angular resistance.

After the recognition of the inconsistencies in the calculations, the problem was corrected by taking θ_o to be the original angle between r_{ij} and r_{ik} regardless of the fact that interacting atoms are first or second neighbors. Therefore θ_os were calculated and stored. This, of course, increased the cost of the runs. A new set of simulations were originated using the new corrected interatomic potentials. Note that the mechanical properties of both solids, i.e., the old 2D-LJCOVa.2 and the new COR.LJCOVa.2 solids are identical in the temperature range of interest, i.e., as long as the interatomic interactions are between the original near neighbors.

Simulations results for these series are summarized in the following section. The sample-size and the initial internal crack were identical to those of the III.4B runs, i.e., similar to the III.4B series a sample consisted of a two-dimensional triangular arrays of 2296 atoms arranged in 39 rows, and a centrally located internal crack of 14 broken bonds was used in these simulations.

Note that at the moment of the heating up of the system, for the purpose of considerable savings in the computation time and cost, the specimen is always scaled in both dimensions according to the appropriate coefficient of linear expansion. Every increase in the applied load is also accompanied by the vertical scaling of the positions of the constituent atoms according to the corresponding Young's modulus.

III.6A1. The heating, loading, and the process of the introduction of the internal crack to the system was identical to those of III.4B1 runs, except that the increase in the applied load was more gradual in the present run. At step 10000, the applied load at the horizontal boundaries of the system was increased from 2.20 to the critical fracture tensile stress of σ_c=2.30 necessary for the initiation of the brittle propagation of the cleavage crack in this system. The equilibrium temperature of this critically loaded sample is K_BT=0.0193 ε_o with MSTFL of $1.16X10^{-4}$. The simulations results are tabulated in Table III.6A1 and illustrated in Fig. III.6A1. The first LHSCT interatomic bond broke at time step 10543. Later on at time step 10599 the first RHSCT interatomic bond broke (Fig. III.6A1b). The propagation was very brittle and nearly symmetrical. At time step 11083 (Fig. III.6A1c) there were 12 new broken interatomic bonds at each crack-tip. At time step 11500 (Fig. III.6A1d) there were 25 new broken LHSCT interatomic bonds, and 26 new broken RHSCT bonds. There is an attempt to emit a dislocation at step 11500, but it does not blunt the crack-tip. It could be a result of sample-size effect, because both crack-tips are very close to the vertical boundaries of the specimen at this point (Fig. III.6A1d).

We may conclude that the 2D-COR.LJCOVa.2 solid at the equilibrium temperature of K_BT=0.0193 ε_o, and the critical applied constant tensile load of σ_c=2.30 is perfectly brittle. Comparison of the simulations results of III.4B1 and III.6A1 leads us to the conclusion that the 2D-COR.LJCOVa.2 solid is more brittle than the 2D-LJCOVa.2 solid.

III.6A2. The pre-cracked pre-loaded sample of III.6A1 run at $K_BT=0.02\ \varepsilon_o$ and $\sigma_a=1.80$ was heated up by randomly displacing its constituent atoms from their new equilibrium positions with the amplitude ch=0.08 at the time step 8000. The system was then allowed to relax in time. At time step 10000 the specimen under the critical load of $\sigma_c=2.10$ was at the equilibrium temperature of $K_BT=0.0634\ \varepsilon_o$ with MSTFL=$1.16X10^{-4}$. The simulations results are tabulated in Table III.6A2 and illustrated in Fig. III.6A2. The brittle propagation of the internal crack was initiated by breaking of the first LHSCT interatomic bond at time step 10645. The second LHSCT interatomic bond broke at step 10697, while even though the first RHSCT bond was stretched significantly it has not broken yet (Fig. III.6A2a). At time step 10869 the third LHSCT interatomic bond and the first RHSCT interatomic bond broke simultaneously. Both crack-tips propagated by the sequential breaking of the interatomic bonds along the initial crack-line (Table III.6A2). There was no observable plasticity anywhere in the solid during the brittle propagation of the cleavage crack. Fig. III.6A2c represents the cleaved specimen at 11159 where there are nine new LHSCT and seven new RHSCT interatomic broken bonds. Later, the moving crack-tips showed a tendency to emit dislocations. This struggle resulted in the nucleation of dislocations at the crack-tips which up to the end of the run were unable to separate themselves from the attractive influence of the crack and were stuck to the crack-tip. As predicted by Brede and Haasen [39, 60] these disable dislocations finally were absorbed back to the crack-tips, and the crack continued its brittle propagation by the sequential breaking of the interatomic bonds. At the final stage of the run, at time step 11500, there were 17 broken LHSCT and 14 broken RHSCT interatomic bonds.

We may conclude that the pre-cracked c_o=3.75d critically loaded σ_c=2.10 2D-COR.LJCOVa.2 solid is relatively brittle at the equilibrium temperature of K_BT=0.0625 ε_o. There is a considerable plastic deformations at the running crack-tips, but the nucleated dislocations at the crack-tips were unable to glide away from the crack-tips and were eventually absorbed back to crack and the brittle propagation of the crack-tips continued.

III.6A.2*. Since the III.4B2 run had not shown any activity at σ_c=2.10 up to the time step 10500, the applied load was increased to σ_c=2.20 at this step. But later on III.6A2 pre-cracked specimen cleaved at 2.10. Therefore III.6A2* run is *overloaded* by five percent and we may investigate the effect of the overloading by analyzing its simulations results.

The pre-cracked specimen under the applied load of 2.20 was at the equilibrium temperature of K_BT=0.062 ε_o. The simulations results are tabulated in Table III.6A2* and illustrated in Fig. III.6A2*. The first LHSCT interatomic bond broke at time step 10568, the next one followed it at time step 10686. On the other hand, the first RHSCT interatomic bond broke at time step 10728 (Fig. III.6A2*a). Both crack-tips were propagating brittlely by the consecutive breaking of the interatomic bonds at the crack-tips along the initial crack-line up to time step 10949, where both crack-tips showed very strong tendencies to get blunted and to nucleate a dislocation. At time step 11000, both crack-tips were sufficiently blunted, but the generated dislocations were unable to move away from the crack-tips. There were five new broken interatomic crack-tip bonds at each tip at time step 11000 (Fig. III.6A2*b).

We may conclude that the pre-cracked c_o=3.75d specimen at K_BT=0.0620 ε_o is relatively brittle under the applied load of 2.20 which is about five percent higher than the critical stress for the initiation of the brittle propagation of an internal crack of this size in this solid (Fig. III.6A2). Compared to the III.6A2 series, the plastic deformations in the immediate vicinity of the running crack-tips started earlier here. Similar to III.6A2 runs, the nucleated dislocations were unable to separate themselves from the attractive influence of the crack-tips, but both crack-tips were considerably deformed and blunted in this overloaded run. Apparently the higher strain rate or *overloading* has induced ductility.

III.6A3. The III.6A2 pre-cracked sample c_o=3.75d under the externally applied constant load of σ_a=1.80 and at the equilibrium temperature of K_BT=0.065 ε_o was heated up by the random displacements of its constituent atoms from their present equilibrium positions by a relatively small amplitude of ch=0.03. The equilibrium temperature of the system was K_BT=0.0700 ε_o at time step 11000. The applied load was then increased by 0.10 every 500 time steps.

The simulations results are tabulated in Table III.6A3 and illustrated in Fig. III.6A3. The applied load was increased from 2.00 to the critical load of σ_c=2.10 at time step 12500. Both crack-tips responded to this increase in the applied load almost immediately by showing strong tendencies to get blunted and emit a blunting dislocation at time step 12562 (Fig. III.6A3a_1). Both crack-tips were completely blunted by the time step 12708 as demonstrated in Fig. III.6A3b_1, but the nucleated dislocations at the crack-tips were stuck to the

lower lips of both crack-tips. These nucleated dislocations never succeeded to break away from the crack-tips, and finally, as predicted by Brede and Haasen [60, 62], were absorbed back to the crack-tip and resharpened both of them (Fig. III.6A3c_1). Since the resharpened crack-tips did not show any further activities, the applied load was increased to 2.15 at step 13000. Surprisingly, this increase in the applied load was completely useless and both crack-tips were totally inactive for 500 time steps and were very sharp at time step 13500 (Fig. III.6A3a_2).

The applied load was then increased from 2.15 to σ_c=2.20 at time step 14000. The crack-tips responded to this increase in the externally applied load by breaking the first LHSCT interatomic bond at step 14054 (Fig. III.6A3a_3). The first RHSCT bond broke at time step 14122. The brittle propagation of the crack was continued by the sequential breaking of the interatomic crack-tip bonds along the initial crack-line. At time step 14377 there were five new LHSCT and three new RHSCT broken interatomic bonds and even though the RHSCT was still relatively sharp, the LHSCT was relatively blunted and was struggling to nucleate a dislocation (Fig. III.6A3b_3). The nucleated dislocation at the blunted LHSCT was unable to move away from the tip and resulted in the creation of a micro-hole at the upper lips of the already blunted LHSCT (Fig. III.6A3c_3). At the time step 14500 where the run was terminated, the LHSCT was still blunted and inactive and the created micro-hole had stuck to its upper lips, and there were four newly broken RHSCT interatomic bonds and the tip was getting blunted (Fig. III.6A3d_3).

We may conclude that the pre-cleaved c_0=3.75d specimen under the applied load of σ_c=2.20 and at the equilibrium temperature of 0.0678 ε_o is relatively brittle. Clearly, by raising the temperature of the specimen, plastic deformation in the immediate vicinity of crack-tips is increased significantly. The generated dislocations at the crack-tips are unable to break away from them.

By comparing the simulations results of this run with those of III.4B2, it is interesting to note that

1. While the critical load for the initiation of the brittle propagation of the crack at K_BT=0.063 ε_o was 2.10 for III.4B2 runs, the applied load of σ_c=2.20 was needed to start the brittle propagation of the crack in III.6A3.

2. The thermally generated dislocations at the crack-tips do not get enough energy to glide away from the blunted crack. They are either absorbed back to the crack-tip (Fig. III.6A3b_3), or resulted in the creation of a micro-hole in the immediate vicinity of the already blunted crack-tip (Fig. III.6A3d_3).

III.6A4. The III.6A2 solid under the constant applied load of σ_a=1.80 and the equilibrium temperature of K_BT=0.065 ε_o was heated up by randomly displacing its constituent atoms from their equilibrium positions by the relatively small amplitude of ch=0.05 at time step 9000. The system was allowed to relax to the equilibrium temperature of K_BT=0.0808 ε_o with MSTFL of $2.55X10^{-4}$. The

simulations results are tabulated in Table III.6A4 and illustrated in Fig. III.6A4. The external load was first increased to 1.90 at time step 11500 and later to the critical stress of σ_c=2.00 at time step 11900. The system immediately responded to this increase in the applied load by breaking the first RHSCT interatomic bond which was rehealed at time step 11997. The crack did not show any particular activity up to time step 12200. The equilibrium temperature of the critically loaded pre-cleaved system was K_BT=0.0790 ε_o with MSTFL of $1.08X10^{-4}$. At time step 12200, while the RHSCT was showing a tendency to get blunted and nucleate a dislocation, the first LHSCT interatomic bond broke (Fig. III.6A4a). As demonstrated in Fig. III.6A4b the LHSCT propagated brittlely by consecutively breaking three interatomic bonds along the original crack-line up to time step 12487, but the nucleated dislocation at the RHSCT was unable to move away from the crack-tip and finally resulted in the creation of a micro-crack at the lower lips of the blunted RHSCT. The LHSCT kept propagating brittlely. By time step 12737, there were six new broken LHSCT interatomic bonds, where, the crack tip started to get blunted and nucleate a dislocation at its upper lips which resulted in a complete blunting and arresting of the LHSCT. Similar to the generated dislocation at the RHSCT, the nucleated dislocation at the LHSCT was also unable to move away from the crack-tip and resulted in the creation of a micro-hole at the upper corner of the arrested and blunted LHSCT. Both micro-holes had started propagating brittlely by the time the run was terminated.

Since the RHSCT was arrested and finally blunted by the nucleation of a blunting dislocation while six LHSCT interatomic bonds cleaved along the

original crack-line, we may conclude that the pre-cleaved c_o=3.75d specimen under the critical fracture stress of σ_c=2.0 and the equilibrium temperature of K_BT=0.0790 ε_o is relatively brittle and may be in the brittle-to-ductile transition zone. The increase in the temperature of the specimen has increased the plastic deformations in the immediate vicinity of the crack-tips. Unlike the nucleated dislocations in the III.4B runs, the generated dislocations in III.6A4 are unable to separate themselves from the attractive influence of the crack-tip. Eventually as a direct result of this immobility a self propagating micro-hole is produced in the immediate vicinity of the blunted-arrested crack-tip. Note the dramatic reduction of the critical fracture stress from 2.20 at K_BT=0.0675 ε_o (III.6A3 run) to 2.00 at K_BT=0.0790 ε_o.

III.6A5. The III.6A4 pre-cracked c_o=3.75d pre-loaded σ_a=1.90 specimen at the equilibrium temperature of K_BT=0.080 ε_o was heated up to the new equilibrium temperature of K_BT=0.0868 ε_o by the random displacements of its constituent atoms from their new equilibrium positions by the relatively small amplitude of ch=0.03 at time step 11900. The externally applied load at the horizontal boundaries of the solid was increased to 1.95 at time step 12500. Since no activity was observed at any of the crack-tips for 500 time steps, the applied load was increased to the critical fracture stress of σ_c=2.00 at time step 13000. The internal crack did not show any significant activity for 700 time steps. The simulations results are tabulated in Table III.6A5 and illustrated in Fig. III.6A5. The first LHSCT interatomic bond broke at time step 13700 as illustrated in Fig. III.6A5a. The struggle for the dislocation nucleation at time step 13767 at the upper lips of the LHSCT (Fig. III.6A5b) was aborted by time step 13900, and the

blunted-arrested LHSCT was resharpened. While the arrested LHSCT was inactive for a few hundred time steps, the RHSCT was propagating brittlely by the sequential breaking of the interatomic bonds along the original crack-line. At time step 13938 there were one broken LHSCT and two broken RHSCT interatomic bonds (Fig. III.6A5c). At this point the RHSCT staged a struggle to nucleate a dislocation downwards, but the nucleated dislocation was unable to break away from the attracted influence of the blunted-arrested RHSCT and eventually resulted in the creation of a micro-hole in the lower corner of the RHSCT. The nucleated micro-hole also got blunted and emitted a dislocation upward which surprisingly was able to glide away from the crack-tip (Fig. III.6A5d). Meanwhile the resharpened LHSCT propagated brittlely by the sequential breaking of the crack-tip interatomic bonds along the crack-line. By time step 14284 there were eight newly broken LHSCT interatomic bonds (Fig. III.6A5d). Fig. III.6A5e demonstrates the last step of this run. Note that both crack-tips as well as the generated hole are blunted, and the emitted dislocation from the blunted micro-hole is moving upwards toward the loaded horizontal surface of the specimen.

We may conclude that the pre-cleaved c_o=3.75d 2D-COR.LJCOVa.2 solid at the equilibrium temperature of K_BT=0.0857 ε_o under the externally applied critical load of σ_c=2.00 is in the brittle-to-ductile transition zone.

III.6A6. The equilibrium temperature of the pre-cracked c_o=3.75d specimen under the applied load of σ_a=1.80 was K_BT=0.107 ε_o with MSTFL=1.91X10^{-4} at time step 10000. The crack-tips responded to the heating of the old sample

immediately by competition between the struggle to break the interatomic crack-tip bond, re-healing it, and dislocation nucleation at the crack-tip. By time step 10000 the crack had attained back its initial configuration where it was decided to increase the applied load to 1.85. Surprisingly the crack did not show any reaction to this increase in the applied load for 500 time steps. The applied load was increased to 1.90 at time step 10500. The internal crack did not respond to this increase in the applied load either. Hence the externally applied load at the horizontal boundaries of the solid was increased to its critical value of 1.95 at time step 11000. The simulations results are tabulated in Table III.6A6 and illustrated in Fig. III.6A6. The equilibrium temperature of the critically loaded pre-cracked specimen was $K_BT=0.104\ \varepsilon_o$ with MSTFL=$1.24X10^{-4}$. The LHSCT got blunted and nucleated a dislocation at its lower lips (Fig. III.6A6a). The generated dislocation was unable to break away from the crack-tip and was finally absorbed back to the crack-tip and resulted in the resharpening of the LHSCT. The first LHSCT bond broke at time step 12012 (Fig. III.6A6b). Meanwhile the RHSCT got blunted and generated a dislocation at its upper lips which was unable to move away from the crack-tip either and resulted in the creation of a micro-hole at the upper lips of the RHSCT (Fig. III.6A6b). The process of the dislocation nucleation and the creation of a micro hole in the immediate vicinity of the blunted-arrested crack-tip as a result of the inability of the generated dislocation to break away from the crack tip, was repeated many times at both crack tips and as illustrated in Fig. III.6A6c the fracture took very complex and peculiar form as a result.

We may conclude that pre-cracked $c_o=3.75d$ critically loaded $\sigma_c=1.95$

2D-COR.LJCOVa.2 solid at the equilibrium temperature of $K_BT=0.104\ \varepsilon_o$ is in the brittle-to-ductile transition zone. As demonstrated in Fig. III.6A6c the fracture is not brittle. On the other hand, it is not perfectly ductile either, because the nucleated dislocations are unable to glide away from the crack tip and result in the creation of multi-micro-holes in the immediate vicinity of the crack-tips. The specimen is fractured by the process of multiple creations of blunting micro-holes.

III.6A7-III.6A9. The temperature of these runs are $0.12\ \varepsilon_o < K_BT < 0.17\ \varepsilon_o$ at the critical load. All of these runs are in trouble due to the loss of various atoms of the loaded horizontal surfaces of the sample. These losses are equivalent to the pealing off of the loaded surface atoms of laboratory specimen at high temperatures. The reason for this behavior is the relatively large-amplitude fluctuations of these loaded surface atoms. Even though we tried to repair the specimen by putting the lost atoms back to their proper positions, eventually, another loaded surface atom was lost after a while. The loss of these loaded surface atoms are very serious and may alter the behavior of the fracture significantly, because their loss is equivalent to the local unloading of the system. This would alter the local configuration and eventually may affect the behavior of the fracture.

Another problem which these high temperature runs face is the inability of the generated dislocations to glide away from the crack-tip. After the nucleation of these dislocations, the crack-tip gets blunted. But since none of these generated dislocations are able to move away from the crack-tip, either

they are absorbed back to the crack-tip and resharpen it, or they result in the creation of a micro-hole in the immediate vicinity of the crack-tip. The fracture then propagates with the multiple micro-hole growth mechanism.

The critical applied load is about twenty percent lower than the critical (Griffith) stress to initiate the brittle propagation of the internal cleavage crack at low temperatures.

Simulations results are reviewed briefly below:

III.6A7. The equilibrium temperature of the pre-cracked c_o=3.75d specimen was K_BT=0.120 ε_o at the externally applied load of σ_a=1.90. Even though the crack-tips showed a strong tendency to propagate brittlely at σ_a=1.70, the two LHSCT and one RHSCT broken bonds by time step 10441 (Fig. III.6A7a) were rehealed later on by time step 12000 where the applied load was increased to 1.80. Both crack-tips were inactive afterwards but as illustrated in Fig. III.6A7c a loaded atom at the upper horizontal surface of the specimen was getting pealed off. Since both crack-tips had not shown any significant activity for about 800 steps, we went back to time step 12500 and increased the applied load from 1.80 to 1.90. The crack-tips did not respond for this increase in the applied load either, but the same troubled loaded upper horizontal surface atom created problems again after about 200 time steps. The crack-tips were still sharp at time step 12845, where it was decided to terminate the run because all attempts to correct the trouble at the upper horizontal loaded surface of the sample failed.

III.6A8. This is the best high temperature run and we may get sufficient simulations data to interpret the behavior of the fracture. The system was obtained by heating up of a pre-cracked sample c_o=3.75d under the applied load of σ_a=1.60 at time step 12000. Even though a lower corner atom was lost, it was repaired later and the system accepted this repair. Since the crack did not show any significant activity, the applied load was increased to 1.70 at step 13000 and later on to 1.80 at time step 13501.

The simulations results are tabulated in Table III.6A8 and illustrated in Fig. III.6A8. The equilibrium temperature of the pre-cracked specimen c_o=3.75d under the applied critical load of 1.80 was K_BT=0.136 ε_o with MSTFL=2.7X10^{-4}. The first RHSCT interatomic bond broke at time step 13716 (Fig. III.6A8a). At time step 13767 the second RHSCT bond broke (Fig. III.6A8b). Both crack-tips were getting blunted and the LHSCT had already nucleated a dislocation at its lower lips (Fig. III.6A8b). By time step 13839 as illustrated in Fig. III.6A8c, the second broken RHSCT bond was rehealed and the RHSCT was resharpened, but the nucleated dislocation at the LHSCT was unable to move away from the crack-tip and resulted in the nucleation of a micro-hole in the immediate vicinity of the LHSCT. By the time step 14313 both crack-tips were completely blunted and as demonstrated in Fig. III.6A8f, the RHSCT also nucleated a dislocation downwards, but the created hole in the vicinity of the LHSCT was attracted back to the crack-tip and was stuck to its lower lips. The generated dislocation at the lower corner of the RHSCT, too, was unable to move away from the crack-tip and resulted in the generation of a micro hole at the lower lips of the RHSCT (Fig. III.6A8g). Note that both crack-tips are completely blunted. By

time step 14468, the nucleated dislocation at the lower corner of the LHSCT was absorbed back to the crack-tip (Fig. III.6A8h). By time step 14577 as illustrated in Fig. III.6A8i, the LHSCT attempted to emit another dislocation downwards. By time step 14641, both crack-tips were completely blunted and arrested, and the emitted dislocation from the lower corner of the LHSCT was gliding away from the crack-tip. On the other hand, the nucleated dislocation at the lower corner of the RHSCT resulted in the creation of a micro-hole in the vicinity of the crack-tip. At this point few loaded atoms at the upper horizontal surface of the specimen started to get in trouble. The generated micro-hole at the lower corner of the LHSCT got blunted by time step 14849 and as illustrated in Fig. III.6A8j emitted a dislocation down wards which eventually broke away from the blunted hole and glided downwards towards the lower loaded horizontal boundary of the specimen. From this point on, the trouble with the few disturbed atoms at the upper horizontal surface of the specimen was uncontrollable, and the simulations results were therefore unreliable. Hence, the simulations were terminated.

Even though there were uncontrollable trouble with a few loaded atoms at the upper surface of the specimen, since this disturbance had started late enough, the simulations results up to step 14849 (Fig. III.6A8j) is certainly reliable. Therefore, based on the behavior of the crack-tips discussed above, we may conclude that the fracture is ductile, and the crack grows by a complex process of blunting, dislocation emission, and nucleation of micro-holes.

III.6A9. The pre-cracked sample c_o=3.75d under the externally applied load of σ_a=1.60 was at K_BT=0.170 ε_o at time step 13500. The RHSCT got blunted and emitted a dislocation upwards, but before a reasonable thermal equilibrium was achieved few of the loaded atoms at the upper horizontal surface of the solid were lost (Fig. III.6A9a). The surface of the specimen was then repaired, and the run was continued. The repair of the specimen cooled down the system to the temperature of K_BT=0.165 ε_o. The emitted dislocation shown in Fig. III.6A9a was absorbed back to the crack-tip a few hundred steps later. After about 1000 steps, the first RHSCT interatomic bond broke at step 14700 (Fig. III.6A9b) which was rehealed by time step 14881 (Fig. III.6A9c). As demonstrated in Fig. III.6A9d, the RHSCT got blunted by time step 14953 and the generated dislocation produced a micro-hole at the lower corner of the RHSCT, which was absorbed back to the crack-tip by time step 15036 (Fig. III.6A9e). The blunted RHSCT nucleated another dislocation downwards at time step 15060 (Fig. III.6A9f). This dislocation, too, got absorbed back to the crack tip and by time step 15452 the RHSCT was resharpened again, but as demonstrated in (Fig. III.6A9g), the LHSCT attempted to emit a dislocation downwards at this step. Later on, due to the uncontrollable troubles with the few loaded atoms at the upper surface of the specimen (Fig. III.6A9h) and our inability to overcome them, the run was terminated.

Even though simulations results are insufficient, based on the behavior of the crack-tips, since there were multiple generation of dislocations at the crack-tips although none of these dislocations were able to move away from the crack-tips, and since none of the crack-tip bonds broke brittlely, we may

conclude that the system is completely ductile at $K_BT=.165\ \varepsilon_o$. Probably the critical load is slightly higher than 1.60, but due to the uncontrollable troubles given by a few atoms at the upper loaded surface of the specimen and worsening of it at still higher applied loads, we were unable to raise the applied load further.

III.7. *Simulations Results of the Investigation of the Brittle-to-Ductile Transition Temperature of the Pre-Cleaved Two-Dimensional Triangular Johnson Solid*

Our first attempt to study the brittle-to-ductile transition temperature was performed on a 2D-triangular Johnson solid. The criterion used for the recognition of ductility was that of the emission of blunting dislocations from the crack-tip prior to the breakage of any crack-tip interatomic bonds. In these simulations the generated dislocations were unable to glide away from the blunted crack-tips and eventually resulted in the nucleation of multiple micro-holes in the immediate vicinity of the crack-tips which propagated and finally joined the original crack. Therefore, it was difficult to interpret the simulations results based on the adopted criterion for the recognition of ductility of the fracture, and we decided to use the 2D-LJCOVa.2 solid instead (III.4A & B runs). Even though the simulations data is not detailed enough to pinpoint the brittle-to-ductile transition temperature in the pre-cracked critically loaded 2D-Johnson solid, due to the similarity of the behavior of III.6A runs (2D-COR.LJCOVa.2 solid) with those of III.7A (2D-Johnson crystal) it is instructive to review the results of these investigations. Note that, here the equilibrium temperature of the system is given in Kelvin.

III.7A1. A sample of size 36x19 was chosen for the present simulations. The simulations were performed at absolute zero temperature. The critical applied load of σ_c=2.40 was needed for the emission of the first blunting dislocation from the tip of a narrow internal crack of c_o=3.75d. As clearly demonstrated in

figure III.7A1, the emitted dislocations gradually glide away from the crack-tips towards the lower horizontal loaded surface of the solid, creating a step there. The 2D-triangular Johnson solid of relatively small size is therefore ductile at absolute zero temperature.

III.7B1. To study BDT temperature a solid is needed which is perfectly brittle at least at absolute zero temperature. The 2D-triangular Johnson solid is in the vicinity of brittle-to-ductile behavior and its conduct is sample-size dependent. Larger the sample-size, the more brittle the system would be. A relatively large sample of 64x39 was therefore chosen for the present simulations.

The equilibrium temperature of the system was 294 Kelvin with MSTFL of 1.6×10^{-4} at the externally applied critical load of σ_c=2.50. As illustrated in figure III.7B1a, the LHSCT got blunted first and tried to emit a blunting dislocation at time step 3190. Later on at time step 3240, the RHSCT too got blunted and nucleated a blunting dislocation at its lower corner (Fig. III.7B1b). As demonstrated in figures III.7B1c-f, both crack-tips were blunted-arrested from this point on. But, generated dislocations were unable to glide away from the already blunted crack-tips and finally resulted in the creation of two micro-holes in the immediate vicinity of the crack. These micro-holes propagated and eventually joined the blunted-arrested original crack.

Even though the nucleated blunting dislocations at both crack-tips were unable to move away from the crack, but since the original crack was blunted and arrested for a considerable amount of time and never propagated, we may

therefore consider the fracture of the ductile type.

III.7C Series. To make sure that the observed behavior in III.7B1 was not an artifact of the sample size, a larger sample of 68x79 containing an initial internal crack of c_o=3.75d was chosen for this series of finite non-zero temperature fracture simulations.

III.7C1. The system was at the equilibrium temperature of 0 K at time step 2000 when the externally applied load was increased to the critical load of σ_c=3.37. Simulations results are illustrated in figure III.7C1. The initial crack propagated brittlely by the sequential breaking of crack-tip bonds. At time step 2640, after nine LHSCT and nine RHSCT bonds broke sequentially, both crack-tips got blunted by the emission of a pair of blunting dislocations. The blunted crack-tips were arrested for a substantial amount of time (Fig. III.7C1d).

The pre-cracked c_o=3.75d, critically loaded σ_c=3.37, 2D-Johnson solid of 68x79 sample size is therefore brittle at 0 K.

III.7C2. The system under the externally applied critical load of σ_c=2.80 was at the equilibrium temperature of 109 K at time step 10000. The LHSCT got blunted by time step 10500, and as demonstrated in figure III.7C2a, tried to nucleated a blunting dislocation at its upper corner. By time step 11059 the LHSCT was completely blunted, but the RHSCT was still sharp (Fig. III.7C2b). Two RHSCT bonds were broken by time step 11059, but as illustrated in figure III.7C2b-c, the nucleated dislocation at the upper corner of the LHSCT was

unable to move away from the crack-tip and as a result a micro-hole was opened at the upper corner of the LHSCT. This micro-hole propagated and finally joined the original crack, creating a complex configuration (Fig. III.7C2d). After four new RHSCT bonds were sequentially broken it, too, got blunted and similar to the LHSCT, its tendency to generate a blunting dislocation at its upper corner was unsuccessful and resulted in the generation of a propagating micro-hole at its immediate vicinity which finally joined the original crack (Fig. III.7C2d).

The 2D-triangular Johnson solid containing an initial internal crack of c_o=3.75d and under the externally applied critical load of σ_c=2.80, therefore fractures in a complex manner at 110 K, and we may conclude that the system is in the brittle-to-ductile transition zone.

III.7C3. The pre-cracked c_o=3.75d sample is at the equilibrium temperature of 296 K under the externally applied critical load of σ_c=2.60 at time step 11000. Both crack-tips got blunted by time step 11500 as illustrated in figure III.7C3a. The blunted crack-tips remained arrested for the rest of the run, and as demonstrated in figure III.7C3b-d all attempts by both crack-tips to nucleate a blunting dislocation failed, and as a result multiple micro-holes were produced in the immediate vicinity of the already blunted-arrested crack-tips. Later on, these generated micro-holes got blunted themselves, and produced further generations of micro-holes.

Based on the simulations data reviewed briefly, we may conclude that the pre-cracked c_o=3.75d critically loaded σ_c=2.60 2D-Johnson solid of 68x79 sample size is at the brittle-to-ductile transition zone at the equilibrium temperature of 296 K.

It is very instructive to compare the illustrations of figure III.7C3 and those of figure III.6A6. The similarity between the behavior of the 2D-triangular COR.LJCOVa.2 solid at K_BT=0.104 ε_o and those of the 2D-triangular Johnson solid at 296 K is amazing. In both cases, the system failed in a complex manner. None of the nucleated dislocations at the crack-tip were able to move away from the crack, and eventually multiple micro-holes were opened in the immediate vicinity of the crack which later on grew and finally joined the blunted-arrested original crack.

Probably, the activation energy to nucleate a blunting dislocation at the crack-tip of both of these systems are higher than those which could be provided by the thermal energy of the system. We may also argue that the reason for this particular behavior is due to the inability of these solids to support dislocation. The later argument, at least for the case of the 2D-triangular Johnson solid at 0 K, is not valid, because as clearly demonstrated in figure II.2.13 and III.7A1 the 2D-triangular Johnson solid may support dislocations at least at absolute zero.

III.7C4. The sample under the externally applied critical load of σ_c=2.30 is at the equilibrium temperature of 404 K with MSTFL of 9.5×10^{-4} at time step 8000. As

illustrated in figure III.7C4a the RHSCT is blunted by step 8402, while the LHSCT is still sharp. Later on, by time step 8974 as demonstrated in figure III.7C4b, the LHSCT also got blunted. Similar to the III.7C3 series, blunted crack-tips remained arrested for the rest of the run and all attempts to nucleate a blunting dislocation at both crack-tips failed, and as a result of this failure multiple micro-holes were created in the immediate vicinity of the crack-tips. As illustrated in figure III.7C4c-f, the generated micro-holes also got blunted and produced further generations of micro-holes. The behavior of the fracture resembles those of III.6A6&8 series.

Even though none of the nucleated dislocations at the crack-tips were able to move away from the crack and the solid failed eventually by the process of micro-hole growth, but since the initial crack is blunted and remained arrested for more than 1000 time steps, we may conclude that the system is ductile at 404 K. The only significant difference between III.7C3 and III.7C4 is the ten percent reduction in the critical stress, i.e., from σ_c=2.60 at 296 K to σ_c=2.30 at 404 K. Similar reduction in the magnitude of the fracture stress was observed between III.6A6 and III.6A8 series, i.e., from σ_c=1.95 at K_BT=0.104 ε_o to σ_c=1.80 at K_BT=0.136 ε_o.

III.7C4*. Since the sample at 404 K under the externally applied critical load of σ_c=2.30 had not shown any observable activity by time step 8000, the applied load was increased to σ_a=2.40. Therefore the system is overloaded by about five percent and we may study the overloading effect by comparing simulations results of III.7C4 and III.7C4*. By time step 8421 as illustrated in figure

III.7C4*a&b, two crack-tip bonds were broken brittlely at each crack-tips. By time step 8666, the LHSCT got blunted and attempted to emit a blunting dislocation upwards (Fig. III.7C4*c), but this struggle was unsuccessful and resulted in the creation of a micro-hole at the upper corner of the LHSCT (Fig. III.7C4*c-e). On the other hand, the RHSCT remained sharp throughout the run and propagated brittlely. By time step 8846, there were 12 newly broken RHSCT bonds.

By comparing figures III.7C4 and III.7C4*, we may conclude that *overloading* has caused the *embrittlement* of the system. Note that overloading induces ductility in the pre-cleaved 2D-triangular LJCOVa.2 solid as well as 2D-COR.LJCOVa.2 (compare Fig. III.6A2-3, III.4B3-3*, and III.4A2-3).

III.8. *Brittle-to-Ductile Transition Temperature; Summary*

Because of the rather very long and bulky volume of the simulations results discussed in detail in the previous sections, it is constructive to summarize the most significant aspects of them. Simulations data are tabulated in a summary format in Table III.4B, III.5-9.

First, the effect of increasing of the equilibrium temperature of the system on the behavior of the internal crack, on the magnitude of the externally applied critical fracture stress, and on the fracture and related properties of the solid will be outlined. Then, the brittle-to-ductile transition temperature of the simulated solids will be discussed briefly, and similarities and differences between them will be high-lighted.

III.8A. Increasing the equilibrium temperature of the system has the following effects

i. The externally applied critical fracture stress σ_c decreases and finally saturates to a constant value as the equilibrium temperature of the system is increased.

ii. As the equilibrium temperature of the system is increased, plastic deformations at the crack-tip zone are increased gradually. After a certain point the crack-tip gets blunted and possibly arrested by emitting a blunting dislocation, provided that the thermal energy is higher than the activation

energy for the generation of dislocations in the crystal. Immediately after the emission of the blunting dislocation, the crack-tip gets blunted and remains arrested afterwards up to a point where the emitted dislocation gets sufficiently far away from the crack-tip zone. If the nucleated dislocation is unable to separate itself sufficiently fast enough from the attractive influence of the crack and can not glide away from the crack-tip zone, it is eventually absorbed back to the blunted crack-tip and resharpens it (see Fig. III.4A9-10; III.4B3*c, III.6A3b_1-c_1, III.6A5b-c, III.6A6a-b). The resharpened crack-tip may resume its brittle propagation. Sometimes the generated dislocation at the crack-tip, neither moves away from the crack-tip, nor is absorbed back to it. As a result, a micro-hole is generated in the immediate vicinity of the blunted-arrested crack-tip. Eventually, the nucleated micro-hole may either propagate itself and finally join the original crack (see Fig. III.4A5-6, III.6A4-5, III.7C2), or gets blunted and possibly produces further generations of micro-holes. The solid may therefore fractures by the complicated process of hole-growth (Fig. III.6A6&8, III.7C3-4). If the original internal crack remains blunted-arrested throughout the major part of the run, even though the solid fails by the process of multiple micro-hole generation instead of the emission of blunting dislocations from the crack-tip, we may consider the fracture to be ductile (Fig. III.6A6&8, III.7C3-4).

iii. While due to the spatial symmetry of the system, the behavior of both crack-tips are necessarily identical at absolute zero temperature (Table III.4A1), increasing the equilibrium temperature of the solid breaks this symmetry. At higher temperatures, crack-tips develop almost independent from each other,

except for the fact that activities in one of the crack-tips may influence and alter the behavior of the other. The emission of a blunting dislocation from one of the crack-tips may alter the spatial configuration of the crack, and may resharpen the other crack-tip (see Fig. III.4A3C, III.4A8, III.6A5-6). The resharpened crack-tip may resume its brittle propagation (Fig. III.4A9-10).

iv. At absolute zero temperature, the crack-tip velocity increases smoothly and finally saturates to a maximum constant value V_T (Fig. II.3.5-9). As the equilibrium temperature of the system is increased, the crack-tip velocity (if any) becomes very irregular, jumping up and down without showing any sign of saturation to a single stable value (Table III.4A2-4, III.4B1, III.6A1,2,2*,3). The reason for this particular behavior is the thermal vibration of the crack-tip atoms. It may be also due to the increasing plastic deformations at the crack-tip zone as the equilibrium temperature of the system is increased.

v. At finite non-zero temperatures, the loading history of the system has a profound effect on the behavior of the crack (see Fig. III.4A6-9).

vi. At finite non-zero temperatures, overloading of the system may induce ductility in the 2D-triangular LJCOVa.2 (Fig. III.4A2&3, III.4A5&5*, and III.4B3&3*) and the 2D-triangular COR.LJCOVa.2 solids (III.6A2&2*), while it induces brittleness in the 2D-triangular Johnson solid (III.7C4&4*).

III.8B1. *BDTT in the 2D-triangular LJCOVa.2 solids*

The necessary and sufficient condition for the ductile behavior of the fracture at the atomic level is the emission of the first blunting dislocation from the crack-tip prior to breakage of any crack-tip interatomic bonds. The simulations results are tabulated in a summary format in Table III.8-9 and briefly reviewed below

i. Ductile-to-brittle transition in the pre-cracked c_o=3.75d, critically loaded 2D-triangular LJCOVa.2 solid is gradual (soft). The system is in the BDT zone where the fracture is neither perfectly brittle nor completely ductile for considerably wide range of temperatures (Table III.8&9)

$.056\varepsilon_o \leq$ BDTT $\leq .0628\varepsilon_o$	sample size: 32x19	(Fig. III.4A5-8)
$.068\varepsilon_o \leq$ BDTT $\leq .0904\varepsilon_o$	sample size: 64x39	(Fig. III.4B2-3)

Note that the upper and lower limits for the BDTT are not absolute, and the brittle-to-ductile transition zone is probably much wider than the reported one. This is due to the fact that the finite temperature simulations are quite expensive and economically we are restricted to simulate only a limited number of temperatures. Besides, the aim of the present simulations was not that of pin-pointing of the exact range of the BDTT.

ii. The BDTT is sample size dependent.

iii. As the equilibrium temperature of the system is increased the externally

applied critical fracture stress σ_c is decreased and eventually saturated to 1.80, well below the zero temperature critical stress of σ_c=2.40 for the larger sample and σ_c=2.20 for the smaller one.

$$\sigma_{c,BDTT} = 1.80 \qquad \text{Sample: 32x19}$$

$$2.20 \geq \sigma_{c,BDTT} \geq 1.80 \qquad \text{Sample: 64x39}$$

Note that we did not observe any sharp increase in the externally applied critical fracture stress at BDTT. It was either missed due to the fact that the simulations were performed on a finite number of temperatures, or this is another indication of the fact that the brittle-to-ductile transition in this solid is gradual. Because, macroscopically the sharp increase in the fracture stress is a characteristic of the sharp BDT.

iv. The small sample of size 32x19 is perfectly ductile at $K_BT=.075\varepsilon_o\approx.23T_M$ (Fig. III.4A10), and the larger sample of size 64x39 is completely ductile at $K_BT=.105\varepsilon_o\approx.32T_M$ (Fig. III.4B4).

III.8B2. *BDTT in the 2D-triangular COR.LJCOVa.2 solids*

The simulations results are summarized in Table III.6,8&9. The thermally generated dislocations at the crack-tip in this crystal are unable to move away from the attractive influence of the crack, and eventually a micro-hole is nucleated in the immediate vicinity of the blunted-arrested crack-tip which itself may get blunted and produce further generations of micro-holes. Therefore, if under the externally applied critical load none of the crack-tip interatomic bonds are broken and the initial internal crack is completely blunted-arrested, and the system fails by the process of multi micro-hole production, we may conclude that the fracture is ductile (Fig. III.6A8). The simulations results indicate that

i. Brittle-to-ductile transition in the pre-cracked c_o=3.75d critically loaded 2D-triangular COR.LJCOVa.2 crystal is gradual (Table III.6,8-9). The fracture in the temperature range of

$$.0675\varepsilon_o \leq (K_BT)_{BDTT} \leq .104\varepsilon_o \qquad \text{(see Fig. III.6A3-6)}$$

is neither perfectly brittle nor totally ductile, therefore we may conclude that the fracture is in the brittle-to-ductile transition zone. Note that as discussed earlier in III.8B1, due to the economic restrictions, the reported upper and lower limits for the brittle-to-ductile transition temperature by no means are absolute and the BDTT zone may be much wider than the observed range.

ii. The critical fracture stress σ_c decreases by increasing the equilibrium temperature of the system

$$2.10 \geq \sigma_{BDT} \geq 1.95$$ (see Fig. III.6A2-6)

Note that contrary to the experimentally observed sharp increase in the externally applied load during the brittle-to-ductile transition in Si, we did not observe any sharp increase in the externally applied critical fracture stress in the pre-cracked 2D-triangular COR.LJCOVa.2 crystals. Even though we may have missed this point, but based on the observed behavior of the fracture in the atomistic level, this may be due to the fact that the brittle-to-ductile transition in this solid is gradual.

iii. The pre-cracked c_o=3.75d sample is "perfectly" ductile at the equilibrium temperature of $K_BT=0.136\varepsilon_o \approx .41T_M$ under the critical stress of σ_c =1.80.

iv. At elevated temperatures a few loaded surface atoms may be lost (Fig. III.6A7&9). This phenomenon is totally legitimate and is equivalent to the experimentally observed sublimation of the surface atoms of the solid. Since external loads are directly applied on the atoms of the uppermost and lowermost surfaces of the solid, any loss of these atoms may alter the behavior of the fracture, and therefore the simulations data in these cases must be discarded.

III.8B3. ***BDTT in the 2D-Triangular Johnson solid***

The simulations results are summarized in table III.7. As discussed earlier in section III.7, the data are not sufficiently detailed to explore the brittle-to-ductile transition in Johnson solid. Only, the similarities of the behavior of the crack in high temperatures in this solid (Fig. III.7B1, III.7C2-4*) to those of the 2D-triangular Cor.LJCOVa.2 (Fig. III.6A2-9) makes these simulations results of particular interest. In both cases at elevated temperatures the pre-cracked critically loaded solid may fracture by the process of multi-hole growth. Our observations suggest that

i. The pre-cracked c_o=3.75d critically loaded 2D-triangular Johnson solid of sample size 68x79 is brittle at 0 K (Fig. III.7C1). It is in the BDT zone at 110 K to 296 K (Fig. III.7C2-3). It is ductile at 404 K and above (Fig. III.7C4). Since there are only two runs in the brittle-to-ductile transition zone (III.7C2,3), it is difficult to judge the shape of the BDTT in this solid.

Note that even though at 0 K the emitted dislocation glides away from the blunted-arrested crack-tips (Fig. II.2.13, III.7A1), at higher temperatures, similar to the 2D-COR.LJCOVa.2 solid, the thermally generated blunting dislocation at the blunted-arrested crack-tip is unable to separate itself from the crack-tip. As a result a micro-hole is nucleated in the immediate vicinity of the crack-tip which either propagates itself (Fig. III.7B1) or gets blunted and produce further generations of micro-holes (Fig. III.7C2-4). The system then fails by the process of multi micro-hole growth. If none of the crack-tip

bonds are broken and the original crack is blunted-arrested, and the system fails by the process of hole-growth, we may interpret the fracture to be of the ductile type.

ii. The behavior of the fracture is sample size dependent. While the pre-cracked c_o=3.75d critically loaded sample of size 68x79 is brittle at 0 K (Fig. III.7C1), the sample of size 36x19 is perfectly ductile at 0 K (Fig. III.7A1).

iii. The externally applied critical fracture stress decreases by the increase in the equilibrium temperature of the system. It decreases from 3.37 at 0 K to 2.30 at 404 K for the sample of size 68x79.

iv. The externally applied critical fracture stress is sample size dependent.

v. Overloading the system has caused the embrittlement of it (Fig. III.7C4-4*).

Tables

[Table. II.1.1] Conversion factors and units for the two-dimensional triangular Lennard-Jones solid.

---

1 broken bond = d/2

1 time step = $0.02\ d\sqrt{(m/\varepsilon_o)}$

1 broken bond / time step = $1/0.04 = 25\ \sqrt{(\varepsilon_o/m)}$

Longitudinal sound velocity, $C_0 = \sqrt{(M/\rho)}$

Dilational wave velocity, $C_1 = \sqrt{(9M/8\rho)}$

For the perfect-unstrained system:

Young's modulus, $M = 83.14\ \varepsilon_o/d^2$

Mass per triangle = $3(m/6) = m/2$

Area of a triangle = $(\sqrt{3}/4)d^2$

Density of the material, $\rho = 2/\sqrt{3}\ (m/d^2)$

Longitudinal sound velocity, $C_0 = 8.485\ \sqrt{(\varepsilon_o/m)}$

1 broken bond / time step = $2.946\ C_1$

[Table. II.1.2] The Johnson Potential [125]. See Fig. II.1.3a-b.

Range	The Potential (ε_o)
$r_1 \leq r \leq r_2$	$-8.7267265(Br-3.09791)^3+28.1179634r-29.552166$
$r_2 \leq r \leq r_3$	$-2.5402761(Br-3.115829)^3 + 4.969104r - 6.28510$
$r_3 \leq r \leq r_4$	$-4.4311074(Br-3.066403)^3 + 4.8549901r-6.151563$

Where;

r_1 = 0.7261224 d.

r_2= 0.9172073 d.

r_3 = 1.1465091 d.

r_4 = 1.3147000 d.

B = 2.6166387.

Unit of d = 2.6166387 A°.

Unit of ε_o = 0.25163806 eV.

[Table. II.1.3] Conversion factors and units for the two-dimensional triangular Johnson solid.

Unit of d = 2.6166387 A°.

Unit of ε_o = 0.25163806 ev.

1 broken bond = d/2

1 time step = 0.02 d $\sqrt{(m/\varepsilon_o)}$

1 broken bond / time step = 1/0.04 = 25 $\sqrt{(\varepsilon_o/m)}$

Longitudinal sound velocity, C_0 = $\sqrt{(M/\rho)}$

Dilational wave velocity, C_1= $\sqrt{(9M/8\rho)}$

For the perfect-unstrained system:

Young's modulus, M_O = 60.13 ε_o/d^2

Mass per triangle = 3(m/6) = m/2

Area of a triangle = $(\sqrt{3}/4)d^2$

Density of the material, $\rho = 2/\sqrt{3}\ (m/d^2)$

Dilational wave velocity, C_1= 7.6539774 $\sqrt{(\varepsilon_o/m)}$

1 broken bond / time step = 3.266 C_1

[Table. II.1.4] Energetics of the quasi-static crack extension in a 2D-triangular array of 10704 atoms interacting via the Johnson potential and arranged in 79 rows (79X135) subjected to the remotely applied constant tensile load of, s_a=1.50<s_c. M_o=60.13. See Fig. II.3.25.

c_o	e	ε=ln(1+e)	σ=s(1+e)	M*	ΔE_{el}	ΔW	$-\Delta E_{me}$	$\Delta W/\Delta E_{el}$
0.00	0.025519	0.025520	1.538280	59.2464	0.0000	0.0000	0.0000	———
3.75	0.025778	0.025451	1.538667	58.6503	1.8288	3.5490	1.7202	1.9406
4.75	0.025941	0.025610	1.538912	58.2819	2.9784	5.7782	2.8000	1.9489
5.75	0.026147	0.025811	1.539220	57.8240	4.4300	8.5894	4.1594	1.9388
6.75	0.026397	0.026055	1.539596	57.2755	6.1986	12.0162	5.8176	1.9385
9.75	0.027451	0.027080	1.541765	55.2786	13.6512	26.4290	12.7730	1.9356

c_o	$\pi\sigma^2c^2/M^*$	$\pi s^2c^2/M^*$	$\pi\varepsilon^2c^2M^*$	$\pi\varepsilon^2c^2M$	$\pi\varepsilon^2c^2M_o$	(Δ%)	$\pi e^2c^2M^*$	πe^2c^2 M
0.00	0.0000	0.0000	0.0000	0.0000	0.0000	(———)	0.0000	0.0000
3.75	1.7833	1.6948	1.6784	1.6955	1.7208	(.034%)	1.7218	1.7393
4.75	2.8802	2.7364	2.7095	2.7543	2.7955	(.162%)	2.7800	2.8260
5.75	4.2557	4.0416	4.0013	4.0998	4.1609	(.036%)	4.1062	4.2072
6.75	5.9238	5.6230	5.5653	5.7568	5.8427	(.432%)	5.7126	5.9092
9.75	12.8790	12.2000	12.1072	12.9762	13.1698	(3.01%)	12.4403	13.3333

NBB = Total Number of Broken Bonds in the half-sample.
c = Half crack-length = (2NBB+1)/4.
M* = "Effective" Young's modulus of the loaded solid.
ΔE_{el} = The change in the elastic energy of the solid.
ΔW = Work done by the external load on the solid.
ΔE_{me} = The change in the mechanical energy of the solid.
s = The applied external load = 1.50 (ε_o/d^2)
Δ% = % difference between $\pi\varepsilon^2c^2M_o$ and ΔE_{me}.
e = The conventional (engineering) strain.
ε = ln(1+e) = True strain.
σ = s(1+e) = True stress.

[Table. II.1.5a] The comparison of the critical engineering stress, S_C, true stress, σ_c, engineering strain, e_C, and true strain, ε_C, values from the simulations and the corresponding Griffith stress, σ_G, and e_G. Sample size: 79x135.

c_o	M	σ_G	¤	S_C	σ_c	ε_G	e_c	ε_c	Δ%
3.75	57.4205	3.195	3.196	3.37	3.427	.053	.0597	.0580	7.2%
6.75	58.5270	2.381	2.384	2.45	2.480	.040	.0424	.0415	4.1%
9.75	58.9850	1.982	1.986	1.90	1.917	.033	.0325	.0320	3.2%

[Table. II.1.5b] The effect of the height of the specimen on the critical load. The width of the sample (2W=135), and the initial half-crack-length (c_o=9.75) are identical. Griffith stress, σ_G , is 1.982 for all of the cases.

sample size	S_c
39x135	1.45
79x135	1.90
159x135	2.15

¤ ≡ $\{(2W/\pi c)\tan(\pi c/2W)\}^{1/2}\sigma_G$
NBB_{tot} ≡ Total Number of Broken Bonds.
c_o ≡ Initial half crack-length ≡ $(NBB_{tot}+1)/4$.
M ≡ Young's modulus of the critically loaded sample.
E ≡ Young's modulus of the nominally loaded sample.
S_C ≡ "Engineering" critical stress.
σ_C ≡ True critical stress = $S_C(1+e)$.
σ_G ≡ Griffith's (fracture) stress= $(2E\gamma/\pi c_o)^{1/2}$.
e_C ≡ "Engineering" critical strain.
ε_C ≡ True critical strain = $\ln(H/H_o) = \ln(1+e)$.
ε_G ≡ Griffith's (fracture) strain $=\sigma_G/E=(2\gamma/\pi E c_o)^{1/2}$.

[Table. II.2.1] Mechanical properties of the two-dimensional triangular (modified) Johnson solid with the angular resistance, a*. Sample size: 18x19, defect-free sample under the constant applied load, S, and absolute zero temperature.

[Table. II.2.1A] The simulation results. See Fig. II.2.3, 5, 7b & 9a.

	a*=0.0		a*=1.0		a*=3.0	
S	e	M	e	M	e	M
0.005	.000083	60.13	.000069	72.25		
1.000	.01688	59.57	.01414	70.91	.011306	88.45
2.000	.03437	58.79	.02904	69.25	.023246	86.04
3.000	.05270	57.80	.04498	67.24	.036062	83.90
4.000	.07214	56.55	.06238	64.28	.050112	79.82
5.000	.09313	54.99	.08186	61.91	.065982	75.79
6.000	.11640	53.01	.10454	58.39	.084751	70.83
7.000	.14320	50.44	.13270	53.82	.10899	64.32
8.000	.17690	46.80	.17332	47.31	.14968	53.69
	M=60.13-37.37e		M=72.25-86e		M=90.7-206e	
good for	e < .035		e < .04		e < .04	

The shear modulus, μ, for the Johnson potential may be calculated from :

$$M/2\mu = 1+\nu$$

for the $\nu=1/3$, we obtain $\mu= (3/8)M = 22.5$, in a reasonable agreement with the theoretical calculations listed in Table II.2.1B.

[Table II.2.1B] Analytical calculation of Young's Modulus, M, Shear Modulus, μ, and Poisson's ratio, ν, for nominal applied strain, e, for the pair-wise Johnson Potential, i.e., a*=0. See Fig. II.2.3, 5 & 9a.

STRAIN e	YOUNG's MODULUS M	SHEAR MODULUS μ
.000001	60.0865	22.5324
.000002	60.1195	22.5448
.000003	60.1305	22.5489
.000004	60.1359	22.5510
.000005	60.1392	22.5522
.00001	60.1456	22.5546
.00002	60.1484	22.5556
.00003	60.1490	22.5559
.00004	60.1490	22.5559
.0001	60.1470	22.5551

[Table II.2.2] Mechanical properties of the two-dimensional "modified" Lennard-Jones, LJCOVa.2, solid with the angular resistance of a*=0.2 as a function of temperature. See Fig.. II.2.6a, 7a, b.

[Table II.2.2A] Simulations results for LJCOVa a*=0.2, sample: 32x19, temperature $K_BT=0.00\ \varepsilon_o$.

LOAD S	STRAIN e	YOUNG's MODULUS M
0.20	.002368	84.51309
0.45	.005429	83.01547
0.70	.008603	81.55376
0.95	.011901	80.07158
1.20	.015337	78.54114
1.70	.022690	75.31852
2.20	.030866	71.74990
2.70	.040140	67.79881
3.20	.050980	63.34601
3.70	.064230	58.19040
4.20	.081732	51.95533
4.70	.108750	43.71801

[Table II.2.2B] Simulations results, for LJCOVa a*=0.2, sample:18X19, applied load, σ =0.25. See Fig. II.2.7a, III.3.1-2, 5.

TEMPERATURE K_BT (ε_o)	L.C. of EXPANSION $\langle\alpha\rangle_t$	STRAIN $\langle 1000\ e\rangle_t$	YOUNG'S MODULUS $\langle M\rangle_t$	KOSTERLITZ THOULESS K
0.00000		2.96	84.42	
0.02144	1.0021	2.98	83.83	4608.19
0.03038	1.0031	3.02	82.52	3201.31
0.05349	1.0054	3.34	74.44	1640.17
0.09564	1.0100	3.52	70.57	869.63
0.09929	1.0104	3.63	68.87	817.49
0.10154	1.0113	3.78	65.48	723.47
0.13855	1.0150	4.19	58.90	501.03
0.15095	1.0165	4.50	55.56	433.80
0.16496	1.0185	4.88	51.22	365.95
0.18317	1.0211	5.07	48.36	311.16

[Table II.2.2C] Simulations results, for LJCOVa.2 a*=0.2, sample:18X19.

S	K_BT $(100\varepsilon_o)$	$<10^3e>_t$	$<M>_t$
0.50	2.116	6.31	79.20
1.00	2.075	13.09	76.50
1.50	2.026	20.57	73.17
1.70	2.000	23.75	71.86
1.80	1.988	25.47	70.95
1.90	1.973	27.17	70.26
2.40	1.907	30.65	66.22
2.90	1.833	47.16	61.93
3.40	1.723	60.27	56.88
3.90	1.619	79.55	49.48

S	K_BT $(100\varepsilon_o)$	$<10^3e>_t$	$<M>_t$
0.25	3.038	3.02	82.52
0.50	3.009	6.34	78.75
0.75	2.981	9.65	77.70
1.00	2.947	13.33	75.07

S	K_BT $(100\varepsilon_o)$	$<10^3e>_t$	$<M>_t$
0.25	5.349	3.34	74.43
0.50	5.303	6.86	72.62
0.75	5.241	10.45	71.55
1.00	5.168	14.14	70.61
1.50	5.040	21.88	68.55

S	K_BT $(100\varepsilon_o)$	$<10^3e>_t$	$<M>_t$
0.25	9.56	3.68	67.42
0.50	9.45	7.36	67.35
0.75	9.31	11.24	66.25
1.00	9.21	15.49	64.20
1.25	9.08	19.75	62.99
1.50	8.93	24.14	61.89
1.75	8.74	29.90	58.34

[Table II.2.2C] continued,

S	K_BT ($100\varepsilon_o$)	$\langle 10^3 e \rangle_t$	$\langle M \rangle_t$
0.00			
0.25	10.667	3.78	65.48
0.50	10.605	7.27	68.09
0.75	10.466	11.41	65.21
1.00	10.349	15.79	62.89
1.25	10.153	20.60	60.33
1.50	9.958	25.19	59.23
1.75	9.808	33.67	51.97
2.00	9.619	39.01	51.26

S	K_BT ($100\varepsilon_o$)	$\langle 10^3 e \rangle_t$	$\langle M \rangle_t$
0.00	16.903	----	----
0.25	16.670	3.77	65.08
0.50	16.280	7.99	61.63
0.75	15.974	14.27	51.83

S	K_BT ($100\varepsilon_o$)	$\langle 10^3 e \rangle_t$	$\langle M \rangle_t$
0.00	14.095	---	----
0.25	13.991	3.62	68.17
0.50	13.602	7.32	67.43
0.75	13.464	12.07	61.48
1.00	13.359	17.05	58.11
1.25	12.890	21.45	57.82
1.50	12.973	26.01	57.29

[Table. II.3.1] Experimentally observed limiting crack-tip velocities, V_T [169].

Material	C_2 (m/s)	C_1 (m/s)	C_2/C_1	V_T (m/s)	V_T/C_2	V_T/C_1
Glass (soda-lime-silica)	1921.7	3140	.578	1540	.49	.300
Glass (silica)	2264.0	3700	.578	2190	.59	.361
Cellulose acetate	416.2	680		300	.44	.269
Steel	1934.0	3160	.542	1500	.47	.288
Columbia resin	575.0	940		550	.59	.361

E ≡Young's modulus of the nominally loaded sample.
C_0 ≡ Longitudinal Wave velocity = $\sqrt{(E/\rho)}$.
C_1 ≡ Dilational wave velocity = $\sqrt{(9E/8\rho)}$ for ν =.25
C_2 ≡ The shear wave velocity = $\sqrt{(\mu/\rho)} = 0.63C_0$ for ν =0.25.
C_R ≡ The Rayleigh velocity = $0.58C_0$ for ν = 0.25.
V_T ≡ Experimentally observed crack-tip terminal velocity.

[Table. II.3.2] Simulations results for the crack-tip velocity as a function of the amplitude of the angular resistance, a*. See Fig. II.3.7-8.

Angular resistance amplitude	Modified Lennard-Jones potential		Modified Johnson potential	
a*	V_T/C_1	dislocation generation at c/c_o	V_T/C_1	dislocation generation at c/c_o
0.00	0.12	*	0.24	**
0.30			0.28	2.5
0.50	0.28	2.0		
0.75			0.35	none
1.00	0.32	none	0.40	none
3.00	0.42	none	0.41	none
5.00	0.42	none		

* a*=0.0, 2D-triangular Lennard-Jones solid had to be simulated at constant applied strain, due to the fact that at constant externally applied load (Fig. II.2.11) the system behaved in a ductile manner by the emission of blunting dislocation at the crack tip.

** a*=0.0, Modified 2D-triangular Johnson solid: V_T/C_1 is the average value for all values of c at both constant critical applied tensile load and constant applied strain for 159x135, 79x135, and 39x63 sample sizes. The crack is propagated brittlely but in all cases a pair of dislocation is generated at the crack tip at $c/c_o \approx$ 2.5-3.0. The fast running crack-tip is arrested for a substantial amount of time immediately after the emission of the dislocation.

*** For all other cases: c_o=3.75, sample size: 39x63, σ_a=3.0 for LJCOVa, and σ_a=4.0 for the covalently modified 2D-Johnson solid.

[Table. II.3.3] Approximate values of the elastic wave velocities for common engineering materials [188].

	Steel	Cu	Al	Glass	Rubber
E(Gpa)	210	120	70	70	20
ρ (kg/m^3)	7800	8900	2700	250	900
C_R (m/s)	2980	2120	2920	3080	26
C_2 (m/s)	3220	2250	3100	3350	27
C_0 (m/s)	5190	3670	5090	5300	46
C_1 (m/s)	5940	4560	6320	5800	1040
ν	0.29	0.34	0.34	0.25	0.5

E = Young's modulus of the nominally loaded sample.
C_0 = Longitudinal Wave velocity = $\sqrt{(E/\rho)}$.
C_1 = Dilational wave velocity = $\sqrt{(9E/8\rho)}$ for ν =.25
C_2 = The shear wave velocity = $\sqrt{(\mu/\rho)}$ = $0.63C_0$ for ν =0.25.
C_R = The Rayleigh velocity = $0.58C_0$ for ν = 0.25.

[Table. II.3.4] The theoretical values of the limiting terminal velocity of brittlely propagating cleavage crack. Eshelby and Mott's theoretical predictions for the crack-tip velocity for c_o=3.75. Eshelby's velocity is normalised to the Shear velocity, C_2=0.612C_1, and Mott-Robert-Wells velocity is normalised to V_T=.25C_1 and V_T=.44C_1. See Fig. II.3.7.

			Eshelby		Mott-Robert-Wells	
NBB	c	c_o/c	V_C/C_2	V_C/C_1	.44C_1	.25C_1
8	4.25	.882	.125	.076		
9	4.75	.790	.232	.142	.093	.053
10	5.25	.714	.324	.199		
11	5.75	.652	.403	.247	.153	.087
12	6.25	.600	.471	.288		
13	6.75	.556	.528	.323	.195	.111
14	7.25	.517	.578	.354		
15	7.75	.484	.621	.380	.227	.129
16	8.25	.455	.658	.402		
17	8.75	.429	.690	.422	.252	.143
18	9.25	.405	.718	.439		
19	9.75	.385	.742	.454	.271	
20	10.25	.366	.764	.468		
21	10.75	.349	.783	.479	.287	
22	11.25	.333	.800	.490		

[Table. II.3.4.] Continued,

NBB	c	c_o/c	Eshelby V_C/C_2	Eshelby V_C/C_1	Mott-Robert-Wells $.44C_1$	Mott-Robert-Wells $.25C_1$
23	11.75	.319	.815	.499	.300	
24	12.25	.306	.829	.507		
25	12.75	.294	.841	.515	.311	
26	13.25	.283	.852	.521		
27	13.75	.273	.862	.527	.320	.182
29	14.75				.328	
33	16.75				.342	
35	17.75				.347	
37	18.75				.352	.200
39	19.75				.357	
43	21.75				.364	
47	23.75				.371	.211
59	28.75				.382	.217

Theory	V_T	Formulation
Mott [3]	$C\equiv(2\pi/K)^{1/2}C_0$	$V_C = C\,(1 - c_o/c)^{1/2}$
Roberts & Wells[32]	$0.38C_0$	$V_C = 0.38C_0\,(1 - c_o/c)$
Eshelby [7]	C_2	$V_C = C_2[1-(c_o/c)^2]/[1-(c_o/c)^2]$
Stroh [189]	C_R	"relativistic" effect
Yoffe [173]	$0.62C_2$	"crack curving"
Freund [4,6]	C_R	$V_C = C_R\,(1 - c_o/c)$

[Table. II.3.5] Forces acting on atoms near the crack-tip for 2D-triangular Lennard-Jones solid of 10704 atoms arranged in 79 rows. The initial half-crack length is 9.75d. At the start of the run the first broken bond is at the atomic position #59 [1]. See Fig. II.2.29.

Time		in (ε_o/d) on atom (row 39) at position:					
step	e/e_G	53	54	55	56	57	58
3600	1.036	2.756	3.011	3.422	4.182	3.764	1.527
3640	1.054	2.800	3.065	3.504	4.336	3.401	1.417
3680	1.054	2.824	3.105	3.577	4.463	3.033	1.324
3720	1.054	2.859	3.178	3.719	4.557	2.386	1.003
3760	1.054	2.930	3.278	3.884	4.425	1.891	0.905
3800	1.054	2.982	3.362	4.042	4.100	1.633	0.449
3840	1.054	3.078	3.535	4.402	3.229	1.362	0.533

Time		in (ε_o/d) on atom (row 40) at position:					
step	e/e_G	53	54	55	56	57	58
3600	1.036	2.663	2.870	3.193	3.747	4.557	2.272
3640	1.054	2.704	2.919	3.259	3.847	4.495	1.996
3680	1.054	2.725	2.952	3.310	3.938	4.340	1.784
3720	1.054	2.749	3.002	3.405	4.139	3.980	1.578
3760	1.054	2.806	3.079	3.534	4.399	3.253	1.380
3800	1.054	2.848	3.146	3.657	4.550	2.680	1.241
3840	1.054	2.928	3.279	3.890	4.448	1.891	0.906

[Table. II.3.6] Dynamic simulations results of brittlely propagating internal cracks in a two-dimensional triangular Lennard-Jones solid under constant critical applied strain [1]. See Fig. II.3.9.

Run	A	N_R	N_O	e/e_G	$e/e_G x(1+\Delta)$	Δ %	NBB	V_T/C_0	c/c_o
1	1227.2	27	55	1.679	1.696	1.0%	59	0.053	1.36
2	3445.9	47	87	1.246	1.257	0.9%	40	0.093	1.51
3	4746.7	59	95	1.125	1.136	1.0%	50	0.108	1.62
4	9085.5	79	135	1.036	1.046	1.0%	45	0.113	1.56
5	9085.5	79	135	1.036	1.054	1.7%	22	-----	----

A ≡ Area of the sample in units of d
N_R ≡ Number of rows of the sample.
N_O ≡ Number of atoms in the odd rows ($N_{even}=N_{odd}+1$)
e_G ≡ Griffith's critical strain = 0.028
NBB ≡ Total number of broken bonds in the half-sample.
V_T ≡ Terminal crack-tip velocity.
C_0 ≡ Longitudinal sound velocity.
c ≡ Crack half-length at which V_T is achieved.
c_o ≡ initial crack half-length.
Run5: Critical damping used to study stress profile.

[Table II.3.7] Comparison of the simulations results regarding the change in the mechanical energy of varieties of systems during the brittle propagation of the internal cracks. The slopes are calculated graphically from Fig. II.3.24, 26, 30-31.

[Table II.3.7A] Constant Applied Load (see Fig. II.3.24, 26, 30-31).

c_o	σ_c	s_1	s_{th1}	$\Delta s_1\%$	s_2	s_{th2}	$\Delta s_2\%$	sample
3.75	3.37				33.34	35.68	6.6%	79x135
6.75	2.45				17.94	18.86	4.9%	79x135
9.75	1.45							39x135
9.75	1.90*				11.11	11.34	2.0%	79x135
9.75	1.90				10.00	11.34	11.8%	79x135
9.75	2.15	.206	.258	20%				159x135

c_o ≡ Initial half crack-length.
s_1 ≡ Slope of $-\Delta E_{me}$ vs c^2 (simulations results).
$s_{th1} \equiv \pi\sigma^2/E$ (the theoretical prediction).
s_2 ≡ Slope of $-\Delta E_{me}$ vs c^2/M^* (simulations results).
$s_{th2} \equiv \pi\sigma^2$ (the theoretical prediction).

[Table II.3.7B] Constant Applied Strain (see Fig. II.3.32).

c_o	e_c	s_1	s_{th1}	$\Delta s_1\%$	s_2	s_{th2}	$\Delta s_2\%$
3.75	0.0615				.001020	.001190	14%
6.75	0.0470				.000574	.000694	17%
9.75	0.0410*	.213	.309	31%	.000498	.000527	6%
9.75	0.0410				.000442	.000527	16%

$c_o \equiv$ Initial half crack-length.
$s_1 \equiv$ Slope of $-\Delta E_{me}$ vs c^2 (simulations results).
$s_{th1} \equiv \pi e^2 M^*$ (the theoretical prediction).
$s_2 \equiv$ Slope of $-\Delta E_{me}$ vs $c^2 M^*$ (simulations results).
$s_{th2} \equiv \pi e^2$ (the theoretical prediction).

[Table II.3.8A1] Run: JN7LD, Type of loading: "fast", sample size: 79x135, c_o=3.75, critical load, σ_C= 3.37. All energies are given for the half-sample. See Fig. II.3.30-31.

STEP	NBB	c	M*	ΔW	ΔE_{el}	ΔE_{ke}	$-\Delta E_{me}$
1998	0	0.00	57.5671	—	—	—	—
3000	7	3.75	57.4917	0.000	0.000	0.0000	0.000
3250	8	4.25	56.8446	10.549	9.199	0.3541	1.350
3285	9	4.75	56.6852	13.180	10.561	0.6240	2.619
3308	10	5.25	56.5834	14.869	10.884	1.0053	3.985
3325	11	5.75	56.5116	16.065	10.551	1.5636	5.514
3342	12	6.25	56.4438	17.197	10.119	2.1148	7.078
3359	13	6.75	56.3809	18.253	9.352	2.9540	8.901
3374	14	7.25	56.3298	19.112	8.313	3.8821	10.799
3388	15	7.75	56.2862	19.847	7.060	4.8687	12.787
3403	16	8.25	56.2441	20.560	5.586	6.1232	14.974
3417	17	8.75	56.2067	21.194	3.797	7.5523	17.397
3436		Incipient Dislocation Generation at the Crack Tip[1] .					

[1] The fast running crack was arrested for a substantial amount of time after the emission of the blunting dislocation.

[Table II.3.8A2] Run: JN7LD, Type of loading: "fast", sample size: 79x135, c_o=3.75, critical load σ_c= 3.37. All energies are given for the half-sample. See Fig. II.3.30-31, 34-35.

STEP	NBB	c	e	ΔW	ΔE_{el}	$-\Delta E_{me}$	c^2/M^*	$(cV_c)^2$
1998	0	0.00	.0595	0.000	0.000	0.000	0.00	0.0
3000	7	3.75	.0596	———	———	——	—	0.0
3250	8	4.25	.0603	11.792	5.837	5.955	0.32	5.9
3285	9	4.75	.0604	14.423	7.199	7.224	0.40	19.6
3308	10	5.25	.0606	16.112	7.522	8.590	0.49	45.8
3325	11	5.75	.0606	17.308	7.189	10.119	0.59	69.8
3342	12	6.25	.0607	18.437	6.757	11.680	0.69	84.4
3359	13	6.75	.0608	19.496	5.990	13.506	0.81	135.4
3374	14	7.25	.0608	20.355	4.951	15.404	0.93	156.2
3388	15	7.75	.0609	21.090	3.698	17.392	1.10	178.5
3403	16	8.25	.0609	21.803	2.224	19.579	1.21	202.3
3417	17	8.75	.0610	22.437	0.435	22.002	1.36	227.6
3436		Incipient Dislocation Generation at the Crack Tip[2] .						

[2] The fast running crack was arrested for a substantial amount of time after the emission of the blunting dislocation.

[Table II.3.8B1] Run: JN13LD, Type of loading: "fast", sample size: 79x135, c_o=6.75, critical load, σ_c= 2.45. All energies are given for the half-sample. See Fig. II.3.31.

STEP	NBB	c	M*	ΔW	ΔE_{el}	ΔE_{ke}	$-\Delta E_{me}$
3999	0	0.00	58.527	—	—	—	—
5000	13	6.75	58.362	0.000	0.000	0.000	0.000
5294	14	7.25	56.104	19.121	16.946	1.190	2.175
5329	15	7.75	55.672	22.948	19.580	1.380	3.368
5354	16	8.25	55.388	25.498	20.855	1.653	4.643
5372	17	8.75	55.201	27.187	21.229	1.969	5.958
5390	18	9.25	55.032	28.724	21.321	2.427	7.403
5407	19	9.75	54.890	30.018	21.078	2.985	8.940
5423	20	10.25	54.774	31.086	20.521	3.606	9.497
5438	21	10.75	54.680	31.950	19.713	4.278	12.237
5453	22	11.25	54.601	32.678	18.534	5.216	14.144
5481	24	12.25	54.492	33.682	15.722	7.046	17.960
5495	25	12.75	54.456	34.024	14.189	7.942	19.835
5509	26	13.25	54.426	34.297	12.339	9.067	21.958
5524	27	13.75	54.388	34.656	10.703	10.051	23.953
5538	28	14.25	54.313	35.370	9.216	11.312	26.154
5554	29	14.75	54.171	36.710	8.418	12.420	28.292
5564		Incipient Dislocation Generation at the Crack Tip[3] .					

[3] The fast running crack was arrested for a substantial amount of time after the emission of the blunting dislocation.

[Table II.3.8B2] Run: JN13LD, Type of loading: "fast", sample size: 79x135, c_o=6.75, critical load, σ_c= 2.45. All energies are given for the half-sample. See Fig. II.3.30-31, 34-35.

Step	NBB	c	e	ΔW	ΔE_{el}	- ΔE_{me}	$(cV_c)^2$
3999	0	0.00	.0424	0.000	0.000	0.000	0.00
5000	13	6.75	.0425	1.350	-6.148	4.798	0.00
5294	14	7.25	.0442	20.471	11.298	9.173	14.27
5329	15	7.75	.0446	24.298	13.932	10.366	45.88
5354	16	8.25	.0448	26.848	15.207	11.641	96.38
5372	17	8.75	.0449	28.537	15.581	12.956	56.56
5390	18	9.25	.0451	30.074	15.673	14.401	205.56
5407	19	9.75	.0452	31.368	15.430	15.938	274.76
5423	20	10.25	.0453	32.436	14.873	17.563	303.67
5438	21	10.75	.0454	33.300	14.065	19.235	334.01
5453	22	11.25	.0454	34.028	12.886	21.142	365.81
5481	24	12.25	.0455	35.032	10.074	24.958	433.73
5495	25	12.75	.0455	35.374	8.541	26.833	469.86
5509	26	13.25	.0457	35.647	6.691	28.956	507.44
5524	27	13.75	.0460	36.006	5.055	30.951	546.46
5538	28	14.25	.0467	36.720	3.568	33.152	586.92
5554	29	14.75	.0458	38.060	2.770	35.290	628.83
5564			Incipient Dislocation Generation at the Crack Tip[4] .				

[4] The fast running crack was arrested for a substantial amount of time after the emission of the blunting dislocation.

[Table II.3.8C1] Run: JN19LD, Type of loading: "fast", sample size: 79x135, c_o=9.75, critical load, σ_c= 1.90. All energies are given for the half-sample.

STEP	NBB	c	M*	ΔW	ΔE_{el}	ΔE_{ke}	$-\Delta E_{me}$
5110	19	9.75	58.159	0.000	0.000	0.000	0.000
5364	20	10.25	53.232	26.414	24.049	1.367	2.365
5395	21	10.75	52.631	29.962	26.575	1.383	3.387
5418	22	11.25	52.241	32.311	27.731	1.572	4.580
5435	23	11.75	51.855	33.862	28.019	1.833	5.843
5453	24	12.25	51.749	35.314	28.075	2.225	7.239
5469	25	12.75	51.568	36.432	27.771	2.647	8.661
5485	26	13.25	51.415	37.383	27.198	3.175	10.208
5500	27	13.75	51.297	38.120	26.330	3.795	11.790
5515	28	14.25	51.203	38.710	25.247	4.487	13.463
5529	29	14.75	51.136	39.131	23.935	5.219	15.196
5543	30	15.25	51.089	39.430	22.544	5.901	16.886
5556	31	15.75	51.061	39.606	21.023	6.621	18.583
5570	32	16.25	51.046	39.702	19.412	7.334	20.290
5584	33	16.75	51.038	39.754	17.628	8.181	22.126
5611	35	17.75	50.935	40.427	14.804	9.690	25.623
5624	36	18.25	50.825	41.143	13.938	10.267	27.205
5671	39	19.75	50.232	45.040	11.994	13.146	33.046
5673			Incipient Dislocation Generation at the Crack Tip[5] .				

[5] The fast running crack was arrested for a substantial amount of time after the emission of the blunting dislocation.

[Table II.3.8C2] Run: JN19LD, Type of loading: "fast", sample size: 79x135, c_o=9.75, critical load, σ_C= 1.90. All energies are given for the half-sample. See Fig. II.3.30-31, 34-35.

Step	NBB	c	e	ΔW	ΔE_{el}-	ΔE_{me}	$(cV_C)^2$	
3999	0	0.00	.0325	0.000	0.000	0.000	0.0	
5110	19	9.75	.0330	1.277	-6.403	7.680	0.0	
5364	20	10.25	.0360	30.421	19.327	11.094	22.8	
5395	21	10.75	.0364	33.969	21.853	12.116	102.1	
5418	22	11.25	.0367	36.318	23.009	13.309	220.5	
5435	23	11.75	.0369	37.869	23.297	14.572	282.3	
5453	24	12.25	.0371	39.321	23.353	15.968	355.9	
5469	25	12.75	.0372	40.439	23.049	17.390	431.9	
5485	26	13.25	.0373	41.390	22.470	18.920	495.5	
5500	27	13.75	.0374	42.127	21.613	20.514	559.3	
5515	28	14.25	.0375	42.717	20.525	22.192	680.0	
5529	29	14.75	.0375	43.138	19.213	23.925	735.0	
5543	30	15.25	.0375	43.437	17.822	25.615	785.7	
5556	31	15.75	.0376	43.613	16.301	27.312	838.0	
5570	32	16.25	.0376	43.709	14.690	29.019	892.1	
5611	35	17.75	.0377	44.434	10.082	34.352	1064.4	
5671	39	19.75	.0382	49.047	7.272	41.775	764.5	
5673		Incipient Dislocation Generation at the Crack Tip[6].						

[6] The fast running crack was arrested for a substantial amount of time after the emission of the blunting dislocation.

[Table II.3.8D] Run: JN19LD, Type of loading: gradual, sample size:79x135, c_o=9.75, critical load, σ_c= 1.90 (see Fig. II.3.9, 21, 23, 31). All energies are given for the half-sample.

STEP	NBB	c	M*	ΔW	ΔE_{el}	ΔE_{ke}	$-\Delta E_{me}$
3999	0	0.00	58.985	0.000	0.000	0.000	0.000
6710	19	9.75	55.130	——	——	1.691	——
6746	20	10.25	54.501	23.182	12.218	1.976	10.964
6788	21	10.75	53.647	28.022	15.718	2.314	12.304
6821	22	11.25	52.960	32.359	18.853	2.515	13.506
6845	23	11.75	52.348	35.705	21.176	2.540	14.529
6864	24	12.25	51.926	38.276	22.763	2.533	15.513
6884	25	12.75	51.527	40.768	24.258	2.522	16.510
6904	26	13.25	51.178	42.972	25.477	2.513	17.495
6923	27	13.75	50.920	44.625	26.078	2.564	18.547
6941	28	14.25	50.798	45.422	25.787	2.656	19.635
6960	29	14.75	50.760	45.671	24.835	2.858	20.836
6978	30	15.25	50.636	46.479	23.265	3.237	23.214
6997	31	15.75	50.394	48.060	23.386	3.726	24.674
7015	32	16.25	50.315	49.181	23.369	4.252	25.814
7033	33	16.75	50.257	48.962	23.147	4.862	25.815
7050	34	17.25	50.147	48.345	21.079	5.702	27.266
7067	35	17.75	50.105	49.957	19.665	6.349	30.292
7084	36	18.25	49.980	50.782	18.492	7.380	32.290

[Table II.3.8D] Run: JN19LDFAST continued,

STEP	NBB	C	M*	ΔW	ΔE_{el}	ΔE_{ke}	$-\Delta E_{me}$
7100	37	18.75	49.895	51.341	17.203	8.240	34.138
7115	38	19.25	49.777	52.130	16.073	9.150	36.057
7130	39	19.75	49.660	52.912	14.435	10.593	38.477
7144	40	20.25	49.532	53.762	13.674	11.191	40.088
7158	41	20.75	49.367	54.563	12.014	12.996	42.554
7172	42	21.25	49.187	56.090	11.540	13.684	44.550
7185	43	21.75	49.010	57.293	9.722	15.761	47.576
7200	44	22.25	48.760	59.021	9.409	16.771	49.612
7213	45	22.75	48.553	60.452	7.512	19.204	52.940
7227	46	23.25	48.282	62.359	7.215	20.332	55.144
7240	47	23.75	48.032	64.135	5.459	22.930	58.676
7253	48	24.25	47.774	65.981	4.900	24.312	61.081
7266	49	24.75	47.477	68.138	3.319	27.116	64.819
7279	50	25.25	47.173	70.376	2.662	28.956	67.714
7292	51	25.75	46.841	70.851	1.459	31.687	69.392
7305	52	26.25	46.477	75.609	0.918	33.997	74.691
7317	53	26.75	46.126	78.312	0.021	36.637	78.291
7330	54	27.25	45.715	81.532	-0.337	39.176	81.869
7342	55	27.75	45.288	84.933	-0.771	42.062	85.704
7355	56	28.25	44.815	88.777	-0.800	44.925	89.577
7368	57	28.75	44.307	92.999	-0.811	48.245	93.810

[Table II.3.8D] Run: JN19LDFAST continued,

STEP	NBB	c	M*	ΔW	ΔE_{el}	ΔE_{ke}	$-\Delta E_{me}$
7380	58	29.25	43.817	97.168	-0.752	51.317	97.920
7393	59	29.75	43.281	101.835	-0.541	54.834	102.373
7405	60	30.25	42.723	106.807	-0.168	58.421	106.975
7421	61	30.75	41.968	113.759	1.523	62.739	112.236

7431 Incipient Dislocation Generation at the Crack Tip[7] .

[7] The fast running crack was arrested for a substantial amount of time after the emission of the blunting dislocation.

[Table II.3.8E] Run: JN7SRN, Type of loading: gradual, sample size: 79x135, c_o=3.75, critical strain, ε_C=0.0615. All energies are given for the half-sample. See Fig. II.3.27, 32, 34-35.

Step	NBB	c	M*	ΔE_{ke}	$-\Delta E_{me} \equiv -\Delta E_{el}$	V_c	$(cV_c)^2$
∞	0	0.00	57.358	0.000	0.000	0.000	0.000
3900	7	3.75		----	----	----	----
4081	8	4.25	56.500	0.103	5.963	0.580	6.076
4115	9	4.75	56.450	0.383	7.045	0.920	19.097
4136	10	5.25	56.372	0.751	8.565	1.271	44.526
4154	11	5.75	56.355	1.502	9.965	1.531	77.497
4170	12	6.25	56.350	1.665	11.553	1.648	106.091
4187	13	6.75	56.358	2.251	12.885	1.648	123.743
4203	14	7.25	56.377	3.148	14.860	1.648	142.755
4217	15	7.75	56.400	4.012	16.730	1.648	163.124
4232	16	8.25	56.430	4.902	18.713	1.648	184.851
4246	17	8.75	56.460	5.902	20.712	1.648	207.936
4261	18	9.25	56.500	7.101	22.811	1.648	232.380
4276			Incipient Dislocation Generation at the Crack Tip[8] .				

[8] The fast running crack was arrested for a substantial amount of time after the emission of the blunting dislocation.

[Table II.3.8F] Run: JN13SRN, Type of loading: gradual, sample size:79x135, c_o=6.75, critical strain, ε_c= 0.0470. All energies are given for the half-sample. See Fig. II.3.9, 28, 32, 34-35.

Step	NBB	c	M*	ΔE_{ke}	$-\Delta E_{me}=-\Delta E_{el}$	V_c	$(cV_c)^2$
2850	0	0.00	58.227	0.000	0.000	0.000	0.000
4002	13	6.75	57.399	0.004	8.660	0.000	0.000
4200	14	7.25	55.519	0.421	10.070	0.570	17.100
4231	15	7.75	55.226	0.655	11.300	1.160	80.800
4252	16	8.25	55.093	0.944	12.590	1.450	143.100
4270	17	8.75	55.028	1.267	13.920	1.510	174.600
4288	18	9.25	55.011	1.624	15.270	1.550	205.600
4304	19	9.75	55.039	1.991	16.580	1.600	243.400
4321	20	10.25	55.109	2.394	18.020	1.620	275.700
4337	21	10.75	55.210	2.819	19.450	1.690	330.600
4352	22	11.25	55.332	3.397	21.010	1.780	401.100
4367	23	11.75	55.474	3.787	22.400	1.797	446.000
4381	24	12.25	55.616	4.532	24.130	1.797	484.800
4395	25	12.75	55.750	4.921	25.520	1.797	525.200
4409	26	13.25	55.806	5.817	27.400	1.797	567.200
4424	27	13.75	55.478	6.306	28.910	1.797	610.800
4438	28	14.25	54.445	7.388	30.940	1.797	656.000
4452	29	14.75	53.651	7.979	32.560	1.797	702.900
4465	30	15.25	53.794	8.973	34.510	1.797	751.300

[Table II.3.8F] JN13SRNGRADUAL, continued,

Step	NBB	c	M*	ΔE_{ke}	$-\Delta E_{me}=-\Delta E_{el}$	V_c	$(cV_c)^2$
4479	31	15.75	52.592	9.642	36.210	1.797	801.400
4493	32	16.25	51.564	10.715	38.200	1.797	853.100
4506	33	16.75	51.131	11.619	40.170	1.797	906.400
4520	34	17.25	50.265	12.243	41.780	1.797	961.300
4534	35	17.75	49.312	13.707	44.180	1.690	899.000
4549	36	18.25	48.967	13.913	45.490	1.480	730.600
4567	37	18.75	47.142	14.752	47.310	1.330	624.300

4568 Incipient Dislocation Generation at the Crack Tip[9] .

[9] The fast running crack was arrested for a substantial amount of time after the emission of the blunting dislocation.

[Table II.3.8G] Run: JN19SRN, Type of loading: "fast", sample size:79x135, c_o=9.75, critical strain, ε_C= 0.0410. All energies are given for the half-sample. See Fig. II.3.29, 32, 34-35.

Step	NBB	c	M*	ΔE_{ke}	$-\Delta E_{me} \equiv -\Delta E_{el}$	V_C	$(cV_C)^2$
3000	0	0.00	58.609	0.000	0.000	0.00	0.0
3700	19	9.75	58.054	0.019	11.161	0.00	0.0
3899	20	10.25	53.294	2.204	14.299	0.51	27.3
3924	21	10.75	52.402	2.262	15.372	1.19	163.6
3940	22	11.25	51.898	2.427	16.547	1.46	269.8
3958	23	11.75	51.399	2.738	17.866	1.77	434.5
3973	24	12.25	51.117	3.017	19.151	1.77	472.3
3989	25	12.75	50.895	3.419	20.666	1.77	511.6
4003	26	13.25	50.794	3.796	21.938	1.77	552.5
4017	27	13.75	50.782	4.121	23.263	1.77	595.0
4031	28	14.25	50.857	4.487	24.628	1.77	639.1
4045	29	14.75	51.017	4.806	25.939	1.77	684.7
4058	30	15.25	51.233	5.067	27.189	1.77	731.9
4071	31	15.75	51.528	5.336	28.469	1.77	780.7
4086	32	16.25	51.864	5.704	29.825	1.77	831.0
4100	33	16.75	52.195	5.965	31.090	1.77	883.0
4113	34	17.25	52.326	6.413	32.524	1.77	936.5
4127	35	17.75	51.779	6.686	33.807	1.77	991.5
4141	36	18.25	50.437	7.246	35.352	1.77	1048.2

[Table II.3.8G] Run: JN19SRNFAST, continued,

Step	NBB	c	M*	ΔE_{ke}	$-\Delta E_{me} \equiv -\Delta E_{el}$	V_c	$(cV_c)^2$
4156	37	18.75	49.912	7.539	36.663	1.77	1106.4
4170	38	19.25	49.147	8.231	38.322	1.77	1166.2
4185	39	19.75	47.622	8.504	39.626	1.77	1227.6
4200	40	20.25	47.700	8.714	40.971	1.77	1290.5
4216	41	20.75	45.991	9.605	42.681	1.50	971.9
4232	42	21.25	45.668	9.624	43.737	1.45	949.4
4249	43	21.75	44.077	9.922	45.026	1.22	699.4
4271	44	22.25	43.764	10.142	46.237	0.88	380.9

4276 Incipient Dislocation Generation at the Crack Tip[10] .

[10] The fast running crack was arrested for a substantial amount of time after the emission of the blunting dislocation.

[Table II.3.8H] Run: JN19SRN, Type of loading: gradual, sample size:79x135, c_o=9.75, critical strain, ε_C= 0.0410. All energies are given for the half-sample. See Fig. II.3.12, 29, 32, 34-35.

Step	NBB	c	M*	ΔE_{ke}	$-\Delta E_{me} \equiv -\Delta E_{el}$	V_c	$(cV_c)^2$
∞	0	0.00	58.6092	0.000	0.000	0.00	0.0
5500	19	9.75			0.000	0.00	0.0
5813	20	10.25	54.3617	0.254	14.631	0.36	13.4
5858	21	10.75	54.3213	0.427	15.804	0.60	41.9
5896	22	11.25	54.4383	0.661	17.037	0.71	64.5
5930	23	11.75	54.6476	0.809	18.183	0.90	110.1
5957	24	12.25	54.7124	1.059	19.424	1.06	168.6
5976	25	12.75	54.7421	1.256	20.621	1.23	245.9
5997	26	13.25	54.7159	1.521	21.890	1.25	274.3
6018	27	13.75	54.6487	1.893	23.248	1.34	339.5
6037	28	14.25	53.9277	2.197	24.558	1.36	375.6
6056	29	14.75	52.4323	2.528	25.889	1.38	414.3
6074	30	15.25	53.0614	2.927	27.265	1.44	482.2
6092	31	15.75	52.0351	3.370	28.724	1.46	528.8
6110	32	16.25	51.2585	3.858	30.204	1.48	578.4
6128	33	16.75	51.2082	4.246	31.597	1.55	674.0
6144	34	17.25	49.9438	4.773	33.114	1.60	761.8
6161	35	17.75	50.9159	5.378	34.699	1.65	857.8
6177	36	18.25	49.2445	5.817	36.145	1.70	906.8

[Table II.3.8H] Run: JN19SRNGRADUAL, continued,

Step	NBB	c	M*	ΔE_{ke}	$-\Delta E_{me} \equiv -\Delta E_{el}$	V_c	$(cV_c)^2$
6192	37	18.75	49.5049	6.409	37.742	1.73	1052.2
6207	38	19.25	48.0669	6.965	39.251	1.75	1134.9
6220	39	19.75	47.7690	7.561	40.877	1.78	1235.9
6234	40	20.25	46.7860	7.969	42.285	1.83	1377.8
6248	41	20.75	46.2660	8.688	43.973	1.83	1446.6
6262	42	21.25	45.9000	8.948	45.272	1.83	1517.2
6275	43	21.75	44.9540	9.690	47.002	1.83	1589.4
6289	44	22.25	44.7440	9.839	48.170	1.83	1663.4
6302	45	22.75	44.2210	10.684	49.990	1.83	1738.9
6315	46	23.25	43.2270	10.727	51.067	1.83	1816.2
6328	47	23.75	42.9370	11.604	52.935	1.83	1895.2
6341	48	24.25	42.3851	11.518	53.847	1.83	1975.8
6355	49	24.75	41.3061	12.575	55.887	1.83	2058.1
6369	50	25.25	41.1874	12.876	56.522	1.83	2142.1
6382	51	25.75	40.0134	13.328	58.633	1.83	2227.8
6397	52	26.25	39.6051	13.831	59.183	1.83	2315.2
6410	53	26.75	39.1688	13.628	60.929	1.83	2404.2
6423	54	27.25	37.7550	13.541	61.904	1.83	2494.9
6437	55	27.75	38.0527	13.924	63.242	1.83	2587.3
6524	61	30.75	33.7722	15.530	70.898	1.83	3177.0
6525	Incipient Dislocation Generation at the Crack Tip[11] .						

[11] The fast running crack was arrested for a substantial amount of time after the emission of the blunting dislocation.

[Table II.3.8.1] Summary: Normalised Crack-Tip velocity, V_c / C_1, sample size: 79x135, c_o=9.75. JN19SRN: critical strain, ε_C= 0.0410. JN19LD: critical load, σ_C= 1.90. See Fig. II.3.5-7, 9.

Crack-tip velocities, V_C, are calculated graphically from the graph of c(t) vs t. Note that the normalised crack-tip terminal velocity lies in the range of 0.249-0.273. Only, the acceleration period is effected by the loading scheme. It is slower for the gradual type of loading.

			V_c / C_1			
			FAST		GRADUAL	
NBB	c	c^2	JN19SRN	JN19LD	JN19SRN	JN19LD
19	9.75	95.06	0.000	0.000	0.000	0.000
20	10.25	105.06	0.072	0.065	0.050	0.052
21	10.75	115.56	0.167	0.131	0.085	0.093
22	11.25	126.56	0.205	0.185	0.100	0.132
23	11.75	138.06	0.249	0.200	0.125	0.169
24	12.25	150.06	0.249	0.216	0.149	0.178
25	12.75	162.56	0.249	0.229	0.173	0.178
26	13.25	175.56	0.249	0.235	0.175	0.179
27	13.75	189.06	0.249	0.241	0.188	0.187
28	14.25	203.06	0.249	0.257	0.191	0.187
29	14.75	217.56	0.249	0.257	0.193	0.187
30	15.25	232.56	0.249	0.257	0.200	0.187
31	15.75	248.06	0.249	0.257	0.205	0.207

[Table II.3.8.1] Summary: V_C / C_1, continued,

			V_c / C_1			
			FAST		GRADUAL	
NBB	c	c^2	JN19SRN	JN19LD	JN19SRN	JN19LD
32	16.25	264.06	0.249	0.257	0.208	0.207
33	16.75	280.56	0.249	0.257	0.218	0.207
34	17.25	297.56	0.249	0.257	0.224	0.207
35	17.75	315.06	0.249	0.257	0.232	0.207
36	18.25	333.06	0.249	0.257	0.239	0.220
37	18.75	351.56	0.249	0.257	0.242	0.226
38	19.25	370.56	0.249	dislocation*	0.246	0.231
39	19.75	390.06	0.249		0.249	0.241
40	20.25	410.06	0.249		0.257	0.251
41	20.75	430.56	0.249		0.257	0.256
42	21.25	451.56	0.249		0.257	0.259
43	21.75	473.06	0.249		0.257	0.273
44	22.25	495.06	0.249		0.257	0.273
45	22.75	517.56	Dislocation*		0.257	0.273
46	23.25	540.56			0.257	0.273
47	23.75	564.06			0.257	0.273
48	24.25	588.06			0.257	0.273
49	24.75	612.56			0.257	0.273
50	25.25	637.56			0.257	0.273

[Table II.3.8.1] Summary: V_C / C_1, continued,

			V_c / C_1			
			FAST		GRADUAL	
NBB	c	c^2	JN19SRN	JN19LD	JN19SRN	JN19LD
51	25.75	663.06			0.257	0.273
52	26.25	689.06			0.257	0.273
53	26.75	715.56			0.257	0.273
54	27.25	742.56			0.257	0.273
55	27.75	770.06			0.257	dislocation*
60	30.25	915.06			0.257	
61	30.75	945.56			Dislocation*	

* The fast running crack was arrested for a substantial amount of time after the emission of dislocation.

[Table II.3.8.2] Summary: Change in the "normalised" mechanical energy of the system as a function of crack length. See Fig. II.3.30-32.

JN19SRN: critical strain, ε_C= 0.0410, sample size: 79x135, c_o=9.75.

JN19LD: critical load, σ_C= 1.90, sample size: 79x135, c_o=9.75.

			GRADUAL	
NBB	c	c^2	JN19SRN	JN19LD
			$-\Delta E_{me}/\pi c^2\varepsilon^2 M^*$	$-\Delta E_{me}/\pi c^2\sigma^2$
19	9.75	95.06	0.000	0.000
20	10.25	105.06	1.072	1.109
21	10.75	115.56	1.159	1.224
22	11.25	126.56	1.247	1.326
23	11.75	138.06	1.326	1.411
24	12.25	150.06	1.414	1.494
25	12.75	162.56	1.501	1.578
26	13.25	175.56	1.594	1.661
27	13.75	189.06	1.695	1.752
28	14.25	203.06	1.814	1.850
29	14.75	217.56	1.967	1.962
30	15.25	232.56	2.047	2.181
31	15.75	248.06	2.199	2.307
32	16.25	264.06	2.347	2.409
33	16.75	280.56	2.458	2.470
34	17.25	297.56	2.641	2.536

[Table II.3.8.2] continued,

NBB	c	c^2	GRADUAL JN19SRN $-\Delta E_{me}/\pi c^2\varepsilon^2 M^*$	GRADUAL JN19LD $-\Delta E_{me}/\pi c^2\sigma^2$
35	17.75	315.06	2.715	2.816
36	18.25	333.06	2.924	2.994
37	18.75	351.56	3.037	3.160
38	19.25	370.56	3.253	3.329
39	19.75	390.06	3.409	3.545
40	20.25	410.06	3.601	3.683
41	20.75	430.56	3.786	3.897
42	21.25	451.56	3.929	4.065
43	21.75	473.06	4.165	4.325
44	22.25	495.06	4.289	4.488
45	22.75	517.56	4.504	4.768
46	23.25	540.56	4.706	4.939
47	23.75	564.06	4.912	5.228
48	24.25	588.06	5.061	5.413
50	25.25	637.56	5.467	5.926
51	25.75	663.06	5.838	6.030
52	26.25	689.06	5.953	6.440
53	26.75	715.56	6.197	6.699
55	27.75	770.06	6.621	7.200
56	28.25	798.06	7.072	7.447

[Table II.3.8.2] continued,

NBB	c	c^2	GRADUAL JN19SRN $-\Delta E_{me}/\pi c^2 \varepsilon^2 M^*$	GRADUAL JN19LD $-\Delta E_{me}/\pi c^2 \sigma^2$
57	28.75	826.56	7.203	7.711
58	29.25	855.56	7.594	7.959
59	29.75	885.06	7.658	8.219
60	30.25	915.06	8.096	8.478
61	30.75	945.56	8.363	8.738

Incipient Dislocation Generation at the Crack Tip.[12]

[12] The fast running crack was arrested for a substantial amount of time after the emission of the blunting dislocation.

[Table II.3.9] Summary. Comparison of the major simulations results concerning the magnitude of the terminal crack-tip velocity, V_T, the change in the mechanical energy of the system during the brittle propagation of the cleavage crack, ΔE_{me}, and theoretical predictions. See Fig. II.3.5-6, 9 and II.3.30-32.

RUN	NBB	e_c	s_1	s_{th1}	Δ%	V_c/C_1	c/c_o
JN7SRN	7	.0615	.01020	.01190	14.0%	.2460	2.47
JN13SRN	13	.0470	.00574	.00694	17.0%	.2389	2.19
JN19SRNFAST	19	.0410	.00498	.00528	5.7%	.2490	2.28
JN19SRNGRAD	19	.0410	.00442	.00528	16.3%	.2573	3.15

RUN	NBB	σ_c	s_2	s_{th2}	Δ%	V_c/C_1	c/c_o
JN7LD	7	3.37	33.34	35.68	6.5%	.2440	2.33
JN13LD	13	2.45	17.94	18.86	4.9%	.2538	2.78
JN19LDFAST	19	1.90	11.11	11.34	2.0%	.2570	2.03
JN19LDGRAD	19	1.90	10.00	11.34	11.8%	.2726	3.15

s_{th1} $\equiv \pi e^2 \equiv$ The theoretical slope of $-\Delta E_{me}$ vs c^2M^*.
s_1 $\equiv$ The slope of $-\Delta E_{me}$ vs c^2M^*.
s_{th2} $\equiv \pi\sigma^2 \equiv$ The theoretical slope of $-\Delta E_{me}$ vs c^2/M^*.
s_2 $\equiv$ The slope of $-\Delta E_{me}$ vs c^2/M^*.
c/c_o $\equiv$ The normalised crack length, where the fast running crack-tip was arrested by the emission of blunting dislocations.

[Table II.3.10A] The simulation results for the 2D-triangular modified Lennard-Jones solid, LJCOVa, with the angular resistance, a*=1.0, and a*=3.0. Initial crack half-length is, c_o=3.75, and the applied load is, S_a=3.00. Sample size is 39X65. Time interval=0.01. See Fig. II.3.7-8, 36.

		a*=1.00				a*=3.00			
NBB	c	V_c/C_1	M*	⊗	ΔE_{ke}	V_c/C_1	M*	⊗	ΔE_{ke}
9	4.75	.30	69.49	4.20	3.79	.34	77.88	4.51	1.91
10	5.25	.33	68.13	6.38	4.29	.37	77.29	6.32	2.23
11	5.75	.34	66.83	8.60	4.79	.39	76.35	8.54	2.62
12	6.25	.34	65.67	10.65	5.33	.40	76.27	11.07	3.06
13	6.75	.34	64.61	12.84	5.97	.42	75.77	13.87	3.57
14	7.25	.34	63.65	15.26	6.70	.43	75.27	16.99	4.15
15	7.75	.34	62.71	17.97	7.62	.44	74.80	20.22	4.75
16	8.25	.34	61.77	20.99	8.70	.45	74.31	23.65	5.42
17	8.75	.34	60.80	24.37	10.00	.45	73.85	27.43	6.09
18	9.25	.34	59.88	28.07	11.42	.45	73.31	31.69	6.88
19	9.75	.34	58.89	32.25	13.18	.45	72.75	36.05	7.55
20	10.25	.34	57.88	36.89	15.11	.45	72.20	40.81	8.62
21	10.75	.34	56.86	42.05	17.09	.45	71.54	45.72	9.66
22	11.25	.34	55.74	47.92	19.32	.45	70.83	51.09	10.81
23	11.75	.34	54.66	54.36	21.53	.45	70.04	56.99	12.08
24	12.25	.34	53.45	61.80	24.19	.45	69.17	63.51	13.49
25	12.75	.34	52.33	69.84	26.85	.45	68.12	70.94	15.16

[Table II.3.10A] continued,

		a*=1.00				a*=3.00			
NBB	c	V_C/C_1	M*	⊗	ΔE_{ke}	V_C/C_1	M*	⊗	ΔE_{ke}
26	13.25	.34	51.03	79.32	30.13	.45	67.05	79.08	16.89
27	13.75	.34	49.83	89.58	33.36	.45	65.79		18.94
28	14.25	.34	48.48	101.65	37.29	.45	64.45		21.19
29	14.75	.34	47.11	115.33	41.35	.45	63.14		23.47
30	15.25	.34	45.59	131.64	45.99	.45	61.66		26.13
31	15.75	.34	44.04	150.47	50.99	.45	60.12		28.99
32	16.25	.34	42.37	171.43	55.99	.45	58.56		32.05
33	16.75	.34	41.05	195.89	61.88	.45	56.96		35.37
34	17.25	.34			67.88	.45	55.35		38.89
35	17.75	.34			74.32	.45			

⊗ ≡ $(cV_C/C_1M^*)^2 \times 10^4$.
LJCOVa, a*=1.0: M=75.52, C_1=8.072: ΔE_{ke} vs ⊗ is linear.
LJCOVa, a*=3.0: M=87.50, C_1=8.725: ΔE_{ke} vs ⊗ is linear.

[Table II.3.10B] The simulation results for the 2D-triangular modified Johnson solid, JOHNCOVa, with the angular resistance, a*=0.30, a*=0.75, a*=1.0, and a*=3.0. Initial half-crack length is, c_o=3.75, and the applied load is, S_a=4.00. Sample size is 39X65. See Fig. II.3.7-8, 19.

		a*=0.30				a*=0.75			
NBB	c	V_c/C_1	M*	⊗	ΔE_{ke}	V_c/C_1	M*	⊗	ΔE_{ke}
08	4.25	.19	60.56	1.78	2.62	.20	63.59	1.79	1.85
09	4.75	.23	59.87	3.27	3.77	.25	63.14	3.48	2.68
10	5.25	.25	59.20	5.07	4.99	.28	62.65	5.51	3.63
11	5.75	.27	58.39	7.28	6.43	.30	62.04	7.73	4.74
12	6.25	.29	57.64	9.89	7.88	.32	61.46	10.33	5.88
13	6.75	.30	56.80	12.54	9.57	.33	60.79	13.59	7.22
14	7.25	.30	55.95	15.31	11.53	.34	60.12	17.01	8.77
15	7.75	.30	55.14	18.26	13.64	.35	59.48	21.27	10.39
16	8.25	.30	54.36	21.57	16.22	.36	58.83	25.49	12.38
17	8.75	.30	53.57	24.98	18.84	.37	58.23	30.25	14.39
18	9.25	.31	52.75	28.79	22.20	.37	57.63	35.27	16.83
		Dislocation Emission				----	-----	------	-----
19	9.75	.26	51.71	24.58	25.94	.37	57.00	40.49	19.39
20	10.25	.24	50.47	24.58	30.15	.37	56.29	46.38	22.31
21	10.75	.32	49.50	48.61	35.16	.38	55.52	52.72	25.46
22	11.25	.35	48.11	72.07	38.39	.38	54.65	59.59	28.87
23	11.75	.33	46.99	69.33	43.28				

[Table II.3.10B] continued,

		a*=0.30			
NBB	c	V_C/C_1	M*	⊗	ΔE_{ke}
24	12.25	.32	45.86	75.58	48.52
25	12.75	.32	44.57	82.48	55.39
26	13.25	.35	44.37	125.80	62.77
27	13.75	.37	42.37	162.20	66.81
28	14.25	.35	41.24	146.30	75.91
29	14.75	.38	40.03	199.70	90.11
30	15.25	.38	39.02	235.30	100.12
31	15.75	.36	37.96	221.90	108.19
32	16.25	.38	36.82	281.30	118.95

		a*=1.00				a*=3.00			
NBB	c	V_C/C_1	M*	⊗	ΔE_{ke}	V_C/C_1	M*	⊗	ΔE_{ke}
09	4.75	.23	64.96	3.89	2.12	.27	79.86	2.62	1.63
10	5.25	.29	64.56	5.87	2.90	.31	79.37	4.21	2.09
11	5.75	.30	64.13	8.23	3.73	.33	78.68	5.89	2.72
12	6.25	.33	63.62	10.76	4.75	.35	78.00	7.87	3.39
13	6.75	.33	63.03	13.88	5.90	.36	77.25	10.12	4.23
14	7.25	.35	62.63	17.37	7.25	.37	76.50	12.56	4.96
15	7.75	.37	61.83	21.51	8.66	.38	75.76	15.27	5.94
16	8.25	.37	61.24	26.07	10.39	.39	75.08	18.37	7.06

[Table II.3.10B] continued,

		a*=1.00				a*=3.00			
NBB	c	V_C/C_1	M*	⊗	ΔE_{ke}	V_C/C_1	M*	⊗	ΔE_{ke}
17	8.75	.39	60.68	31.06	12.22	.40	74.43	21.67	8.38
18	9.25	.39	60.13	36.74	14.36	.40	73.80	25.39	9.97
19	9.75	.37	59.54	42.94	16.90	.41	73.16	29.57	11.89
20	10.25	.42	58.96	49.32	19.42	.41	72.55	34.21	13.06
21	10.75	.39	58.26	56.68	22.45	.42	71.88	38.71	15.73
22	11.25	.42	57.52	65.45	25.49	.42	71.07	44.20	18.20
23	11.75	.39	56.68	73.47	29.20	.42	70.25	48.18	20.79
24	12.25	.42	55.81	83.47	32.97	.43	69.42	56.78	23.35
25	12.75	.42	54.87	93.01	36.95	.43	68.42	61.43	26.53
26	13.25	.42	53.89	106.13	41.66	.43	67.35	71.56	29.78
27	13.75	.42	52.86	126.51	46.25	.43	66.30	79.90	33.22
28	14.25	.42	51.77	131.71	51.69	.43	65.07	89.50	37.07
29	14.75	.44	50.72	149.66	57.02	.43	63.79	99.78	41.28

⊗ ≡ $(cV_C/C_1M^*)^2 \times 10^4$.
JOHNCOVa, a*=0.30: M=62.0, C_1=7.328: ΔE_{ke} vs ⊗ is linear.
JOHNCOVa, a*=0.75: M=64.3, C_1=7.460: ΔE_{ke} vs ⊗ is linear.
JOHNCOVa, a*=1.00: M=65.0, C_1=7.503: ΔE_{ke} vs ⊗ is linear.
JOHNCOVa, a*=3.00: M=80.0, C_1=8.324: ΔE_{ke} vs ⊗ is linear.
Slope=4070, S_a=4.0 → K=12.72.

[Table II.3.10C] The simulations results for the 2D-triangular modified Johnson solid, JOHNCOVa, with the angular resistance, a*=0.30, a*=0.75, a*=1.0, and a*=3.0, and the 2D-triangular Lennard-Jones solid, LJCOVa, with a*=0.5 and a*=3.0. The change in the mechanical energy, $-\Delta E_{me} \equiv \Delta(E_{el}-W)$, is given with respect to c=4.25. Initial half crack-length is, c_o=3.75, and the applied load is, (S_a=3.00 for LJCOVa, and S_a=4.00 for JOHNCOVa). Sample size is 39X65. See Fig. II.3.7-8.

			LJCOVa		JOHNCOVa			
NBB	c	⊕	a*= 0.5	a*=3.0	a*=0.75	a*=1.0	a*=3.0	a*=5.0
09	4.75	2.832	1.471	1.290	1.824	1.568	1.308	1.19
10	5.25	3.467	2.968	2.606	3.771	3.303	2.762	2.38
11	5.75	4.168	4.621	3.998	5.881	5.173	4.382	3.61
12	6.25	4.938	6.457	5.076	8.022	6.194	6.065	4.86
13	6.75	5.575	8.338	6.944	10.365	9.345	7.905	6.14
14	7.25	6.683	10.492	8.524	12.913	11.697	9.634	7.45
15	7.75	7.661	12.831	10.126	15.537	14.005	11.613	8.81
16	8.25	8.713	15.318	11.792	18.529	16.748	13.730	10.23
17	8.75	9.838	18.018	13.464	21.539	19.669	16.053	11.72
18	9.25	11.040	20.851	15.257	24.977	22.808	18.640	13.29
19	9.75	12.320	23.869	17.123	28.536	26.346	21.427	14.96
20	10.25	13.670	27.078	18.999	32.454	29.871	24.329	16.68
21	10.75	15.110	30.557	21.039	36.606	33.896	27.399	18.58
22	11.25	16.640	34.117	23.185	41.013	38.127	30.878	20.60

[Table II.3.10C] continued,

			LJCOVa		JOHNCOVa		
NBB	c	⊕	a*= 0.5	a*=3.0	a*=0.75	a*=3.0	a*=5.0
23	11.75	18.250	38.499	25.458	42.643	34.468	22.65
24	12.25	19.950	42.901	27.863	47.413	38.023	24.82
25	12.75	21.750	47.693	30.542	52.400	42.202	27.10

⊕ ≡ -lncos($\pi c/2w$) x 100.
2w ≡ The width of the specimen = 63.
LJCOVa a*=0.50 : M_o=88.2, M=74.70 at S_a=3.0.
LJCOVa a*=1.00 : M=75.52 at S_a=3.0.
LJCOVa a*=3.00 : M_o=110.0, M=87.50 at S_a=3.0.
LJCOVa a*=5.00 : M_o=123.0, M=100.4 at S_a=3.0.
JOHNCOVa a*=0.75 : M=64.00 at S_a=4.0.
JOHNCOVa a*=1.00 : M_o=72.3, M=64.13 at S_a=4.0.
JOHNCOVa a*=3.00 : M_o=90.5, M=79.20 at S_a=4.0.

[Table II.3.10D] The simulation results for the 2D-triangular modified Lennard-Jones solid, LJCOVa, with the angular resistance, a* = 2.0, 4.0, 6.0, 8.0, and 10.0. Initial half crack-length is, c_o=3.75, and the applied load is, S_a=3.00. Sample size is 39X65. Time interval is 0.01. See Fig. II.3.8.

		Δt between breaking of two consecutive crack-tip bonds for the LJCOVa solid with				
NBB	c	**a*=2.0**	**a*=4.0**	**a*=6.0**	**a*=8.0**	**a*=10.0**
08	4.25	11	11	6	5	4
09	4.75	10	10	7	6	4
10	5.25	9	10	6	5	5
11	5.75	11	10	7	6	5
12	6.25	11	9	7	5	4
13	6.75	13	10	7	6	5
14	7.25	13	9	7	6	4
15	7.75	13	10	7	7	5
16	8.25	14	9	6	6	6
17	8.75	14	8	7	7	5
18	9.25	12	8	7	6	6
19	9.75	12	8	6	6	5
20	10.25	12	8	7	6	6
21	10.75	11	9	7	6	5
22	11.25	12	8	7	6	5
23	11.75	11	9	7	6	5
24	12.25	10	9	8	6	5

[Table II.3.10D] continued,

NBB	c	Δt between breaking of two consecutive crack-tip bonds for the LJCOVa solid with a*=2.0	a*=4.0	a*=6.0	a*=8.0	a*=10.0
25	12.75	11	10	8	7	5
26	13.25	12	9	8	6	6
27	13.75	11	9	8	7	6
28	14.25	10	9	8	7	6
29	14.75	11	9	9	8	7
30	15.25	11	8	8	7	7
31	15.75	11	9	8	8	6
32	16.25		9	9	7	7
34	17.25		9	8	7	7
36	18.25		9	8	7	6
37	18.75		9	8	8	7
38	19.25		9	8	7	7
40	20.25		9	8	7	7
41	20.75		9	8	8	7
42	21.25		9	9	7	6
43	21.75		9	8	8	7
44	22.25		9	7	7	7
47	23.75		9	7	8	7
V_T		2.20	2.84	3.23	3.55	4.23

[Table III.4A1] Temperature K_BT= 0 ε_o, LJCOVa.2 a*=.2, sample size: 32x19, c_o=3.75d, time interval is 0.01, critical load, σ_C =2.10. See Fig. III.4A1.

TIME	LHSCT BEHAVIOR			RHSCT BEHAVIOR		
STEP	NNBB	CT		NNBB	CT	
5744	1	\	SH	1	/	SH
5783	2	/	SH	2	\	SH
5823	3	\	SH	3	/	SH
5892	5	\	SH	5	/	SH
5925	6	/	SH	6	\	SH
5965	7	\	SH	7	/	SH
5996*	8	/	SH	8	\	SH
6062	10	/	SH	10	\	SH
6092	11	\	SH	11	/	SH
6143	13	\	SH	13	/	SH
6176	15	\	SH	15	/	SH
6228	17	\	SH	17	/	SH
6278	18	/	SH	18	\	SH
6328	20	/	SH	20	\	SH
6355*	21	\	SH	21	/	SH
6376	22	/	SH	22	\	SH

BEHAVIOR: The fracture is BRITTLE.

SH ≡ Sharp.
* ≡ Picture is provided, see Fig. III.4A1.

[Table III.4A2] Temperature K_BT= 0.02 ε_o, LJCOVa.2 a*=.2, sample size: 32x19, c_o= 3.75d, time interval is 0.01, critical load, σ_C = 1.90. See Fig. III.4A2.

TIME STEP	LHSCT BEHAVIOR NNBB		CT	RHSCT BEHAVIOR NNBB		CT
13012	0	/	SH	1	/	SH
13103*	1	\	SH	2	\	SH
13142	1	\	SH	3	/	SH
13244	3	\	SH	4	\	SH
13286	4	/	SH	5	/	SH
13386*	7	\	SH	8	\	SH
13406	7	\	Xup	9	/	SH
13454	8	/	Xup & Xdown	10	\	Xup
13474	9	\	Xup & Xdown	10	\	Xup & Xdown
13506	10	/	Xup	11	/	Xdown
13528	11	\	Xup	11	/	Xdown
13563	12	/	SH	13	\	Xup
13576	13	\	SH	13	/	SH
13606*	14	/	SH	15	/	Xup & Xdown
13629	15	\	SH	16	\	Xup & Xdown

BEHAVIOR: <u>The fracture is BRITTLE.</u>

SH ≡ Sharp.
Xup ≡ A disturbance at the upper corner of the CT which may result in the emission of a blunting dislocation upward.
Xdown ≡ A disturbance at the lower corner of the CT which may result in the emission of a blunting dislocation downward.
* ≡ Picture is provided, see Fig. III.4A2.

[Table III.4A3] Temperature K_BT= 0.02 ε_o, LJCOVa.2 a*=.2, sample size:32x19, c_o= 3.75d, time interval is 0.01. Applied load σ_a=2.0 > critical load σ_c=1.90. See Fig. III.4A3.

TIME	LHSCT BEHAVIOR			RHSCT BEHAVIOR		
STEP	NNBB	CT		NNBB	CT	
12735*	1	\	SH	1	/	SH
12832*	4	/	SH	2	>	Xdown
12981*	8	/	SH	2	>	Xdown→dislocation
13000	9	\	Xup	2	>	dislocation downwards
13106*	13	\	SH	2	>	lowermost surface slips
13202	16	/	Xup	2	>	Xup

BEHAVIOR: <u>The fracture is BRITTLE</u> : The LHSCT propagates brittlely, while the RHSCT behaves in a ductile manner.

SH ≡ Sharp.
Xup ≡ A disturbance at the upper corner of the CT which may result in the emission of a blunting dislocation upward.
Xdown ≡ A disturbance at the lower corner of the CT which may result in the emission of a blunting dislocation downward.
* ≡ Picture is provided, see Fig. III.4A3.

[Table III.4A4] Temperature $K_BT=0.046\varepsilon_o$, LJCOVa.2 a*=.2, sample size: 32x19, c_o= 3.75d, time interval is 0.01, critical load, σ_C = 1.90. See Fig. III.4A4.

TIME	LHSCT BEHAVIOR			RHSCT BEHAVIOR		
STEP	NNBB	CT		NNBB	CT	
13338	1	\	SH	0	\	SH
13420	2	/	SH	0	\	SH
13502*	3	\	SH	0	\	Xup
13584	5	\	Xup	0	\	Xup
13621	5	Dislocation Upwards		1	/	SH
13683	5	<	Blunted	2	\	Xdown
13736	5	<	Blunted	3	/	SH
13758	5	<	Blunted	4	\	SH
13797	5	<	Blunted	5	/	SH
13821*	5	Uppermost Surface Slips		5	/	SH
13897	8	<	Xup	6	\	SH
13921*	8	Uppermost Surface Slips		7	/	SH

BEHAVIOR: <u>The fracture is BRITTLE</u> : The RHSCT propagates brittlely, while, the LHSCT behaves in a ductile manner.

SH ≡ Sharp.
Xup ≡ A disturbance at the upper corner of the CT which may result in the emission of a blunting dislocation upward.
Xdown ≡ A disturbance at the lower corner of the CT which may result in the emission of a blunting dislocation downward.
* ≡ Picture is provided, see Fig. III.4A4.

[Table III.4A5] Temperature $K_BT=0.056\varepsilon_o$, LJCOVa.2 a*=.2, sample size: 32x19, c_o= 3.75d, time interval is 0.01, critical load, σ_C= 1.80. See Fig. III.4A5.

TIME	LHSCT BEHAVIOR		RHSCT BEHAVIOR	
STEP	NNBB	CT	NNBB	CT
12669*	1	\ SH	0	> Blunted, Hole Down
12703	2	/ Xdown	0	> Blunted, Hole Down
12722	2	/ SH	0	> Blunted, Hole Down
12753	1	Healed→ SH	0	> Blunted, Hole Down
12801	1	\ SH	0	> Blunted, Hole Down
12846*	2	SH → Blunted	0	> Hole is Propagating
12901	2	< Blunted	0	Dislocation Downwards
12945	2	< Blunted		Propagated Hole & Emitted Dislocation
12984*	2	Dislocation Downwards		

BRITTLE TO DUCTILE TRANSITION? The RHSCT behaves in a ductile manner, while the LHSCT is blunted and emitted a dislocation after breaking two crack-tip bonds.

SH ≡ Sharp.
Xup ≡ A disturbance at the upper corner of the CT which may result in the emission of a blunting dislocation upward.
Xdown ≡ A disturbance at the lower corner of the CT which may result in the emission of a blunting dislocation downward.
* ≡ Picture is provided, see Fig. III.4A5.

[Table III.4A5*] Temperature $K_BT=.056\varepsilon_o$, LJCOVa.2 a*=.2, sample size: 32x19, c_o= 3.75d, time interval is .01, applied load σ_a=1.90 > critical load σ_c=1.80: *OVERLOADED*. See Fig. III.4A5*.

TIME	LHSCT BEHAVIOR			RHSCT BEHAVIOR		
STEP	NNBB	CT		NNBB	CT	
12558*	0	/	SH	0	>	Blunted, <> down
12571	1	\	SH	0	>	Blunted, <> down
12656	2	/	SH	0	>	Blunted, <> down
12697	2	<	Blunted, Xdown	0	>	Blunted, <> prop.
12796*	2	<	Blunted, Xdown	0	>	<> is also Blunted
12826	2	<	Blunted, Xdown	0	2nd <> is opened down	
12930*	2	<	—| Down	0	2nd <> is propagating	
13062	2	lowermost surface slips				
13088	3	\	Propagation is resumed.			
13149*	5	\	SH	0	2nd <> is propagating	

BRITTLE-TO-DUCTILE TRANSITION? The fracture's behavior is different from that of III.4A5. After breaking 2 CT bonds, the LHSCT emits a blunting dislocation downwards, but the RHSCT propagates by the process of hole growth.

—| ≡ Emitted Dislocation from the LHSCT.
<> ≡ Hole.
SH ≡ Sharp.
Xup ≡ A disturbance at the upper corner of the CT which may result in the emission of a blunting dislocation upward.
Xdown ≡ A disturbance at the lower corner of the CT which may result in the emission of a blunting dislocation downward.
* ≡ Picture is provided, see Fig. III.4A5*.

[Table III.4A6] Temperature $K_BT=0.060\varepsilon_o$, LJCOVa.2 a*=.2, sample size: 32x19, c_o= 3.75d, time interval is 0.01, critical load, σ_C= 1.80. See Fig. III.4A6.

TIME	LHSCT BEHAVIOR			RHSCT BEHAVIOR		
STEP	NNBB		CT	NNBB		CT
13548*	1	\	SH	1	/	SH
13659	0	/	SH, Healed	2	\	SH
13751	2	/	SH, Xdown	2	\	SH, Xup
13781	2	/	SH, Xdown	3	>	Blunted, |— UP
13808	1	\	SH, Healed	3	>	|— Moving UP
13851	2	<	Blunted, Xdown	3	>	|— Moving UP
13888*	2	<	Blunted, —|			" " "
			Moving Downwards			
13950*	2	<	—| → <>			" " "
14027	2	<	Blunted CT & <>			Uppermost surface slips
14130*	2	<	<> is propagated			2nd |— Emitted

BRITTLE-TO-DUCTILE TRANSITION? The RHSCT is blunted and behaves in a ductile manner but only after 3 RHSCT bonds are broken. Initially the LHSCT behaved similar to RHSCT, but finally it is propagated by the process of "hole" growth.

|— ≡ Emitted Dislocation from the RHSCT.
—| ≡ Emitted Dislocation from the LHSCT.
<> ≡ Hole.
SH ≡ Sharp.
Xup ≡ A disturbance at the upper corner of the CT which may result in the emission of a blunting dislocation upward.
Xdown ≡ A disturbance at the lower corner of the CT which may result in the emission of a blunting dislocation downward.
* ≡ Picture is provided, see Fig. III.4A6.

[Table III.4A7] Temperature $K_BT=0.060\varepsilon_o$, LJCOVa.2 a*=.2, sample size: 32x19, c_o= 3.75d, time interval is 0.01, critical load, σ_C = 1.80. The history of the run is different from that of III.4A6. See Fig. III.4A7.

TIME	LHSCT BEHAVIOR			RHSCT BEHAVIOR		
STEP	NNBB		CT	NNBB		CT
11878*	1	\	SH	1	/	SH
11912	2	/	SH	1	/	SH
11951	3	\	SH, Xdown	1	/	SH
11972	4		Getting Blunted	1	/	SH
12004	4		Getting Blunted	1	/	SH
12049*	4		Getting Blunted	2	>	Getting Blunted
12101	4	<	Blunted, —| down	2	>	Blunted, |—down
12223*	4	<	—| Moving Down	2	>	|— Moving Down
12365*	4	<	—| moved to the lowermost surface.	2	>	|— moved to the lowermost surface.

BRITTLE-TO-DUCTILE TRANSITION? The RHSCT is blunted and behaves in a ductile manner but only after 2 RHSCT bonds are broken. The LHSCT is also blunted and behaves in a ductile manner but only after 4 RHSCT bonds are broken.

|— ≡ Emitted Dislocation from the RHSCT.
—| ≡ Emitted Dislocation from the LHSCT.
SH ≡ Sharp.
Xdown ≡ A disturbance at the lower corner of the CT which may result in the emission of a blunting dislocation downward.
* ≡ Picture is provided, see Fig. III.4A7.

[Table III.4A8] Temperature $K_BT=.0628\varepsilon_o$, LJCOVa.2 a*=.2, sample size: 32x19, c_o= 3.75d, time interval is 0.01, critical load, σ_c = 1.80. See Fig. III.4A8.

TIME	LHSCT BEHAVIOR		RHSCT BEHAVIOR		
STEP	NNBB	CT	NNBB		CT
12158*	0	Getting Blunted	1	/	SH
12278	0	Xdown, " "	2	\	SH
12321	0	Blunted, A —| is emitted down.	2	\	SH
12361*	0	The emitted —| is gliding downwards.	2	\	SH
12387	0	" "	3	/	SH
12399	0	" "	4	\	SH
12454	0	—| is moved to the lowermost surface.	4	\	SH
12499*	0	The CT is blunted & lowermost surface slips.	6	\	SH

BRITTLE-TO-DUCTILE TRANSITION? The LHSCT is blunted and behaves in a ductile manner, while, the RHSCT is remained sharp and propagated brittlely.

—| ≡ Emitted Dislocation from the LHSCT.
SH ≡ Sharp.
Xup ≡ A disturbance at the upper corner of the CT which may result in the emission of a blunting dislocation upward.
Xdown ≡ A disturbance at the lower corner of the CT which may result in the emission of a blunting dislocation downward.
* ≡ Picture is provided, see Fig. III.4A8.

[Table III.4A9] Temperature $K_BT=.0625\varepsilon_o$, LJCOVa.2 a*=.2, sample size: 32x19, c_o= 3.75d, time interval is 0.01, critical load, σ_C = 1.80. The history of the run is different from that of the III.4A8 run.See Fig. III.4A9.

TIME	LHSCT BEHAVIOR			RHSCT BEHAVIOR		
STEP	NNBB		CT	NNBB		CT
14457	1	\	SH	0	\	SH
14651*	0	/	Rehealed —|down	1	>	Xup
14675*	2	<	Blunted, Xdown	1	>	Xup, Blunted
14754	2	<	—| Down.	1	>	Xup, Xdown.
14819*	2	<	—| → <>?	1	/	Resharpening
14902	2	<	—| Moving down	3	/	SH
15003*	2	<	—| Moved to the Lowermost Surface→ Slip.	6	\	SH
15129	2	<	2nd —| is Emitted.	7	>	Xup, Blunted

BRITTLE-TO-DUCTILE TRANSITION? The LHSCT is blunted and behaves in a ductile manner but only after 2 crack-tip bonds are broken, while, the RHSCT is remained sharp and propagated brittlely.

—| ≡ Emitted Dislocation from the LHSCT.
<> ≡ Hole.
SH ≡ Sharp.
Xup ≡ A disturbance at the upper corner of the CT which may result in the emission of a blunting dislocation upward.
Xdown ≡ A disturbance at the lower corner of the CT which may result in the emission of a blunting dislocation downward.
* ≡ Picture is provided, see Fig. III.4A9.

[Table III.4A10] Temperature $K_BT=0.075\varepsilon_o$, LJCOVa.2 a*=.2, sample size: 32x19, c_o= 3.75d, time interval = 0.01, critical load, σ_c=1.80. See Fig. III.4A10.

TIME	LHSCT BEHAVIOR			RHSCT BEHAVIOR		
STEP	NNBB	CT		NNBB	CT	
22282*	0	<	Blunting, Xdown	0	<	Blunting, Xdown
22447	0	<	Blunted, —|down	0	>	Resharpening
22598	0	<	—| Moving Down.	0	\	SHARPENED.
22639*	0	<	—| Moved to the Lowermost Surface→ Slip.	0	\	Sharp.
22732	0	<	Blunted / Slip	1	/	Sharp.
22803	0		Slip	4	\	Sharp.
22938	0		Slip	4	\	SH, |— Down
22995	1		Slip	4	>	Blunted, |—
23024	2		Slip	4	>	Blunted, Slip
23463*						

DUCTILE. The LHSCT is blunted and behaves in a ductile manner. The RHSCT remained inactive till the emitted dislocation from the LHSCT glided to the lower surface of the specimen.

|— ≡ Emitted Dislocation from the RHSCT.
—| ≡ Emitted Dislocation from the LHSCT.
<> ≡ Hole.
SH ≡ Sharp.
Xdown ≡ A disturbance at the lower corner of the CT which may result in the emission of a blunting dislocation downward.
* ≡ Picture is provided, see Fig. III.4A10.

[Table III.4A] **SUMMARY**: III.4A SERIES; Brittle-to-Ductile Transition Temperature in the covalently modified Lennard-Jones solid, LJCOVa.2 a*=.2, c_o=3.75d, sample size: 32x19, time interval = 0.01.

RUN	K_BT (ε_o)	FINAL STEP	CRITICAL STRESS	LHSCT BB,CT	RHSCT BB,CT	CONCLUSION BEHAVIOR
III.4A1	.0000	6376	2.1	22, /	22, \	BRITTLE
III.4A2	.0200	13629	1.9	15, \	16, \	BRITTLE
III.4A3	.0200	13202	2.0*	16, /	2, >, |—	BRITTLE
III.4A4	.0460	13921	1.9	8, <, —|	7, /	BRITTLE
III.4A5	.0560	12984	1.8	2, <, —|	0, >, |—	BDT
III.4A5*	.0560	13149	1.9*	5, \, —|	0, >, <>	BDT
III.4A6	.0600	14130	1.8	2, <, —|	3, >, |—	BDT
III.4A7	.0600	12365	1.8	4, <, —|	2, >, |—	BDT
III.4A8	.0628	12499	1.8	0, <, —|	6, \	BDT
III.4A9	.0625	15129	1.8	2, <, —|	7, >	BDT
III.4A10	.0750	22639	1.8	0, <, —|	0, \	DUCTILE

Brittle-to-Ductile Transition, BDT, is gradual (soft).

* ≡ Overloaded runs
/ or \ ≡ Sharp CT.
< ≡ Blunted LHSCT.
> ≡ Blunted RHSCT.
|— ≡ Emitted Dislocation from the RHSCT.
—| ≡ Emitted Dislocation from the LHSCT.
BDT ≡ Brittle-to-Ductile TRANSITION.

[Table III.4B1] Temperature $K_BT=0.0193\varepsilon_o$, LJCOVa.2 a*=.2, sample size: 64x39, c_o= 3.75d, time interval = 0.01, critical load, σ_c = 2.40. See Fig. III.4B1.

TIME	LHSCT BEHAVIOR			RHSCT BEHAVIOR		
STEP	NNBB	CT		NNBB	CT	
10816	0	/	SH	1	/	SH
10981	1	\	SH	4	\	SH
11087*	4	/	SH	7	/	SH
11263*	9	\	SH	7	>	|—— Down.
11400	13	\	SH	8	>	|—UP, |—Down
11537*	18	/	SH	8	>	|—UP, |—Down
11592	20	/	SH	8		Lower Surface Slips
11618	21	\	SH	8	>	|—UP, $SLIP_{down}$
11691	23	\	SH	9		Upper Surface Slips
11700*	24	/	SH	9	/	$SLIP_{up}$. $SLIP_{down}$

BRITTLE. The LHSCT propagated brittlely and remained sharp throughout the run. The RHSCT, also, propagated brittlely, but after 7 crack-tip bonds were broken, it was arrested by the emission of a pair of blunting dislocations up and down towards the loaded surface of the sample.

|— ≡ Emitted Dislocation from the RHSCT.
SH ≡ Sharp.
* ≡ Picture is provided, see Fig. III.4B1.

[Table III.4B2] Temperature $K_BT=0.0680\varepsilon_o$, LJCOVa.2 a*=.2, sample size: 64x39, c_o= 3.75d, time interval = 0.01, critical load, σ_c = 2.20. See Fig. III.4B2.

TIME	LHSCT BEHAVIOR			RHSCT BEHAVIOR		
STEP	NNBB		CT	NNBB		CT
9456	0	/	SH	1	/	SH
9481*	1	<	Xup, Blunting	2	\	SH
9528	1	<	Xup, Blunting	3	/	SH
9569	1	<	Blunted	4	>	Blunting
9602*	1	<	Blunted,—| up	4	>	Blunted, <>down.
9701*	1	<	Blunted,—| up	4	>	Blunted, <>down.
9845	1	<	Blunted,—| up	4	>	Blunted, <>down,
						<> Blunted, |—down.
9822*	1	<	—| Moving Up	4	>	<>, |— Moving Down
10000			—| Moving Up			|— Moving Down
		<	Crack Blunted.			Crack Blunted, <>Blunted

BRITTLE-TO-DUCTILE TRANSITION? The LHSCT is blunted and behaves in a ductile manner. The RHSCT is also blunted and emitted a blunting dislocation downwards, but only after three crack-tip bonds are brittlely broken.

|— ≡ Emitted Dislocation from the RHSCT.
—| ≡ Emitted Dislocation from the LHSCT.
<> ≡ Hole.
SH ≡ Sharp.
Xup ≡ A disturbance at the upper corner of the CT which may result in the emission of a blunting dislocation upward.
* ≡ Picture is provided, see Fig. III.4B2.

[Table III.4B3] Temperature $K_BT=0.0904\varepsilon_o$, LJCOVa.2 a*=.2, sample size: 64x39, c_o= 3.75d, time interval = 0.01, critical load, σ_c = 2.00. See Fig. III.4B3.

TIME	LHSCT BEHAVIOR			RHSCT BEHAVIOR		
STEP	NNBB		CT	NNBB		CT
8600	0	/	SH, Xup	0	\	SH
8621*	1	<	Blunting, Xup	1	/	SH
8674	1	<	—| up, Blunted	2	\	SH, Xup
8730	1	<	—| up, Blunted	3	>	Blunted
8908	1	<	—| up, Blunted	3	>	|—up, Blunted
8994*	1	<	—| up, Blunted	3	>	|—up, Blunted

BRITTLE-TO-DUCTILE TRANSITION? The LHSCT is blunted and behaves in a ductile manner, while, the RHSCT is, also, blunted and emitted a blunting dislocation, but after 3 crack-tip bonds are broken.

|— ≡ Emitted Dislocation from the RHSCT.
—| ≡ Emitted Dislocation from the LHSCT.
SH ≡ Sharp.
Xup ≡ A disturbance at the upper corner of the CT which may result in the emission of a blunting dislocation upward.
* ≡ Picture is provided, see Fig. III.4B3.

[Table III.4B3*] Temperature $K_BT=0.0892\varepsilon_o$, LJCOVa.2 a*=.2, sample size: 64x39, c_o= 3.75d, time interval = 0.01, applied load σ_a = 2.10 > critical load σ_c= 2.0: "*OVERLOADED*". See Fig. III.4B3*.

TIME	LHSCT BEHAVIOR			RHSCT BEHAVIOR		
STEP	NNBB		CT	NNBB		CT
8618*	0	/	SH	1	/	SH
8631	1	<	Xup	2	\	SH
8663	1	<	Xup	2	>	Xup, Blunting CT
8689	1	<	Blunted	3	>	Xup, Blunting CT
8731	1	<	—| up, Blunted	3	>	Xup, Blunting CT
8828*	1	<	—| up, Blunted	3	>	|— up, CT Blunted
8850*	1	<	—| up, Blunted	3	/	|— Being Absorbed
8901*	1	<	—| up, Blunted	3	>	|— up, CT Blunted
9000*	1	<	—| up, Blunted	3	>	|—up & |—down.

BRITTLE-TO-DUCTILE TRANSITION? The LHSCT is blunted and behaves in a ductile manner, while, the RHSCT is, also, blunted and emitted a blunting dislocation, but after 3 crack-tip bonds are broken.

\|— ≡ Emitted Dislocation from the RHSCT.
—\| ≡ Emitted Dislocation from the LHSCT.
SH ≡ Sharp.
Xup ≡ A disturbance at the upper corner of the CT which may result in the emission of a blunting dislocation upward.
* ≡ Picture is provided, see Fig. III.4B3*.

[Table III.4B4] Temperature $K_BT=0.105\varepsilon_o$, LJCOVa.2 a*=.2, sample size: 64x39, c_o= 3.75d, time interval is 0.01, critical load, σ_c = 1.80. See Fig. III.4B4.

TIME	LHSCT BEHAVIOR			RHSCT BEHAVIOR		
STEP	NNBB		CT	NNBB		CT
9400*	0	<	Xdown	0	>	Xdown
9618*	0	<	Xdown	0	\	SHARPENED
10000*	0	<	—| Moving Down	0	\	SH
10146*	0	<	—| Moving Down	0	\	SH

DUCTILE. The LHSCT emitted a blunting dislocation downwards, and as a result, it is blunted. The RHSCT, on the other hand, remained inactive throughout the run.

|— ≡ Emitted Dislocation from the RHSCT.
SH ≡ Sharp.
Xdown ≡ A disturbance at the lower corner of CT which may result in the emission of a blunting dislocation downward.
* ≡ Picture is provided, see Fig. III.4B4.

[Table III.4B] **SUMMARY**: III.4B SERIES; Brittle-to-Ductile Transition Temperature in the covalently modified Lennard-Jones solid, LJCOVa.2 a*=.2, c_o=3.75d, sample size: 64x39, time interval = 0.01.

RUN	K_BT (ε_o)	FINAL STEP	CRITICAL STRESS	LHSCT BB,CT	RHSCT BB,CT	CONCLUSION BEHAVIOR
III.4B1	.0193	11715	2.4	24, \	10, |—	BRITTLE
III.4B2	.0680	10000	2.2	1,<,—|	4,>,|—	BDT
III.4B3	.0900	8955	2.0	1,<,—|	3,>,|—	BDT
III.4B4	.1060	10000	1.8	0,<,—|	inactive	DUCTILE

Brittle-to-Ductile transition, BDT, is gradual (soft).

/ or \ ≡ Sharp CT.
< ≡ Blunted LHSCT.
> ≡ Blunted RHSCT.
|— ≡ Emitted Dislocation from the RHSCT.
—| ≡ Emitted Dislocation from the LHSCT.
BDT ≡ Brittle-to-Ductile TRANSITION.

[Table III.5] **Summary**. The simulations results of the search for the brittle-to-ductile transition temperature in III.4A and III.4B series are summarised and compared to each other.

K_BT	CRITICAL LOAD		FRACTURE BEHAVIOR		RUN	
(ε_o)	III.4A	III.4B	III.4A	III.4B	III.4A	III.4B
0.0000	2.1		B		4A1	
0.0200	1.9	2.4	B	B	4A2	4B1
0.0460	1.9		B		4A4	
0.0560	1.8		BDT		4A5	
0.0600	1.8		BDT		4A6	
0.0628	1.8		BDT		4A8	
0.0680		2.2		BDT		4B2
0.0750	1.8		D		4A10	
0.0904		2.0		BDT		4B3
0.1050		1.8		D		4B4

B ≡ BRITTLE.
D ≡ DUCTILE.
BDT ≡ BRITTLE-TO-DUCTILE TRANSITION.

[Table III.6A1] Temperature $K_BT=0.0193\varepsilon_o$, COR.LJCOVa.2, sample size: 64x39, c_o= 3.75d, time interval = 0.01, critical load, σ_c = 2.30. See Fig. III.6A1.

TIME	LHSCT BEHAVIOR			RHSCT BEHAVIOR		
STEP	NNBB	CT		NNBB	CT	
10500	0	/	SH	0	\	SH
10543	1	\	SH	0	\	SH
10599*	1	\	SH	1	/	SH
10725	2	/	SH	2	\	SH
10744	2	/	SH	3	/	SH
10789	4	/	SH	3	/	SH
10826	5	\	SH	4	\	SH
10891	6	/	SH	6	\	SH
11025	10	/	SH	10	\	SH
11083*	12	/	SH	12	\	SH
11113	13	\	SH	12	\	SH
11164	15	\	SH	13	/	SH
11176	15	\	SH	14	\	SH
11468	24	/	SH	24	\	SH
11500*	25	\	SH	26	\	SH

BEHAVIOR: BRITTLE. Both crack-tips propagated brittlely and remained sharp throughout the run.

SH ≡ Sharp.

* ≡ Picture is provided, see Fig. III.6A1.

[Table III.6A2] Temperature $K_BT=0.0634\varepsilon_o$, COR.LJCOVa.2, sample size: 64x39, c_o= 3.75d, time interval = 0.01, critical load, σ_c = 2.10. See Fig. III.6A2.

TIME	LHSCT BEHAVIOR			RHSCT BEHAVIOR		
STEP	NNBB		CT	NNBB		CT
10697*	2	/	SH	0	\	SH
10930	4	/	SH	1	/	SH
10964	4	/	SH	2	\	SH
11000*	6	/	SH	3	/	SH
11017	6	/	SH	4	\	SH
11090	7	\	SH	5	/	SH
11102	7	\	SH	6	\	SH
11159*	9	\	SH	7	/	SH
11188	10	/	SH	8	\	SH
11239	12	/	SH	9	/	Xup
11363	15	\	Xdown, Blunting	10	/	Xup, Xdown
11500	18	\	Xup, Xdown	12	/	Xup, |— down

BEHAVIOR: BRITTLE. Both crack-tips propagated brittlely and remained sharp for the major part of the run. The RHSCT emitted a blunting dislocation downwards towards the end of the run.

|— ≡ Emitted Dislocation from the RHSCT.
SH ≡ Sharp.
Xup ≡ A disturbance at the upper corner of the CT which may result in the emission of a blunting dislocation upward.
Xdown ≡ A disturbance at the lower corner of the CT which may result in the emission of a blunting dislocation downward.
* ≡ Picture is provided, see Fig. III.6A2.

[Table III.6A2*] Temperature $K_BT= 0.062\varepsilon_o$, COR.LJCOVa.2, sample size: 64x39, $c_o= 3.75d$, time interval = 0.01, critical load, $\sigma_c = 2.20$. See Fig. III.6A2*.

TIME	LHSCT BEHAVIOR			RHSCT BEHAVIOR		
STEP	NNBB		CT	NNBB		CT
10686	2	/	SH	0	\	SH
10728*	2	/	SH	1	/	SH
10791	3	\	Xup	2	\	SH
10759	4	<	Xup, Blunting	1	/	SH, CT Rehealed
10853	4	<	Xup, Blunting	3	/	SH
10944	4	<	Xup, Blunting	4	>	Xdown, Blunting
10954	5	<	Xup, Blunting	4	>	Xdown, Blunting
11000*	5	<	Xup, Blunting	5	>	Xdown, Blunting

BEHAVIOR: Brittle-to-Ductile transition? The LHSCT is blunted and struggling to emit a blunting dislocation upwards but only after breaking 4 crack-tip interatomic bonds. The RHSCT, also, started to struggle to get blunted and emit a dislocation downwards after breaking 4 crack-tip atomic bonds. It seems that overloading enhanced ductility.

< ≡ Blunted LHSCT.
> ≡ Blunted LHSCT.
SH ≡ Sharp.
Xup ≡ A disturbance at the upper corner of the CT which may result in the emission of a blunting dislocation upward.
Xdown ≡ A disturbance at the lower corner of the CT which may result in the emission of a blunting dislocation downward.
* ≡ Picture is provided, see Fig. III.6A2*.

[Table III.6A3] Temperature $K_BT= 0.0675\varepsilon_o$, COR.LJCOVa.2, sample size: 64x39, $c_o= 3.75d$, time interval = 0.01, critical load, $\sigma_c = 2.20$. See Fig. III.6A3.

TIME STEP	Applied Load	LHSCT BEHAVIOR NNBB		CT	RHSCT BEHAVIOR NNBB		CT
12562*	2.10	0	/	SH	0	>	Blunting, Xdown
12708*	2.10	0	<	Blunted	0	>	Blunted
12964*	2.10	0	<	Sharpening	0	>	Sharpening
13500*	2.15	0	/	SH	0	\	SH
14054*	2.20	1	\	SH	0	\	SH
14167	2.20	2	/	SH	1	/	SH
14326	2.20	3	\	Blunting	2	\	SH
14377*	2.20	4	<	Blunted	3	/	SH
14467*	2.20	4	<	Blunted, <>up	3	/	SH
14500*	2.20	4	<	Blunted, <>up	4	>	Blunting, Xdown

BEHAVIOR: DUCTILE TO BRITTLE TRANSITION? Both crack-tips are blunted under the applied load of 2.10 by step 12788, but since they were unsuccessful in the emission of blunting dislocations, eventually, they were sharpened by the end of the run. None of the crack-tips responded to the increase of the applied load to 2.15. Under the critical load of 2.20, the LHSCT got blunted after breaking 3 crack-tip bonds, but its struggle to emit a dislocation upward resulted in the creation of a hole at the upper corner of the blunted LHSCT. The RHSCT remained sharp for the major part of the run and propagated brittlely by breaking 3 crack-tip bonds. Toward the end of the run RHSCT, too, was getting blunting.

< ≡ Blunted LHSCT.
> ≡ Blunted LHSCT.
<> ≡ Hole.
SH ≡ Sharp.
* ≡ Picture is provided, see Fig. III.6A3.

[Table III.6A4] Temperature $K_BT= 0.0790\varepsilon_o$, COR.LJCOVa.2, sample size: 64x39, $c_o= 3.75d$, time interval = 0.01, critical load, $\sigma_c = 2.00$. See Fig. III.6A4.

TIME	LHSCT BEHAVIOR			RHSCT BEHAVIOR		
STEP	NNBB		CT	NNBB		CT
12200*	1	\	SH	0	\	Blunting
12487*	3	\	SH	0	>	Blunted,<>down
12548	4	/	SH, Xup	0	>	Blunted,<>down
12737	6	<	Blunting, Xup	0	>	Blunted,<>down
12915	7	<	Blunted, <>up	0	>	Blunted,<>down
12943	7	<	Blunted, <>up	0	>	Blunted,<>down

BEHAVIOR: Brittle-to-Ductile TRANSITION. The RHSCT is completely blunted but its struggle to emit a blunting dislocation have resulted in the creation of an opening in the lower corner of the crack-tip. The RHSCT, on the other hand, propagated brittlely by breaking 4 crack-tip bonds. Later on, the LHSCT also got blunted.

< ≡ Blunted LHSCT.
> ≡ Blunted LHSCT.
<> ≡ Hole.
SH ≡ Sharp.
Xup ≡ A disturbance at the upper corner of the CT which may result in the emission of a blunting dislocation upward.
Xdown ≡ A disturbance at the lower corner of the CT which may result in the emission of a blunting dislocation downward.
* ≡ Picture is provided, see Fig. III.6A4.

[Table III.6A5] Temperature $K_BT= 0.0857\varepsilon_o$, COR.LJCOVa.2, sample size: 64x39, $c_o= 3.75d$, time interval = 0.01, critical load, $\sigma_c = 2.00$. See Fig. III.6A5.

TIME	LHSCT BEHAVIOR			RHSCT BEHAVIOR		
STEP	NNBB		CT	NNBB		CT
13700*	1	\	SH	0	\	SH
13767*	1	<	Blunted, <>up	0	\	SH
13938*	1	\	SH	2	\	SH, Xdown
13955	2	<	Blunting	2	>	Blunting, Xdown
14079	3	\	SH	2	>	Blunted, <>down
14284*	8	/	SH	2	>	|—up, <>down
14408	9	<	Blunting, Xup	2	>	|— up, <>down
14488*	10	<	Blunted, <>down	2	>	|— up , <>down

BEHAVIOR: Brittle-to-Ductile TRANSITION? The RHSCT was blunted after breaking 2 crack-tip interatomic bonds. Its struggle to emit a dislocation was resulted in the creation of a hole at its lower corner, which itself got blunted and emitted a dislocation upward. On the other hand, the LHSCT remained sharp for the major part of the run and propagated brittlely by breaking 8 crack-tip bonds. The LHSCT, too, got blunted finally.

< ≡ Blunted LHSCT.
> ≡ Blunted LHSCT.
|— ≡ Emitted Dislocation from the RHSCT.
<> ≡ Hole.
SH ≡ Sharp.
Xup ≡ A disturbance at the upper corner of the CT which may result in the emission of a blunting dislocation upward.
Xdown ≡ A disturbance at the lower corner of the CT which may result in the emission of a blunting dislocation downward.
* ≡ Picture is provided, see Fig. III.6A5.

[Table III.6A6] Temperature $K_BT = 0.104\varepsilon_o$, COR.LJCOVa.2, sample size: 64x39, $c_o = 3.75d$, time interval = 0.01, critical load, $\sigma_c = 1.95$. See Fig. III.6A6.

TIME	LHSCT BEHAVIOR			RHSCT BEHAVIOR		
STEP	NNBB	CT		NNBB	CT	
11654*	0	<	Blunted, <>down	0	\	SH
12012*	1	\	SH	1	>	Blunted, <>up
12272	4	<	Blunted	2	>	Blunted, <>up
12349	5	<	Blunted, <>down	2	>	Blunted, <>up
12480*	6	<	Blunted, <>down	2	>	Blunted, <>up

BEHAVIOR: DUCTILE-TO-BRITTLE TRANSITION. The RHSCT was blunted and grew by the process of micro hole growth. The LHSCT, too, got blunted initially, but after a while, resharpened, broke 4 CT bonds, and finally blunted again.

< ≡ Blunted LHSCT.
> ≡ Blunted LHSCT.
|— ≡ Emitted Dislocation from the RHSCT.
<> ≡ Hole.
SH ≡ Sharp.
Xup ≡ A disturbance at the upper corner of the CT which may result in the emission of a blunting dislocation upward.
Xdown ≡ A disturbance at the lower corner of the CT which may result in the emission of a blunting dislocation downward.
* ≡ Picture is provided, see Fig. III.6A6.

[Table III.6A6*] Temperature $K_BT= 0.104\varepsilon_o$, COR.LJCOVa.2, sample size: 64x39, $c_o= 3.75d$, time interval = 0.01, applied load $\sigma_a=2.0$ > critical load of 1.95 "OVERLOADED".

TIME	LHSCT BEHAVIOR			RHSCT BEHAVIOR		
STEP	NNBB		CT	NNBB		CT
11510	0	<	Blunting, Xdown	0	\	SH
11639	0	<	Blunted, <>down	0	\	SH
11666	0	<	Blunted, <>Healed	0	\	SH
11790	0	<	Blunted	0	>	Blunted, <>down
11850	0	<	Blunted, <>down	0	>	Blunted, <>down
11940	0	<	Blunted, <>Healed	0	>	Blunted, <>up
11990	0	<	Blunted,	0	>	Blunted, <>up

BEHAVIOR: DUCTILE? This overloaded run is definitely more ductile than III.6A6 run. Both crack-tips are blunted, and remained inactive for the major part of the run. No dislocation was emitted from the crack-tips.

< ≡ Blunted LHSCT.
> ≡ Blunted LHSCT.
<> ≡ Hole.
SH ≡ Sharp.
* ≡ Picture is provided, see Fig. III.6A6*.

[Table III.6A8] Temperature $K_BT= 0.136\varepsilon_o$, COR.LJCOVa.2, sample size: 64x39, $c_o= 3.75d$, time interval = 0.01, critical load, $\sigma_c = 1.80$. See Fig. III.6A8.

TIME	LHSCT BEHAVIOR			RHSCT BEHAVIOR		
STEP	NNBB		CT	NNBB		CT
13716*	0	/	SH	1	/	SH
13767*	0	<	Blunted, Xdown	2	>	Blunting
13854	0	<	Blunted, <>down	1	/	SHARPENED
14088*	0	<	Blunted, <>down	2	>	Blunting, Xdown
14257*	0	<	Blunted, <>healed	1	>	Blunting, Xdown
14313*	0	<	Blunted, <>down	1	>	Blunted, |—down
14400*	0	<	Blunted, <>down	1	>	Blunted, <>down
14468	0	<	Blunted, <>healed	1	>	Blunted, <>down
14577*	0	<	Blunted, —| down	1	>	Blunted, <>down

BEHAVIOR: DUCTILE.

< ≡ Blunted LHSCT.
> ≡ Blunted LHSCT.
|— ≡ Emitted Dislocation from the RHSCT.
—| ≡ Emitted Dislocation from the LHSCT.
<> ≡ Hole.
SH ≡ Sharp.
Xup ≡ A disturbance at the upper corner of the CT which may result in the emission of a blunting dislocation upward.
Xdown ≡ A disturbance at the lower corner of the CT which may result in the emission of a blunting dislocation downward.
* ≡ Picture is provided, see Fig. III.6A8.

[Table III.6] **Summary:** BDT in the 2D-triangular COR.LJCOVa.2 solid, a*=0.2, sample size: 64x39, c_o=3.75d, time interval = 0.01.

Run	Temperature K_BT	Final step	Applied stress	LHSCT BB, CT	RHSCT BB,CT	Conclusion: Behavior
III.6A1	.0193	11500	2.30	25,\ , SH	26, \ , SH	Brittle
III.6A2	.0634	11500	2.10	18, \ , X	12, / , X	Brittle
III.6A2*	.0620	11000	2.20*	5, <, X_{up}	5, >, X_{down}	D/B
III.6A3	.0675	14500	2.20	4,<, <>up	4, >, X_{down}	BDT
III.6A4	.0790	13000	2.00	7, <,<>up	0, >, <>down	BDT
III.6A5	.0857	14500	2.00	10,<,<>down	2, >, |—up	BDT
III.6A6	.104	12500	1.95	6,<, <>	2, >, <>	BDT
III.6A6*	.104	12000	2.00*	0,<	0,>	Ductile?
III.6A7	.120	13000	1.90	uppermost surface atoms are in trouble		
III.6A8	.136	15000	1.80	0,<,<>dn,|–dn	1,>,<>down	Ductile
III.6A9	.170	15800	1.60	uppermost surface atoms are in trouble		

< ≡ Blunted LHSCT.
> ≡ Blunted LHSCT.
|— ≡ Emitted Dislocation from the RHSCT.
—| ≡ Emitted Dislocation from the LHSCT.
<> ≡ Hole.
SH ≡ Sharp.
Xup ≡ A disturbance at the upper corner of the CT which may result in the emission of a blunting dislocation upward.
Xdown ≡ A disturbance at the lower corner of the CT which may result in the emission of a blunting dislocation downward.
* ≡ Overloaded runs. All other runs are critically loaded.
BDT ≡ Brittle-to-Ductile Transition.

[Table III.7] **Summary** of the search for the brittle-to-ductile transition temperature in the 2D-triangular Johnson solids, c_o=3.75d, time interval = 0.01.

Run	Temperature (Kelvin)	Sample size	Applied stress	LHSCT BB, CT	RHSCT BB,CT	Conclusion: Behavior
III.7A1	0	36x19	2.40	0,<, |—down	0.>, |—down	Ductile
III.7B1	295	64x39	2.50	0,<, <>down	0, >, <>down	Ductile
III.7C1	0	68x79	3.37	10, /, SH	10, \ , SH	Brittle
III.7C2	110	68x79	2.80	2,<, <>	4,>, <>	BDT
III.7C3	296	68x79	2.60	0,<, <>	0,>, <>	Ductile
III.7C4	404	68x79	2.30	0,<, <>	0,>, <>	Ductile
III.7C4*	404	68x79	2.40*	0,<, <>	13, /, <>	BDT

< ≡ Blunted LHSCT.
> ≡ Blunted LHSCT.
|— ≡ Emitted Dislocation from the RHSCT.
—| ≡ Emitted Dislocation from the LHSCT.
<> ≡ Hole.
SH ≡ Sharp.
* ≡ Overloaded runs. All other runs are critically loaded.
BDT ≡ Brittle-to-Ductile Transition.

[Table III.8] **Overall summary** of the search for the brittle-to-ductile transition temperature of the 2D-LJCOVa.2 and 2D-COR.LJCOVa.2 solids.

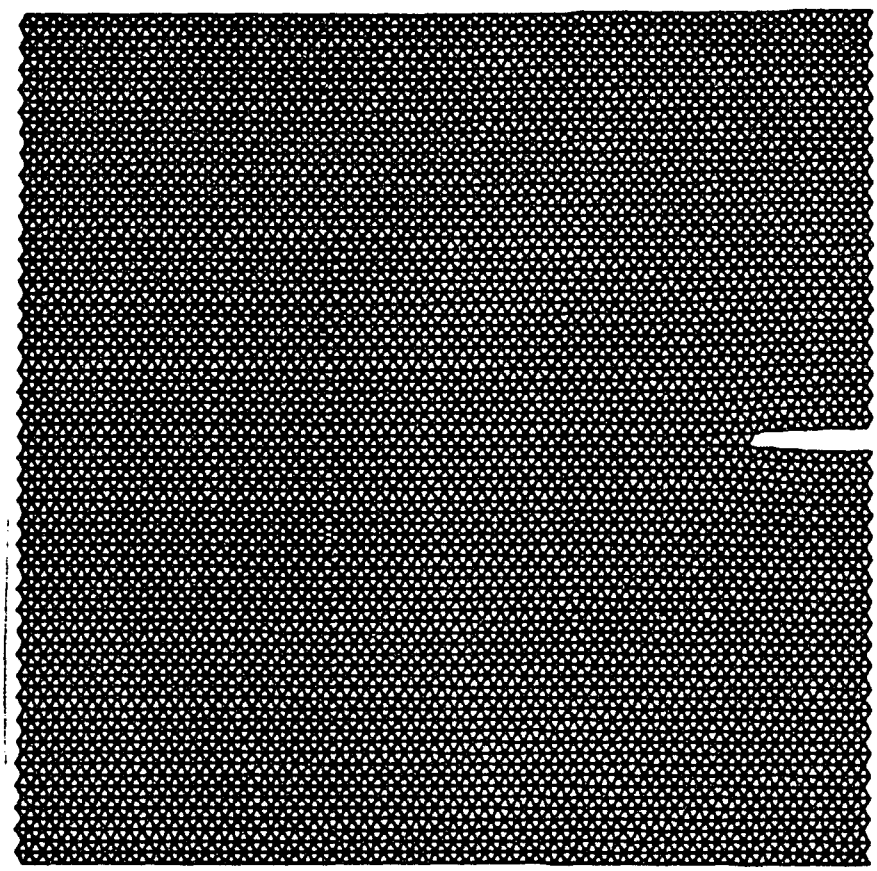
K_BT	LJCOVa.2 [32x19]					LJCOVa.2 [64x39]					COR.LJCOVa.2 [64x39]				
	III.4A series					I II.4B series					III.6A series				
(ε_0)	Run	σ_a	LHSCT	RHSCT	?	Run	σ_a	LHSCT	RHSCT	?	Run	σ_a	LHSCT	RHSCT	?
.0000	4A1	2.1	21,\	21,/	B										
.0200	4A2	1.9	14,\	15,\	B	4B1	2.4	24, \	10,>,|–	B	6A1	2.3	25, \	26,\	B
.0200	4A3	2.0*	13,\	2,>,–|	B										
.0460	4A4	1.9	8,<,–|	7,/	B										
.0560	4A5	1.8	2,<,–|	0,>,|–	B										
.0560	4A5*	1.9*	2,<,–|	0,>,<>	B										
.0600	4A6	1.8	3,<,<>	3,>,|–	BDT										
.0600	4A7	1.8	4,<,–|	2,>,|–	BDT										
.0620											6A2*	2.2*	5<X_u	5>X_d	BDT
.0625	4A9	1.8	2,<–|	6\	BDT										
.0625	4A8	1.8	0,<–|	6\	BDT										
.0634											6A2	2.1	9, \	7,/	BDT
.0675											6A3	2.2	4<,<>	4>X_d	BDT
.0680						4B2	2.2	1,<–|	4,><>|–	BDT					
.0750	4A10	1.8	0,<–|	0,<|–	D										
.0790											6A4	2.0	7,<,<>	0,>,<>	BDT
.0857											6A5	2.0	10,<,<>	2,>,<>	BDT
.0892						4B3*	2.1*	0,<–|	3,>|–	BDT					
.0904						4B3	2.0	1,<–|	3,>|–	BDT					
.1040											6A6	1.95	6,<,<>	2,>,<>	BDT
.1050						4B4	1.8	0,<–|	0,\	D					
.1200											6A7	surface atoms in trouble.			
.1360											6A8	1.8	0,<,<>–|	1,>,<>	D
.1700											6A9	surface atoms in trouble			

[Table III.9] **Conclusion**. Brittle-to-Ductile Transition Temperature in the 2D-LJCOVa.2 and 2D-COR.LJCOVa.2 solids.

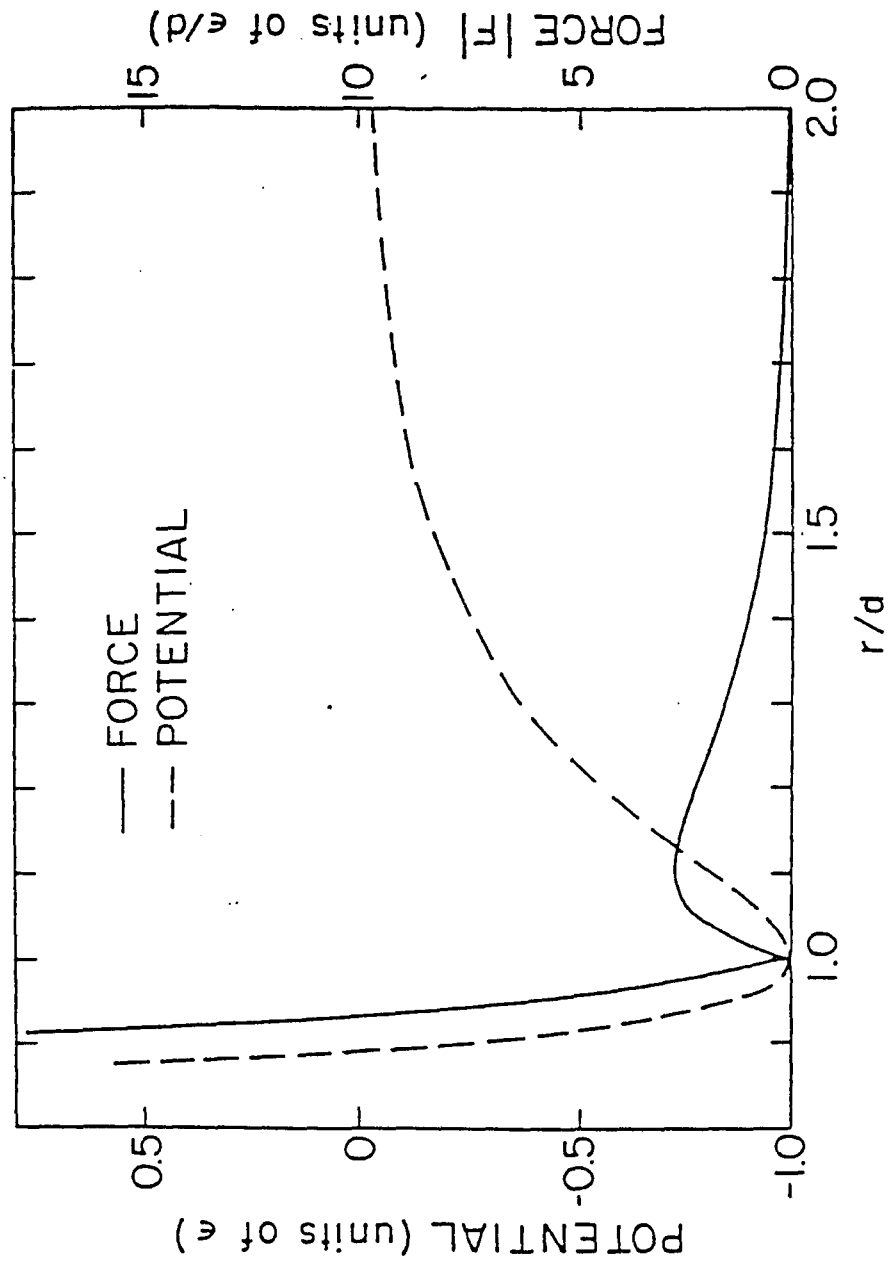
LJCOVa.2 [32x19] III.4A series	LJCOVa.2 [64x39] III.4B series	COR.LJCOVa.2 [64x39] III.6A series
$.056\varepsilon_o \leq$ BDTT $\leq .0628\varepsilon_o$	$.068\varepsilon_o \leq$ BDTT $\leq .0904\varepsilon_o$	$.0675\varepsilon_o \leq$ BDTT $\leq .104\varepsilon_o$
$1.80 \leq \sigma_c \leq 1.80$	$2.20 \leq \sigma_c \leq 2.00$	$2.20 \leq \sigma_c \leq 1.95$
$\Delta_{BDTT} \approx .0068\varepsilon_o \approx .02T_M$	$\Delta_{BDTT} \approx .0224\varepsilon_o \approx .07T_M$	$\Delta_{BDTT} \approx .0365\varepsilon_o \approx .11T_M$
$T_{ductile} \geq .075\varepsilon_o \approx .23T_M$	$T_{ductile} \geq .105\varepsilon_o \approx .23T_M$	$T_{ductile} \geq .136\varepsilon_o \approx .41T_M$
Dislocation Emission	Dislocation Emission	Hole Growth

BDTT ≡ Brittle-to-Ductile Transition Temperature.
Δ_{BDTT} ≡ BDTT range.
T_M ≡ Melting point temperature.

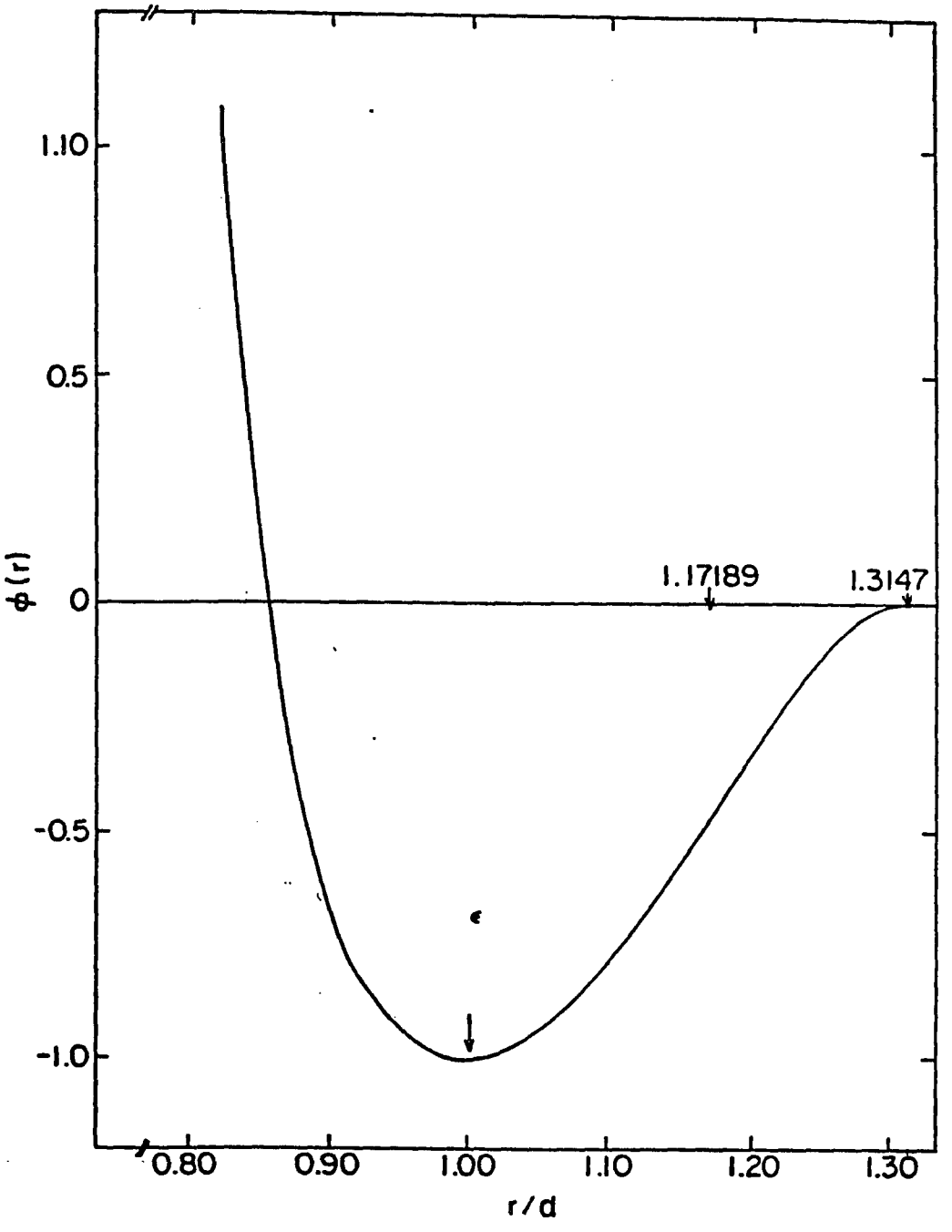
ILLUSTRATIONS



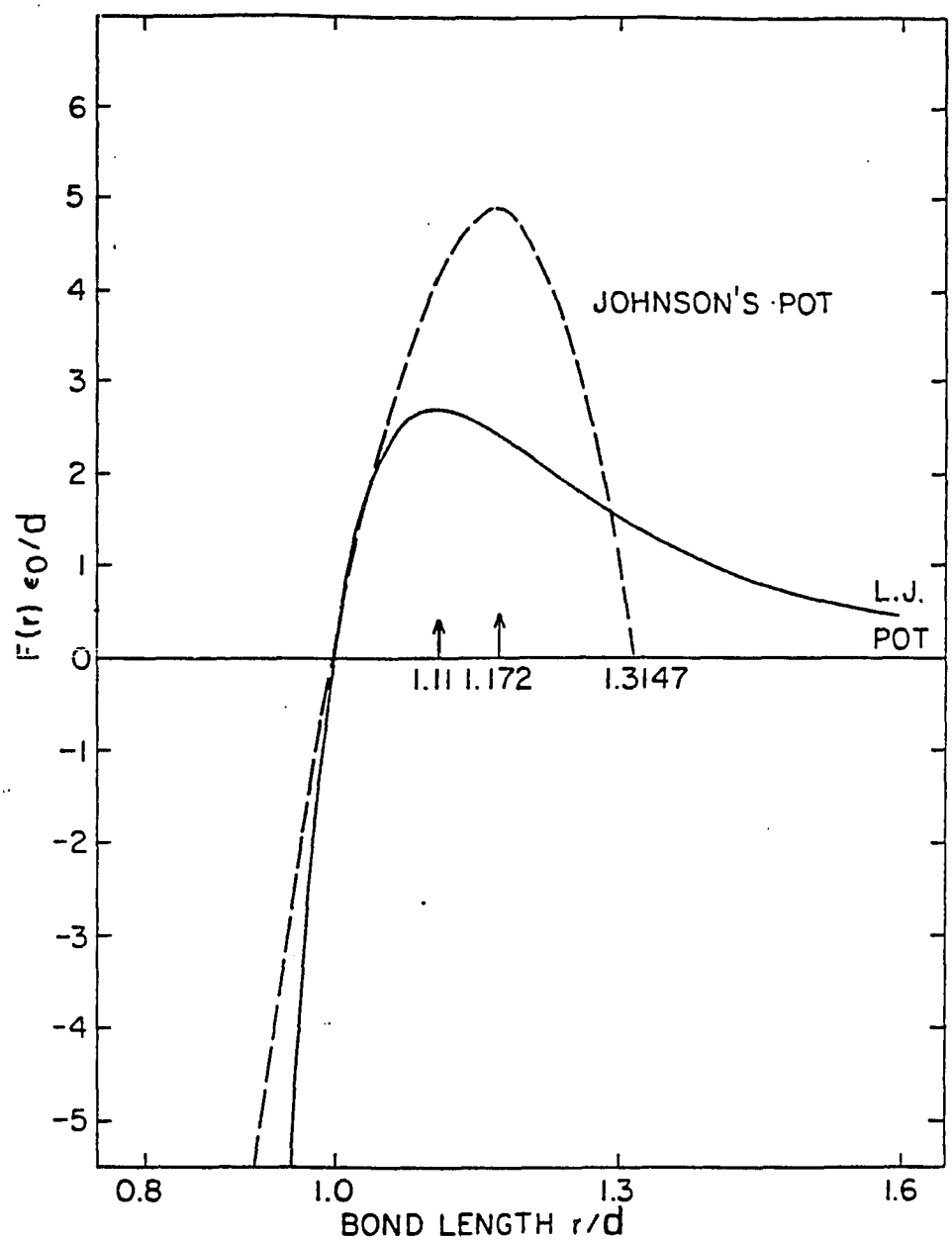
[Fig. II.1.1.] The two-dimensional triangular lattice of 79 rows and 135 columns in odd rows with the centrally located internal crack of 38 broken bonds (correspondent to the initial half-crack length c_o=9.75d between the 39th and 40th rows. Mirror symmetry about the central vertical axis is used. The half-sample mode I opening is illustrated.



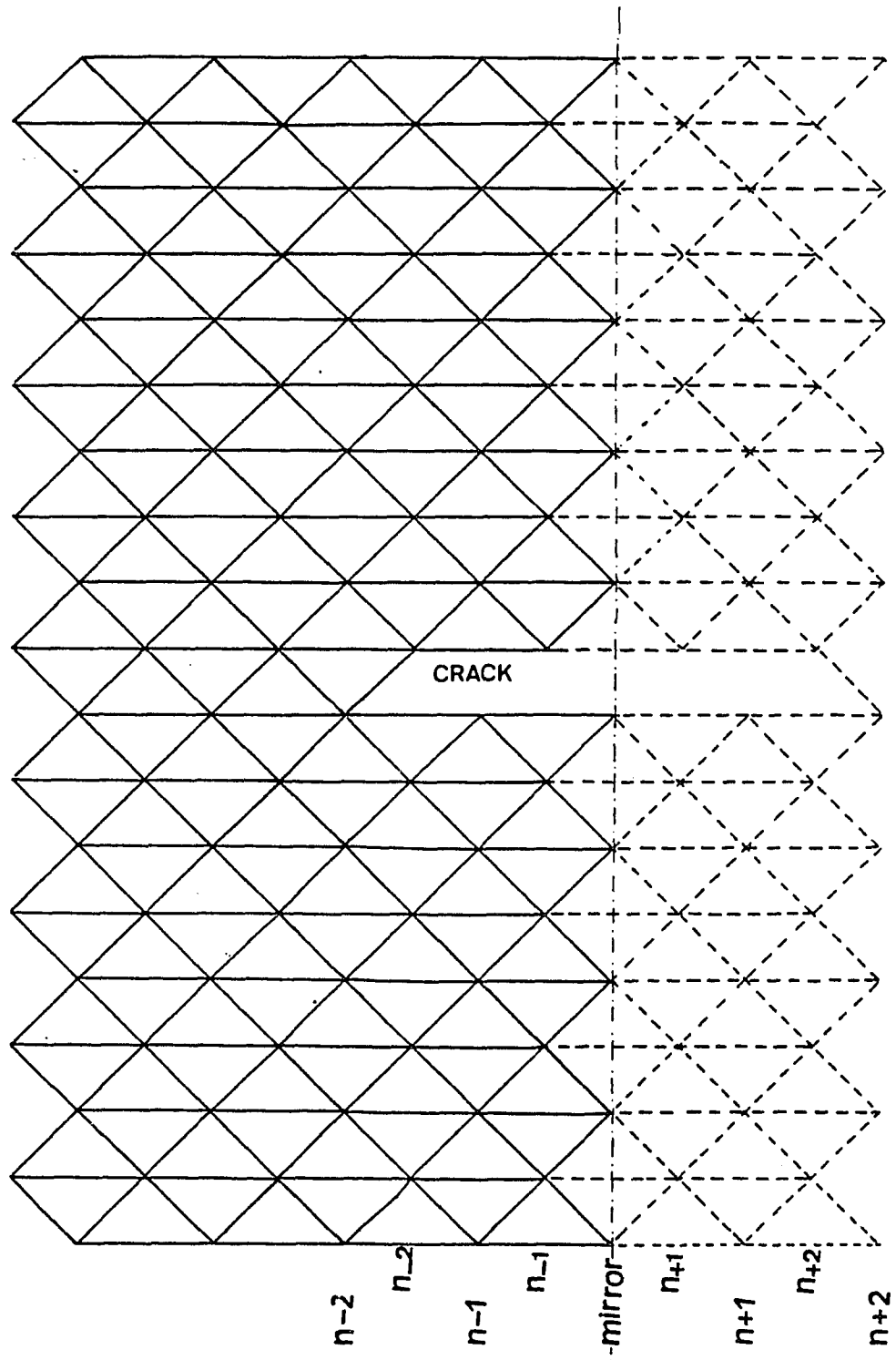
[Fig. II.1.2.] Pair-wise 6-12 Lennard-Jones interatomic potential and the correspondent interatomic force against the interatomic spacing.



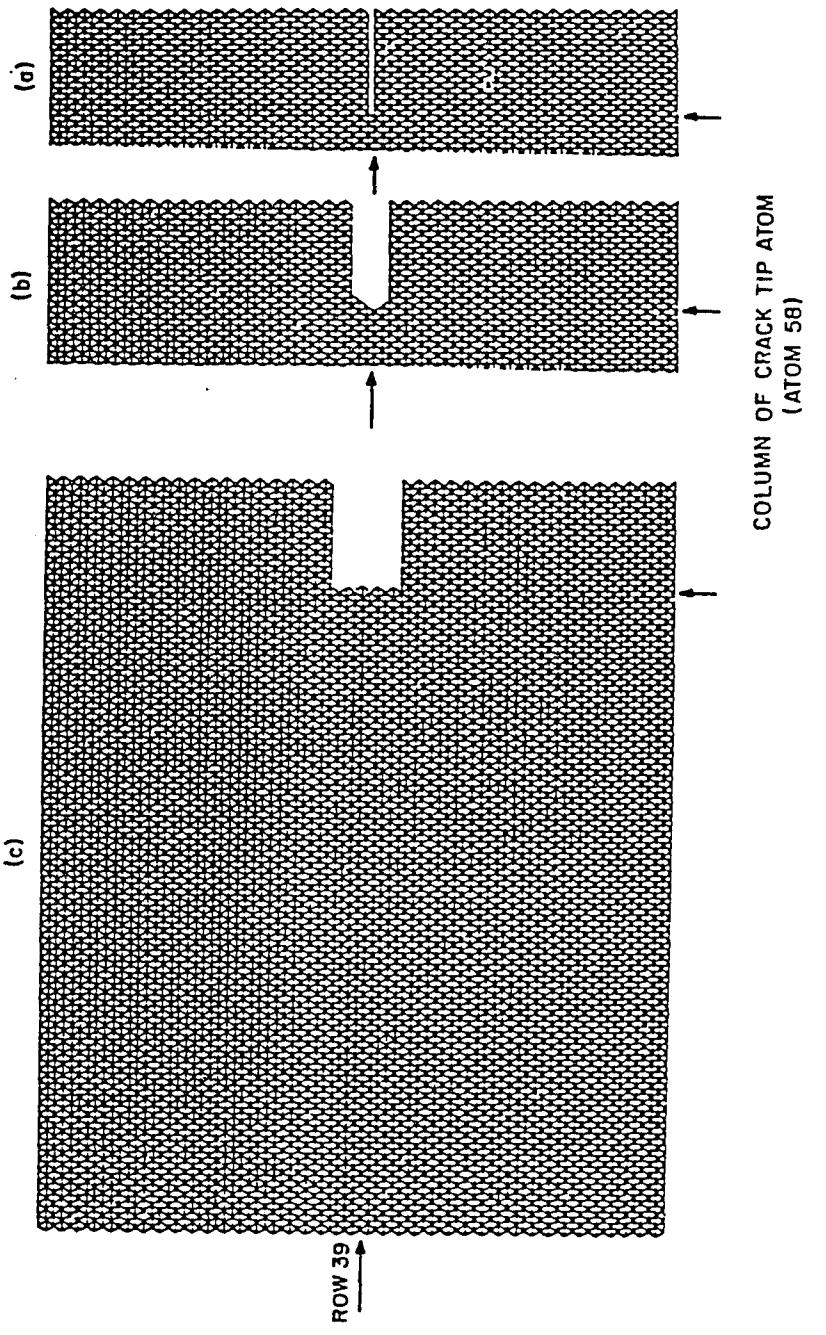
[Fig. II.1.3a] Pair-wise Johnson empirical interatomic potential [125] versus the interatomic spacing. The potential has an inflection point at r/d=1.17189 (maximum in the force) and goes to zero at r/d=1.3147. See Table. II.1.2.



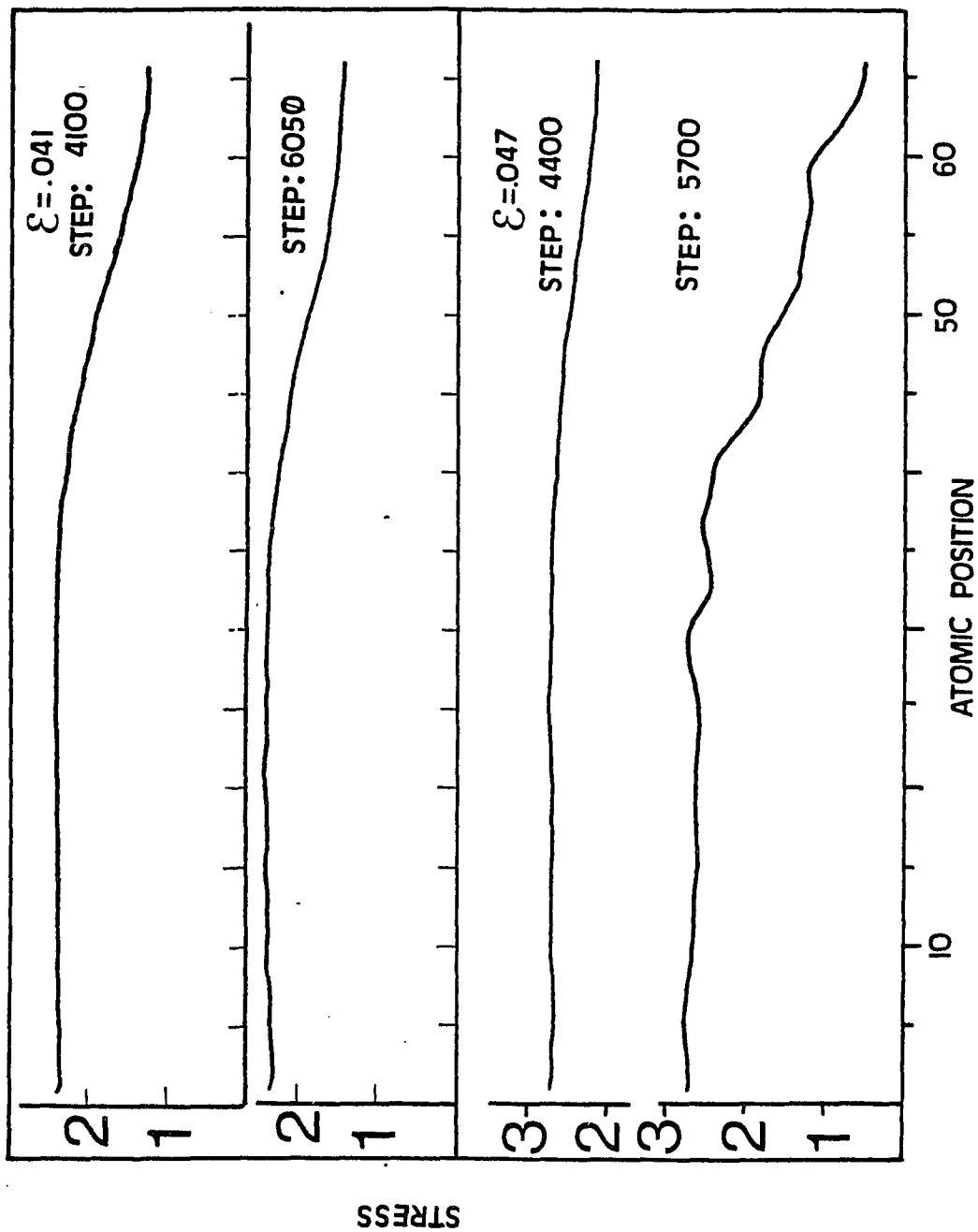
[Fig. II.1.3b] Interatomic forces versus interatomic distance for Lennard-Jones and Johnson potentials [125]. The arrow indicates the maximum force the bond may sustain at the r values indicated. Note that the shapes of the forces are quite different. The Johnson interatomic force falls off much more rapidly past the maximum than is the case with the Lennard-Jones interatomic force. See Table. II.1.2.



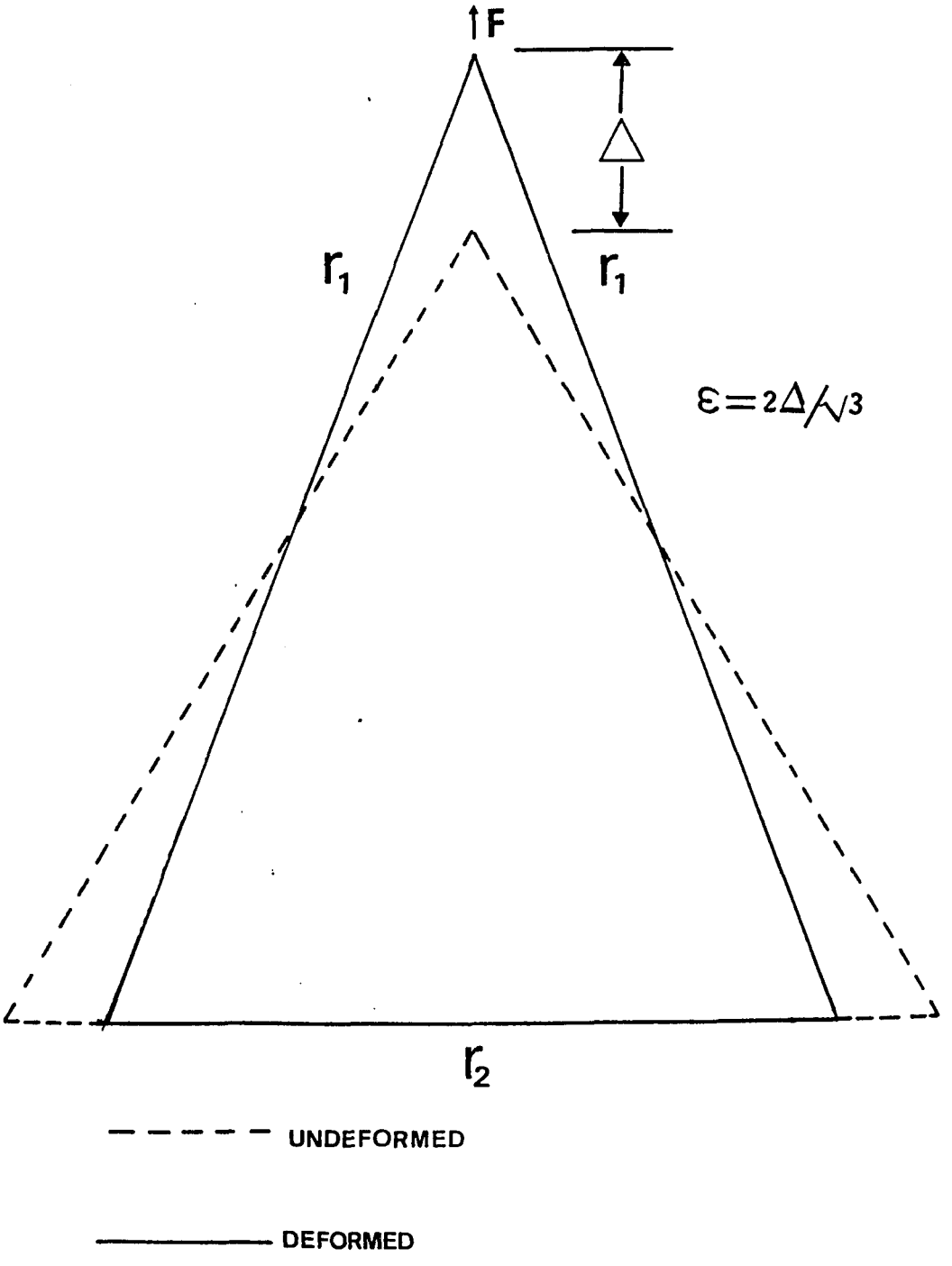
[Fig. II.1.4] Half-sample with two extra columns of atoms. The column n+1 and n+2 are mirror images of columns n-1 and n-2 about the central axis n, respectively.



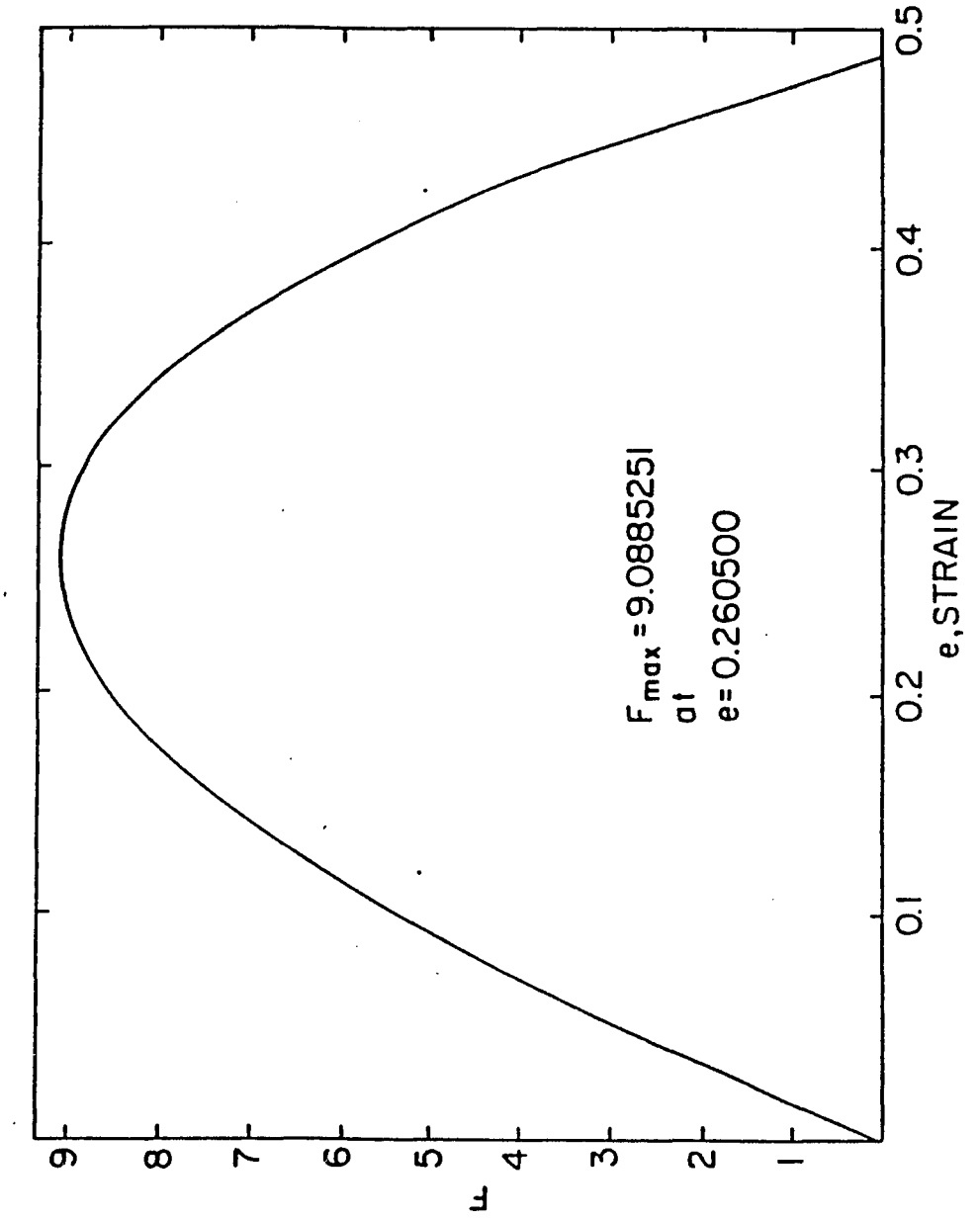
[Fig. II.1.5.] The crack shapes investigated (only a portion of the half-sample is shown): (a) A narrow crack of 38 broken bonds c_o=9.75d; (b) The wide crack. In this configuration the narrow crack was widened by removing four rows of atoms; (c) The "wide-jagged crack" created by removing 8 rows of atoms. The crack-tip atom is atom no. 58 on the 39th row. The crack-length is the same for all of these cracks.



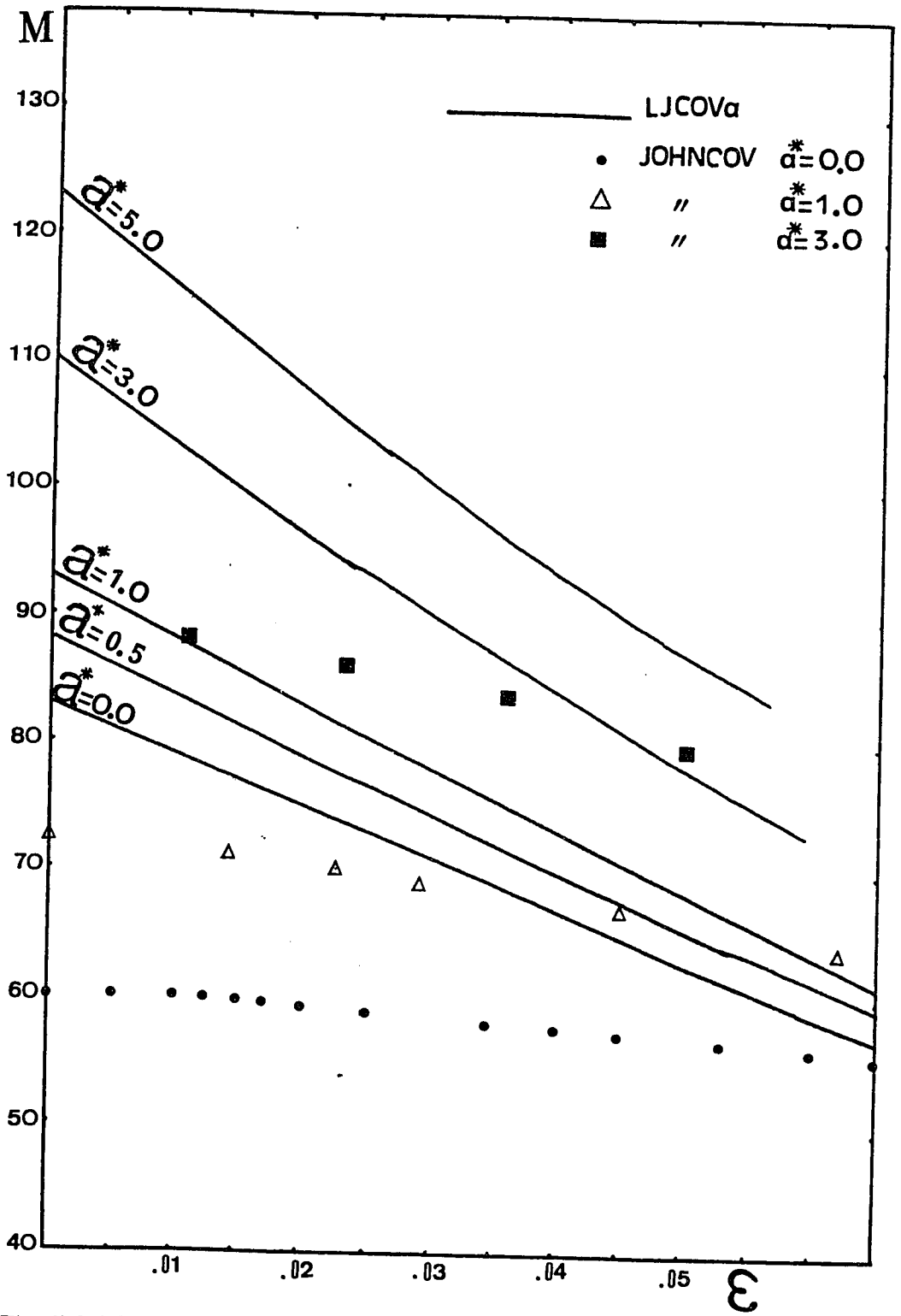
[Fig. II.1.6.] In the case of the constant external displacement simulations, the calculated forces (stresses) on the individual atoms in the uppermost and lowermost rows are not constant.



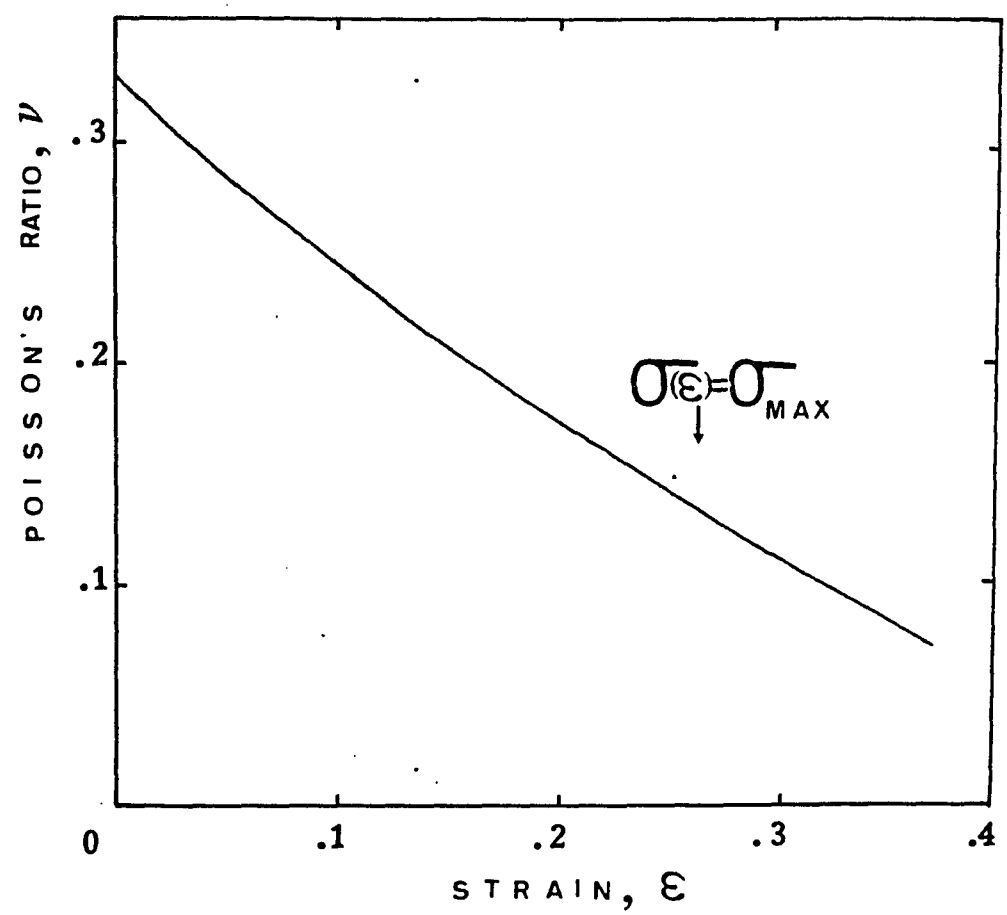
[Fig. II.2.1.] The deformed elementary triangular cell under a uniform tensile strain, ε.



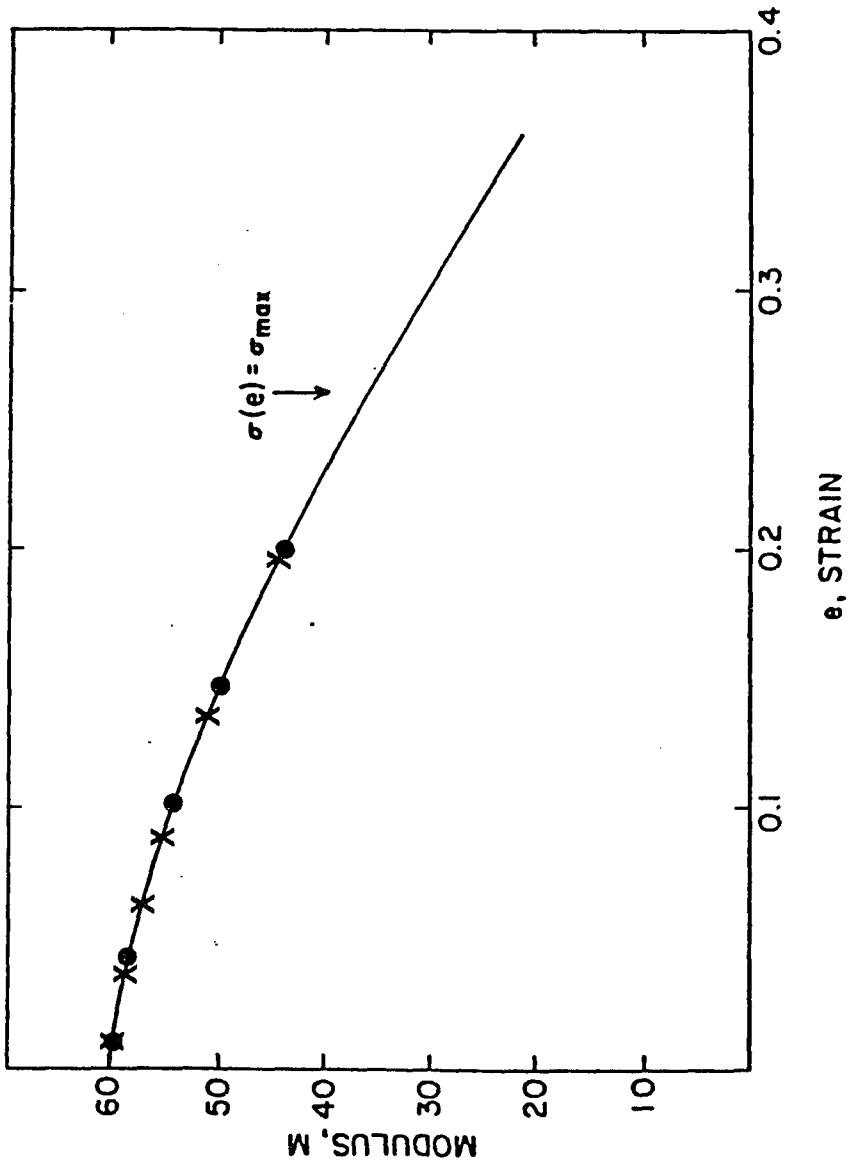
[Fig. II.2.2.] The tensile force, F, versus the applied strain for the two dimensional triangular Johnson solid.



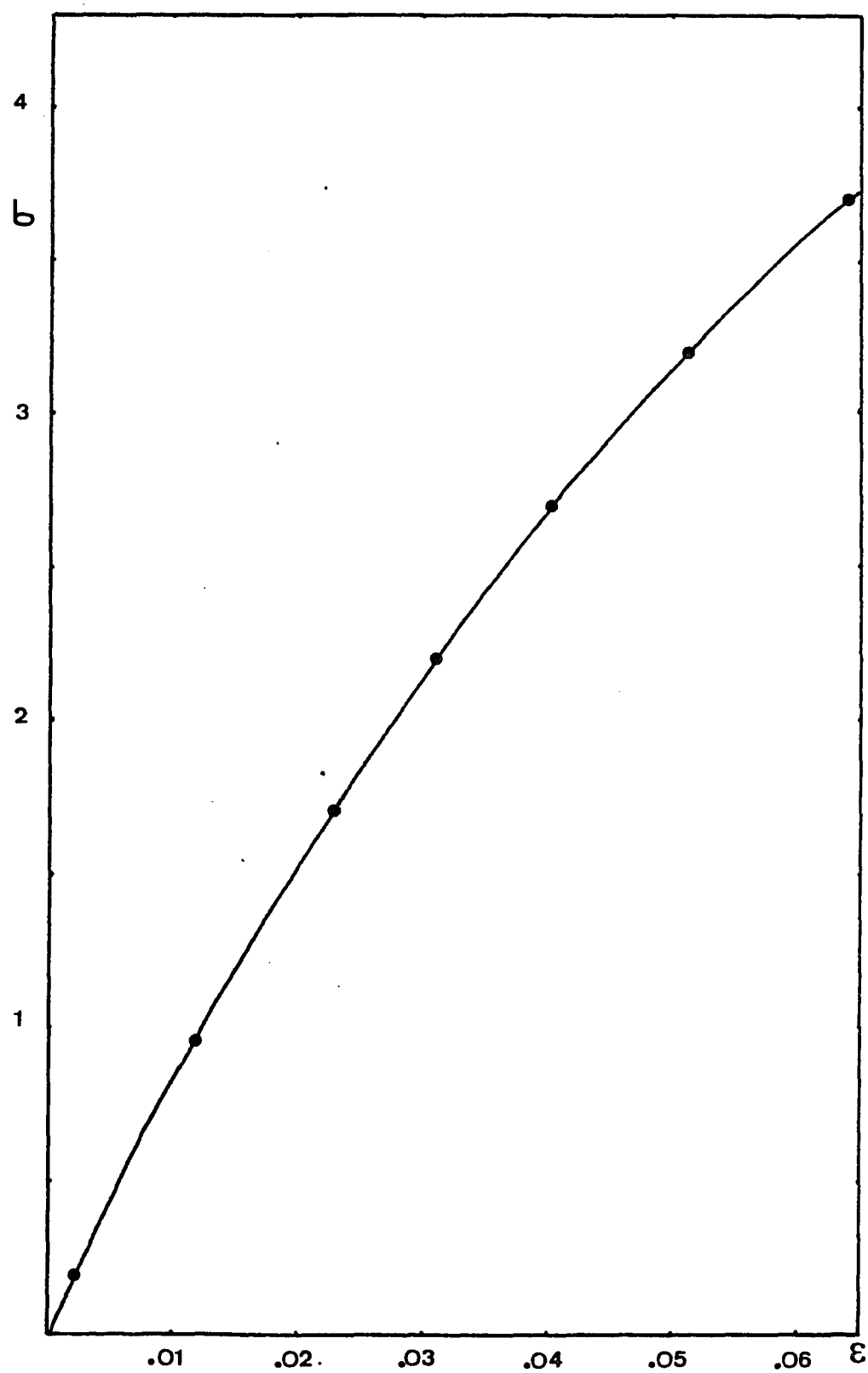
[Fig. II.2.3.] Young's Modulus, M, versus the applied strain, ε, for the two-dimensional triangular covalently modified Johnson and Lennard-Jones solids.



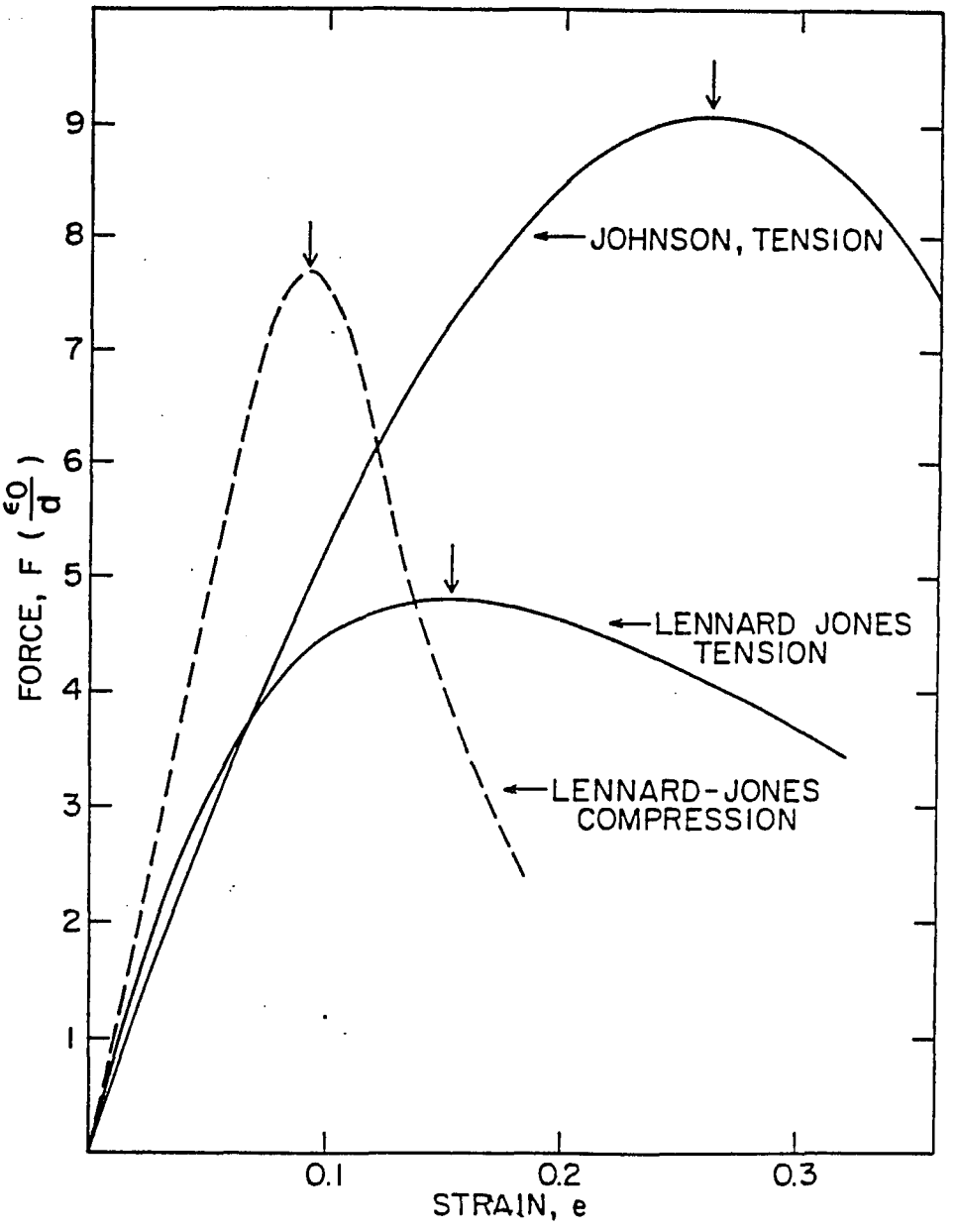
[Fig. II.2.4.] Poisson's ratio, ν, versus the applied strain for the two-dimensional triangular Johnson solid.



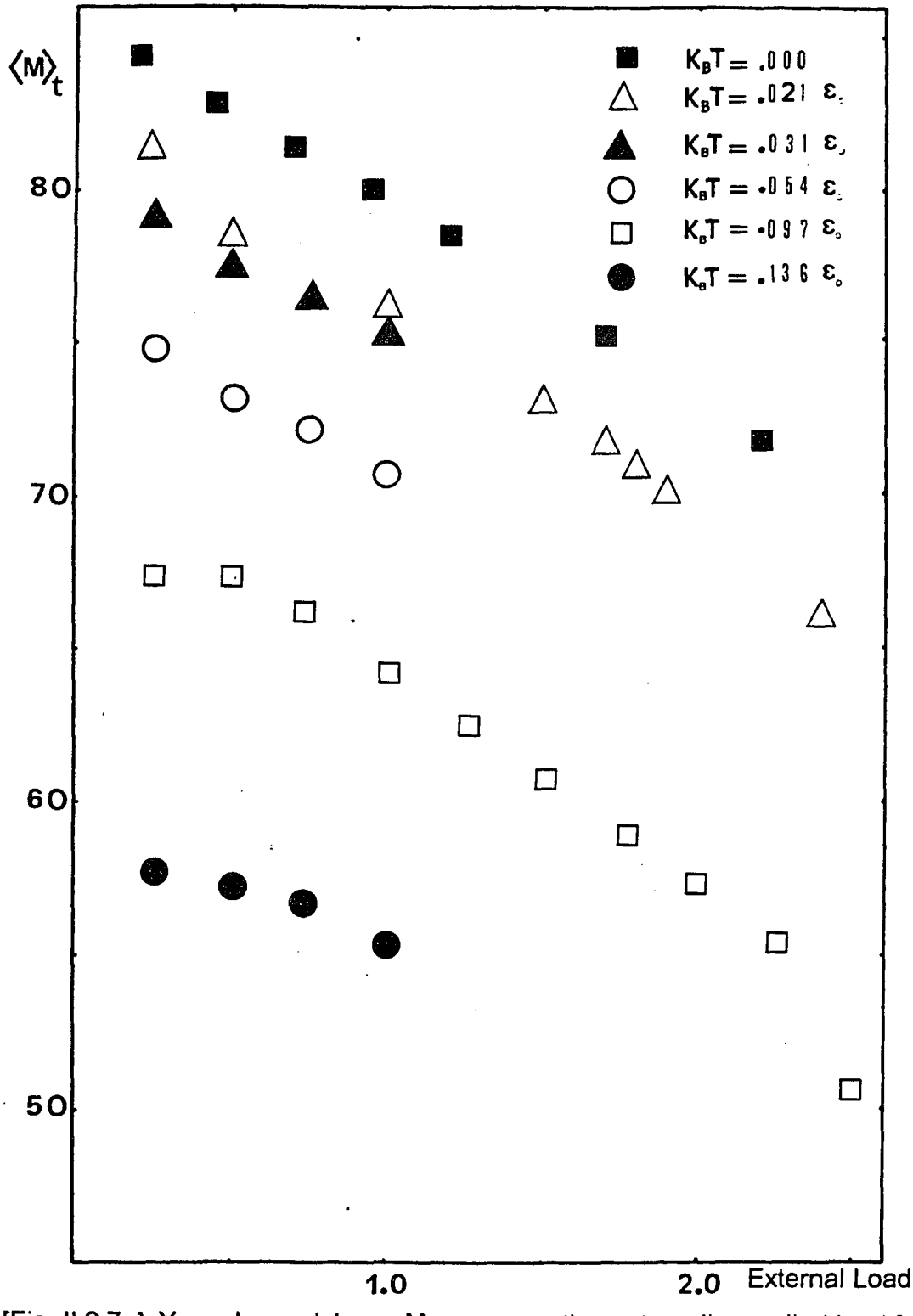
[Fig. II.2.5] Young's Modulus, M, versus the applied strain. The crosses (full circles) represent simulations results of a defect-free 2D-triangular Johnson solid under a given constant applied strain (or stress). The line is the theoretical behavior of the modulus of elasticity of the system against strain (Table. II.2.1).



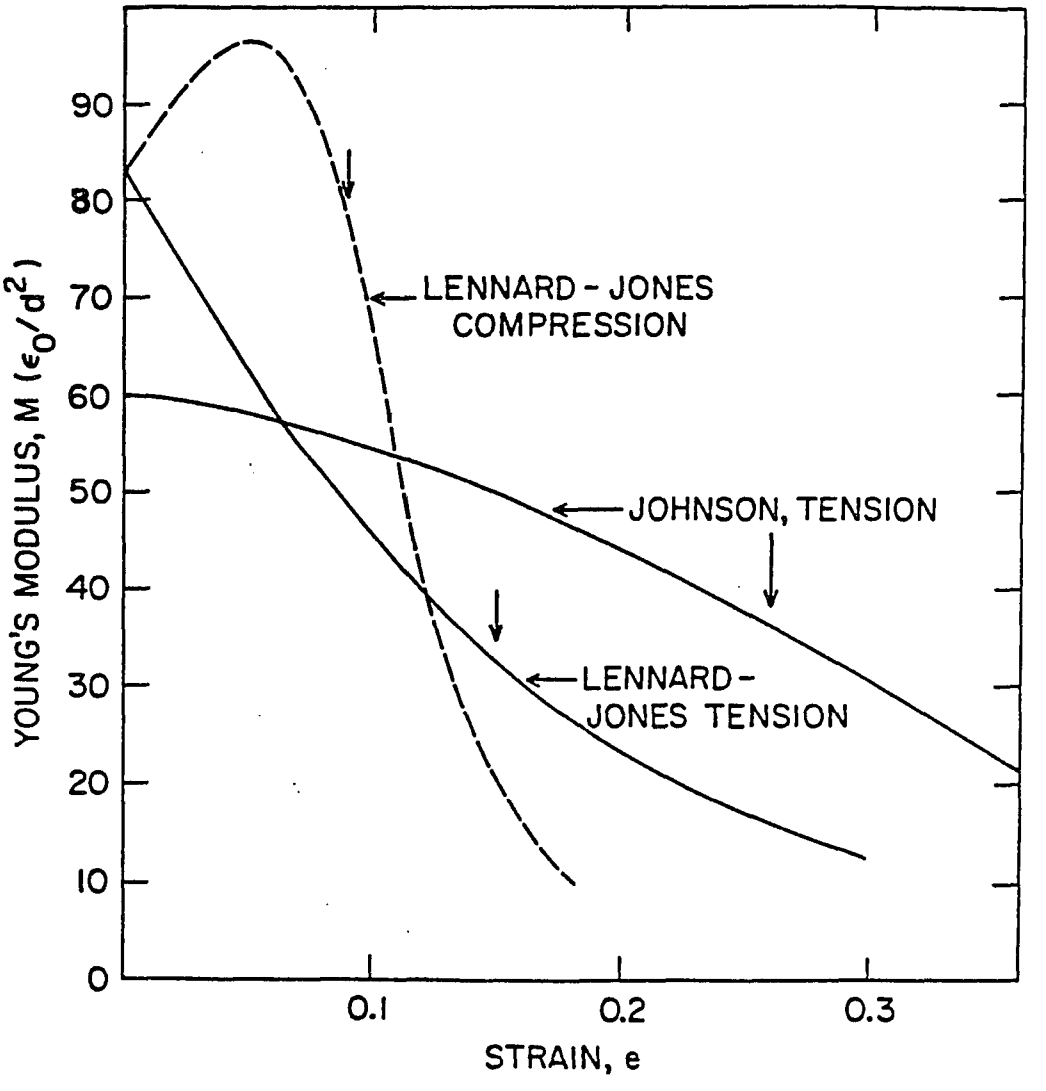
[Fig. II.2.6a.] Stress, σ, versus the applied strain, ε, for the 2DLJCOVa.2 solid.



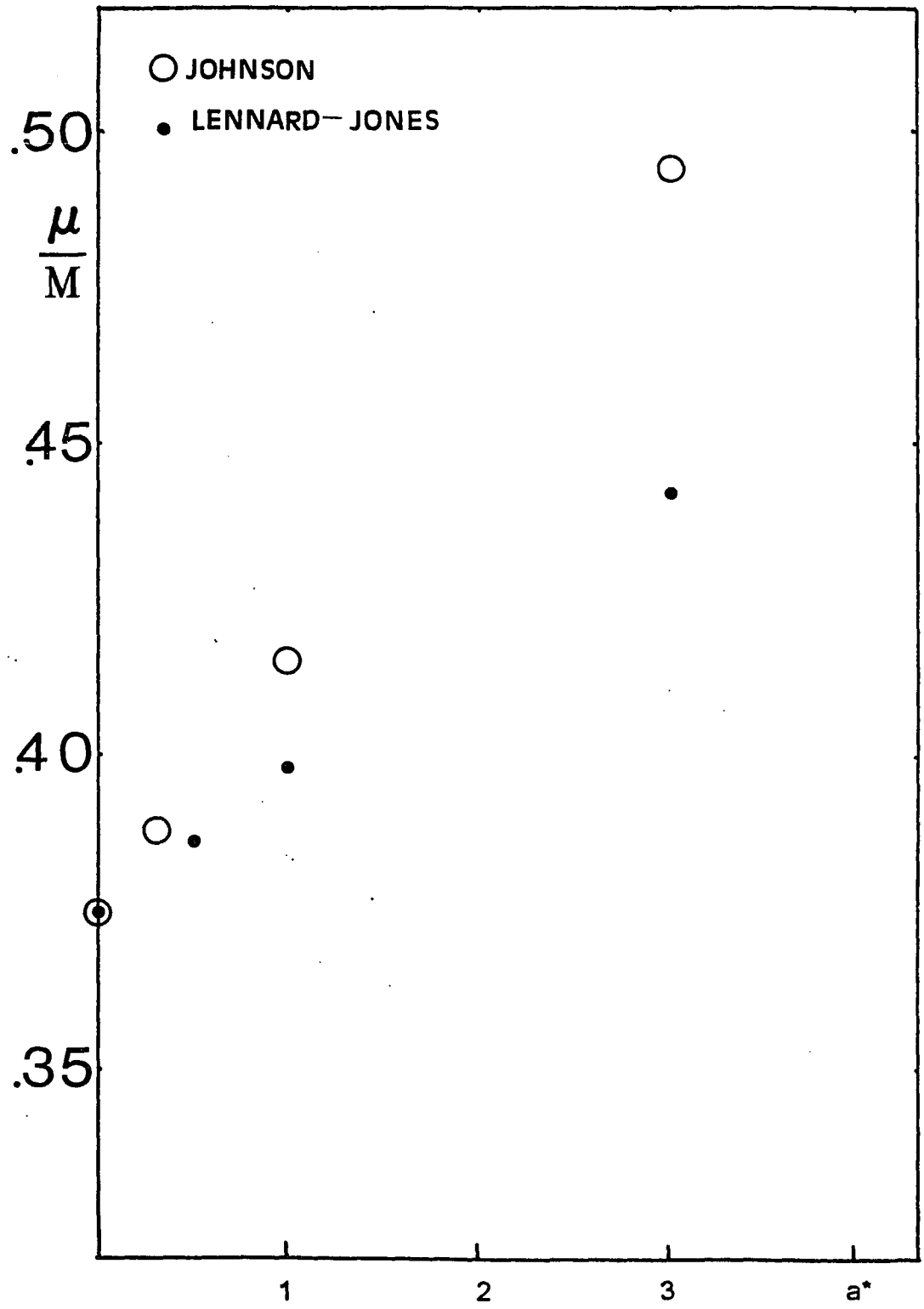
[Fig. II.2.6b.] The force versus strain curves for the Johnson and Lennard-Jones 2D-triangular solid. The arrow indicate the points of instability.



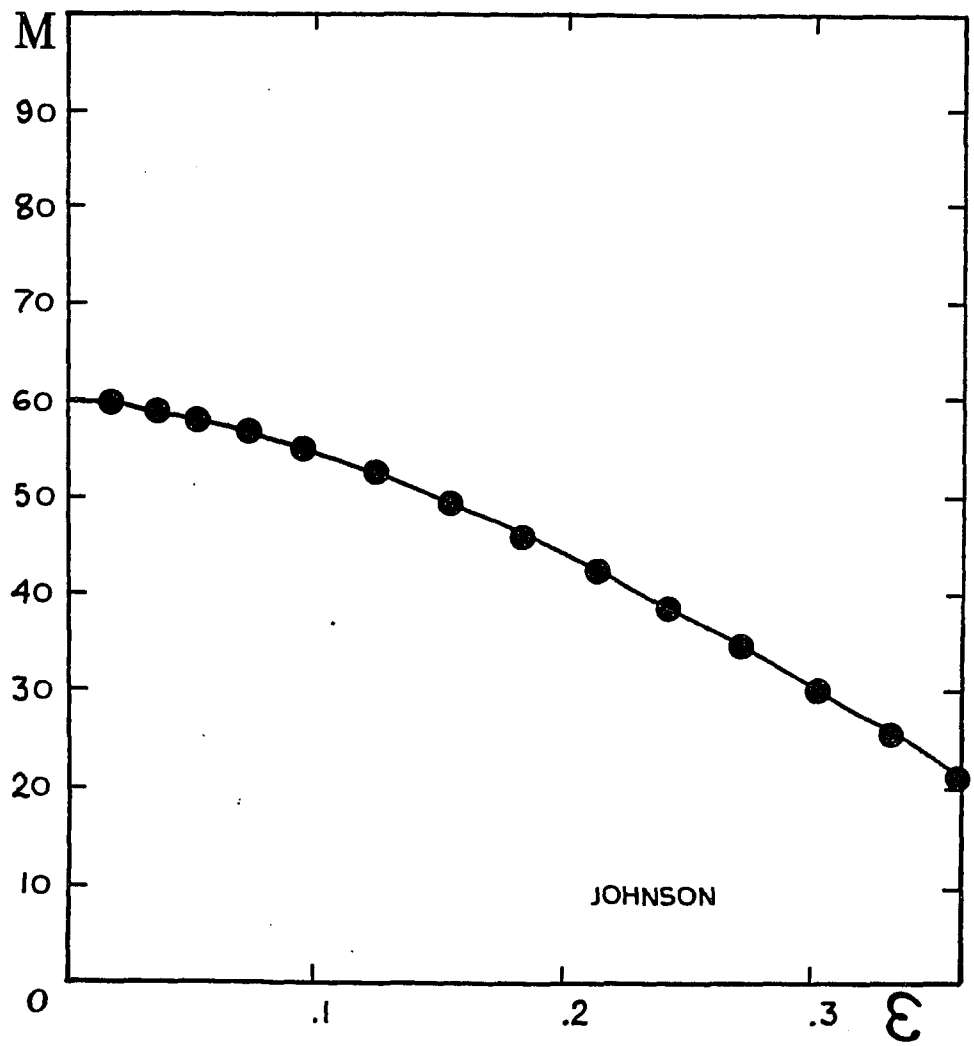
[Fig. II.2.7a] Young's modulus, <M>$_t$, versus the externally applied load for the 2D-LJCOVa.2 solid as a function of temperature. See Table II.2.2C.



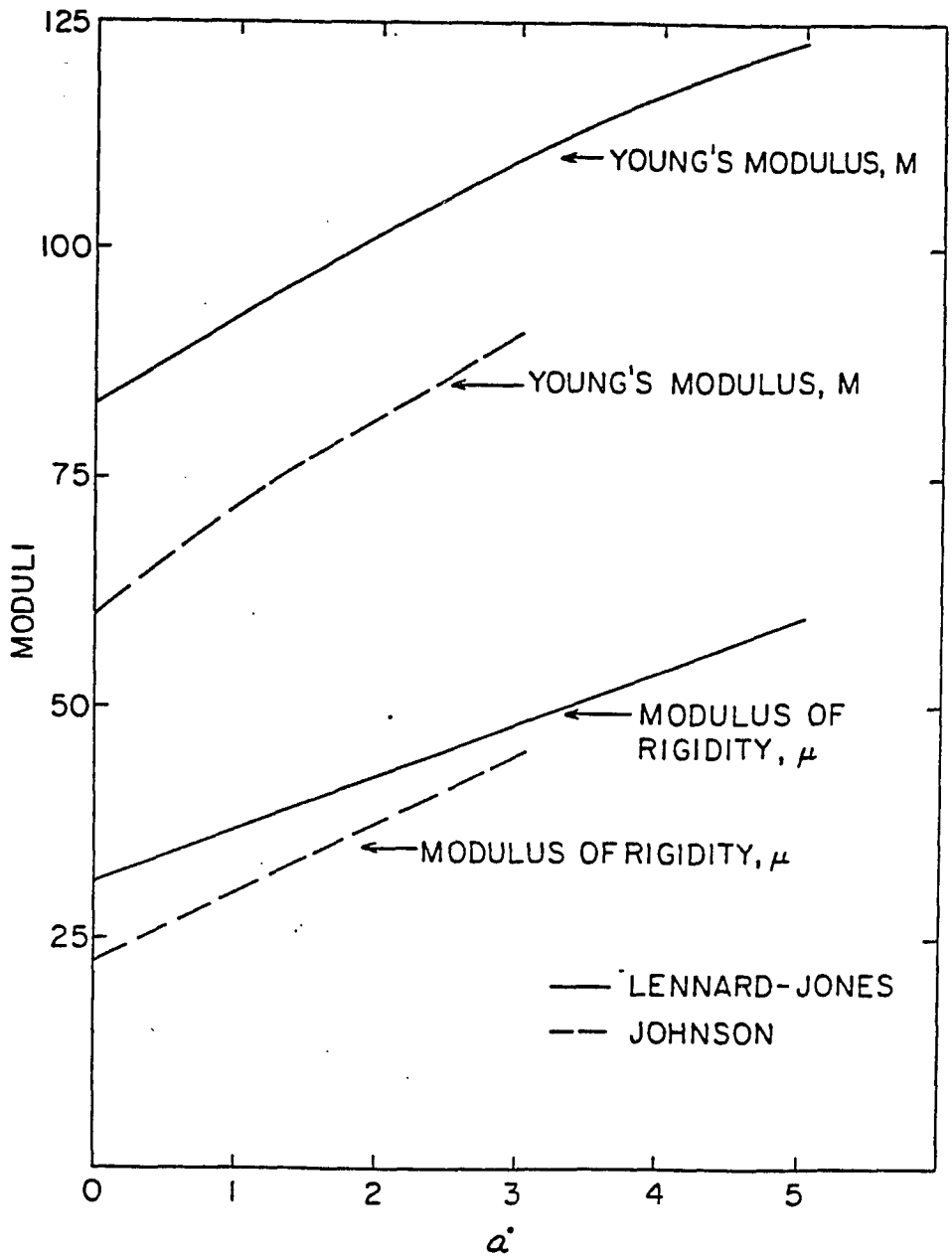
[Fig. II.2.7b] Modulus of elasticity, M, versus strain curves for Johnson and Lennard-Jones solids. The arrows indicate points of instability of the solids. See Table. II.2.1A.



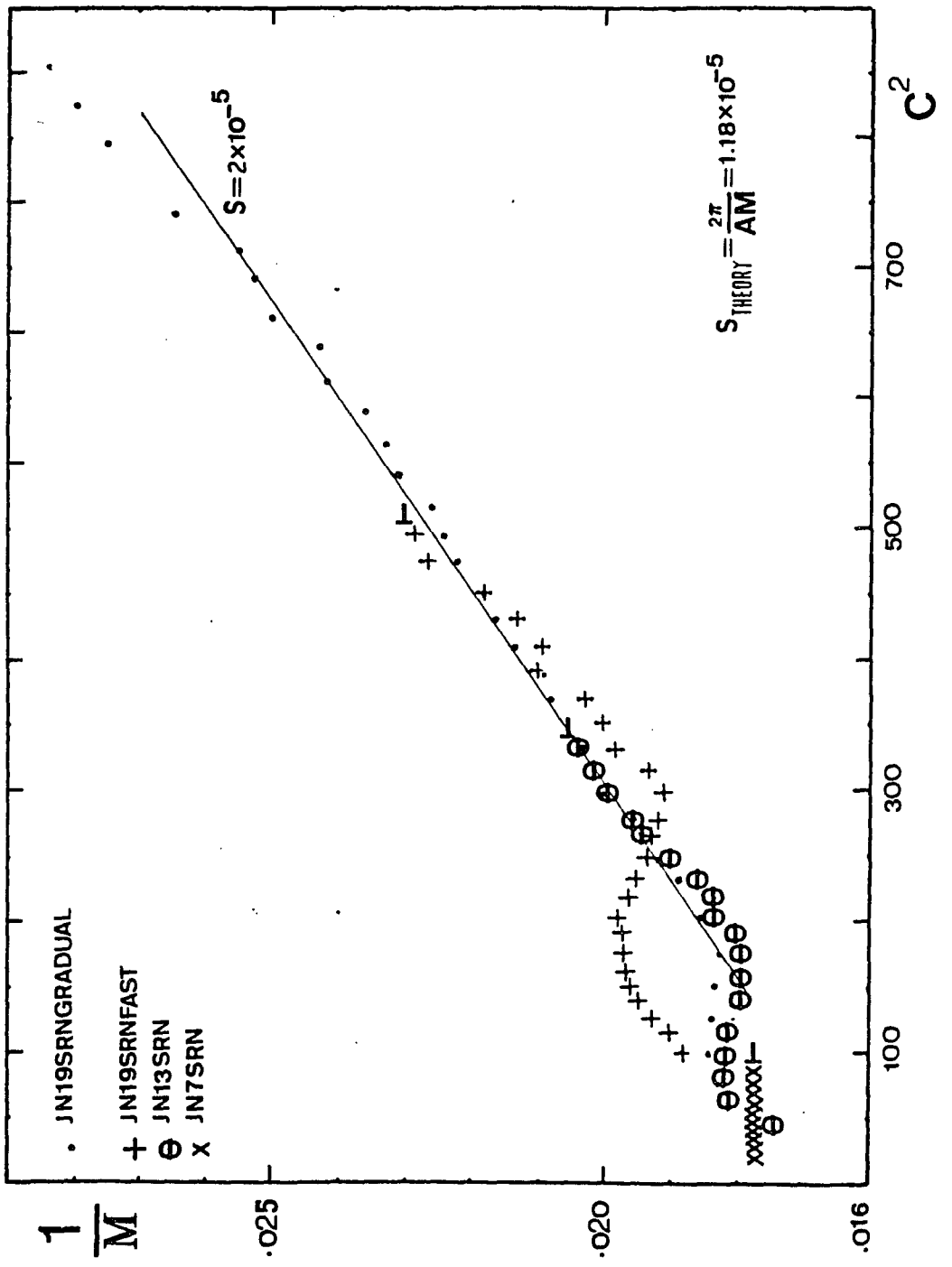
[Fig. II.2.8.] μ/M ratio versus a* for the covalently modified Lennard-Jones and Johnson solids.



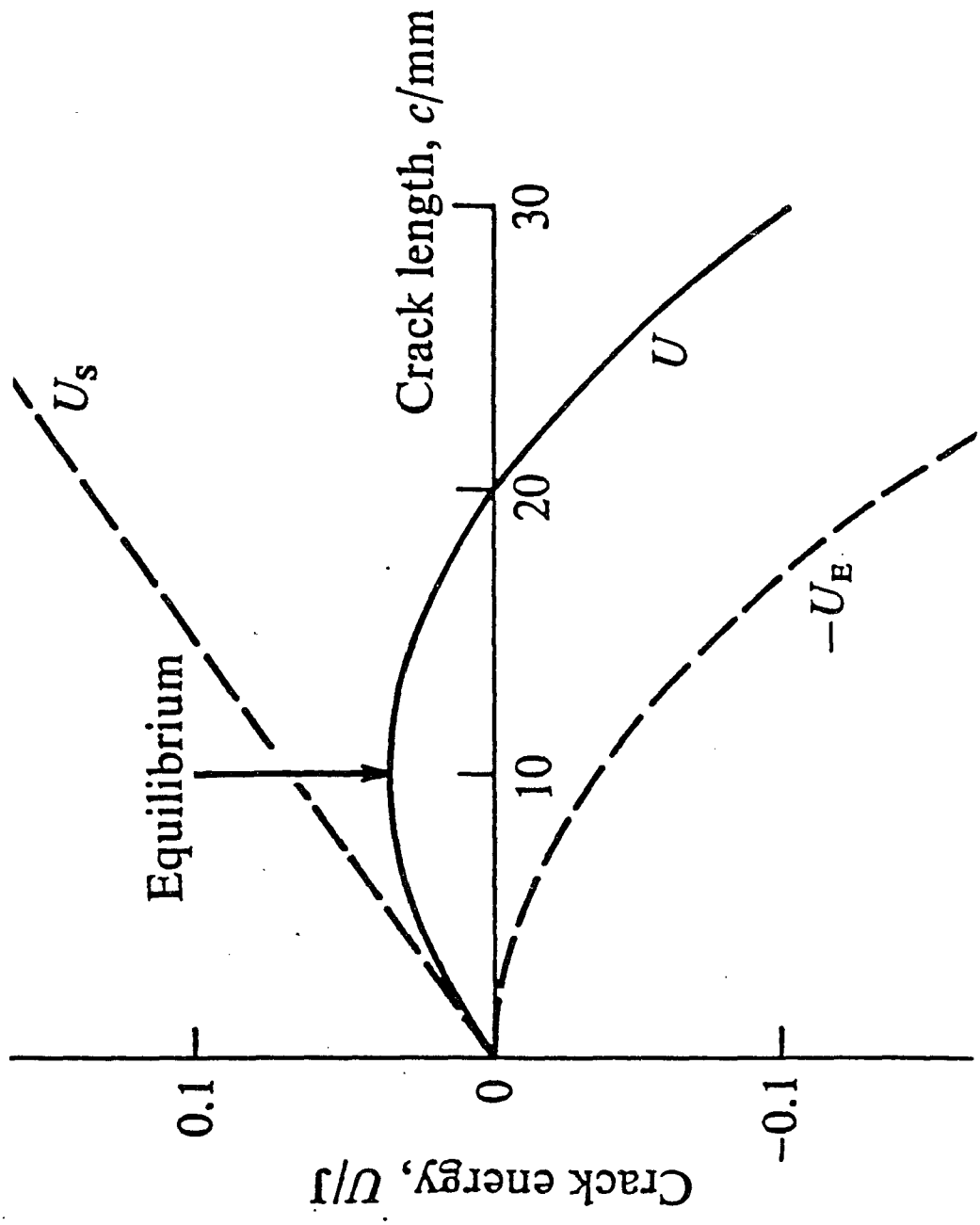
[Fig. II.2.9a.] Young's modulus, M, versus the applied strain. The full circle represents three sample-sizes spanning a factor of 4 in the plate-area. The moduli are identical within 0.1% independent of the sample-size. The straight line is the theoretical behaviour of the modulus against strain for a perfect sample.



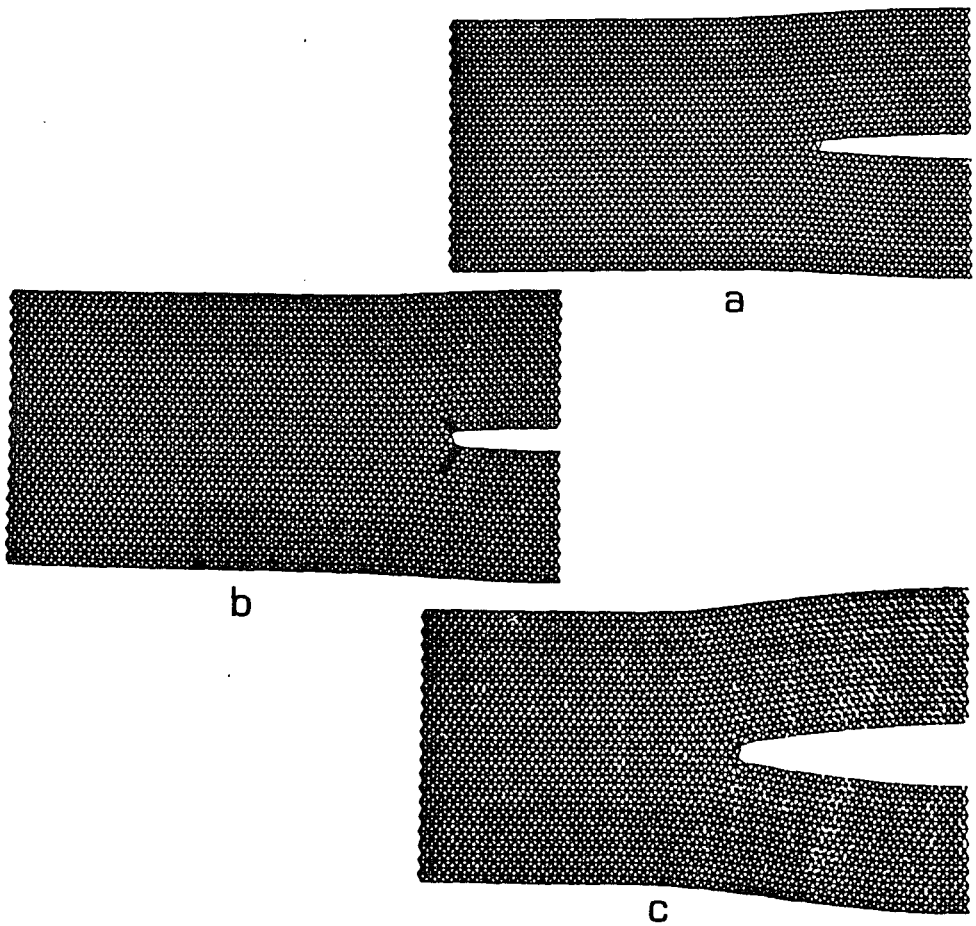
[Fig. II.2.9b.] Young's modulus, M, and the shear moduli versus the increase in the amplitude of the angular resistance, a*, for a 2D-triangular "covalent" solid held together by the modified Lennard-Jones and Johnson potential.



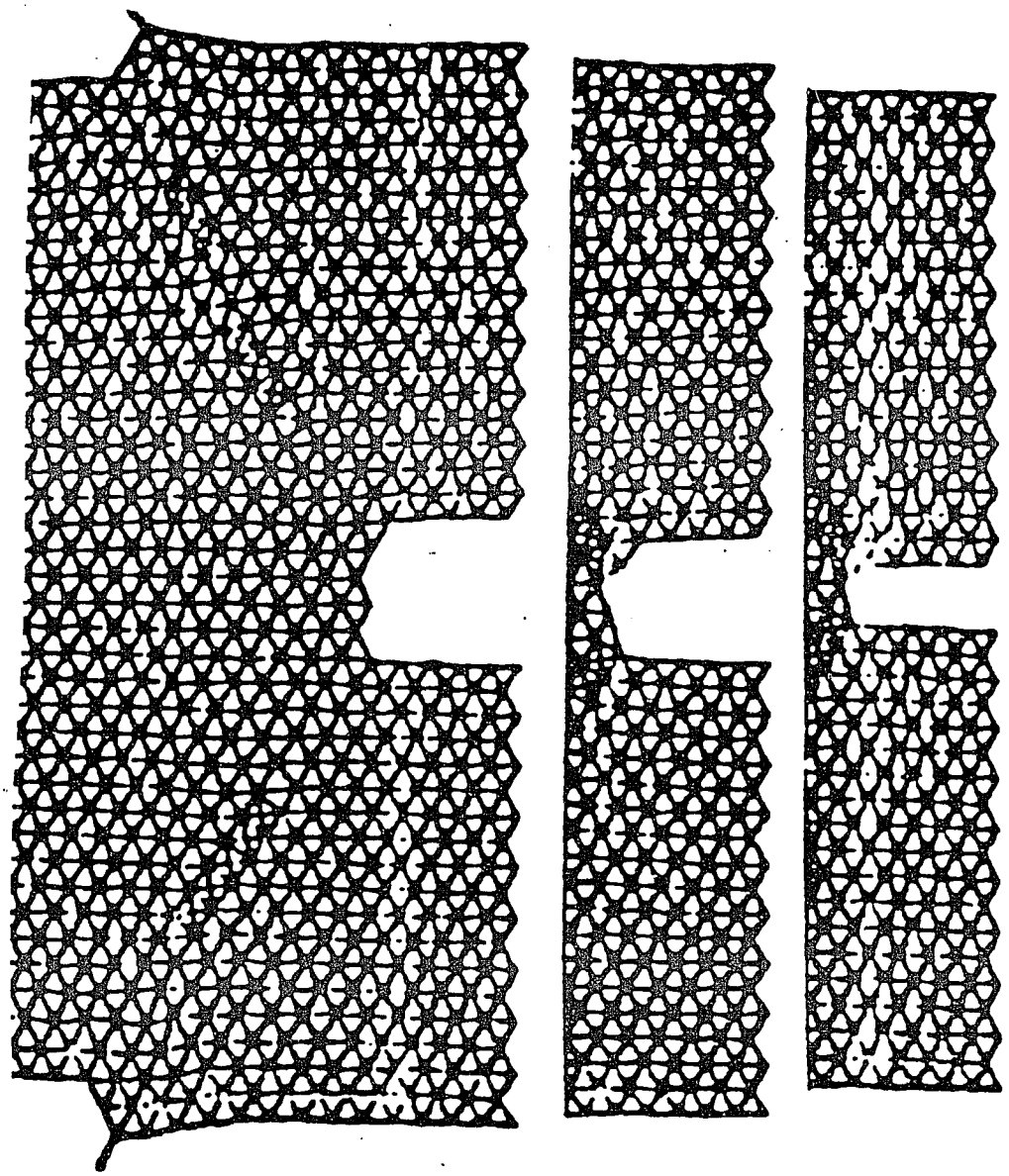
[Fig. II.2.9c.] The functional dependence of the modulus of elasticity, M*, on the sample-size. The simulation data is plotted as 1/M* against c^2. The straight line is the empirical fit to Simulations results. All samples have the identical sample size of 79x135 under the critical constant external strain, and containing varieties of centrally located internal crack of initial half-crack length c_o={3.75, 6.75, and 9.75}.



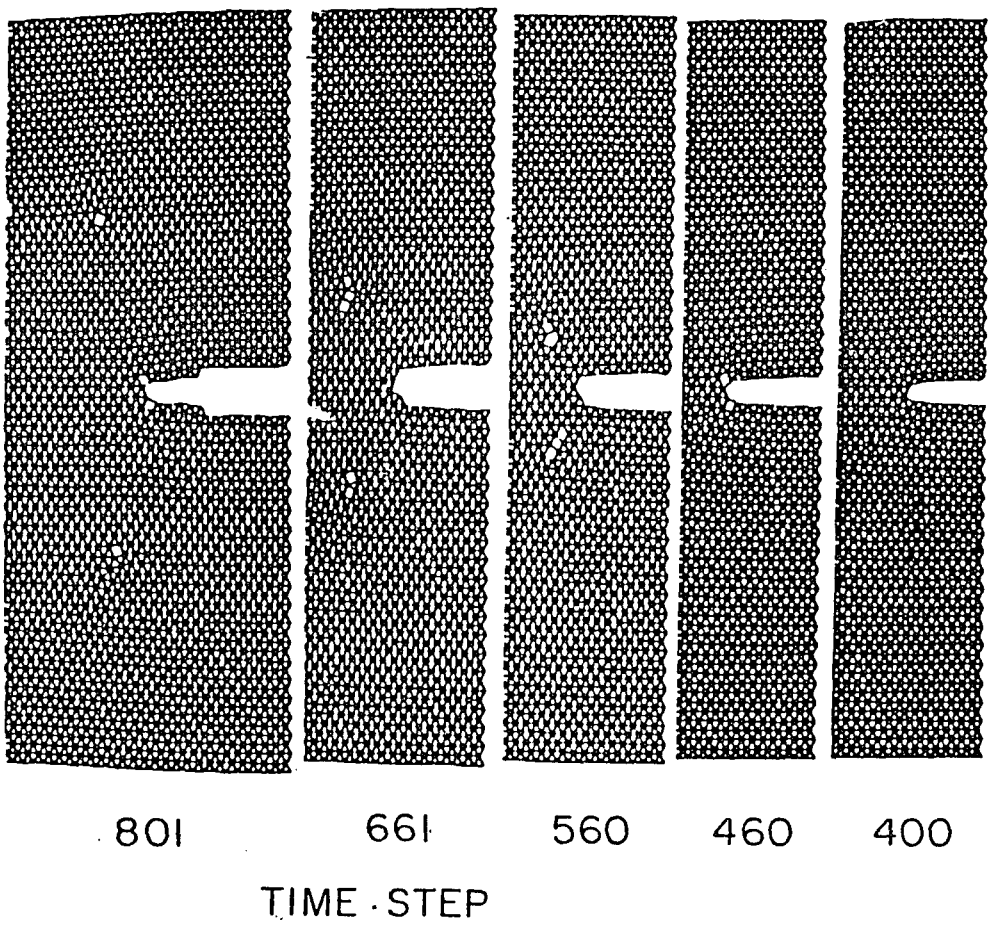
[Fig. II.2.10] Energetics of the Griffith crack in uniform tension. Data for glass from Griffith's paper: γ_S=1.75Jm^{-2}, E=6.2X10^{10}Nm^{-2}, σ=2.63X10^{6}Nm^{-2}. selected to give equilibrium at c=10 mm [p.8, Fig. 1.5, [33]].



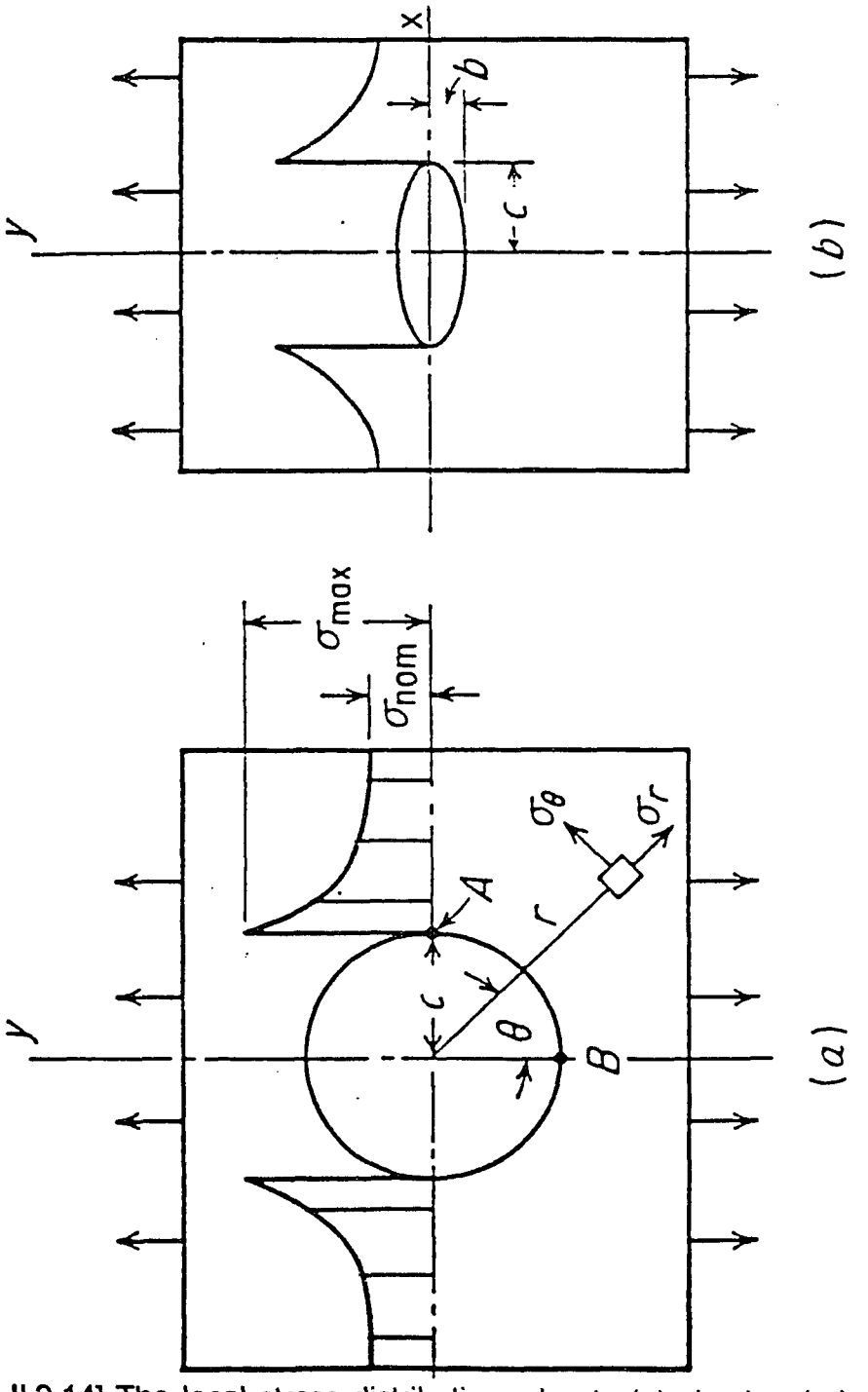
[Fig. II.2.11] The pre-cleaved two-dimensional triangular Lennard-Jones solid under the externally applied critical tensile load. Due to the mirror symmetry used in these simulations only half-sample is demonstrated in this figure. The whole sample may be obtained by the reflection about the right-hand side vertical column of this figure. External constant tensile forces (loads, σ_a) are applied to the individual atoms of the uppermost and lowermost horizontal boundaries, i.e., 1st and 39th rows. Lines are drawn between the interacting atoms, i.e., between those atoms which are less than 1.6d apart. (a) Brittle propagation of the cleavage crack of initial half crack-length c_o=19.75d under the applied constant tensile load of σ_a=0.50. (b) The incipient dislocation nucleation at the crack-tip of initial half crack-length c_o=9.75d under the applied tensile load of σ_a=1.30. The extra lines designate the atoms which have moved into the interaction range of their second neighbors. (c) Dislocation formed at the lower end of the crack tip at σ_a=1.30 and c_o=19.75d. The generated dislocation is, eventually, moved away from the crack-tip towards the loaded horizontal surfaces of the specimen. Note that the system is heavily overloaded [2, 15].



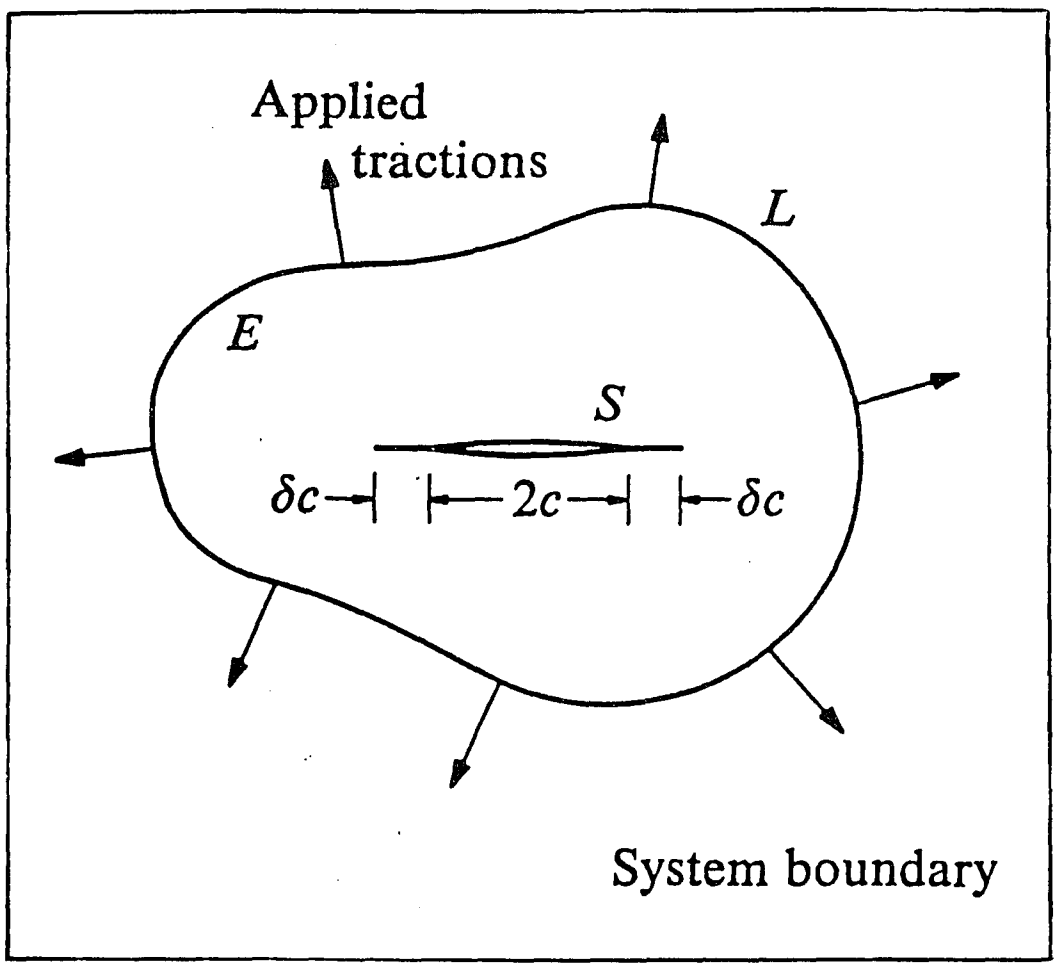
[Fig. II.2.12] The arrest and blunting of an internal crack in a two-dimensional triangular Lennard-Jones crystal, subjected to the remotely applied constant tensile critical load at the horizontal boundaries of the specimen, due to the emission of blunting dislocations at the crack-tip. The emitted dislocations, eventually, moved to the loaded horizontal surfaces of the sample and produced a jug there. Only a portion of the specimen is illustrated [15, 114, 121].



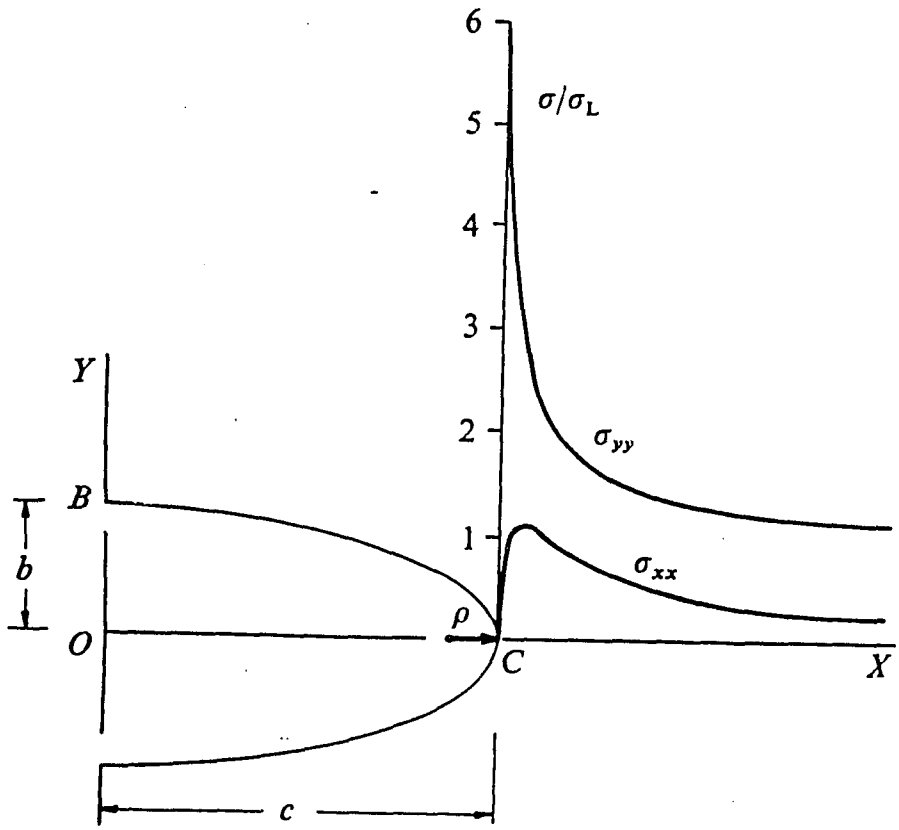
[Fig. II.2.13] The arrest and blunting of brittlely propagating cleavage crack of initial half crack-length c_o=3.75d in a two-dimensional triangular Johnson crystal subjected to the critical applied constant tensile load of 3.37 at the horizontal surfaces of the specimen. Immediately after the emission of blunting dislocations at the crack-tip the brittlely propagating internal crack got blunted. As illustrated in Fig. II.3.14 the blunting dislocations were generated at step 460, the crack was then arrested for about 200 time steps, and the brittle propagation of the blunted crack-tip renewed at time step 645 as the emitted dislocations moved away from the crack-tip zone and their shielding effect was, therefore, removed. A new set of dislocations were emitted at step 801, and the above process was repeated again. The emitted dislocations, finally, propagated to the loaded horizontal boundaries of the specimen. In the 2D-triangular Johnson solid the dislocation shows up as missing bonds as atoms move out of the short range of the interatomic potential, i.e., r>1.3147d.



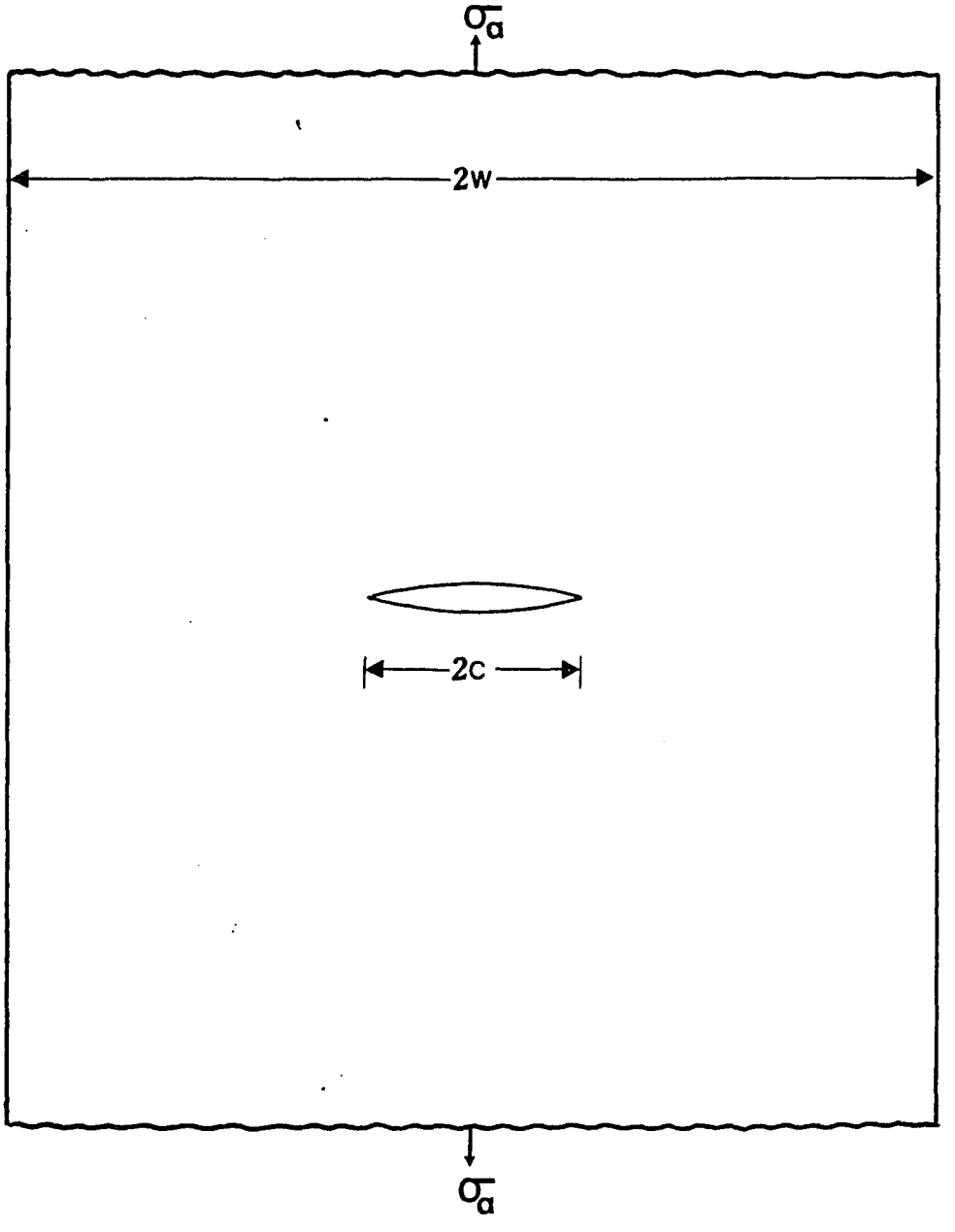
[Fig. II.2.14] The local stress distributions due to (a) circular hole and (b) elliptical hole in an infinite plate subjected to the remotely applied constant tensile loads at the horizontal boundaries of the specimen (Fig. 2.20 [190]).



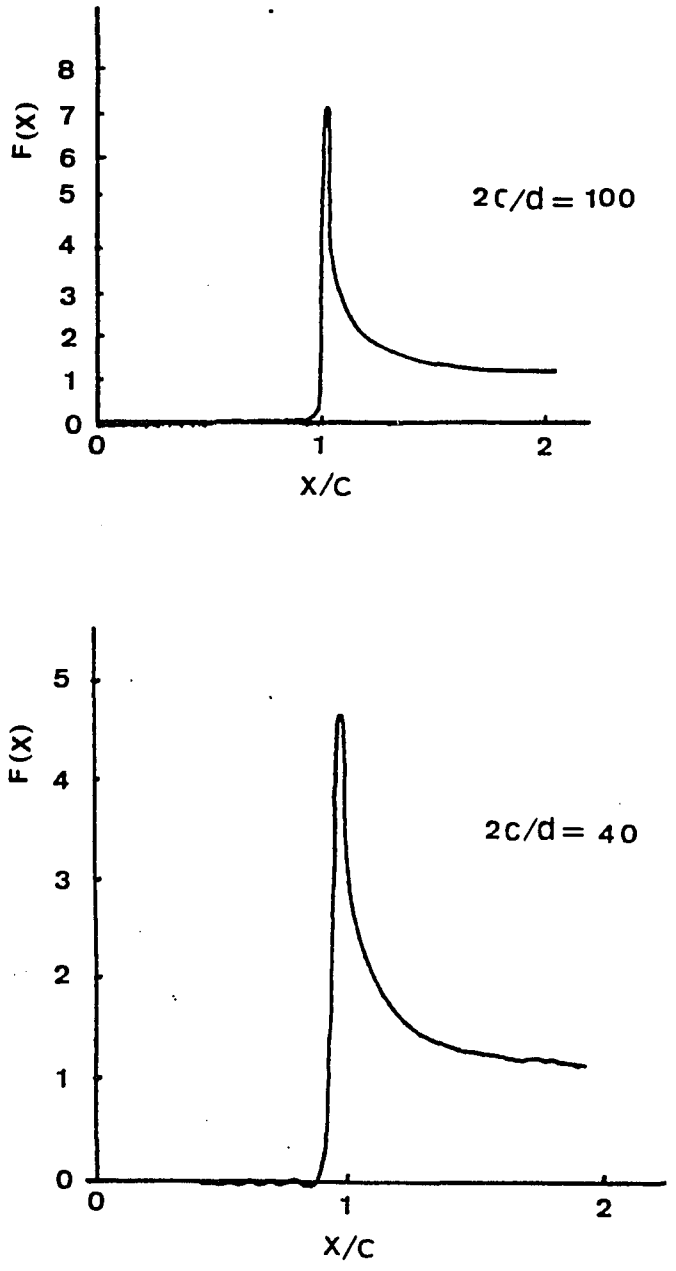
[Fig. II.2.15] Griffith's model for a crack system: a pre-cleaved plate subjected to the remotely applied loads at the boundaries. The important elements of the system are illustrated as: an elastic body E containing an internal crack S of length 2c subjected to the externally applied loads L at the boundaries (Fig. 1.4 [33]).



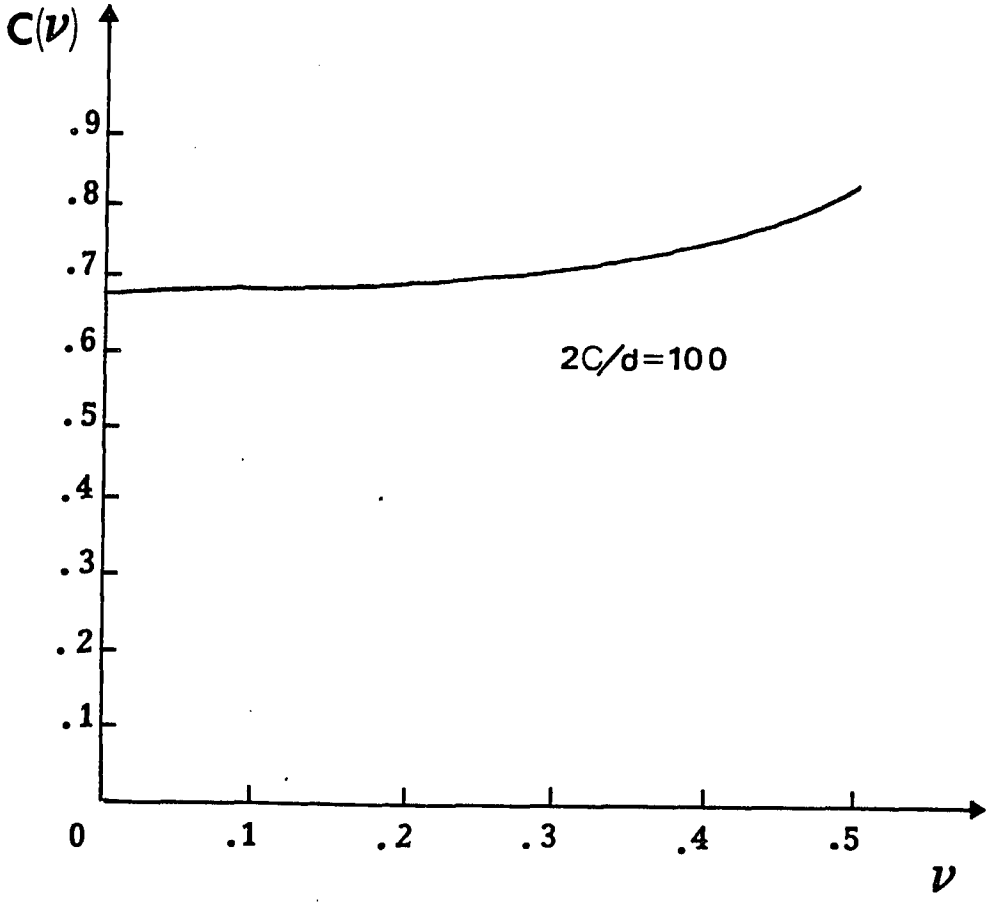
[Fig. II.2.16] The local stress concentration factor σ_y/σ_a of an internal elliptical hole of c=3b. Note that the major perturbations to the applied stress field occur only within the characteristic length of c from the physical boundaries of the hole, with the greatest stress gradients confined to the highly localised region within the distance of the order of the radius of curvature of the hole, ρ, surrounding the position of the maximum concentration (Fig. 1.2 [33]).



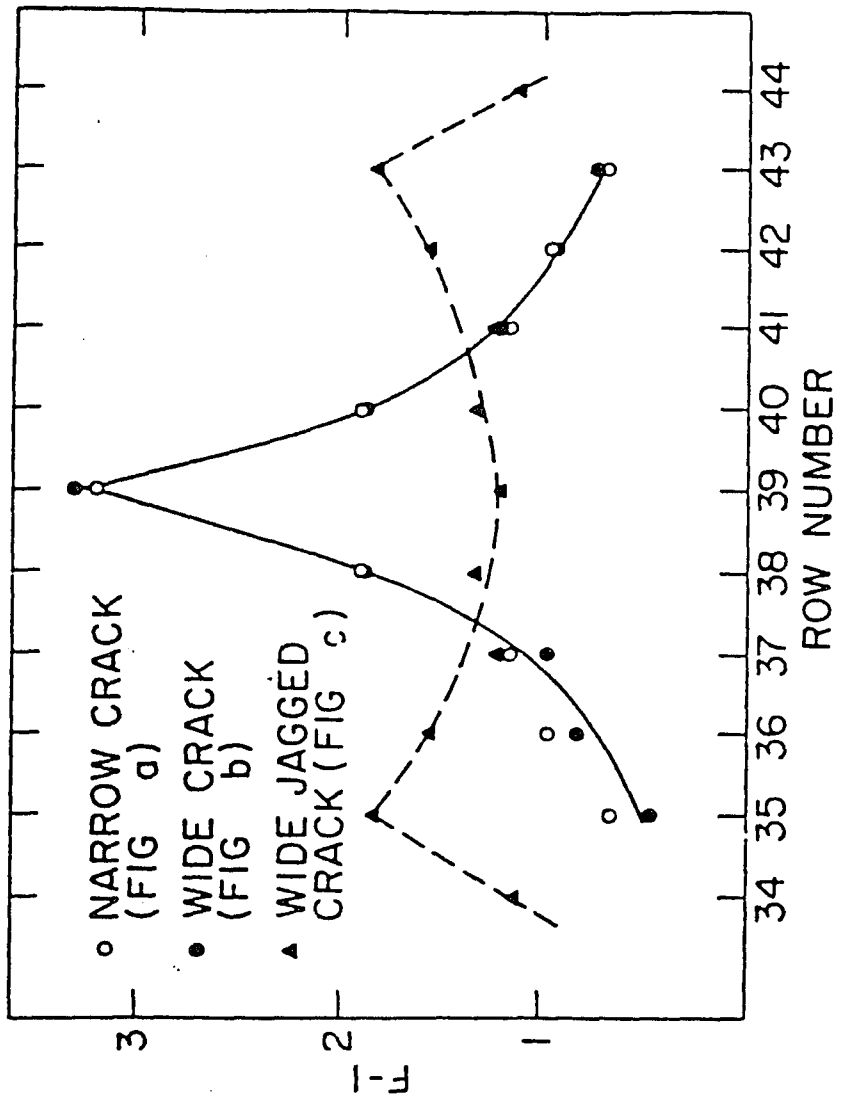
[Fig. II.2.17] Uniform loading configurations for plane cracks with straight fronts. This model is used for the derivations of the local stresses in the vicinity of the internal cracks. The thickness of the plate is conveniently taken to be unity in the two-dimensional problem, and infinity in the 3D problems (Fig. 3.7 [33]).



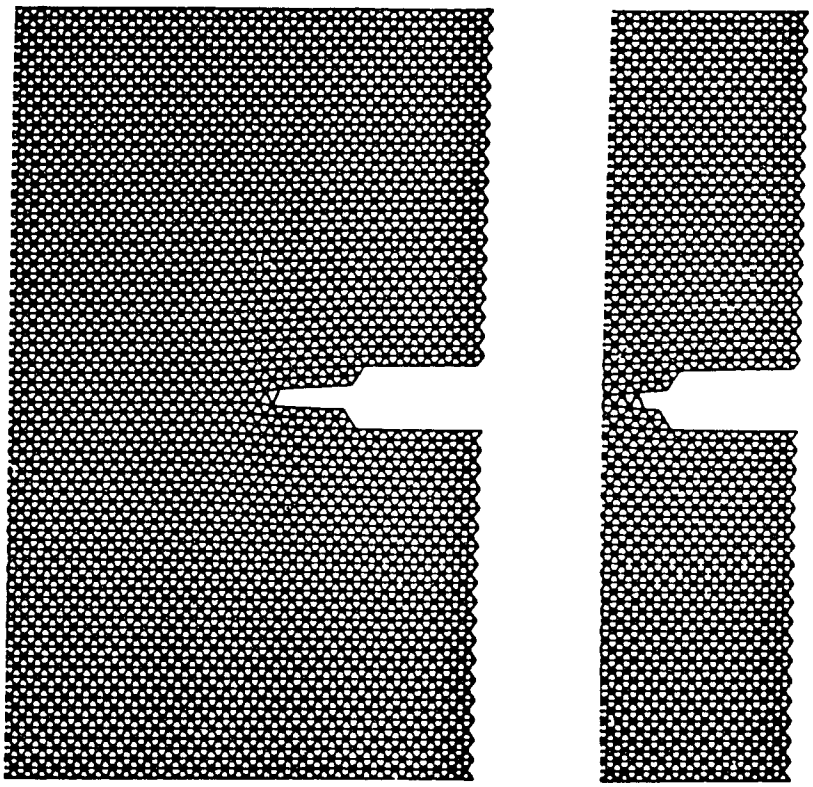
[Fig. II.2.18] Hoop's stress distribution along the crack-line, $F(x)=\sigma_y(x,0)/\sigma_a$, versus x/c for the variety of the crack-lengths from Eringen's [108] non-local treatment of the crack problem.



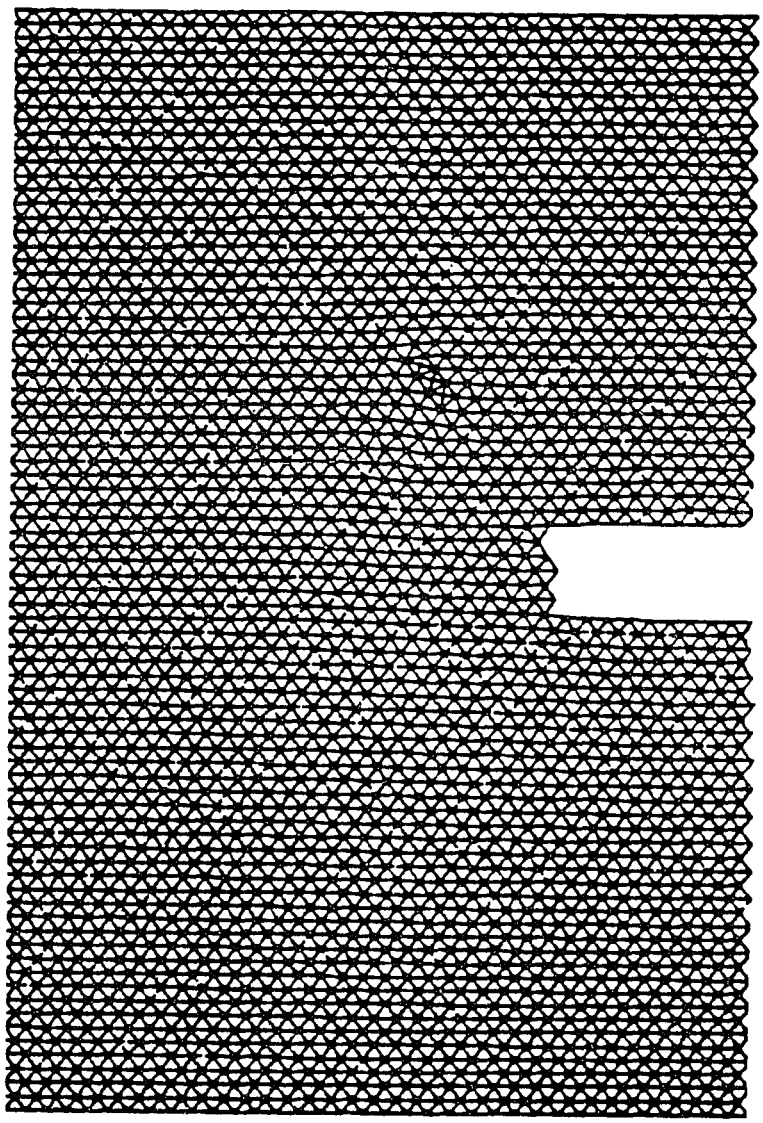
[Fig. II.2.19] Eringen's [108] Material Function, C(ν), depends on the Poisson's ratio only, and it falls into the region $0.845 \geq C(\nu) \geq 0.676$ for $\nu=0$ to 0.5. For $\nu=0.25$, $C(\nu)=0.713$.



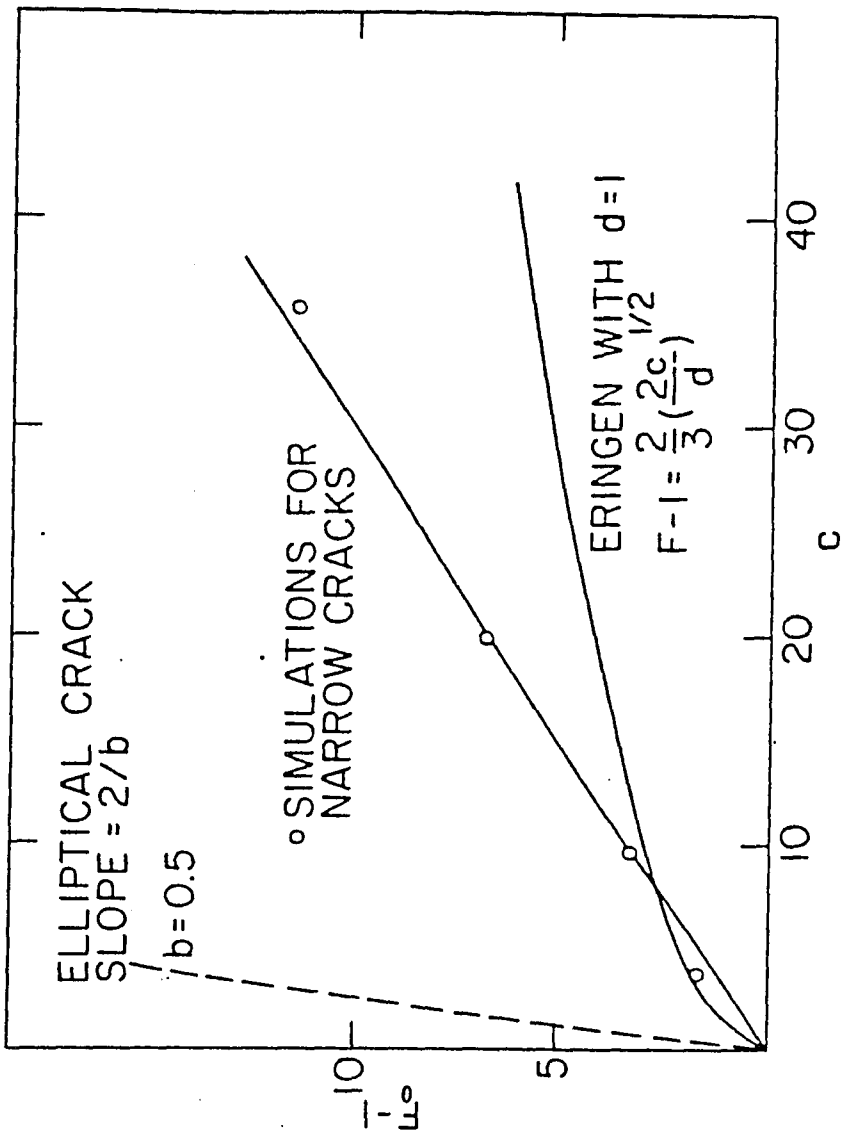
[Fig. II.2.20] The stress concentration (distribution) factor F-1 along the column of the crack-tip atom, i.e., at r=0, atom no. 58 of Fig. II.1.5 at the central crack row (row 39 of Fig. II.1.5) and at several surrounding rows. F-1 is the contribution from the crack itself, and the remotely applied nominal tensile stress is about E/10000 in magnitude. E is the Young's modulus of the solid.



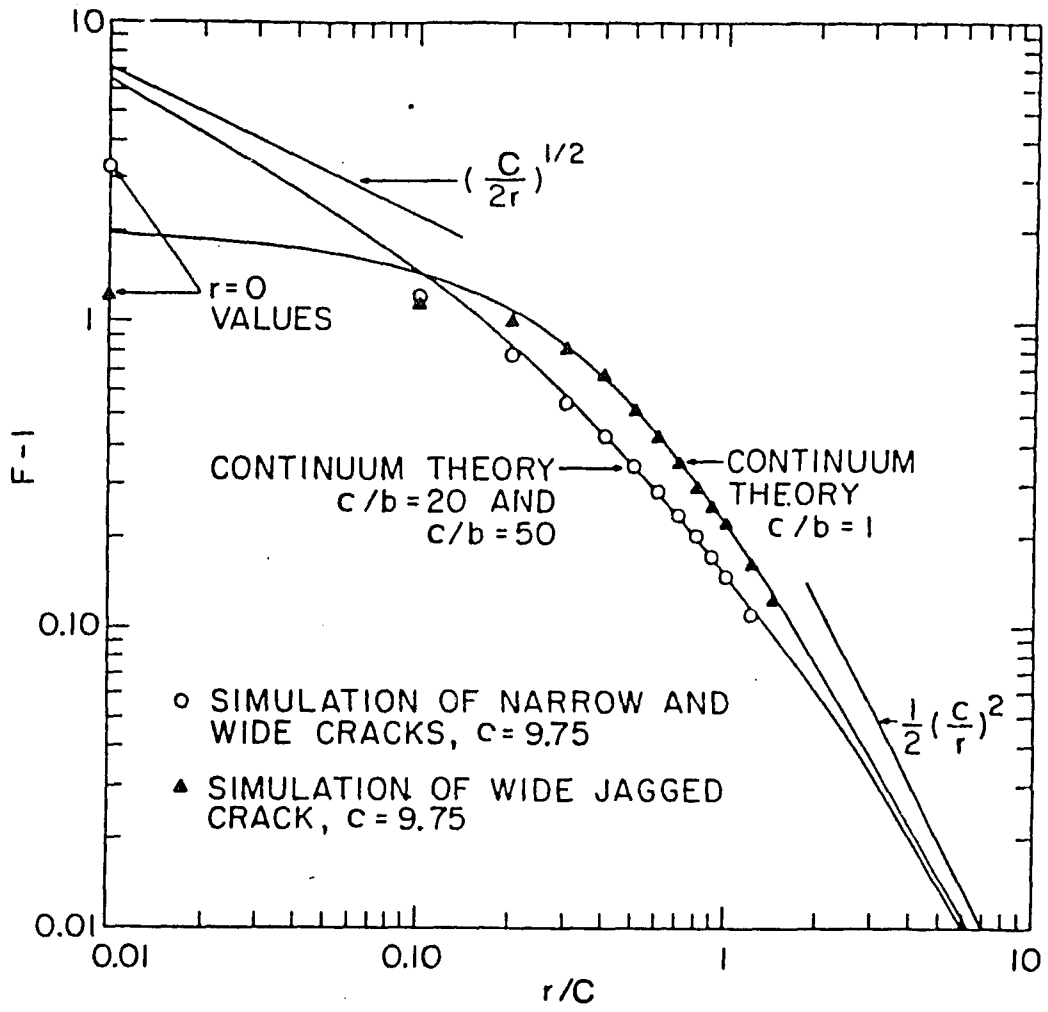
[Fig. II.2.21.] Brittle propagation of the "wide" crack of Fig. II.1.5b at a constant critical applied strain of 0.0305.



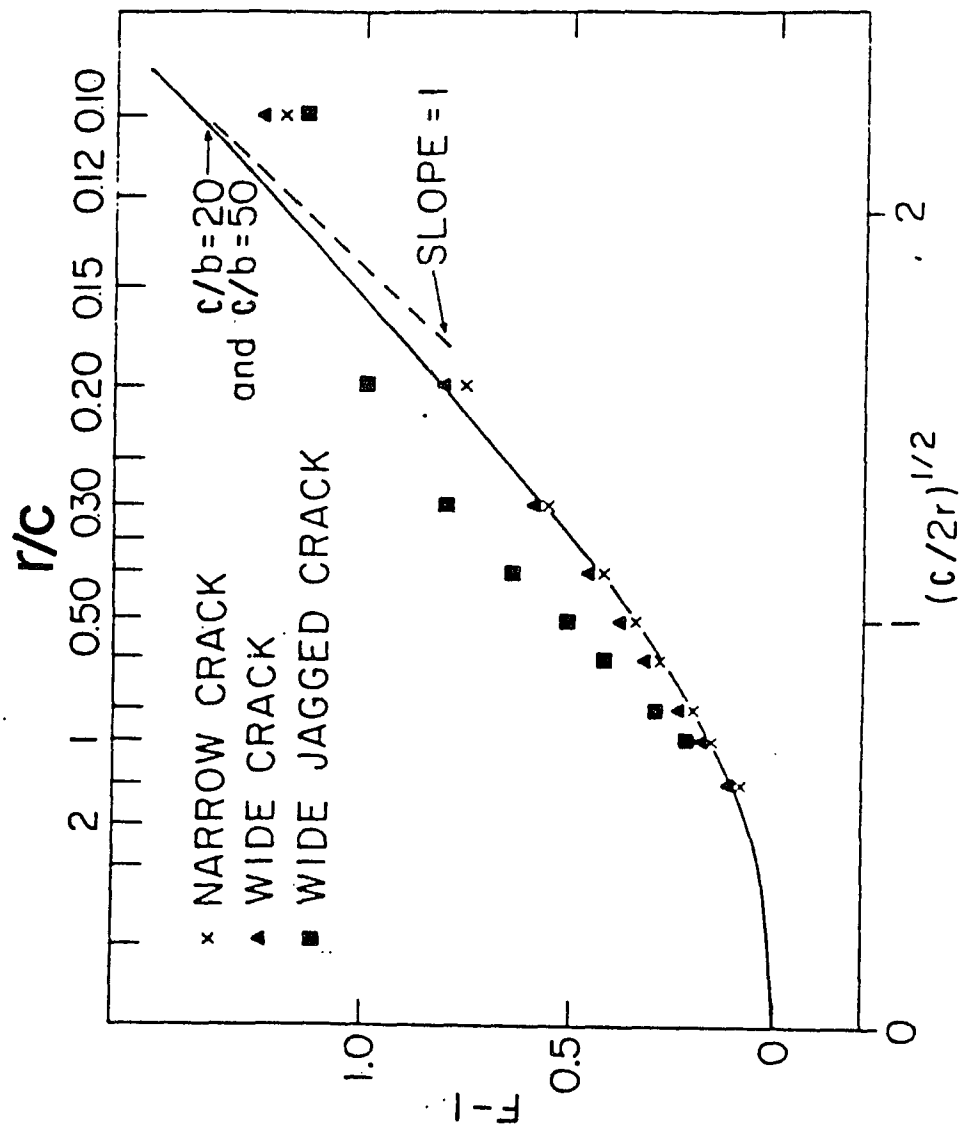
[Fig. II.2.22.] Dislocation generation at the sharp corner of the wide jagged crack of Fig II.1.5c at the critical externally applied strain of 0.0350. The emitted dislocation, characterised by the cross hatching has left a ledge at the crack-tip by gliding away from the crack-tip toward the loaded horizontal surface of the specimen.



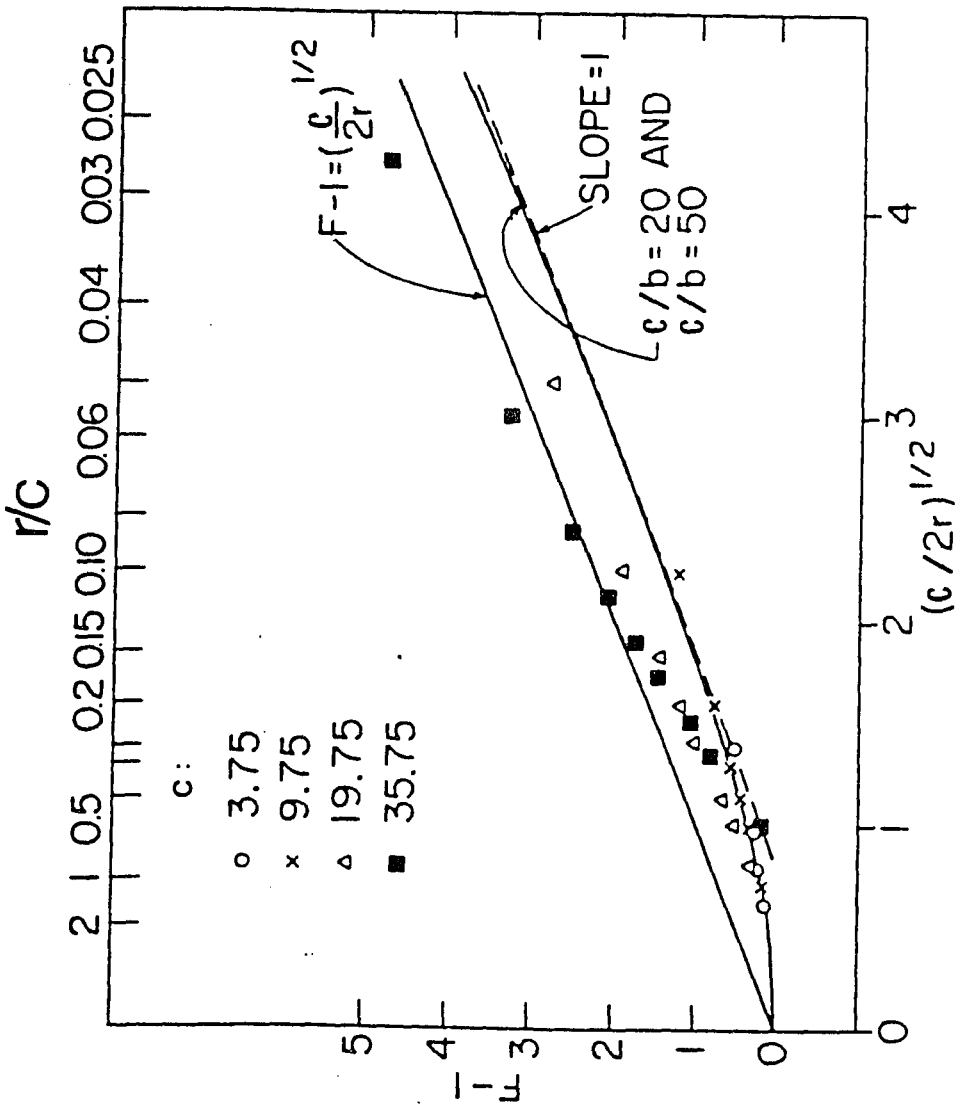
[Fig. II.2.23] Local stress concentration factor F-1 at the crack-tip, i.e., at r=0 as a function of half-crack length for four narrow cracks. Simulations results are illustrated as open circles. The solid line passing through these points demonstrate a linear dependency of stress concentration factor, F-1, on the crack length. The broken line represents the theoretical calculation of Inglis-Griffith-Goodier (IGG) for an elliptical hole of b=0.5d (equations II.2.51-52). Eringen's [108] non-local prediction for the stress concentration factor (eq. II.2.58) is also shown for the purpose of comparisons.



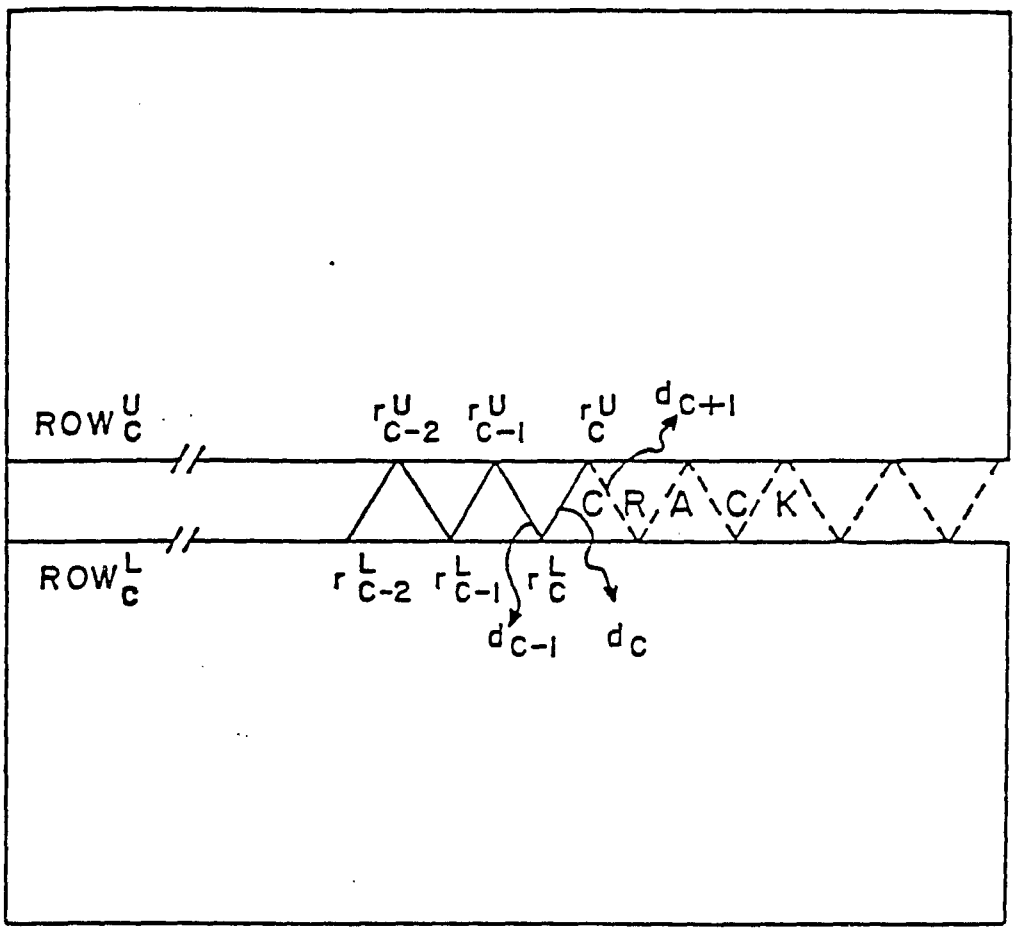
[Fig. II.2.24] Log-Log plot of the stress distribution factor F-1 as a function of r/c. Simulations results for the narrow and wide cracks of c_o=9.75d are indistinguishable and, therefore, illustrated with a single symbol (open circles). The wide-jagged crack simulations results are shown as solid triangle. The solid lines are IGG's theoretical predictions for an elliptic hole of c/b=20 (or 50), and for a circle c/b=1 calculated by means of equations II.2.51-53.



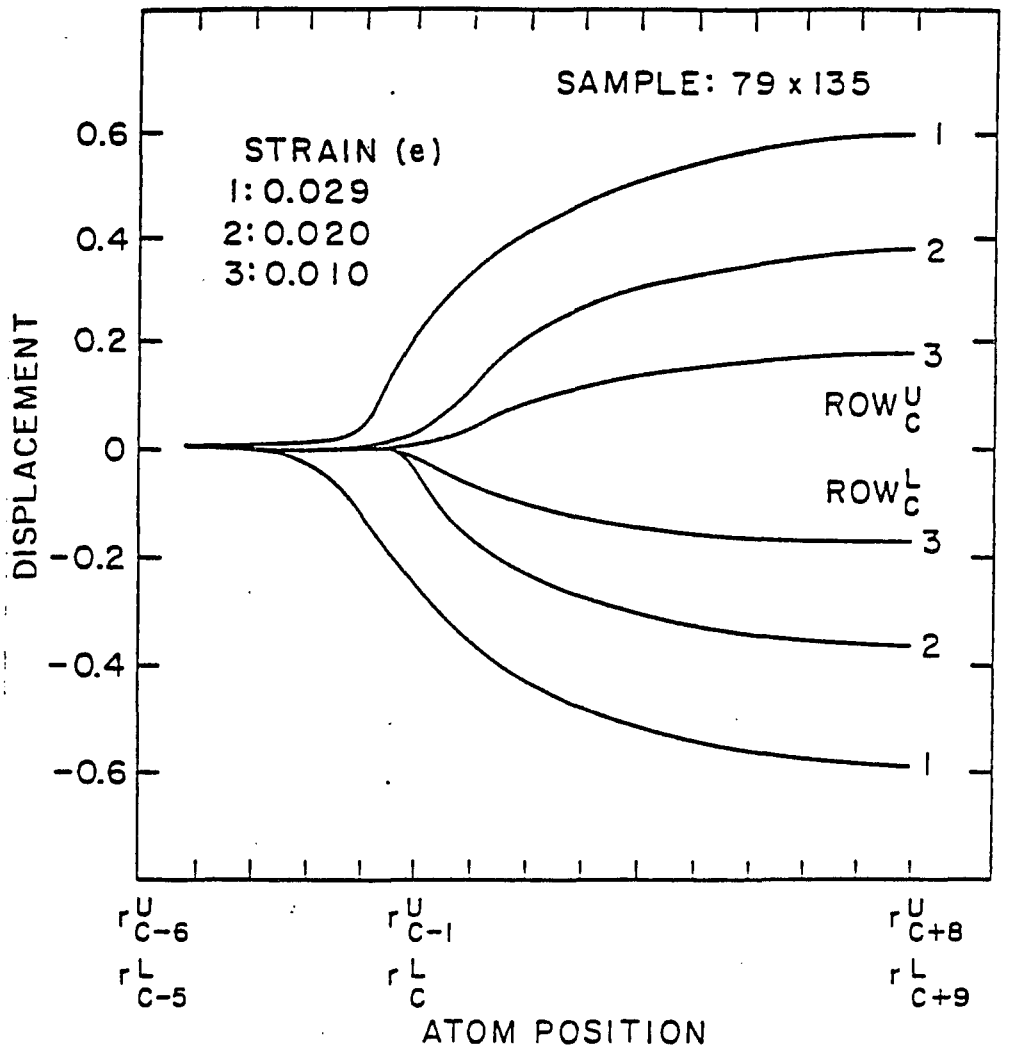
[Fig. II.2.25] Simulations data of Fig. II.1.5 plotted as F-1 versus $(c/2r)^{1/2}$. The theoretical prediction of IGG is given as broken line (slope=1). Note that the solid line fit to the data has neither the correct slope nor does it pass through the origin.



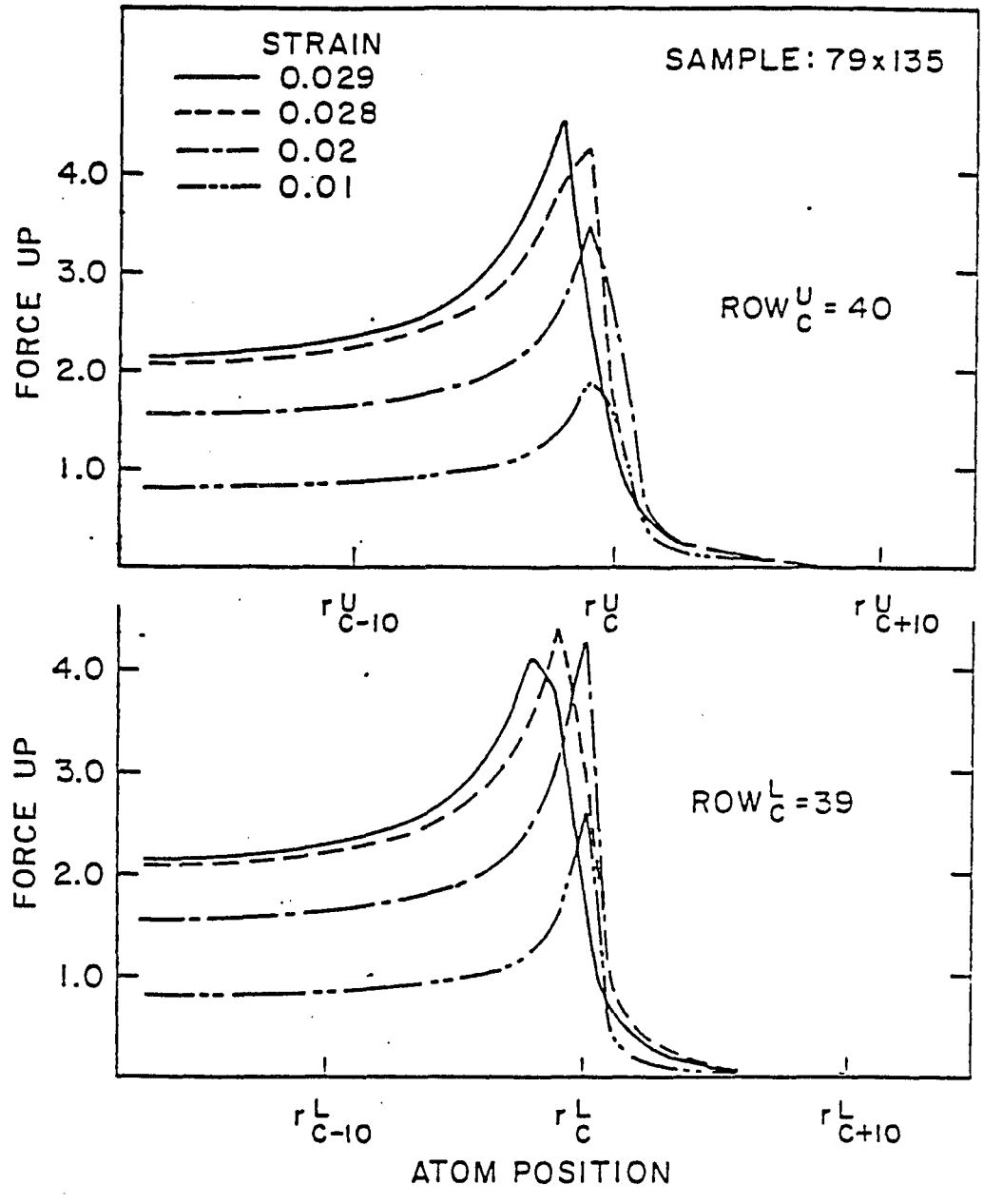
[Fig. II.2.26] Simulations data for four narrow cracks of different lengths plotted as F-1 versus $(c/2r)^{1/2}$. The number adjacent to the symbols are the half crack lengths, c. The broken line illustrates the correct theoretical slope of one. Note that the solid line fit to the data has neither the correct slope nor does it pass through the origin. Most of the simulation data fall between the thin elliptical c/b=20, and infinitely thin crack $F-1=(c/2r)^{1/2}$ lines. No systematic $r^{-1/2}$ dependence is observed.



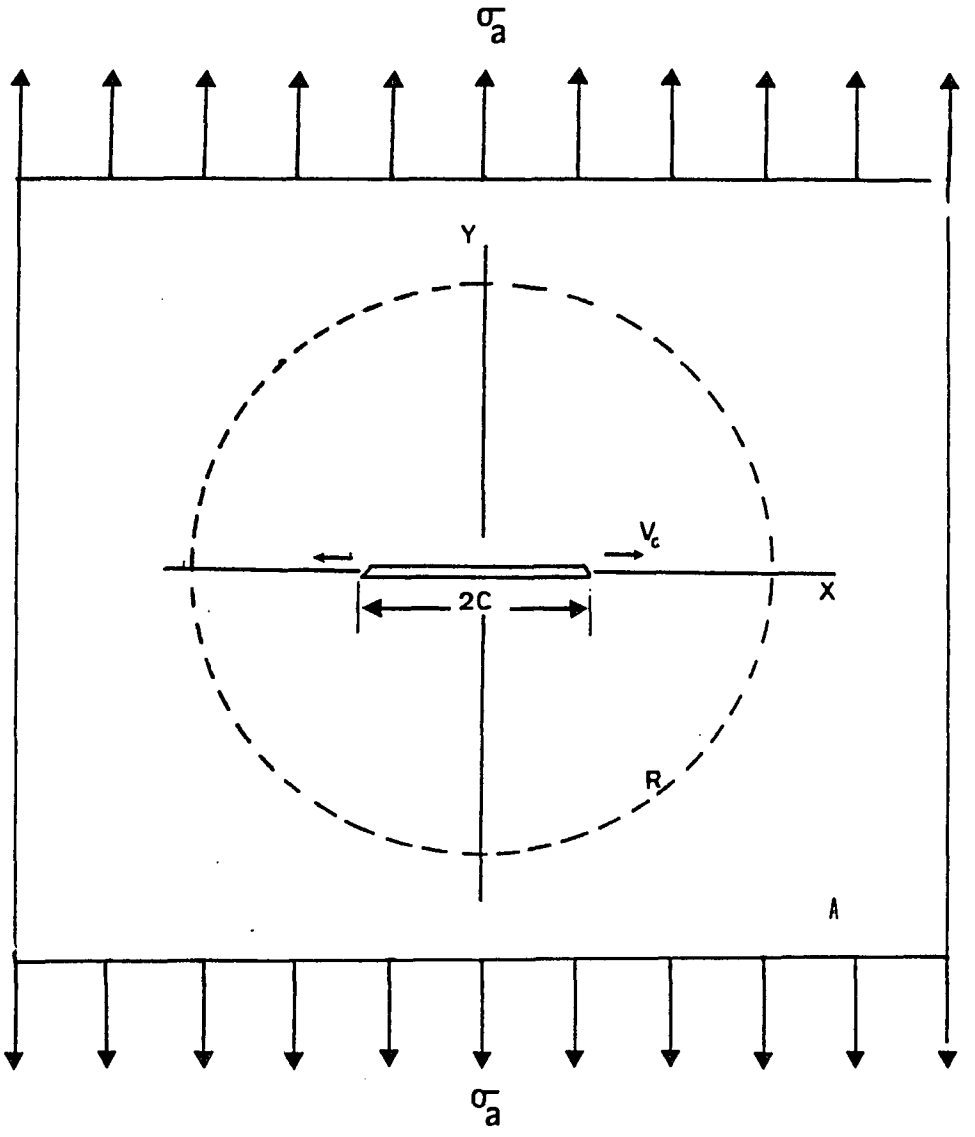
[Fig. II.2.27] Labelling of the interatomic bonds and mass points (atoms) at the immediate vicinity of the crack-tip.



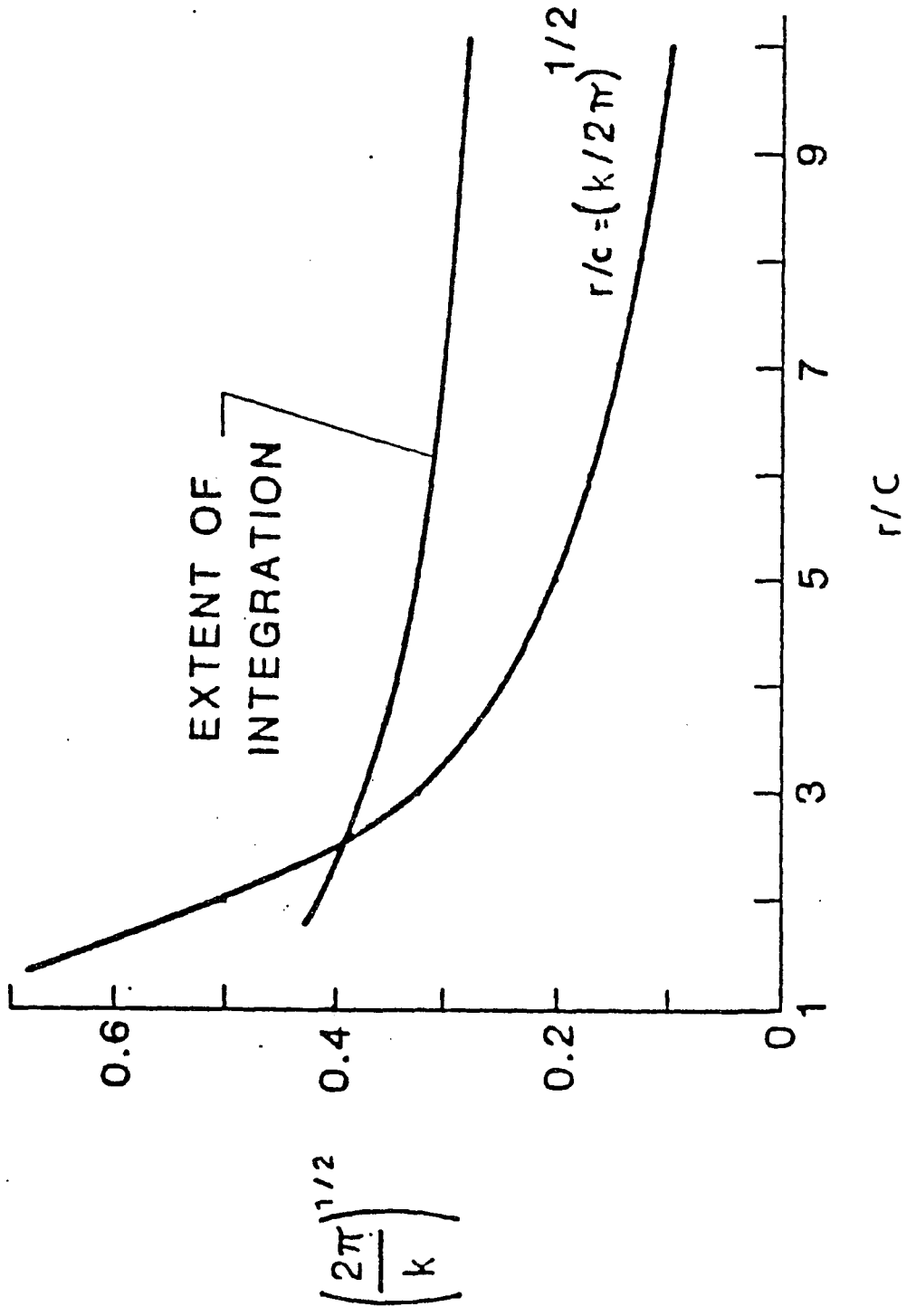
[Fig. II.2.28.] Displacements of few atoms on the two central rows at the vicinity of the crack-tip are plotted against the atomic positions for a 2D-triangular Lennard-Jones solid (79X135) subjected to varieties of remotely applied constant displacements, containing an internal crack of c_o=9.75d.



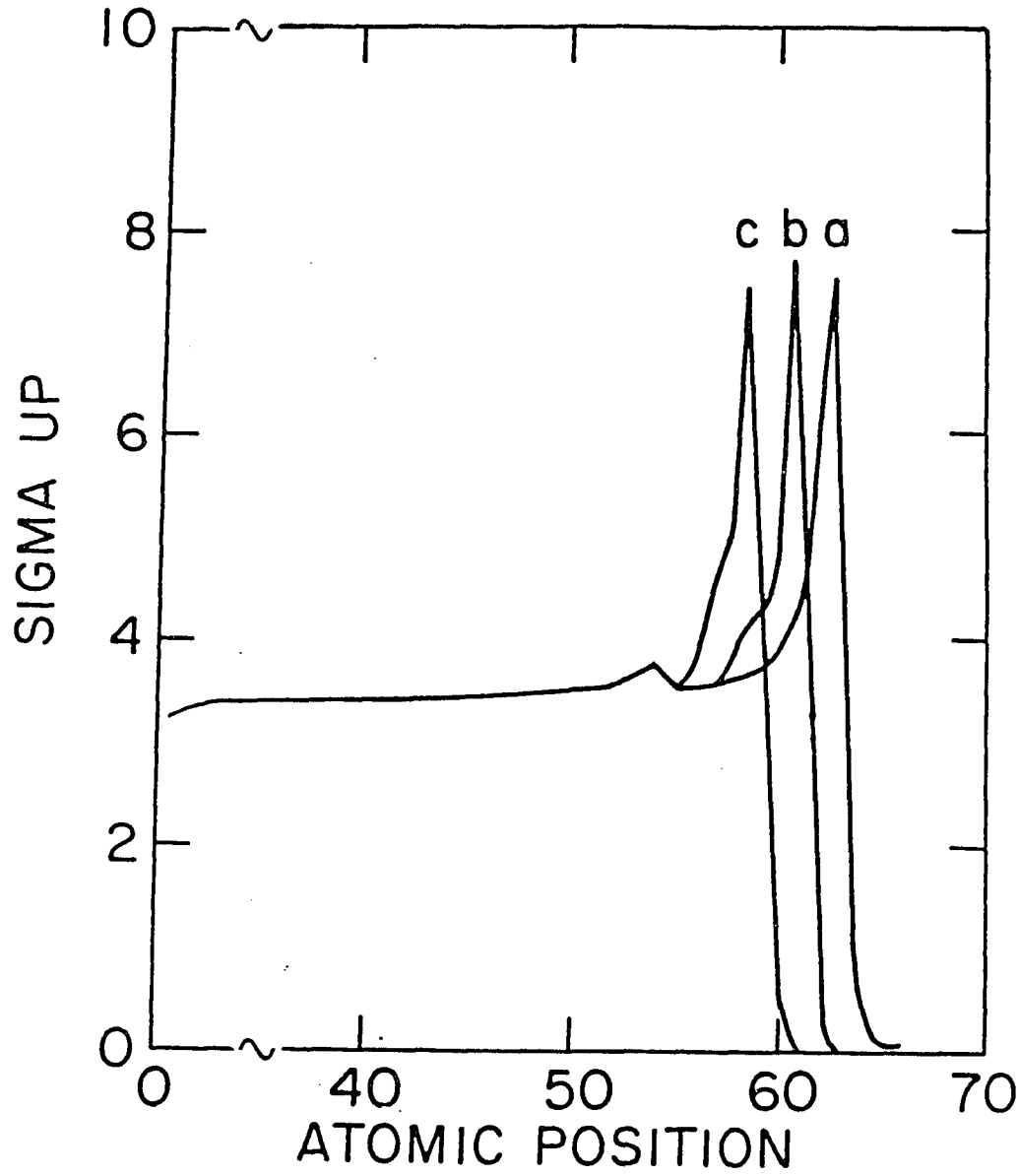
[Fig. II.2.29] The local forces acting on the individual atoms on the two central rows in the vicinity of a narrow crack, c, in a 2D-triangular Lennard-Jones solid subjected to four very different applied constant strain, i.e., ε= 0.01, 0.02, 0.028, 0.029. Note that the critical strain for the initiation of fracture for this crack (c_o=9.75) in the same sample size i.e., 79 rows by 135 columns was 0.0293. See Table. II.3.5



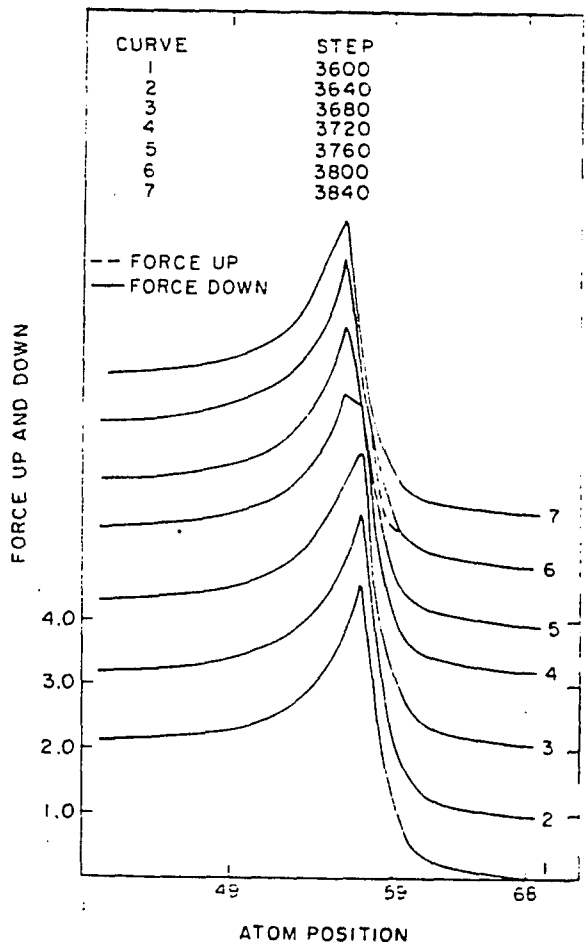
[Fig. II.3.1] Dynamic plane-crack system. V_C is the crack-tip velocity. R denotes the domain which receives the stress-wave "message" from the crack-tip.



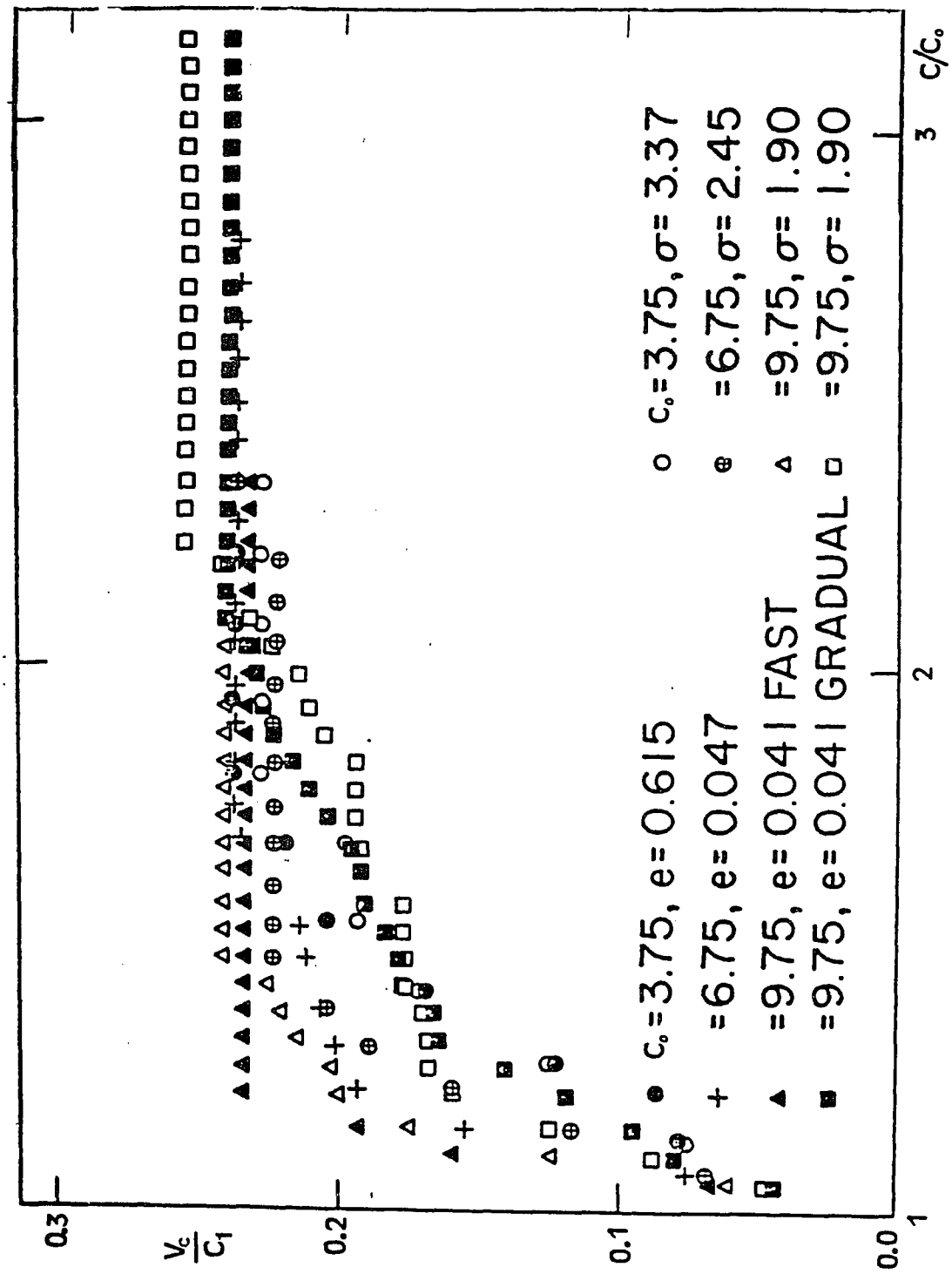
[Fig. II.3.2] The calculations of Roberts and Wells that provided their limiting crack-tip velocity of $0.38C_1$ [191].



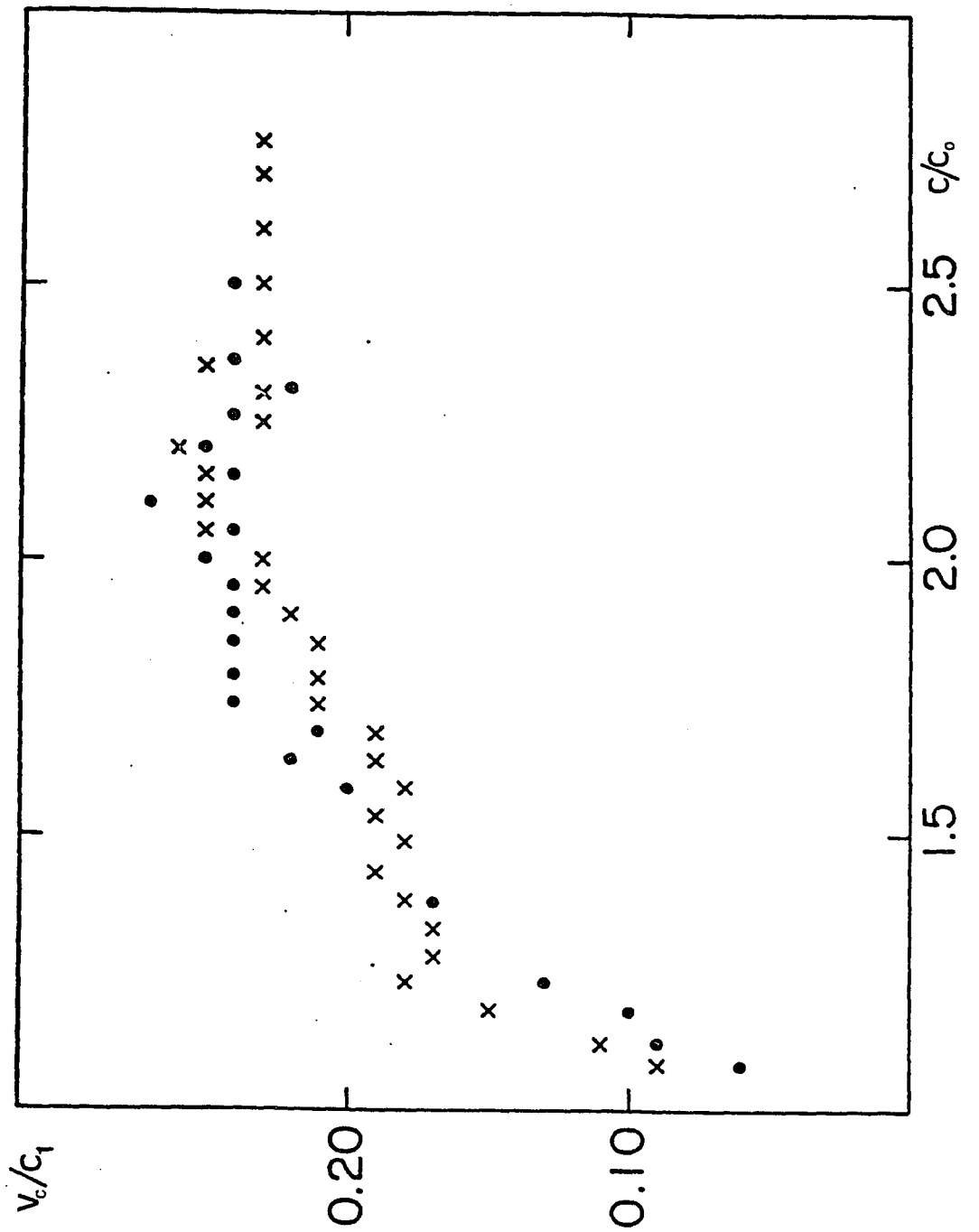
[Fig. II.3.3.] Dynamic stress distribution in the 2D-triangular Johnson solid. Curve (a) is the static stress distribution for the centrally located internal crack of the initial half-crack length c_o=3.75 correspondent to 7 broken bonds in the half-sample. Curve (b) is 331 steps later where there are 11 broken bonds in the half sample, and the crack-tip is accelerating. Curve (c) represents the system 93 steps later, where there are 15 broken bonds in the half-sample and the crack-tip velocity is saturated to its constant terminal value. The static and dynamic local stress distributions are very similar and is obviously crack-tip velocity independent. The critical (fracture) stress is 3.37.



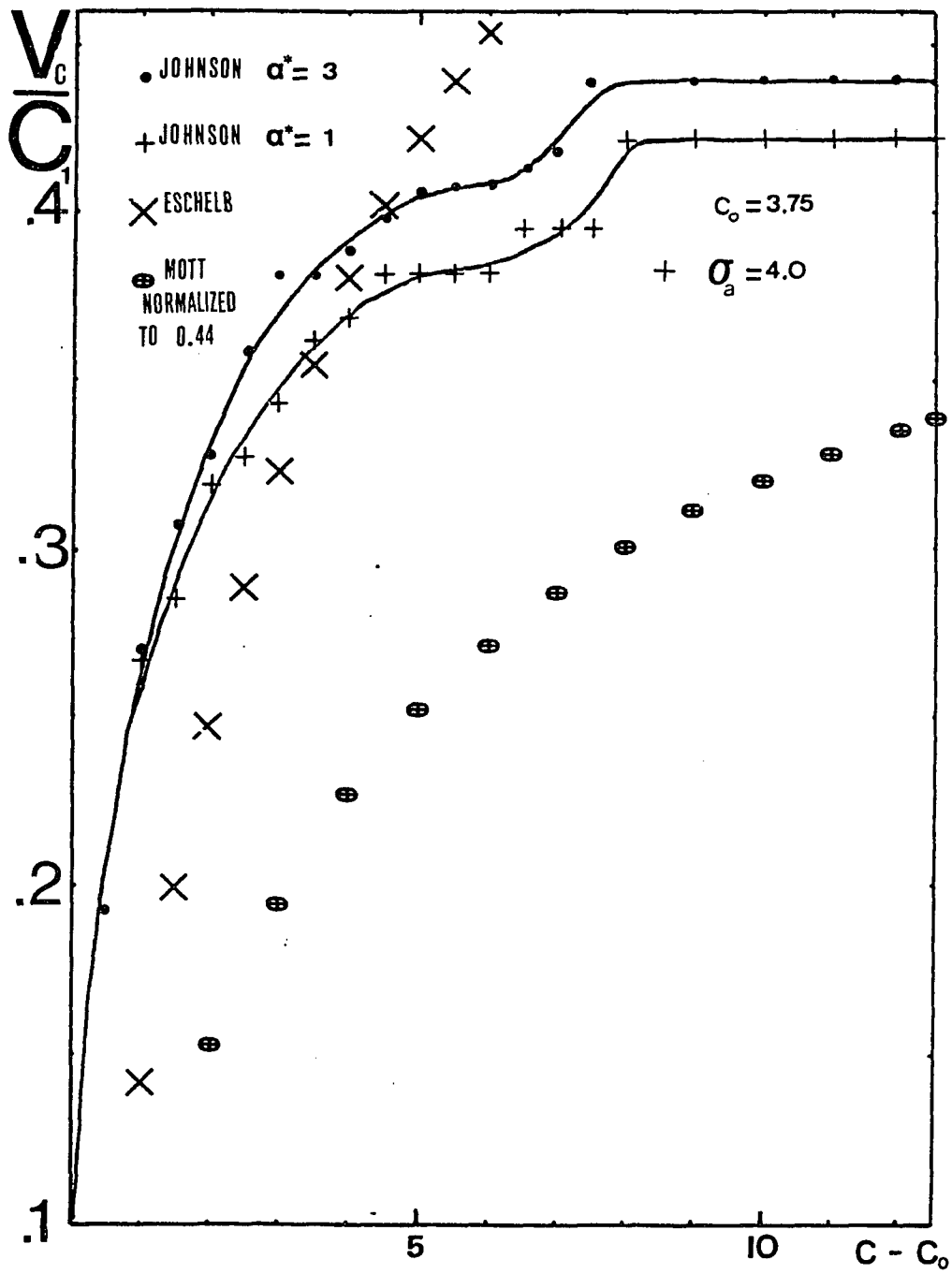
[Fig. II.3.4.] Dynamic stress distribution in the 2D-triangular Lennard-Jones solid of 10704 atoms arranged in 79 rows (79X135). Curve #1 is the static stress distribution for an initial crack of 19 broken bonds in the half-sample. Curve 2-7 are those of the propagating cleavage crack. The relative strain, e/e_G is 1.036 at time step 3600 (stable crack). The relative strain is 1.054 for all other curves [1] (see Table II.3.5). The static and dynamic stress concentration (& distributions) are very similar.



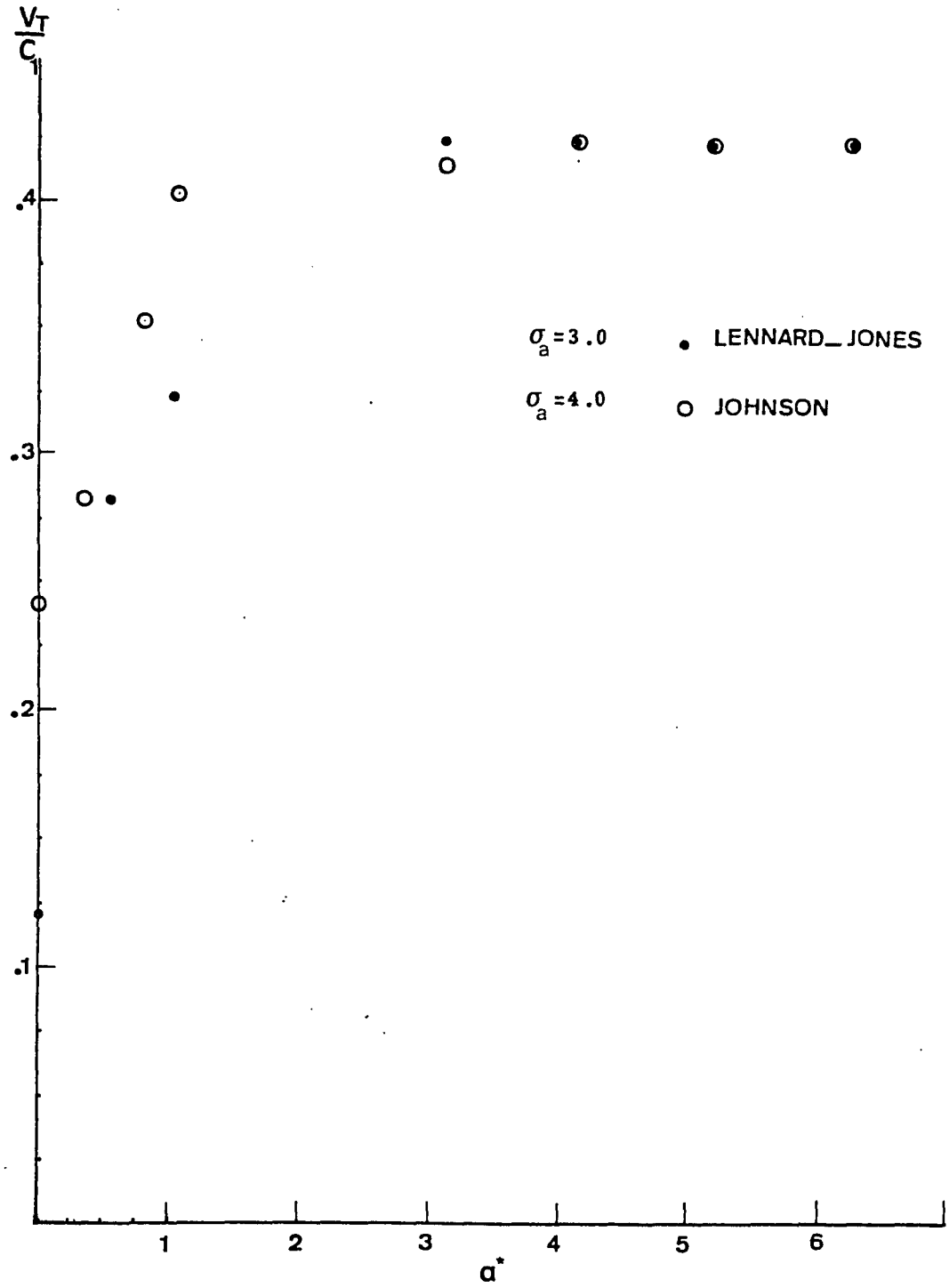
[Fig. II.3.5] Normalised crack-tip velocity versus the normalised crack-length, c/c_o, where c_o is the initial half-crack length. $C_1 = (9E/8\rho)^{1/2}$ is the velocity of the waves of dilation. The sample size is 79X135. See Table II.3.8A-H, II.3.8.1.



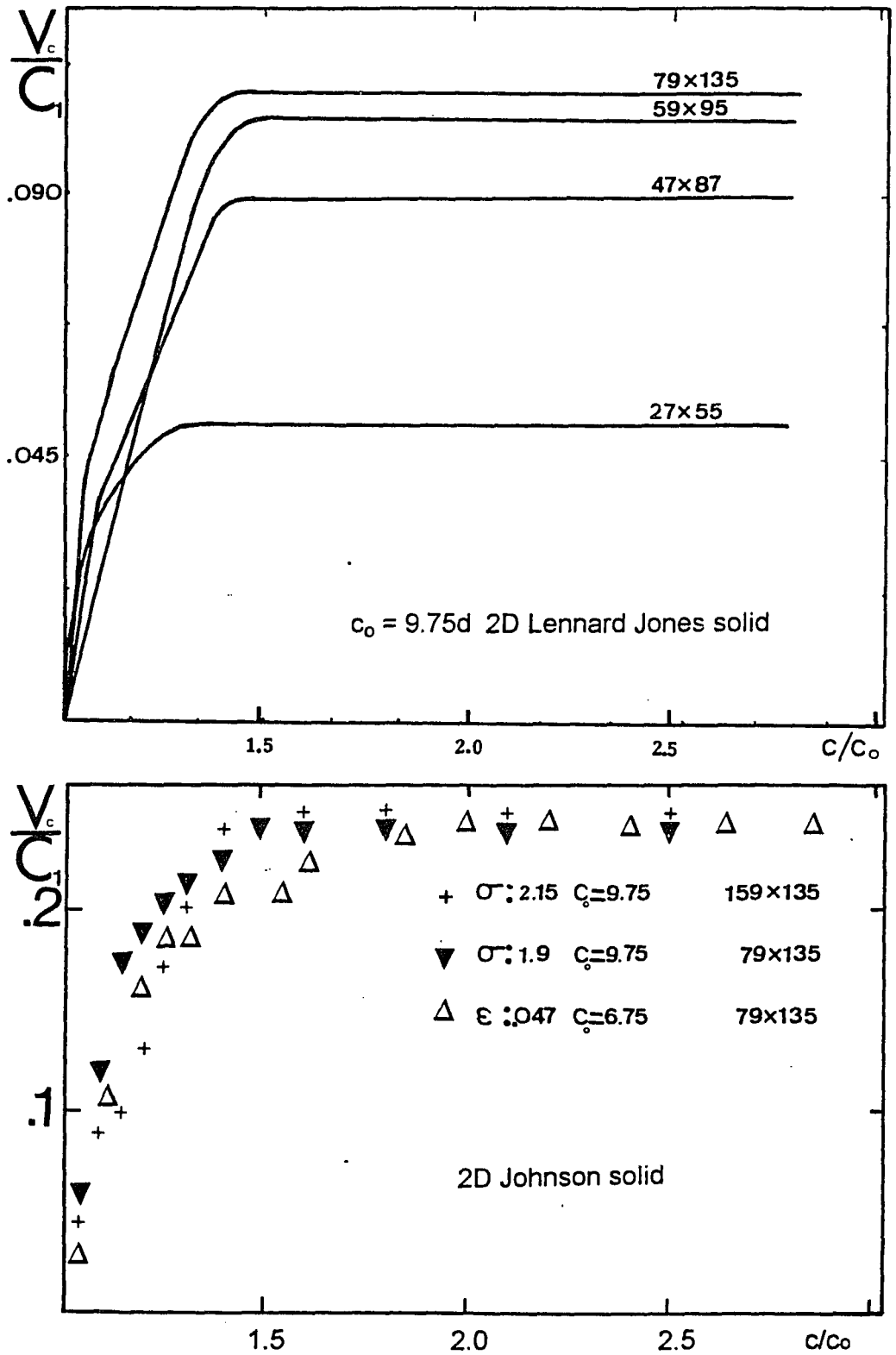
[Fig. II.3.6.] Normalised crack-tip velocity versus the normalised crack-length. c_o is the initial half-crack length. C_1 is the velocity of the waves of dilation in the 2D-Johnson solid = $[E/\rho(1-\nu^2)]^{1/2} = (9E/8\rho)^{1/2}$ =7.65 Sample size : (•) 159X135, σ_C=2.15; (X) 79X135, σ_C=1.90.



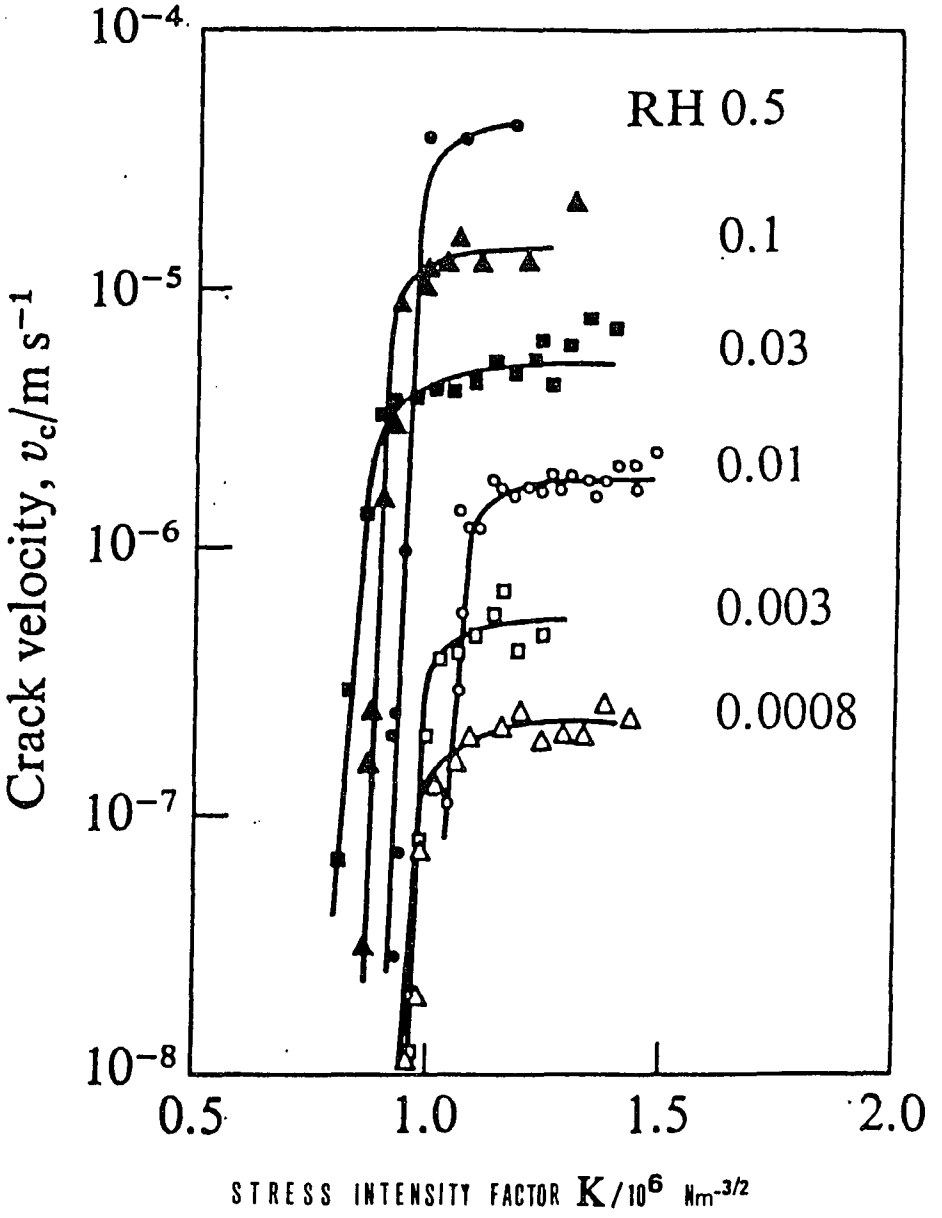
[Fig. II.3.7] Normalised crack-tip velocity versus the normalised crack-length, $c-c_o$, where c_o is the initial half-crack length. $C_1=(9E/8\rho)^{1/2}$ is the velocity of the waves of dilation in the 2D-covalently modified Johnson solid for $\nu=1/3$. The shape of this curve is representative of the development of the crack-tip velocity in varieties of the covalently bonded Johnson solid (Table II.3.2, 4, 10B-C).



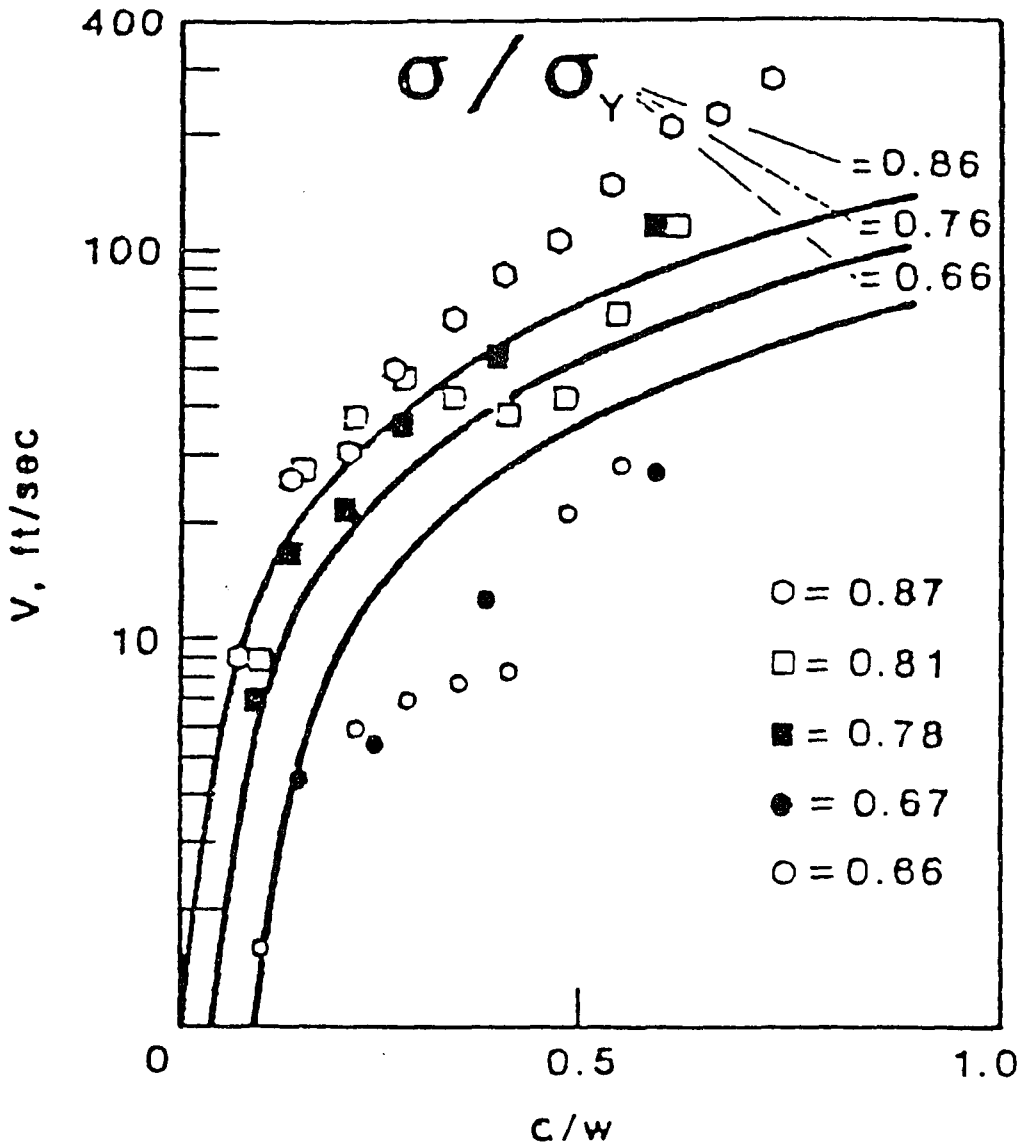
[Fig. II.3.8] The variation of the normalised terminal crack-tip velocity with the amplitude of the angular resistance, a*. See Table. II.3.2, II.3.10A-D.



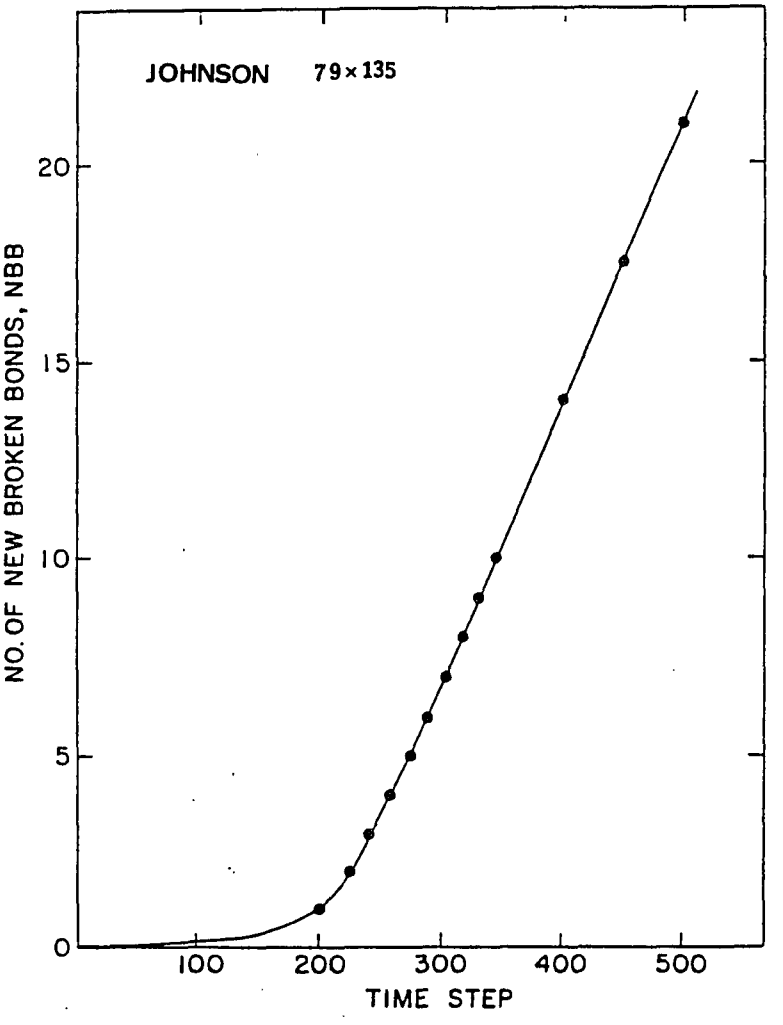
[Fig. II.3.9] Plots of the crack-tip velocity against crack-half length in the 2D-triangular Lennard Jones and Johnson solid. See Table. II.3.6, 8D-F.



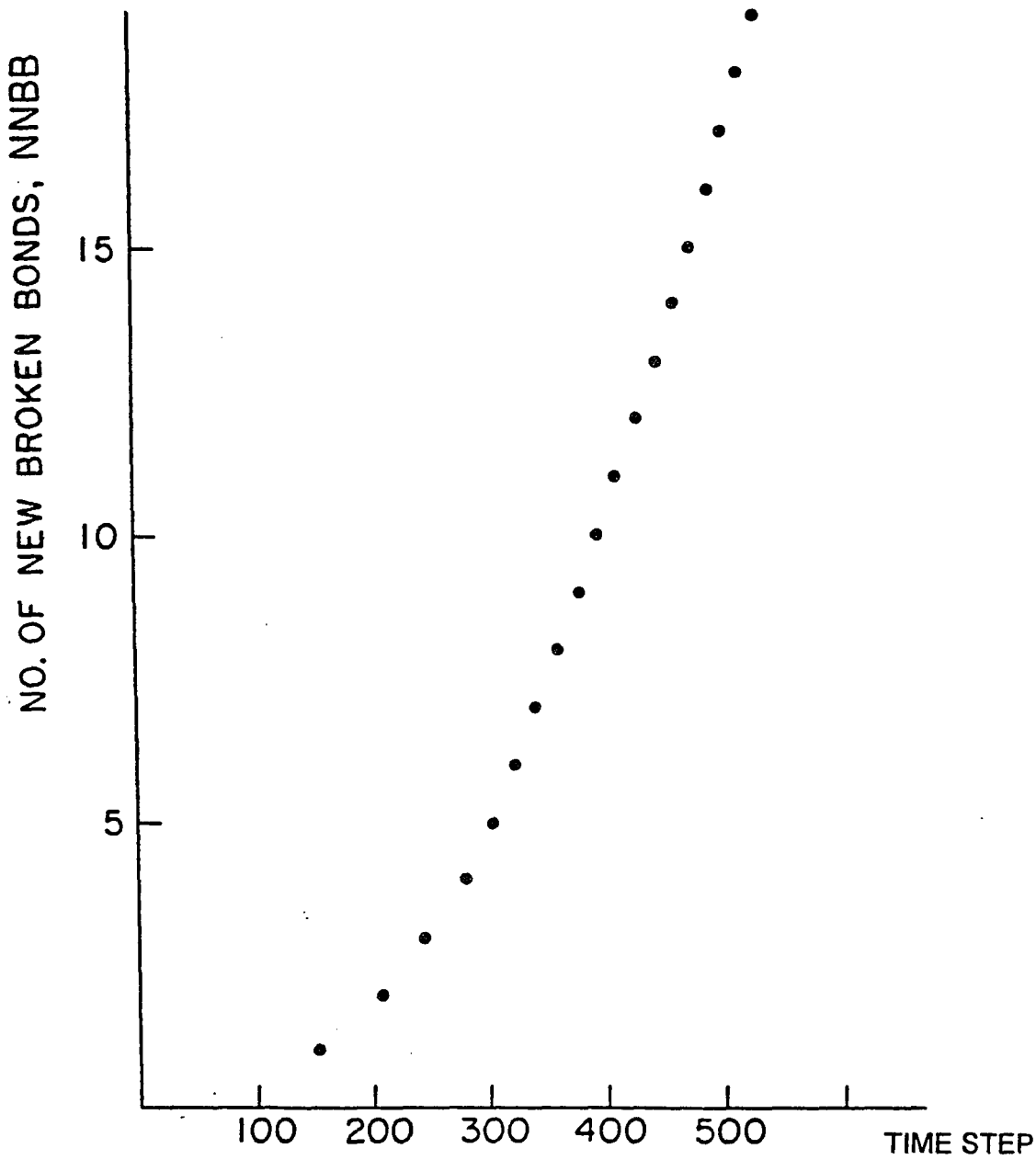
[Fig. II.3.10] Experimental results for the crack-tip velocity in sapphire tested in the moistened nitrogen gas (relative humidities indicated) [After [192]].



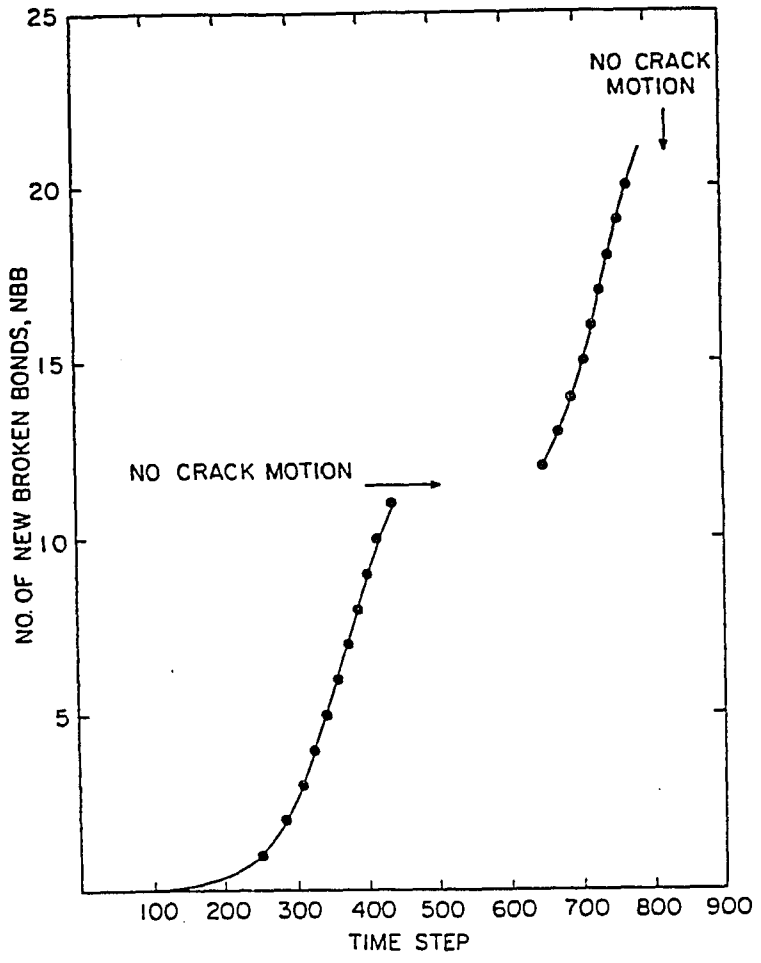
[Fig. II.3.11] Comparison of the observed crack propagation results with predictions of a propagating strip yield zone model for steel foil sheet in tension [Fig. 4.36, p. 256 [151]].



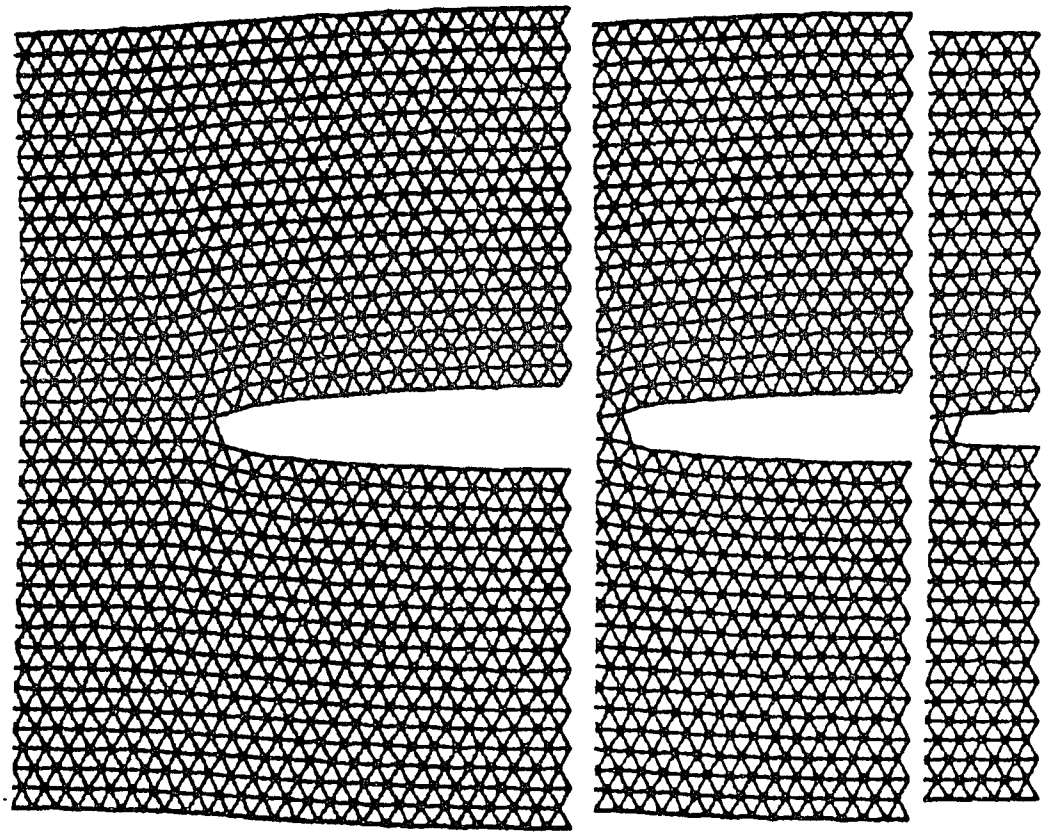
[Fig. II.3.12] A typical dynamic brittle propagation. Number of new sequential breaking of the interatomic bonds between rows 39 and 40, NNBB, is plotted against the time step. Initial number of broken bonds in half-sample was 19, corresponding to c_o=9.75d. The sample is under remotely applied constant critical strain of 0.041. See Table II.3.8H.



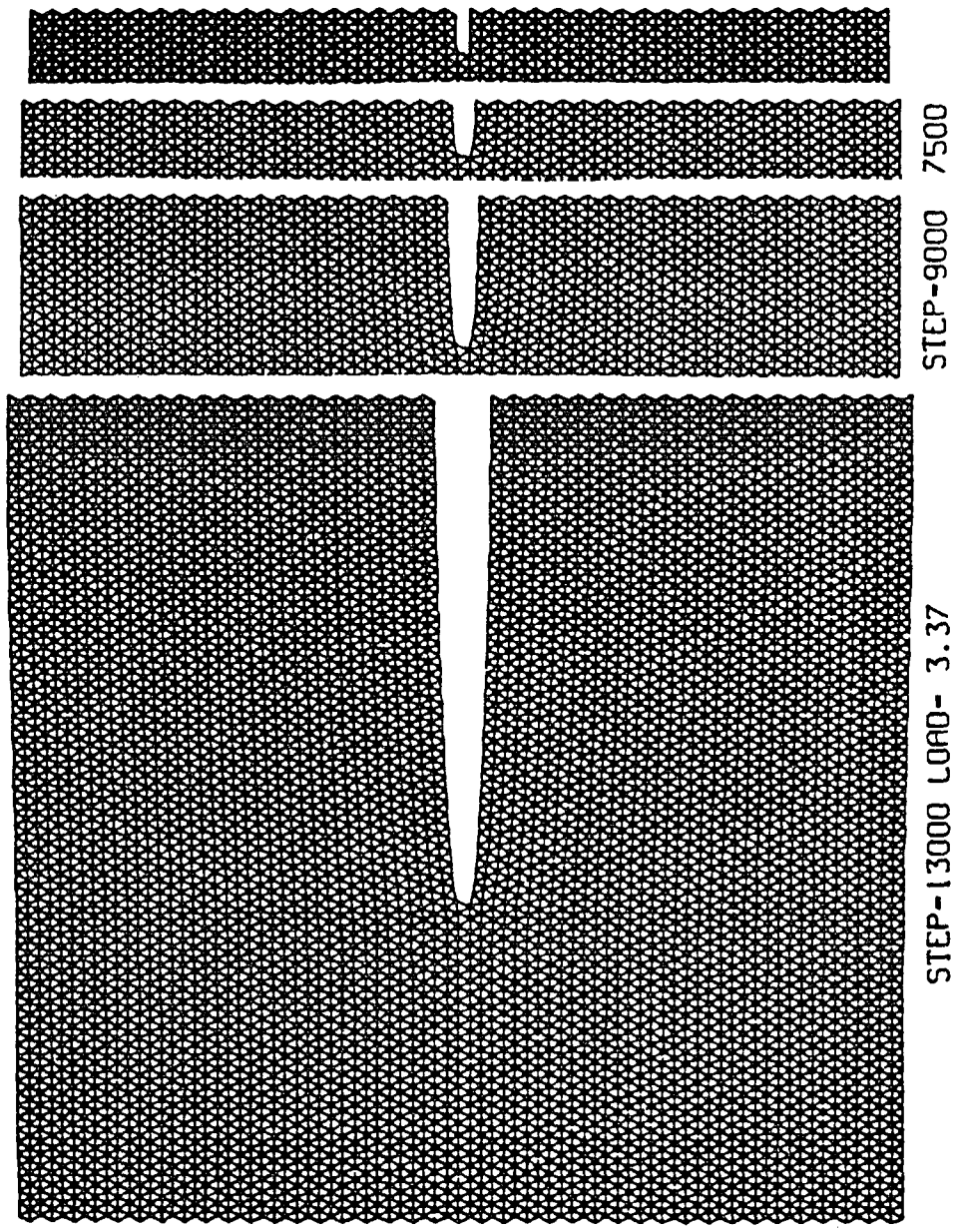
[Fig. II.3.13.] Simulations results of the brittle propagation of the centrally located internal crack of c_o=9.75d, in a 2D Johnson's solid of 21544 atoms arranged in 159 rows, subjected to a remotely applied constant critical load of 2.15. Number of new broken bonds, NNBB, is plotted against the time step. The slope of this curve at a given time step is the instantaneous crack-tip velocity.



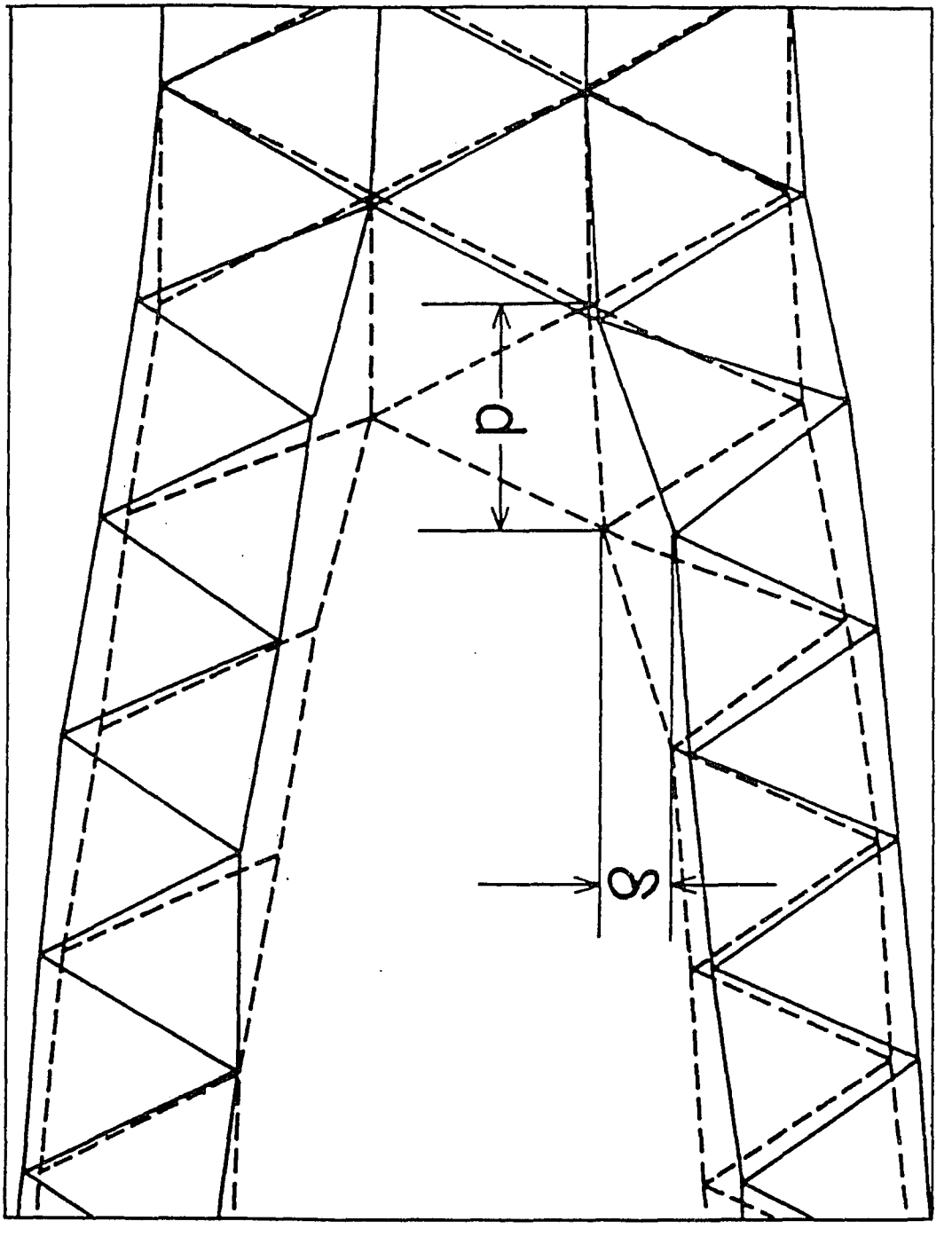
[Fig. II.3.14.] The crack arrest caused by dislocation generation at the crack-tip of a running crack of the initial half-crack length of c_0=3.75d, in a 2D-triangular Johnson solid of 10704 atoms arranged in 79 rows under the remotely applied constant critical tensile load of 3.37. A pair of dislocations were emitted, symmetrically, from the crack-tip (Fig. II.2.13) 460 time steps after the removal of the critical damping. Immediately after dislocations nucleation, the crack-tip got blunted, the principal stresses at the crack-tip was reduced for a considerable length of time. By the time step 645, where the brittle propagation of the crack-tip was renewed along its initial path, the emitted dislocations had moved away from the crack-tip toward the loaded horizontal surfaces of the specimen, and the normal stresses at the crack-tip had risen back to the theoretical cohesive (fracture) strength of the material. 801 time step after the removal of the critical damping, a second pair of blunting dislocations were emitted from the fast-running crack-tip, and the crack was arrested again for a significant amount of time.



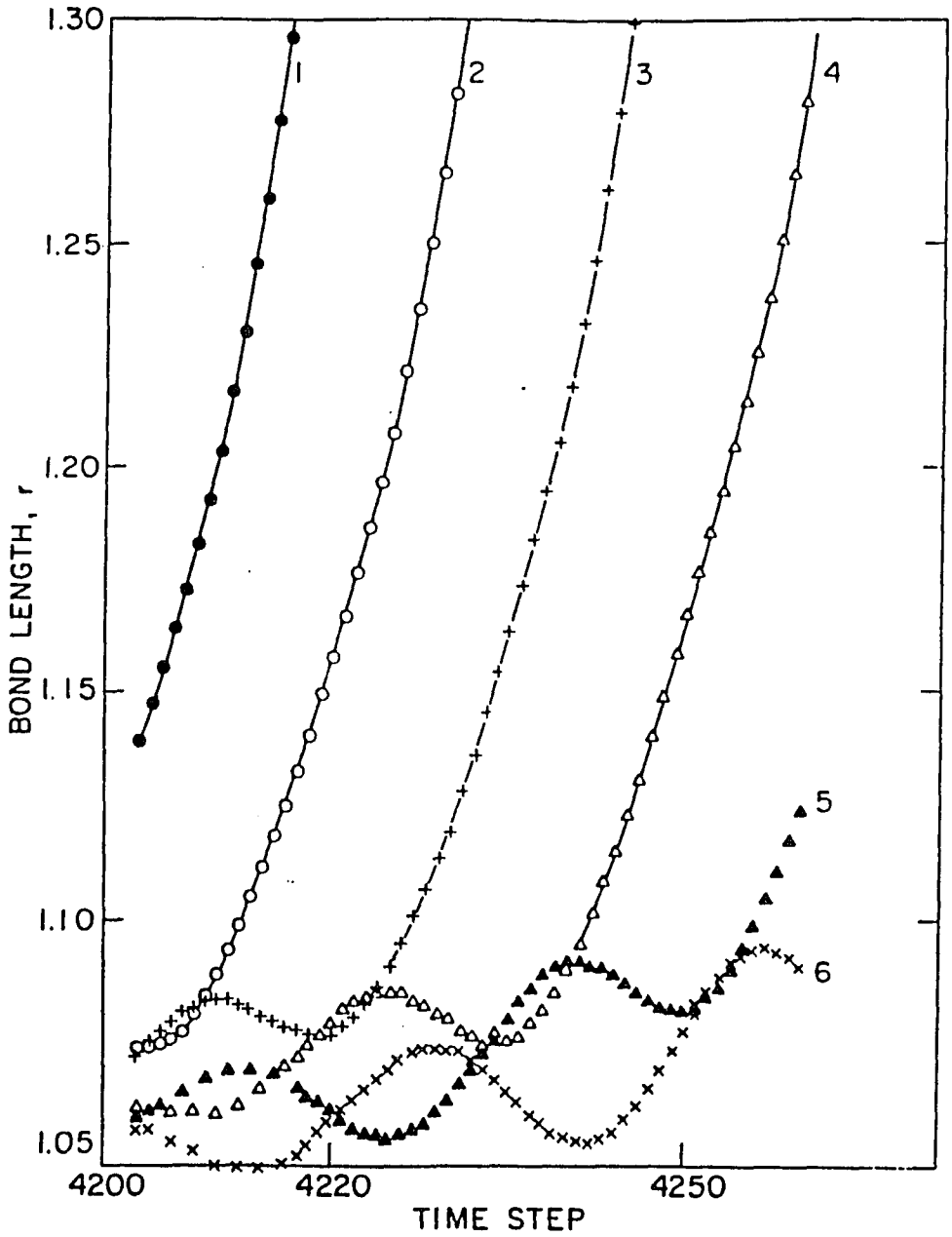
[Fig. II.3.15] The simulations results illustrated in this figure for the two-dimensional triangular covalent Lennard-Jones solid of $a^*=1.0$ is typical of these series. The internal crack of $c_o=3.75$ has propagated brittlely to a crack of instantaneous half crack-length $c=16.25$, i.e., $c/c_o=4.33$ by the end of this run as demonstrated in the last image in this figure. Note that the crack surface is very clean, and no evidence of any plastic deformation is present.



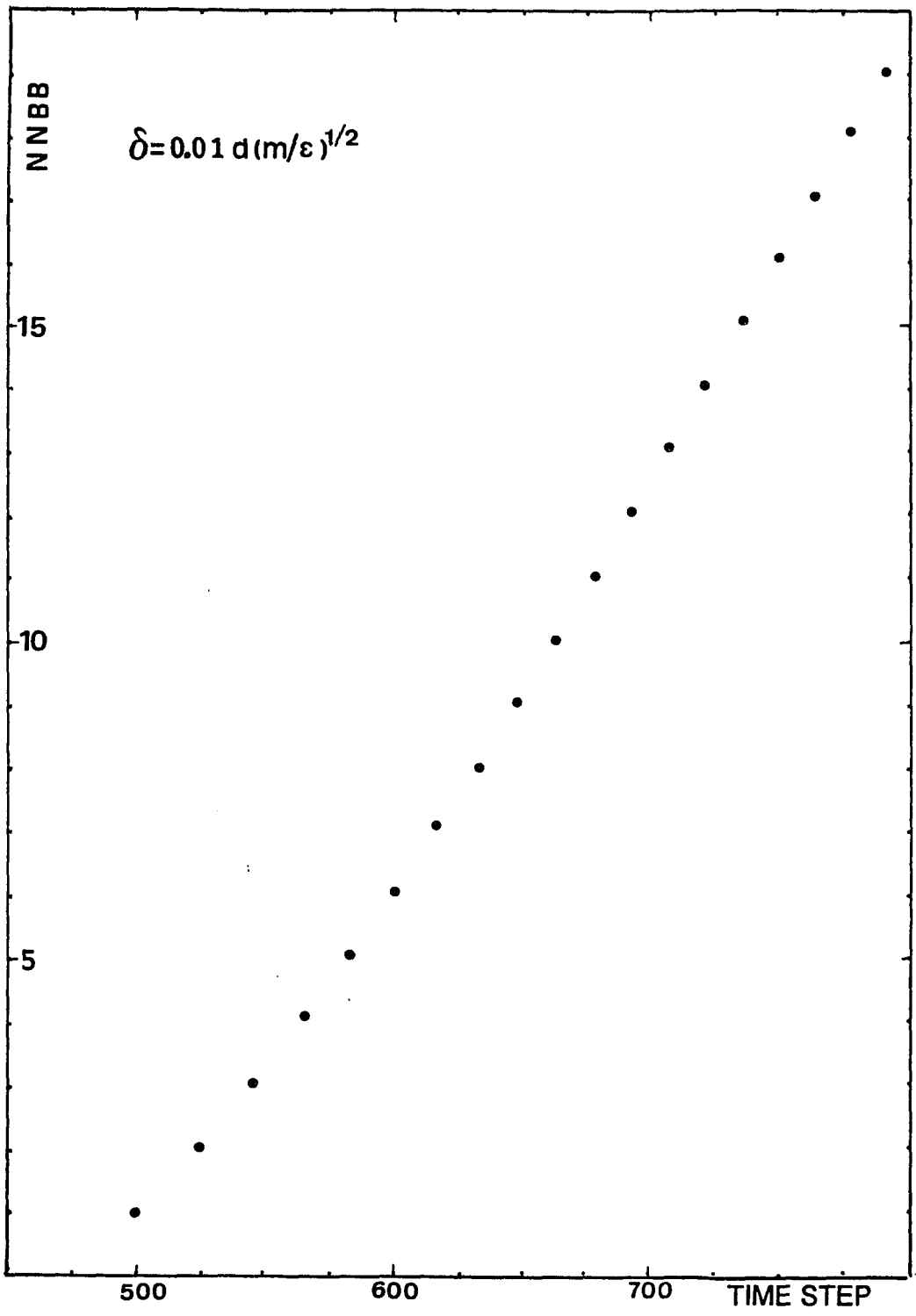
[Fig. II.3.16] Simulations results of the brittlely propagating internal crack of c_o=3.75 in a 2D Johnson solid of sample size 79x135, subjected to the critical external load of 3.37. The system is damped, i.e. the kinetic energy of the sample is reduced at every step. Note that there is no observable plastic deformation in the vicinity of the running crack-tip. Comparison of these results with those of JN7LD run reveals the fact that, indeed, the observed generation of a pair of dislocations at the tip of the running crack-tip in JN7LD run is due to the generated adiabatic heating in the vicinity of the running crack-tip. Note also the very smooth surface of the propagated crack.



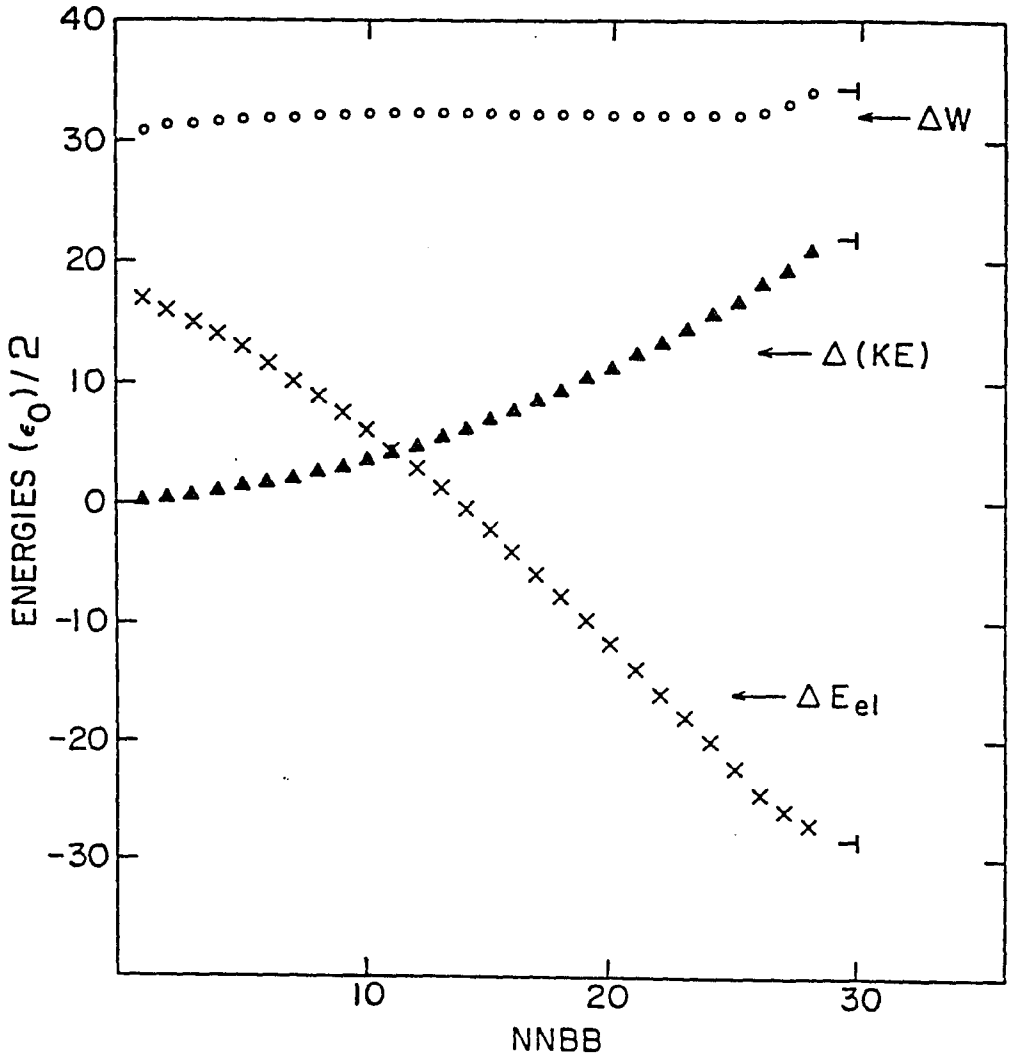
[Fig. II.3.17] The schematic representation of the distance parameters at the crack-tip.



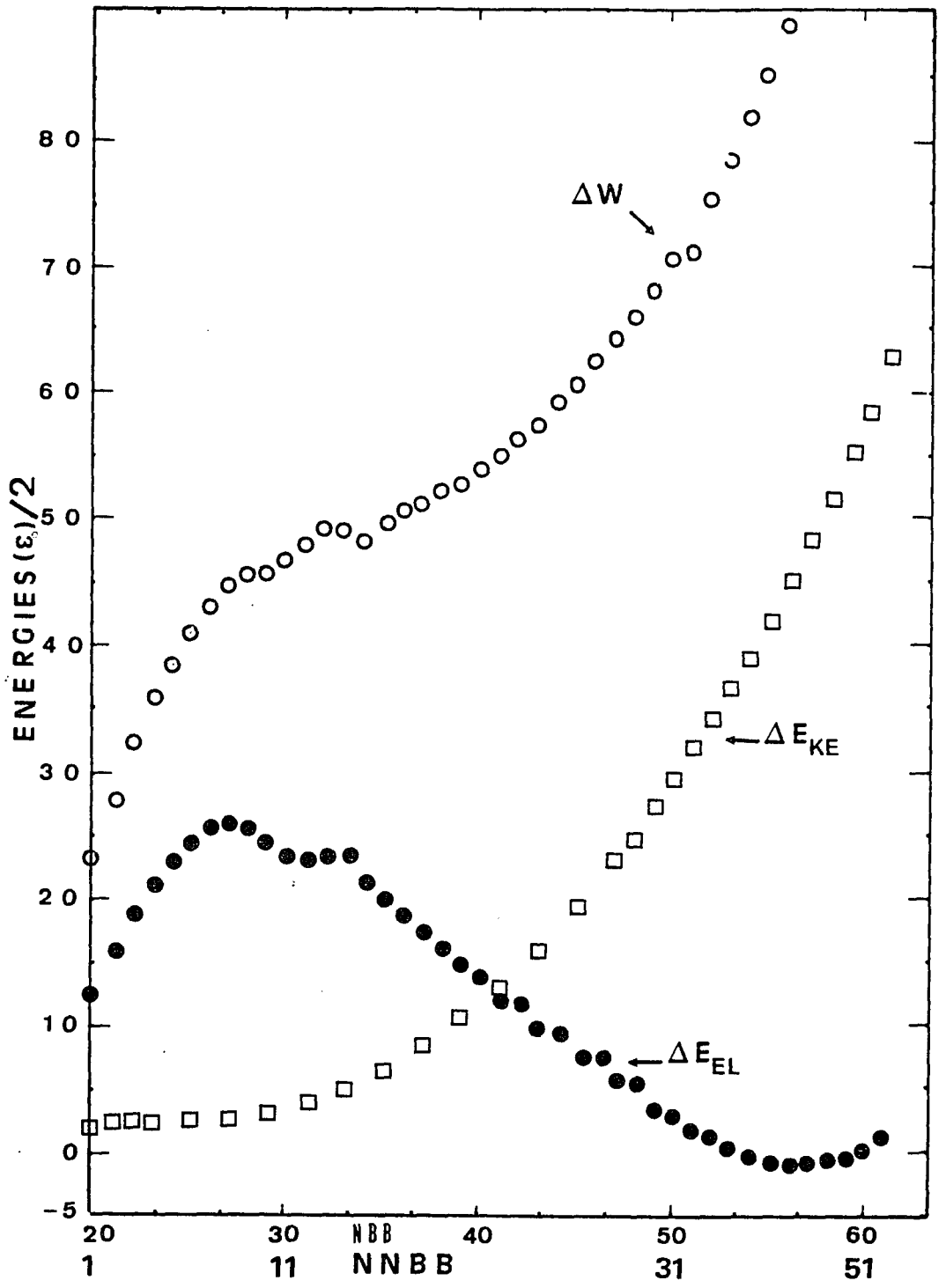
[Fig. II.3.18] Interatomic bond lengths against the time step during the steady propagation for the several interatomic bonds in the vicinity of the crack-front.



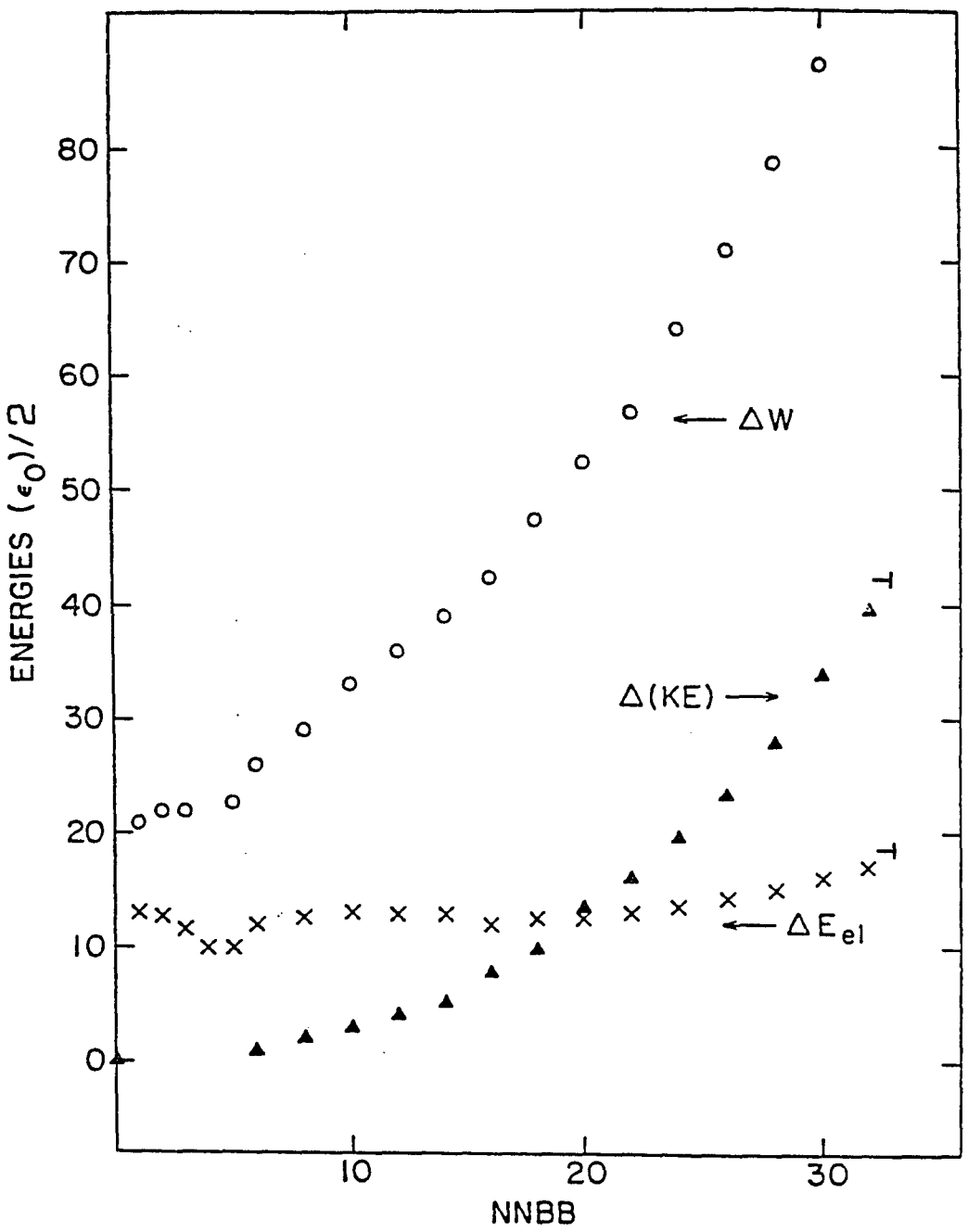
[Fig. II.3.19] Typical raw data of the Number of New Broken Bonds vs the time step for the covallently modified Johnson solid, a*=3. See Table II.3.10B.



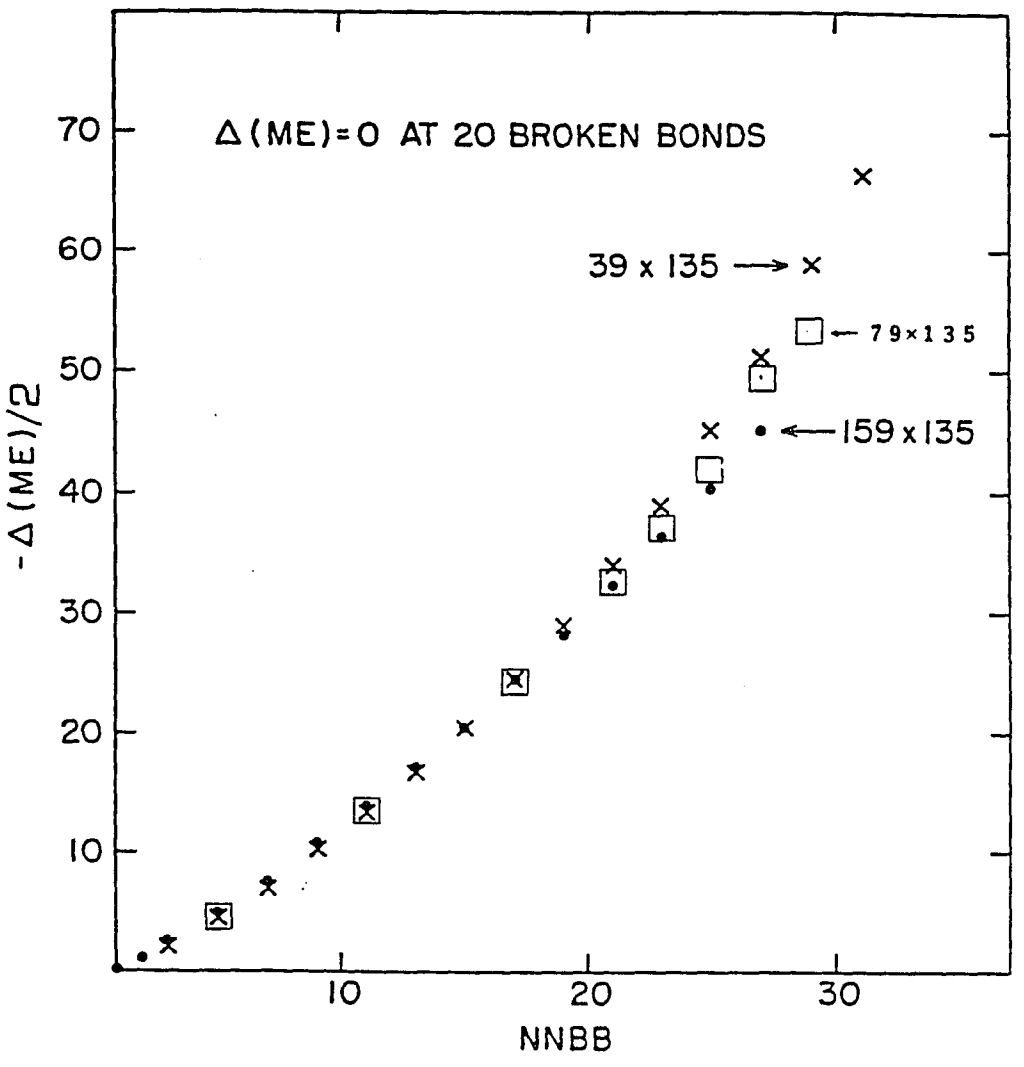
[Fig. II.3.20] The change in the energies of the critically loaded, σ_c=2.15, pre-cleaved, c_o=9.75, sample of 159x135 as a function of the number of new broken bonds, NNBB, during the brittle propagation of internal crack.



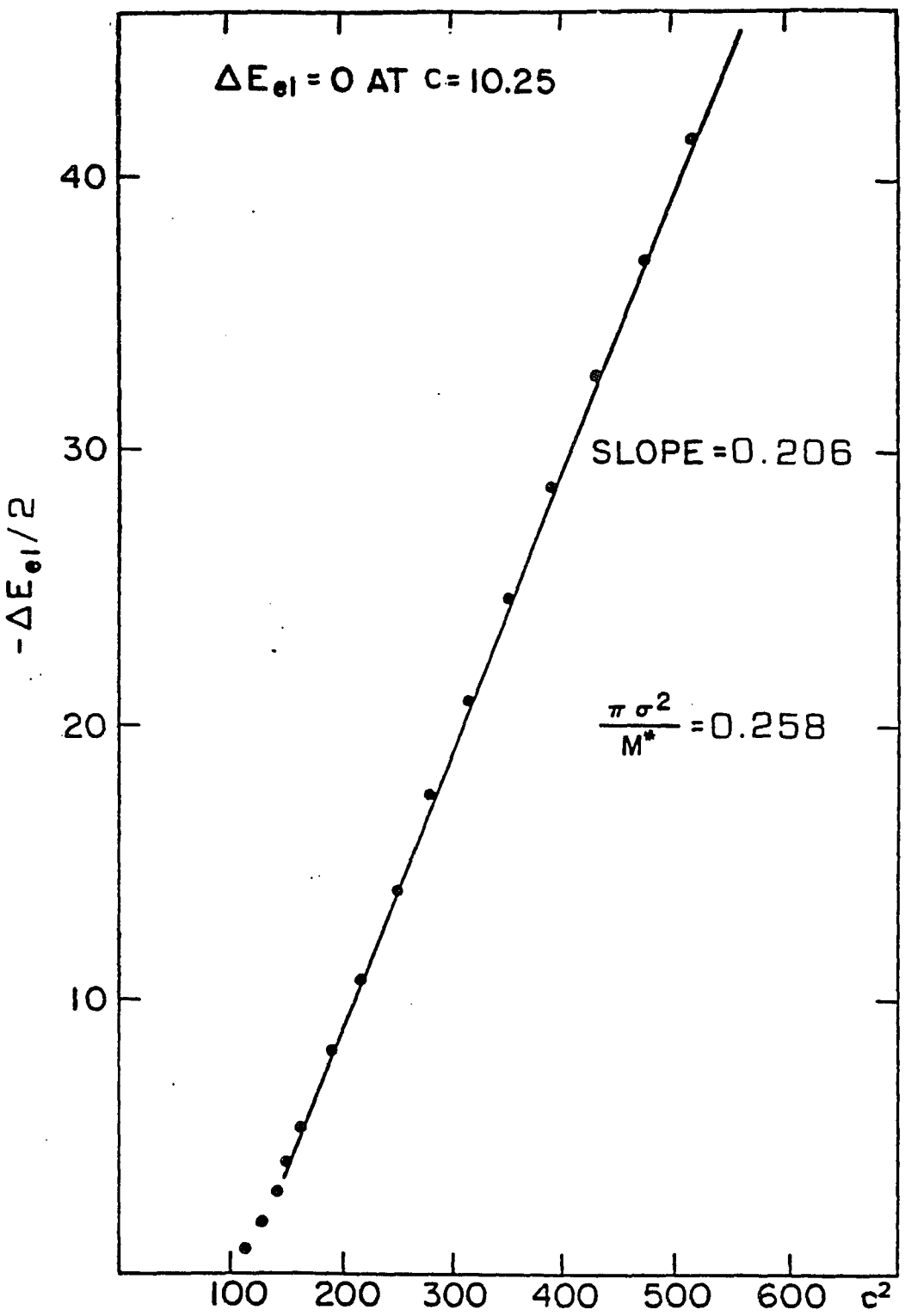
[Fig. II.3.21] The change in the energies of the critically loaded, σ_c=1.90, pre-cleaved, c_o=9.75, sample of 79x135 versus the number of new broken bonds, NNBB, during the brittle propagation of the internal crack (Table II.3.8D).



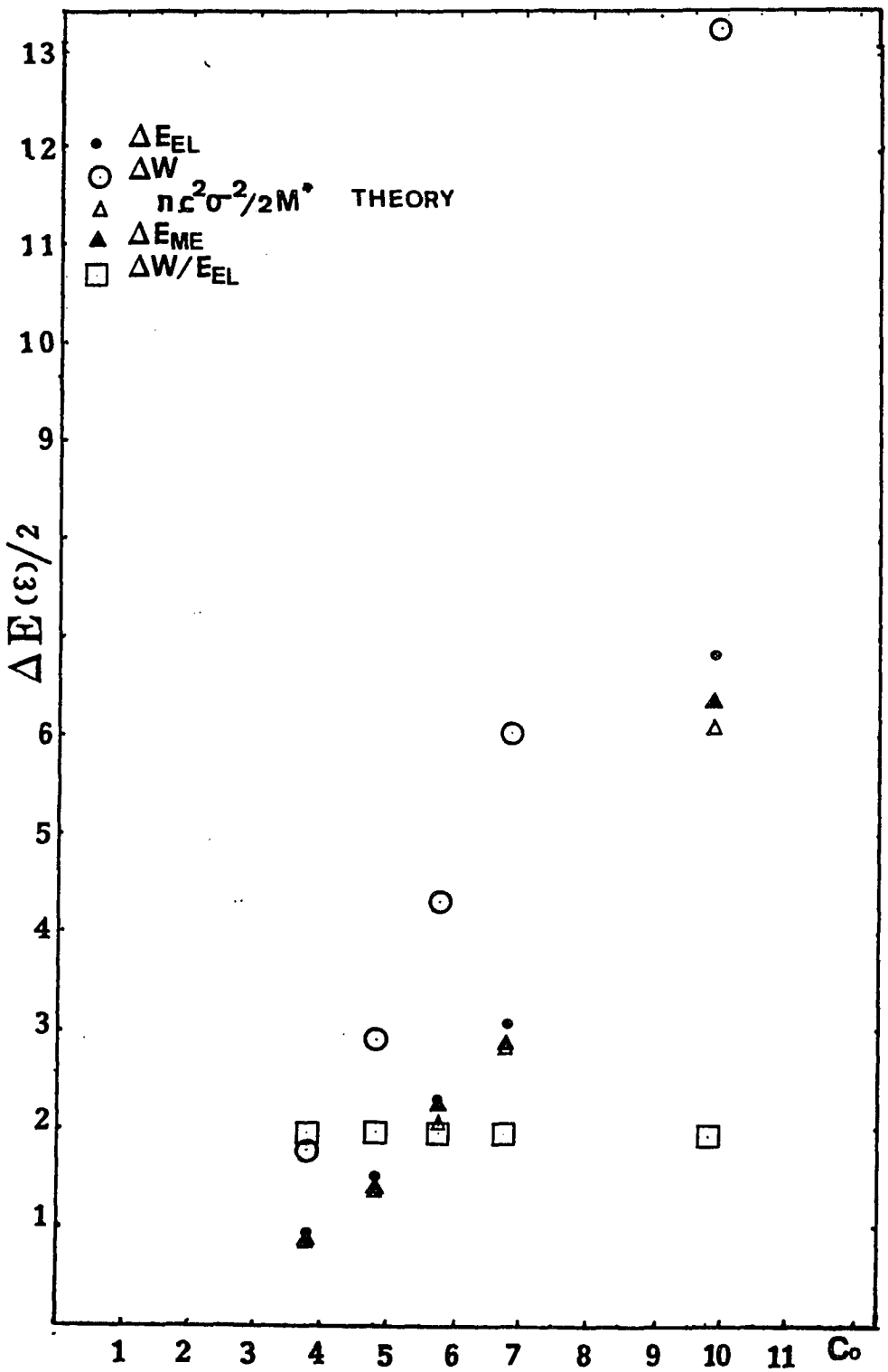
[Fig. II.3.22] The change in the energies of the critically loaded, σ_c=1.45, pre-cleaved, c_o=9.75, sample of 39x135 as a function of the number of new broken bonds, NNBB, during the brittle propagation of internal crack.



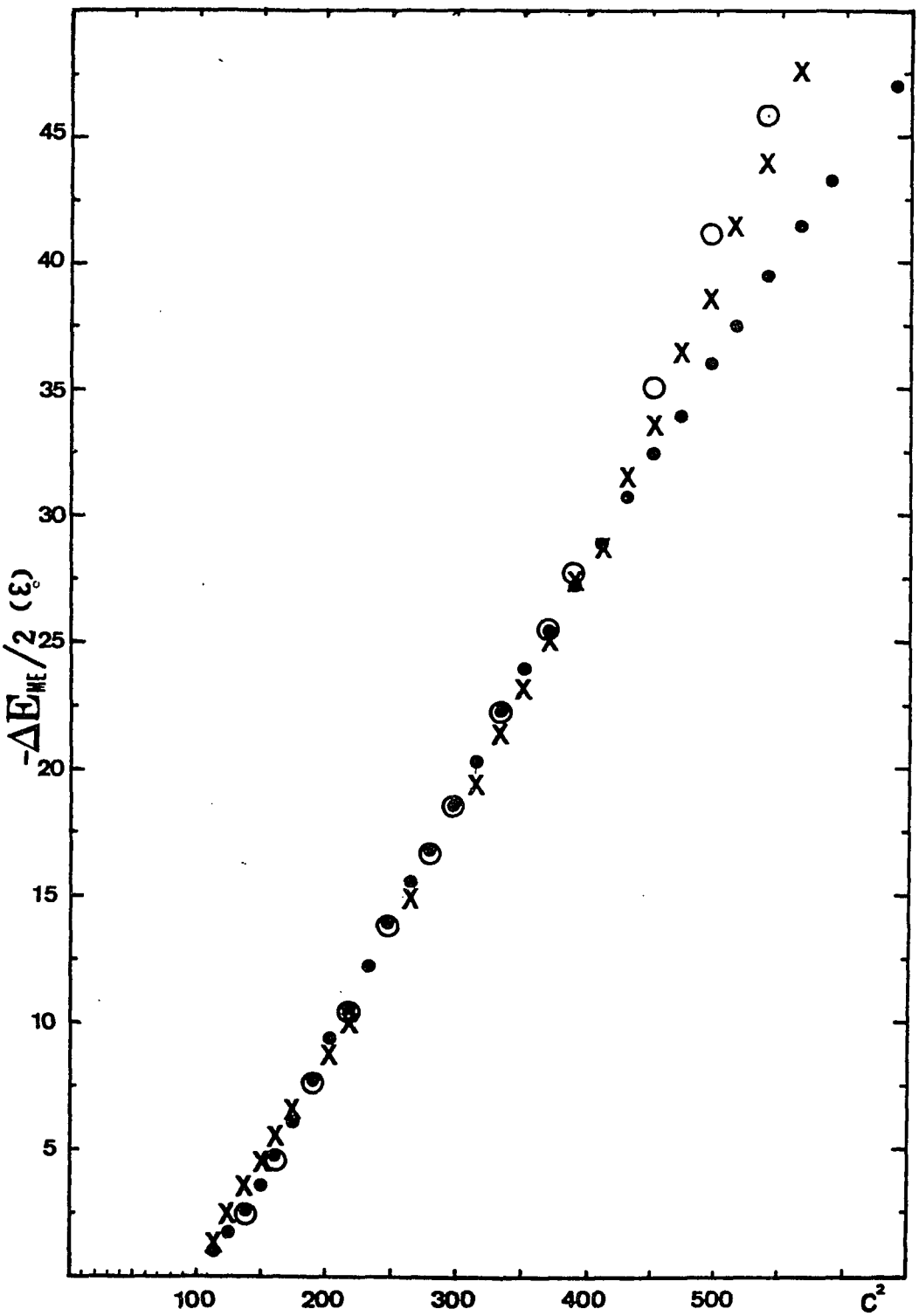
[Fig. II.3.23] The change in the mechanical energy of the pre-cleaved critically loaded 2D-triangular Johnson solid versus the number of new broken bonds, NNBB, during the brittle propagation of the internal crack of c_o=9.75d (Table II.3.8D). (•) 159x135, σ_c=2.15; (x) 39x135, σ_c=1.45; (□) 79x135, σ_c=1.90.



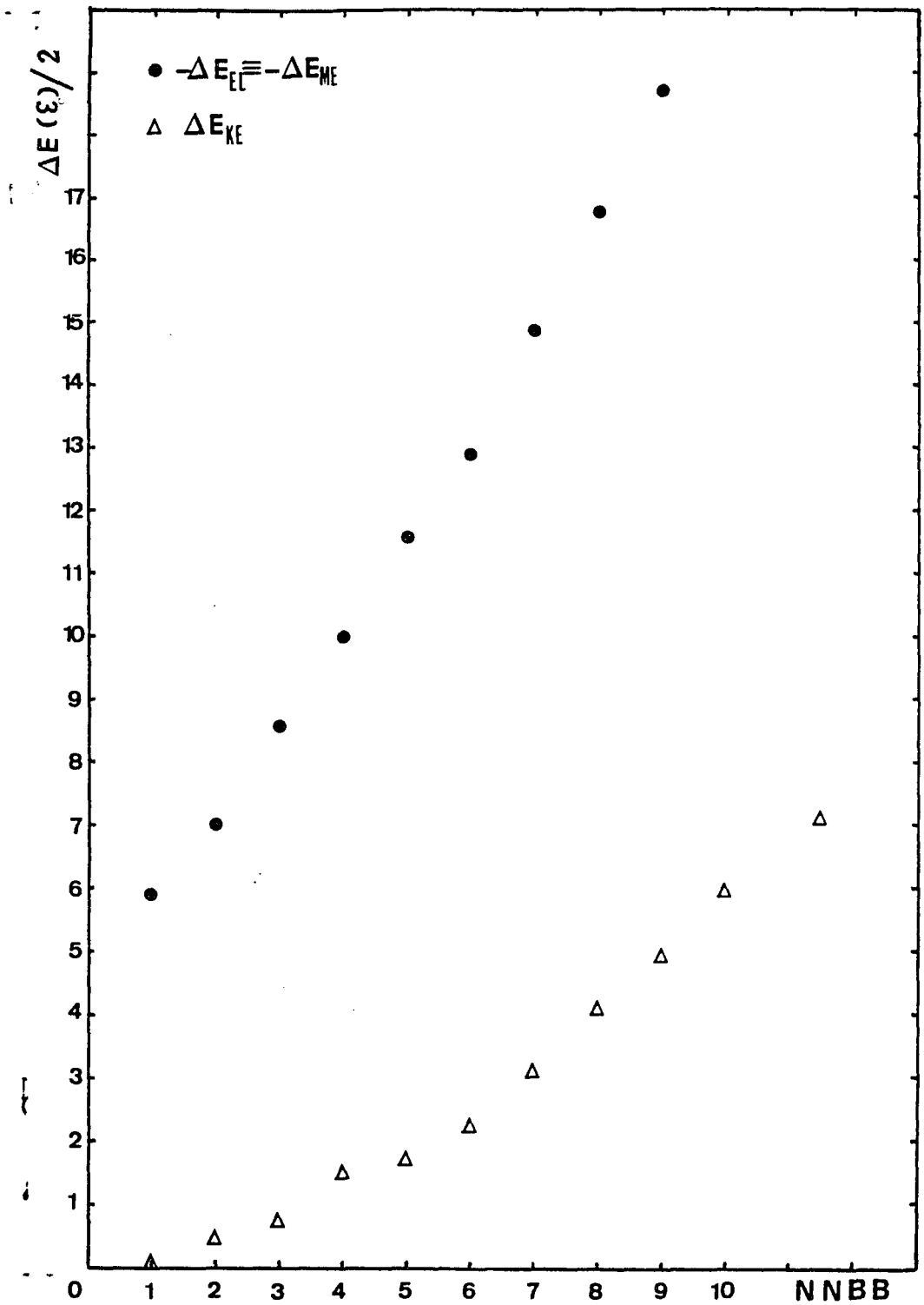
[Fig. II.3.24] The decrease in the elastic strain energy, ΔE_{el}, of the pre-cleaved, c_o=9.75, critically loaded, σ_c=2.15, 2D-triangular Johnson solid of sample size 159x135 vs c^2 during the brittle propagation of the internal crack (Table II.3.7).



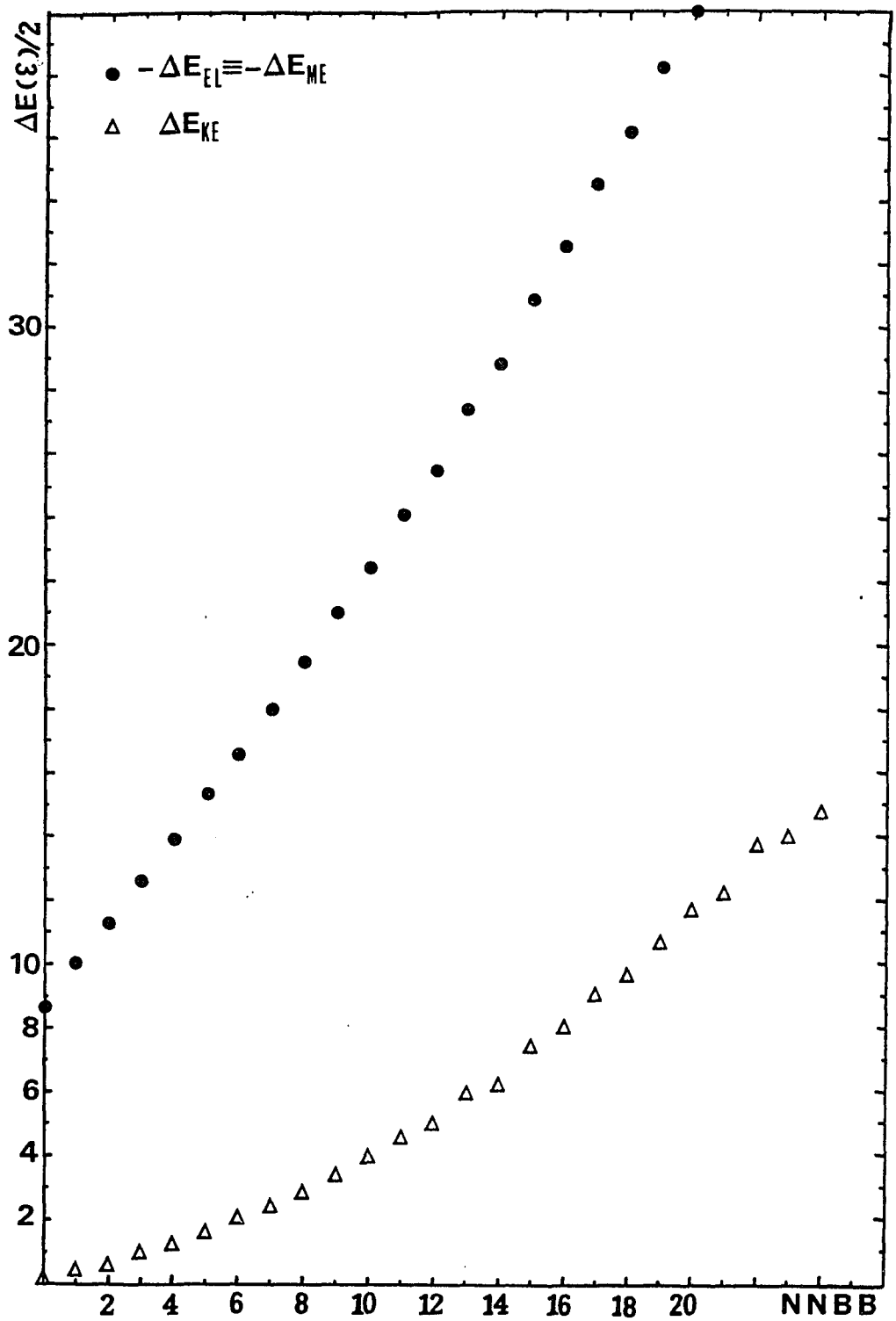
[Fig. II.3.25] Energetics of the quasi-static crack extension as a function of c. The predictions of the quasi-static continuum theories are illustrated as $\pi c^2\sigma^2 / 2M^*$, for the comparison purposes (see Table. II.1.4).



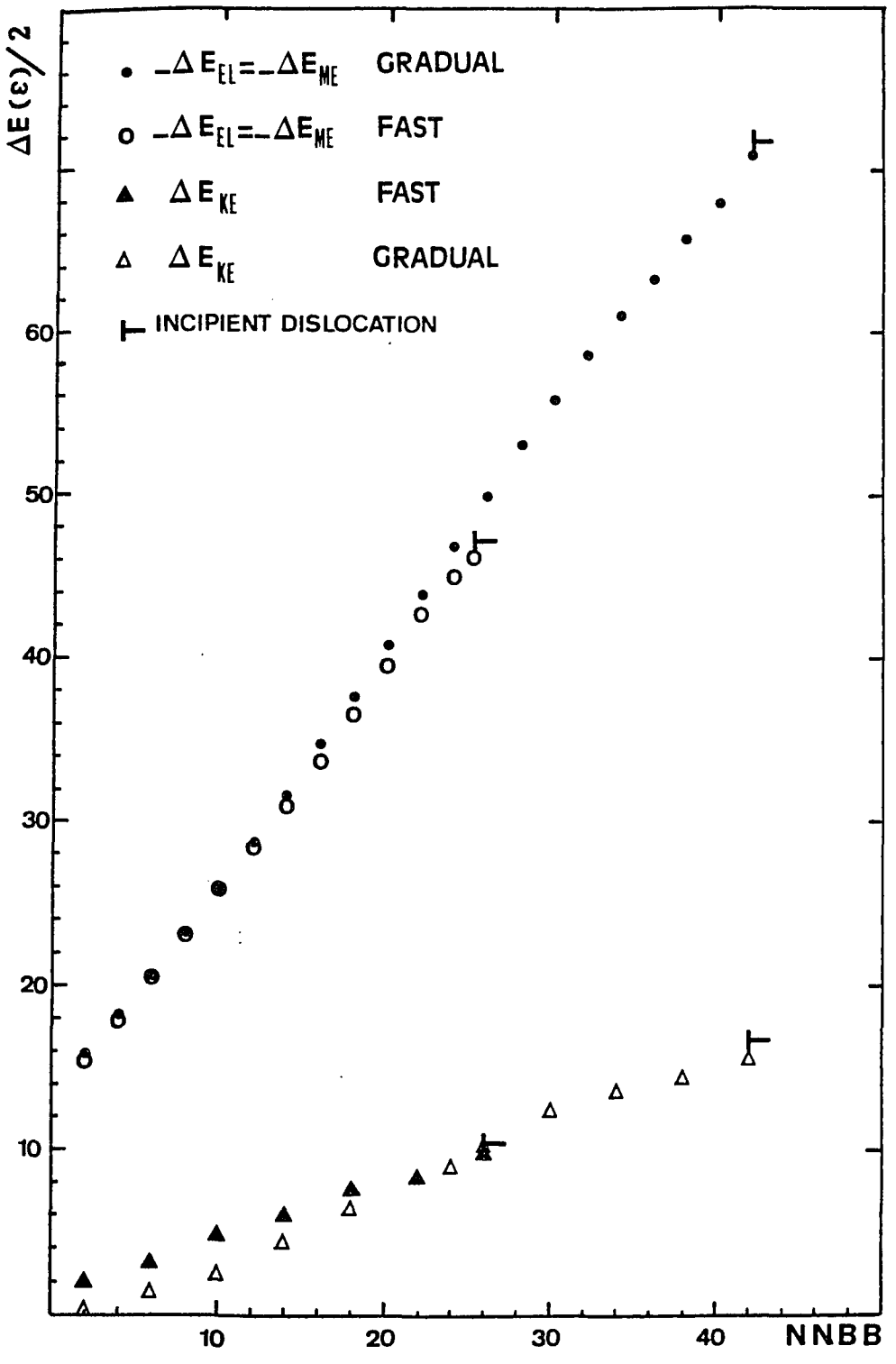
[Fig. II.3.26] The change in the mechanical energy of the critically loaded pre-cleaved (c_o=9.75) 2D Johnson solid vs c^2 during the brittle propagation of the internal crack. (•) 159x135, σ_c=2.15; (x) 79x135, σ_c=1.90; (o) 39x135, σ_c=1.45.



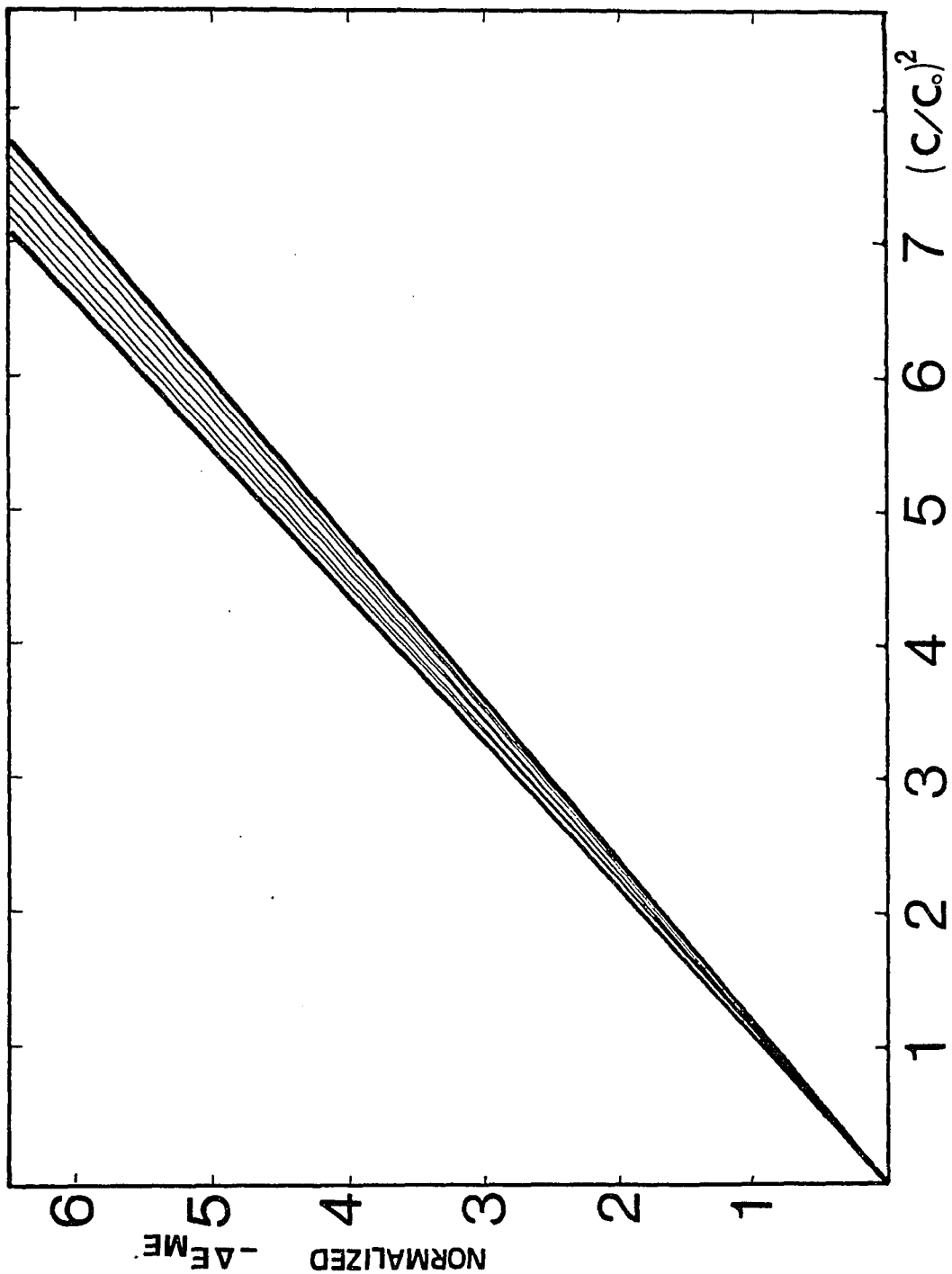
[Fig. II.3.27] The change in the energies of the critically loaded, ε_c= 0.061, pre-cleaved, c_o=3.75, Johnson solid of 79x135 versus the number of new broken bonds, NNBB, during the brittle propagation of the internal crack (Table II.3.8E).



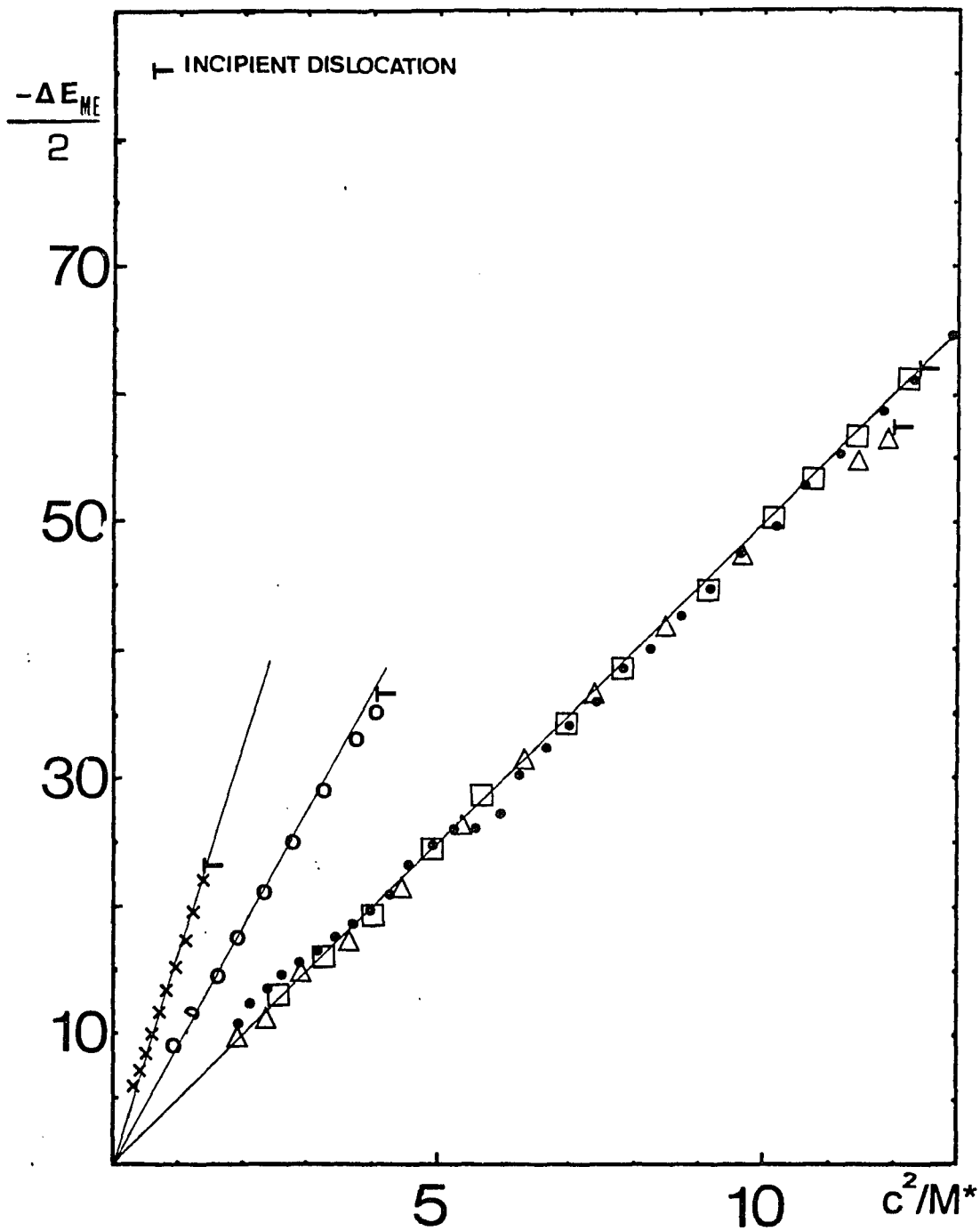
[Fig. II.3.28] The change in the energies of the critically loaded, ε_c= 0.047, pre-cleaved, c_o=6.75, Johnson solid of 79x135 versus the number of new broken bonds, NNBB, during the brittle propagation of the internal crack (Table II.3.8F).



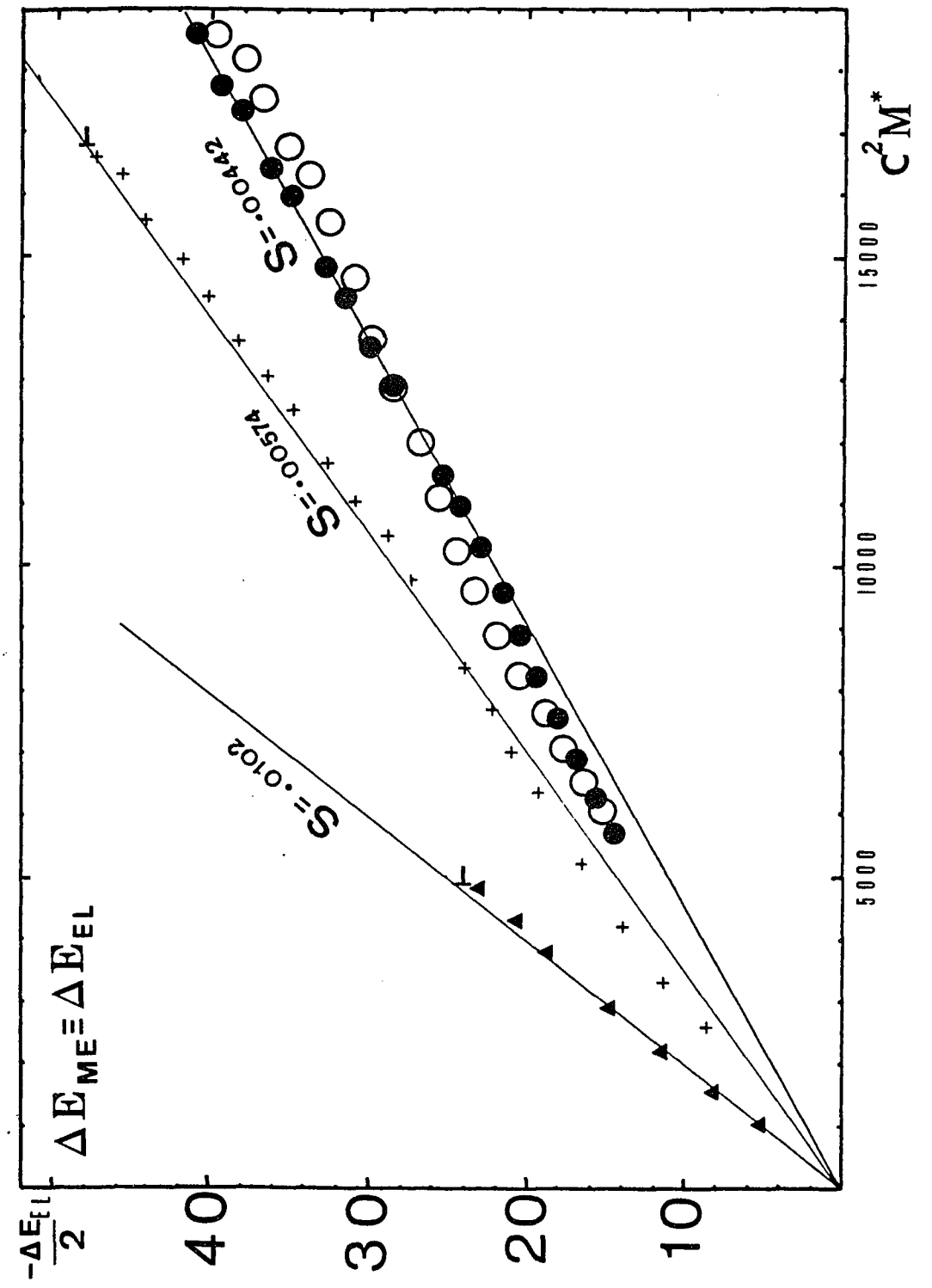
[Fig. II.3.29] The change in the energies of the critically loaded, ε_c=0.041, pre-cleaved, c_o=9.75, Johnson solid of 79x135 versus the number of new broken bonds during the brittle propagation of the internal crack (Table II.3.8G-H).



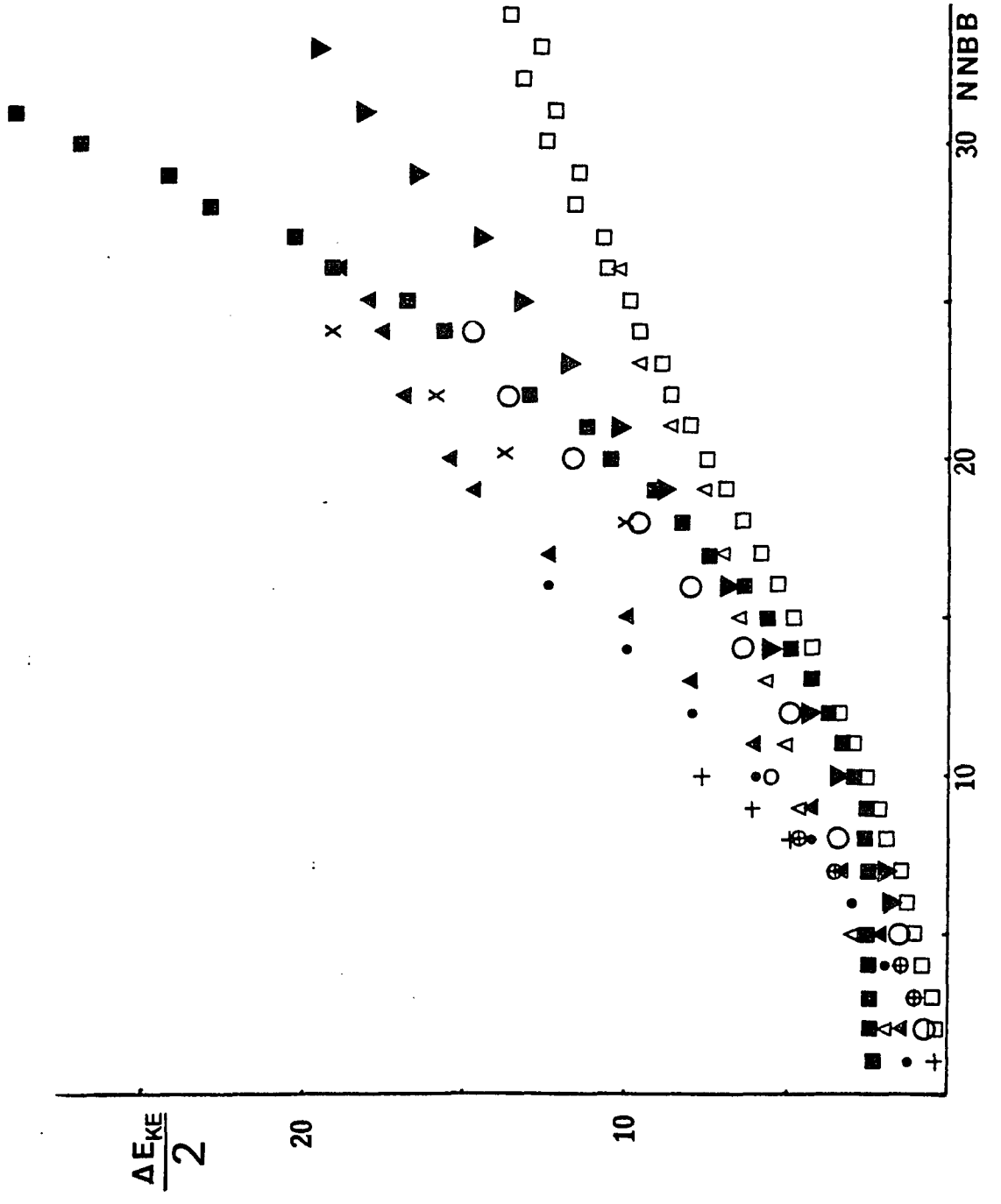
[Fig. II.3.30] The change in the "normalised mechanical energy" of the critically loaded pre-cleaved 2D Johnson solid, $-\Delta E_{me}/(\pi c^2 e^2 M^*)$ [for constant external strain] and $-\Delta E_{me} M^*/(\pi c^2 s^2)$ [for constant external stress] versus "normalised square of crack length", $(c/c_o)^2$ during the brittle propagation of the internal crack for varieties of sample sizes, loading conditions, and initial crack lengths.



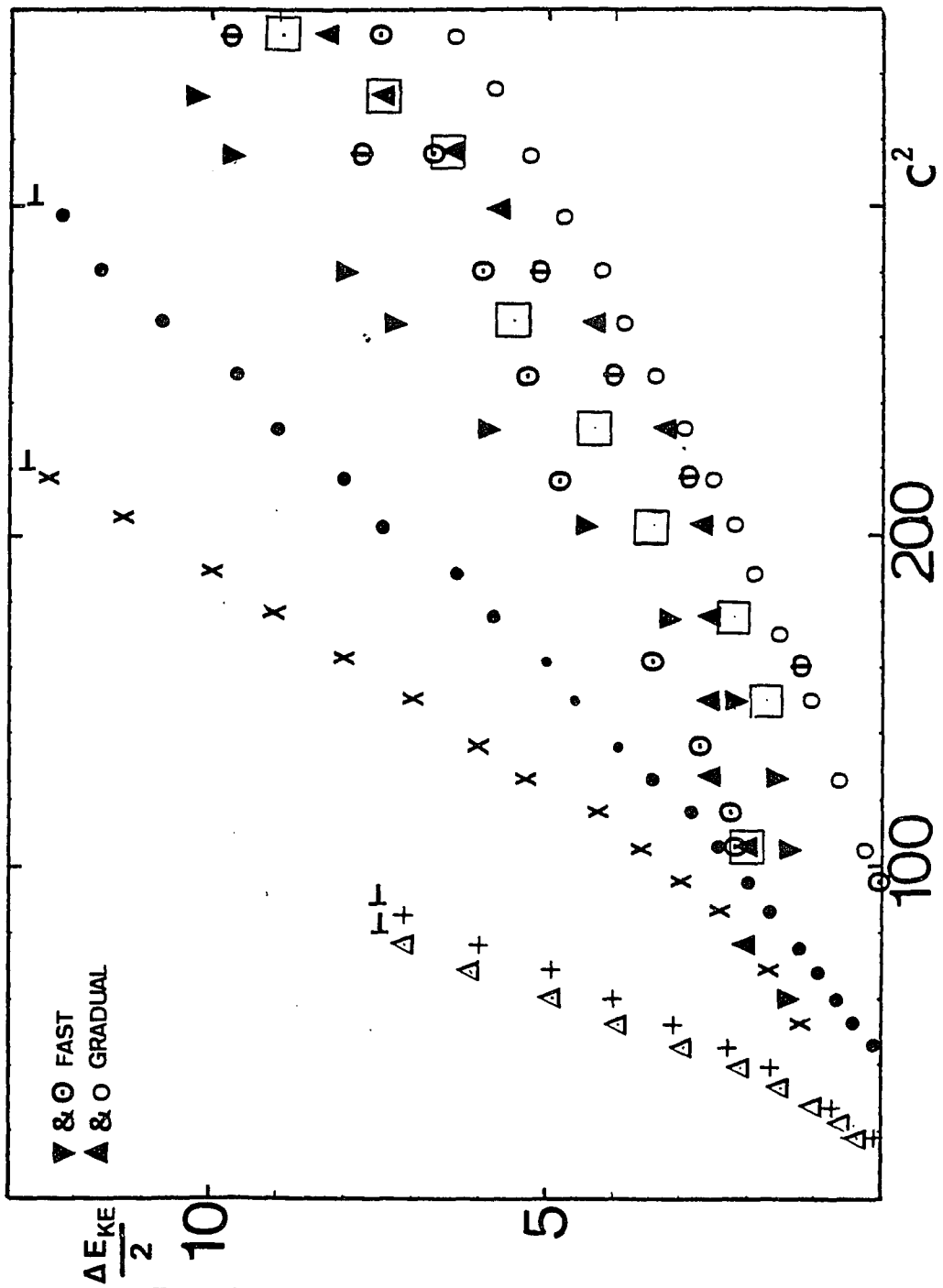
[Fig. II.3.31] The change in the mechanical energy of the critically loaded pre-cleaved 2D Johnson solid, $-\Delta E_{me}$ vs c^2/M^* during the brittle propagation of the internal crack. (Δ) 159x135, σ_c=2.15, c_o=9.75; (●) 79x135, σ_c=1.90, c_o=9.75; (□) 39x135, σ_c=1.45, c_o=9.75; (x) 79x135, σ_c=3.37, c_o=3.75; (o) 79x135, σ_c=2.45, c_o=6.75. See Table II.3.7, II.3.8A1-D2, II.3.8.2.



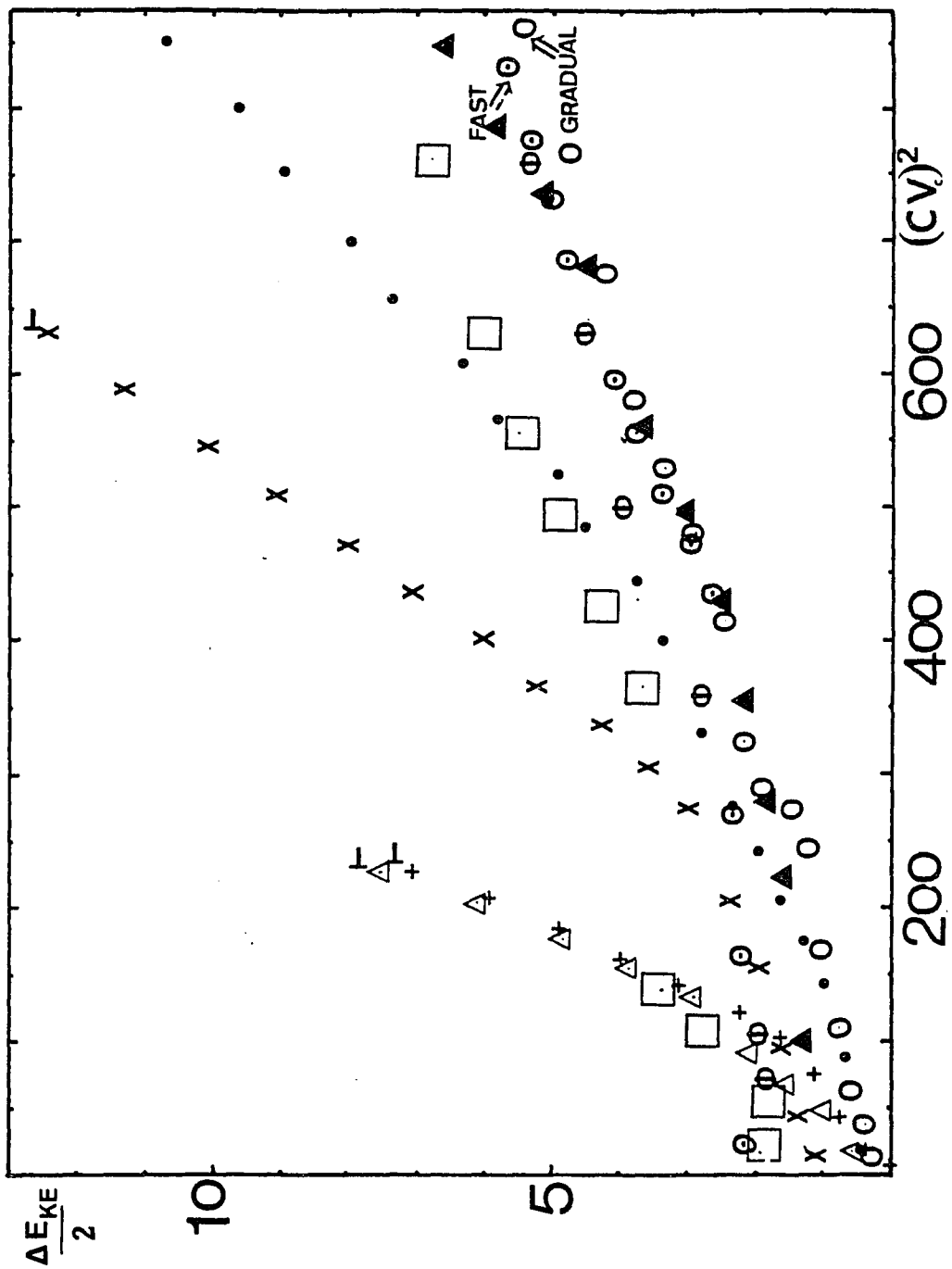
[Fig. II.3.32] The change in the mechanical energy of the critically loaded pre-cleaved 2D Johnson solid, $-\Delta E_{me}$, vs c^2M^* (Table II.3.8E-H).Sample: 79x135. (▲) ε_c=0.061, c_o=3.75; (+) ε_c=0.047, c_o=6.75; (●) c_o=9.75, ε_c=0.041 (O fast).



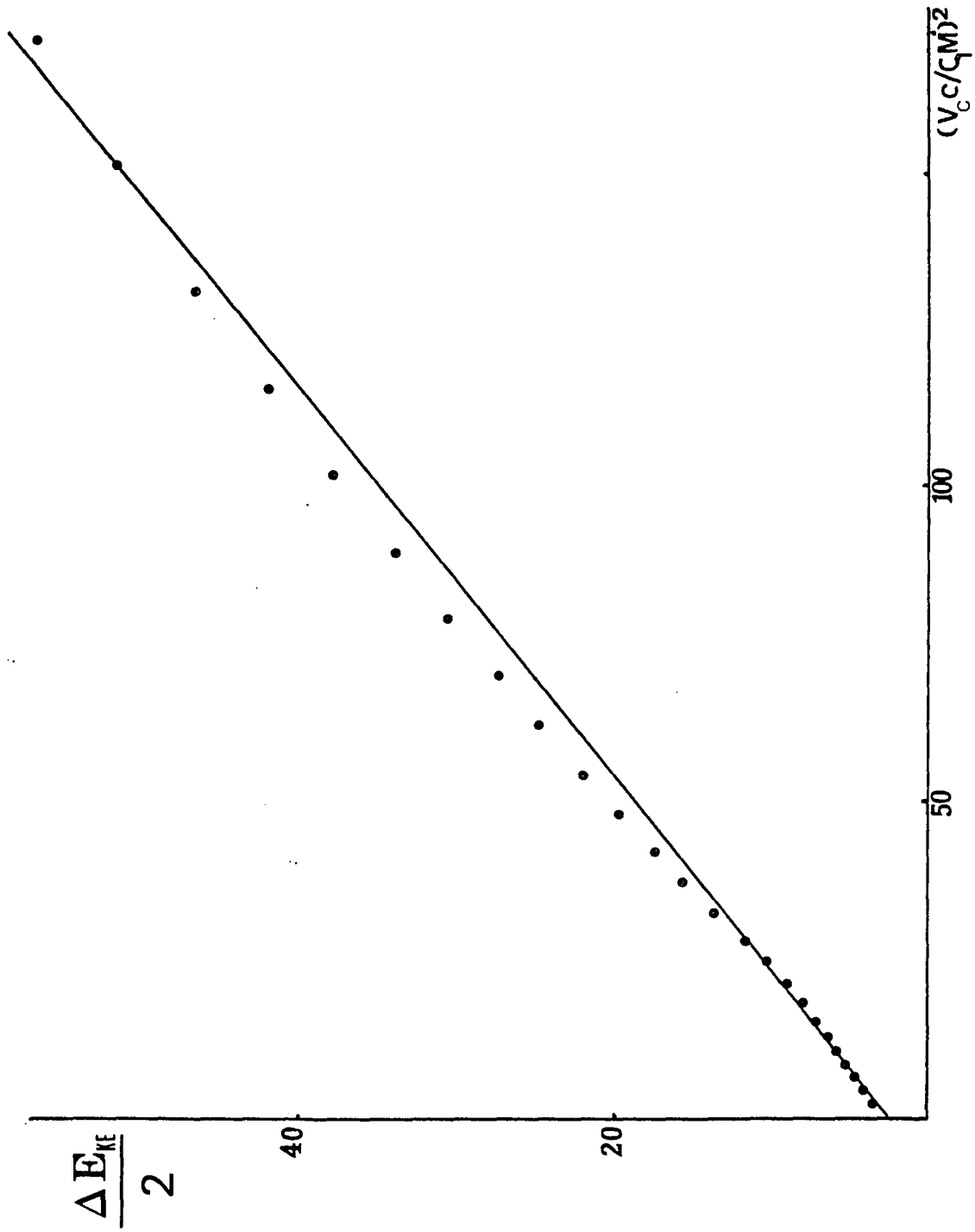
[Fig. II.3.33] The change in the kinetic energy of the critically loaded pre-cleaved 2D-triangular Johnson solid, ΔE_{ke}, vs the Number of New broken bonds during the brittle propagation of the internal crack. (▽)159x135, σ_c=2.15, c_o=9.75; (■)79x135, σ_c =1.90, c_o=9.75; (x)39x135, σ_c=1.45, c_o=9.75; (+)79x135, σ_c=3.37, c_o=3.75; (⊕)79x135, ε_c=0.061, c_o=3.75; (•)79x135, σ_c=2.45, c_o=6.75; (o)79x135, ε_c=0.047, c_o=6.75; (□)79x135, c_o=9.75, ε_c=0.041 (Table II.3.8A-H).



[Fig. II.3.34] The change in the kinetic energy of the critically loaded pre-cleaved 2D-triangular Johnson solid, ΔE_{ke}, vs c^2. (□)159x135, σ_c=2.15, c_o=9.75; (⊥) 79x135, σ_c=1.90, c_o=9.75; (Φ) 39x135, σ_c=1.45, c_o=9.75; (Δ)79x135, σ_c=3.37, c_o=3.75; (+) 79x135, ε_c=0.061, c_o=3.75; (x) 79x135 σ_c=2.45, c_o=6.75; (•) 79x135, ε_c=0.047, c_o=6.75; (o)79x135, c_o=9.75, ε_c=0.041.

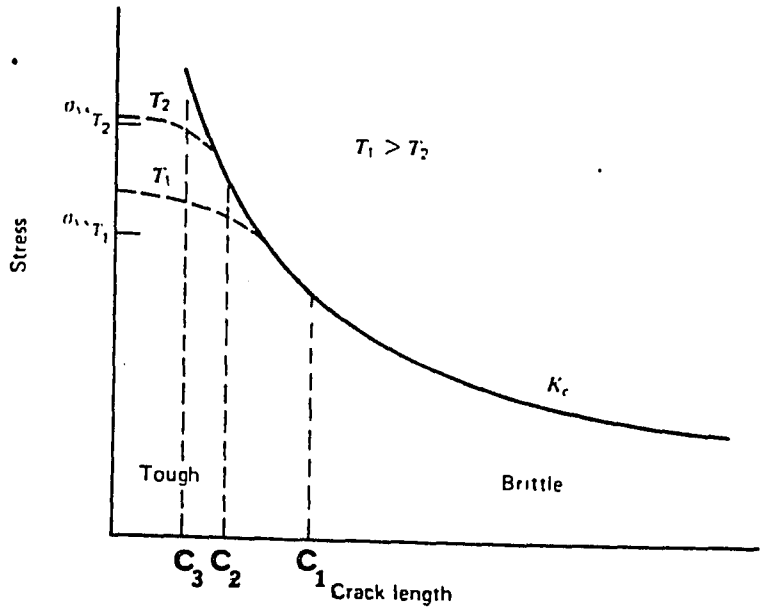


[Fig. II.3.35] The change in the kinetic energy of the critically loaded pre-cleaved 2D Johnson solid, ΔE_{ke}, vs $(cV_c)^2$. (□)159x135, σ_c=2.15, c_o=9.75; (▲)79x135, σ_c=1.90, c_o=9.75; (Φ)39x135, σ_c=1.45, c_o=9.75; (Δ)79x135, σ_c=3.37, c_o=3.75; (+)79x135, ε_c=0.061, c_o=3.75; (x)79x135, σ_c=2.45, c_o=6.75 (•)79x135, ε_c=0.047, c_o=6.75; (o)79x135, c_o=9.75, ε_c=0.041. Simulations results do not reveal any particular functional c^2, and/or $(cV_c)^2$ dependency.

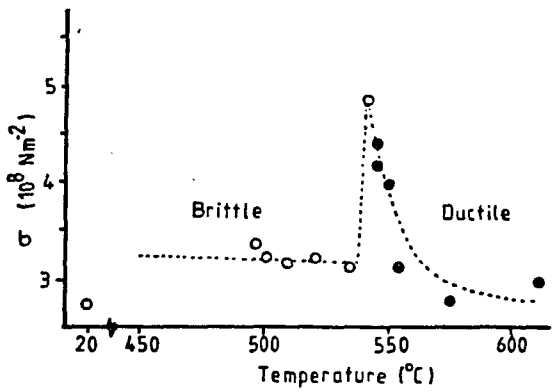


[Fig. II.3.36] The change in the kinetic energy of the critically loaded pre-cleaved 2D-triangular covalently modified Lennard-Jones solid with $a^*=1.0$, ΔE_{ke}, versus $(V_C.c/C_1M^*)^2$ during the brittle propagation of the internal crack.

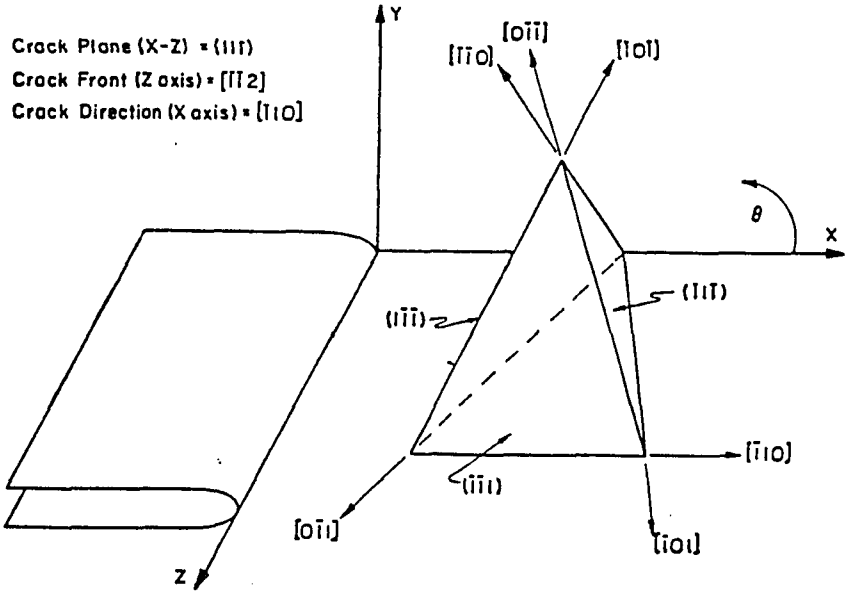
See Table II.3.10A.



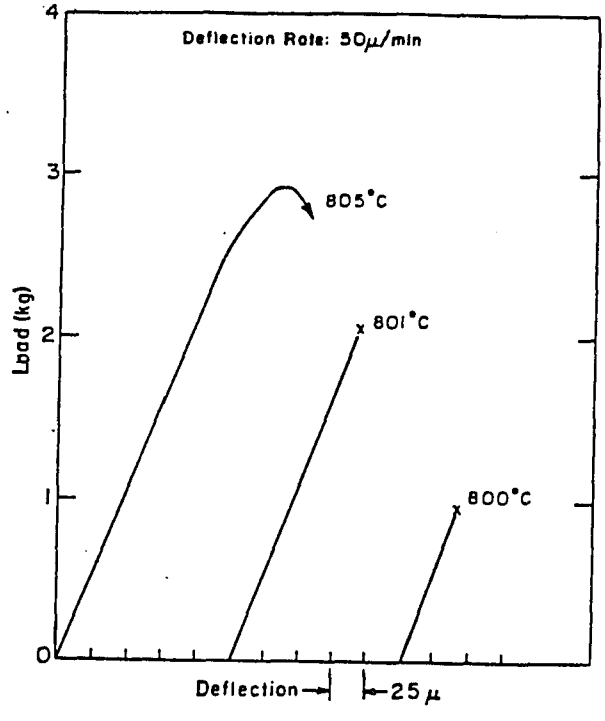
[Fig. III.1A] Schematic diagram showing the relationship between allowable stress level and flow size. Solid line represents material fracture toughness K_C. dashed lines show the effect of plasticity (Fig. 9.15, [42]).



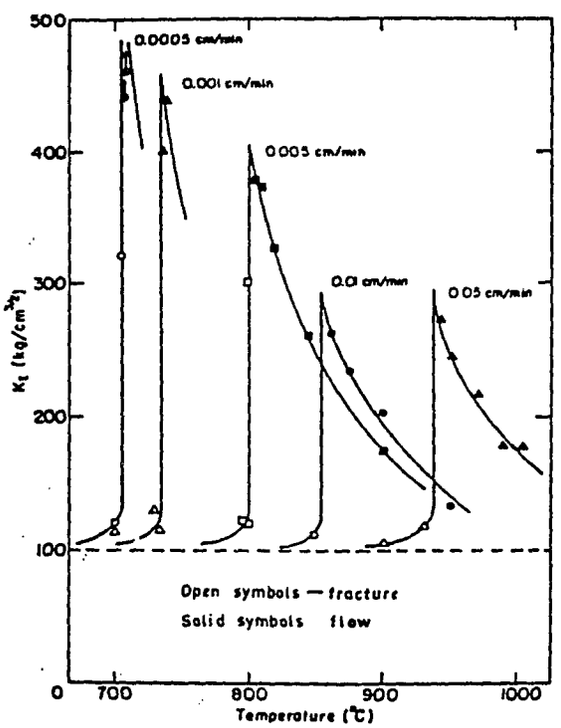
[Fig. III.1B] Failure stress against temperature for intrinsic silicon; (O) brittle cleavage, (●) ductile failure (Fig. 1, [11]).



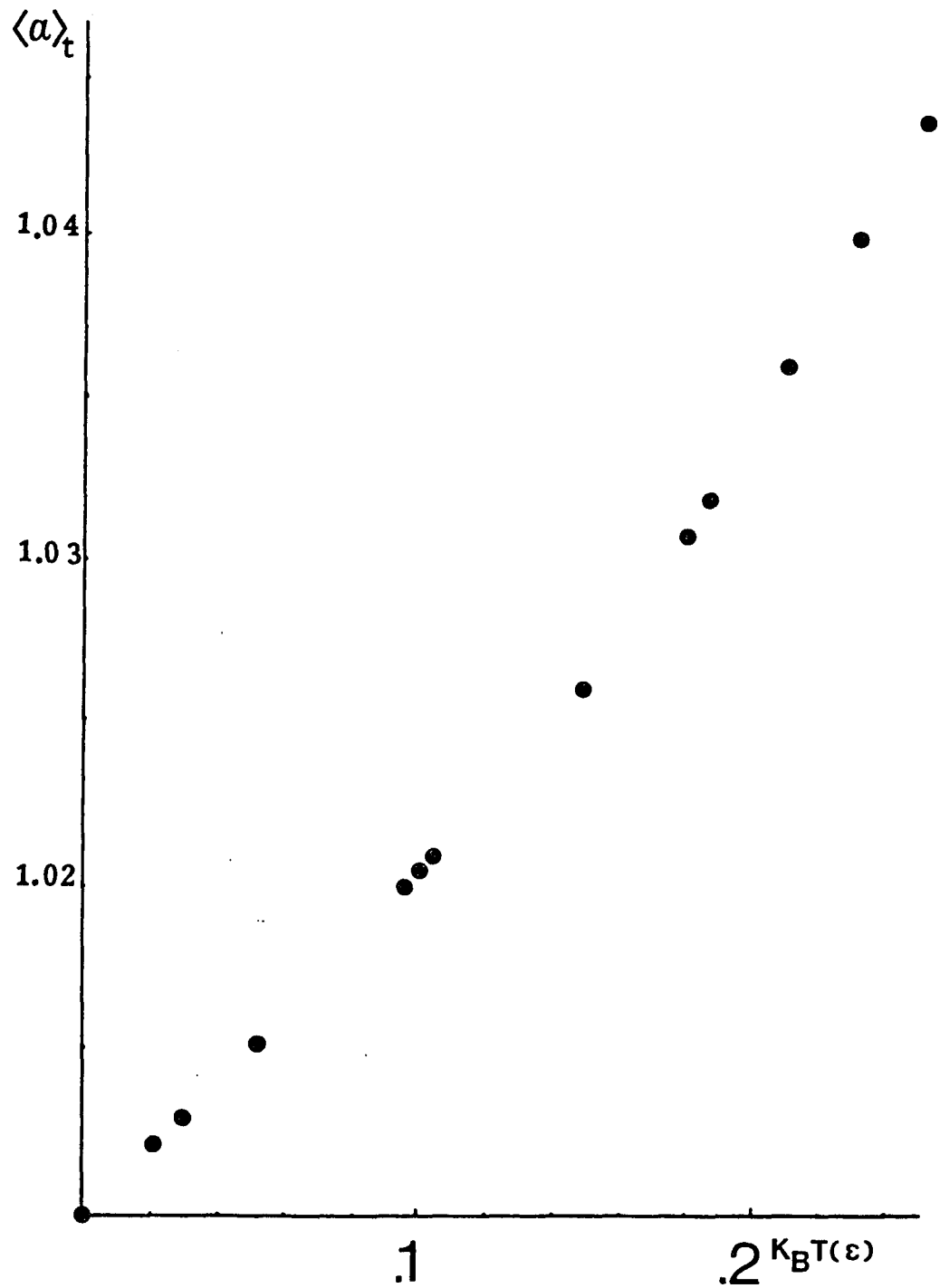
[Fig. III.2] Orientation between the crack and the dislocation glide planes in 3D Si (Fig. 2, [54]).



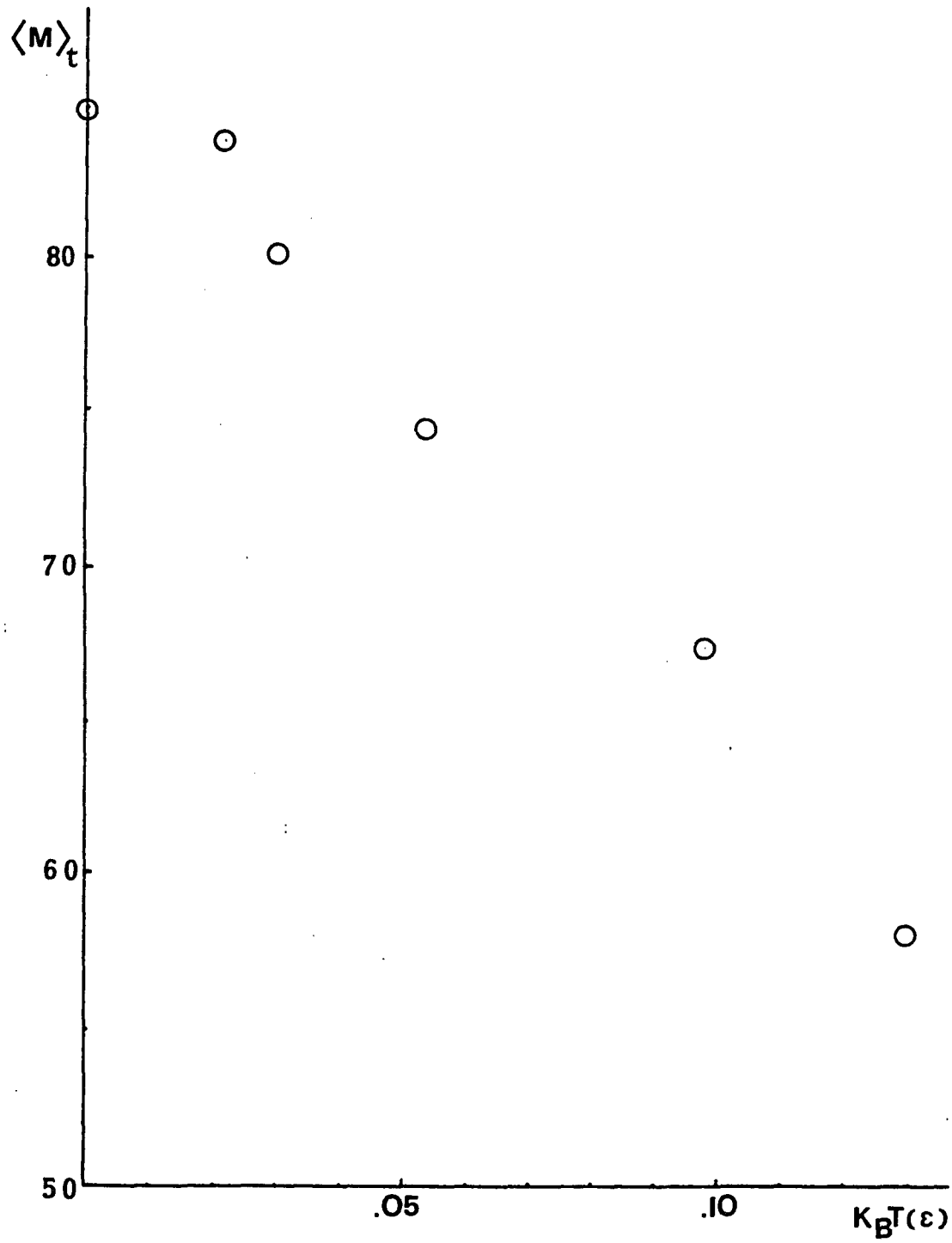
[Fig. III.3] Load-deflection curves for three temperatures bracketing a brittle-to-ductile transition, BDT (Fig. 7, [54]).



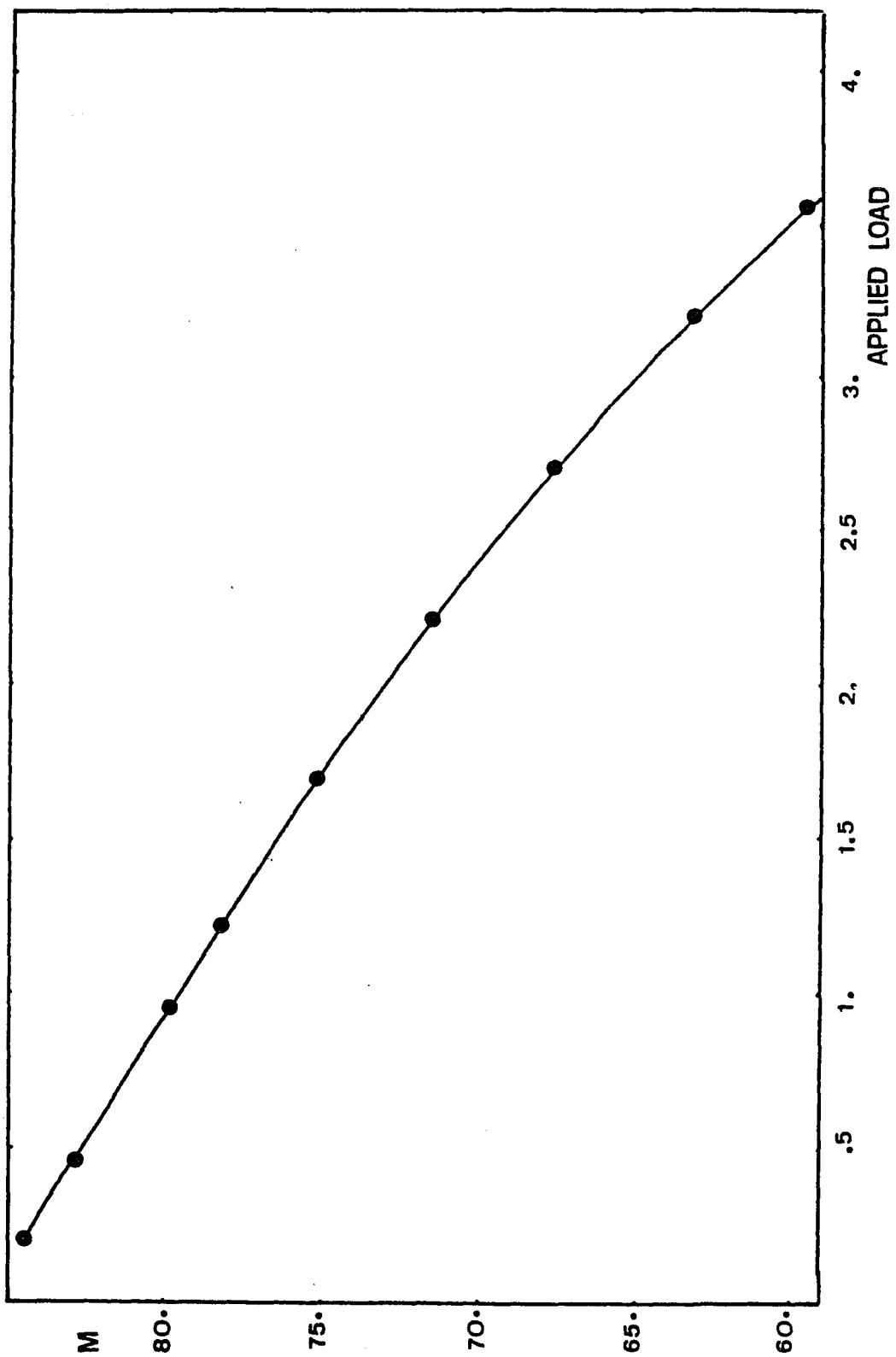
[Fig. III.4] Critical stress intensity factors at fracture or flow versus temperature for five cross-head speeds showing the respective brittle-to-ductile transition, BDT (Fig. 8, [54]).



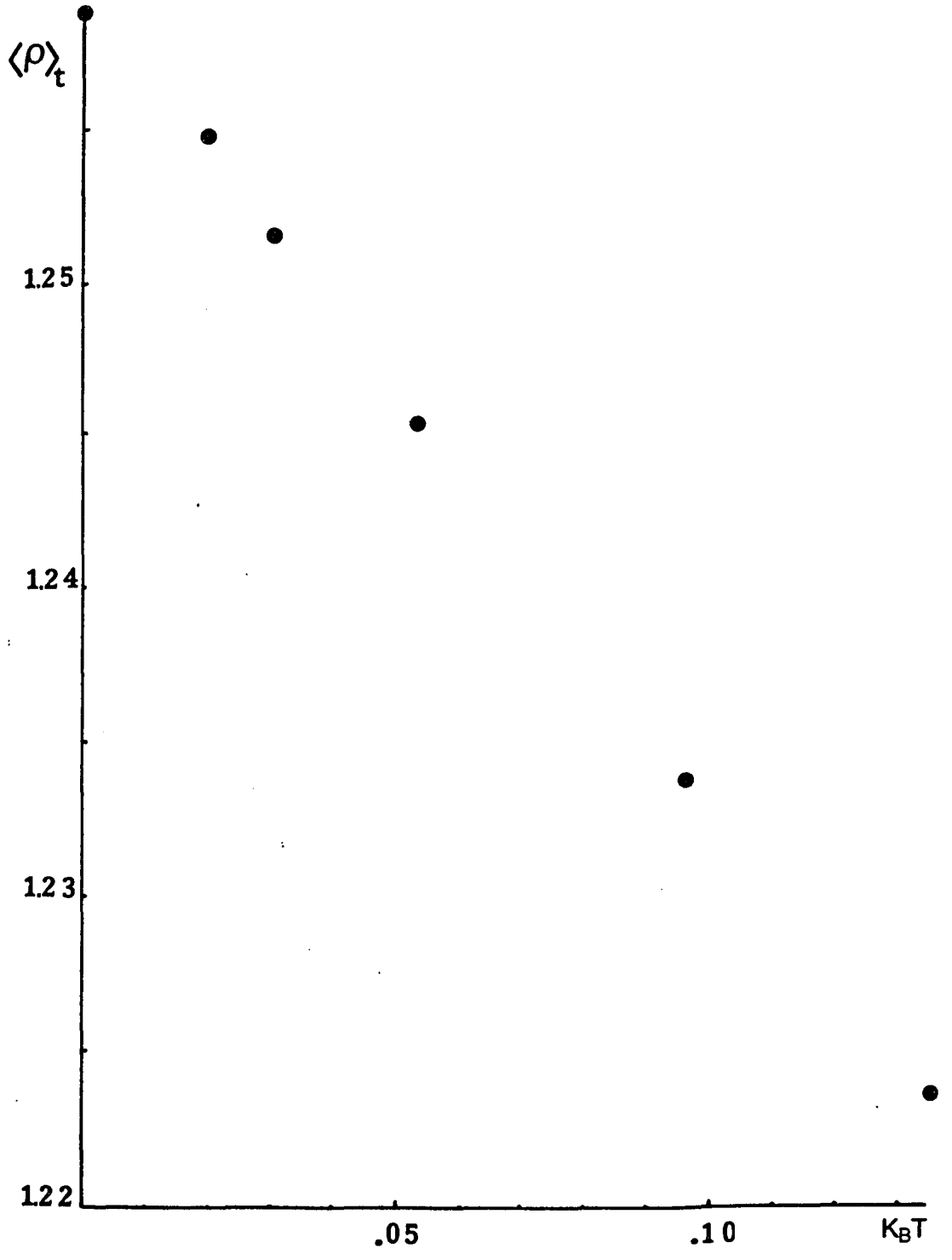
[Fig. III.3.1] The (time averaged) linear coefficient of expansion of the LJCOVa.2 solid, <α>t , as a function of the temperature. See Table II.2.2B.



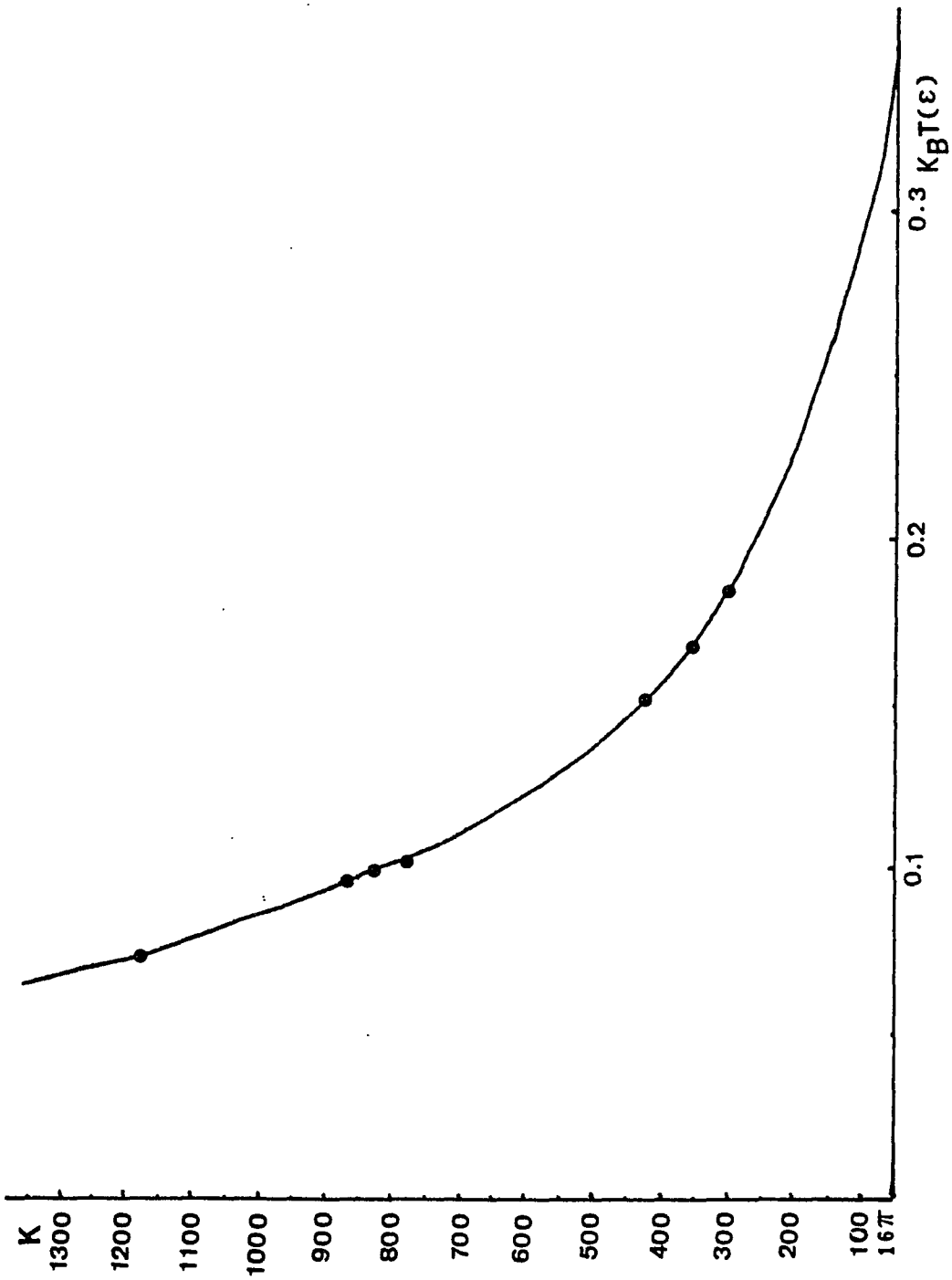
[Fig. III.3.2] The (time averaged) modulus of elasticity, $\langle M \rangle_t$ versus the equilibrium temperature of the 2D LJCOVa.2 solid, K_BT. See Table II.2.2B.



[Fig. III.3.3] Young's modulus, M, versus σ for 2D LJCOVa.2 solid at zero K.



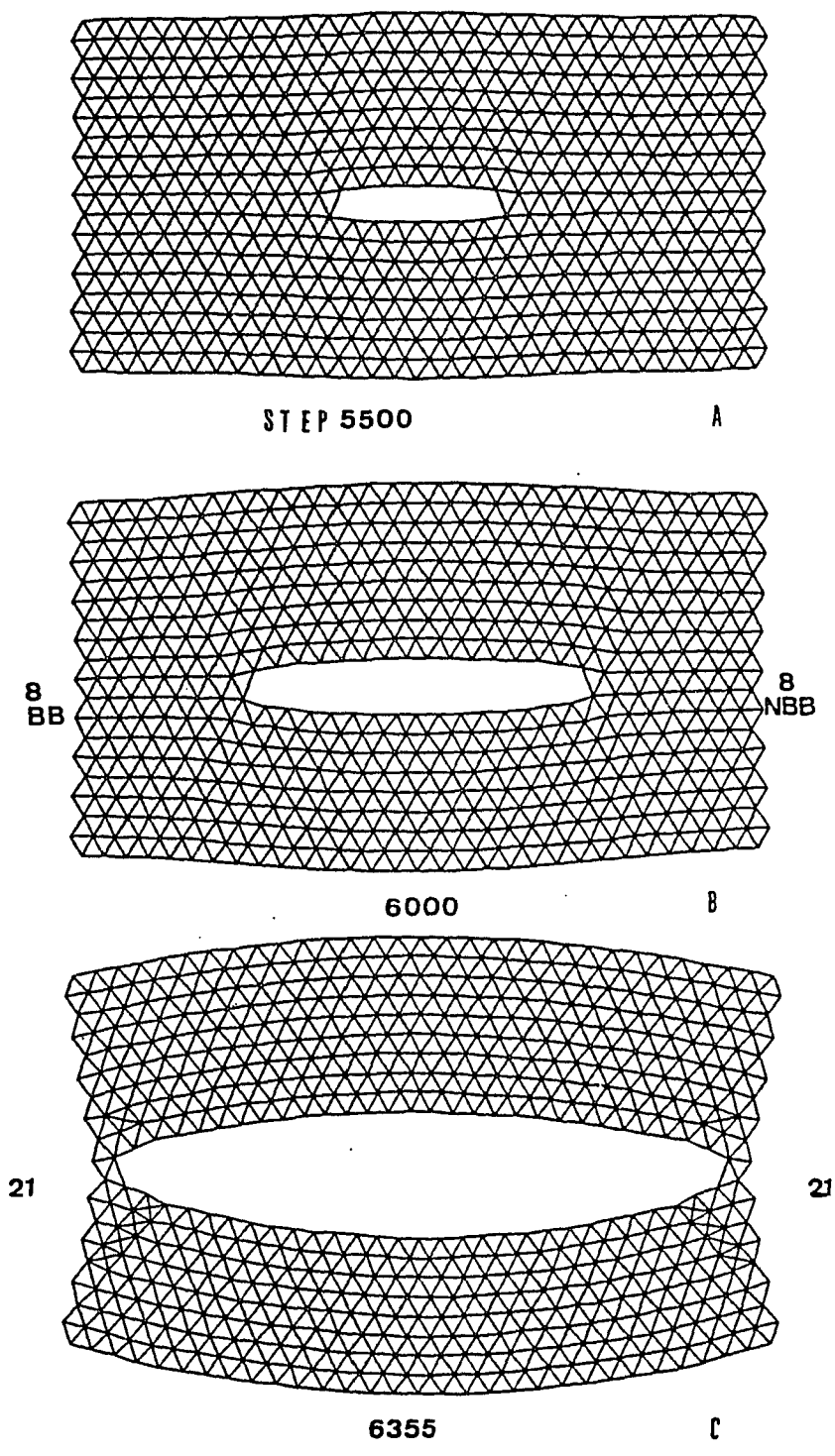
[Fig. III.3.4] The (time averaged) density of the LJCOVa.2 solid, $\langle\rho\rangle_t$, as a function of the equilibrium temperature of the system, K_BT.



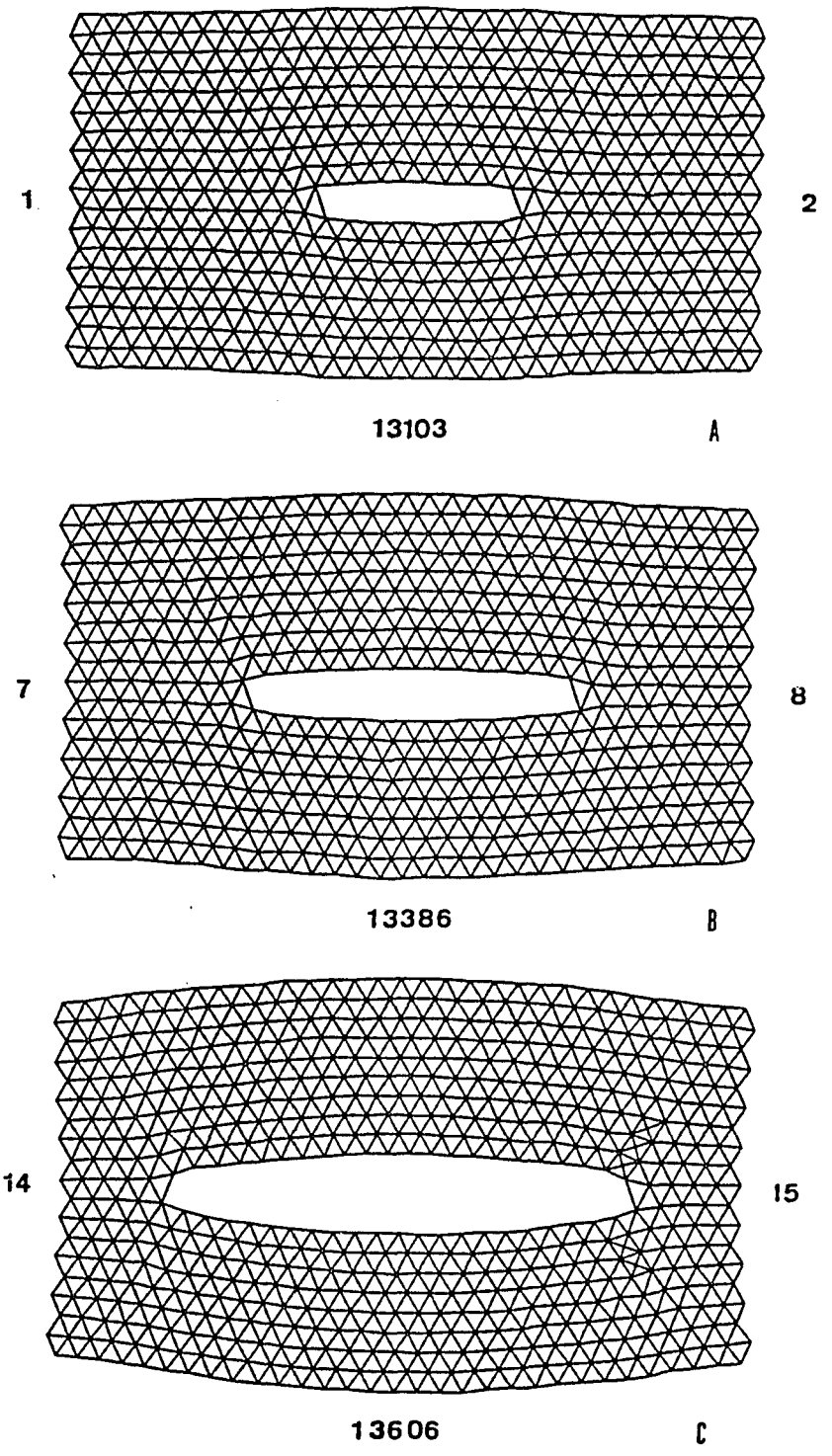
[Fig. III.3.5] Kosterlitz-Thouless parameter,

$$\mathbf{K} = [33d/28][M/K_BT] \geq 16\pi \qquad \text{for Solid} \qquad \text{III.3.4}$$

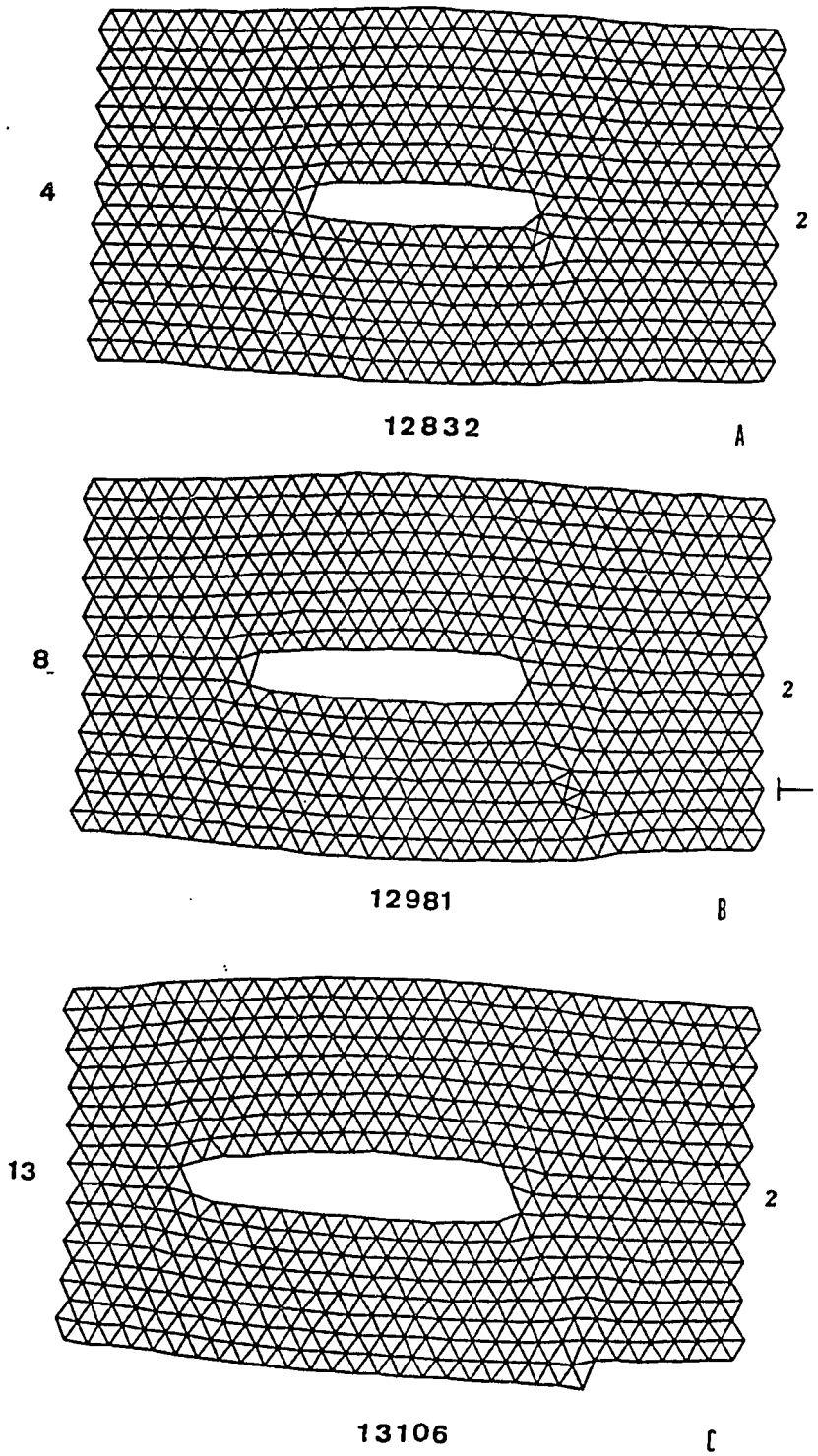
is plotted against K_BT. The extrapolation of **K** to 16π discloses $K_BT \approx 0.34\ \varepsilon_o$ for the melting temperature of the 2D-LJCOVa.2 solid, which is in good agreement with the simulations results. See Table II.2.2B.



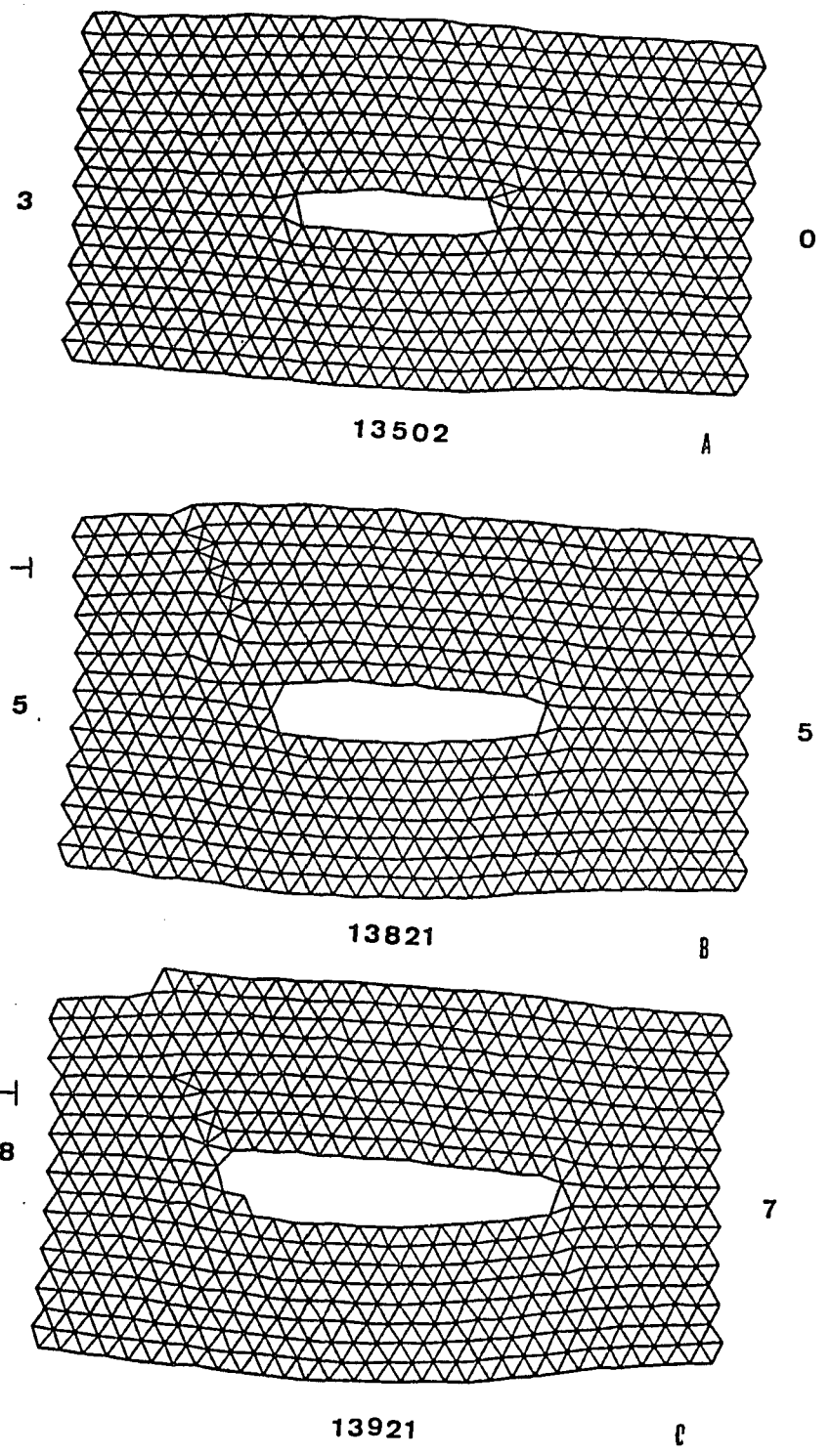
[Fig. III.4A1] The critically loaded, σ_c=2.1, pre-cleaved, c_o=3.75d, LJCOVa.2 solid is at K_BT=0. Simulations results are tabulated in Table III.4A1.



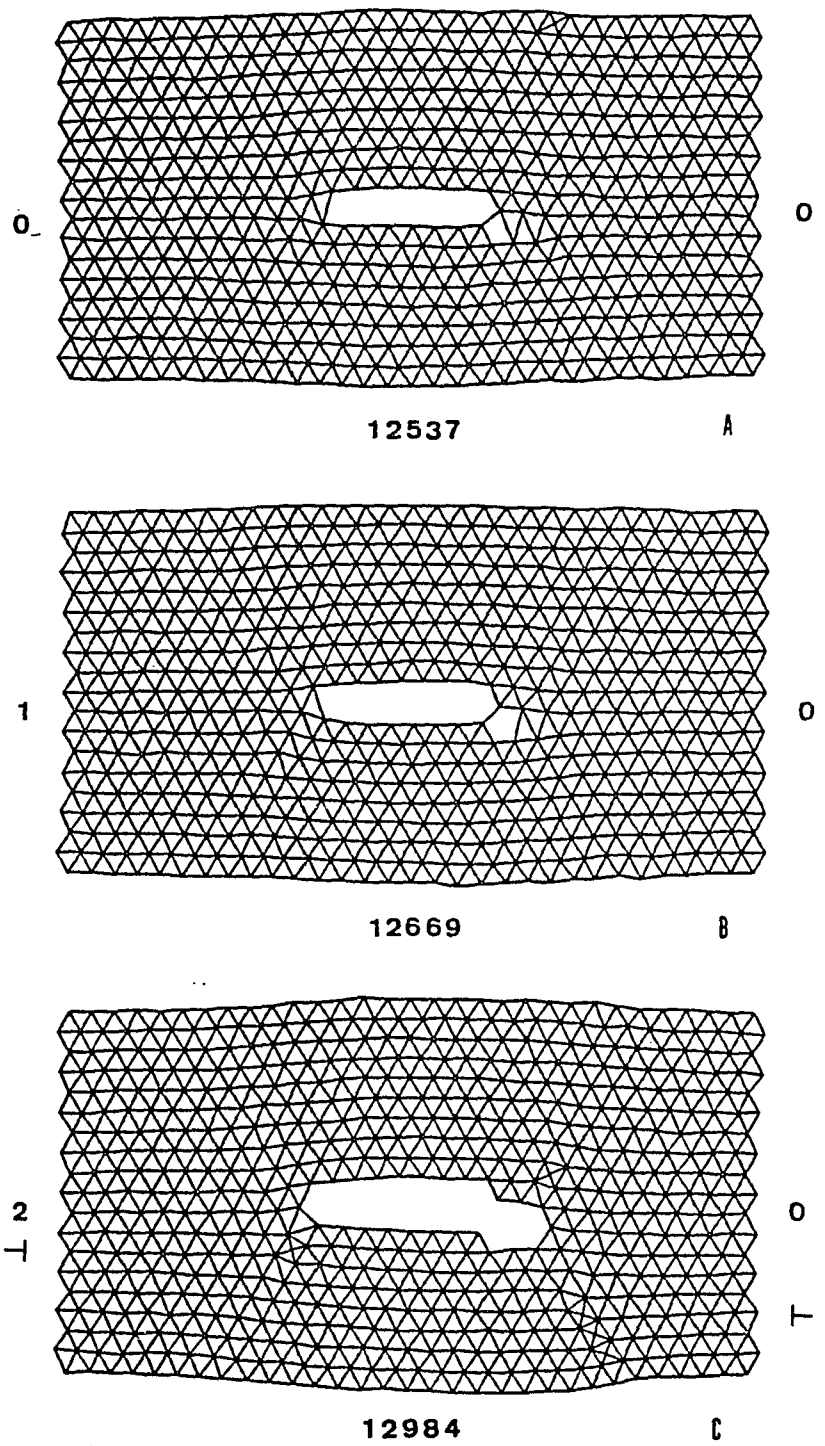
[Fig. III.4A2] The critically loaded (σ_C=1.9) pre-cleaved (c_o=3.75d) LJCOVa.2 solid is at K_BT=0.02 ε_o. Simulations results are tabulated in Table III.4A2.



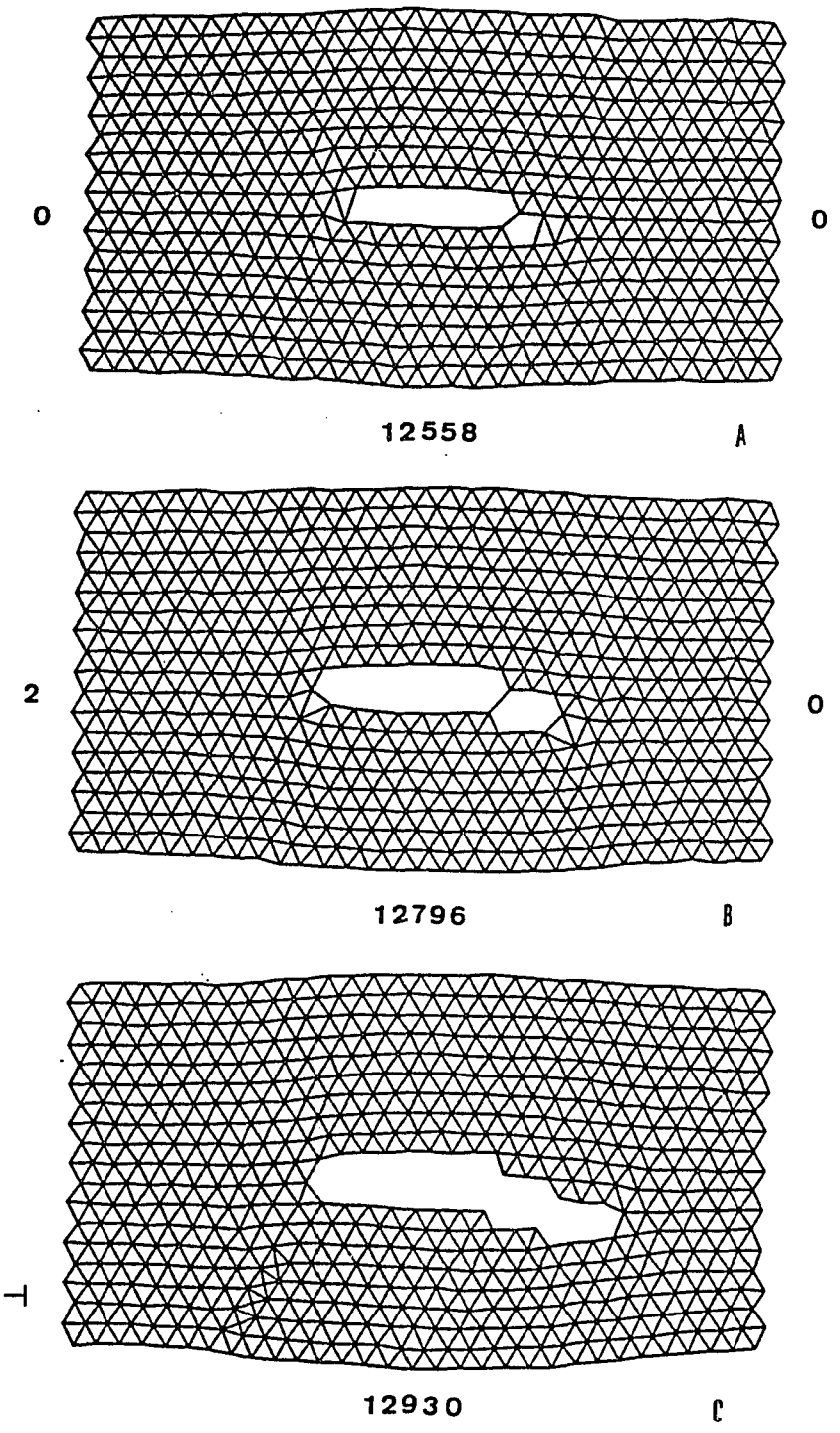
[Fig. III.4A3] The overloaded (σ=2.0) pre-cleaved (c_o=3.75d) LJCOVa.2 solid is at K_BT=0.02 ε_o. Simulations results are tabulated in Table III.4A3.



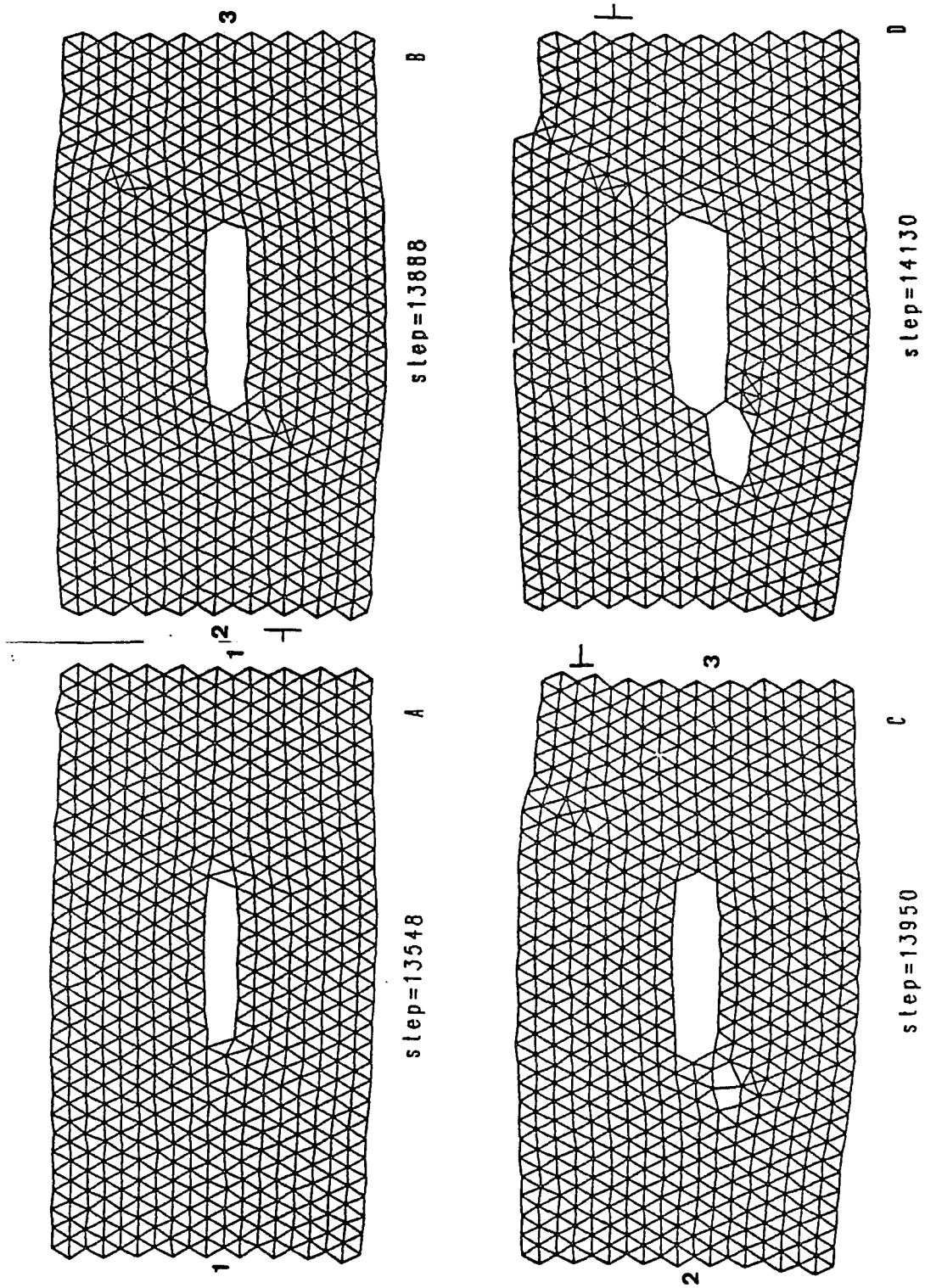
[Fig. III.4A4] The critically loaded (σ_C=1.90) pre-cleaved (c_o=3.75d) LJCOVa.2 solid is at K_BT=0.046 ε_o. Simulations results are tabulated in Table III.4A4.



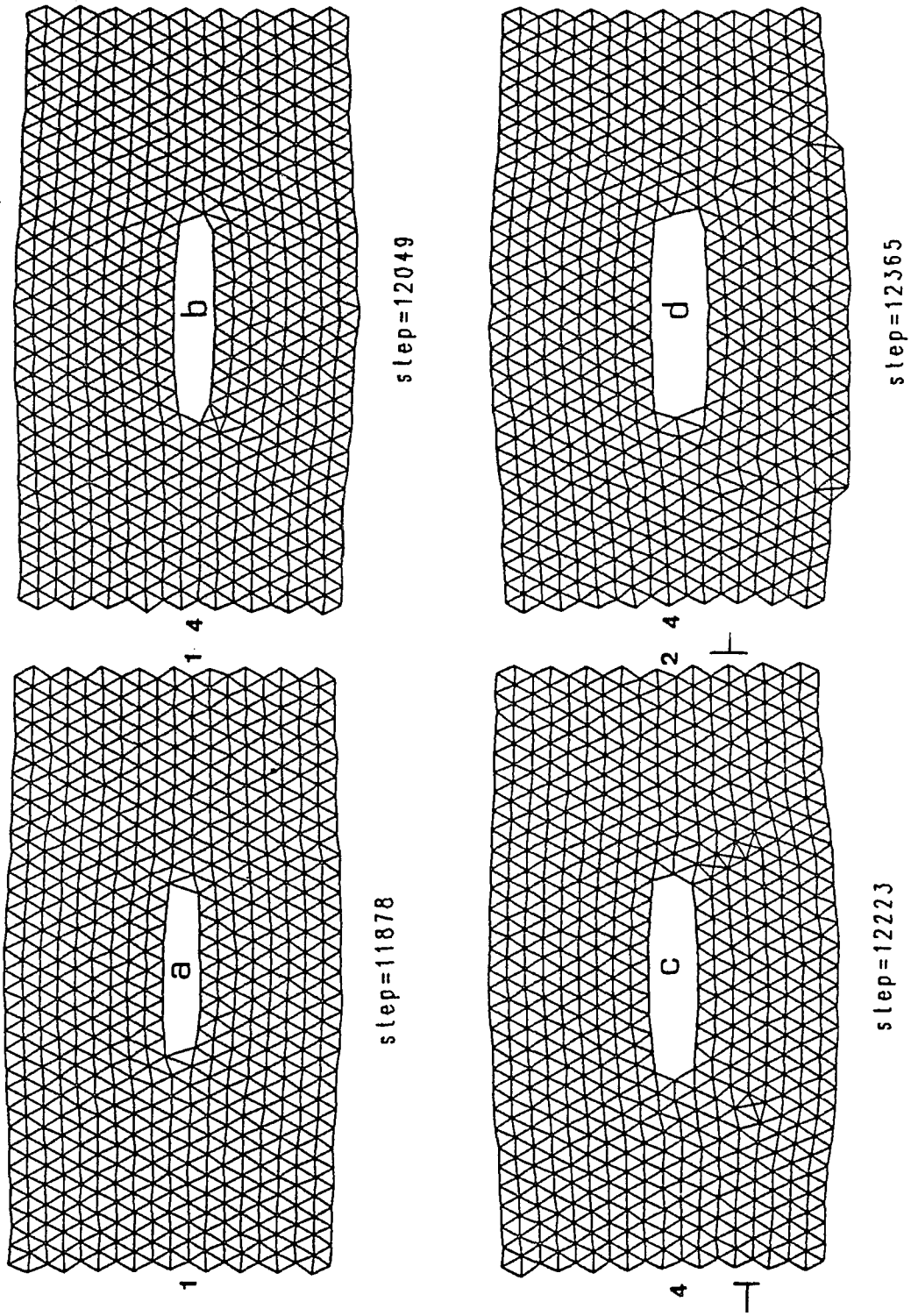
[Fig. III.4A5] The critically loaded (σ_C=1.80) pre-cleaved (c_o=3.75d) LJCOVa.2 solid is at K_BT=0.056 ε_o. Simulations results are tabulated in Table III.4A5.



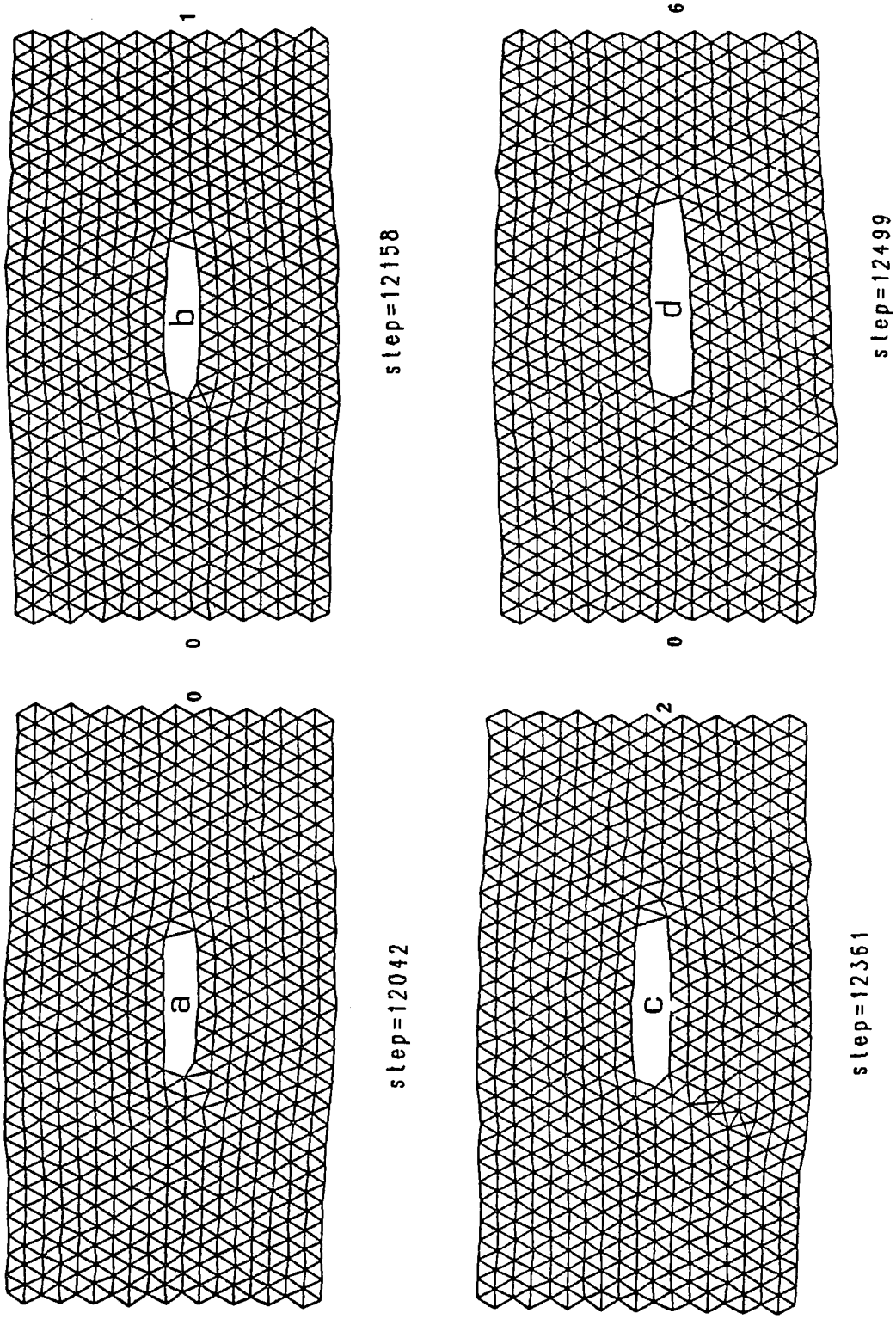
[Fig. III.4A5*] The overloaded (σ=1.90) pre-cleaved (c_o=3.75d) LJCOVa.2 solid is at K_BT=0.056 ε_o. Simulations results are tabulated in Table III.4A5*.



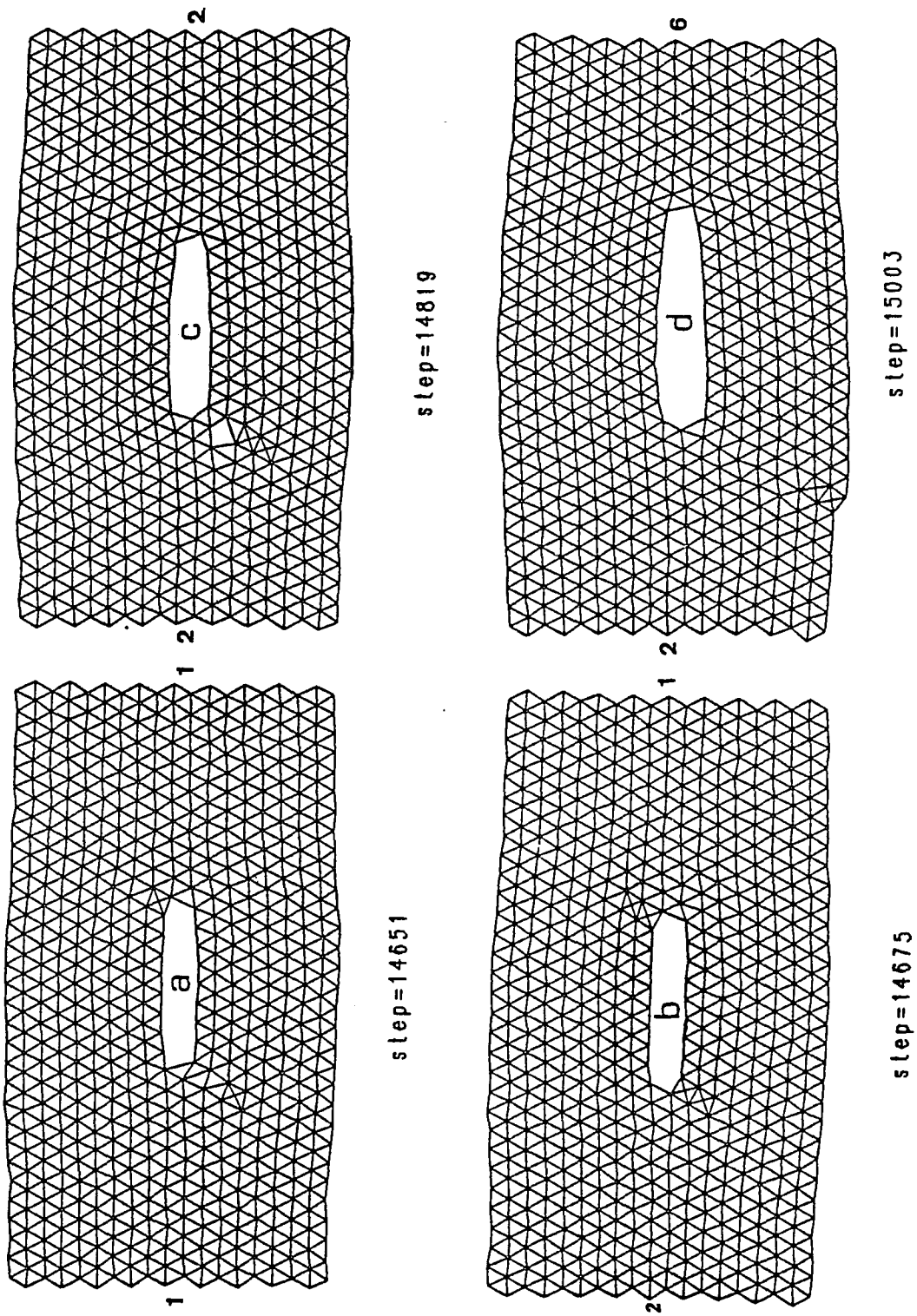
[Fig. III.4A6] The critically loaded (σ_c=1.80) pre-cleaved (c_o=3.75d) LJCOVa.2 solid is at K_BT=0.060 ε_o. Simulations results are tabulated in Table III.4A6.



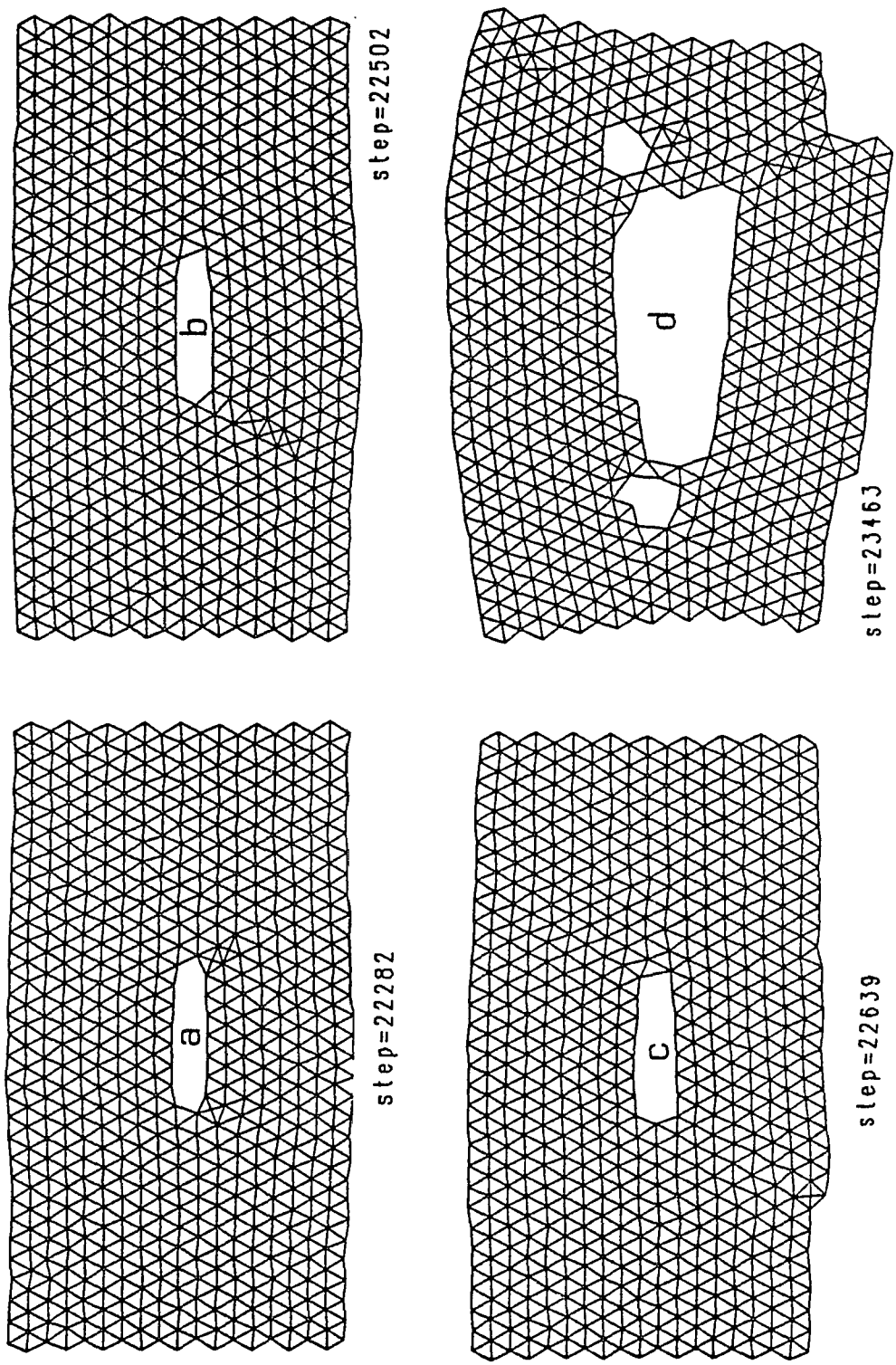
[Fig. III.4A7] The critically loaded (σ_C=1.80) pre-cleaved (c_o=3.75d) LJCOVa.2 solid is at K_BT=0.060 ε_o. Simulations results are tabulated in Table III.4A7. The history of the run is different from that of III.4A6.



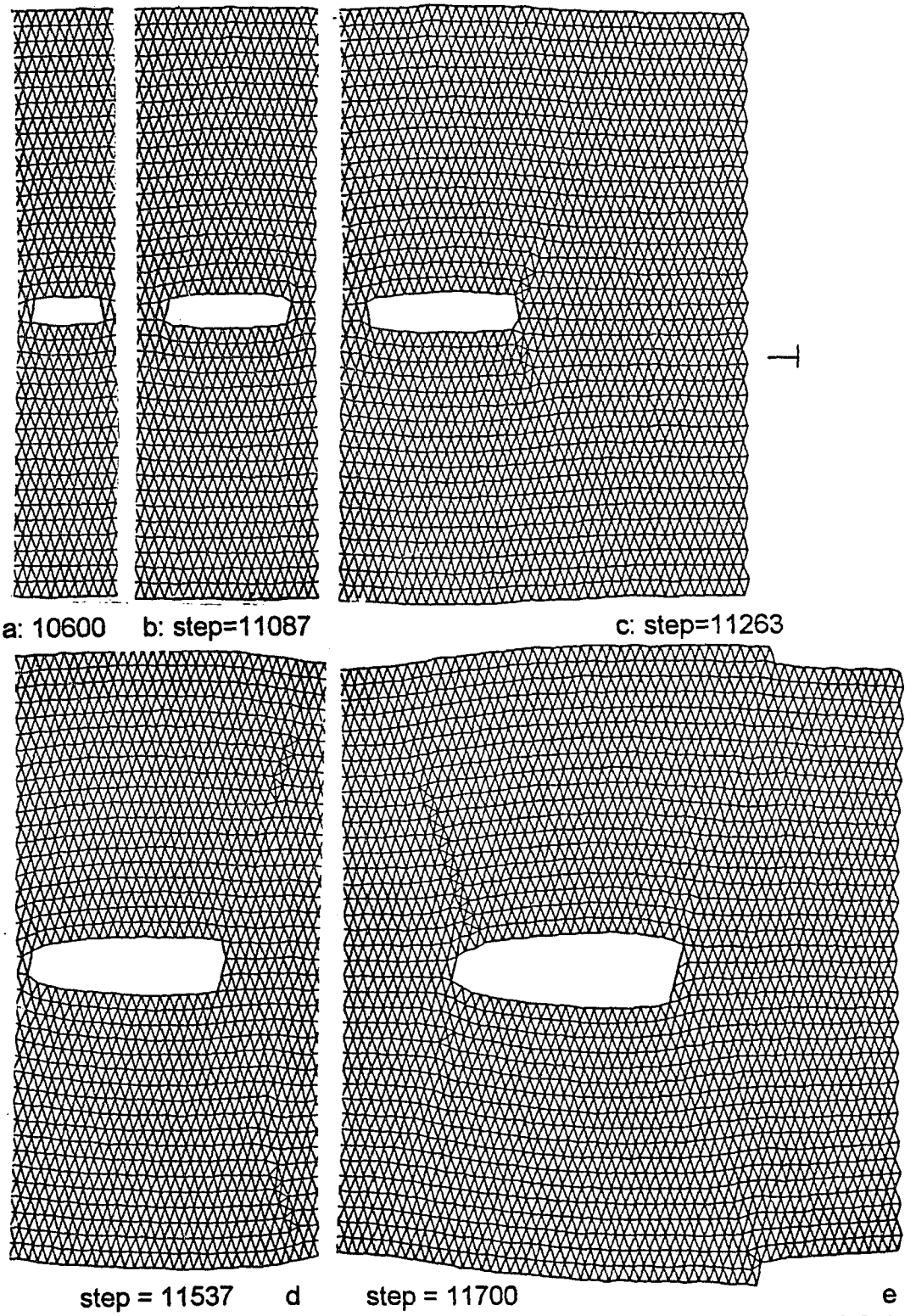
[Fig. III.4A8] The critically loaded (σ_c=1.80) pre-cleaved (c_o=3.75d) LJCOVa.2 solid is at K_BT=0.0628 ε_o. Simulations results are tabulated in Table III.4A8.



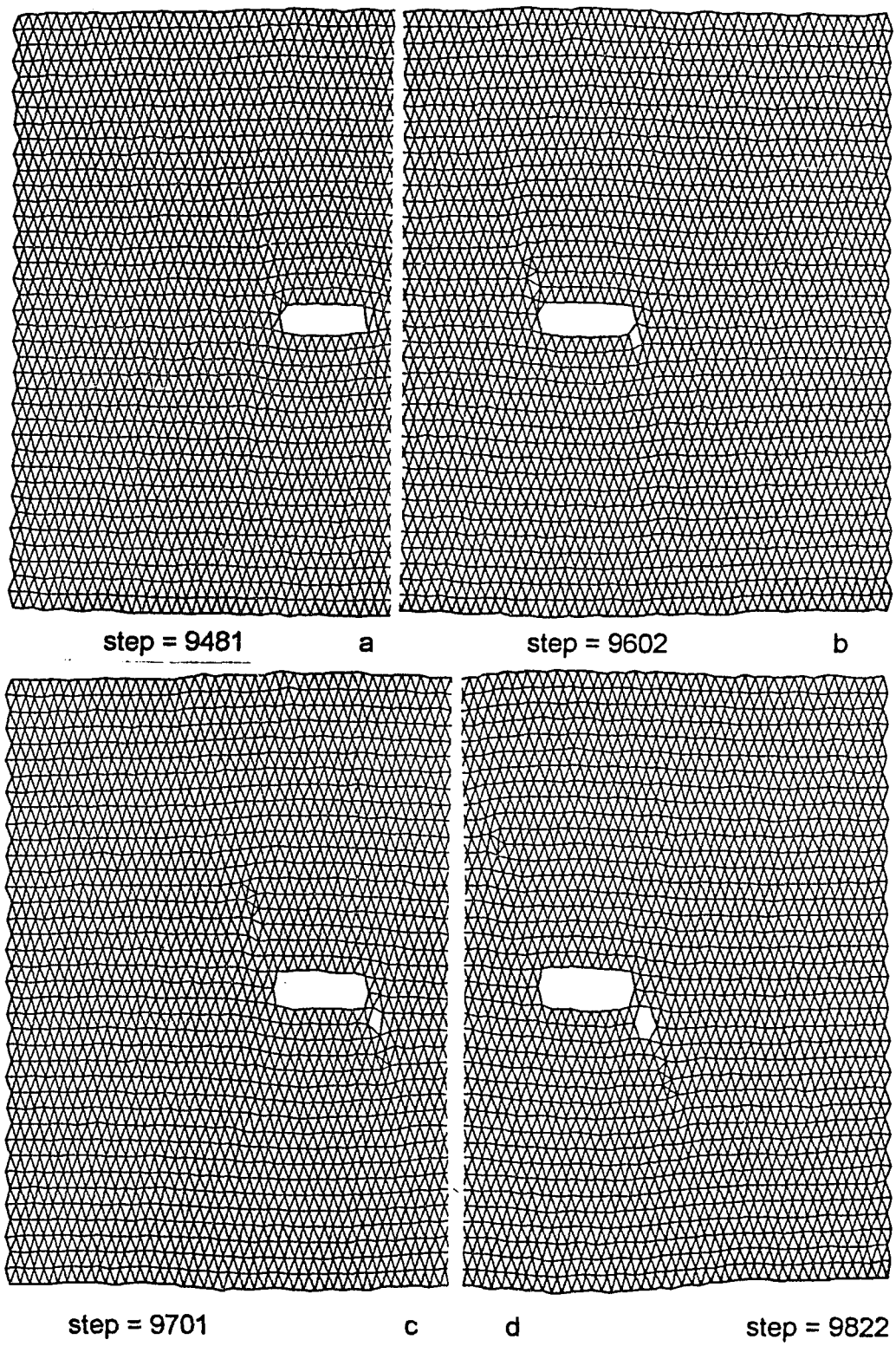
[Fig. III.4A9] The critically loaded (σ_C=1.80) pre-cleaved (c_o=3.75d) LJCOVa.2 solid is at K_BT=0.0625 ε_o. Simulations results are tabulated in Table III.4A9. The history of the run is different from that of III.4A8.



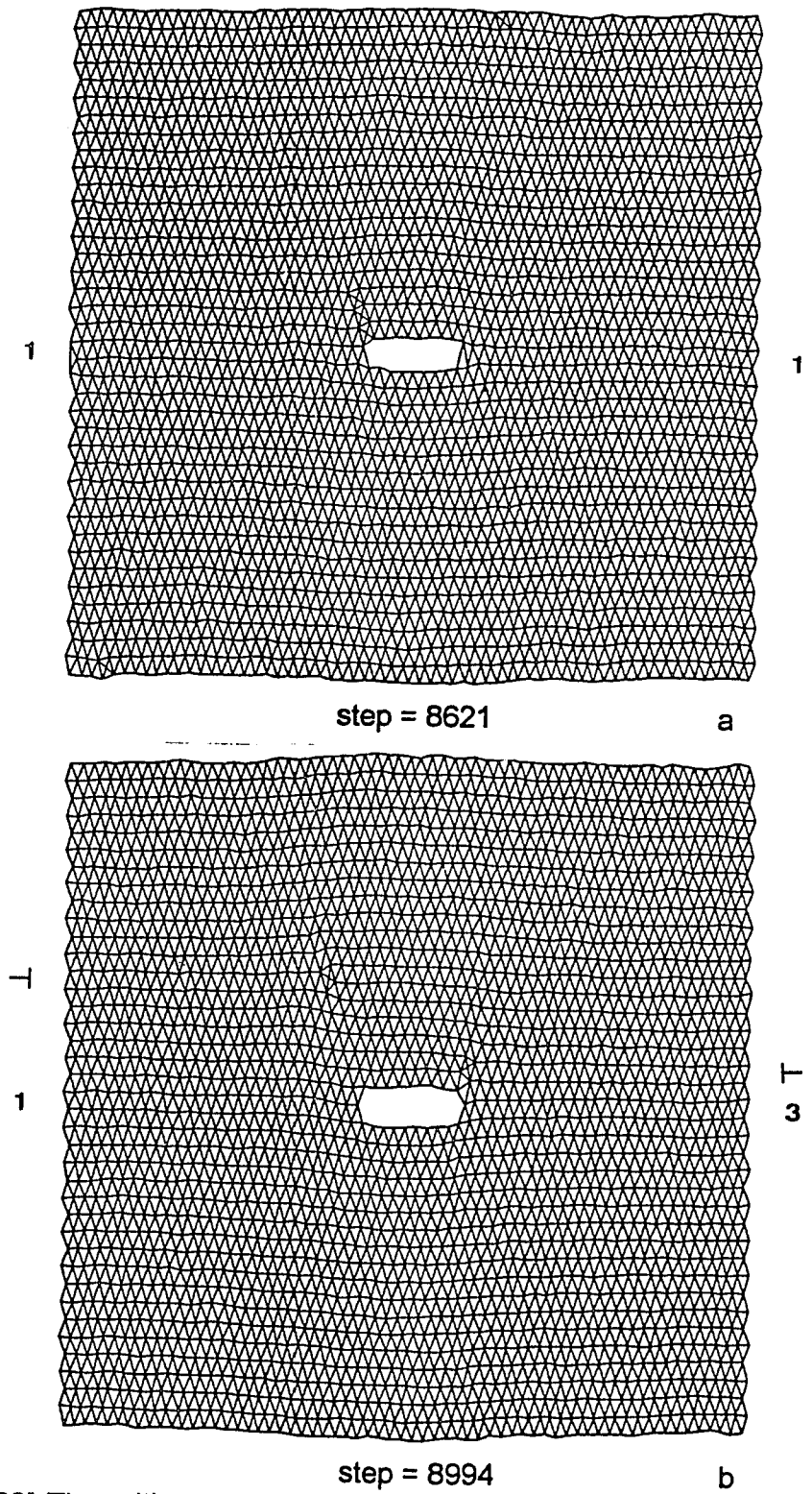
[Fig. III.4A10] The critically loaded (σ_C=1.80) pre-cleaved (c_o=3.75d) LJCOVa.2 solid is at K_BT=0.075 ε_o. Simulations results are tabulated in Table III.4A10.



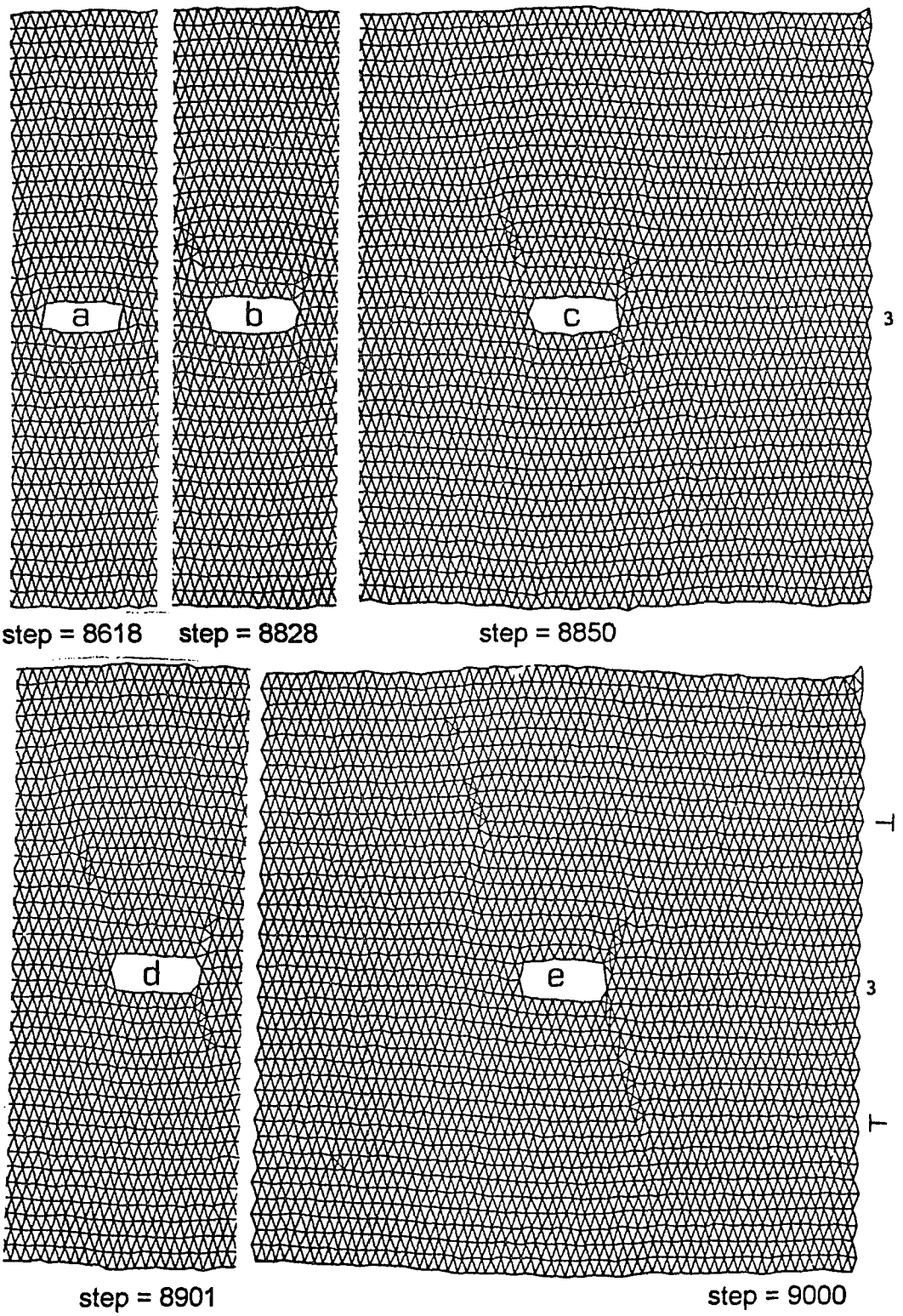
[Fig. III.4B1] The critically loaded (σ_c=2.40) pre-cleaved (c_o=3.75d) LJCOVa.2 solid is at K_BT=0.0193 ε_o. Simulations results are tabulated in Table III.4B1.



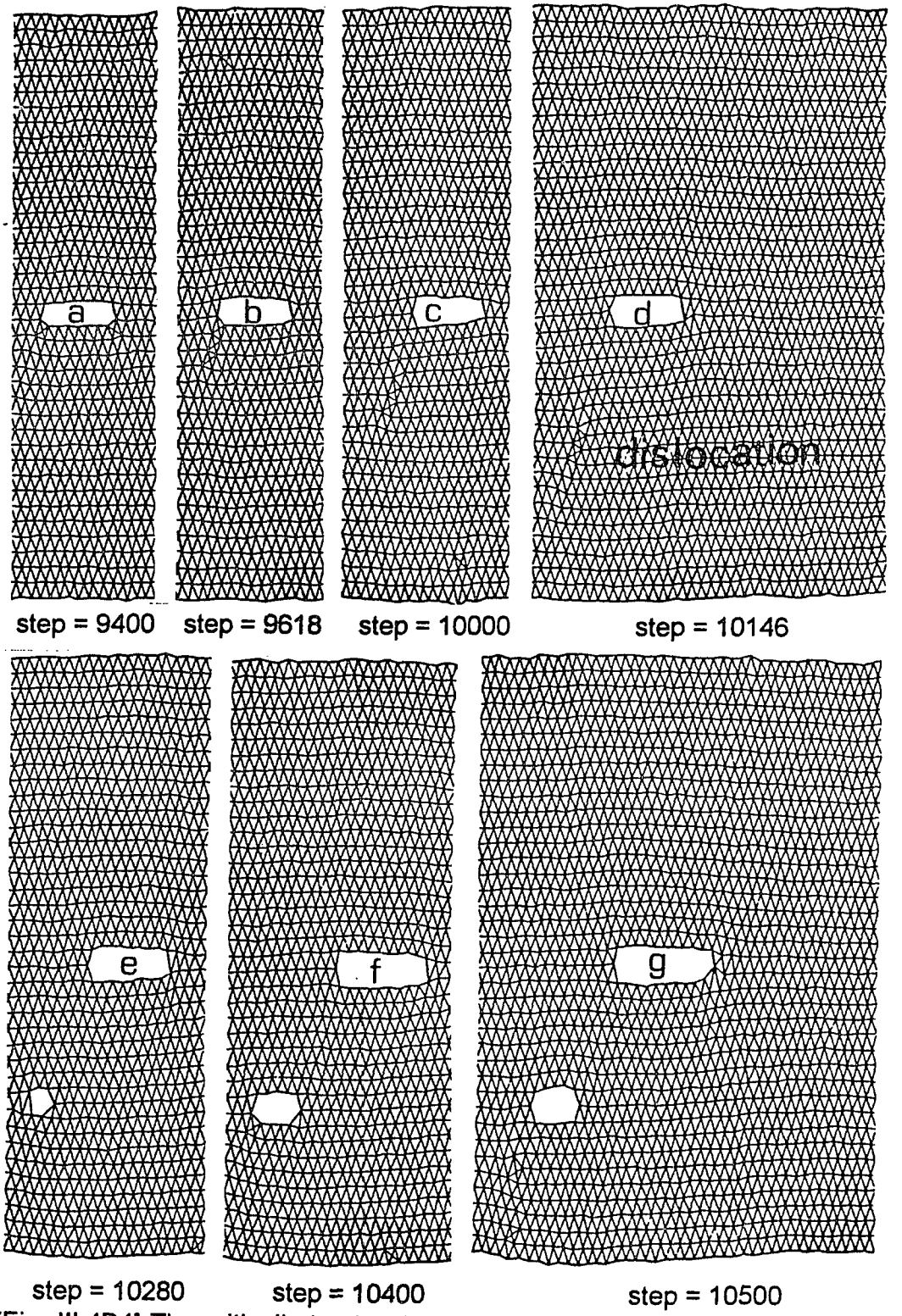
[Fig. III.4B2] The critically loaded (σ_c=2.20) pre-cleaved (c_o=3.75d) LJCOVa.2 solid is at K_BT=0.068 ε_o. Simulations results are tabulated in Table III.4B2.



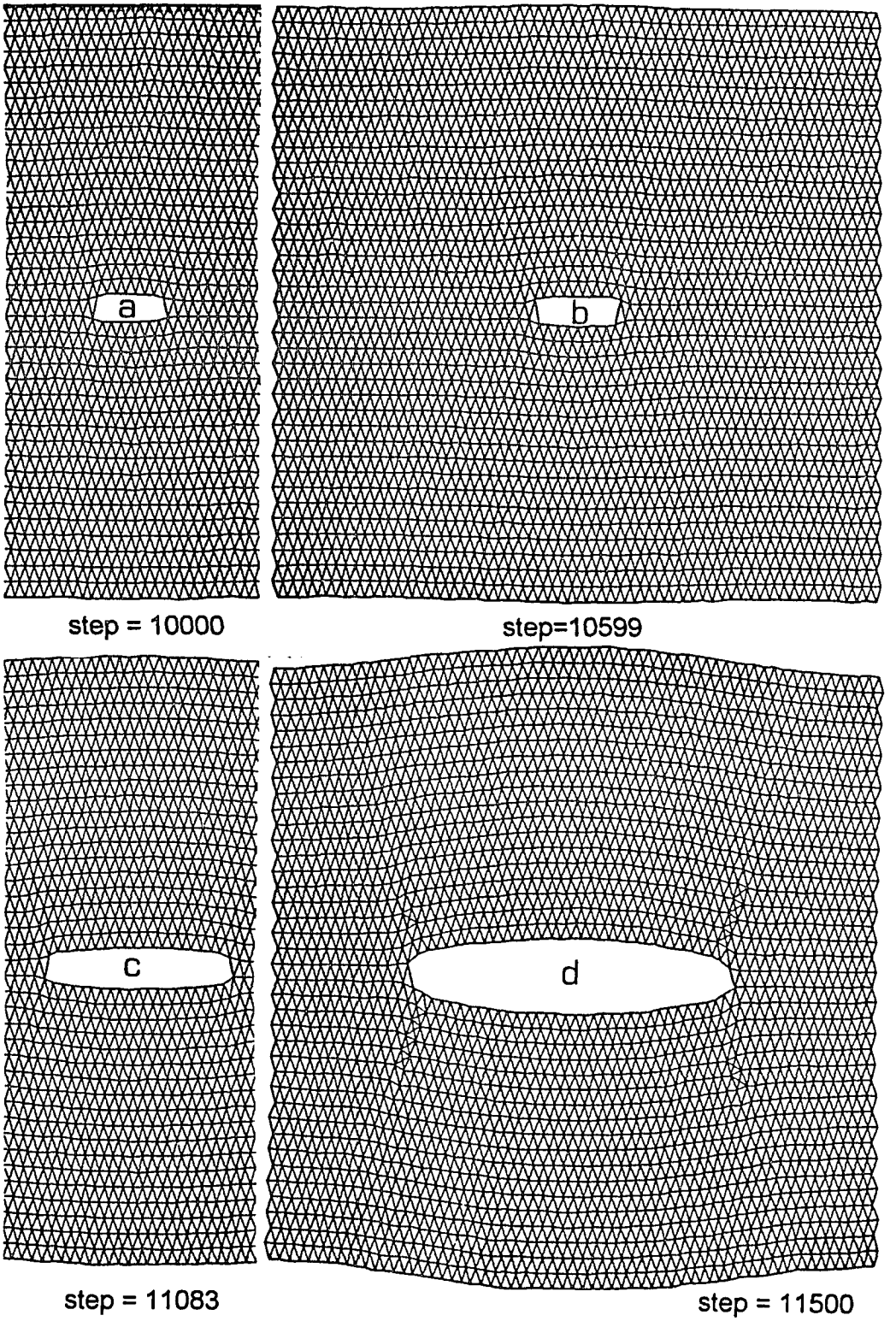
[Fig. III.4B3] The critically loaded (σ_c=2.00) pre-cleaved (c_o=3.75d) LJCOVa.2 solid is at K_BT=0.0904 ε_o. Simulations results are tabulated in Table III.4B3.



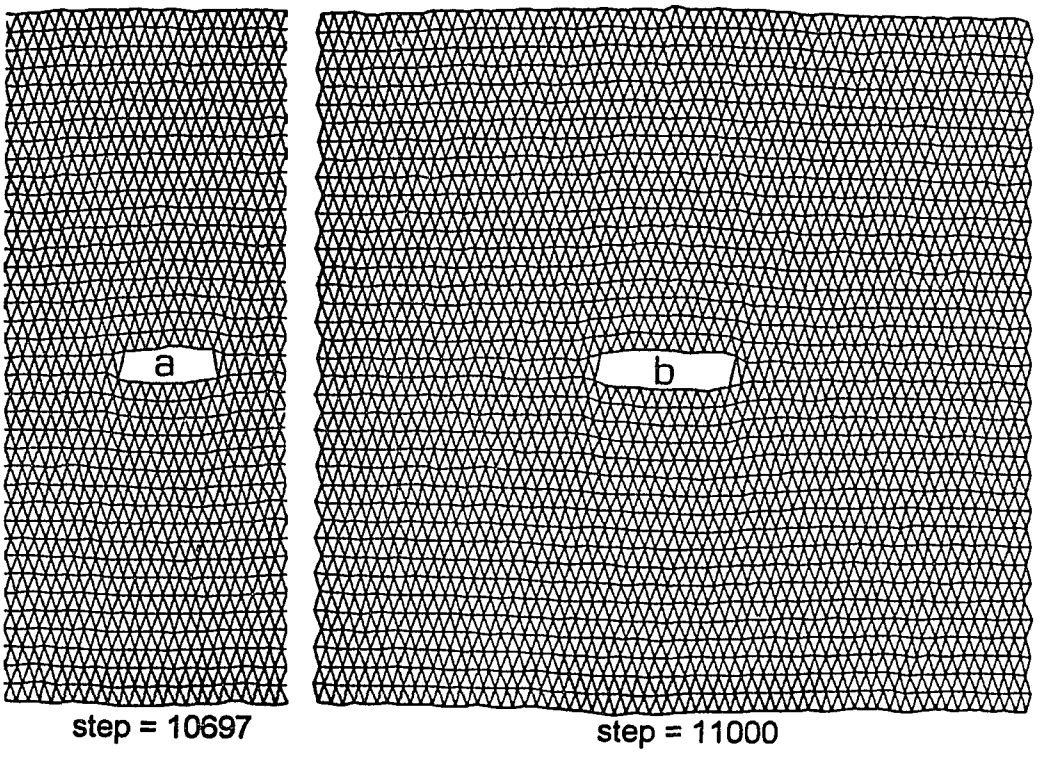
[Fig. III.4B3*] The over loaded (σ_a=2.10) pre-cleaved (c_o=3.75d) LJCOVa.2 solid is at K_BT=0.0892 ε_o. Simulations results are tabulated in Table III.4B3*.

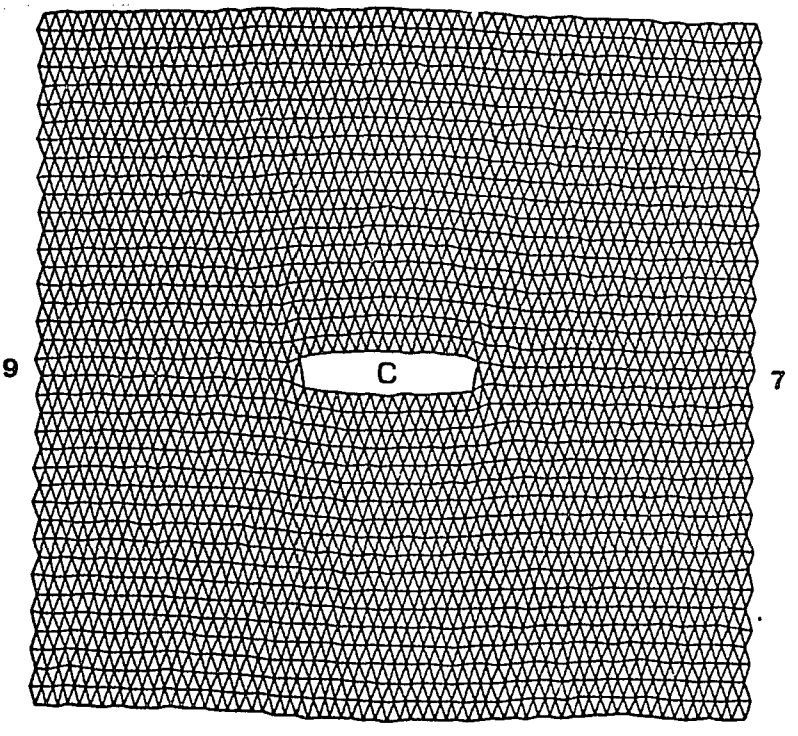


[Fig. III.4B4] The critically loaded (σ_C=1.80) pre-cleaved (c_o=3.75d) LJCOVa.2 solid is at K_BT=0.105 ε_o. Simulations results are tabulated in Table III.4B4.

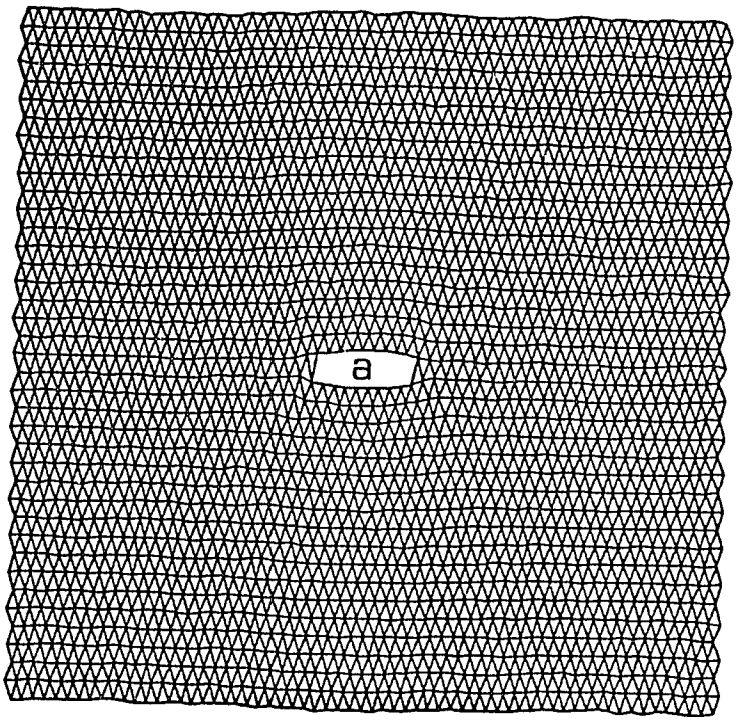


[Fig. III.6A1] Critically loaded (σ_C=2.30) pre-cleaved (c_o=3.75d) COR.LJCOVa.2 solid at K_BT=0.0193 ε_o. Simulations results are tabulated in Table III.6A1.

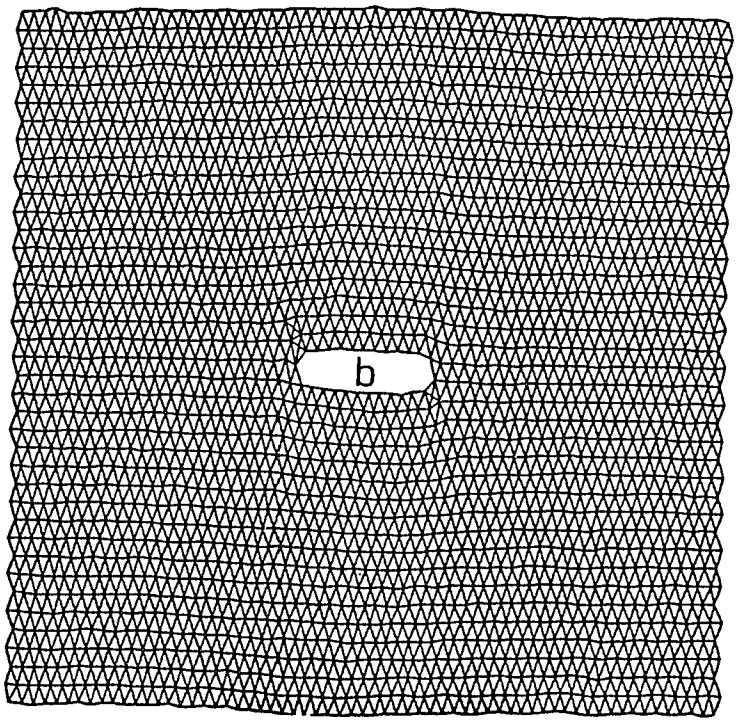




[Fig. III.6A2] Critically loaded (σ_C=2.10) pre-cleaved (c_o=3.75d) COR.LJCOVa.2 solid at K_BT=0.0634 ε_o. Simulations results are tabulated in Table III.6A2.

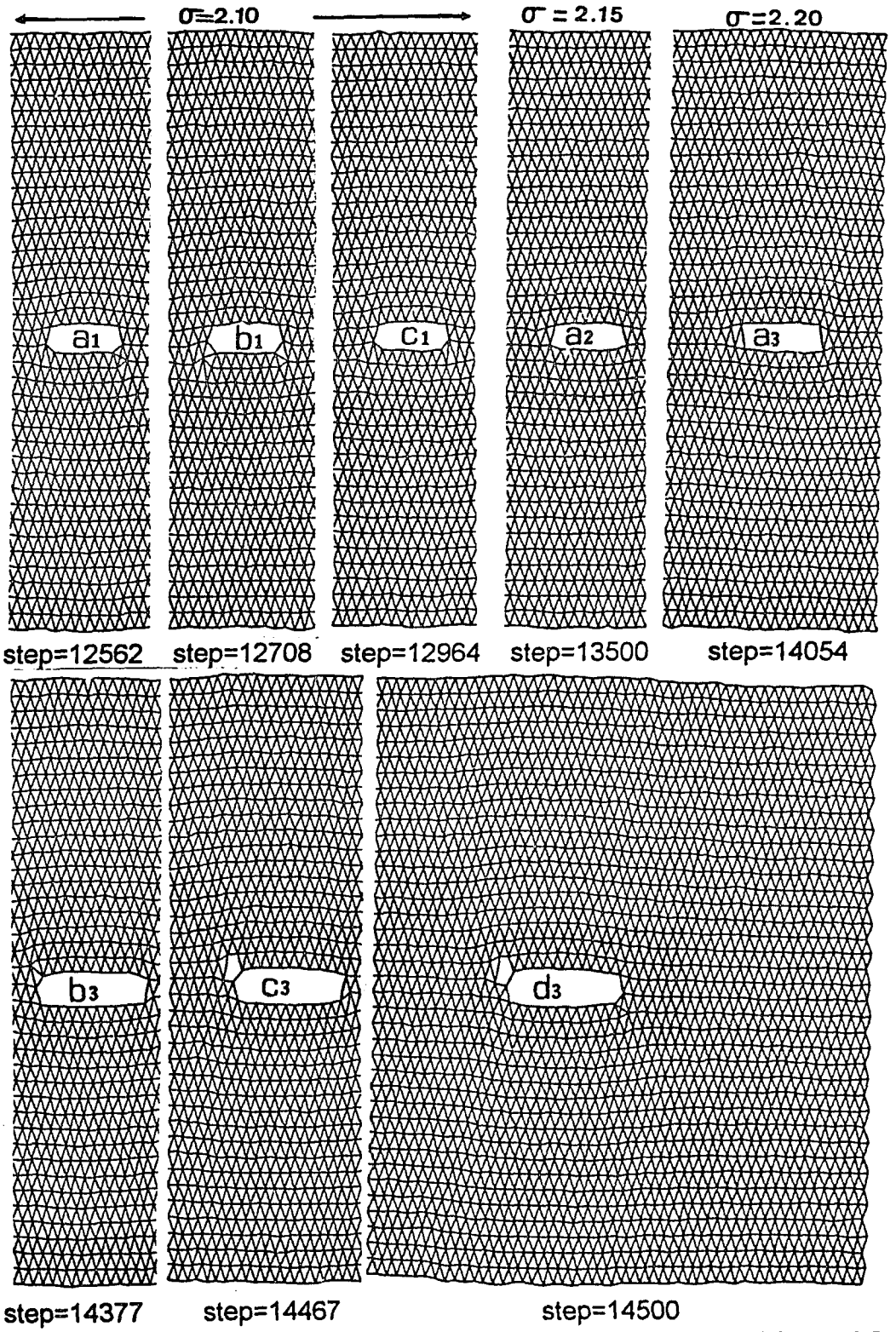


step = 10728

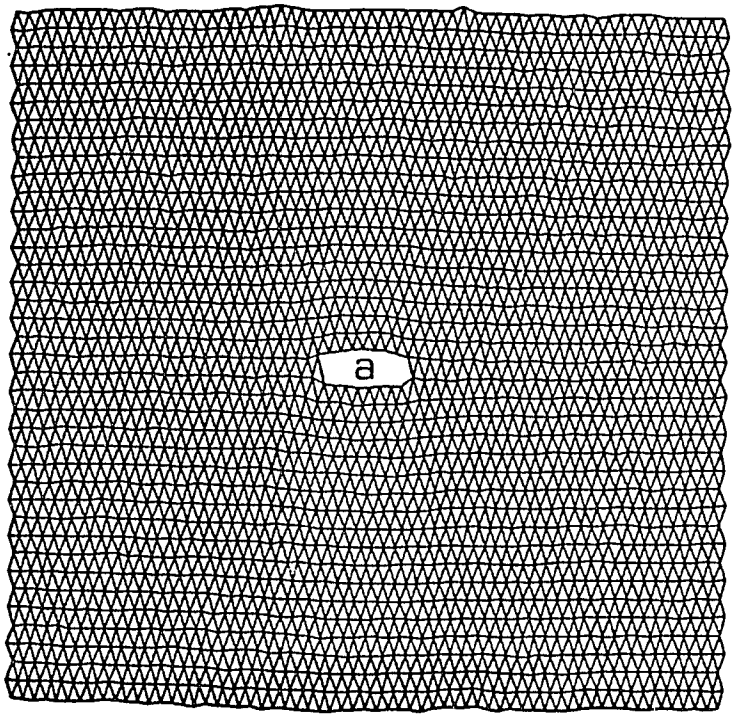


step = 11000

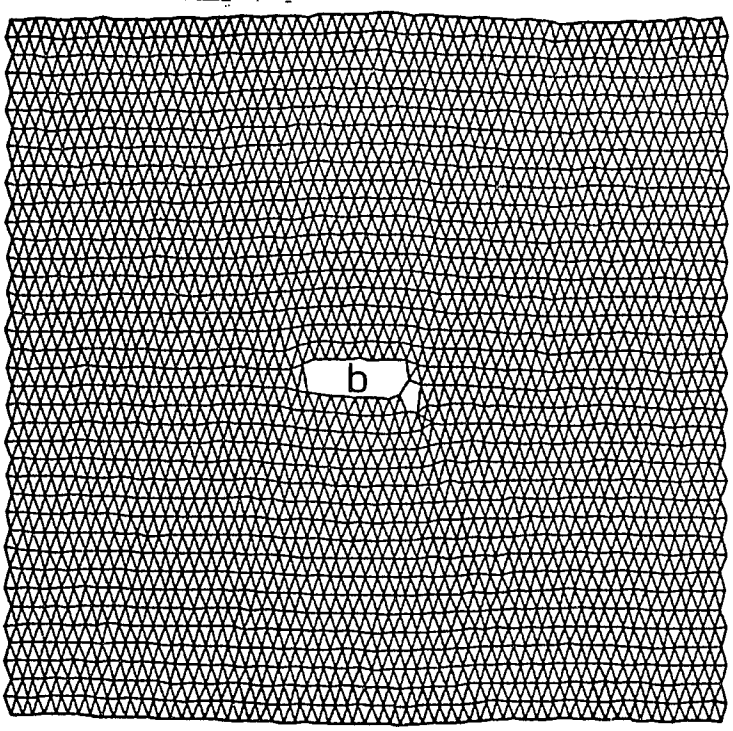
[Fig. III.6A2*] The overloaded (σ_a=2.2) pre-cleaved (c_o=3.75d) COR.LJCOVa.2 solid is at K_BT=0.062 ε_o. Simulations results are tabulated in Table III.6A2*.



[Fig. III.6A3] Critically loaded (σ_c=2.20) pre-cleaved (c_o=3.75d) COR.LJCOVa.2 solid at K_BT=0.0675 ε_o. Simulations results are tabulated in Table III.6A3.

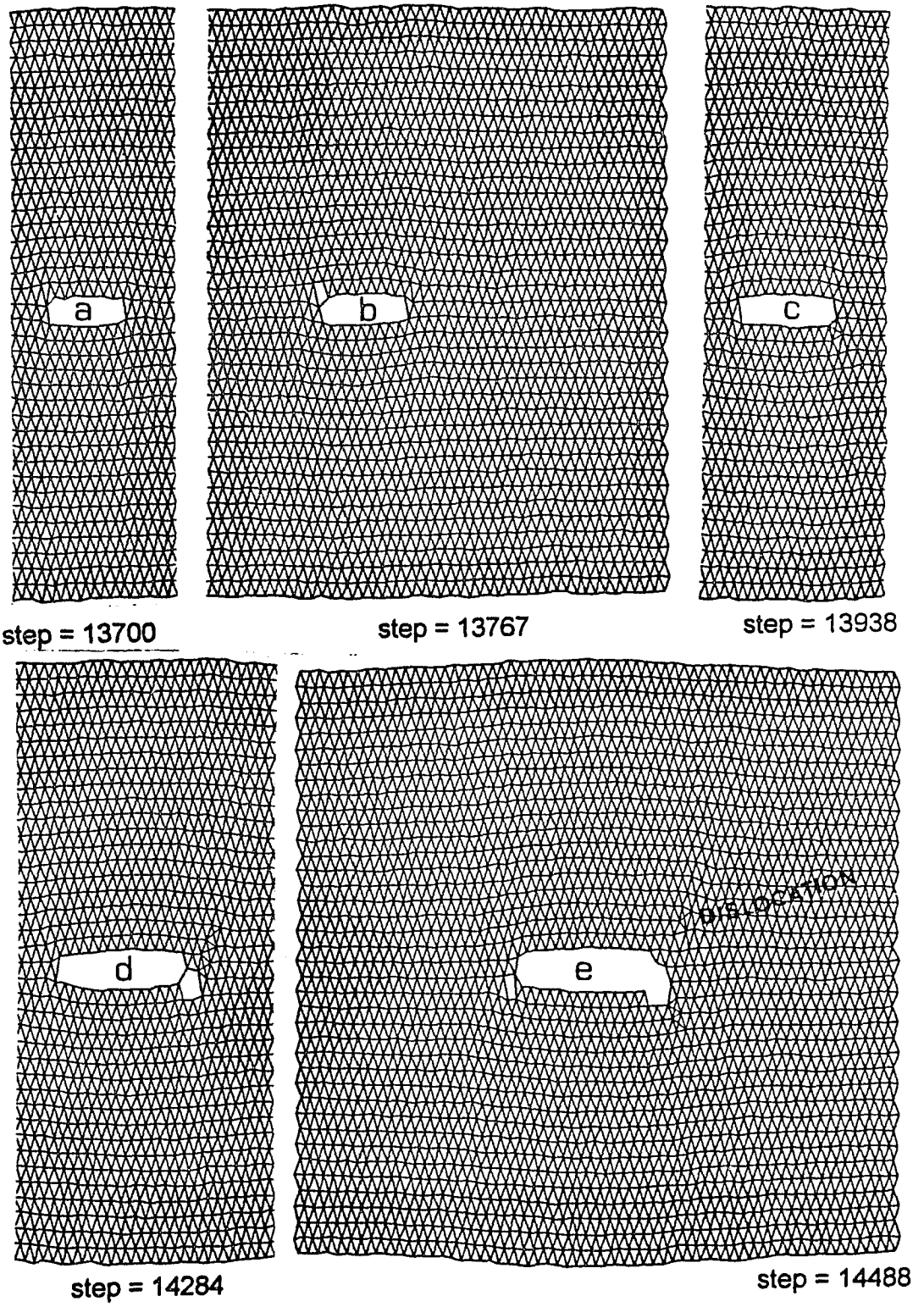


step = 12200

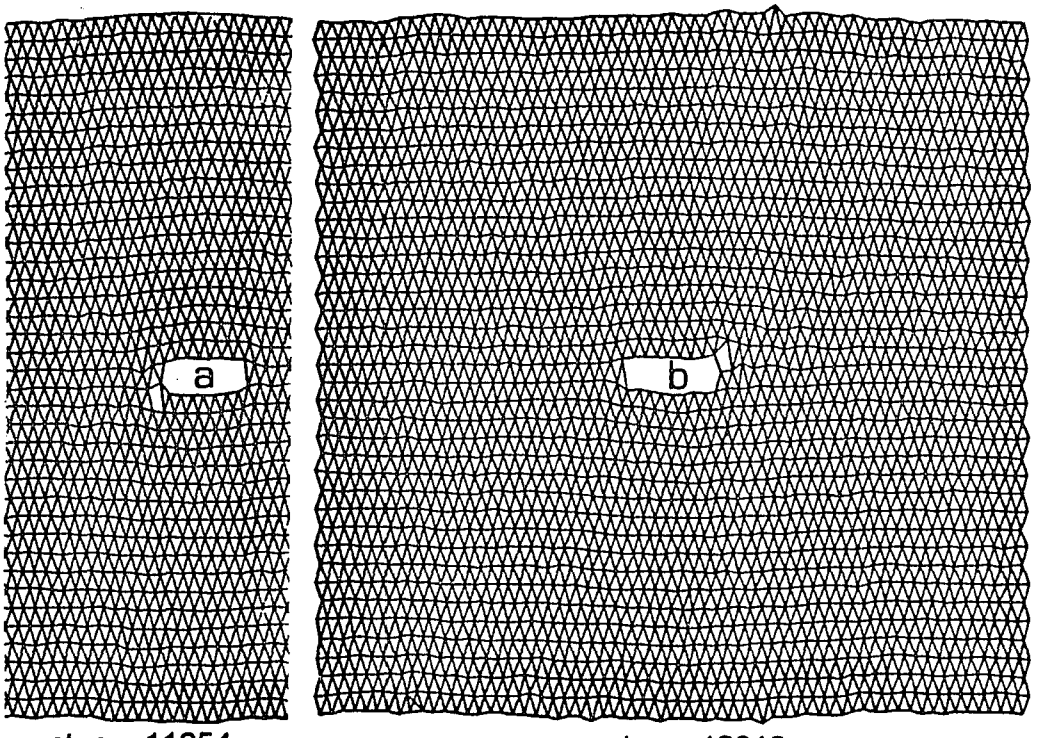


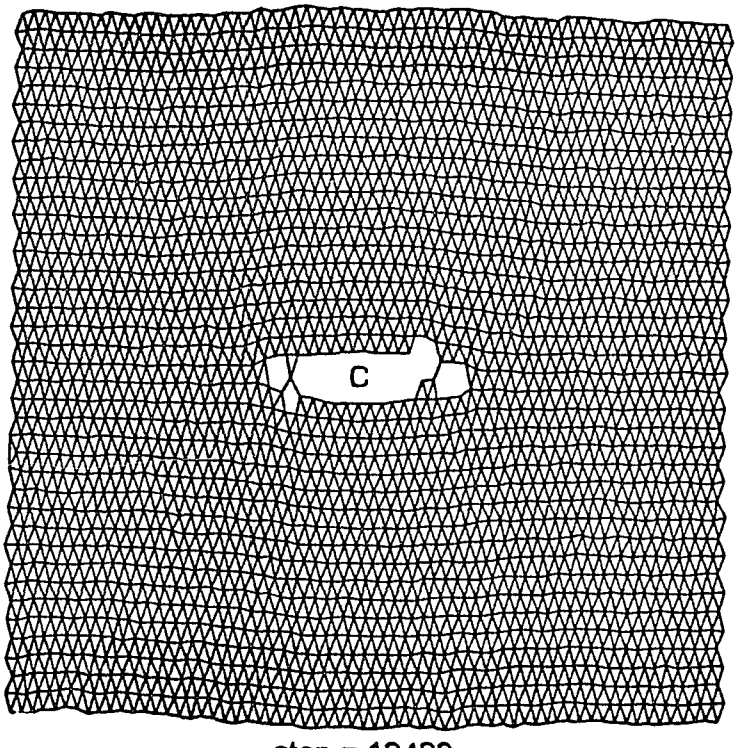
step = 12487

[Fig. III.6A4] Critically loaded (σ_c=2.00) pre-cleaved (c_o=3.75d) COR.LJCOVa.2 solid is at K_BT=0.0790 ε_o. Simulations results are tabulated in Table III.6A4.

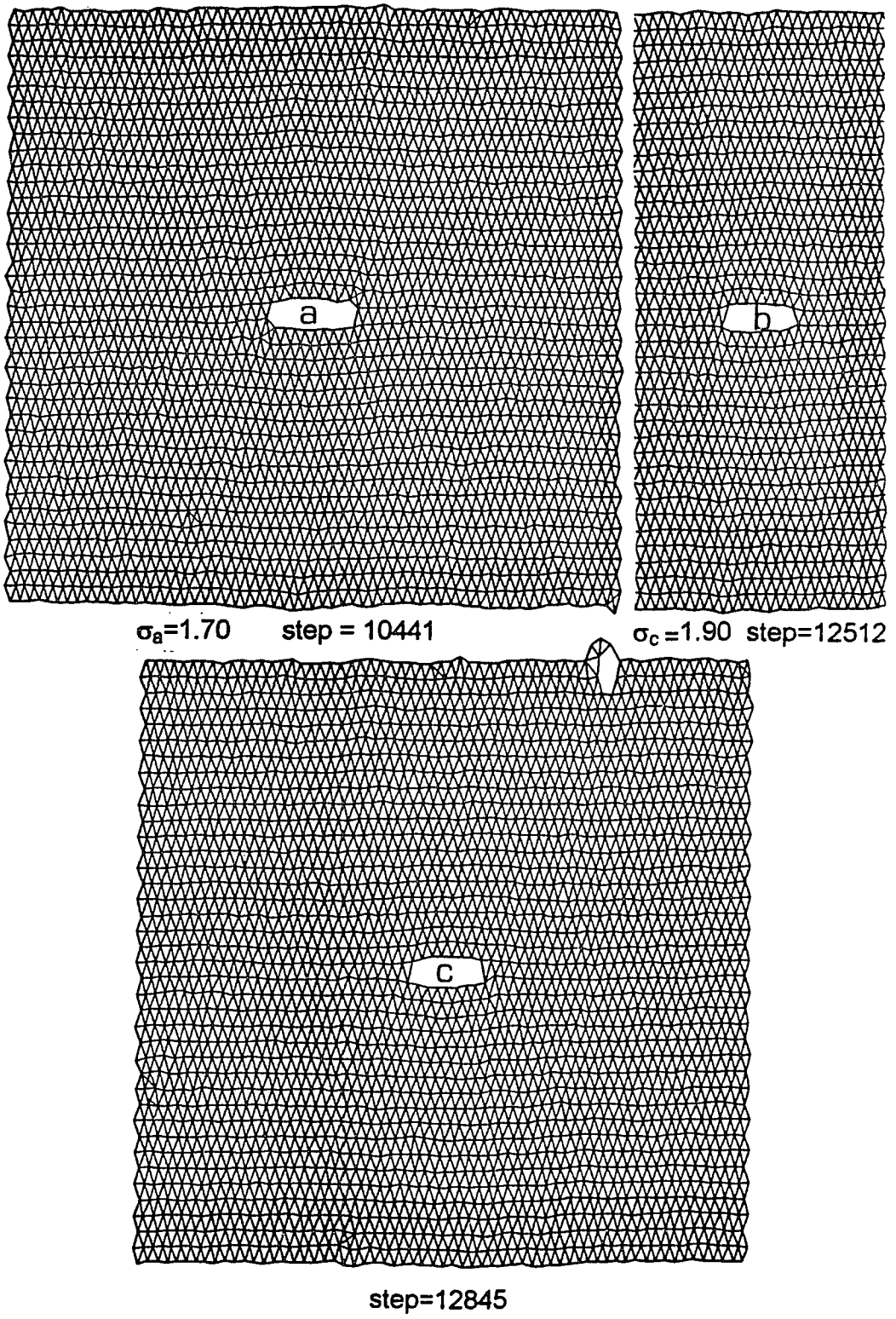


[Fig. III.6A5] Critically loaded (σ_c=2.00) pre-cleaved (c_o=3.75d) COR.LJCOVa.2 solid at K_BT=0.0857 ε_o. Simulations results are tabulated in Table III.6A5.

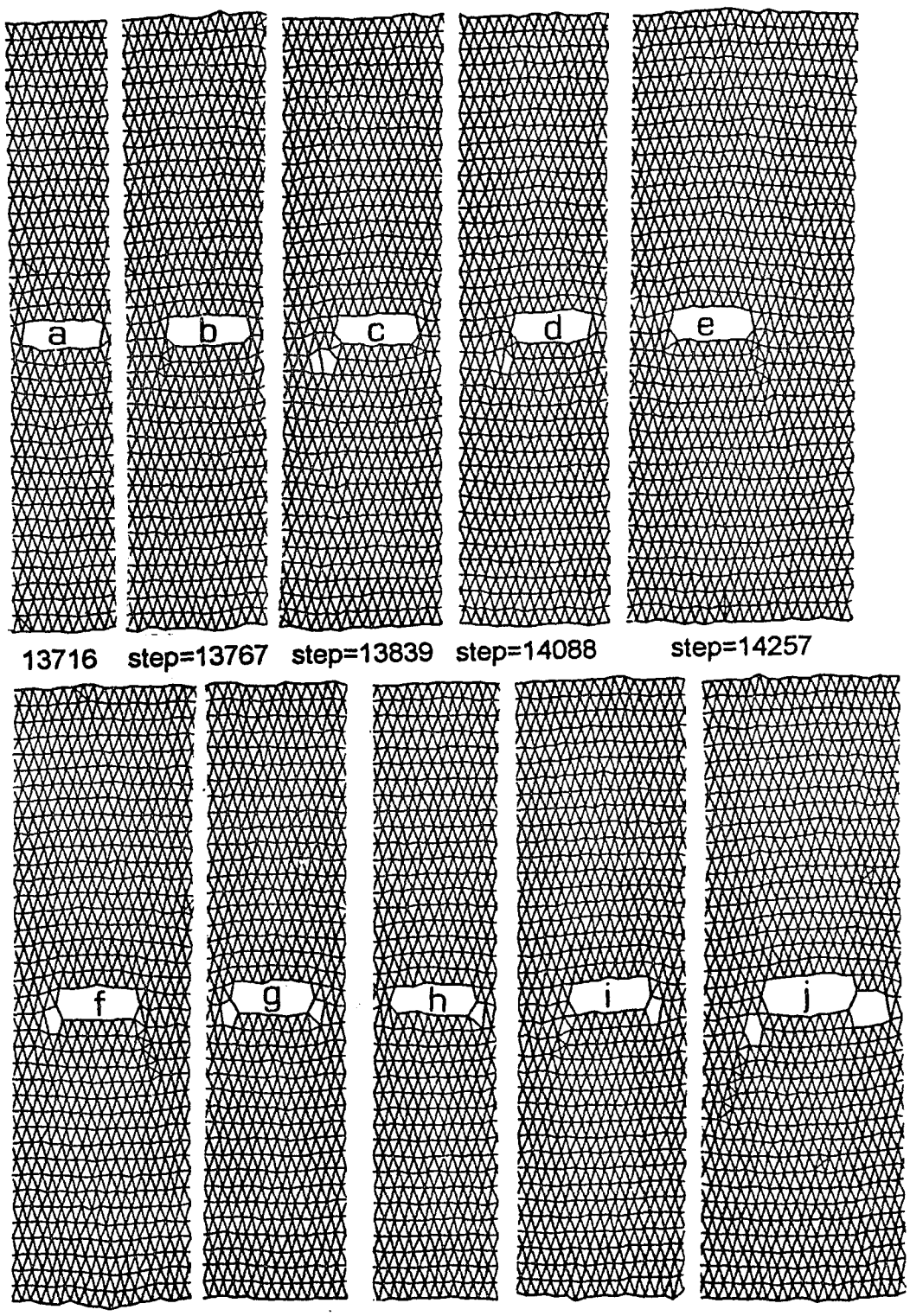




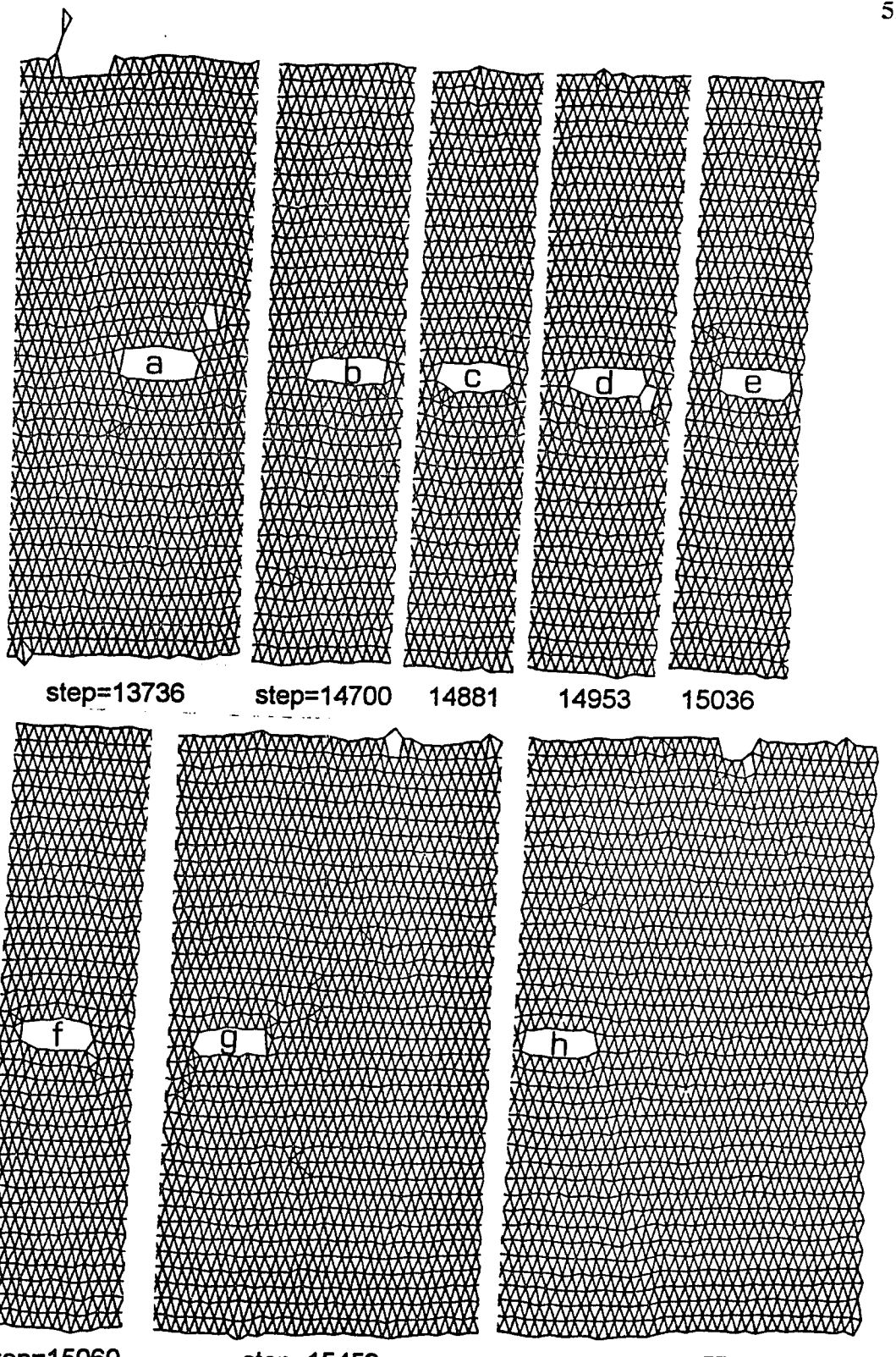
[Fig. III.6A6] Critically loaded (σ_c=1.95) pre-cleaved (c_o=3.75d) COR.LJCOVa.2 solid at K_BT=0.104 ε_o. Simulations results are tabulated in Table III.6A6.



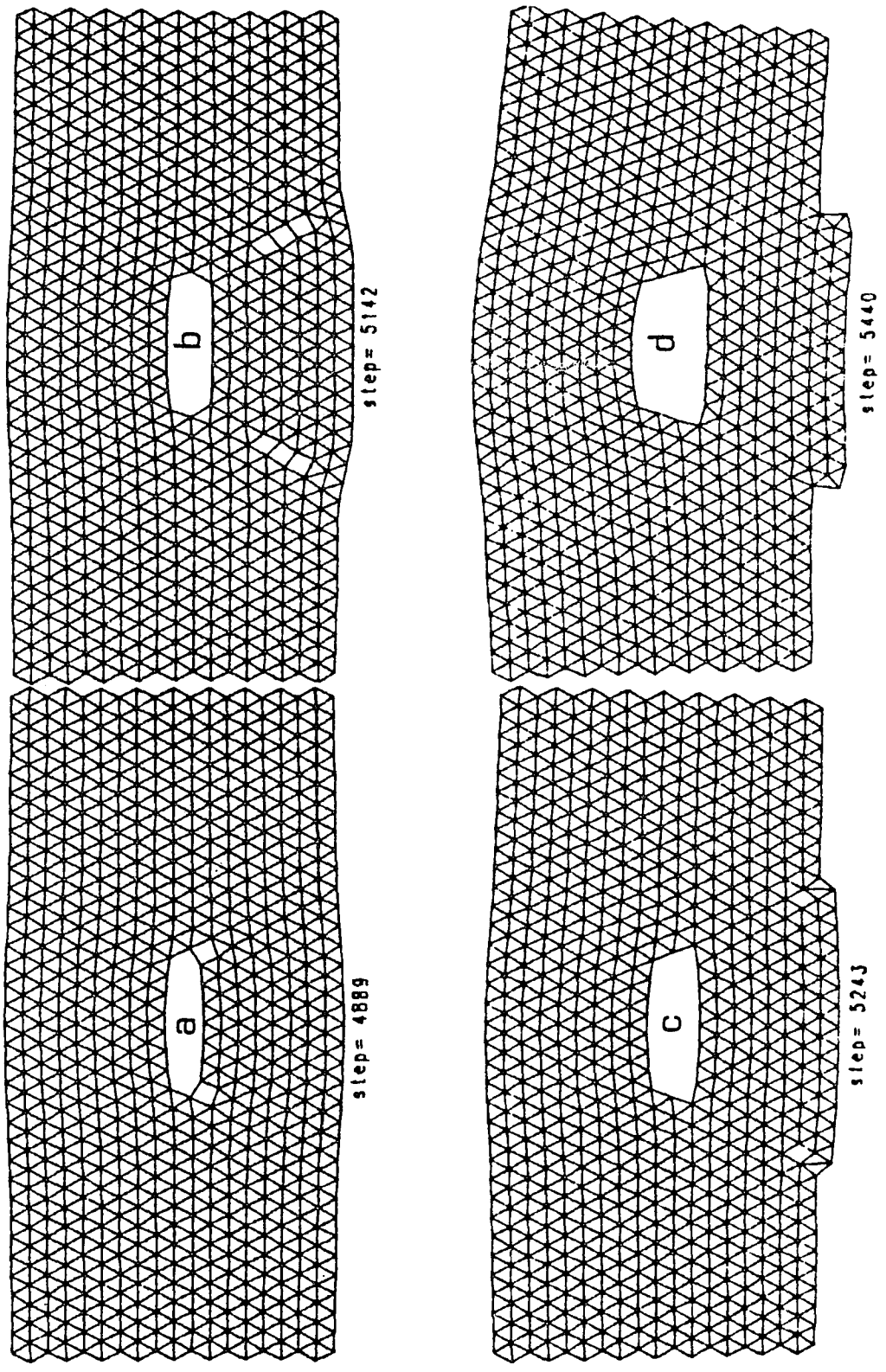
[Fig. III.6A7] The "critically" loaded (σ=1.90) pre-cleaved (c_o=3.75d) COR.LJCOVa.2 solid is at K_BT=0.120 ε_o.



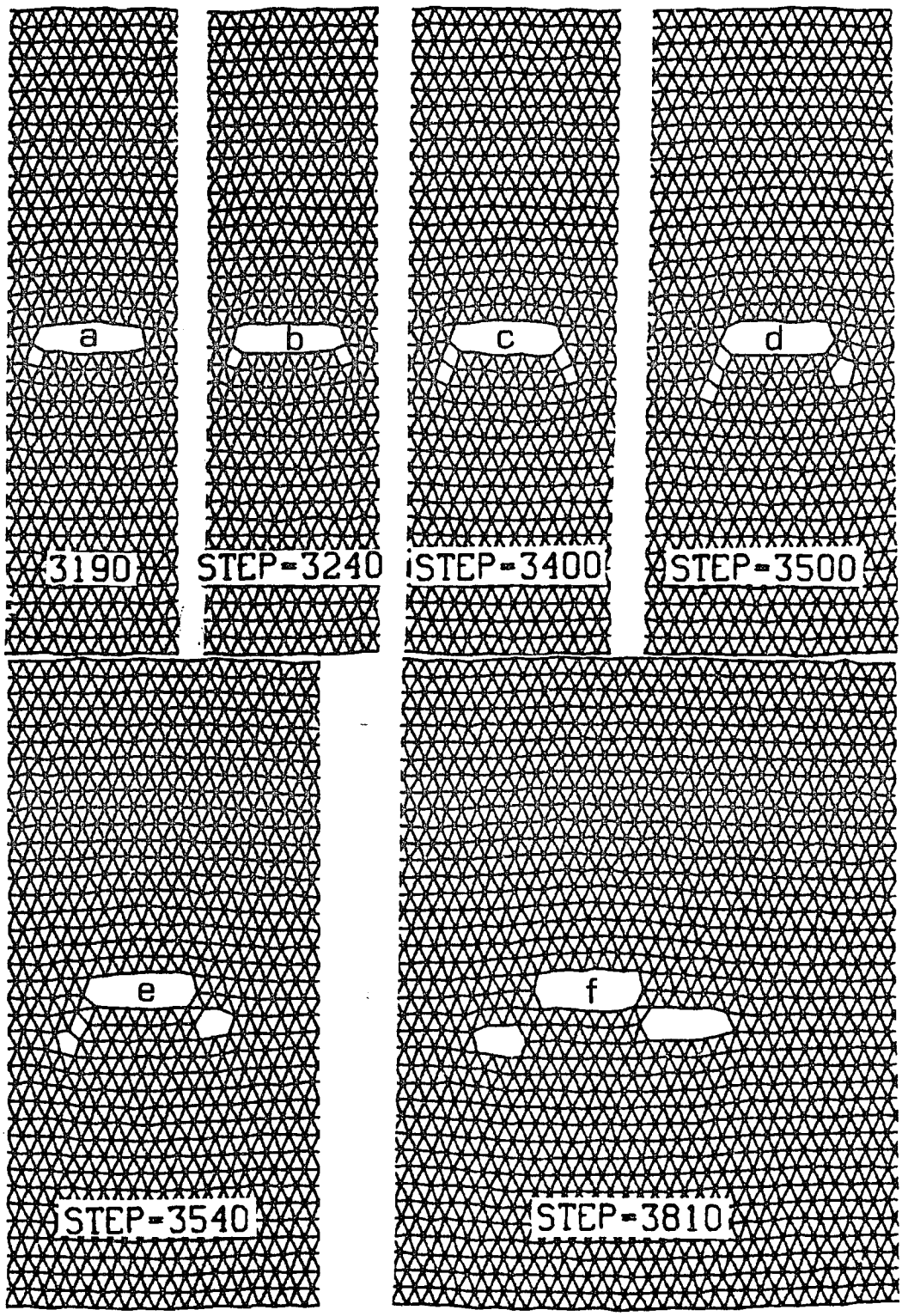
[Fig. III.6A8] "Critically" loaded (σ_c=1.80) pre-cleaved (c_o=3.75d) COR.LJCOVa.2 solid at K_BT=0.136 ε_o. See Table III.6A8.



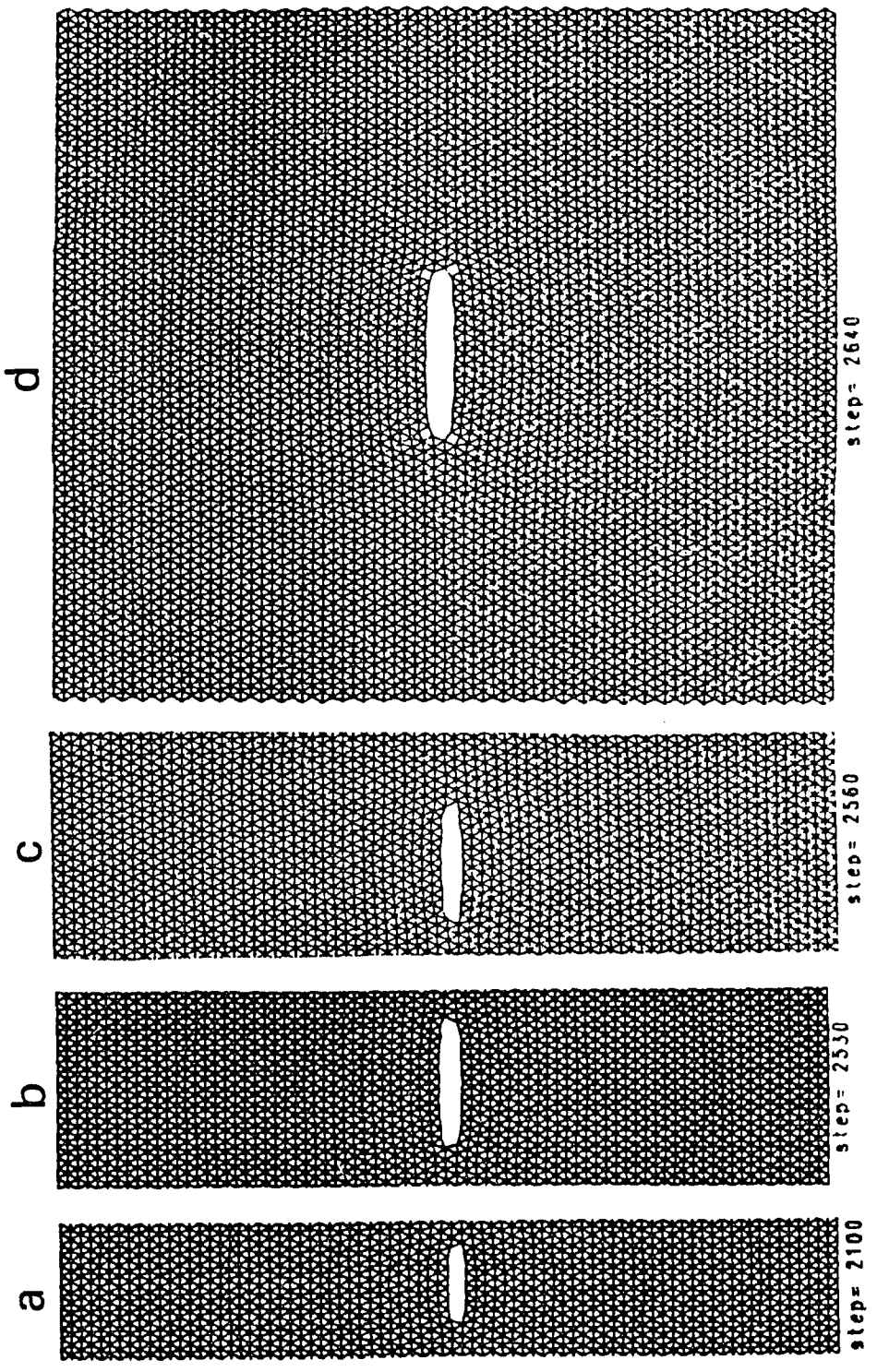
[Fig. III.6A9] The "critically" loaded (σ=1.60) pre-cleaved (c_o=3.75d) COR.LJCOVa.2 solid is at K_BT=0.170 ε_o.



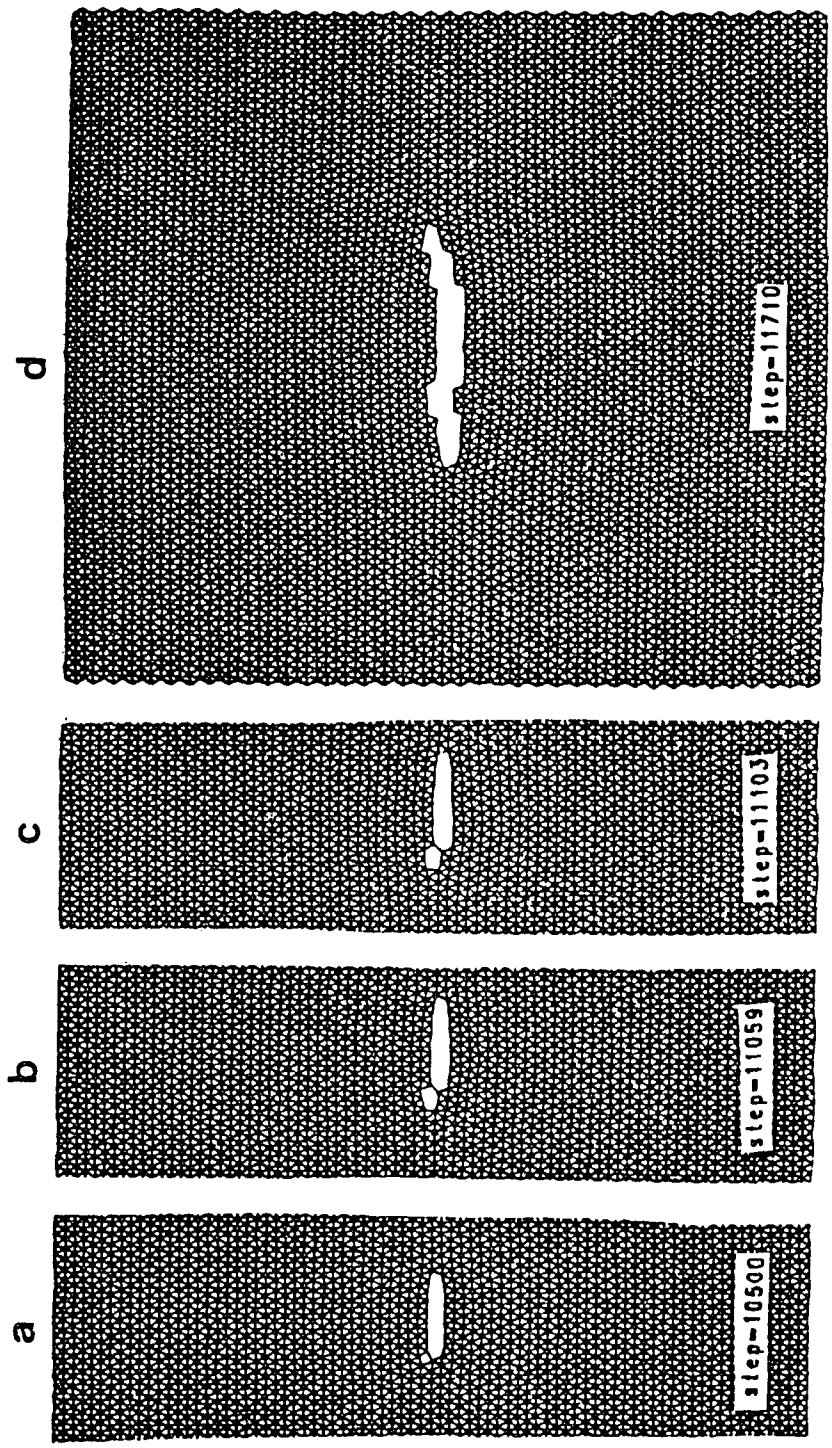
[Fig. III.7A1] Critically loaded (σ_c=2.40) pre-cleaved 2D Johnson solid at 0 K.



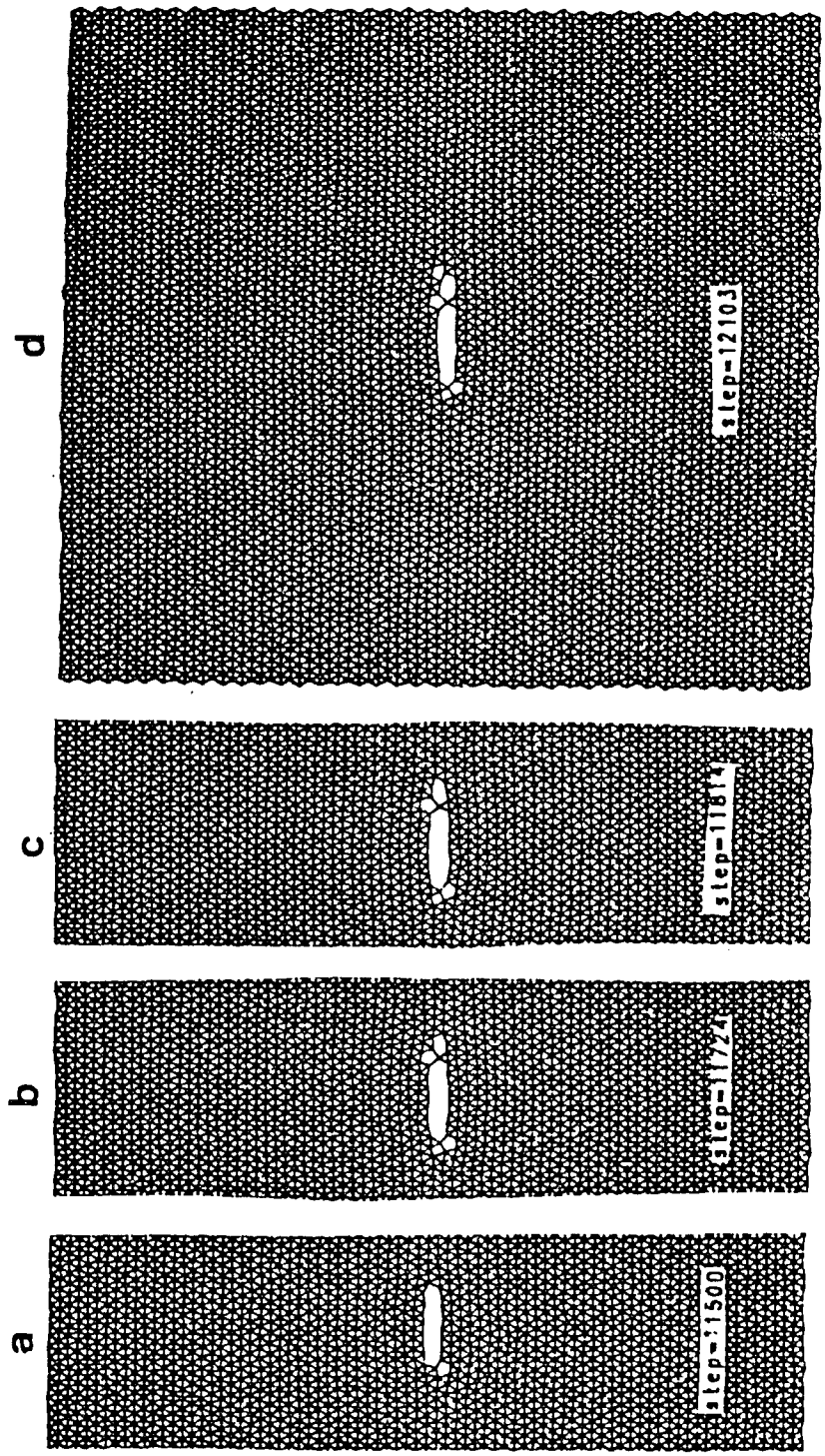
[Fig. III.7B1] The critically loaded (σ_c=2.50) pre-cleaved (c_o=3.75d) 2D-triangular Johnson solid is at 295 Kelvin . Sample size is 39x64.



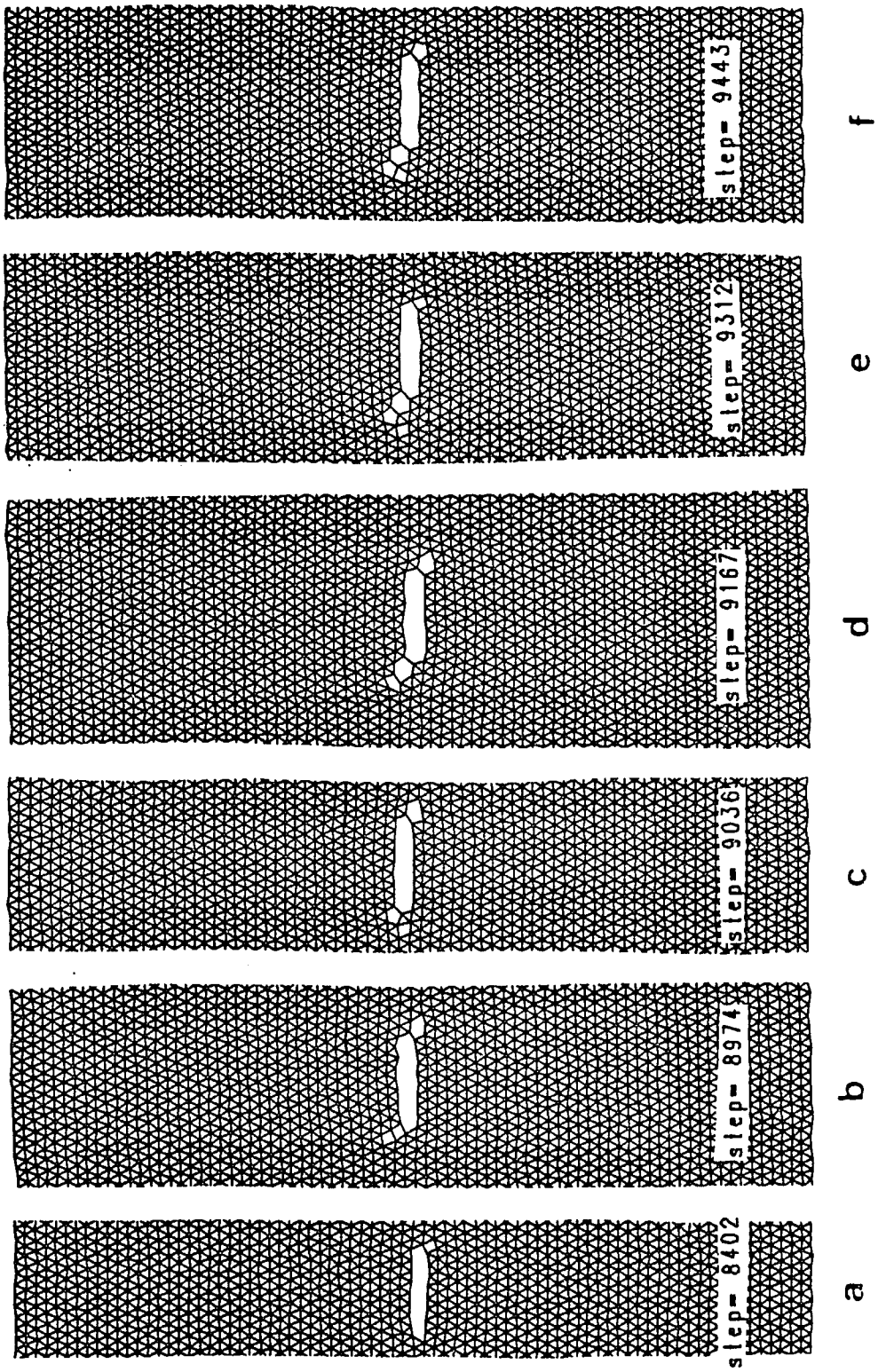
[Fig. III.7C1] The critically loaded (σ_c=3.37) pre-cleaved (c_o=3.75d) 2D-triangular Johnson solid is at 0 Kelvin . Sample size is 79x68.



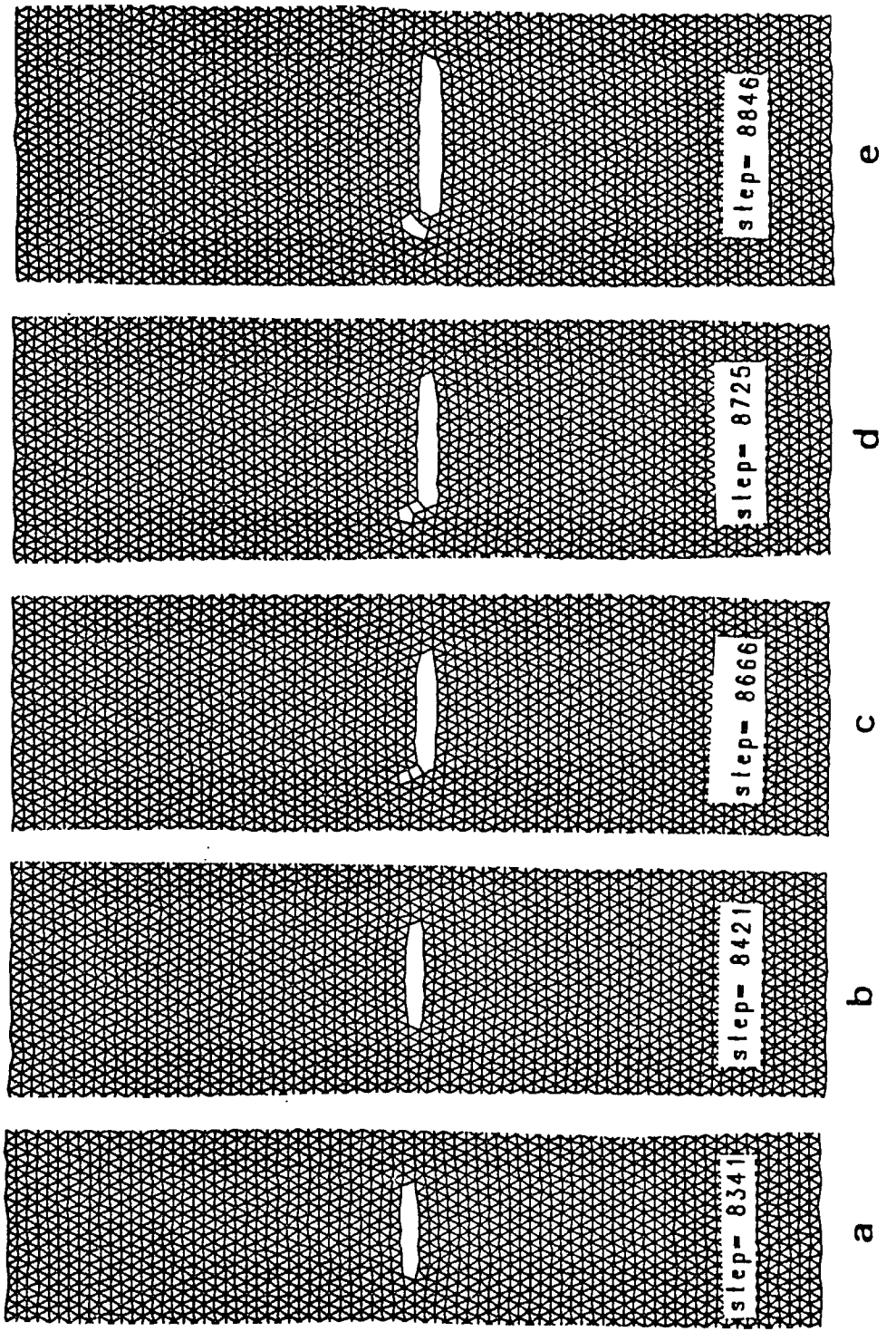
[Fig. III.7C2] The critically loaded (σ_c=2.80) pre-cleaved (c_o=3.75d) 2D-triangular Johnson solid is at 110 Kelvin . Sample size is 79x68.



[Fig. III.7C3] The critically loaded (σ_c=2.60) pre-cleaved (c_o=3.75d) 2D-triangular Johnson solid is at 296 Kelvin . Sample size is 79x68.



[Fig. III.7C4] The critically loaded (σ_c=2.30) pre-cleaved (c_o=3.75d) 2D-triangular Johnson solid is at 404 Kelvin . Sample size is 79x68.



[Fig. III.7C4*] The overloaded, σ_a=2.40, pre-cleaved, c_o=3.75d, 2D-triangular Johnson solid is at 404 Kelvin . Sample size is 79x68. The critical load is 2.30.

Appendix A

The Question Of The Thermal Equilibrium

To introduce the temperature to a given solid in the present molecular dynamic simulations the constituent interacting atoms of the crystal are given some initial perturbation from their static equilibrium positions. Then the dynamic system of the interacting atoms is allowed to relax to its thermal equilibrium.

Real systems at thermal equilibrium generally exhibit a remarkable constancy and almost no fluctuations could be detected by the ordinary measurements. However in a dynamic system of a limited number of atoms, the question of the thermal equilibrium is a somewhat subtle one. As the increase in the potential energy of the dynamic system caused by the disturbance in the atomic positions of the constituent atoms is, gradually, converted into the kinetic energy of the system, the solid is heated up, and the temperature of the crystal calculated from the kinetic energy of the ensemble rises, and the initially large fluctuations in temperature decrease, progressively, in magnitude until they reach to a value characteristic of the thermal equilibrium. The magnitude of the fluctuation in the temperature (or the kinetic energy) of the system at the thermal equilibrium depends upon the total number of atoms, N, in the system.

For a canonical ensemble, the average energy per system is U, and the deviation from this average by some system of the ensemble with energy, K_i, is

(K_i-U). The mean square deviation, $\langle(\delta K)^2\rangle=\langle\Sigma_i f_i(K_i-U)^2\rangle$, is a measure of the spread of the statistical distribution and is, therefore, a suitable measure of the fluctuation in the energy of the system and, hence, in the temperature of it. Here, f_i is the canonical distribution function

$$f_i = (1 / Z) e^{- K_i / K_B T} \qquad \text{A.1}$$

where, Z is the partition function

$$Z = \Sigma_i \; e^{- K_i / K_B T} \qquad \text{A.2}$$

where, K_B is the Boltzmann's constant. We may express the mean square deviation in the energy of the system as

$$\langle(\delta K)^2\rangle=\langle\Sigma_i f_i(K_i-U)^2\rangle= \langle\Sigma_i f_i(K_i^2 + U^2 - 2K_iU)\rangle = \langle K^2\rangle - U^2 \qquad \text{A.3}$$

For the canonical distribution, the average energy is given by

$$U = \langle K\rangle = \{\Sigma_i \; K_i e^{- K_i / K_B T}\}/\{\Sigma_i \; e^{- K_i / K_B T}\} \qquad \text{A.4}$$

and $\langle K^2\rangle$ is defined as

$$\langle K^2\rangle = \{\Sigma_i K_i^2 e^{- K_i / K_B T}\}/\{\Sigma_i \; e^{- K_i / K_B T}\} \qquad \text{A.5}$$

We may differentiate the average energy, U, to obtain the specific heat at constant volume, C_v

$$C_V=(\partial U/\partial T)_V=(\langle K^2\rangle - U^2) / (K_B T^2) \quad \text{A.6}$$

The relative mean square deviation is therefore given by

$$(\langle K^2\rangle - U^2) / U^2 = C_V K_B T^2 / \langle K\rangle^2 \quad \text{A.7}$$

In general, average energy of system, U, is proportional to the number of particles, N, in the system. Therefore, heat capacity, C_V, is also proportional to N. Taking the harmonic limit, in a 2D crystal

$$U = \langle K\rangle = NK_B T \quad \text{A.8}$$

and

$$C_V=NK_B \quad \text{A.9}$$

We may conclude that

$$\langle(\delta K)^2\rangle / \langle K\rangle^2 = (NK_B)(K_B T^2) / (NK_B T)^2 = 1/N \quad \text{A.10}$$

For example, N is 2500 for the crystal of size 64x39 used in the major part of this simulation, and the mean square fluctuation in the temperature, MSTFL, at the thermal equilibrium is expected to be about 4×10^{-4}. Indeed, as is apparent from the reported simulations results in the earlier sections, MSTFL at the thermal equilibrium is of the expected order of 10^{-4} for the crystal of about 2500 atoms.

BIBLIOGRAPHY

[1] A. Paskin, D. K. Som, and G. J. Dienes "The Dynamic Properties of Moving Cracks": Acta Metall. Vol. **31**, No. 11, pp. 1841-1848, (1983).

[2] A. Paskin, A. Gohar, and G. J. Dienes "Computer Simulation of Crack Propagation": Phy. Rev. Letters, Vol. **44**, No. 14, pp. 940-943, (1980).

[3] N.F. Mott: "Fracture of Metals: Theoretical Considerations", Engineering **165**, pp. 16-19, (1948).

[4] L. B. Freund: "Crack Propagation in an Elastic Solid Subjected to General Loading-I. Constant Rate of Extension", J. Mech. Phy. Solids, **20**, pp. 129-140, (1972).

[5] L. B. Freund: "Crack Propagation in an Elastic Solid Subjected to General Loading-II. Uniform Rate of Extension", J. Mech. Phy. Solids, **20**, pp. 141-152, (1972).

[6] L. B. Freund: "Crack Propagation in an Elastic Solid Subjected to General Loading-III. Stress Wave Loading", J. Mech. Phy. Solids, **21**, pp. 47-61, (1973).

[7] J. D. Eshelby: "The Starting of a Crack" in "Physics of Strength and Plasticity" (edited by A. S. Argon), pp. 263-275, MIT Press, Cambridge, Mass. (1968).

[8] P. B. Hirsch, S. G. Roberts, and J. Samuels: "The Brittle-Ductile Transition in Silicon-II. Interpretation"; Proc. Roy. Soc. London A **421**, pp. 25-53, (1989).

[9] P. B. Hirsch, S. G. Roberts, and J. Samuels: "The Dynamics of Dislocation Generation at Crack Tips and the Ductile-Brittle Transition"; Scripta Metall, Vol. **21**, pp. 1523-1528, (1987).

[10] P. B. Hirsch, S. G. Roberts: "The Dynamics of Edge Dislocation Generation Along a Plane Orthogonal to a Mode I Crack"; Scripta Metall., Vol. **23**, pp. 925-930, (1980).

[11] P. B. Hirsch, S. G. Roberts: "The Brittle-Ductile Transition in Silicon"; Phil. Mag. A. Vol. **64**, No. 1, pp. 55-80, (1991).

[12] W. E. Anderson, and P. C. Paris; Metals. Eng. Quart. **1**, p. 33, (1961).

[13] K. J. Hsia, and A. S. Argon: " Experimental Study of the Mechanisms of Brittle-To-Ductile Transition of Cleavage Fracture in Silicon Single Crystals"; Material Science and Engineering, **A176**, pp. 111-119, (1994) [Fourth International Conference on the Fundamentals of Fracture, Urabandai, Japan 93] .

[14[C.F. Tipper: "The Fracture of Metals", Metallurgica **39**, pp. 133-137, (1949).

[15] G. J. Dienes, and A. Paskin: "Computer Modelling of Cracks" in Atomistic of Fracture (Ed. by R.M. Latanision , and , J.R. Pickens) pp. 671-705, Plenum Press, New York, (1983).

[16] S. P. Timoshenko: " History of the Strength of Materials", p. 51, McGraw Hill, New York (1953).

[17] A. Nadai: "Theory of Flow and Fracture of Solids", pp. 207-228, McGraw Hill, New York, (1950).

[18] A. A. Griffith: "The Phenomenon of Rupture and Flow in Solids.", Phil. Trans. Roy. Soc. London, Ser. **A221**, pp. 163-198, (1920).

[19] A. A. Griffith: "The Theory of Rupture", in Proc. First Inter Nat. Congr. Appl. Mech., Delft, The Netherlands 1924, (Ed. C.B. Biezeno and J.M. Burgers), J. Waltman Jr., Delft, pp. 55-63 (1925).

[20] W. Weibull: "A Statistical Theory of the Strength of Metals.", Proc. Roy. Swed. Inst. Eng. Res., No. **151**, (1939).

[21] F. A. McClinton, J. Appl. Mech., **25**, p. 582, (1958).

[22] J. M. Krafft, and G. R. Irwin, Symposium on Fracture Toughness Testing and its Applications, STP **381**, p. 114, Philadelphia, (1965).

[23] G. I. Barenblatt, Adv. Appl. Mech. **7**, p. 55, (1962).

[24] F. Erdogan, G. C. Sih, Trans. ASME Ser. D.J. Basic Eng. **85**, p. 519, (1963).

[25] R. S. Rivlin, and A. G. Thomas: J. Polymer Sci. V. **10** , p. 291, (1952).

[26] M. L. Williams: in "Fracture of Solids" (D. Drucker, and J .J. Gilman, Eds.), p. 157, Wiley (Inter-Science), New York, (1963).

[27] M. L. Williams: Intern. J. Fracture Mech. **1**, p. 292, (1965).

[28] W. G. Knauss, in "Proceeding of the First Int. Conf. on Fracture", Sendai, (T. Yokobori, T. Kawasaki, J. L. Swedlow, Eds.) Vol. **2**, p. 1139, (1966), Jap. Soc. for Strength and Fracture of Materials, Tokyo.

[29] T. L. Smith, J. Polymer Sci., **A1**, p. 3597, (1963).

[30] E. Orowan, J. Welding (N.Y.), Res. Supply **34**, 157, (1955).

[31] G. R. Irwin, in "Handbuch der Physik", V. **6**, p. 551, Springer, Berlin, (1958).

[32] D. K. Roberts, and A. A. Wells: "The Velocity of Brittle Fracture", Engineering **24**, p. 820, (1954).

[33] B. R. Lawn, and T. R. Wilshaw: "Fracture of Brittle Solids", Cambridge University Press, Cambridge, (1975).

[34] E. R. Fuller Jr., and R. M. Thomson: in "Fracture Mechanics of Ceramics", (R. C. Broadt, D. P. H. Hasselman, and F. F. Lange, Eds.), Vol. **4**, Plenum, New York, pp. 507-548, (1978).

[35] D. M. Esterling: "Lattice Statistics Approach to Fracture and Plasticity", Comments in Solid State Physics, **9**, p.105, (1979).

[36] J. E. Sinclair, and B. R. Lawn: "An Atomistic Study of Cracks in Diamond Structure Crystals", Proc. Roy. Soc. London, **A329**, p.83, (1972).

[37] P. C. Gehlen: "Crack Extension in a Model of α-iron, Scripta Metall. **7**, p. 1115, (1973).

[38] J. E. Sinclair: "The Influence of the Interatomic Force Law and of Kinks on the Propagation of Brittle Cracks", Phil. Mag. **31**, pp.347-671 (1975).

[39] Tong Yi Zhang, and Peter Haasen: "The Influence of Ionised Hydrogen on the Brittle-to-Ductile Transition in Silicon", Phil. Mag. A, Vol. **60**, No. 1, pp. 15-38, (1989).

[40] W. R. Tyson : "Atomistic Simulation of the Ductile- Brittle Transition"; Fracture 1977, Vol. **2**, ICF4, Canada, June 19-24, (1977).

[41] Gerard Michot, and A George: "In Situ Observation by X-Ray Synchrotron Deformed Region Around Crack Tips in Silicon Under Creep Conditions"; Scripta Metall., **16**, p. 519, (1982).

[42] Richard W. Hertzberg: "Deformation and Fracture Mechanics of Engineering Material", John Wiley and Sons, (1976).

[43] A. Kelly, W. R. Tyson, and A. H. Cottrell: "Ductile and Brittle Crystals", Phil. Mag. **15**, pp. 567-586, (1967).

[44] N. Davidenkov, and F. Wittman: "Mechanical Analysis of Impact Brittleness", Tech. Phys. USSR, **4**, pp. 3-17, (1937).

[45] J. Samuels, and S. G. Roberts: "The Brittle-to- Ductile Transition in Silicon. I. Experiments"; Proc. Roy. Soc. Lond. A. **421**, pp. 1-23, (1989).

[46] J. R. Rice, and R. Thomson: "Ductile Versus Brittle Behavior of Crystals", Phil. Mag. **29**, pp. 73-97, (1974).

[47] Peter Haasen: "Electronic Processes at Dislocation Cores and Crack Tips"; In Atomistics of Fracture, NATO Conf. Sr. VI [ed. by R.M. Latanision and J.R. Pickens], pp. 707-730, New York: Plenum Press, (1983).

[48] A. George; J. Phys, Paris **40**, C6, pp. 133-137, (1979).

[49] A. S. Argon: "Brittle To Ductile Transition in Cleavage Fracture"; Acta. metall. Vol. **35**, No. 1, pp. 185-196, (1987).

[50] S. M. Ohr, Mater. Sci. Engng **72**, pp. 1-35, (1985).

[51] Robb Thomson: "Physics of Fracture", Solid State Physics, Vol. **39**, pp. 1-129, (H. Ehrenreich and D. Turnbull (Eds.)) Academic Press, Orlando, Fl. (1986).

[52] I. H. Lin; J. Mater. Sci. Lett **2**, 295, (1983).

[53] H. Alexander, and P. Haasen: "Dislocation and Plastic Flow in the Diamond Structure", Sol. St. Physics, **22**, pp. 27-158, (1968).

[54] C. St. John: "The Brittle-to-Ductile Transition in Pre-Cleaved Silicon"; Phil. Mag., **32**, pp. 1193-1212, (1975).

[55] A. George, and G. Champier; Physica Status Solidi A. **53**, pp. 529-540, (1979).

[56] M. Imai, and K. Sumino; Phil. Mag. **A47**, p. 599-621, (1983).

[57] V. C. Kannan, Ph.D. Thesis, University of Berkeley, (1969).

[58] J. E. Dorn, J. Mitchell and F. Hauser; Expl. Mech. **5**, 9, (1965).

[59] J. P. Hirth, and J. Lothe: "Theory of Dislocations" New York, McGraw-Hill, p. 488, (1968).

[60] M. Brede, and P. Haasen: "The Brittle-to-Ductile Transition in Doped Silicon as a Model Substance"; Acta Metall, Vol. **36**, No. 8, pp. 2003-2018, (1988).

[61] G. Michot, Thèse d'Etat, L'Institut National Polytechnique de Lorrain, Nancy, (1982).

[62] R. Behrensmeier, M. Brede, and P. Haasen; Scripta Metall, **21**, p. 1481, (1987).

[63] G. Michot; Crystal Properties and Preparation; **17 / 18**, 55, (1988).

[64] I. H. Lin, and R. Thomson: "Cleavage, Dislocation Emission, and Shielding for Cracks Under General Loading"; Overview No. 47, Acta Metall., Vol. **34**, No. 2, pp. 187-206, (1986).

[65] Y. H. Chiao, and D. R. Clarke; Acta Metal, **37**, p. 203 (1989).

[66] G. Michot, A. George: "On the Brittle-to-Ductile Transition of Silicon", private communications.

[67] M. Khantha, D. P. Pope, and V. Vitek: " Dislocation Screening and the Brittle-to-Ductile Transition: A Kosterlitz-Thouless Type Instability"; Phys. Rev. Lett., Vol. **73**, No. 5, (1994).

[68] M. Khantha, D. P. Pope and V. Vitek: "The Brittle-To-Ductile Transition I: A Cooperative Dislocation Generation Instability"; Scripta Metallurgica et Materialia, Vol. **31**, No. 10, pp. 1349-1354, (1994).

[69] M. Khantha: "The Brittle-To-Ductile Transition - II: Dislocation Dynamics and the Strain-rate Dependence of the Transition Temperature"; Scripta Metallurgica et Materialia, Vol. **31**, No. 10, pp. 1355-1360, (1994).

[70] G. Schoeck, Philos. Mag. A **63,** 111 (1991).

[71] J. R. Rice: "Dislocation Nucleation From A Crack Tip: An Analysis Based on the Peierls Concept"; J. Mech. Phys. Solids, **40**, p. 239, (1992).

[72] W. W. Gerberich, H. Huang, W. Zielinski and P. G. Marsh, Metall. Trans. A. **24A,** 535 (1993).

[73] James R. Rice and Glenn E. Beltz: "The Activation Energy for Dislocation Nucleation at a Crack"; J. Mech. Phys. Solids, Vol. **42**, No. 2, pp. 333-360, (1994).

[74] J. F. Knott: "Fundamentals of Fracture Mechanics"; Butterworths, London, (1979).

[75] H. Vehoff, in High-Temperature Ordered Intermetallic Alloys V, edited by I. Baker, R. Darolia, J. D. Whittenberger and M. H. Yoo, MRS Symposia Proceedings No. **288**, p.71, Materials Research Society, Pittsburgh (1993).

[76] J. M. Kosterlitz and D. J. Thouless, J. Phys. Vol. **6,** p. 1181, (1973).

[77] A. P. Young, Phys. Rev. B, Vol. **19**, p. 1855, (1979).

[78] S. Fujita, K. Madea and S. Hyodo: "Dislocation- mobility-controlled cracking in GaAs caused by constant-rate indentation"; Phil. Mag. A, Vol. **65**, No. 1, pp.131-147, (1992).

[79] V. R. Nitzsche and K. J. Hsia: "Modelling of Dislocation Mobility Controlled Brittle-To-Ductile Transition"; Material Science and Engineering, A**176**, pp. 155-164, (1994) [Fourth International Conference on the Fundamentals of Fracture, Urabandai, Japan 93].

[80] D. R. Nelson, and B. I. Halperin, Phys. Rev. B. Vol. **19**, p. 2457, (1979).

[81] R. W. Lardner, Mathematical Theory of Dislocations and Fracture, UT Press, Toronto, (1974).

[82] G. L. Pearson, W. T. Read Jr. and W. L. Feldmann, Acta Metall, **5**, 181 (1957).

[83] M. Brede: " The Brittle-to-Ductile Transition in Silicon"; Acta metall. mater. Vol. **41**, No. 1, pp. 211-228, 1993.

[84] M. Brede, K. J. Hsia and A. S. Argon: "Brittle crack propagation in silicon single crystala"; J. Appl. Phys., **70**, pp.758-771 (1991).

[85] D. K. Dewald, T. C. Lee, I. M. Robertson and H. K. Birnbaum, Scripta Metall., **23**, p. 1307, (1989).

[86] S. J. Burns and W. W. Webb, J. Appl. Phys., **41**, p. 2086, (1970).

[87] L. B. Freund and J. W. Hutchinson, J. Mech. Phys. Solids, **33**, p. 169, (1985).

[88] K. Maeda, H. Nishioka, N. Narita and S. Fujita: "Brittle-To-Ductile Transition Studied by Constant-Rate Indentation";Material Science and Eng., **A176**, pp. 121-126, [Fourth Int. Conf. on the Fund. of Fracture, Urabada, Japan 93] (1994).

[89] B. R. Lawn, A. G. Evans and D. B. Marshall, J. Am. Ceram. Soc., **59**, p.371, (1976).

[90] Hibbit, Karlson, and Sorenson, Inc., **ABAQUS** Version **4.9**, (1993).

[91] Gerard Michot, and A George, in S. G. Roberts (ed.), Proc. 6th Int. Conf. on Dislocations in Semiconductors, IOP Conference Series **104**, IOP Publications, Bristol, p. 385, (1989).

[92] Z. Suo, C. F. Shih and A. G.Varias, Acta Metall. Mater., **41**, p. 1551, (1993).

[93] D. Hull, P. Beardmore and A. P. Valintine: "Crack Propagation in Single Crystals of Tungston", Philos. Mag., **12**, pp. 1021-1041, (1965).

[94] Amand George and Gérard Michot: "Dislocation Loops at Crack Tips: Nucleation and Growth; an Experimental Study in Silicon", Materials Science Engineering, A **164,** pp. 118-134, (1993).

[95] S. G. Roberts, M. and P. B. Hirsch: "Dislocation Dynamics and Brittle-to-Ductile Transition"; Mater. Sci. Eng. A, **164**, pp. 135-140, (1993).

[96] S. G. Roberts, A. S. Booth and P. B. Hirsch: "Dislocation Activity and Brittle-Ductile Transitions in Single Crystals"; Material Science and Eng., **A176**, pp. 91-98, [Fourth Int. Conf. on the Fund. of Fracture, Urabada, Japan 93] (1994).

[97] H. Azzouzzi, G. Michot and A. George, in D. G. Brandon, R. Chaim and A. Rosen (Eds.), Proc. 9th Conf. on the Strength of Metals and Alloys, Haifa, July 1991, Freund, London, p. 317, (1991)

[98] P. D. Warren: "The Brittle-Ductile Transition in Silicon: The Influence of Pre-Existing Dislocation Arrangements"; Scripta Metall. Vol. **23**, pp. 637 - 642, (1989).

[99] M. J. Lii, X. F. Chen, Y. Katz and W. W. Gerberich, Acta Metall. Mater., **38**, p. 2435, (1990).

[100] M. Ellis, Ph.D. thesis, Univ. of Oxford (1992).

[101] S. G. Roberts, H. S. Kim and P. B. Hirsch, in D. G. Brandon, R. Chaim and A. Rosen (Eds.), Proc. 9th Conf. on the Strength of Metals and Alloys, Haifa, July 1991, Freund, London, p. 783, (1991).

[102] F. C. Serbena and S. G. Roberts: "The Brittle-To-Ductile Transition in Germanium"; Acta metall. mater. Vol. **42**, No. 7, pp. 2505-2510, (1994).

[103] A. S. Booth and S. G. Roberts, J. Am. Ceram. Soc., to be published.

[104] H. Vehoff, in C. T. Liu, R. W. Cahn and Sauthoff (Eds.), Ordered Intermetallics-Physical Metallurgy and Mechanical Behaviour, NATO Advanced Science Institutes Series, Vol. **213** (Series E, Applied Sciences), Kluwer, Dordrecht, p. 299, (1992).

[105] J. R. Patal and A. R. Chaudhari, Phys. Rev. **143**, p. 601 (1966).

[106] F. Ericsson, S. Johansson and J. Schweitz, Mater. Sci. Engng A **105/106**, p. 131 (1988).

[107] R. D. Dukino and M. V. Swain, J. Am. Ceram. Soc. **75**, p.304 (1992).

[108] A.C. Eringen: "Continuum Mechanics at the Atomic Scale", Crystal Lattice Defects, Vol. **7**, pp. 109-130, (1977).

[109] R. Taylor: "Interatomic Potentials and Crystalline Defects", (ED. J.K. Lee), AIME **71**, (1981).

[110] M. Mullins, M. A. Dokainish: "Simulation of the 001 Plane Crack in α-Fe Employing a New Boundary Scheme", Phil. Mag. A, Vol. **46**, No. 5, pp. 771-787, (1982).

[111] J. H. Weiner, and W. Pear, J. Ap. Phys. **46**, p. 2398, (1975).

[112] W. T. Ashurst, and W. G. Hoover, Phys. Rev. **B14**, p. 1465, (1976).

[113] M. F. Kanninen, and P. C. Gehlen: "A study of crack propagation in α-iron." In "Interatomic Potentials and Simulations of Lattice Defects", (Eds. P. C. Gehlen et al.), pp. 713-722, Plenum, NY, (1972).

[114] A. Gohar: "A Microscopic Fracture Study in the Two-Dimensional Triangular Lattice", Ph.D. Thesis, City University of New York, New York, unpublished, (1979).

[115] D. Som: "Computer Modelling of Cracks", Ph.D. Thesis City University of New York, New York, unpublished, (1982).

[116] A. Paskin, Behzad Massoumzadeh, K. Sieradzki, and G. J. Dienes: "Enhancement of Dislocation Generation Induced by Film on Crack Surfaces", Scripta Metall., Vol. **18**, pp. 1135-1138, (1984).

[117] G. J. Dienes, K. Sieradzki, A. Paskin, and Behzad Massoumzadeh: "Critical Film Properties for Epitaxy", Surface Science **144**, pp. 273-289. (1984).

[118] A. Paskin, D.K. Som, and G. J. Dienes; J. Phys. C. **14**:L171, (1981).

[119] Mayes Mullins: "Molecular Dynamic Simulations of Propagating Cracks", Scripta Met., Vol. **16**, pp. 663-666, (1982).

[120] R. J. Arsenault, J. R. Beeler Jr., and J. A. Simmons, "Computer Simulations for Material Applications", Nuclear Metallurgy, Vol. **20**, (1976).

[121] A. Paskin, B. Massoumzadeh, K. Shukla, K. Sieradzki and G. J. Dienes: "Effect of Atomic Crack-Tip Geometry on Local Stresses", Acta Metall. Vol. **33**, No. 11, pp. 1987-1996, (1985).

[122] K. Sieradzki, G. J. Dienes, A. Paskin, and Behzad Massoumzadeh: "Atomistics of Crack Propagation" Acta Metall. Vol. **36**, No. 3, pp. 651-663, (1988).

[123] G. J. Dienes, K. Sieradzki, A. Paskin, and Behzad Massoumzadeh: "Molecular Dynamic Simulation of Crack Growth" in "Modelling Environmental Effects on Crack Growth Processes", (Eds. R.H. Jones, and W.W. Gerberich), pp. 85-98, AIME, Warreendale, Pa. (1986).

[124] G. J. Dienes: "Molecular Dynamic Studies of Crack Propagation: The Role of Interatomic Potentials", presented at the "Role of Hungarians in science", Budapest, Hungary, Aug. (1986). [Brookhaven National Laboratory Report No. **BNL37960**].

[125] R. A. Johnson: Interstitials and Vacancies in α-iron, Phys. Rev., **134**, A1329-A1336, (1964).

[126] L. Verlet: Computer Experiments on Classical Fluids Phys. Rev. **159**, pp. 98-103, (1967).

[127] D. O. Welch, G. J. Dienes, A. Paskin: "A Molecular Dynamic Study of The Equation of State of Solids at High Temperature and Pressure", J. Phys. Chem. Solids, Vol. **39**, pp. 589-603, (1978).

[128] A. Paskin, K. Sieradzki, D. K. Som, and G. J. Dienes: "Environmentally Induced Crack Nucleation and Brittle Fracture", Acta Metall., Vol. **30**, pp. 1781-1788, (1982).

[129] A. Paskin, K. Sieradzki, D. K. Som, and G. J. Dienes: "Dislocation Enhancement and Inhibition Induced by Films on Crack Surfaces", Acta Metall. Vol. **31**, No. 8, pp. 1253-1265, (1983).

[130] P. O. Esbjorn, and E. J. Jensen; J. Phys. Chm. Solids **37**, 1081, (1976).

[131] M. Born and K. Huang: The Dynamic Theory of Crystal Lattice, Oxford, University Press, London, (1954).

[132] J. P. Berry: "Some Kinetic Consideration of The Griffith Criterion for Fracture", JMPS, **8**, pp. 194-216, (1960).

[133] C. E. Inglis: "Stress in a Plate Due to the Presence of Cracks and Sharp Corners", Trans. Inst. Naval Archit. **55**, p. 219, (1913).

[134] H. F. Buckner: "The Propagation of Cracks and the Energy of Elastic Deformation", Trans. of the American Soc. for Mech. Eng., **80**, pp. 1225-1230, (1958).

[135] H. M. Westergaard: "Bearing Pressure and Cracks", Trans. of the American Soc. for Mech. Eng., **61**, pp. A49-A53, (1939).

[136] J.F. Knott: "Mechanics of Fracture", in "Atomistics of Fracture", (Eds. R.M. Latanision, and J.R. Pickens), pp. 671-705, Plenum Publ. Co. (1983).

[137] Webster's New World Dictionary of American Language The World Publishing Co. (1966).

[138] P. Ludwik: "Elemente der Technologischen Mechanik", Springer-Verlag OHG, Berlin, (1909).

[139] George R. Irwin: "Fracture", In Handbuch der Physik Springer-Verlag, Berlin, Vol. **6**, pp. 551-590, (1958).

[140] J. Weertman: "Three Dimensional Constitutive Relations and L Fracture", [Ed.: S. Nemat Nasser], pp. 111-122, North-Holland, Ams. (1980).

[141] J. Friedel, in "Fracture", [Eds.: B.L. Avenbach, D.K. Felbeck, G.T. Hahn and D.A. Thomas], pp. 498-522, MIT Press, Cambridge, Mass., (1959).

[142] I. N. Sneddon: "The Dislocation of Stress in the Neighborhood of a Crack in an Elastic Solid", Proceedings of the Royal Society of London, **A187**, pp. 229-260, (1946).

[143] M. L. Williams: "On The Stress Distribution at the Base of a Stationary Crack", Journal of Applied Mechanics, **24**, pp. 109-114, (1957).

[144] G. R. Irwin: "Analysis of Stresses and Strains Near the End of a Crack Traversing a Plate", Journal of Applied Mechanics, **24**, pp. 361-364, (1957).

[145] P. C. Paris, and G.C.M. Sih: "Stress Analysis of Cracks", in "Fracture Toughness Testing", [Eds: J. E. Srawley, and W.F. Brown], p. 30, STP NO. **381**, Pa, (1965).

[146] G. C. Sih, P. C. Paris, and F. Erdogan: "Crack Tip, Stress-Intensity Factors for Plane Extension and Plate Bending Problems", Journal of Applied Mechanics, **29**, pp. 306-312, (1962).

[147] G. C. Sih, P. C. Paris, and G. R. Irwin: "On Cracks in Rectilinearly Anisotropic Bodies", Int. J. of Fracture Mechanics, **1**, pp. 189-203 (1965).

[148] J.N. Goodier: "Mathematical Theory of Equilibrium Cracks", Fracture, [Ed.: H. Liebowitz], Vol. II. Academic Press, New York, pp. 1-66, (1968).

[149] A. Ç. Eringen, and B. S. Kim, Mech. Res. Commun., **1**, p. 233, (1974).

[150] D. S. Dugdale: "Yielding of Steel Sheets Containing Slits", J. Mech. Phys. Solids, **8**, p. 100, (1960).

[151] M. F. Kanninen, and G.H. Popelar: "Advanced Fracture Mechanics", Clarendon Press, Oxford, (1985).

[152] D. Broek: Elementary Engineering Fracture Mechanics Noordhoff, Leyden, The Netherlands, (1974), Third Revised Edition, (1985).

[153] H. Liebowitz [ed.]: Treatise on Fracture, in Seven Volumes, Academic Press, New York, pp. 497-590, (1968).

[154] F. Erdogan: "Crack Propagation Theories", in "Fracture Vol. II", [Ed.: H. Liebowitz], Academic Press, New York, pp. 497-590, (1968).

[155] J. D. Achenbach: Dynamic Effects in Brittle Fracture Mechanics Today, Vol. **1**, [Ed.: S. Nemat Nasser], Pergamon Press, Oxford, pp. 1-54, (1974).

[156] L. B. Freund: "Dynamic Crack Propagation", in "The Mechanics of Fracture" [Ed.: F. Erdogan], ASME, **AMD-19**, pp. 105-134, (1976).

[157] L. R. F. Rose: "Recent Theoretical and Experimental Results on Fast Brittle Fracture", Int. J. of Fracture, **12**, pp. 799-813, (1976).

[158] D. Francois: "Dynamic Crack Propagation and Arrest" Developments in Pressure Vessel Technology-flaw Analysis, [Ed.: R.W. Nicholos], Applied Science Publ., pp. 151-167, (1979).

[159] M. F. Kanninen: "A Critical Appraisal of Solution Techniques in Dynamic Fracture Mechanics", in "Numerical Methods in Fracture Mechanics", [Eds.: A. Luxmoore, and R. Owen], U. Swansea, pp. 612-633, (1978); & "Whiter Dynamic Fracture Mechanics?", in "Numerical Methods in Fracture Mechanics", [Eds.: R.D.G. Owen and A.R. Luxmoore], Pineridge, Swansea, U.K., (1980).

[160] M. S. Kamath: "Crack Propagation and Arrest", The Welding Institute Research Bulletin, Part I: "Wide Plate Crack Arrest Studies and the Empirical Tests of Pellini and others", pp. 14-25; Part II: "Dynamic Aspects, Mechanisms and the Static LEFM Approach", pp. 193-203, (1980).

[161] F. Nilsson, B. Brickstad: "Dynamic Fracture Mechanics, Rapid Crack Growth in Linear and Non-Linear Materials", Report No. **49**, The Royal Institute of Technology, Stockholm, Sweden, (1983).

[162] G. C. Sih [Ed.]: "Dynamic Crack Propagation", Noordhoff, International Leyden, The Netherlands, (1973).

[163] G. T. Hahn, and M. F. Kanninen [Eds.]: "Fast Fracture and Crack Arrest", ASTM **STP 627**, American Society for Testing and Materials, Philadelphia, (1972).

[164] G. T. Hahn, and M. F. Kanninen [Eds.]: "Crack Arrest Methodology and Applications", ASTM **STP 711**, American Society for Testing and Materials, Philadelphia, (1980).

[165] L. B. Freund: Mech. Today **3**, p. 55, (1976).

[166] E. N. Dulaney, and W.F. Brace: "Velocity Behavior of a Growing Crack", Journal of Applied Physics, **31**, pp. 2233-2236, (1960).

[167] S. Winkler, D.A. Shockey, and D.R. Curran: "Crack Propagation at Supersonic Velocities", Int. J. of Fracture Mech. **6**, pp. 151-158, and pp. 271-278, (1970).

[168] J. E. Field: "Brittle Fracture : Its Study and Application", Contemp. Physics, V. **12**, p. 1, (1971).

[169] J. I. Bluhm: "Fracture Arrest", in Fracture Vol. **v**, [Ed. H. Liebowitz], Academic Press, New York, pp. 1-63, (1969).

[170] T. Kobayashi, and J.W. Dally: "Fast Fracture, and Crack Arrest", [Eds: G.T. Hahn, and M. F. Kanninen], p. 257, Am. Soc. Test. Mater., Philadelphia, Pa., (1977).

[171] A. E. H. Love: "A Treatise on the Mathematical Theory of Elasticity", 4th ed., Dover Publications Inc., New York, (1949).

[172] A. H. Cottrell: The Mechanical Properties of Matter John Wiley & Sons, Inc., New York, (1964).

[173] E. H. Yoffe: The Moving Griffith Crack", Phil. Mag. **42**, pp. 739-750, (1951).

[174] B. Cotterel: "On Brittle Fracture Paths", Int J. of Fracture Mechanics, **1**, pp. 96-103, (1965).

[175] A. B. J. Clark, and G. R. Irwin: "Crack-Propagation Behaviors", Exp. Mech., **6**, pp. 321-330, (1966).

[176] H. Schardin: "Velocity Effect in Fracture", in "Fracture", [Eds.: B. L. Avenbach, D. K. Felbeck, G. T. Hahn, and D. A. Thomas], MIT Press, Cambridge, Mass., pp. 297-330, (1959).

[177] J. Congleton, and N. J. Petch: "Crack Branching", Phil. Mag. **16**, pp. 749-760, (1967).

[178] A. N. Stroh: "A Simple Model of a Propagating Crack", J. Mech. Phys. Solids, **8**, pp. 119-122, (1960).

[179] H. Bateman: "Electrical and Optical Wave-motion", Cambridge, Cambridge University Press, p. 138, (1915).

[180] B. deCelis, A. S. Argon, and L. Yip: "Molecular Dynamics Simulations of Crack Tip Process in α-iron and Copper"; J. Appl. Phys. **54** (9), pp. 4864-4878, (1983).

[181] G. Michot and Amand George: "Dislocation Emission From Cracks-Observations by X-ray Topography in Silicon"; Scripta Metall, Vol. **20**, pp. 1495-1500, (1986), View Point Set No. **10**.

[182] G. Michot, K. Badawi, A. R. Abd el Halim, and A. George: "Observation Par Topographie Aux Rayon X Des Configurations De Dislocations Développ'ees a l'extrémite d'une Fissure Dans Le Silicum", Phil. Mag. A **42**, pp. 195-215 (1980) [X-Ray Top. Study of CT Disl. Pat. in Silicon].

[183] G. Michot, A. George, G. Champier: "Dislocation Developed Around Crack Tips in Silicon and Their Influence on Fracture Toughness"; "Proceedings of the fourth European Conference on Fracture", Leoben, Austria, **V1**, 30, (1982).

[184] S. M. Ohr: "Electron Microscope Studies of Dislocation Emission from Cracks"; Scripta Metall., Vol. **20**, Viewpint Set No. 10, pp. 1501-1505, (1986).

[185] A. R. Lang: Modern Diffraction and Imaging Techniques in Material Science; [Eds. S. Amelinckx, R. Gevers, G. Remault, J. Van Landuyt], North Holland Pub. Co., Amsterdam, (1987).

[186] B. Tanner; X-Ray Diffraction Topography, Pergamon Press, (1978).

[187] Robb Thomson: "Fracture", Physical Metallurgy, Vol. **2**, [Ed. by R. W. Cahn and P. Haasen), Amsterdam, North-Holland, p. 1487, (1983).

[188] H. Kolsky: "Stress Waves in Solids", Dover, New York, (1963).

[189] A. N. Stroh: "A Theory of the Fracture of Metals", Advances in Physics, **6**, pp. 418-465, (1957).

[190] G.E. Dieter: Mechanical Metallurgy, Third Edition, McGraw-Hill Book Company, (1986).

[192] G. R. Irwin and A. A. Wells: "A Continuum Mechanics View of Crack Propagation," Metallurgical Reviews, **10**, pp. 223-270, (1965).

[192] S. M. Wiederhorn: Mechanical and Thermal Properties of Ceramics, [Ed: J. B. Wachtman Jr.], N. B. S. Special Publication, **303**, p. 217, (1969).